NAUČNOM VEĆU INSTITUTA ZA FIZIKU U BEOGRADU

Predmet:

Molba za pokretanje postupka za sticanje zvanja: naučni saradnik

S obzirom da ispunjavam kriterijume propisane od strane Ministarstva prosvete nauke i tehnološkog razvoja za sticanje naučnog zvanja naučnog saradnika, kao i kriterijume propisane Pravilnikom o sticanju naučnih zvanja u Institutu za fiziku, molim Naučno veće Instituta za fiziku da pokrene postupak za moj izbor u navedeno zvanje. U prilogu dostavljam:

(1) Mišljenje rukovodioca projekta sa predlogom članova komisije

(2) Kratku biografiju

(3) Pregled naučne aktivnosti

(4) Elemente za kvalitativnu ocenu naučnog doprinosa uz sedam referenci

(5) Elemente za kvantitativnu ocenu naučnog doprinosa

(6) Spisak objavljenih naučnih publikacija i njihovih kopija

(7) Podatke o citiranosti

(8) Kopiju doktorske diplome sa sertifikatima uz dokaz o nostrifikaciji

(9) Priloge

Valjevo, 18. decembra 2017. godine

S dužnim poštovanjem,

Dr Dejan M. Đokić

1. MIŠLJENJE RUKOVODIOCA PROJEKTA SA PREDLOGOM ČLANOVA KOMISIJE ZA PISANJE IZVEŠTAJA

Dr Dejan M. Đokić je angažovan kao spoljnji saradnik u Centru za fiziku čvrstog stanja i nove materijale Instituta za fiziku u Beogradu na projektu ON 171032 "Fizika nanostrukturnih oksidnih materijala i jako korelisanih sistema" Ministarstva prosvete nauke i tehnološkog razvoja Republike Srbije.
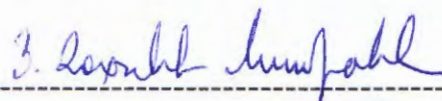
Pošto ispunjava sve uslove predviđene Pravilnikom za izbore u naučno-istraživačka zvanja, saglasna sam sa pokretanjem postupka za izbor dr Dejana M. Đokića u zvanje naučni saradnik. Stoga molim Naučno veće Instituta za fiziku u Zemunu da pokrene odgovarajući postupak.

Predlog članova Komisije za pisanje izveštaja:

1. Dr Zorana Dohčević-Mitrović, naučni savetnik, Institut za fiziku
2. Dr Antun Balaž, naučni savetnik, Institut za fiziku
3. Dr Željko Šljivančanin, naučni savetnik, Nuklerani institut Vinča
4. Dr Dimitrije Stepanenko, viši naučni saradnik, Institut za fiziku

Beograd, 18. decembar 2017. godine

Rukovodilac projekta :

Dr Zorana Dohčević-Mitrović

Dr Dejan M. Đokić

Privremena adresa:
Avenue Eglantine 24/76
CH-1006 Lausanne
Vaud, Switzerland
☎ : +41 (0) 78 692 15 59
✉ : djokic@ipb.ac.rs

Stalna adresa:
Dimitrija Tucovića 26
14 000 Valjevo
Republika Srbija
☎ : +381 (0) 69 651 004
✉ : dejan.m.djokic@gmail.com

2. BIOGRAFIJA

Dejan Đokić je rođen 07. 02. 1980. godine u Valjevu od oca Milorada (✝) i majke Milene Đokić. U Valjevu je završio osnovnu školu i gimnaziju kao nosilac Vukove diplome. Bio je učesnik brojnih srednjoškolskih takmičenja iz fizike i matematike osvojivši mnogobrojne prve nagrade na državnim nivoima. Nakon gimnazijskog obrazovanja je upisao osnovne studije na Fizičkom fakultetu Univerziteta u Beogradu, na smeru Teorijska i eksperimentalna fizika. Diplomirao je 2004. godine sa radom pod nazivom *"Visoko temperaturske popravke u teoriji Fermijeve tečnosti nuklearnog modela tečne kapi"*. Prosečna ocena za vreme studija bila je 9.63. Tokom studija je dobio nagradu i stipendiju fonda *Studenice* za 2004. godinu. Nakon osnovnih studija fizike 2005. godine upisao je magistarske studije na Fizičkom fakultetu Univerziteta u Beogradu, na smeru Fizika kondenzovanog stanja materije. Početkom 2005. godine se zaposlio u Centru za fiziku čvrstog stanja i nove materijale Instituta za fiziku gde je pod rukovodstvom akademika Prof. Dr Zorana Popovića bio angažovan na projektu *"Fizika niskodimenzionih nanostruktura i materijala"*. Tokom svog angažovanja je uspešno završio magistarske studije sa prosečnom ocenom 10.00 i bio uključen u razne naučno-istraživačke delatnosti eksperimentalnog i teorijskog sadržaja u oblasti spektroskopije čvrstih tela. Svoje magistarske studije zaokružuje uspešno 2008. godine odbranivši magistarsku disertaciju pod nazivom *"Uticaj spinskih korelacija antiferomagnetno uređene faze na infracrvene spektre α-MnSe"*. Iste godine se upisuje na doktorske studije u Švajcarskoj na *Ecole Polytechnique Fédérale de Lausanne* (EPFL). Kao post-diplomski student doktorske škole fizike EPFL-a se priključuje Institutu za fiziku kondenzovanog stanja materije (*Institute of Condensed Matter Physics*) sa afilijacijom u Laboratoriji za fiziku kompleksnih materijala (*Laboratory of Physics of Complex Matter*), gde mu je i definisana tema doktorske disertacije. Bio je angažovan na različitim projektima pomenute laboratorije koji su uključivali studije elektron spinske rezonance niskodimenzionih struktura počev od jako korelisanih organskih provodnika i superprovodnika, preko molekularnih magneta, multiferoičnih materijala i drugo. Svoju doktorsku tezu pod naslovom *"Electron Spin Resonance of Novel Materials"* brani 2012. godine čiji je rukovodilac bio Prof. Dr László Forró, inače inostrani član Srpske akademije nauka i umetnosti. Tokom svog akademskog angažmana na EPFL-u, Dejan je bio aktivni učesnik u radu sa studentima diplomskih i post-diplomskih studija fizike, medicine, i inženjerstva o materijalima, te se tako pokazao kao izuzetan predavač što je potvrđeno brojnim sertifikatima. Inostrana

doktorska diploma je sertifikovana od strane Ministartsva prosvete nauke i tehnološkog razvoja pod rednim brojem: 612-01-00057/2016-06. Posle uspešno završenih doktorskih studija, pridružuje se Laboratoriji za primenjene superprovodne tanke filmove (*Applied Superconducting Thin Films Laboratory*) pri Univerzitetu u Ženevi (*University of Geneva* - UNIGE) gde je u saradnji sa Prof. Dr Michel Decroux radio kao post-doktorant na istraživačkom projektu u kooperaciji sa industrijskim partnerom ABB iz Badena u Švajcarskoj. Pored svoje istraživačko-industrijske delatnosti na uređajima superprovodnih strujnih graničnika visokih snaga, uporedo je radio i kao univerzitetski predavač opšteg kursa fizike. Zaokruživši svoj rad na Univerzitetu u Ženevi aprila 2015. godine zapošljava se kao naučni saradnik pri Laboratoriji za nanobiotehnologiju (*Laboratory of Nanobiotechnology*) na Institutu hemijskih nauka i inženjerstva (*Institute of Chemical Sciences and Engineering*) na EPFL-u u Lozani, gde je radio u oblasti sinteze i spektroskopije funkcionalizovanih karbonskih nanotuba kao biomedicinskih senzora. Inače, Dejan je strastveni sportista, zaljubljenik u muziku, medicinu, filozofiju prirodnih i društvenih nauka, kulinarstvo, horsko pevanje i ostalo. Tečno govori engleski i francuski jezik.

Trenutno je angažovan kao spoljnji saradnik u Centru za fiziku čvrstog stanja i nove materijale Instituta za fiziku u Beogradu na projektu ON171032 "Fizika nanostrukturnih oksidnih materijala i jako korelisanih sistema" Ministarstva prosvete nauke i tehnološkog razvoja Republike Srbije, čiji je rukovodilac Dr Zorana Dohčević-Mitrović. Bavi se ispitivanjem električnih i magnetnih osobina nanostruktura na bazi multiferoičnog bizmut-ferita. U isto vreme promoviše i podiže fiziku na viši nivo radeći kao nastavnik fizike u Valjevskoj gimnaziji u specijalizovano-matematičkim odeljenjima kao i u bilingvalnim odeljenjima. Kreator je sajta fizike https://dejanphysics.wordpress.com/ koji prati čitav region, a i šire.

✧ ✧ ✧ ✧ ✧ ✧ ✧ ✧ ✧

3. PREGLED NAUČNE AKTIVNOSTI

Istraživački rad Dejana Đokića se do sada odvijao u okviru različitih tematskih celina fizike čvrstog stanja sa akademskog, primenjenog, i industrijskog aspekta. Tu spadaju eksperimentalna i teorijska istraživanja na jako korelisanim niskodimenzionim sistemima, magnetnim i multiferoičnim materijalima, fotonskim kristalima, superprovodnim tankim filmovima, karbonskim i titanijumskim nanostrukturama, organskim provodnicima i molekularnim magnetima, grafenu, biološkim polimerima, i drugo. Ovladao je nizom eksperimentalnih tehnika kao što su Raman i infracrvena spektroskopija, tehnike magnetne rezonance, magnetometrija, skenirajuća elektronska mikroskopija, rendgenska i neutronska difrakcija, diferencijalno skenirajuća kalorimetrija, kriogenika, deponovanje tankih filmova magnetnim raspršivanjem i koevaporacijom, fluorescentna mikroskopija, uključujući i razne hemijske metode u sintezi organskih superprovodnika i funkcionalizaciji karbonskih nanotuba. Sa teorijske strane, poseduje značajno iskustvo u tehnikama kvantne teorije polja mnogočestičnih sistema kao i programerske veštine zasnovane na metodu konačnih elemenata u licenciranim i nekomercijalnim softverima. Kao što je elaborirano u onome što sledi, njegovi dosadašnji naučno-istraživački rezultati su plod rada na četiri akademske institucije, visoko kotirane u svetu (pogledati tabelu).

Period	Afilijacija	Zvanje
2005-2008	**Centar za fiziku čvrstog stanja i nove materijale** - Institut za fiziku u Zemunu - - Univerzitet u Beogradu -	Magistar fizičkih nauka
2008-2012	**Laboratory of Physics of Complex Matter** - Institute of Condensed Matter Physics - - Ecole Polytechnique Fédérale de Lausanne (EPFL) -	Doktor nauka
2013-2015	**Applied Superconducting Thin Films Laboratory** - Department of Quantum Matter Physics - - University of Geneva (UNIGE) -	Postdoktorant
2015-2016	**Laboratory of Nanobiotechnology** - Institute of Chemical Sciences and Engineering - - Ecole Polytechnique Fédérale de Lausanne (EPFL) -	Naučni saradnik

3.1

Institut za fiziku - Univerzitet u Beogradu (2005-2008)

– Centar za fiziku čvrstog stanja i nove materijale –

3.1.1 Infracrveni spektri niskodimenzionog η-Na$_{1.3}$V$_2$O$_5$

Natrijum vanadijumovi oksidi tipa x-Na$_{1+\epsilon}$V$_2$O$_5$ ($\epsilon \geq 0$) ispoljavaju svoje stabilne kristalne strukture u sedam različitih x faza, $x \in \{\alpha, \alpha', \beta, \delta, \eta, \kappa, \tau\}$. Ova jedinjenja se ističu po tome što se vanadijumovi atomi nalaze u izmešanim valentnim stanjima V^{4+} i V^{5+} koja se, istim redom, razlikuju po svojim spinskim stanjima $S = 1/2$ i $S = 0$. U slučaju η-Na$_{1.3}$V$_2$O$_5$, naizmenična magnetna i nemagnetna vanadijumova stanja zajedno sa niskom dimenzijom kristalne strukture dovode do magnetnih fluktuacija na niskim temperaturama ispod ca 120 K što je opaženo u merenjima spinske susceptibilnosti kroz otvaranje spinskog procepa veličine od oko 35 K. Ova magnetno neuređena faza je propraćena strukturalnim faznim prelazom drugog reda usled spontanog uređivanja naelektrisanja te samim tim i udvostručavanjem parametra kristalne rešetke duž b-ose. Na taj način se ovaj sistem pokazao podesnim za ispitivanje fononske dinamike na niskim i visokim temperaturama jer je ona u neposrednoj sprezi sa promenama koje se javljaju na parametrima kristalne rešetke. Ustanovljeno je da se ispod približno 120 K pojavljuju novi infracrveno aktivni fononski modovi kao i da pozicije učestanosti već postojećih fononskih oscilatora trpe nagli pomeraj pri snižavanju temperature. Ova pojava je interpretirana kroz postojanje izražajnih promena na fononskim spektrima nastalih usled evolucije kristalne strukture kao posledice uređenja naelektrisanja u niskodimenzionoj magnetno neuređenoj fazi. Eksperimentalni rezultati su uspešno obrađeni, analizirani, i objavljeni u [C1], i predstavljaju jedan značajan doprinos u razumevanju faznog prelaza η-Na$_{1.3}$V$_2$O$_5$ kao i njemu srodnih sistema sa niskotemperaturskim spinskim fluktuacijama oslanjajući se na spektroskopske tehnike.

3.1.2 Magnon-fononska interakcija u antiferomagnetnom α-MnSe

Usled svojih izuzetnih optičkih, magnetnih, i transportnih osobina, halogenidi i oksidi mangana ne prestaju da zaokupljaju pažnju u istraživanjima koja su od značaja za realizaciju spintroničkih uređaja. Oni predstavljaju $3d$ prelazne metal komplekse i hlađenjem uspostavljaju dugodometna magnetna uređenja. Kubični (fcc) α-MnSe se uređuje antiferomagnetno ispod temperature Néel-a na oko $T_N = 130$ K. Pri tom se spinovi Mn^{2+} jona orjentišu paralelno i antiparalelno duž (111) kristalografskih ravni. Studije Raman spektroskopije na α-MnSe ne pokazuju prisustvo optičkih fonona u skladu sa teorijskim predviđanjima, izuzev magnonskog prisustva u antiferomagnetnoj fazi. Sa druge strane, simetrijska pravila predviđaju postojanje jednog infracrvenog optički aktivnog fononskog oscilatora F_{1u} u paramagnetnoj i antiferomagnetnoj fazi. Takođe, ne isključuje se postojanje aktivnih fononskih oscilatora viših redova, poput kombinovanih dvo-fononskih modova. Hlađenjem se očekuje porast (tzv. otvrdnjavanje) u fononskim energijama na osnovu modela koji uvodi anharmonijske efekte, kao što je fonon-fononska interakcija. U slučaju α-MnSe primećeno je dodatno otvrdnjavanje dva moda (LO F_{1u} i dvo-fononski kombinacioni mod) ispod temperature faznog prelaza koje je nemoguće objasniti anharmonijskim efek-

tima koji potiču od čisto fononskih interakcija. Ipak, kombinujući efekte magnon-fononske interakcije zajedno sa magnetnom anizotropijom u okviru formalizma Green-ovih funkcija $1/z$ perturbativnog razvoja, dodatno otvrdnjavanje se može čak i kvantitativno objasniti. Poreklo magnetne anizotropije leži u spin-orbitalnom sprezanju, dok je magnon-fononska interakcija izvedena na osnovu modulacije Heisenberg-ovog modela od strane jonskih pomeraja tokom fononskih vibracija rešetke. α-MnSe je $3D$ antiferomagnet što ga svrstava u grupu klasičnih antiferomagneta gde se kvantne fluktuacije zanemaruju, dok se u perturbativnom razvoju svojstvene energije fononskog propagatora ne ide dalje od $(1/z)^1$. Ovom aproksimacijom je zanemarena i interakcija između magnona. Na taj način je uspešno objašnjeno dodatno otvrdnjavanje fonona u antiferomagnetnoj fazi usaglašavajući teoriju sa postojećim eksperimentom. Pogledati dve publikacije na ovu temu [B1 i J1], od kojih druga predstavlja magistarsku disertaciju. Predstavljeni model ima i svoje mikroskopsko značenje. Utvrđeno je i da bezdimenzioni parametar magnetne anizotropije mora biti veći od 0.01 kako bi došlo do fononskog otvrdnjavanja što je u skladu sa procenjenom vrednošću od 0.03 na osnovu magnona koji se pojavljuje u Raman spektrima. Dinamika magnona kao i fonona spregnutih slobodnim magnonima je razrađena u okvirima Abrikosovljeve fermionske reprezentacije spina $S = 1/2$, koja je u ovom slučaju uz izvesnu aproksimaciju primenjena i na manganov spin $S = 5/2$. Aproksimacija je zasnovana na postojanju jedino temperaturskih, a ne kvantnih, fluktuacija u magnetizaciji antiferomagnentne podrešetke α-MnSe.

3.1.3 Fazna stabilnost $Mo_6S_3I_6$ nanožica praćena Raman spektroskopijom

Rezultat sistematske potrage za novim kvazi-jednodimenzionim materijalima koji bi efikasno mogli da zamene karbonske nanotube u nanotehnološkim primenama predstavlja otkriće nanožica prečnika od približno 1 nm sa stehiometrijskom formulom $Mo_6S_{9-x}I_x$, pri čemu je $3 < x \leq 6$. Od posebnog interesa za realizaciju optičkih uređaja baziranih na molibdenskim nanožicama predstavljaju pikovi u elektronskoj gustini stanja koji potiču od Van Hove-ovih singulariteta i odražavaju se kroz oštre optičke karakteristike. Poseban slučaj se odnosi na $x = 6$. U tom slučaju su proučavane fononske osobine $Mo_6S_3I_6$ nanožica i izvršena je asignacija najintenzivnijih eksternih i internih modova, imajući u vidu da je taj zadatak nemoguće u potpunosti izvršiti bez polarizacionih Raman merenja na monokristalima. Proučavana je termička stabilnost $Mo_6S_3I_6$ nanožica korišćenjem Raman spektroskopije u opsegu od sobne temperature do 600 °C. Prostorna grupa koja opisuje $Mo_6S_3I_6$ nanostrukturu je triklinična $P\bar{1}$ (br. 2) sa jediničnom ćelijom $Mo_{12}S_6I_{12}$. Na osnovu dostupnih podataka o pozicijama atoma u jediničnoj ćeliji, zaključeno je da se svi atomi nalaze na (2i) Wyckoff pozicijama. Analiza faktor grupe daje $\Gamma = 45A_g + 42A_u$ za optički aktivne modove. Prema tome, u Raman spektrima nanožica može se očekivati 45 Raman aktivnih modova. Generalno, kod molekulskih kristala je karakteristično da Raman spektri mogu da se podele na niskofrekventni opseg kojem pripadaju eksterni modovi, i visokofrekventni opseg sa internim modovima, između kojih postoji vibracioni procep. Ispitivana termostabilnost nanožica metodom Raman spektroskopije je izvedena variranjem upadne snage lasera $(1 - 9 \text{ mW})$ i zagrevanjem uzorka $(25 - 600 \text{ °C})$. Ustanovljeno je da se pri upadnim snagama lasera većim od 4 mW ili na temperaturama višim od 300 °C pojavljuju novi modovi koji potiču od MoO_3. Termostabilnost $Mo_6S_3I_6$ nanožica nestaje između 300 i 400 °C, kada dolazi do fazne separacije odnosno formiranja oksidnog sloja. U Raman spektrima na visokim temperaturama fazna separacija je praćena pojavljivanjem novog fononskog moda na 819 cm^{-1} koji je karakterističan za MoO_3 fazu. Na niskim temperaturama Raman spektri

ukazuju na primetnu razliku između fonon-fononske interakcije kod internih i eksternih modova. Ova izuzetna vibraciona svojstva $Mo_6S_3I_6$ nanožica mogu poslužiti kao baza u poboljšavanju sinteze materijala, električne i termičke provodnosti, funkcionalnih svojstava i slično. Eksperimentalni rezultati su objavljeni u dva članka [B2 i G1] od kojih je jedan iz vrhunskog međunarodnog časopisa.

3.1.4 Simetrijska analiza u dvodimenzionim GaAs fotonskim kristalima

Dvodimenzioni GaAs fotonski kristali koji operišu u infracrvenom delu spektra važe za izuzetne kandidate u realizaciji novih integrisanih optičkih uređaja poput optičkih logičkih kola, mikro-elektro-mehaničkih aparata, senzora i drugo. Iz tih razloga je važno izučavati optička svojstva fotonskih kristala koji potiču od Blohovih stanja u analogiji sa elektronskim stanjima u čvrstim telima. Kombinujući razvoj ravanskih talasa sa selekcionim pravilima teorije prostornih grupa moguće je analizirati ponašanja propagirajućih i evanescentnih modova u fotonskim kristalima. U slučaju dvodimenzione kvadratne rešetke uočeni su slobodni modovi B-tipa koji se ne mogu pobuditi spolja usled zabrane od strane selekcionih pravila. Postojanje ovakvih modova koji nisu spregnuti spoljnim elektromagnetnim pobudama dovodi do pojave stvaranja nespregnutih fotonskih procepa unutar kojih je transmisija zabranjena. Na taj način se procepi kod dvodimenzionih fotonskih kristala kvadratnih rešetki mogu podeliti u dve grupe: spregnuti i nespregnuti. Videti publikaciju [B4, D1].

3.2

Institute of Condensed Matter Physics - EPFL (2008-2012)

– Laboratory of Physics of Complex Matter –

3.2.1 Metaličnost kagomé faze organskog $(EDT\text{-}TTF\text{-}CONH_2)_6Re_6Se_8(CN)_6$

Kagomé rešetka, sačinjena od isprepletane mreže oprečnih trouglova u ravni, zauzima centralno mesto u istraživanjima fizike kondenzovanog stanja materije usled svoje mogućnosti da generiše magnetna stanja sa visokim stepenom frustriranosti, čak i na temperaturi apsolutne nule. Na temu magnetno frustriranih stanja postoji veliki broj studija koje se tiču slučaja lokalizovanih antiferomagnetno spregnutih spinova u neorganskim sistemima. Ovaj slučaj je vrlo prisutan u literaturi za razliku od slučaja provodnih elektrona na kagomé rešetki. Jedna takva struktura je realizovana po prvi put u $(EDT\text{-}TTF\text{-}CONH_2)_6Re_6Se_8(CN)_6$ organskom sistemu, gde TTF organski dimeri igraju vodeću ulogu u elektronskoj strukturi. Njegova kagomé topologija u kombinaciji sa $2/3$ elektronskog popunjavanja na čvoru rešetke dovodi do formiranja Dirakovog polumetalnog stanja sa istovetnim topološkim karakterom kao kod grafena. Međutim, postojanje kulonovske interakcije između elektrona kao za posledicu ima formiranje novih egzotičnih stanja koja su slabo istražena teorijski, a eksperimentalno su potpuno neistražena. Na osnovu temperaturski zavisnih transportnih merenja, rendgenske difrakcije, magnetometrije, i elektron spinske rezonance zaključeno je da ovaj sistem trpi strukturalni fazni prelaz na približno 180 K. Na visokim temperaturama $(EDT\text{-}TTF\text{-}CONH_2)_6Re_6Se_8(CN)_6$ je u svojoj romboedarskoj fazi i ponaša se kao dvodimenzioni metal sa $2/3$ elektronskog popunjavanja uz prisustvo jake kulonovske interakcije - korelacija koje se vide u magnetnim merenjima kroz izuzetno visoku vrednost magnetne susceptibilnosti Curie-Weiss-ovog karaktera ($\chi_{300K} = 0.0015$ emu/mol). Metaličnost ovog stanja je procenjena kao izuzetno slaba ($\rho_{300K} = 0.17$ Ωm) usled dinamičkog neuređenja rešetke što je čest slučaj kod organskih sistema. Dominantni nosioci naelektrisanja su jako korelisani polaroni što je u skladu sa transportnim merenjima i asimetrijom u lorencovom elektron spin rezonantnom profilu, tzv. Dysonian-u. Na niskim temperaturama, sistem postaje Mott-ov izolator dok je kristalna struktura triklinična. Ovo izolatorsko stanje se odlikuje postojanjem slabo interagujućih antiferomagnetnih ($J \sim 65$ K) spinskih lanaca koji su interpretirani u okviru anizotropnog modela spinskih tečnosti. Oshikawa-Affleck-ova teorija je korišćena u usaglašavanju sa eksperimentalnim rezultatima temperaturske zavisnosti poluširine rezonantne linije. Budući da su organski sistemi izuzetno kompresibilni, izvedena su transportna i elektron spin rezonantna merenja pod pritiskom sve do 15 kbar. Na osnovu oba eksperimenta je zaključeno da visoki pritisci pomeraju niskotemperatursku izolatorsku fazu ka višim temperaturama pa sve do temperature sobe. Prateći ponašanje poluširine rezonantne linije sa povećanjem pritiska na oko 220 K ustanovljeno je da se spinska relaksacija pokorava Elliott-Yafet-ovom mehanizmu (svojstven metalima) sve do 8 kbar. Iza ovih vrednosti sistem se stabilizuje u izolatarskom stanju spinskih lanaca. Istovetan rezultat je izveden na osnovu transportnih merenja pod pritiskom, s tim što se sve do *ca* 8 kbar primećuje porast u aktivacionoj elektronskoj energiji koja potiče od kompresibilnosti TTF dimera i elektron-fononske interakcije. Rezultati su objavljeni u [F1, F2, F3, F4, F9, i I1] i u jednom nedavno poslatom radu u *Physical Reviews Letters* pod naslovom: *Correlated Polarons in an Organic Dirac Cone*

Kagomé System as Seen by ESR; D. M. Djokić, A. Olariu, J. Jaćimović, P. Batail, L. Forró, and E. Tutiš. U pripremi je još jedan rukopis: *Tracing the Origin of Bad Dirac Cone Metallicity in a Molecular Kagomé Compound*; D. M. Djokić, J. Jaćimović, P. Batail, L. Forró, and E. Tutiš, koji će zbog svoje izvrsnosti i revolucionarnih rezultata biti poslat u *Nature Physics*.

3.2.2 Magnetizam u nano-grafenu viđen elektron spinskom rezonancom

Numeričke studije ukazuju na mogućnost formiranja dugodometnog magnetnog uređenja u grafenu kao i grafitnim česticama nanometarskih veličina. Koristeći elektron spinsku rezonancu ispitivana su magnetna svojstva ultra-tankih grafitnih nano-čestica dobijenih jakom ultrazvučnom sonikacijom grafitnih prahova dispergovanih u N-metilpirolidinu. Spinsko rezonantni signal je dekomponovan na dve linije: usku i široku. Za usku liniju je ustanovljeno da potiče od lokalizovanih defekata Curie-vog tipa. Sa druge strane, široka linija je intrizičnog karaktera i ukazuje na formiranje superparamagnetnog stanja ispod 25 K u skladu sa ponašanjem svog intenziteta, g-faktora (oko 2.011), i poluširine. Primećen je značajan porast u spinskoj susceptibilnosti, a takođe i kod poluširine ($20 \rightarrow 80$ Gauss) na 25 K, dok je kod rezonantnog polja uočen pomeraj ka višim poljima ($\delta g/g = 10^{-2}$). U dvodimenzionim sistemima sa feromagnetnim korelacijama, $q = 0$ fluktuacioni mod difuzivnog karaktera koji dominantno doprinosi termodinamičkim veličinama, raste progresivno pri snižavanju temperature prema kritičnoj. Iako sve činjenice sugerišu na postojanje dugodometnog feromagnetnog uređenja, dalja magnetna merenja nisu potvrdila postojanje globalno uređene magnetizacije. Objašnjenje se krije u postojanju malih domena na 25 K koji interaguju vrlo slabo, ali koji se mogu uzeti kao superparamagnetni klasteri. Porast u spinskoj susceptibilnosti i poluširini rezonantne linije se tako objašnjava na osnovu preraspodele lokalnih unutrašnjih polja na grafitnim/grafenskim ostrvcima. Sa teorijske strane izvedeni su DFT proračuni za grafen sa graničnim defektima, poput cik-cak, pentagon-oktagon kolona i slično. Ustanovljeno je postojanje magnetnih momenata na elektronima C-atoma u blizini ovih defekata koji su feromagnetno spregnuti. Ipak, feromagnetne korelacije između momenata nisu u stanju da formiraju dugodometno feromagnetno uređenje. Istovetni zaključci su izvedeni i iz transportnih merenja. Električna otpornost pokazuje nemetalnu temperatursku zavisnost u skladu sa mehanizmom elektronskog preskakanja varirajućih dometa između čestica. Međutim, pri pojavi lokalnog feromagnetnog uređenja na 25 K električna otpornost trpi blagi porast sa sniženjem temperature. Ova obzervacija sugeriše da se klasteri sa lokalnom magnetizacijom ponašaju kao izolatori unutar kojih je transport elektrona otežan. Ovi rezultati su prezentovani u publikacijama [B3, C2, i I1].

3.2.3 Kvantne korelacije u tetramerama magnetno anizotropnog SeCuO$_3$

Već duže od dve decenije familija kuprata postojano drži vodeće mesto u proučavanju visoko temperaturske superprovodnosti, antiferomagnetizma, multiferoičnosti, i lokalizovanih spinskih klastera. U tu familiju spada i monoklinični SeCuO$_3$ kao jedan potencijalni kandidat u istraživanjima kvantnih efekata među spinskim klasterima. Magnetni klasteri u ovom sistemu se sastoje od četiri $S = 1/2$ spina sa vrlo jakom antiferomagnetnom interakcijom u njima i slabim sprezanjem između njih koje igra bitnu ulogu u uspostavljanju dugodometnog uređenja. SeCuO$_3$ je antiferomagnet sa prelaznom temperaturom od $T_N = 8$ K, dok vrednost intratetramerne antiferomagnetne izmenske interakcije, koja je odgovorna za antiferomagnetno uređenje, iznosi oko $J = 200$ K. Ovo ukazuje na prisutnost jakih

kvantnih fluktuacija i frustriranosti budući da je $J/T_N \approx 20 \gg 1$. Izvedena su merenja rendgenske difrakcije, magnetizacije, i elektron spinske rezonance na SeCuO$_3$ sistemu. Strukturno ovaj sistem se može shvatiti kao trodimenziona mreža sačinjena od tetramera. Vrednosti intratetramernih izmenskih interakcija su procenjene na osnovu spinske susceptibilnosti koje se poklapaju u oba slučaja: SQUID-a i elektron spinske rezonance. Primećena je neuobičajena temperaturska zavisnost efektivnog g-tenzora uz rotaciju makroskopske magnetne ose. Ovo je pripisano postojanju selektivnih kvantnih korelacija na čvorovima kao i postojanju magnetne anizotropije koja je jednim delom formirana od strane fluktuacija magnentih momenata sa različitih bakarnih čvorova. Monokliničnost strukture je takođe zaključena na osnovu ugaone zavisnosti efektivnog g-tenzora na 50 K i pokazano je da se tenzor transformiše po odgovarajućoj simetriji. Temperaturska zavisnost ovog tenzora je objašnjena preko formiranja singleta na centralnom bakarnom paru unutar tetramere. Isti model je korišćen u usaglašavanju teorije sa spinskom susceptibilnošću na visokim temperaturama. Takođe je uočen jedan zavojak u susceptibilnosti na oko 70 K. Ova pojava je objašnjena uvođenjem novih članova u spinski Hamiltonijan. Dodavanjem J_{22} (2 predstavlja kristalografsku numeraciju čvora) interakcije koja spreže tetramere duž a kristalografske ose uspešno je objašnjena ova anomalija u spinskoj susceptibilnosti, a na isti način i ponašanje poluširine rezonantne linije. Ispod 70 K poluširina obrazuje minimum poput slučaja jednodimenzionih antiferomagnetnih $S = 1/2$ spinskih lanaca. Međutim, preliminarna merenja neutronske difrakcije upućuju na postojanje linijskog magnetizma, krivolinijskog tetramernog lanca u tri dimenzije, pre nego na postojanje pravolinijskih spinskih lanaca. Kao zaključak, primećena temperaturska zavisnost magnetne ose nastaje usled postojanja kvantnih korelacija sa neekvivalentnih bakarnih čvorova (1 i 2). Predpostavljajući slabu temperatursku zavisnost osnovnog g-tenzora ($g_1 = (2.335, 2.14, 2.07)$, $g_2 = (2.153, 2.33, 2.07)$, i $J_{11} = 290$ K), što je vrlo čest slučaj kod ovakvih sistema, ovaj efekat se može iskoristiti u cilju uvođenja jedne nove eksperimentalne metode u dobijanju magnetne susceptibilnosti koja potiče od pojedinih čvorova rešetke. Frustriranost antiferomagnetnog stanja SeCuO$_3$ predstavlja poseban slučaj koji je predmet narednih studija. Eksperimentalni podaci kao i teorijski model je objavljen u jednom vrhunskom međunarodnom časopisu uključujući opširnu analizu u doktorskoj disertaciji i prezentaciju na domačoj konferenciji [B5, I1, i F5]. U pripremi je još jedan rad: *Infrared Reflectivity and Transmissivity Spectra of Antiferromagnetic SeCuO$_3$*; K. Miller, D. M. Djokić, H. Berger, and D. Tanner (*Physical Review B*).

3.2.4 Magneto-električno sprezanje u multiferoičnom Cu$_2$OSeO$_3$

Materijali u kojima istovremeno koegzistira dugodometno magnetno i polarno uređenje se nazivaju multiferoicima. U ovakvoj grupi materijala magnetni i električni stepeni slobode su međusobno spregnuti na mikroskopskom nivou što se može iskoristiti kao osnovni mehanizam u magnetnom čuvanju informacija koje bi se očitavale električnim putem. Kubični Cu$_2$OSeO$_3$ je multiferoik sa frustriranom magnetnom interakcijom koja formira ferimagnetno stanje ispod 57 K. Magneto-električno sprezanje u ovom sistemu potiče od anharmonijske spin-fononske interakcije kako je zaključeno na osnovu ponašanja imaginarne i realne vrednosti dielektrične konstante čija anomalna vrednost na 57 K nestaje pri primeni magnetnog polja. Ovo sprezanje je praćeno preko spin talasne rezonance koristeći jednu novu rezonantnu tehniku koja je zasnovana na *lock-in* modulaciji električnim poljem. Inače, standardna paramagnetno rezonantna merenja se izvode koristeći modulacije magnetnim poljima, ali je u slučaju multiferoika prednost u tome što se mogu koristiti električna polja. Na taj način razvijena je

nova eksperimentalna metoda kojom se mogu izučavati multiferoici rezonantnim tehnikama. Merenja su vršena na tankim monokristalima (1×1 mm^2) debljine 100 μm. Temperaturska zavisnost magneto-električne konstant prati spinsku susceptibilnost i naglo opada iznad temperature faznog prelaza. Asignacija rezonantnih linija spinsko talasnih modova desetog reda je uspešno izvedena i potkrepljena modelom u kojem bitnu ulogu igra debljina uzorka. Ovi modovi su uočeni u oba slučaja, sa magnetnom i sa električnom modulacijom. U drugom slučaju, za indukovanu magnetizaciju je ustanovljeno da se ponaša na isti način kao i kod mionskih rezonantnih merenja. Odnos konstante magneto-električnog sprezanja i spinske susceptibilnosti ne pokazuje prisutnost anomalija na 57 K što ukazuje da magneto-električno sprezanje ne nastaje kao rezultat dugodometnog uređenja, već je u potpunosti mikroskopske prirode. Rezultati kao i predlog novog spin rezonantnog metoda za multiferoike su objavljeni u *Physical Review Letters* [A1], koji dostiže citiranost na zavidnom nivou. Takodje je jedan deo rezultata predstavljen na *APS March Meeting*-u u Baltimoru, SAD (2013). Videti [F10].

3.2.5 Sinteza TiO$_2$ nanotuba dopiranih manganom

TiO$_2$ je postao predmet mnogobrojnih istraživanja usled svoje temperaturske i hemijske stabilnosti, rasprostranjenosti, kao i bezazlenosti po životnu sredinu. Nanostrukturni TiO$_2$ se već uveliko koristi u proizvodnji fotoanoda u solarnim ćelijama, gasnim senzorima, i superkondenzatorima. Od posebnog interesa je sinteza novih TiO$_2$ nanostruktura poput TiO$_2$ nanotuba dopiranih manganom u širokom opsegu koncentracija. U pomenutoj sintezi Mn^{2+} joni su inkorporirani u kristalnu nanostrukturu TiO$_2$ metodom jonske izmene formirajući tako Mn$_x$H$_{2-x}$Ti$_3$O$_7$. Tokom toplotnog tretiranja ovo jedinjenje je dalje transformisano u Mn$_y$Ti$_{1-y}$O$_2$, gde je $y = x/(3 + x)$. Oksidaciona stanja mangana kao i priroda njegovog lokalnog okruženja su praćeni elektron spinskom rezonancom u oba slučaja: Mn$_x$H$_{2-x}$Ti$_3$O$_7$ i Mn$_y$Ti$_{1-y}$O$_2$. Uočeno je da Mn^{2+} joni ravnomerno okupiraju dve kristalografske pozicije. Prva je u potpunosti kubične simetrije, dok je druga pozicija jako narušenog oktaedarskog okruženja. Udeo u naseljenosti ove dve kristalne pozicije od strane mangana ne zavisi od stepena dopiranja i iznosi $15{:}85$ u Mn$_x$H$_{2-x}$Ti$_3$O$_7$ i $5{:}95$ u Mn$_y$Ti$_{1-y}$O$_2$. U slučaju merenja spinske susceptibilnosti putem elektron spinske rezonance i uz pomoć SQUID-a utvrđeno je da ne dolazi do formiranja nikakvog dugodometnog uređenja sve do 2 K. Intenzitet rezonantne linije se nije razlikovao u slučajevima pre i posle toplotnog tretiranja što ukazuje na činjenicu da manganovi joni ostaju u svom 2+ stanju tokom formacije Mn$_y$Ti$_{1-y}$O$_2$. Dalje je uočeno da su Mn^{2+} joni ravnomerno raspoređeni u uzorku i da nema formiranja klastera tokom toplotnog tretiranja. Široka rezonantna linija potiče od Mn^{2+} spinskog stanja u narušenom oktaedarskom okruženju, dok prisutni spinski sekstet na $g = 2.001$ potiče od manganovih jona visokosimetrijskog kubičnog okruženja. Sekstetna stanja su primećena pri niskim koncentracijama i rezultat su postojanja hiperfinog spin nuklearnog sprezanja. Pri visokim koncentracijama dolazi do dipolarnog širenja glavne linije što ekranira spin nuklearno sprezanje, a za posledicu ima nestajanje seksteta. Konstanta hiperfinog spin nuklearnog sprezanja je procenjena na $A_{iso} = 12$ mT. Na ovaj način je demonstrirano da se rezonantno aktivni jonski izmenljivi katjoni mangana homogeno raspoređuju u TiO$_2$ nanotubama, što utire put jednoj alternativnoj metodi u pripremanju i sintezi razređenih magnetnih nanostruktura i njihovih derivata. Rezultati ovih istraživanja su dati u radu [A2], koji je do sada citiran 24 puta (*web of science*).

Department of Quantum Matter Physics - UNIGE (2013-2015)

– Applied Superconducting Thin Films Laboratory –

3.3.1 Propagacija normalne zone u superprovodnim strujnim graničnicima

Superprovodni strujni graničnici predstavljaju uređaje zasnovane na visokotemperaturskim superprovodnim tankim filmovima koji služe u ograničavanju i kontrolisanju neželjenih visokih struja. Ideja leži u činjenici da pri visokim gustinama struja visokotemperaturski superprovodnici na bazi kuprata prelaze u normalno izolatorsko stanje što za posledicu ima nagli porast u električnoj otpornosti, a samim tim i regulaciju visokih struja. Ovaj proces je praćen burnim oslobađanjem toplote, u literaturi poznat kao *quench* (kvenč), koji se radi zaštite uređaja mora kontrolisati kriogeničkim putem. Zarad industrijske primenljivosti, glavni cilj inženjera i istraživača u ovom polju je da se formiranje kvenča uspostavi na najbrži mogući način kako bi superprovodni strujni graničnici operisali na željenom funkcionalnom nivou. Brzina kojom se kvenč prostire je poznata pod nazivom brzina prostiranja normalne zone, tj. toplotnog fronta na $T = T_C$. U posebnu grupu superprovodnih strujnih graničnika spadaju oni koji su presvučeni tankim slojevima plemenitih metala koji dovode do dodatne kriostabilnosti uređaja. Međutim, ovi uređaji pate od izuzetno sporih propagacija normalnih zona što dovodi u pitanje stepen izdržljivosti tokom kvenča. U cilju povećanja ove brzine neophodno je uspostaviti odgovarajuću konfiguraciju supstratnih slojeva kod ovih uređaja kao i njihov dizajn. Predloženi dizajn se sastoji od YBCO (YBa$_2$Cu$_3$O$_7$) superprovodnih uzoraka (1×20 cm^2) debljine 300 nm koji su presvučeni sa 40 nm srebra (Ag) kao stabilizatorom. YBCO+Ag je deponovan na visokoj temperaturi pri isparavanju odgovarajućih konstituenata: Y, Ba, Cu, i Ag u atmosferi argona i kiseonika, nakon čega su uzorci testirani rendgenskom difrakcijom, skenirajućim elektronskim mikroskopom, i magnetometrijom. U početnim fazama merenja je proveravan hemijski sastav i stepen monokristaličnosti, dok je kasnije merena kritična temperatura od $T_C = 92$ K. Uzorcima je na slobodnoj YBCO površini deponovan sloj od oko 4 μm MgO kao amortizujućeg sloja (*buffer layer*). Ovaj električno izolujući sloj je formiran pulsirajućom laserskom depozicijom i služi kao povezujući sloj sa supstratom koji je u ovom slučaju hasteloj debljine 90 μm. Čitava struktura je uronjena u tečni azot. Izvršena su merenja brzine prostiranja normalne zone (v_{NZP}) uzduž superprovodnih pisti pri strujnim gustinama većim od 1 MA/cm^2 za vrednost kritične strujne gustine od $J_C = 0.9$ MA/cm^2. Za $J = 1$ MA/cm^2 pronađeno je da $v_{NZP} = 12$ cm/s eksponencijalno raste sa porastom gustine struje, a u skladu sa teorijom. Takođe je i razvijen $2D/3D$ elektro-termalni model u MATLAB/COMSOL-u koji kombinuje analitičke proračune i numerički metod konačnih elemenata, tzv. hibridni model. Pokazano je vrlo dobro slaganje između merenih brzina propagacije normalne zone pri različitim strujama sa onim dobijenim u simulacijama bez uvođenja novih slobodnih parametara. U cilju realizacije novih prototipova superprovodnih strujnih graničnika simulirani su rezultati za različite debljine supstrata i različite vrednosti u termalnoj provodnosti ekstremno tankog međusloja između supstrata i MgO. Praćene su propagacije normalne zone duž superprovodne piste i popreko, pri čemu je ustanovljeno da se dobar deo toplotnog fronta prostire lateralno i pored niske termalne provodnosti supstrata. Projekat je realizovan pod pokroviteljstvom kompanije ABB iz Badena u Švajcarskoj

i dobar deo rezultata je ostao neobjavljen kako je ugovoreno sa industrijskim partnerom. Pogledati radove predstavljene na konferencijama [F6 i F7].

3.3.2 Poboljšanje u preraspodeli toplote u $YBa_2Cu_3O_7$ tankim filmovima

Glavni problem u srebrom presvučenim superprovodnim strujnim graničnicima, zasnovanim na YBCO ($YBa_2Cu_3O_7$) tankim filmovima, leži u neadekvatnoj preraspodeli toplote nakon pojavljivanja toplotnog fronta na 92 K. Značajno poboljšanje bi se očekivalo pojačanjem termalne provodnosti vodećeg supstrata kao i podešavanjem geometrije superprovodnih pisti. Jedno rešenje je električni izolovana višeslojna supstratna struktura koja sadrži nekoliko mikrona bakra deponovanog na 100 μm masivnog supstrata kvarcnog stakla. U cilju sprečavanja međuslojne difuzije između kvarcnog stakla i bakra deponovano je nekoliko submikronskih slojeva titanijum dioksida i niobijuma. Tehnika deponovanja tankih filmova magnetnim raspršivanjem je korišćena u ovom slučaju. Sa druge strane kontaminacija supeprovodnih pisti od strane supstratnog bakarnog sloja je sprečena zaštitnim električno izolujućim slojem od 4 μm MgO. Predložena konfiguracija superprovodnih pisti je meandarskog tipa čime je otvoren novi lateralni kanal za propagaciju toplotnog fronta. Eksperiment se odvijao uporedo sa kompjuterskim simulacijama zasnovanih na metodu konačnih elemenata u COMSOL Multiphysics. Predloženi teorijski model za ovu strukturu se pokazao sasvim precizan na osnovu poređenja sa eksperimentalnim rezultatima za tanke filmove deponovane na safiru i hasteloju. U slučaju predloženog višeslojnog supstrata na bazi bakra i kvarcnog stakla procenjeno je da brzina prostiranja normalne zone dostiže maksimalnu vrednost od 4.5 m/s za oko jedan mikron bakra. Pokazano je takođe i da povećavanjem debljine bakarnog sloja ne dolazi do porasta u brzini prostiranja normalne zone, što je u skladu sa teorijom kvazi-adijabatskog prostiranja toplote. Ovaj rezultat je korišćen u eksperimentu budući da deponovanje bakarnih slojeva debljih od jednog mikrona dovodi do problema vezanog za amorfnost. Ispitivana je i termodinamička stabilnost superprovodnog tankog filma u slučaju submikronske varijacije debljine bakarnog sloja. Ustanovljeno je da 1 μm bakra predstavlja maksimum debljine neophodan za kristalizaciju, dok sa druge strane, neophodan minimum u uspostavljanju termodinamičke stabilnosti. Rezultati su objavljeni u konferencijskom radu [E1] kao i u radu koji je objavljen u *International Journal of Thermal Sciences* [A3].

3.4

Institute of Chemical Sciences and Engineering - EPFL (2015-2016)

– Laboratory of Nanobiotechnology –

3.4.1 Kvantna efikasnost DNK-funkcionalizovanih karbonskih nanotuba

Već duže od dve decenije karbonske nanotube drže vodeće mesto u polju istraživanja nanometarskih materijala. Od posebnog interesa za istraživanja u medicinskim naukama su poluprovodne nanotube usled njihovog svojstva da apsorbovanu vidljivu svetlost emituju u blisko infracrvenom delu spektra. Na taj način one mogu poslužiti kao optički biosenzori znajući da su biološka tkiva potpuno transparentna u ovom delu spektra. Međutim, glavni problem kod optičkih svojstava karbonskih nanotuba leži u tome da su one sklone formiranju snopova usled van der Waals-ovih interakcija. Korišćenjem bioloških polimera, poput DNK i slično, nanotube postaju potpuno razdvojene i obmotane polimerima koji nekovalentno funkcionalizuju slobodnu površinu nanotuba što u velikoj meri poboljšava njihova optička svojstva. Sa druge strane funkcionalizacijom nanotube gube svoja toksična svojstva koja su rezultat postojanja slobodnih površina na kojima se mogu odvijati brojne kataboličke hemijske reakcije. U literaturi je ustanovljeno da fluorescencija poluprovodnih karbonskih nanotuba potiče od eksitonskih stanja i urađeno je mnogo na proučavanju ovih stanja i njihovih radijativnih i neradijativnih vremena života u slučaju golih nanotuba bez prisustva obmotavajućih polimera. Posebna pažnja je posvećena proceni kvantne efikasnosti koja predstavlja odnos intenziteta emitovane i apsorbovane svetlosti. U slučaju DNK-obmotanih poluprovodnih nanotuba jako malo se zna o ponašanju kvantne efikasnosti sa promenom tipa polimera ili obmotavajućeg ugla. U pratećoj publikaciji je po prvi put predložen model koji uvodi ovu zavisnost i zasnovan je na difuznoj dinamici eksitona. Eksitoni su tretirani kao tačkaste čestice na sobnoj temperaturi koji se podvrgavaju dvodimenzionom slučajnom hodu (*random walk*) na površini nanotube. Kanali neradijativnih eksitonskih raspada su sadržani u difuznim procesima koji potiču od vibracija kristalne rešetke karbonske nanotube. Ispostavilo se da je model u stanju da predvidi jaku zavisnost kvantne efikasnosti od svojstva polimera, tj. DNK-ove sekvence. Sa druge strane nije primećena izrazita zavisnost od obavijajućeg ugla za vrednosti kvantne efikasnosti koje su veće od 10^{-4} što je vrednost koja se sreće u literaturi. Ovo se objašnjava visokom anizotropnošću nanotuba koje su prečnika 1 nm i karakterističnih dužina od 100 nm i više. Za vrednosti kvantne efikasnosti manje od 10^{-4} uočena je ugaona zavisnost, preciznije, pad efikasnosti sa rastućim uglom što se može očekivati budući da gusto obmotavajući polimeri, koji su u stanju da apsorbuju eksitone, utiču na porast neradijativnih procesa. Pri tom, vrednosti kvantne efikasnosti koje su niže od 10^{-4} nisu od eksperimentalnog značaja jer ih je vrlo teško meriti. Iz tih razloga je sasvim dovoljno osloniti se na model koji ne tretira ugaonu zavisnost ($\phi = 0$) koji je inače rešen analitički za razliku od opšteg slučaja koji je rešen numerički. Rezultati su prezentovani ispred *Swiss Chemical Society* [F8], dok je ostatak objavljen u vrhunskom međunarodnom časopisu *Nanotechnology* pod naslovom: *Quantum Yield in Polymer Wrapped Single Walled Carbon Nanotubes: A Computational Model* [B6]. Eksperimentalna verifikacija predloženog i poboljšanog modela je u finalnom procesu recenzije u međunarodnom časopisu *ACS Nano*, koji je izuzetne vrednosti impakt faktora oko 14. Naslov rada je *Towards Engineering SMaRT Nanosen-*

sors: Elucidating the Effects of Polymer Wrapping on Exciton Dynamics in Single-Walled Carbon Nanotubes, dok su autori A. Chiappino-Pepe, V. Zubkovs, A. Goswami, B. Lambert, J. Kupis-Rozmyslowicz, D. M. Djokić, J. N. Longchamp, i A. A. Boghossian.

✧ ✧ ✧   ✧ ✧ ✧   ✧ ✧ ✧

4. ELEMENTI ZA KVALITATIVNU OCENU NAUČNOG DOPRINOSA

4.1 Kvalitet naučnih rezultata

4.1.1 Naučni nivo i značaj rezultata, uticaj naučnih radova

Dr Dejan M. Djokić je do sada objavio 13 radova u međunarodnim časopisima sa <u>web of science</u> liste, pri čemu je u svim radovima imao ključni doprinos. U časopisima kategorije M20 kandidat je objavio 12 radova, od toga 3 rada kategorije M21a, 6 radova kategorije M21, 2 rada kategorije M22 i 1 rad kategorije M23. Na međunarodnim konferencijama objavio je jedan rad u celini (M33) i 10 radova u izvodima (M34). Objavio je i jedan rad u nacionalnom časopisu kategorije M52, kao i jedan rad u izvodu na nacionalnoj konferenciji (M64). Pri izradi ovih publikacija kandidat je učestvovao u formulaciji problema i osmišljavanju i realizaciji eksperimentalnih merenja, kao i u tumačenju rezultata i pisanju objavljenih radova. Kao tri najznačajnija rada kandidata mogu se uzeti:

[1] *Influence of Antiferromagnetic Spin Ordering on the Far-Infrared Active Optical Phonon Modes of α-MnSe*; <u>D. M. Djokić</u>, Z. V. Popović, and F. R. Vukajlović, Physival Review **B77**, 01430 (2008).

[2] *Finite Element Method Simulation Study of Heat Propagation in a Novel YBCO-Based Coated Conductor for Resistive Fault Current Limiters*; <u>D. M. Djokić</u>, L. Antognazza, and M. Decroux, International Journal of Thermal Sciences **111**, 160 (2017).

[3] *Quantum Yield in Polymer Wrapped Single Walled Carbon Nanotubes: A Computational Model*; <u>D. M. Djokić</u> and A. Goswami, Nanotechnology **28**, 465204 (2017).

U prvom radu, autor je kombinujući efekte magnon-fononske interakcije zajedno sa magnetnom anizotropijom u okviru formalizma Green-ovih funkcija $1/z$ perturbativnog razvoja, objasnio dodatno otvrdnjavanje fonona sa temperaturom ispod temperature antiferomagnentog faznog prelaza α-MnSe. α-MnSe je $3D$ antiferomagnet što ga svrstava u grupu klasičnih antiferomagneta gde se kvantne fluktuacije zanemaruju, dok se u perturbativnom razvoju svojstvene energije fononskog propagatora ne ide dalje od $(1/z)^1$. Ovom aproksimacijom je zanemarena i interakcija između magnona. Na taj način je uspešno objašnjeno dodatno otvrdnjavanje fonona u antiferomagnetnoj fazi usaglašavajući teoriju sa postojećim eksperimentom. Predstavljeni model ima i svoje mikroskopsko značenje. Utvrđeno je i da bezdimenzioni parametar magnetne anizotropije mora biti veći od 0.01 kako bi došlo do fononskog otvrdnjavanja što je u skladu sa procenjenom vrednošću od 0.03 na osnovu magnona koji se pojavljuje u Raman spektrima. Dinamika magnona kao i fonona spregnutih slobodnim magnonima je razrađena u okvirima Abrikosovljeve fermionske reprezentacije spina $S = 1/2$, koja je u ovom slučaju uz izvesnu aproksimaciju primenjena i na manganov spin $S = 5/2$. Aproksimacija je zasnovana na postojanju jedino temperaturskih, a ne kvantnih, fluktuacija u magnetizaciji antiferomagnentne podrešetke.

U drugom radu je ispitivano prostiranje kvenča u srebrom presvučenim superprovodnim prekidačima, zasnovanim na YBa$_2$Cu$_3$O$_7$ tankim filmovima. Predložena je konfiguracija superprovodnih YBaCuO-pisti meandarskog tipa čime je otvoren novi lateralni kanal za propagaciju toplotnog fronta. Eksperi-

ment se odvijao uporedo sa kompjuterskim simulacijama zasnovanih na metodu konačnih elemenata u COMSOL Multiphysics. Dat je i teorijski model za ovu strukturu koji se pokazao sasvim precizan na osnovu poređenja sa eksperimentalnim rezultatima za tanke filmove deponovane na safiru i hasteloju. U slučaju predloženog višeslojnog supstrata na bazi bakra i kvarcnog stakla procenjeno je da brzina prostiranja normalne zone dostiže maksimalnu vrednost od 4.5 m/s za oko jedan mikron bakra. Pokazano je takođe i da povećavanjem debljine bakarnog sloja ne dolazi do porasta u brzini prostiranja normalne zone, što je u skladu sa teorijom kvazi-adijabatskog prostiranja toplote. Ovaj rezultat je korišćen u eksperimentu budući da deponovanje bakarnih slojeva debljih od jednog mikrona dovodi do problema vezanog za amorfnost.

Treći rad je baziran na izučavanju kvantne efikasnosti DNK-obmotanih poluprovodnih nanotuba. Autor je predložio model koji uvodi ugaonu zavisnost obmotavanja i zasnovan je na difuznoj dinamici eksitona. Eksitoni su tretirani kao tačkaste čestice na sobnoj temperaturi koji se podvrgavaju dvodimenzionom slučajnom hodu (*random walk*) na površini nanotube. Kanali neradijativnih eksitonskih raspada su sadržani u difuznim procesima koji potiču od vibracija kristalne rešetke karbonske nanotube. Ispostavilo se da je model u stanju da predvidi jaku zavisnost kvantne efikasnosti od svojstva polimera, tj. DNK-ove sekvence. Sa druge strane nije primećena izrazita zavisnost od obavijajućeg ugla za vrednosti kvantne efikasnosti koje su veće od 10^{-4} što je vrednost koja se sreće u literaturi. Ovo se objašnjava visokom anizotropnošću nanotuba koje su prečnika 1 nm i karakterističnih dužina od 100 nm i više. Za vrednosti kvantne efikasnosti manje od 10^{-4} uočena je ugaona zavisnost, preciznije, pad efikasnosti sa rastućim uglom što se može očekivati budući da gusto obmotavajući polimeri, koji su u stanju da apsorbuju eksitone, utiču na porast neradijativnih procesa. Pri tom, vrednosti kvantne efikasnosti koje su niže od 10^{-4} nisu od eksperimentalnog značaja jer ih je vrlo teško meriti. Iz tih razloga je sasvim dovoljno osloniti se na model koji ne tretira ugaonu zavisnost ($\phi = 0$) koji je inače rešen analitički za razliku od opšteg slučaja koji je rešen numerički.

4.1.2 Pozitivna citiranost naučnih radova kandidata

Prema *ISI Web of Knowledge* bazi ukupan broj citata radova kandidata na dan 08.02.2018 je $72 = 72 + 0$, tj. redom 100 % heterocitata i 0 % autocitata. Videti 6. odeljak.

4.1.3 Parametri kvaliteta časopisa

Bitan element za procenu kvaliteta naučnih rezultata je i kvalitet časopisa u kojima su radovi objavljeni, odnosno njihov impakt faktor − IF. U kategoriji M21a, M21, M22 i M23, kandidat je objavio radove u sledećim časopisima:

- 1 rad u *Physical Review Letters* (IF=7.33)
- 1 rad u *Journal of Physical Chemistry C* (IF=4.55)
- 1 rad u *International Journal of Thermal Sciences* (IF=3.90)
- 1 rad u *Journal of Raman Spectroscopy* (IF=2.52)
- 1 rad u *Photonics and Nanostructures - Fundamentals and Applications* (IF=1.80)
- 3 rada u *Physical Review B* (IF=3.57, 3.26, 3.16)
- 1 rad u *Nanotechnology* (IF=2.91)

- 1 rad u *European Physical Journal B* (<u>IF=1.18</u>)
- 1 rad u *Physica Status Solidi B* (<u>IF=1.65</u>)
- 1 rad u *Acta Physica Polonica A* (<u>IF=0.74</u>)

Ukupan faktor uticaja radova kandidata je 36.57. Časopisi u kojima je kandidat objavljivao su po svom ugledu veoma cenjeni u oblastima kojima pripadaju. Među njima, posebno se ističu: *Physical Review Letters*, *Journal of Physical Chemistry C*, i *International Journal of Thermal Sciences*.

Dodatni bibliometrijski pokazatelji kvaliteta časopisa u kojima je kandidat objavljivao radove je dat u sledećeoj tabeli. Ona sadrđi impakt faktore (IF) radova, M poene radova po srpskoj kategorizaciji naučno-istraživačkih rezultata, kao i impakt faktor normalizovan po impaktu citirajućeg clanka (SNIP). U tabeli su date ukupne vrednosti, kao i vrednosti svih faktora usrednjenih po broju članaka i po broju autora po članku.

	IF	M	SNIP
Ukupno	36.57	91	13.024
Usrednjeno po članku	3.048	7.583	1.085
Usrednjeno po autoru	8.033	20.242	2.905

4.2 Angažovanost u formiranju naučnih kadrova

(i) Doprinos u izradi diplomske teze Jelene Todorović tokom (2007-2008) na Institutu za fiziku u Zemunu u Centru za fiziku čvrstog stanja i nove materijale.

(ii) Angažman, aktivno učešće, i doprinos predavanjima na kursu Jako korelisanih elektronskih sistema na smeru Fizika kondenzovane materije Doktorskih studija Fizičkog fakulteta 2008. godine pod nadzorom Prof. Dr Milice Milovanović (**DOC0**).

(iii) Rad sa studentima prve godine fizike na EPFL-u u periodu od (2009-2010) kroz angažman na kursu metrologije (videti referencu **DOC1**).

(iv) Doprinos u izradi master rada Pétera Szirmaia tokom 2010. godine u Laboratoriji za fiziku kompleksnih materijala na EPFL-u (videti rad [A2]).

(v) Rad sa studentima prve godine medicine na Univerzitetu u Lozani u periodu od (2010-2011) kroz angažman na opštem kursu fizike (videti referencu **DOC2**).

(vi) Rad sa studentima druge godine masterskih studija fizike i inženjerstva na EPFL-u tokom (2011-2012) kroz angažman na kursu fizike novih materijala uz doprinos u izgradnji kursa (videti referencu **DOC2**).

(vii) Rad sa studentima prve godine fizike i geologije na Univerzitetu u Ženevi u periodu od (2013-2014) kroz angažman na opštem kursu fizike (videti referencu **DOC3**).

(viii) Mentorstvo u radu sa izmenskim studentom Aranya Goswami u Laboratoriji za nanobiotehnologiju na EPFL-u u periodu od (2015-2016) godine (*Quantum Yield in Polymer Wrapped Single Walled Carbon Nanotubes: A Computational Model*).

(ix) Vođenje i mentorstvo nad studentima doktorantima u Laboratoriji za nanobiotehnologiju na EPFL-u u periodu od (2015-2016) godine (videti referencu **DOC4**).

4.3 Angažovanost u razvoju uslova za naučni rad

(i) Angažovanost na projektu *Fizika niskodimenzionih nanostruktura i materijala* tokom (2005−2008) na Institutu za fiziku u Zemunu u Centru za fiziku čvrstog stanja i nove materijale pod rukovodstvom Prof. Dr Zorana V. Popovića.

(ii) Angažovanost na projektu *Physics of novel carbon based materials* tokom (2008 − 2012) u Laboratoriji za fiziku kompleksnih materijala na EPFL-u (videti referencu **DOC5**).

(iii) Saradnja sa Univerzitetom u Strazburu 2011. godine (Prof. Dr Philippe Turek) na projektu *Physics of molecular magnets* (videti referencu **DOC6**).

(iv) Saradnja sa Univerzitetom u Cirihu 2012. godine (Prof. Dr Hugo Keller) na projektu *Novel electron spin resonance technique development* (videti referencu **DOC7**).

(v) Angažovanost na industrijskom projektu *Novel YBCO coated conductors for superconducting fault current limiters* tokom (2013 − 2015) u Laboratoriji za primenjene superprovodne tanke filmove na Univerzitetu u Ženevi u saradnji sa industrijskim gigantom ABB iz Badena u Švajcarskoj (videti referencu **DOC3**).

(vi) Angažovanost na projektu *Nanotube sensors* kao naučni saradnik (*Collaborateur scientifique*) u Laboratoriji za nanobiotehnologiju na EPFL-u 2015. godine (videti referencu **DOC4**).

(vii) Učešće u podizanju laboratorije za nanobiotehnologiju na EPFL-u 2015. godine uključujući izgradnju blisko infracrvenog fluorescentnog mikroskopa (videti referencu **DOC4**).

(viii) Pogledati priloženi svezak sertifikata koji potvrđuje akademsko i industrijsko usavršavanje u postdiplomskom periodu (videti referencu **DOC3**).

(ix) Angažman u vidu spoljnjeg saradnika pri Centru za fiziku čvrstog stanja i nove materijale Instituta za fiziku u Zemunu na projektu $ON171032$ *Fizika nanostrukturnih oksidnih materijala i jako korelisanih sistema* Ministarstva prosvete, nauke i tehnološkog razvoja Republike Srbije (2017−).

4.4 Naučno-istraživačko angažovanje u industrijskom sektoru

ABB je globalni lider u visoko-naponskim tehnologijama i automatizaciji odgovarajućih uređaja i svake godine investira oko 1.5 milijardi dolara za finansiranje istraživanja i razvojnih aktivnosti iniciranih od strane velikog broja (oko 8500) tehnologa, naučnika, i inženjera raspoređenih po sedam korporativnih istraživačkih centara širom sveta. Jedan od ABB-ovih korporativnih centara, smešten u Argovijanskom švajcarskom kantonu u blizini Ciriha, najveći deo svojih razvojno-istraživačkih aktivnosti usmerava ka visoko-naponskim zaštitama. Jedno od rešenja se sastoji u korišćenju visoko-temperaturskih

superprovodnih tankih filmova kao strujnih limitatora koji uranjanjem u tečni azot ne gube na svojoj funkcionalnosti, što znatno smanjuje industrijske troškove u odnosu na upotrebu tečnog helijuma. Budući da je rad na ovakvim sistemima izrazito kompleksan i zahteva rad unutar multidisciplinarnih laboratorija, ABB uglavnom uspostavlja saradnju sa akademskim istraživačkim centrima lansirajući projekte povereničkih komisija za inovativne tehnologije (tzv. *CTI projects*) u Švajcarskoj i na taj način omogućava postdoktorskim istraživačima akademskih titula da svoje sposobnosti oprobaju u industrijskom sektoru. Rad ovog tipa prevashodno nije usmeren ka objavljivanju rezultata, već ima predominatno industrijski karakter u pronalaženju novih ideja koje bi se mogle komercijalizovati na tržištu. Strujni limitatori, u slobodnom prevodu ograničavači, se koriste u cilju zaštite od iznenadnog kratkog spoja čak u prvobitnim blagim porastima visokih pogonskih struja u instaliranim mrežama. Pri tom su strujni limitatori ovog tipa primarno osetljivi na dinamiku trenutnog strujnog rasta (di/dt) što pruža veću stabilnost u odnosu na bespotrebna strujna prekidanja. Moj rad je obuhvatao sledeće:

(1) simulacije konačnih elemenata u sprezi sa dizajnerskim softverima,

(2) merenja koeficijenta zapreminske specifične toplote,

(3) merenja koeficijenta toplotne provodnosti,

(4) induktivna merenja gustina kritičnih struja u superprovodnicima,

(5) deponovanje tankih filmova,

(6) energetsko-disperzionu rendgensku spektrometriju,

(7) analizu kvarova (*Failure Analysis*).

Videti objavljene radove [E1, F6, i F7] u saradnji sa ABB-om čiji je rukovodilac na zajedničkom projektu u periodu od (2013-2014) bio Dr Markus Abplanalp, adresa: ABB Corporate Research Center, Baden-Dättwil, Switzerland. Radi potvrde, u kontakt je moguće stupiti i elektronskim putem slanjem pošte na: markus.abplanalp@ch.abb.com.

✦ ✦ ✦ ✦ ✦ ✦ ✦ ✦ ✦

5. ELEMENTI ZA KVANTITATIVNU OCENU NAUČNOG DOPRINOSA

5.1 Ostvareni rezultati u periodu pre izbora

Kandidat se po prvi put bira u zvanje naučni saradnik, pa se uzimaju u obzir svi do sada objavljeni rezultati. U časopisima kategorije M20 kandidat je do sada objavio 12 radova, od toga 3 rada kategorije M21a, 6 radova kategorije M21, 2 rada kategorije M22 i 1 rad kategorije M23. Na međunarodnim konferencijama objavio je jedan rad u celini (M33) i 10 radova u izvodima (M34). Objavio je i jedan rad u nacionalnom časopisu kategorije M52, kao i jedan rad u izvodu na nacionalnoj konferenciji (M64).

Kategorija	M bodova po radu	Broj radova	M bodova	**Normirano**
M21a	10	3	30	27.14
M21	8	6	48	41.71
M22	5	2	10	9.17
M23	3	1	3	3
M33	1	1	1	1
M34	0.5	10	5	5
M52	1.5	1	1.5	1.5
M64	0.2	1	0.2	0.2
M70	6	1	6	6

5.2 Poređenje sa minimalnim kvantitativnim uslovima za izbor u zvanje naučni saradnik

Minimalni broj M bodova		Ostvareno	**Normirano**
Ukupno	16	104.7	94.72
M10+M20+M31+M32+M33+M41+M42	10	92	82.02
M11+M12+M21+M22+M23	6	91	81.02

Prema bazi podataka *Web of Science*, radovi kandidata su citirani ukupno 72 puta bez autocitata, a njegov h-index je 5.

✧ ✧ ✧　✧ ✧ ✧　✧ ✧ ✧

6. SPISAK NAUČNIH PUBLIKACIJA

6.1 Radovi u međunarodnim časopisima izuzetnih vrednosti (**M21a**):

[A1] *Magnetoelectric Coupling in Single Crystal Cu_2OSeO_3 Studied by a Novel Electron Spin Resonance Technique*; A. Maisuradze, A. Shengelaya, H. Berger, D. M. Djokić, and H. Keller, Physical Review Letters **108**, 247211 (2012).
- citirano $16 = 16 + 0$ puta (hetero- i autocitati tim redom).

[A2] *Synthesis of Homogeneous Manganese Doped Titanium Oxide Nanotubes from Titanate Precursors*; P. Szirmai, E. Horváth, B. Náfrádi, Z. Micković, R. Smajda, D. M. Djokić, K. Schenk, L. Forró, and A. Magrez, The Journal of Physical Chemistry **C117**, 697 (2013).
- citirano $24 = 24 + 0$ puta (hetero- i autocitati tim redom).

[A3] *Finite Element Method Simulation Study of Heat Propagation in a Novel YBCO-Based Coated Conductor for Resistive Fault Current Limiters*; D. M. Djokić, L. Antognazza, and M. Decroux, International Journal of Thermal Sciences **111**, 160 (2017).
- citirano $0 = 0 + 0$ puta (hetero- i autocitati tim redom).

6.2 Radovi u vrhunskim međunarodnim časopisima (**M21**):

[B1] *Influence of Antiferromagnetic Spin Ordering on the Far-Infrared Active Optical Phonon Modes of α-MnSe*; D. M. Djokić, Z. V. Popović, and F. R. Vukajlović, Physical Review **B77**, 01430 (2008).
- citirano $5 = 5 + 0$ puta (hetero- i autocitati tim redom).

[B2] *Investigation of Thermostability and Phonon-Phonon Interactions in $Mo_6S_3I_6$ Nanowires by Raman Scattering Spectroscopy*; J. M. Todorović, Z. D. Dohčević-Mitrović, D. M. Djokić, D. Mihailović, and Z. V. Popović, Journal of Raman Spectroscopy **41**, 978 (2010).
- citirano $1 = 1 + 0$ puta (hetero- i autocitati tim redom).

[B3] *Magnetism in Nanoscale Graphite Flakes as Seen Via Electron Spin Resonance*; L. Ćirić, D. M. Djokić, J. Jaćimović, A. Sienkiewicz, A. Magrez, M. Lotya, J. N. Coleman, Ž. Šljivančanin, and L. Forró, Physical Review **B85**, 205437 (2012).
- citirano $5 = 5 + 0$ puta (hetero- i autocitati tim redom).

[B4] *Uncoupled Photonic Band Gaps*; Dj. Jovanović, B. Nikolić, T. Radić, D. M. Djokić, and R. Gajić, Photonics and Nanostructures - Fundamentals and Applications **10**, 657 (2012).
- citirano $0 = 0 + 0$ puta (hetero- i autocitati tim redom).

[B5] *Site Selective Quantum Correlations Revealed by Magnetic Anisotropy in the Tetramer System $SeCuO_3$*; I. Živković, D. M. Djokić, M. Herak, D. Pajić, K. Prša, P. Pattison, D. Dominko, Z. Micković, D. Cinčić, L. Forró, H. Berger, and H. Rønnow, Physical Review **B86**, 054405 (2012).
- citirano $6 = 6 + 0$ puta (hetero- i autocitati tim redom).

[B6] *Quantum Yield in Polymer Wrapped Single Walled Carbon Nanotubes: A Computational Model*; D. M. Djokić and A. Goswami, Nanotechnology **28**, 465204 (2017).
- citirano $0 = 0 + 0$ puta (hetero- i autocitati tim redom).

6.3 Radovi u istaknutim međunarodnim časopisima (**M22**):

[C1] *Infrared Reflectivity Spectra of η-$Na_{1.3}V_2O_5$ in the Charge Disordered and Ordered Phase*; Z. V. Popović, <u>D. M. Djokić</u>, Z. D. Dohčević-Mitrović, M. Isobe, and Y. Ueda, European Physical Journal **B65**, 1 (2008).
  - citirano $0 = 0 + 0$ puta (hetero- i autocitati tim redom).

[C2] *Size Dependence of the Magnetic Response of Graphite Oxide and Graphene Flakes - an Electron Spin Resonance Study*; L. Ćirić, A. Sienkiewicz, <u>D. M. Djokić</u>, R. Smajda, A. Magrez, T. Kaspar, R. Nesper, and L. Forró, Physica Status Solidi **B247**, 2958 (2010).
  - citirano $13 = 13 + 0$ puta (hetero- i autocitati tim redom).

6.4 Radovi u međunarodnim časopisima (**M23**):

[D1] *Waveguiding Effect in GaAs $2D$ Hexagonal Photonic Crystal Tiling*; Dj. Jovanović, R. Gajić, <u>D. M. Djokić</u>, and K. Hingerl, Acta Physica Polonica **A116**, 55 (2009).
  - citirano $2 = 2 + 0$ puta (hetero- i autocitati tim redom).

6.5 Saopštenja sa međunarodnog skupa−štampana u celini (**M33**):

[E1] *Heat Propagation Improvement in YBCO-Coated Conductors for Superconducting Fault Current Limiters*; <u>D. M. Djokić</u>, L. Antognazza, M. Abplanalp, and M. Decroux, Excerpt from the Proceedings of the 2014 COMSOL Conference, Cambridge, UK (2014).

6.6 Saopštenja sa međunarodnog skupa−štampana u izvodu (**M34**):

[F1] *High Field ESR Temperature Study on $(EDT\text{-}TTF\text{-}CONH_2)_6Re_6Se_8(CN)_6$ under Pressure*; <u>D. M. Djokić</u>, A. Olariu, P. Batail, and L. Forró, Fifth International School and Conference on Spintronics and Quantum Information Technology - SPINTECH V p. 2, Cracow, Poland (2009).

[F2] *Electron Spin Resonance Study of $1D$ κ-$[(EDT\text{-}TTF\text{-}CO\text{-}NH\text{-}CH_2\text{-}CO_2H)_2]^{\bullet+}[HSO_4]^-$ Organic Charge Transfer Salt*; <u>D. M. Djokić</u>, A. Sienkiewicz, A. Olariu, R. Gaál, P. Batail, and L. Forró, MaNEP Swiss Workshop Meeting on Basic Research and Applications, Les Diablerets, Switzerland (2009).

[F3] *High Field ESR Study on $(EDT\text{-}TTF\text{-}CONH_2)_6Re_6Se_8(CN)_6$ under Pressure*; <u>D. M. Djokić</u>, A. Olariu, L. Forró, and P. Batail, European Science Foundation Meeting - Magnetic Resonance in Highly Frustrated Magnetism, Kranjska Gora p. 41, Slovenia (2010).

[F4] *High Field ESR Study of Organic Kagomé $(EDT\text{-}TTF\text{-}CONH_2)_6Re_6Se_8(CN)_6$ Compound*; <u>D. M. Djokić</u>, A. Olariu, P. Batail, and L. Forró, Swiss Physical Society Annual Meeting p. 6, Basel, Switzerland (2010).

[F5] *Electron Spin Resonance Study of $SeCuO_3$*; <u>D. M. Djokić</u>, Z. Micković, I. Živković, K. Schenk, H. Rønnow, H. Berger, and L. Forró, Joint Annual Meeting of Swiss Physical Society and Austrian Physical Society - Condensed Matter Physics p. 56, Lausanne, Switzerland (2011).

[F6] *Hybrid Model of Quench Propagation in Coated Conductors Applied to Fault Current Limiter Design*; D. M. Djokić, A. Badel, L. Antognazza, M. Abplanalp, and M. Decroux, Swiss Workshop on Materials with Novel Electronic Properties p. 130, Les Diablerets, Switzerland (2013).

[F7] *Improved Heat Propagation in Coated Superconducting Fault Current Limiters*; D. M. Djokić, L. Antognazza, A. Badel, M. Abplanalp, and M. Decroux, EuCAS p. 113, Genoa, Italy (2013).

[F8] *Excitonic Effects and Optical Spectra of Single Walled Carbon Nanotubes for Biosensor Applications in Life Sciences and Medicine*; D. M. Djokić, A. Goswami, V. Zubkovs, and A. A. Boghossian, Swiss Chemical Society - Fall Meeting, Lausanne p. 10, Switzerland (2015).

[F9] *High Frequency Electron Spin Resonance Study of the Organic Kagomé Compound (EDT-TTF-CONH$_2$)$_6$Re$_6$Se$_8$(CN)$_6$ under Hydrostatic Pressure*; A. Olariu, D. M. Djokić, S. Baudron, P. Batail, and L. Forró, MaNEP Swiss Workshop Meeting on Basic Research and Applications, Les Diablerets, Switzerland (2009).

[F10] *Magnetoelectric Coupling in Single Crystal Cu$_2$OSeO$_3$ Studied by a Novel Electron Spin Resonance Technique*; A. Maisuradze, A. Shengelaya, H. Berger, D. M. Djokić, and H. Keller, APS March Meeting, Baltimore, USA (2013).

6.7 Rad u časopisu nacionalnog značaja (**M52**):

[G1] *Ispitivanje Termostabilnosti Mo$_6$S$_3$I$_6$ Nanožica Metodom Raman Spektroskopije*; J. M. Todorović, D. M. Djokić, Z. D. Dohčević-Mitrović, D. Mihailović, and Z. V. Popović, Hem. Ind. **63**, 217 (2009). - citirano $0 = 0 + 0$ puta (hetero- i autocitati tim redom).

6.8 Zbornici apstrakata nacionalnih skupova (**M64**):

[H1] *Electron Spin Resonance Study of SeCuO$_3$*; D. M. Djokić, Z. Micković, I. Živković, K. Schenk, H. Rønnow, and L. Forró, XVIII Symposium on Condensed Matter Physics - SFKM p. 81, Belgrade, Serbia (2011).

6.9 Odbranjena doktorska disertacija (**M70**):

[I1] *Electron Spin Resonance of Novel Materials*; D. M. Djokić, PhD Thesis No **5537**, EPFL, Lausanne, Switzerland, (2012).

6.10 Odbranjena magistarska disertacija:

[J1] *Uticaj Spinskih Korelacija Antiferomagnetno Uređene Faze na Infracrvene Spektre α-MnSe*; D. M. Djokić, Magistarska teza, Fizički fakultet Univerziteta u Beogradu, Beograd, Srbija (2008).

6.11 Citiranost

Prema *ISI Web of Knowledge* bazi ukupan broj citata radova kandidata na dan $08.02.2018$ je $72 = 72 + 0$, tj. redom $100\,\%$ heterocitata i $0\,\%$ autocitata.

✧ ✧ ✧ ✧ ✧ ✧ ✧ ✧

Web of Science	InCites	Journal Citation Reports	Essential Science Indicators	EndNote	Publons		Sign In ▼	Help	English ▼

Web of Science

Clarivate Analytics

Search	Search Results		My Tools ▼	Search History	Marked List	13

Citation report for 13 results from Web of Science Core Collection between [2005 ▼] and [2018 ▼] [Go]

You searched for: **From Marked List: ...More**

This report reflects citations to source items indexed within Web of Science Core Collection. Perform a Cited Reference Search to include citations to items not indexed within Web of Science Core Collection.

Export Data: [Save to Text File ▼]

Total Publications
13
1998   2017

h-index ⓘ
5

Average citations per item ⓘ
5.54

Sum of Times Cited ⓘ
72

Without self citations ⓘ
72

Citing articles ⓘ
70

Without self citations ⓘ
70

Sum of Times Cited per Year

Sort by:	**Times Cited**	Date	[More ▼]	◀ Page	1	of 2 ▶

	2014 ◀	2015	2016	2017	2018 ▶	Total	Average Citations per Year
Use the checkboxes to remove individual items from this Citation Report							
or restrict to items published between [2005 ▼] and [2018 ▼] [Go]	23	13	7	13	0	72	7.20
1. **Synthesis of Homogeneous Manganese-Doped Titanium Oxide Nanotubes from Titanate Precursors** By: Szirmai, Peter; Horvath, Endre; Nafradi, Balint; et al.	10	4	5	4	0	24	4.00

JOURNAL OF PHYSICAL CHEMISTRY C   Volume: 117   Issue: 1   Pages: 697-702   Published: JAN 10 2013

2. Magnetoelectric Coupling in Single Crystal Cu2OSeO3 Studied by a Novel Electron Spin Resonance Technique

By: Maisuradze, A.; Shengelaya, A.; Berger, H.; et al.
PHYSICAL REVIEW LETTERS   Volume: 108   Issue: 24   Article Number: 247211   Published: JUN 13 2012

4	4	1	5	0	16	2.29

3. Size dependence of the magnetic response of graphite oxide and graphene flakes - an electron spin resonance study

By: Ciric, Luka; Sienkiewicz, Andrzej; Djokic, Dejan M.; et al.
Conference: 24th International Winterschool on Electronic Properties of Novel Materials - Molecular Nanostructures (IWEPNM 2010) Location: Kirchberg/Tirol, AUSTRIA Date: MAR 06-13, 2010
Sponsor(s): Appl Nanofluorescence; Bruker Opt; Graphene Ind Ltd; HORIBA Jobin Yvon GmbH; NACALAI TESQUE, INC; SINEUROP Nanotech GmbH; Wiley-VCH Verlag GmbH & Co.
PHYSICA STATUS SOLIDI B-BASIC SOLID STATE PHYSICS   Volume: 247 Issue: 11-12   Pages: 2958-2961   Published: DEC 2010

4	2	0	1	0	13	1.44

4. Site-selective quantum correlations revealed by magnetic anisotropy in the tetramer system SeCuO3

By: Zivkovic, I.; Djokic, D. M.; Herak, M.; et al.
PHYSICAL REVIEW B   Volume: 86   Issue: 5   Article Number: 054405   Published: AUG 6 2012

2	0	1	2	0	6	0.86

5. Magnetism in nanoscale graphite flakes as seen via electron spin resonance

By: Ciric, Luka; Djokic, Dejan M.; Jacimovic, Jacim; et al.
PHYSICAL REVIEW B   Volume: 85   Issue: 20   Article Number: 205437   Published: MAY 22 2012

1	2	0	1	0	5	0.71

6. Influence of antiferromagnetic spin ordering on the far-infrared active optical phonon modes of alpha-MnSe

By: Djokic, D. M.; Popovic, Z. V.; Vukajlovic, F. R.
PHYSICAL REVIEW B   Volume: 77   Issue: 1   Article Number: 014305   Published: JAN 2008

2	1	0	0	0	5	0.45

7. Waveguiding Effect in GaAs 2D Hexagonal Photonic Crystal Tiling

By: Jovanovic, D.; Gajic, R.; Djokic, D.; et al.
Conference: Symposium on Raman Scattering in Materials Science Location: Warsaw, POLAND Date: SEP 15-19, 2008
Sponsor(s): Renishaw; NanoCharm
ACTA PHYSICA POLONICA A   Volume: 116   Issue: 1   Pages: 55-57   Published: JUL 2009

0	0	0	0	0	2	0.20

8. Investigation of thermostability and phonon-phonon interactions in Mo6S3I6 nanowires by Raman scattering spectroscopy

By: Todorovic, J. M.; Dohcevic-Mitrovic, Z. D.; Dokic, D. M.; et al.
JOURNAL OF RAMAN SPECTROSCOPY   Volume: 41   Issue: 9   Pages: 978-982   Published: SEP 2010

0	0	0	0	0	1	0.11

9. Quantum yield in polymer wrapped single walled carbon nanotubes: a computational model

By: Djokic, Dejan M.; Goswami, Aranya
NANOTECHNOLOGY   Volume: 28   Issue: 46   Article Number: 465204   Published: NOV 17 2017

0	0	0	0	0	0	0.00

10. Finite Element Method simulation study of heat propagation in a novel YBCO-based Coated Conductor for resistive fault current limiters

By: Djokic, Dejan M.; Antognazza, Louis; Decroux, Michel

0	0	0	0	0	0	0.00

INTERNATIONAL JOURNAL OF THERMAL SCIENCES   Volume: 111
Pages: 160-167   Published: JAN 2017

☐ Select Page

Save to Text File ▾

Sort by: **Times Cited**   Date | More ▾ |

◀ Page 1 of 2 ▶

13 records matched your query of the 28,289,080 in the data limits you selected.

Web of Science

Clarivate Analytics

Search   Search Results   My Tools ▼ | Search History | Marked List | 13

Citation report for 13 results from Web of Science Core Collection between [2005 ▼] and [2018 ▼] [Go]

You searched for: **From Marked List: ...More**

This report reflects citations to source items indexed within Web of Science Core Collection. Perform a Cited Reference Search to include citations to items not indexed within Web of Science Core Collection.

Export Data: [Save to Text File ▼]

Total Publications
13

1998   2017

***h*-index** ⓘ
5

Average citations per item ⓘ
5.54

Sum of Times Cited ⓘ
72

Without self citations ⓘ
72

Citing articles ⓘ
70

Without self citations ⓘ
70

Sum of Times Cited per Year

Sort by: **Times Cited**   Date   [More ▼]   ◀ Page [2] of 2 ▶

Use the checkboxes to remove individual items from this Citation Report

or restrict to items published between [2005 ▼] and [2018 ▼] [Go]

	2014 ◀	2015	2016	2017	2018 ▶	Total	Average Citations per Year
	23	13	7	13	0	72	7.20
11. **Uncoupled photonic band gaps** By: Jovanovic, Dj; Nikolic, B.; Radic, T.; et al. PHOTONICS AND NANOSTRUCTURES-FUNDAMENTALS AND APPLICATIONS Volume: 10 Issue: 4 Pages: 657-666 Published: OCT	0	0	0	0	0	0	0.00

2012

☐ 12. **INVESTIGATION OF THERMOSTABILITY OF Mo6S3I6**
        NANOWIRES USING RAMAN SPECTROSCOPY

☑   By: Todorovic, Jelena M.; Dokic, Dejan M.; Dohcevic-Mitrovic, Zorana D.; et al.
        Conference: 7th Seminar of Young Researchers Location: Belgrade, SERBIA
        Date: DEC 22-24, 2008
        HEMIJSKA INDUSTRIJA   Volume: 63   Issue: 3   Pages: 217-220   Published:
        MAY-JUN 2009

| | 0 | 0 | 0 | 0 | 0 | 0 | 0.00 |

☐ 13. **Infrared reflectivity spectra of eta-Na1.3V2O5 in the charge**
        disordered and ordered phase

☑   By: Popovic, Z. V.; Dokic, D. M.; Dohcevic-Mitrovic, Z.; et al.
        EUROPEAN PHYSICAL JOURNAL B   Volume: 65   Issue: 1   Pages: 1-4
        Published: SEP 2008

| | 0 | 0 | 0 | 0 | 0 | 0 | 0.00 |

☐ Select Page   🖻 ✉ | Save to Text File ▾

Sort by: **Times Cited**   Date   More ▾   ◀ Page [2] of 2 ▶

13 records matched your query of the 28,289,080 in the data limits you selected.

На основу члана 105б. став 4. Закона о високом образовању („Службени гласник РС", бр. 76/05, аутентично тумачење – 100/07, 97/08, 44/10, 93/12, 89/13, 99/14, 45/15 – аутентично тумачење и 68/15), члана 192. став 1. Закона о општем управном поступку („Службени гласник СРЈ", бр. 33/97 и 31/01, „Службени гласник РС", број 30/10) и члана 23. став 2. Закона о државној управи („Службени гласник РС", бр. 79/05, 101/07, 95/10 и 99/14), решавајући по захтеву Дејана Ђокића из Ваљева, Република Србија, за признавање високошколске исправе издате у Швајцарској Конфедерацији, ради запошљавања,

министар просвете, науке и технолошког развоја доноси

Р Е Ш Е Њ Е

Диплома коју је 2. септембра 2012. године на име Дејан Ђокић, издала Федерална политехничка школа у Лозани (Ecole Polytechnique Federale de Lausanne), Лозана, Швајцарска Конфедерација, о завршеним докторским академским студијама, студијски програм Докторска школа физике, звање/квалификација: Docteur es Sciences, признаје се као диплома докторских академских студија трећег степена високог образовања, у оквиру образовно-научног поља Природно-математичких наука, научна, односно стручна област Физичке науке, ради запошљавања.

Ово решење омогућава имаоцу општи приступ тржишту рада у Републици Србији, али га не ослобађа од испуњавања посебних услова за бављење професијама које су регулисане законом или другим прописом.

О б р а з л о ж е њ е

Овом министарству обратио се Дејан Ђокић из Ваљева, Република Србија, захтевом за признавање дипломе Федералне политехничке школе у Лозани (Ecole Polytechnique Federale de Lausanne), Лозана, Швајцарска Конфедерација, студијски програм Докторска школа физике, звање/квалификација: Docteur es Sciences, ради запошљавања.

Уз захтев, подносилац захтева доставио је:
1) оверену копију дипломе издате 2. септембра 2012. године, коју је издала Федерална политехничка школа у Лозани (Ecole Polytechnique Federale de Lausanne), Лозана, Швајцарска Конфедерација, студије трећег степена високог образовања, студијски програм Докторска школа физике, звање/квалификација: Docteur es Sciences;

2) оверени превод дипломе на српски језик;
3) копију докторске дисертације на изворном језику;
4) проширени апстракт дисертације на енглеском језику;
5) списак објављених научних радова;
6) радну биографију на српском језику;
7) пријавни формулар;
8) доказ о уплати таксе за професионално признавање.

Чланом 105 б. став 4. прописано је да Министар доноси решење о професионалном признавању у року од 90 дана од дана пријема уредног захтева.

Одредбама члана 192. Закона о општем управном поступку прописано је да на основу одлучних чињеница утврђених у поступку орган надлежан за решавање доноси решење у управној ствари која је предмет поступка.

Одредбама члана 23. став 2. Закона о државној управи прописано је да Министар представља Министарство, доноси прописе и решења у управним и другим појединачним стварима и одлучује о другим питањима из делокруга Министарства.

Чланом 104. став 1. Закона о високом образовању, прописано је да признавање стране високошколске исправе јесте поступак којим се имаоцу те исправе утврђује право на наставак образовања, односно на запошљавање. Поступак признавања стране високошколске исправе спроводи се у складу са одредбама овог закона, ако међународним уговором није предвиђено другачије.

Сходно одредбама члана 105. став 1. и 6. Закона о високом образовању и васпитању, ENIC/NARIC центар при Министарству просвете, науке и технолошког развоја, прибавио је релевантне информације о студијском програму на ком је стечена диплома из става 2. тачка 1) образложења овог решења.

У складу са чланом 105. став 4. Закона о високом образовању, комисија коју је именовао министар извршила је прво вредновање студијског програма на коме је стечена диплома из става 2. тачка 1) образложења овог решења, и дала предлог за признавање дипломе ради запошљавања.

Подносилац захтева је доставио доказ о уплати таксе у складу са чланом 2. став 1. Правилника о висини таксе за професионално признавање страних високошколских исправа („Службени гласник РС", број 83/2015).

Имајући у виду наведено, решено је као у диспозитиву овог решења.

Упутство о правном средству: Ово решење је коначно у управном поступку и против истог може се покренути управни спор. Тужба се подноси Управном суду у року од 30 дана од дана пријема овог решења.

Решење доставити:
- Дејану Ђокићу, ул. Димитрија Туцовића бр. 26, 14000 Ваљево;
- Архиви.

МИНИСТАР
др Срђан Вербић

École
Polytechnique
Fédérale
de Lausanne

Doctorat

EPFL

ÉCOLE POLYTECHNIQUE
FÉDÉRALE DE LAUSANNE

Le Président

[signature]

Patrick Aebischer

Le Vice-président
pour les affaires académiques

[signature]

Philippe Gillet

Le Directeur de thèse

[signature]

László Forró

L'École Polytechnique Fédérale de Lausanne
sur proposition de la Faculté des sciences de base
décerne

à Monsieur

Dejan
Djokić

né le 7 février 1980 à
Valjevo (Serbie)

le grade de

Docteur ès Sciences

Le candidat a prouvé son aptitude à la recherche scientifique en présentant la thèse intitulée

Electron Spin Resonance of Novel Materials

et a réussi l'examen oral exigé par l'ordonnance
sur le doctorat dans le cadre du programme
doctoral « Physique » dont il a suivi les cours avec
succès.

Délivré à Lausanne, Suisse, le 2 novembre 2012

0034934

(EPFL

ÉCOLE POLYTECHNIQUE
FÉDÉRALE DE LAUSANNE

TRANSLATION

École Polytechnique Fédérale de Lausanne (EPFL)
upon the recommendation of the School of Basic Sciences

hereby confers
on Mr.

Dejan Djokić

born on 7th February 1980 in Valjevo (Serbia)

the degree of

Docteur ès sciences (PhD)

The candidate has proven his aptitude in scientific research by presenting his thesis entitled:

"Electron Spin Resonance of Novel Materials"

and successfully completed the curriculum of the doctoral program in "Physics" and passed the oral examination required by regulations for doctoral studies at EPFL.

Conferred in Lausanne, Switzerland, on 2nd November 2012

The President   The Vice-president for   Thesis Director
                       academic affairs

Patrick Aebischer   Philippe Gillet   László Forró

(original signatures are on the original diploma in French)

Certified to be a true translation
from original French text
ÉCOLE POLYTECHNIQUE FÉDÉRALE
DE LAUSANNE
Service académique

15. 10. 2012

EPFL

ÉCOLE POLYTECHNIQUE
FÉDÉRALE DE LAUSANNE

Doctoral Program in Physics

Record of ECTS credits

Djokic Dejan

Date of birth : 07.02.1980
Federal number : 08-821-969

MANEP Winter school on Exploring New Phases of Electronic Matter (11.01.09 - 16.01.09) Saas-Fee (Switzerland) *Various lecturers*	2
Electronic properties of solids and superconductivity (PHYS-615) *L. Forro & M. Grioni*	3
Quantum theory of solids (MSE-615) *E. Kaxiras*	4
Statistical Field Theory (Autumn 09) / CUSO *T. Giamarchi*	4
Advanced biomedical imaging methods and instrumentation (PHYS-719) *R. Gruetter*	4
Total ECTS credits :	17

Date of issue : 01 October 2012

Prof. Olivier Schneider
Director of the program

DOC0

Ove beleške su nastale na osnovu predavanja u školskoj 2007/2008 godini na smeru Fizika kondenzovane materije Doktorskih studija Fizičkog fakulteta.

Zahvaljujem se kolegama Darku Tanaskoviću, Antunu Balažu i Dejanu Djokiću na aktivnom učešću i doprinosu predavanjima i studentima Ivani Vidanović i Zlatku Papiću na vrednom praćenju i učešću.

Posebno se zahvaljujem Dejanu Djokiću za tehničku pomoć pri pisanju ovih beležaka.

Beograd
20. 10. 2008.

Milica Milovanović
viši naučni saradnik
Institut za Fiziku

3

Prof. Gérard Gremaud
Faculté des Sciences de Base
Institut de Physique de la Matière Complexe
Groupe de Spectroscopie Mécanique

EPFL SB IPMC GSM	Tel .: +41 21 693 33 60
PH D3 445	Fax: +41 21 693 44 70
Station 3	gerard.gremaud@epfl.ch
CH-1015 Lausanne	http://titan.epfl.ch/gsm

ÉPFL

ÉCOLE POLYTECHNIQUE
FÉDÉRALE DE LAUSANNE

Certificate for Mr Dejan Djokic

Mr Dejan Djokic has been teaching practice in physics laboratories to the physics students of the Swiss Federal Institute of Technology, from September 2009 to June 2010.

Concerning his own capabilities, Mr Djokic was a hard-working, serious and intelligent man, who quickly and thoroughly understood the material which he had to teach to the students,

In his teaching activity, he has shown excellent pedagogical aptitudes, keeping a very good contact with the students, who all enjoyed the clear and efficient explanations and tutorials he provided.

Personally, he is communicative, pleasant and very agreeable to work with.

Ecublens, September 24, 2010

Prof. Gérard Gremaud

**Chef du Service des Travaux Pratiques
et Auditoires de Physique**

EPFL
Prof. Gérard Gremaud
IPMC & TP de Physique
PH-D3445
Station 3
CH-1015 Lausanne

INSTITUT DE PHYSIQUE DE LA MATIERE CONDENSEE (ICMP)

FACULTE DES SCIENCES DE BASE

Laboratoire de Physique de la Matière Complexe

ICMP-LPMC – Bâtiment Physique – Station 3 – CH – 1015 LAUSANNE
Tél. +41 (0)21.693 11 11
Tél. secrétariat : +41 (0)21 693 33 74 Téléfax: +41 (0)21 693 44 70

Professeur László Forró
Téléphone : +41 (0)21 693 43 06
e-mail : Laszlo.Forro@epfl.ch

EPFL

ÉCOLE POLYTECHNIQUE
FÉDÉRALE DE LAUSANNE

Lausanne, November 26th, 2012

CERTIFICAT DE TRAVAIL

I hereby certify that

Mr Dejan DJOKIC

born Frebruary 7th, 1980, has worked in my group in Laboratory of Physics of Complex Matter (LPMC) form 15.10.2008 to 14.10.2012.

During this period, Mr Djokic was in charge of the study of various magnetic materials with an ultimate goal to use his findings in spintronics applications. He has shown ability to perform measurements by electron spin resonance, SQUID magnetometry and neutron diffraction studies. Furthermore, he had the necessary theoretical tools to perform in-depth analysis of his findings.

He has also assisted in teaching several courses – "General physics" for students in medicine, and "Novel electronic materials" for physics students. The students highly appreciated his devotion to help them in their studies.

I am very happy with his performance, and his professional progress. Mr Djokic has become an independent researcher, whom I highly recommend for any academic and research position

Yours sincerely,

Prof. László Forró

DOC3

Pr Michel Decroux
Direct: +41 (0)22 379 63 24
Fax: +41 (0)22 379 68 69
Michel.decroux@unige.ch
Secretariat: +41 (0)22 379 30 13

Je soussigné certifie que

M. Dejan DJOKIC

né le 7 février 1980, a travaillé comme Post-Doc dans mon groupe au Département de Physique de la Matière Quantique (DQMP) du 1 janvier 2013 au 14 avril 2015.

Son travail s'inscrivait dans le cadre de nos recherches sur les limiteurs de courant supraconducteurs en collaboration avec l'entreprise ABB. Nos travaux avaient montré la nécessité de réaliser des substrats ayant une conductibilité thermique supérieure à celle de l'hastelloy. Le projet de recherche de M. Djokic consistait à réaliser une étude par simulation numérique sur l'influence de l'épaisseur d'une couche ayant une excellent conductibilité thermique (cuivre) entre un support mécanique mauvais conducteur thermique et la couche supraconductrice. Ces simulations numériques ont montré que l'épaisseur de cuivre doit être au minimum de $1\mu m$. Des structures artificielles ont été réalisées sur la base des ces résultats et les mesures de conductibilité thermique ont confirmé les prévision des simulations numériques.

Pendant la totalité de son mandat, M. Djokic a également assumé des charges d'enseignement dans les cadre des Travaux Pratiques Elémentaire de Physique pour les orientations en Sciences de la Terre (4h/semaine) et en Physique (4h/semaine). M. Djokic a été très apprécié des étudiants et a donné entière satisfaction aux responsable des TPE

M. Djokic a montré dans son travail un grand esprit critique et une grande indépendance dans la réalisation des objectifs fixés, tout en conservant un esprit d'équipe primordial dans une recherche de groupe. Je ne peux donc que hautement recommander M. Djokic pour toute position qui toucheront à la recherche ou à l'enseignement.

Fait à Genève le 28 avril 2015

Prof. Michel Decroux

DQMP – MaNEP, Ecole de Physique, 24 quai Ernest-Ansermet , CH-1211 Genève 4, http://dqmp.unige.ch/, http://www.manep.ch

The National Centres of Competence in Research (NCCR) are a research instrument of the Swiss National Science Foundation.

DOC4

Pflichtenheft/Cahier des charges/Elenco degli obblighi (Siehe Wegleitung/Voir instructions/Vedere instruzioni)

Erstellt am / établi le / stabilito il	durch / par / da		Stellenplan Seite Nr / Etat des places pages no / Piano dei posti pagina no
25 février 2015	Prof. Ardemis Boghossian		696

Name, Vorname/Nom, prénom/Cognome, nome	Geb.-Jahr / Année de naiss. / Anno di nasc.	Erlernter Beruf/Prof. apprise/Prof. appresa	Eintritt in das heutige Amt/Entrée dans l'office/Entrata nell'ufficio
DOKIC Dejan	1980	Dr ès sciences, EPFL	15.04.2015

Bundesamt, office fédéral / ufficio federale	Bereich, Betrieb / Secteur, unité d' organisation/Settore, unità d' organizzazione
Ecole Polytechnique Fédérale de Lausanne	SB / ISIC / LNB (Laboratory of Nano Biotechnology)

Dienstliche Stellung, Klasse/ Fonction, classe/Funzione, classe gegenwärtig/actuelles/attuali	Kl./cl./cl.	Vorschlag/Proposition/Proposta	Kl./cl./cl.	Termin/A partir du/A partire dal
Collaborateur scientifique	18			

Dienstverhältnis/Rapports de service/Rapporto d'impiego gegenwärtig/actuels/attuale		Vorschlag/Proposition/Proposta	Letzte Beförderung/Dernière promotion/Ultima promozione
CDD			
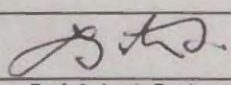
Tätigkeiten in der Reihenfolge ihrer Bedeutung / Activités par ordre d'importance / Attività per ordine d' importanza	%	Art der Erledigung / Manière de traiter les affaires / Modo di trattare
	100 %	

	%	
PROJECT: "Nanotube Sensors" (24 months)		
Computational & theoretical modelling of photophysical observations.	30	i
Microscope setup & application:	35	i
• Construction of near-infrared spectroscopy & imaging microscope		
• Photophysical measurements		
• In vitro/in vivo application		
Teaching duties regarding BSc, MSc and graduate students:	25	d
• Supervision of Semester and MSc projects, practical courses, exercises		
• Exams organization and correction		
Assistance on grant proposals preparation and lab administration	10	d
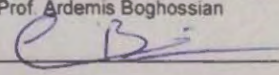
Direkta/r Vorgesetzte/r Supérieur/e direct/e Superiore diretto/a	Prof. Ardemis Boghossian

s selbständig	w nach Weisungen	Pflichtenheft verändert	ja	☐	nein	☐
i indépendante	d selon directives	Cahier des charges changé	oui		non	
i indipendente	d secondo direttive	Elenco degli obblighi cambiato	si		no	

Direkt unterstelltes Personal / Personnel directement subordonné / Personale direttamente subordinato	Total unterstelltes Personal / Total du personnel subordonné / Personale subordinato in totale	Stellenausschreibung vom / Mise au concours de / Messa al concorso del	Kl. / cl. / cl.

Bemerkungen/Remarques/Osservazioni	Unterschrift Stelleninhaber/in Signature du/de la titulaire Firma del/della titolare

	Unterschrift Vorgesetzte/r Signature du/de la supérieur/e Firma del/della superiore	Prof. Ardemis Boghossian
	Entscheid/Décision/Decisione	

DOC5

INSTITUT DE PHYSIQUE DE LA MATIERE CONDENSEE (IPMC)
INSTITUTE OF PHYSICS OF CONDENSED MATTER (IPCM)
FACULTE DES SCIENCES DE BASE

FSB-ECUBLENS - CH - 1015 LAUSANNE, Switzerland
Tél. 41.21.693. 43 37
Tél. secrétariat : 41.21- 693 33 74 Téléfax: 41.21-693.44.70

Dr. Andrzej Sienkiewicz
Laboratory of Complex Matter Physics
Institute of Condensed Matter Physics
EPFL, FSB-ECUBLENS, Station 3
CH-1015 LAUSANNE, Switzerland
Room: PH-L1-491
Phone :   (+41-21) 693-43-37 ; FAX : (+41-21) 693-44-70
E-mail: andrzej.sienkiewicz@epfl.ch

Re: Reference letter concerning professional competence of Dr. Dejan Djokić

To whom it may concern:

I am delighted to be called upon as a reference for Dr. Dejan Djokić. I first became acquainted with Dejan Djokić in the fall of 2008, when he was enrolled into the PhD program under the supervision of Prof. László Forró and joined our Laboratory (Laboratory of Complex Matter Physics, Institute of Physics of Condensed Matter, Faculty of Basic Sciences, EPFL).

During his PhD studies, Dejan Djokić was engaged in several projects devoted to physico-chemical properties of novel carbon-based materials.

In particular, I personally had an opportunity to work with Dejan Djokić and advise him in projects concerning the ultra-thin graphite and quasi one-dimensional organic systems.

I also collaborated with him in the research on graphene-related systems, including strategies of preparing and characterizing graphene-based field-effect transistors.

Actually, the graphene-based systems have become one of the major issues of his PhD thesis, entitled: "Electron Spin Resonance of Novel Carbon Based Materials" (PhD Thesis, EPFL).

During his research devoted to graphene, Dejan Djokić demonstrated a high level of competence and professionalism in using various experimental techniques, including: Electron Spin Resonance (ESR), high-field multi-frequency ESR (HF-MF ESR), as well as X ray diffraction (XRD), just to name a few of them. These skills, together with the high-level theoretical background acquired during his undergraduate studies, enabled him to quickly enter the very rapidly moving field of graphene-related systems and obtain publishable results.

During his PhD studies, Dejan Djokić had also numerous teaching obligations. His skills in teaching have been highly appreciated by both the staff and students at the EPFL.

Finally, Dejan Djokić shared his skills and actively helped many PhD students, postdoctoral fellows and professors from numerous research teams at the EPFL and beyond. His publications record clearly points to this fact.

From my personal perspective, I highly appreciated his constant curiosity, creative approach to do science as well as his well-balanced experimental skills and theoretical insight.

Summarizing, I have no hesitation in recommending Dejan Djokić for a position at your Department.

Yours truly,

Andrzej Sienkiewicz, Ph.D., PD

PS. If I can be of any help, please do not hesitate to reach me through E-mail at: andrzej.sienkiewicz@epfl.ch

Dr. Andrzej Sienkiewicz
Laboratory of Complex Matter Physics (LCMP)
Institute of Condensed Matter Physics (ICPM)
Faculty of Basic Sciences (FSB)
Ecole Polytechnique Fédérale de Lausanne, Station 3
CH-1015 LAUSANNE-EPFL, SWITZERLAND
Phone: (+41) 21 693 43 37
FAX: (+41) 21 693 44 70
E-mail: andrzej.sienkiewicz@epfl.ch

DOC6

To whom it may concern

Letter of recommendation concerning **Dr. Dejan DJOKIC**

Dear Colleague,

I have known Dr. Djokic in the frame of a scientific collaboration with Prof. L. Forró at EPFL.
Dr. Djokic was in charge of the high field Electron Paramagnetic Resonance (EPR) spectrometer.
While being strongly involved in the experimental set up for our experiments, he also had a fair scientific discussion on our topics although being not yet involved at that moment.
Since then, I have been invited as a reviewer of his PhD Thesis work at EPFL. I was much impressed by the broad scope of Dr. Djokic's knowledge and by the deep reflection he could have on such various topics as, *e.g.* frustrated spin systems, carbon nanoworld, and molecular materials.
Dr. Djokic is actually an experienced scientist at a rare level I have ever met for a junior researcher.
It is actually my pleasure to recommend Dr. Djokic as a clever and efficient collaborator to his future welcoming lab.

Sincerely yours,

Strasbourg, Oct. 10 / 2012
Philippe TUREK,

Professor in Physics
University of Strasbourg
Vice-Dean of the Faculty of Physics and Engineering
Director of the POMAM lab

Phone +33 368 855 626 / Mail : turek@unistra.fr

Laboratoire P.O.M.A.M.
http://www-chimie.u-strasbg.fr/~pomam/
INSTITUT DE CHIMIE – UMR 7177 – CNRS / UdS
4 rue Blaise Pascal – CS 90032 – 67081 Strasbourg Cedex

DOC7

Physik-Institut

Universität Zürich
Winterthurerstrasse 190
CH-8057 Zürich
Telefon +41 44 635 57 21
Telefax +41 44 635 57 04
www.physik.uzh.ch

Prof. Dr. Hugo Keller
Telefon +41 44 635 57 48
Telefax +41 44 635 57 04
keller@physik.uzh.ch

Zürich, 23. October 2012

Recommendation Letter for Dr. Dejan M. Djokić

Dear Colleagues,

It is a great pleasure for me to recommend highly Dr. Dejan M. Djokić for a postdoctoral position in the field of experimental condensed matter physics.

As a member of the jury of his PhD thesis I have met Dejan for the first time during his PhD defense at EPFL in Lausanne in September 2012. I am not only very much impressed by the rich scientific content of his thesis, but also how skillfully he answered and discussed the questions during the exam. Even when he did not know the exact answer, he stayed calm, and tried to attack the problem, demonstrating a broad and profound knowledge of physics.

His dissertation provides a thorough account of current research in the area of materials with novel electronic properties. The thesis is focused on a study of the magnetic properties of three different classes of novel magnetic materials which are not only of great fundamental interest, but also have a promising potential for innovative applications, such as spintronics and carbon-based electronics (graphene). These three different materials are:
-    The tetramer system $SeCuO_3$: a cupric oxide quantum antiferromagnet
-    Nanoscale graphite flakes: defected graphene bottled-up in nanographite
-    The organic system $(EDT\text{-}TTF\text{-}CONH_2)_6Re_6Se_8(CN)_6$: a charge transfer, low-dimensional topological insulator with unprecedented Kagomé geometry

The main experimental technique used in the thesis is Electron Spin Resonance (ESR) which is a very sensitive and extremely powerful microscopic tool to probe magnetic interactions and spin dynamics in magnetic solids. In addition, high-frequency (210 GHz) ESR experiments under hydrostatic pressure up to 15 kbar were performed. The ESR results are compared with structural data, resistivity, and magnetization measurements as well as with theoretical predictions. His work provides new and essential information on three classes of novel magnetic systems

which may help to reach a deeper understanding of the complex properties of these interesting materials.

In his thesis Dejan Djokić has clearly demonstrated ability of realizing ambitious research at the forefront of modern condensed matter physics. Although I do not know Dejan very well, in my opinion he is an intelligent, motivated and hard working scientist with a broad and solid background in physics who is able to plan and realize his own research projects. I also would like to mention his ability to give clear and scientifically sound talks. He also is a friendly and very open-mined person who likes to work in a team.

In my opinion Dr. Djokić fulfills all the conditions for becoming an independent and mature researcher in any field experimental condensed matter physics

I would be very glad to supply you with any additional information which you might wish.

Yours Sincerely,

Prof. H. Keller

Magnetoelectric Coupling in Single Crystal Cu_2OSeO_3 Studied by a Novel Electron Spin Resonance Technique

A. Maisuradze,[1,2,*] A. Shengelaya,[3] H. Berger,[4] D. M. Djokić,[4] and H. Keller[1]

[1]*Physik-Institut der Universität Zürich, Winterthurerstrasse 190, CH-8057 Zürich, Switzerland*
[2]*Laboratory for Muon Spin Spectroscopy, Paul Scherrer Institut, CH-5232 Villigen PSI, Switzerland*
[3]*Department of Physics, Tbilisi State University, Chavchavadze av. 3, GE-0128 Tbilisi, Georgia*
[4]*Institute of Condensed Matter Physics, École Polytechnique Fédérale de Lausanne (EPFL), CH-1015 Lausanne, Switzerland*
(Received 25 January 2012; published 13 June 2012)

The magnetoelectric (ME) coupling on spin-wave resonances in single-crystal Cu_2OSeO_3 was studied by a novel technique using electron spin resonance combined with electric field modulation. An external electric field **E** induces a magnetic field component $\mu_0 H^i = \gamma E$ along the applied magnetic field **H** with $\gamma = 0.7(1)$ μT/(V/mm) at 10 K. The ME coupling strength γ is found to be temperature dependent and highly anisotropic. $\gamma(T)$ nearly follows that of the spin susceptibility $J^M(T)$ and rapidly decreases above the Curie temperature T_c. The ratio γ/J^M monotonically decreases with increasing temperature without an anomaly at T_c.

Magnetoelectric (ME) materials exhibiting coupled and microscopically coexisting magnetic (**M**) and electric (**P**) polarizations have attracted considerable interest in recent years [1–4]. This coupling allows one to influence the magnetic state of a ME material via an external electric field, thus opening a broad range of possible technical applications of such materials [3,5]. Moreover, it is very interesting to investigate the microscopic mechanism of ME coupling, since **P** and **M** tend to exclude each other [4]. In order to detect the ME effect, sensitive and reliable experimental techniques are required, since this coupling is generally quite small. Usually, for the determination of the ME coupling either the dielectric properties of ME materials are measured as a function of magnetic field or the magnetization is studied as a function of an applied electric field [3].

Cu_2OSeO_3 is a paraelectric ferrimagnetic material with a Curie temperature of $T_c \simeq 57$ K [6–8]. The ME effect in Cu_2OSeO_3 was first observed by magnetocapacitance experiments [6]. Later on, a small abrupt change of the dielectric constant below T_c was reported by infrared reflection and transmission studies [9,10]. Recent μSR investigations showed a rather small change of the internal magnetic field by applying an electric field [8]. X-ray diffraction [6] and nuclear magnetic resonance [11] studies revealed no evidence of any lattice anomaly below T_c, suggesting that lattice degrees of freedom are not directly involved in the ME effect. Moreover, a metastable magnetic transition with enhanced magnetocapacitance was observed [6] and later on was also investigated under hydrostatic pressure [12]. Very recently, ME Skyrmions were observed in Cu_2OSeO_3 by means of Lorentz transmission electron microscopy [13] and small angle neutron scattering experiments [14].

Here we report a study of the ME coupling in a single crystal of Cu_2OSeO_3. For this investigation, a novel microscopic method for the direct determination of the ME effect based on the standard FMR/EPR technique combined with electric field modulation was developed. As a result, to our knowledge for the first time, spin-wave resonance (SWR) excitations [15] were detected via ME coupling. The linear ME coupling strength γ was determined quantitatively in Cu_2OSeO_3. In particular, the temperature and angular dependence of γ and the SWR excitations were investigated. The temperature dependence of the ME coupling was found to follow nearly that of the spin susceptibility without a sudden change across T_c. By comparing the results of ME Cu_2OSeO_3 with those of standard DPPH ($C_{18}H_{12}N_5O_6$), we further demonstrate that this novel microscopic method is a very sensitive and powerful tool to investigate the ME effect and to search for new ME materials.

High-quality single crystals of Cu_2OSeO_3 were prepared using a procedure described elsewhere [11]. The crystal structure is cubic with symmetry ($P2_13$) [6,7]. Several thin single-crystal samples of approximate dimensions of $\sim 1 \times 1 \times d$ mm with thickness $d \leq 0.1$ mm were studied. The [110] direction of the crystal is oriented perpendicular to the planes of the thin samples [see Fig. 1 (a)]. The FMR and EPR measurements were performed with a standard X-band (9.6 GHz) BRUKER EMX spectrometer. In order to detect the ME effect, a capacitor-like structure consisting of two thin (< 10 μm) isolated gold electrodes separated by $\simeq 0.3$ mm was used [see Fig. 1(a)]. The sample and the DPPH marker [16,17] were placed between the two electrodes. The electrodes were connected to an ac voltage source of amplitude $V_m = 17$ V, synchronized with the frequency of 100 kHz of the magnetic field modulation generator of the spectrometer [16,17]. Two kinds of resonance experiments were
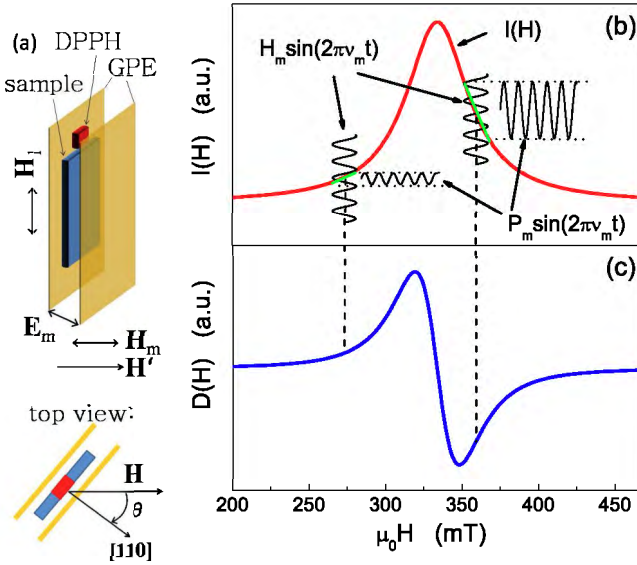
FIG. 1 (color online).   (a) Schematic view of the sample and the magnetic or electric field geometry. The ME sample and the marker sample DPPH are sandwiched between two gold plate electrodes (GPE). $\mathbf{H}'$: static external magnetic field, $\mathbf{H}_m$: magnetic modulation field, $\mathbf{E}_m$: electric modulation field, $\mathbf{H}_1$: microwave field, and $\mathbf{H} = \mathbf{H}' + \mathbf{H}_m$: total external magnetic field. (b) Basic principle of EPR signal detection. Red curve represents the EPR absorption line $I(H)$. The modulation magnetic field $H_m \sin(2\pi\nu_m t)$ and the resulting modulated microwave absorption power $P_m \sin(2\pi\nu_m t)$ are also illustrated. (c) First derivative $D(H)$ signal of the EPR absorption line $I(H)$ after lock-in detection.

performed: (1) EPR/FMR with standard magnetic field modulation (MFM) and (2) EPR/FMR with electric field modulation (EFM) at 100 kHz. The [110] axis of the crystal was perpendicular to the microwave field $\mathbf{H}_1$. For the angular dependent measurements, the sample was rotated with respect to the applied field $\mathbf{H}$ [see Fig. 1(a)].

The EPR/FMR technique is based on the resonance absorption of microwave energy by a Zeeman-split spin system [16,17]. The Zeeman splitting of the spin system is achieved by sweeping an applied magnetic field H. In the simplest case of an effective spin $S = 1/2$ system (as for the present case of Cu^{2+}) the double degenerate ground state is split into two levels by the Zeeman energy $E_Z = g\mu_B H$. When $E_Z = h\nu$, where $\nu = 9.6$ GHz is the frequency of the microwave H_1 field, resonance absorption takes place [see Fig. 1(b)]. In order to increase the sensitivity, the applied magnetic field H is modulated: $H = H' + H_m \sin(2\pi\nu_m t)$, where H' is the static applied magnetic field, H_m is the modulation amplitude, and ν_m is the modulation frequency (typically $\nu_m = 100$ kHz). During signal detection H' is swept slowly. As a result, the detected microwave absorption power $P(t) = P_m \sin(2\pi\nu_m t)$ is also modulated with the frequency ν_m. The amplitude P_m is proportional to the slope $D(H)$ of the absorption signal $I(H)$. Further amplification and lock-in detection of

$P(t)$ results in the EPR derivative signal $D(H)$ as illustrated in Fig. 1(c) [16,17].

Ferromagnetic resonance studies were performed previously on composite ME structures involving piezoelectric and magnetostrictive compounds [18–20]. In these experiments, a static external field E_{st} was used to detect the ME coupling strength. By applying $E_{st} = 1$ kV/mm in the present experiments, a shift of the resonance fields of the order of $\simeq 0.5$ mT was also detected for Cu_2OSeO_3, indicating an additional magnetization induced by E_{st}. However, in order to increase the sensitivity of signal detection and to avoid artifacts related to hysteresis effects of the magnet core, it is advantageous to apply a periodic voltage to detect small changes in the spectra. This technique was previously applied to investigate the electric field effect on the non-Kramers ion Pr^{3+} in $LaMgN_2$ [21]. The main idea of the present experiment is to use EFM to observe EPR/FMR signals in Cu_2OSeO_3 instead of the usual MFM technique. In a spin system without ME effect (e.g., DPPH) no modulated signal $P(t) = P_m \sin(2\pi\nu_m t)$ will occur. However, if the ME effect is present in the sample, modulation by an electric field $E_m \sin(2\pi\nu_m t)$ leads to a modulation of the magnetization $M(t)$ and therefore to a modulation of the magnetic field in the sample $B(t) = \mu_0[H + M(t)]$. In this case the EPR/FMR signal which is proportional to the ME coupling may in principle be detected.

First we describe the FMR/EPR signals obtained in Cu_2OSeO_3 using the conventional MFM technique. For a polycrystalline or arbitrarily shaped single crystal, a very complex signal is observed as reported previously (see Ref. [22]). We found that the signal is substantially simpler for a thin single crystal with a nearly constant effective demagnetization factor [23]. Figure 2(a) shows the FMR signal of a thin single-crystal sample of Cu_2OSeO_3 (thickness $d = 55$ μm) at 14 K with the applied magnetic field H parallel ($H_\parallel$, $\theta = 90°$) and perpendicular ($H_\perp$, $\theta = 0°$) to the plane of the sample [see Fig. 1(a)]. For $H_\parallel$ a slightly skewed single signal is observed, whereas for $H_\perp$, multiple peaks with different signal intensities are evident. These peaks represent resonances of different spin-wave (SW) modes. In thin ferromagnetic samples, SW modes are expected to occur at resonance fields H_n [15,24,25]:

$$H_n = H_0 - S\left(\frac{\pi}{d}\right)^2[(n+1)^2 - 1] \qquad (1)$$

Here, S is a parameter related to the spin stiffness [15,24], n is the order of the spin-wave mode, and d is the thickness of the sample. With increasing n the resonance field H_n decreases, and with decreasing d the difference $H_0 - H_1$ increases. Qualitatively, this behavior agrees with our observation [see Fig. 2(b)]. However, there are quantitative deviations from Eq. (1) as was reported previously for various materials [24,25]. These deviations are often related to stress, magnetic anisotropy, distribution, or variation of
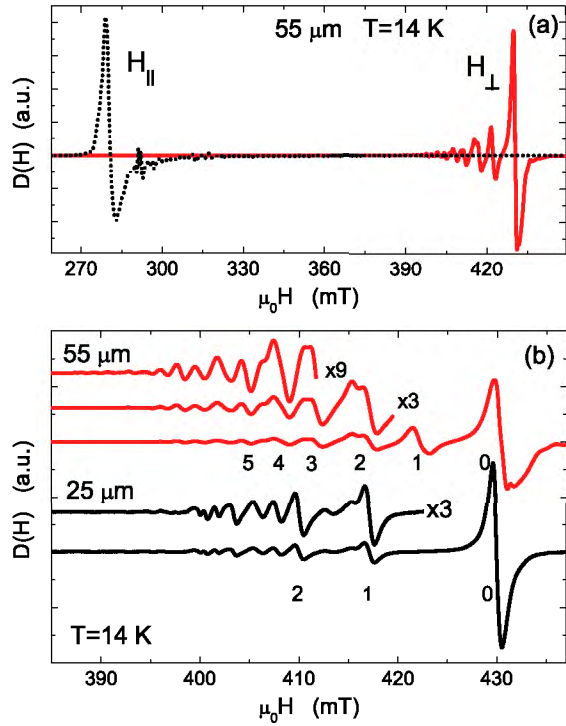
FIG. 2 (color online).   (a) FMR in the 55 μm thick single-crystal sample of Cu_2OSeO_3 at $T = 14$ K for $H_\parallel$ and $H_\perp$ using the conventional MFM technique. (b) SWR in the 25 and 55 μm thick single-crystal samples of Cu_2OSeO_3 at $T = 14$ K for $H_\perp$. The indices $0, 1, 2, \ldots$ indicate the order of the SWR mode.

magnetization across the sample. As shown in Fig. 2, it was possible to detect SW modes with order $n > 10$ in the present experiments. However, due to a slight variation of thickness d across the sample, the modes of high order n interfere. Moreover, with increasing temperature the line widths of the SWR modes increase and overlap [see Fig. 3].

Next we discuss the ME effect using the EFM method by applying an ac electric field $E_m \sin(2\pi\nu_m t)$. Figure 3 shows some typical FMR spectra of the 55 μm-thick single-crystal sample at different temperatures detected by this technique. It is evident that the SWR lines are also observed as for MFM. At 10 K, the SWR signals $D^M(H)$ and $D^E(H)$ detected by MFM and EFM, respectively, have approximately the same amplitudes. With increasing temperature, however, the amplitude of $D^E(H)$ is reduced compared to that of $D^M(H)$. Above 60 K, the intensity of the $D^E(H)$ signal becomes very small. Note that for the marker sample DPPH, no signal is present in the case of EFM as expected. The absence of a DPPH signal unambiguously demonstrates that ME coupling in Cu_2OSeO_3 gives rise to the $D^E(H)$ signal. Thus, the ratio of the signal intensities detected by electric and magnetic modulations is proportional to strength of the ME effect [26],

$$\alpha(H) = \frac{I^E(H)}{I^M(H)} \equiv \frac{\int_0^H D^E(h)dh}{\int_0^H D^M(h)dh}. \quad (2)$$
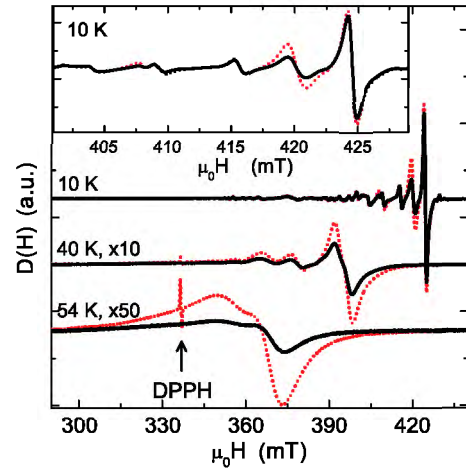
FIG. 3 (color online).   Temperature dependence of SWR signals of single-crystal Cu_2OSeO_3 detected using the MFM technique (dotted line) and the EFM technique (solid line). The sharp peak visible at 340 mT and 54 K is the signal of the marker sample DPPH which is present only in the case of MFM. The inset shows the expanded spectra at 10 K around 415 mT. For better comparison, all the EFM signals are multiplied by a factor of 2.

This ratio is determined by $\alpha = \mu_0 H^i / \mu_0 H_m$, where $\mu_0 H_m^i = \gamma E_m$ is the magnetic field induced by the electric field E_m, and $\mu_0 H_m = 0.1$ mT is the field used in the MFM experiment. Therefore, the ME coupling strength $\gamma = \alpha C$ with a calibration factor $C= \mu_0 H_m / E_m = 1.76 \mu T/(V/mm)$ [1,3]. It is convenient to introduce the spectrally averaged value of $\alpha(H)$,

$$\langle \alpha \rangle = \frac{\int I^M(H)\alpha(H)dH}{\int I^M(H)dH} = \frac{\int I^E(H)dH}{\int I^M(H)dH} = \frac{J^E}{J^M}. \quad (3)$$

Here, $J^\beta = \iint D^\beta(h)d^2h$, $(\beta = E, M)$ are the signal intensities in the EFM and the MFM experiments, respectively. J^M is also a measure of spin susceptibility [16]. The temperature dependence of $\alpha(H)$ for $H_\perp$ is shown in Fig. 4(a). Above 20 K, $\alpha(H)$ has a minimum at around 300 mT, and is nearly constant above 320 mT. The averaged ME effect parameter $\langle \alpha \rangle$ as a function of temperature is plotted in Fig. 4(b), together with the temperature dependencies of J^E and J^M. The ME effect is most pronounced at low temperatures and decreases with increasing temperature. With the above value of C and $\langle \alpha \rangle = 0.4$, one obtains $\gamma = 0.7(1) \mu T/(V/mm)$ at 10 K. Below 20 K, the ME effect is decreasing slightly faster than J^M with increasing temperature as shown in Fig. 4(b). Above 60 K, the ME effect rapidly decreases, although it is still present in the paramagnetic phase. The insert of Fig. 4(b) shows $\langle \alpha \rangle$ at 14 K as a function of the angle θ [see Fig. 1(a)]. The sign change of $\langle \alpha(\theta) \rangle$ at $\theta \simeq 25°$ corresponds to the change of the direction of the induced magnetization M^i with respect to $\mathbf{H}$. The observed $\langle \alpha(\theta) \rangle$ indicates that the ME effect depends not
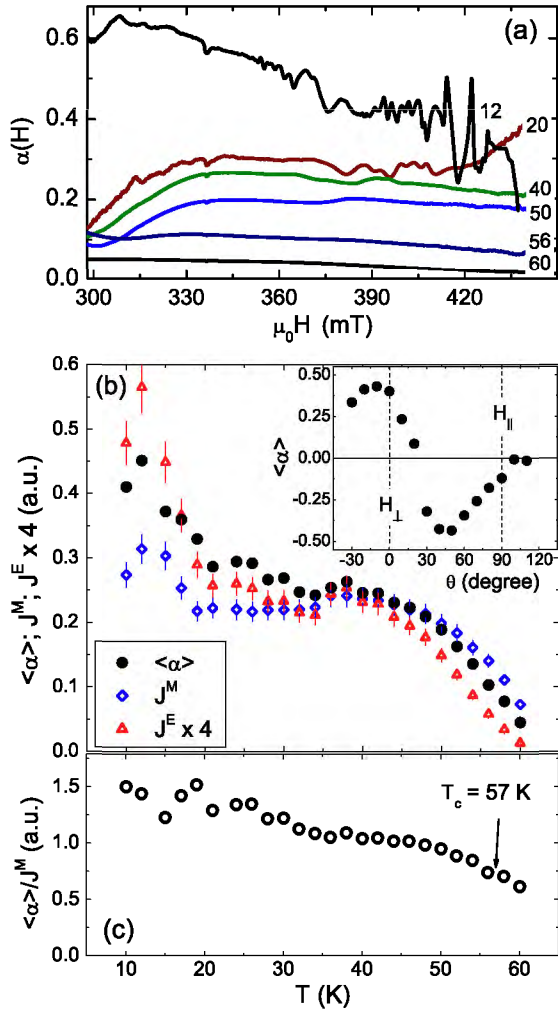
FIG. 4 (color online). (a) Spectrally resolved ME effect parameter $\alpha(H)$ in single-crystal Cu_2OSeO_3 at $T = 12, 20, 40, 50, 56$, and 60 K for $H_\perp$. (b) Temperature dependence of the average ME effect parameter $\langle\alpha\rangle$ and the signal intensities J^E and J^M detected by EFM and MFM, respectively. The inset shows the angular dependence of $\langle\alpha\rangle$ at 14 K. (c) Temperature dependence of the ratio $\langle\alpha\rangle/J^M$ showing no anomaly at T_c.

only on the relative orientation of $\mathbf{E}_m$ and $\mathbf{H}$ [see Fig. 1(a)] but also on the crystal orientation with respect to these fields. In Fig. 4(c), the temperature dependence of the ratio $\langle\alpha\rangle/J^M$ is shown. This ratio decreases gradually with increasing temperature showing no anomaly at $T_c = 57$ K, indicating that the ME coupling mechanism is not related to the onset of long range magnetic order. The ME coupling is linear as is evident from the linear relation between the SWR peak-to-peak amplitude A_{pp} of $D(H)$ and the applied EFM amplitude E_m [see Figs. 5(a) and 5(b)]. In Fig. 5(c), we show A_{pp} as a function of the EFM frequency ν_m. Note that A_{pp} shows no appreciable frequency dependence, indicating that γ is not related to a mechanical resonance of the sample, as observed in some of the composite ME materials [27].
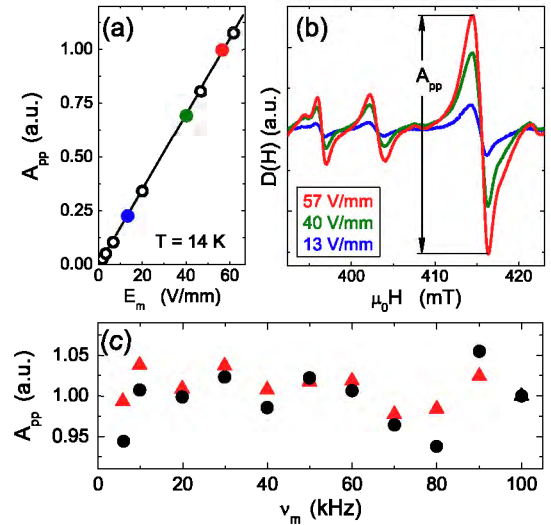
FIG. 5 (color online). (a) Peak-to-peak amplitude A_{pp} of the zero order SWR mode extracted from $D(H)$ shown in (b) as a function of the EFM amplitude E_m in Cu_2OSeO_3. Note that $A_{pp} \propto E_m$ indicating that ME coupling is linear. (c) A_{pp} as a function of the EFM frequency ν_m at $T = 25$ K (dots) and 35 K (triangles).

It is interesting to compare the magnitude of the ME effect $\gamma = \alpha C$ observed in this work with previous results [6,8]. For an applied electric field of $\delta E = 500/3$ (V/mm), a change of the internal magnetic field of $\mu_0\delta\overline{H^i_{\mu SR}} = 0.4(4)$ mT was detected by μSR [8]. This corresponds to an electric field induced magnetization of $\mu_0\delta\overline{M_{\mu SR}} = \mu_0\delta\overline{H^i_{\mu SR}}(1-N)^{-1} \simeq 0.6$ mT (for $N = 1/3$ [28]). For the same electric field and for a mean value of $\overline{\langle\alpha\rangle} \simeq 0.28$ for $T < 50$ K, the average induced magnetization is estimated to be $\mu_0\delta\overline{M_{FMR}} = \mu_0\delta\overline{H^i_{FMR}}(1-N)^{-1} = \overline{\langle\alpha\rangle}C\delta E(1-N)^{-1} \simeq 0.55$ mT, where $N \simeq 0.85$ was used corresponding to the actual geometry of the sample [23]. The present value of $\mu_0\delta\overline{M_{FMR}} \simeq 0.55$ mT is in good agreement with the value of $\simeq 0.6$ mT obtained by μSR [8]. The observed temperature dependence of the ME effect differs slightly from that measured by magnetocapacitance experiments on powder samples [6], but it is in agreement with that observed recently for a single crystal sample [29]. While the ME effect parameter $\langle\alpha\rangle$ is strongly reduced above 60 K, the ME effect reported in Ref. [6] is still substantial up to 65 K.

In summary, the magnetoelectric coupling in single crystal of Cu_2OSeO_3 was studied by means of a novel and highly sensitive magnetic resonance technique. This method is based on the use of electric field modulation instead of conventional magnetic field modulation in standard continuous wave EPR. Resonance lines of spin-wave modes of more than order 10 could be resolved in the FMR spectra. Moreover, spin-wave resonances were observed via the ME coupling by applying an electric field modulation technique. By combining magnetic and electric field

modulation experiments, the temperature and angular dependence of the linear ME effect in Cu_2OSeO_3 was investigated for the electric field parallel to the [110] direction of the crystal. The ME coupling was found to be $\gamma = 0.7(1)$ $\mu T/(V/mm)$ at 10 K. The magnetization induced by the applied electric field is in good agreement with previous μSR results [8]. The temperature dependence of the ratio of ME coupling strength to the spin susceptibility γ/J^M exhibits no anomaly at $T_c = 57$ K. This indicates that the ME coupling mechanism is not related to the presence of long-range magnetic order.

---

*alexander.m@physik.uzh.ch

[1] M. Fiebig, J. Phys. D: Appl. Phys. **38**, R123 (2005).
[2] N. A. Spaldin and M. Fiebig, Science **309**, 391 (2005).
[3] W. Eerenstein, N. D. Mathur, and J. F. Scott, Nature **442**, 759 (2006).
[4] N. A. Hill, J. Phys. Chem. B **104**, 6694 (2000).
[5] M. Bibes and A. Barthélémy, Nature Mater. **7**, 425 (2008).
[6] Jan-Willem G. Bos, C. V. Colin, and T. T. M. Palstra, Phys. Rev. B **78**, 094416 (2008).
[7] H. Effenberger and F. Pertlik, Monatsch. Chem. **117**, 887 (1986).
[8] A. Maisuradze, Z. Guguchia, B. Graneli, H. M. Rønnow, H. Berger, and H. Keller, Phys. Rev. B **84**, 064433 (2011).
[9] K. H. Miller, X. S. Xu, H. Berger, E. S. Knowles, D. J. Arenas, M. W. Meisel, and D. B. Tanner, Phys. Rev. B **82**, 144107 (2010).
[10] V. P. Gnezdilov, K. V. Lamonova, Yu. G. Pashkevich, P. Lemmens, H. Berger, F. Bussy, and S. L. Gnatchenko, Fiz. Nizk. Temp. **36**, 688 (2010).
[11] M. Belesi, I. Rousochatzakis, H. C. Wu, H. Berger, I. V. Shvets, F. Mila, and J. P. Ansermet, Phys. Rev. B **82**, 094422 (2010).

[12] C. L. Huang, K. F. Tseng, C. C. Chou, S. Mukherjee, J. L. Her, Y. H. Matsuda, K. Kindo, H. Berger, and H. D. Yang, Phys. Rev. B **83**, 052402 (2011).
[13] S. Seki, X. Z. Yu, S. Ishiwata, and Y. Tokura, Science **336**, 198 (2012).
[14] T. Adams, A. Chacon, M. Wagner, A. Bauer, G. Brandl, B. Pedersen, H. Berger, P. Lemmens, and C. Pfleiderer, arXiv:1204.3597v1.
[15] C. Kittel, Phys. Rev. **110**, 1295 (1958).
[16] A. Abragam and B. Bleaney, *Electron Paramagnetic Resonance of Transition Ions* (Clarendon, Oxford, 1970).
[17] C. P. Poole, *Electron Spin Resonance: A Comprehensive Treatise on Experimental Techniques* (Dover, New York, 1997), 2nd ed..
[18] Y. Chen, A. Yang, M. R. Paudel, S. Stadler, C. Vittoria, and V. G. Harris, Phys. Rev. B **83**, 104406 (2011).
[19] M. Weiler, L. Dreher, C. Heeg, H. Huebl, R. Gross, M. S. Brandt, and S. T. B. Goennenwein, Phys. Rev. Lett. **106**, 117601 (2011).
[20] S. Shastry, G. Srinivasan, M. I. Bichurin, V. M. Petrov, and A. S. Tatarenko, Phys. Rev. B **70**, 064416 (2004).
[21] P. Wysling and K. A. Müller, J. Phys. C: Solid State Phys. **9**, 635 (1975).
[22] M. I. Kobets, K. G. Dergachev, E. N. Khatsko, A. I. Rykova, P. Lemmens, D. Wulferding, and H. Berger, Low Temp. Phys. **36**, 176 (2010).
[23] G. Zheng, M. Pardavi-Horvath, X. Huang, B. Keszei, and J. Vandlik, J. Appl. Phys. **79**, 5742 (1996).
[24] T. G. Rappoport, P. Redlinski, X. Liu, G. Zaránd, J. K. Furdyna, and B. Jankó, Phys. Rev. B **69**, 125213 (2004).
[25] X. Liu and J. K. Furdyna, J. Phys.: Condens. Matter **18**, R245 (2006).
[26] Provided that the rest of experimental conditions are identical.
[27] U. Laletsin, N. Padubnaya, G. Srinivasan, and C. P. DeVreugd, Appl. Phys. A **78**, 33 (2004).
[28] Assuming an effective demagnetization factor $N = 1/3$ for a randomly shaped domain.
[29] M. Belesi, I. Rousochatzakis, M. Abid, U. K. Rössler, H. Berger, and J.-Ph. Ansermet, arXiv:1204.3783v1.

Synthesis of Homogeneous Manganese-Doped Titanium Oxide Nanotubes from Titanate Precursors

Péter Szirmai,[§] Endre Horváth,[†] Bálint Náfrádi,[†] Zlatko Micković,[†] Rita Smajda,[†] Dejan M. Djokić,[†] Kurt Schenk,[‡] László Forró,[†] and Arnaud Magrez*,[†]

[†]Laboratory of Physics of Complex Matter, Ecole Polytechnique Fédérale de Lausanne, 1015 Lausanne, Switzerland
[‡]Institute of Physics of Biological Systems, Ecole Polytechnique Fédérale de Lausanne, 1015 Lausanne, Switzerland
[§]Department of Physics, Budapest University of Technology and Economics, PO Box 91, Budapest H-1521, Hungary

ABSTRACT: We report a novel synthesis route of homogeneously manganese-doped TiO_2 nanotubes in a broad concentration range. The scroll-type trititanate ($H_2Ti_3O_7$) nanotubes prepared by hydrothermal synthesis were used as precursors. Mn^{2+} ions were introduced by an ion exchange method resulting $Mn_xH_{2-x}Ti_3O_7$. In a subsequent heat treatment, they were transformed into $Mn_yTi_{1-y}O_2$, where $y = x/(3 + x)$. The state and the local environment of the Mn^{2+} ions in the precursor and final products were studied by the electron spin resonance (ESR) technique. It was found that the Mn^{2+} ions occupy two positions: the first having an almost perfect cubic symmetry while the other is in a strongly distorted octahedral site. The ratio of the two Mn^{2+} sites is independent of the doping level and amounts to 15:85 in $Mn_xH_{2-x}Ti_3O_7$ and to 5:95 in $Mn_yTi_{1-y}O_2$. SQUID magnetometry does not show long-range magnetic order in the homogeneously Mn^{2+}-doped nanotubes.
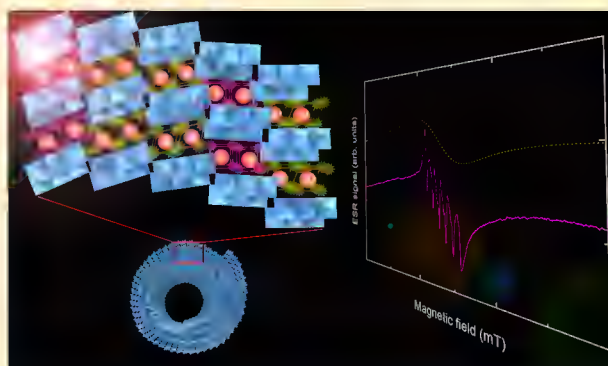
INTRODUCTION

Titanium dioxide has been extensively studied due to its high thermal and chemical stability, abundance, and environmental friendliness. This material is widely used in heterogeneous catalysis and photocatalysis, as white pigment in paints, food and cosmetic products, corrosion-protective coatings, and biocompatible layer of bone implants.[1] Nanostructured TiO_2 films are used as photoanode in solar-to-electric energy conversion devices such as dye-sensitized solar cells[2] (DSSCs), in gas sensors,[3] and in supercapacitors.[4] It is expected that a detailed study of the structural and electronic properties of TiO_2 will help in the understanding of the material's behavior as well as to improve the performances of the previously mentioned applications.[5,6]

Recently, TiO_2 nanotubes and nanowires have received a great deal of attention. These elongated structures possess large surface area and can be used to prepare novel 3D and highly crystalline structures exhibiting large porosity from which efficient DSSCs are built.[7] Titanate nanowires can serve as a scaffold for self-organization of organic molecules. Based on this property, high sensitivity optical humidity sensors with fast response time have been realized.[8] Furthermore, TiO_2 is a popular material in spintronics.[9] It is expected to show room temperature ferromagnetism when doped with transition metal ions.[10,11] TiO_2 thin films have shown this effect above 5% Mn substitutional doping.[12,13] A similar phenomenon has been observed at low doping level in bulk manganese-doped TiO_2 produced by sintering.[14] Ferromagnetism is explained on the basis of the bound magnetic polaron model. However, these results are the subject of controversy as ferromagnetism could arise from impurities, aggregation of doping or magnetic clusters.[15] These flaws could be the product of inhomogeneously prepared TiO_2 precursors or the result of segregation caused by the high-temperature synthesis process.[16] This ambiguity underscores the need to elaborate a reliable synthesis method for homogeneous doping of TiO_2 with transition metal ions.

Here we report a low-temperature synthesis route of homogeneously doped TiO_2 nanotubes (NTs) with Mn^{2+} ions using scroll-type trititanate ($Na_2Ti_3O_7$) nanotube precursor (Na-NTs) produced by an alkali hydrothermal treatment of TiO_2. These multiwalled nanotubes are composed of stepped or corrugated host layers of edge-sharing TiO_6 octahedrons having interlayer alkali metal cations. By ionic exchange, the alkali titanates can be easily modified into $Mn_xH_{2-x}Ti_3O_7$, a transition-metal-doped protonated titanate (MnH-NTs) with maximal concentration of about $x \sim 0.18$. A subsequent heat treatment transforms it into $Mn_yTi_{1-y}O_2$ (Mn-NTs) with $y = x/(x + 3)$. The concentration y reaches a maximum of 5.6 at. %. Here we focus on the spatial distribution of Mn^{2+} in nanotubular titanates and on their magnetic response by using X-ray diffraction (XRD), electron spin

resonance spectroscopy (ESR), and SQUID techniques. We found two Mn^{2+} positions in the structure with cubic and strongly distorted octahedral local symmetries. ESR and SQUID measurements do not show a long-range magnetic order.

■ EXPERIMENTAL METHODS

In a typical synthesis, 1 g of titanium(IV) oxide nanopowder (99.7% anatase, Aldrich) is mixed with 30 mL of 10 M NaOH (97%, Aldrich) solution. The mixture is then transferred to a Teflon-lined stainless steel autoclave (Parr Instrument Co.) and heated to 130 °C and kept at this temperature for 72 h. After the treatment, the autoclave is cooled down to room temperature at a rate of 1 °C min^{-1}. The obtained $Na_2Ti_3O_7$ product is then filtered and washed several times with deionized water and neutralized up to pH ≈ 6.5 with the appropriate amount of 0.1 M HCl solution (Merck). During this step, sodium exchange proceeds to the formation of $H_2Ti_3O_7$ nanotubes. The sample is finally washed with hot (80 °C) deionized water in order to remove any traces of NaCl. To dope $H_2Ti_3O_7$ nanotubes by Mn^{2+}, they are suspended in a $Mn(NO_3)_2·H_2O$ solution at 10 °C for 1 h. The suspension is subsequently filtered and washed with 500 mL of deionized water in order to remove the nonexchanged Mn^{2+} remaining in the solution. As a result, a solid $Mn_xH_{2-x}Ti_3O_7$ phase is obtained with x up to 0.18 (MnH-NTs). For Mn^{2+}-doped TiO_2 NTs, in the final step MnH-NTs undergo heat treatment at 400 °C in a reducing atmosphere (N_2/H_2) in order to prevent Mn^{2+} oxidation into higher oxidation states, and a single phase $Mn_yTi_{1-y}O_2$ is obtained (Mn-NTs).

The manganese content was determined by energy-dispersive X-ray spectroscopy (EDX). XRD measurements were performed in $\Theta/2\Theta$ geometry on powder samples using Cu Kα (λ = 1.540 56 Å) radiation. The morphology of the samples was examined by low-/high-resolution transmission electron microscopy (TEM/HRTEM). Electron spin resonance (ESR) measurements of the nanotubes were carried out in an X-band spectrometer in the 5−300 K temperature range. SQUID measurements were performed on a S600 magnetometer following the zero-field-cooled/field-cooled (ZFC/FC) magnetization measurements.

■ RESULTS AND DISCUSSION

In Figure 1, the manganese ion concentration of MnH-NTs assuming complete ion exchange (nominal) versus the equilibrium manganese concentration (incorporated) after the ion exchange is depicted based on EDX measurements. The line in Figure 1 is a fit to an exponential saturation model $a(1 - e^{-bx})$. It yields $a = 18(1)$ at. % saturation concentration and $b = 0.052(6)$ characteristic exchange ratio. This doping level and Mn^{2+} exchange efficiency are seen as characteristics to the described synthesis method.

The kinetics of alkali metal ion intercalation between the layers of titanate nanotubes and nanofibers from aqueous suspension has been thoroughly studied by Bavykin et al.[17] They found that the limiting stage of the process is likely to be the diffusion of ions inside the solid crystal which strongly depended on the length of the nanotubes. Here we focus on the elucidation of the state, local interaction, and spatial distribution of Mn^{2+} in nanotubular titanates and their derivatives after the steady-state concentration has been reached.
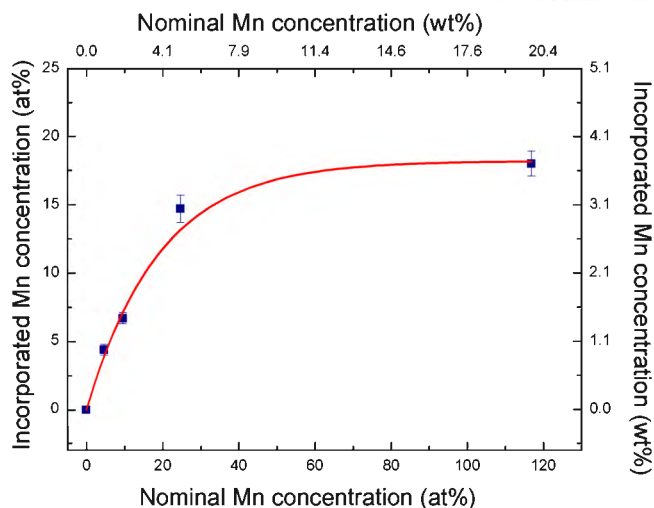
Figure 1. Nominal vs the incorporated Mn concentration ratio for the case of MnH-NTs. Line is a fit to an exponential saturation model $a(1 - e^{-bx})$ with $a = 18(1)$ at. % and $b = 0.052(6)$. The abbreviations contain the incorporated Mn concentration. The incorporated Mn concentration x of MnH-NT translates to $y = x/(x + 3)$ Mn concentration of Mn-NT upon heat treatment.

The powder XRD data measured on the MnH-NTs and Mn-NTs are given in Figure 2. The XRD pattern of the undoped,
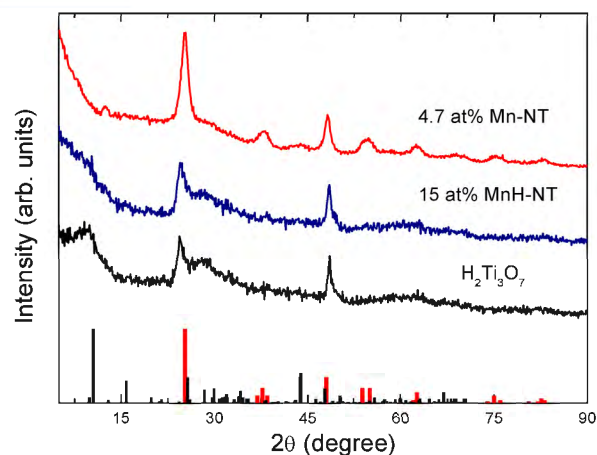
Figure 2. XRD spectra of undoped titanate ($H_2Ti_3O_7$) nanotubes, 15 at. % Mn-doped titanate nanotubes (15 at. % MnH-NT), and 4.7 at. % Mn-doped TiO_2 (4.7 at. % Mn-NT). The peak at $2\Theta = 13°$ in 4.7 at. % Mn-NT originates from the sample holder.

protonated titanate nanotubes can be indexed as the monoclinic trititanate ($H_2Ti_3O_7$) phase.[18,19] The characteristic reflection near $2\Theta = 10°$ is correlated with the interlayer distance d_{200} in the wall of nanotubes. XRD profile of the 15 at. % MnH-NT compared to the undoped, protonated sample ($H_2Ti_3O_7$) shows the weakening of the peak near $2\Theta = 10°$ upon the ion exchange. Similar weakening of this characteristic reflection was found by several authors.[20−22] This could be related to the distortion of crystalline order within the layers due to the ion-exchange.

The heat treatment of MnH-NTs in reduced atmosphere resulted in the creation of Mn-NTs where TiO_2 exists in anatase phase TiO_2 (JCPDS 84_1285). No other peaks of minority phases as manganese titanate, metallic manganese, or its oxides have been observed.

In principle, in a solid the ion-exchange positions are spatially well-defined places. Therefore, we expect that the ionic exchange across the titanate nanoscrolls ensures that manganese ions do not create aggregates in the MnH-NT structure. Furthermore, the relatively low-temperature heat treatment process for making the Mn-NTs suppresses the diffusion and aggregation of Mn ions.

The TEM images of 4.7 at. % Mn-NT produced under heat treatment at 400 °C ascertain the prevailing tubular morphology of the doped TiO$_2$ material. Unlike the pristine trititanate nanotubes, the manganese-doped TiO$_2$ nanotubes are crystallized together near the contact point during the heat treatment, which results in highly aggregated nanotube secondary structure (Figure 3c,d). The effect of calcination
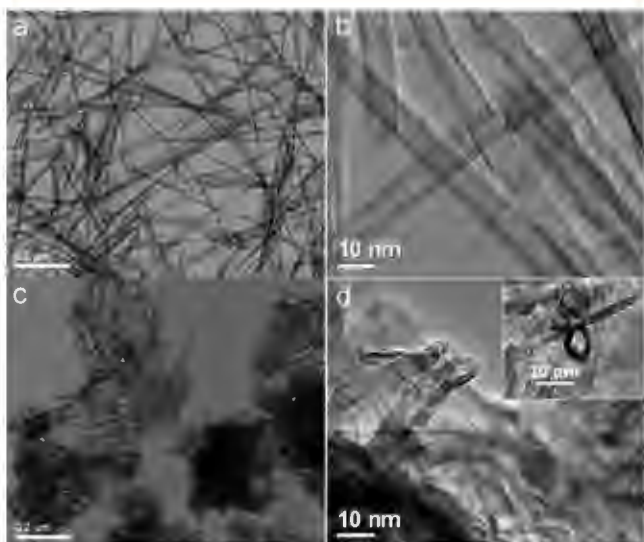
Figure 3. (a) TEM and (b) HRTEM image of pristine titanate nanotubes. (c) TEM and (d) HRTEM image of a 4.7 at. % Mn-NTs produced under heat treatment of MnH-NTs at 400 °C in a reducing atmosphere.

on the morphological evolution and phase transition of protonated titanate nanotubes has been studied by many researchers. It has been reported that upon calcination the gradual interlayer dehydration leads to a titanate-to-anatase crystal phase change accompanied by the transformation of the tubular shape into nanorods. Electron microscopic investigations revealed that the nanotubes still retain the tubular shape at 350−400 °C.[23]

Neither XRD nor TEM measurements find segregated Mn-rich phases in the studied materials. Nevertheless, these techniques are limited to identifying about percent concentration minority phases. ESR, in contrast, is a dopant-specific spectroscopic technique that provides highly detailed microscopic information about the oxidation state and the local environment of the substituent paramagnetic ions in the crystal on ppm levels in principle. Furthermore, ESR is sensitive to the interactions between the paramagnetic ions. ESR spectroscopy has proven to be a very useful method for evaluating success in the synthesis of colloidal Mn^{2+}-doped semiconductor nanocrystals.[24,25] The theoretical background of ESR spectra of a large number of nanocrystals doped with Mn^{2+} has now been largely developed.[26,27] The spin Hamiltonian that describes the spectra of Mn^{2+} is

$$H = H_Z + H_{CF} + H_{HF} + H_{e-e}$$

where first is the Zeeman term and second is the interaction with crystal electric fields. The third term describes the hyperfine coupling between the $S = 5/2$ electron spin and $I = 5/2$ nuclear spin of Mn^{2+}. The last term is the interaction between neighboring Mn^{2+} ions.

Characteristic ESR spectra of MnH-NTs are given in Figure 4a. They confirm the presence of magnetically isolated Mn^{2+}
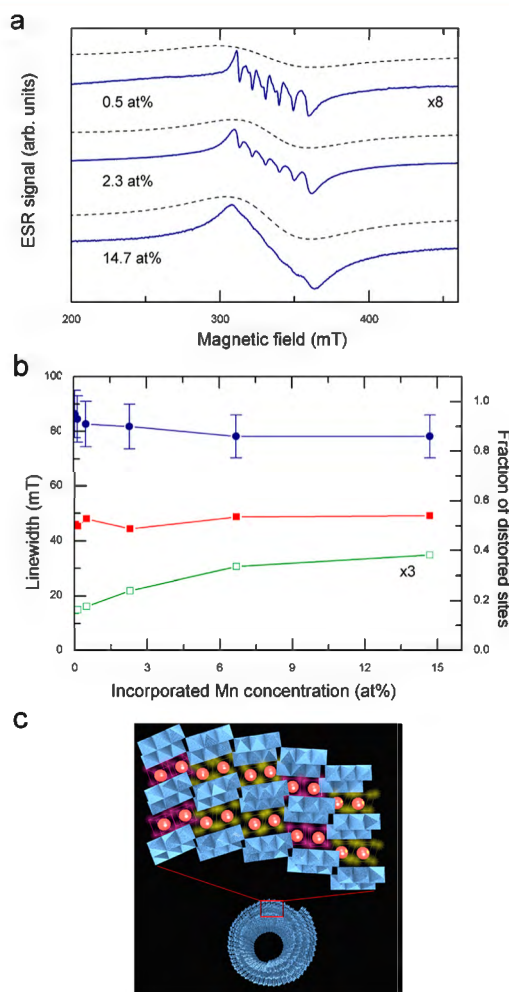
Figure 4. (a) Room-temperature ESR measurements on 0.5, 2.3, and 14.7 at. % MnH-NTs. Spectra are superposition of two ESR signal: a narrow sextet and a 48 mT broad line. Dashed lines are fits to the broad component. (b) ESR line width of individual hyperfine lines (□) and of the broad component (■) as a function of Mn concentration. Mn concentration dependence of the fraction of distorted Mn sites (●). (c) Schematic view of the tubular structure of MnH-NTs. Purple and yellow tetrahedrons represent slightly and strongly distorted Mn sites, respectively.

ions in the titanate nanotube structure. The spectra at all Mn^{2+} concentrations consist of two signals. One set of sextet lines dominates the spectra at low Mn^{2+} concentrations. In contrast, a 48 mT broad line is more pronounced at high Mn^{2+} concentrations.

The sextet signal is characteristic of a hyperfine splitting of ^{55}Mn with $g = 2.001(1)$ g-factor and $A_{iso} = 9.1$ mT hyperfine coupling constant. This spectrum corresponds to allowed ($\Delta m_I = 0$) and forbidden ($\Delta m_I = \pm 1$) hyperfine transitions between the Zeeman sublevels $m_s = \pm 1/2$. It is characteristic to Mn^{2+}
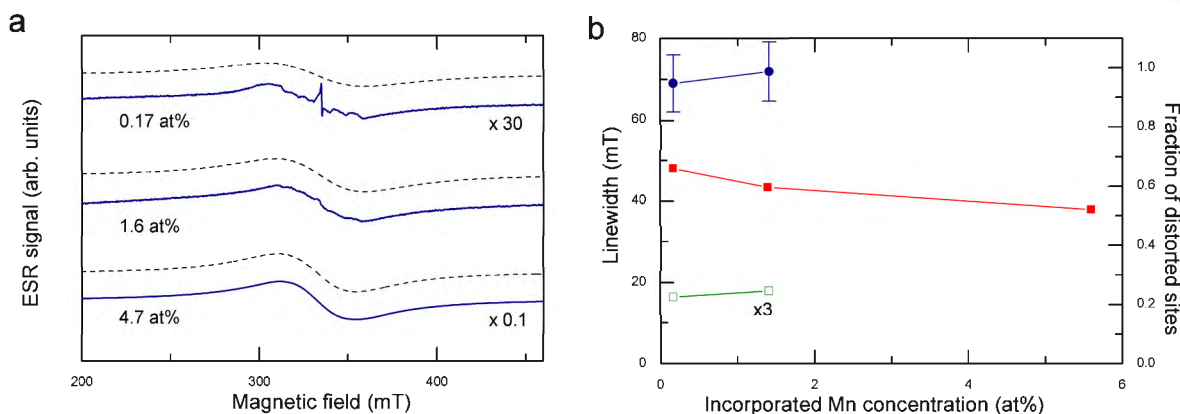
Figure 5. (a) Room-temperature ESR measurements on 0.17, 1.6, and on 4.7 at. % Mn-NTs. Spectra are superposition of three ESR signals: a narrow sextet, a 46 mT broad line (dashed lines), and the SETOV. (b) ESR line width of individual hyperfine lines (□) and of the broad component (■) as a function of Mn concentration. Mn concentration dependence of the fraction of distorted Mn sites (●). At Mn concentration higher than 1.6 at. %, the strong broadening of the sextet lines impedes the sextet lines to be resolved. This explains the absence of data for the line width and fraction of distorted sites.

ions in octahedral crystal fields. However, since forbidden transitions are observable, Mn^{2+} ions do not occupy strictly cubic sites, as strictly cubic centers have zero probability of forbidden transitions, but the distortion relative to the cubic symmetry is small. The hyperfine coupling constant A_{iso} is essentially independent of the Mn^{2+} concentration. The width of the individual hyperfine lines increases by increasing the Mn^{2+} concentration (Figure 4b). Assuming only the dipole–dipole interaction between Mn^{2+} ions as an origin of the broadening following ref 28, the calculation yields $d_{Mn-Mn} = 1$ nm average distance at 15 at. %. This is a lower bound for the average Mn–Mn distance.

The broad Lorentzian signal around $g \approx 2$ (dashed line in Figure 4c) is superimposed to the narrow hyperfine sextet. The intensity of this broad line increases with the initial Mn^{2+} content; thus, it is intrinsic to ion-exchange. The 48 mT width of the broad line is essentially independent of Mn^{2+} concentration. It is about 5 times the $A_{iso} = 9.1$ mT, which is characteristic of Mn^{2+} ions located in strongly distorted octahedral sites. In powdered polycrystalline systems non-central transitions ($m_S \neq 1/2$) are always broadened and unresolved. This is due to the strong angular dependence of the lines and a parameter distribution in both hyperfine- and fine-coupling parameters. Dipolar interactions further broaden the lines. As previously determined, dipole–dipole interaction between Mn^{2+} ions broadens the sextuplet lines corresponding to the central $\Delta m_I = 1$ transition. However, dipole–dipole interaction is not strong enough to smear out the hyperfine structure and thus produce the broad line. These findings are characteristic of Mn^{2+}-doped nanocrystals like Mn:CdS and Mn:TiO$_2$.[24,25]

The width of the broad line and the ratio $I_{broad}/(I_{broad} + I_{hyperfine}) = 0.85$ are found to be independent of the incorporated Mn^{2+} concentration for MnH-NTs (Figure 4c). Here, I_{broad} is the ESR intensity of the broad line and $I_{hyperfine}$ is the ESR intensity of the sextuplet. This also confirms that the broad Lorentzian curves in Figure 4 originate from distorted Mn^{2+} sites.

The question to be answered here is, what is the origin of the two different ion-exchange positions in the TiO$_6$ octahedra built host matrix? We speculate that the otherwise defectless layers of TiO$_6$ ocatahedra are not lined up in perfect registry due to the rolled up morphology of the trititanate nano-

tubes.[29,30] Along this line, the 15% doping-independent fraction of high-symmetry Mn^{2+} positions are more likely a consequence of the incommensurate facing of titanium-centered octahedrons in neighboring walls due to the rolled-up structure of trititanate nanotubes (Figure 4b). Another possible explanation would be that structural imperfections (i.e., defects) have formed during the oriented crystal growth of the nanotubes, when these TiO$_6$ building bricks were arranged in space.[29]

During heat treatment, MnH-NTs undergo dehydration to yield Mn-NTs. During the process, $Mn_xH_{2-x}Ti_3O_7$ is transformed into $Mn_yTi_{1-y}O_2$. Mn/Ti stoichiometry remains constant, so that $y = x/(x + 3)$. For example, 5.6 at. % Mn-NTs originates from 18 at. % MnH-NTs.

Figure 5 depicts ESR on 0.17, 1.6, and 4.7 at. % Mn-NTs obtained after thermal treatment of the corresponding MnH-NTs. The spectra show the coexistence of a sextuplet and a broad Lorentzian line around $g \approx 2$ originating from Mn^{2+} ions similarly to Mn-NTs. Furthermore, a narrow symmetric line close to the free electron g-factor ($g = 2.003$) was also observed. This additional narrow line at $g = 2.003$ can be assigned to the single-electron-trapped oxygen vacancies (SETOV).[18,31,32] The SETOV signal is induced by breaking of the Ti–OH bonds which follows the dehydration upon heat treatment. This is characteristic to all annealed titania nanotubes.[18,24] The line width of the SETOV signal is $\Delta B_{pp} = 0.5$ mT in accordance with the literature.[18,33] As already reported (in the 140–300 K temperature range),[33] ESR intensity of the SETOV satisfies the Curie law, confirming the presence of localized electrons. ESR measurements on the undoped TiO$_2$ (not shown) reveal the presence of the SETOV as well. At doping levels lower than 0.17 at. % (not shown), the SETOV signal dominates the spectra, but at all doping levels the SETOV concentration remains in the ppm level. At high Mn concentration, the broad Lorentzian curve overwhelms other signals.

The ESR intensity is essentially the same before and after the heat treatment of MnH-NTs. This indicates that Mn ions preserve their 2+ valence state during the heat treatment and Mn-NT formation. Furthermore, it is evidenced that the Mn^{2+} distribution remains homogeneous, and no Mn^{2+} clustering occurs during heat treatment. Similarly to MnH-NTs, the broad ESR signal stems from Mn^{2+} ions in distorted sites while the sextuplet at $g = 2.001$ proves that some Mn^{2+} ions occupy high

symmetry sites.[24,25] However, due to the strong broadening of the sextet lines by increasing Mn concentration, the sextet lines were only resolved at low Mn concentrations. The hyperfine coupling constant is $A_{iso} = 12$ mT in the case of Mn-NT. The ratio of the two different Mn^{2+} lines is 5:95, which indicates that most of the Mn^{2+} ions occupy distorted sites (Figure 5b). The ratio increases relative to the MnH-NTs as a consequence of the different tube geometry.

ESR found the Mn-NT samples paramagnetic without a trace of magnetically ordered minority phase. However, X-band ESR is not always detectable on magnetically long-range ordered systems; thus, to further characterize the magnetic properties of Mn-NTs, SQUID measurements are required. Figure 6 depicts
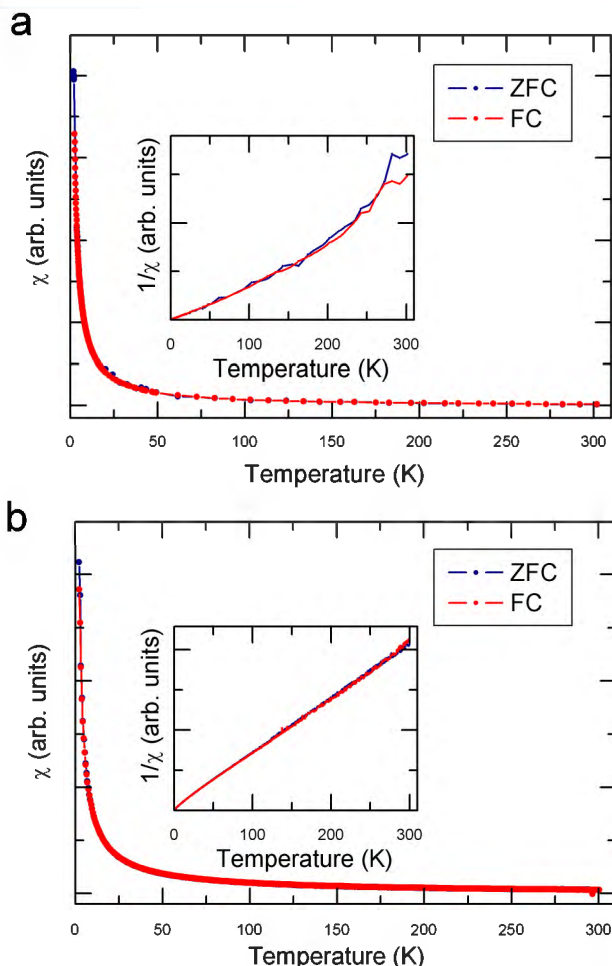
Figure 6. ZFC/FC SQUID measurements (a) for 0.17 at. % and (b) for 4.7 at. % Mn-NT. For FC, the applied field was 0.1 T. In the main panel the susceptibility (χ) is shown as a function of temperature. Inset presents $1/\chi$ as a function of temperature.

the ZFC/FC SQUID measurements for 0.17 and 4.7 at. % Mn-NT. The bulk susceptibility is of a Curie-like paramagnetic temperature dependence. This is further emphasized plotting $1/\chi$ as a function of temperature in the inset of Figure 6. The SQUID susceptibility is in agreement with the ESR intensity of the broad Lorentzian curves assigned to Mn^{2+} ions.

Earlier reports suggest that ferromagnetism in the fourth naturally occurring TiO_2 polymorph called $TiO_2(B)$ is induced by the SETOV.[34] It has been proposed that the ferromagnetic coupling is induced through the F-center exchange mechanism.[35] Our measurements do not contradict these results. ESR

intensity, i.e., the spin susceptibility of the SETOV, is negligible compared to that of Mn^{2+} ions; thus, the paramagnetic behavior of 0.17 at. % Mn-NT is provoked by Mn^{2+} ions.

■ CONCLUSION

We have prepared homogeneously Mn^{2+} substituted $H_2Ti_3O_7$ (MnH-NTs) nanotubes by ion exchange. Two symmetrically different ion-exchange sites are identified by ESR spectroscopy. About 15% of the substituted Mn^{2+} ions occupy cubic sites, whereas 85% shows strongly distorted octahedral local symmetry. Low-temperature heat treatment transforms the titanate structure to $Mn_yTi_{1-y}O_2$ nanotubes (Mn-NTs) while it maintains the homogeneity of the Mn^{2+} substitution. We report on the absence of ferromagnetic properties of single phase $Mn_yTi_{1-y}O_2$ nanotubes which favors the scenario that ferromagnetism is of extrinsic origin in $Mn_yTi_{1-y}O_2$.

The synthesis method presented here opens a novel pathway to synthesizing high-quality homogeneously diluted magnetic semiconducting TiO_2 nanotube powders. Besides the commonly used doping techniques employing vapor deposition or ion bombardment, the ion-exchange-based protocol could be used as a cost-effective, alternative way to obtain materials that cannot be prepared by heating mixtures of different precursors. Whereas these days vacuum deposition techniques are capable of controlling carrier concentrations moderately well, wet chemical methods to electronic doping are only now being developed and still suffer from many of the above-mentioned challenges. Here we have also demonstrated that ESR-active, ion-exchangeable cations can be seen as local probes to extract so far undetected information about the atomic level structure of nanotubular titanates and their derivatives.

The illustrated synthesis method could have long-term importance for the potential use of the ion-exchangable titanate nanotube and nanowire powders in the DMS (diluted magnetic semiconductor) field.

■ AUTHOR INFORMATION

Corresponding Author
*E-mail arnaud.magrez@epfl.ch.
Notes
The authors declare no competing financial interest.

■ REFERENCES

(1) Diebold, U. *Surf. Sci. Rep.* **2003**, *48*, 53−229.
(2) O'Regan, B.; Grätzel, M. *Nature* **1991**, *353*, 737−740.
(3) Garzella, C.; Comini, E.; Tempesti, E.; Frigeri, C.; Sberveglieri, G. *Sens. Actuators, B* **2000**, *68*, 189−196.
(4) Fabregat-Santiago, F.; Randriamahazaka, H.; Zaban, A.; Garcia-Canadas, J.; Garcia-Belmonte, G.; Bisquert, J. *Phys. Chem. Chem. Phys.* **2006**, *8*, 1827−1833.
(5) Forró, L.; Chauvet, O.; Emin, D.; Zuppiroli, L.; Berger, H.; Lévy, F. *J. Appl. Phys.* **1994**, *75*, 633−635.
(6) Jacimovic, J.; Vaju, C.; Magrez, A.; Berger, H.; Forró, L.; Gaál, R.; Cerovski, V.; Zikic, R. *Europhys. Lett.* **2012**, *99*, 57005.
(7) Tétreault, N.; Horváth, E.; Moehl, T.; Brillet, J.; Smajda, R.; Bungener, S.; Cai, N.; Wang, P.; Zakeeruddin, S. M.; Forró, L.; Magrez, A.; Grätzel, M. *ACS Nano* **2010**, *4*, 7644−7650.
(8) Horváth, E.; Ribic, P. R.; Hashemi, F.; Forró, L.; Magrez, A. *J. Mater. Chem.* **2012**, *22*, 8778−8784.

(9) Ogale, S. B. *Adv. Mater.* **2010**, *22*, 3125−3155.

(10) Matsumoto, Y.; Murakami, M.; Shono, T.; Hasegawa, T.; Fukumura, T.; Kawasaki, M.; Ahmet, P.; Chikyow, T.; Koshihara, S.-y.; Koinuma, H. *Science* **2001**, *291*, 854−856.

(11) Coey, J. M. D.; Venkatesan, M.; Fitzgerald, C. B. *Nat. Mater.* **2005**, *4*, 173−179.

(12) Xu, L.; Xing, X.; Yang, M.; Li, X.; Wu, S.; Hu, P.; Lu, J.; Li, S. *Appl. Phys. A: Mater. Sci. Process.* **2010**, *98*, 417−421.

(13) Sharma, S.; Chaudhary, S.; Kashyap, S. C.; Sharma, S. K. *J. Appl. Phys.* **2011**, *109*, 083905.

(14) Tian, Z. M.; Yuan, S. L.; Wang, Y. Q.; He, J. H.; Yin, S. Y.; Liu, K. L.; Yuan, S. J.; Liu, L. *J. Phys. D: Appl. Phys.* **2008**, *41*, 055006.

(15) Coey, J. *Curr. Opin. Solid State Mater. Sci.* **2006**, *10*, 83−92.

(16) Nakajima, T.; Sheppard, L. R.; Prince, K. E.; Nowotny, J.; Ogawa, T. *Adv. Appl. Ceram.* **2007**, *106*, 82−88.

(17) Bavykin, D. V.; Walsh, F. C. *J. Phys. Chem. C* **2007**, *111*, 14644−14651.

(18) Cho, J.; Yun, W.; Lee, J.-K.; Lee, H.; So, W.; Moon, S.; Jia, Y.; Kulkarni, H.; Wu, Y. *Appl. Phys. A: Mater. Sci. Process.* **2007**, *88*, 751−755.

(19) Kijima, T. *Inorganic and Metallic Nanotubular Materials: Recent Technologies and Applications*; Topics in Applied Physics; Springer: New York, 2010; pp 17−32.

(20) Wang, X. W.; Gao, X. P.; Li, G. R.; Gao, L.; Yan, T. Y.; Zhu, H. Y. *Appl. Phys. Lett.* **2007**, *91*, 143102.

(21) Morgado, E.; Marinkovic, B. A.; Jardim, P. M.; de Abreu, M. A.; da Graça C. Rocha, M.; Bargiela, P. *Mater. Chem. Phys.* **2011**, *126*, 118−127.

(22) Sun, X.; Li, Y. *Chem.—Eur. J.* **2003**, *9*, 2229−2238.

(23) Zhang, L.; Lin, H.; Wang, N.; Lin, C.; Li, J. *J. Alloys Compd.* **2007**, *431*, 230−235.

(24) Counio, G.; Esnouf, S.; Gacoin, T.; Boilot, J. *J. Phys. Chem.* **1996**, *100*, 20021−20026.

(25) Saponjic, Z. V.; Dimitrijevic, N. M.; Poluektov, O. G.; Chen, L. X.; Wasinger, E.; Welp, U.; Tiede, D. M.; Zuo, X.; Rajh, T. *J. Phys. Chem. B* **2006**, *110*, 25441−25450.

(26) Allen, B. T. *J. Chem. Phys.* **1965**, *43*, 3820−3826.

(27) Misra, S. K. *Physica B* **1994**, *203*, 193−200.

(28) Van Vleck, J. H. *Phys. Rev.* **1948**, *74*, 1168−1183.

(29) Kukovecz, A.; Hodos, M.; Horváth, E.; Radnóczi, G.; Kónya, Z.; Kiricsi, I. *J. Phys. Chem. B* **2005**, *109*, 17781−17783.

(30) Gateshki, M.; Chen, Q.; Peng, L.-M.; Chupas, P.; Petkov, V. *Z. Kristallogr.* **2007**, *222*, 612−616.

(31) Serwicka, E.; Schlierkamp, M.; Schindler, R. *Z. Naturforsch., Sect. A: J. Phys. Sci.* **1981**, *36*, 226−232.

(32) Serwicka, E. *Colloids Surf.* **1985**, *13*, 287−293.

(33) Cho, J.; Seo, J.; Lee, J.-K.; Zhang, H.; Lamb, R. *Physica B* **2009**, *404*, 127−130.

(34) Huang, C.; Liu, X.; Kong, L.; Lan, W.; Su, Q.; Wang, Y. *Appl. Phys. A: Mater. Sci. Process.* **2007**, *87*, 781−786.

(35) Coey, J. M. D.; Douvalis, A. P.; Fitzgerald, C. B.; Venkatesan, M. *Appl. Phys. Lett.* **2004**, *84*, 1332.

Finite Element Method simulation study of heat propagation in a novel YBCO-based Coated Conductor for resistive fault current limiters

Dejan M. Djokić [a, b, *], Louis Antognazza [a], Michel Decroux [a]

[a] Department of Quantum Matter Physics, University of Geneva, CH-1211, Geneva 4, Switzerland
[b] Institute of Chemical Sciences and Engineering, Ecole Polytechnique Fédérale de Lausanne, CH-1015, Lausanne, Switzerland

ABSTRACT

YBCO-based Coated Conductors (CCs) used for applications in Resistive Superconducting Fault Current Limiters (RSFCLs) are well known to have fairly low values of Normal Zone Propagation Velocity (NZPV) during quench avalanche phenomena. Slow propagating normal zones result in the Joule heating localization that may lead to permanent damages of the devices. A marked improvement can be made by enhancing the thermal conductivity of the underlying substrate of YBCO-based CC. We propose an electrically isolated multilayered substrate containing a micron scaled copper layer on the top of a massive fused silica substrate. In order to compute NZPV values, Finite Element Method (FEM) simulations have been performed in COMSOL Multiphysics on a 3D meander-like configuration of such a novel YBCO-based RSFCL. The simulation results have demonstrated an enhancement in NZPVs by promoting the novel RSFCL multistructure as a radical alternative to earlier studied cases. The relevance of copper thickness variation has also been examined.

© 2016 Elsevier Masson SAS. All rights reserved.

1. Introduction

For industrial purposes, RSFCLs used in large scale applications must satisfy two important but competing requirements: (*i*) desired level of thermal stability during operation on one hand side, and on the other, (*ii*) managing quench propagation severities [1—3]. Unlike their low temperature kin, high temperature YBCO-based CCs for RSFCLs relatively successfully meet the first requirement by virtue of their high operating temperatures, at which no substantial thermal instabilities occur due to the amount of released heat [4]. The weak point of such systems, however, lies in their slowly propagating normal zones with velocities as low as few cm/s [5]. Consequently, use of YBCO-based CCs for RSFCLs may entail a risk of damages because of slowly propagating hot spot proliferations [6,7]. One remarkable solution was reached in RSFCLs made of YBCO on sapphire substrates [8] that has not been industrially acknowledged given the unprofitably high cost. Scientific and engineering communities are investing considerable computational and experimental efforts to provide the most acceptable YBCO-based CC solution to the market [9]. For that reason, it is crucial to understand operationality of novel designs of YBCO-based RSFCLs during quench events [10].

This account presents a computational approach to resolving the quench propagation issue, which is generic to YBCO-based CCs. Our central focus is to improve the thermal property of such devices, as well as, to optimize their geometry in order to guarantee a safe grid integration. We have numerically studied the advantage of multilayered structures grown on a cheap fused silica (SiO^2) with thickness of nearly 100 μm. The multilayer is composed of a several micron thick copper layer used to ameliorate the thermal conductivity, together with a couple of thin layers with the aim of avoiding eventual inter-diffusion events. Quasi-adiabatic mitigation of the thermal influence of the massive lowermost substrate makes the overall heat propagation dominated by the properties of the thermally conductive copper layer. The increased dimensionality up to a meander configuration, on the other hand, leads to the temperature homogenization over the system since there is an extra front of propagation to homogenize the heat generation in such geometries [11—13], thus resulting in thermodynamic stability.

We have also addressed the question of how much copper layer is sufficient for an effective decoupling of the YBCO-based CC from the thermally inertial SiO^2. The proposed numerical model assumes a current transport in YBCO-based CCs only and the existence of a Joule heating source due to a local perturbation across the coated

* Corresponding author. Department of Quantum Matter Physics, University of Geneva, CH-1211, Geneva 4, Switzerland.
E-mail address: dejan.djokic@epfl.ch (D.M. Djokić).

superconductor. Furthermore, we have investigated the variation of copper layer thickness that has turned out to be relevant for both heat propagation improvement and thermal stability. The simulation results have shown a remarkable improvement as compared to the cases considered in the preceding studies [13,14].

2. Computational details

2.1. Description of an idealized structure

A 3D sketch of the novel YBCO-based RSFCL structure is given in Fig. 1. The structure is partitioned into two major components. The first is a multilayered substructure composed of a $\delta_{SiO_2} = 100 \ \mu m$ thick fused silica substrate which is depicted in light blue (see Fig. 1), and a several micron thick (δ_{Cu} varied from nearly 0 up to 10 μm) deposited copper layer represented in reddish brown colour (Fig. 1). The copper deposition is effected by placing a submicron sized interlayer of TiO^2 and Nb on the thick fused silica in order to prevent undesirable interdiffusion processes. The geometry of such extremely fine interlayers is found to have no significant influence on the computational results. However, their thermal properties are captured in a 1D parametric form that will be discussed later throughout the text.

The second part of the structure consists of three coated superconducting lines (violet colour in Fig. 1). The lines are electrically insulated from the underlying copper so that the electric current can pass only through them. The isolation between YBCO and Cu is guaranteed by the existence of buffer layers made of both MgO and hastelloy which are used for avoiding the copper contamination. Due to their fine thicknesses, the buffer layers were computationally treated in the same manner as the Nb/TiO^2 interlayers (1D parameter). The entire structure is immersed into a thermal bath of liquid nitrogen to ensure the reservoir temperature of 77 K.

Each line is L = 20 mm long, d = 6 mm large, $\delta_{Ag} + \delta_{YBCO} = 340$ nm thick, and consists of $\delta_{YBCO} = 300$ nm thick superconducting YBCO coated with $\delta_{Ag} = 40$ nm of silver on the top. The three lines are separated in space by 400 μm. Their experimental realization is envisaged in a meander configuration [15]. However, without loss of generality we will treat only the three geometrically isolated lines which the current is passing through. Such approach considerably simplifies the 3D time consuming simulations as a result of the implementation of symmetry boundary conditions.

Being piloted by the simulation outcomes, the experimental completion of the novel YBCO-based RSFCL structure is still well under way [16]. Most conventionally, one employs three techniques to build up such a novel RSFCL: (1) DC magneto-sputtering system for the multilayer depositions, (2) ion-beam assisted deposition for bi-axially alignment of the MgO template, and (3) co-evaporation technique for silver coating and deposition growth of the YBCO thin film. Pure silver coatings, which are benign to YBCO and do not oxidize, have so far proven difficult to sharply texture. However, fairly thin silver coatings of nearly 40 nm seem very promising in settling the issue with silver purity [17].

2.2. Description of the heat transfer model

In order to investigate the heat transfer processes in the present RSFCL, we have carried out time dependent FEM simulations using COMSOL Multiphysics. It stands for a commercial software which is based on advanced numerical methods for modelling and simulating physics related problems. Specifically, the time dependent differential equations were solved using the Comsol Multiphysics (4.3b) simulation program on a Windows 7 platform: Intel Core i7 PC of 3.4 GHz with 12 GB RAM. In Comsol the time-step adaptation of higher order backward differentiation formula was used with the direct multi-frontal massively parallel sparse direct solver. The number of degrees of freedom solved for the most optimal copper thickness (~µm) is on the order of a half of a million, while the related simulation has been found the shortest having taken around 750 min. The studied geometry (Fig. 1) is implemented in Heat Transfer Module. The heat source is generated in the middle line only and it is due to the Joule heating initialized inside a small defected part of YBCO (Fig. 2). For that purpose, its critical current density value is locally reduced down as $J_{C77}^{def} \rightarrow 0$ in the defect area. The remaining two lines contain no such imperfections. The subscript of 77 refers to the measurement at liquid nitrogen temperature in the absence of magnetic field.

Guided by some of the earlier works on the YBCO-based RSFCLs [8,10,13,14], the deposited superconducting YBCO layers are assumed to have the critical temperature of $T_c = 90$ K and critical current density of $J_{C77} = 2$ MA/cm^2, while the electric leads are attached to the silver layer only, carrying an operational DC current density of $J = 2.5$ MA/cm^2. These assumptions are prone to an eventual redefinition which will fit the upcoming findings of the ongoing experiment [16]. In addition, our guess on the critical current density at 77 K is corroborated with measurements published in a relatively recent work [18] which demonstrates the realization of high critical current density $J_C > 2$ MA/cm^2 at 77 K for

Fig. 1. Novel RSFCL structure composed of fused silica SiO^2 (blue layer), copper Cu (reddish brown layer), together with three coated superconducting lines Ag + YBCO on the top (depicted in violet). Vertical coupling goes via (1) thin buffer-layer between Ag + YBCO and Cu, and (2) thin inter-layer between Cu and SiO^2, both coloured in black. The electric current passing only through the lines is plotted in arrows. The length of the lines is denoted with L. The aspect ratio does not correspond to the proportions of the realistic structure. (For interpretation of the references to colour in this figure legend, the reader is referred to the web version of this article.)
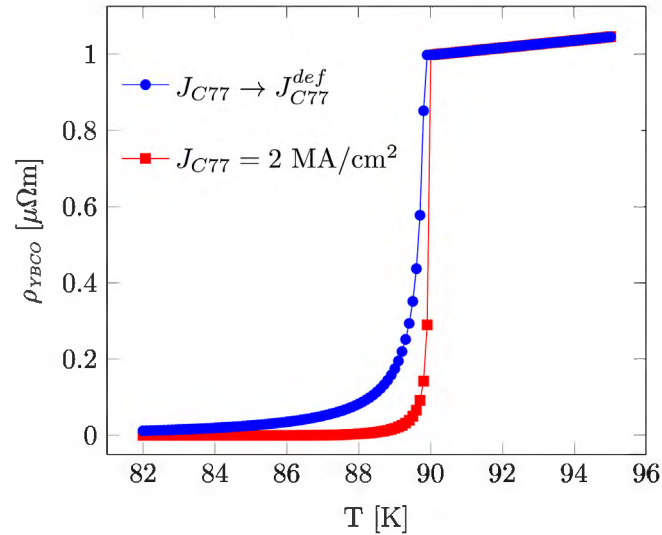

Fig. 2. Cross section of the middle coated superconducting line along its length L. The superconducting YBCO (violet) as thick as $\delta_{YBCO} = 300$ nm is coated with $\delta_{Ag} = 40$ nm of silver (gray). Initially, the current J is bypassing a small defect created deliberately in the centre of the YBCO layer ($\Delta L \ll L$). The critical current density of the defected YBCO part is much lower than that of the rest of the superconductor ($J_{C77}^{def} \ll J_{C77}$), driving the defect into a normal state immediately. (For interpretation of the references to colour in this figure legend, the reader is referred to the web version of this article.)

YBCO coatings on Cu tapes.

It is a common wisdom that the real RSFCL applications are designed for AC grid current limitations. However, the typical thermal times of both diffusive and superconducting transition assisted heat propagations [19] are much shorter than the standard AC period of 20 ms (ν = 50 Hz). This justifies a DC current approach. Once the DC electrical current is switched on, the defected block in the centre of the middle line immediately reaches its normal state. It thereby becomes the trigger for a hot spot proliferation spreading along and sidewise the line. The current density is shared in the Ag-coated YBCO (J_{Ag} in Ag stabilizer and J_{YBCO} in YBCO) as is shown in Fig. 2. Apart from the defect, the current is initially flowing through the entire superconductor. The situation changes latter on as the size of the normal state starts to thermally conquer the rest of the YBCO. The sharing is determined by both silver and YBCO resistivities: $\rho_{Ag}(T)$ and $\rho_{YBCO}(T,J_{C77};J_{YBCO})$. The former depends only on temperature and was borrowed from the COMSOL material library, whereas the latter depends not only on temperature but also on the critical current density (either J_{C77} or J_{C77}^{def}), as well as, the operational current density (J_{YBCO}) passing through the superconductor. Following the Ginzburg-Landau formulation of flux flow below T_c [2], the complex dependence of YBCO resistivity can be written down as follows

$$\rho_{YBCO}(T,J_{C77};J_{YBCO}) =$$

$$\rho_0 \left(\frac{J_{YBCO}}{J_{C77}} \frac{\left(1 - \left(\frac{77}{90}\right)^2\right)\sqrt{1 - \left(\frac{77}{90}\right)^4}}{\left(1 - \left(\frac{T}{T_c}\right)^2\right)\sqrt{1 - \left(\frac{T}{T_c}\right)^4}} - 1 \right)^n, \quad (1)$$

where ρ_0 = 3.2 nΩ m represents the equivalent electrical resistivity at $2J_{C77}$, while n = 1.6 and stands for the order of the power law. Both parameters must feature the properties of the YBCO for a given underlying substrate. Yet, ρ_{YBCO} for $T{\geq}T_C$ is extrapolated in a way that it depends linearly on temperature up to a value of 11.5 μΩ m at 1200 K. See Fig. 3 for visualization of ρ_{YBCO}. In what follows we give an account of how the explicit J_{YBCO} dependence can be bypassed in ρ_{YBCO}.

For simplicity, we have not considered the influence of the electrical resistance of YBCO-Ag interface, that might nevertheless be a subject of a future study. Moreover, it was evidenced [20] that the contact resistivity of YBCO-Ag has quite a low value of nearly 10^{-10} Ω cm². This backs the assumption that the electric fields along both YBCO and Ag stabilizer remain equal all the time so that the current density J_{YBCO} in YBCO can be calculated as

$$J_{YBCO}^{(i+1)}(T,J_{C77}) = \frac{\rho_{Ag}(T)}{\chi\rho_{Ag}(T) + \rho_{YBCO}\left(T,J_{C77};J_{YBCO}^{(i)}\right)}J, \quad (2)$$

where $\chi{\equiv}\delta_{YBCO}/\delta_{Ag}$. J_{YBCO} is computed iteratively until the convergence is reached for given T and J_{C77}. One immediately notices that the spatial dependence of J_{YBCO} is hidden behind temperature's. For that reason, it is necessary to delineate the so-called map of the current sharing regions. These are local regions in the coated superconductor with the uniformly averaged local temperatures. The map is automatically formed in COMSOL software and exactly coincides with the mesh discretization. Each mesh element of infinitesimal small length h along L with temperature T is assigned a value of Joule heating function, $Q(T,J_{C77})$, which is expressed in W/m³. This function can be readily calculated using the circuit laws of Kirchhoff and Ohm for two local resistors connected in parallel. Namely, it follows from $(I_{Ag}^2 R_{Ag} + I_{YBCO}^2 R_{YBCO})/(hd(\delta_{Ag} + \delta_{YBCO}))$, with $R_{Ag,YBCO} = \rho_{Ag,YBCO} \times h/(d\delta_{Ag,YBCO})$, $I_{Ag,YBCO} = J_{Ag,YBCO} \times (d\delta_{Ag,YBCO})$, and $I_{Ag} + I_{YBCO} = J \times (d\delta_{Ag})$ as can be concluded from Fig. 2. The Joule heating function therefore reads as

$$Q(T,J_{C77}) = \frac{J^2}{1+\chi}\left(\eta^2\rho_{Ag} + \frac{(1-\eta)^2}{\chi}\rho_{YBCO}\right), \quad (3)$$

where $\eta{\equiv}J_{Ag}/J$ represents the current sharing function with respect to the silver, as is given in Fig. 4. Another spatial dependence of $J_{YBCO}(T,J_{C77})$ and $Q(T,J_{C77})$ is encapsulated within J_{C77} which varies over the superconductor. It takes on J_{C77} = 2 MA/cm² everywhere but the defect area where $J_{C77}^{def}{\to}0$. This area represents the normal

Fig. 3. A temperature dependent plot of equation (1) extrapolated above T_C = 90 K and drawn for J = 2.5 MA/cm². Two interesting cases are singled out. The first concerns the highest critical current density (red squares) for which the YBCO resistivity becomes non-zero above nearly 82 K prior to the transition at T_C. The second case (blue dots) represents the YBCO resistivity of the normal state where ρ_{YBCO} never falls to zero for any $T{<}T_C$. The two curves coincide above T_C. (For interpretation of the references to colour in this figure legend, the reader is referred to the web version of this article.)

Fig. 4. Surface plot visualization of (T,J_{C77}) dependent current sharing function η ($\equiv J_{Ag}/J$) reaching the plateau of nearly 100% beyond T_C = 90 K. The dependence is computed at J = 2.5 MA/cm² as a parameter for a continuum of the critical current values between $J_{C77}^{def}{\to}0$ and J_{C77} = 2 MA/cm².

block of length $\Delta L = 50$ μm (Fig. 2). The normal block is treated as a new domain in COMSOL with the same thermal properties as the rest of the superconductor except for the intensified Joule heating term of $Q(T, J_{C77}^{def})$. The size of normal block has cautiously been tuned in order to ensure the convergence in the simulation results. On the other hand, the length has been found long enough to exceed the minimum quench energy in 3D heat propagating systems, as reported in Ref. [21].

In order to study the heat propagation in the proposed YBCO-based RSFCL structure, we have used the following thermal balance equation with the (TJ_{C77}) dependent heat sources only existing in the coated superconducting lines:

$$\rho_m C_p(T) \frac{\partial T}{\partial t} = \kappa(T)\nabla^2 T + Q(T, J_{C77}),$$ (4)

where $C_p(T)$, $\kappa(T)$, and ρ_m are specific heat capacity, thermal conductivity, and mass density, respectively, which were adopted from the COMSOL material library. We have treated the Ag-coated YBCO as a single domain with the combined effective thermal properties which read as

$$C_{p,eff} = \frac{1}{1+\chi}C_{p,Ag} + \frac{\chi}{1+\chi}C_{p,YBCO},$$ (5)

$$\kappa_{eff} = \frac{1}{1+\chi}\kappa_{Ag} + \frac{\chi}{1+\chi}\kappa_{YBCO}.$$ (6)

This approximation enables us to circumvent problems generated by extremely thin layers, such as the Ag stabilizer, and is justified by the small variation of temperature along the thickness of the coated YBCO. Moreover, the absolute tolerance scale defined in COMSOL was taken to be as low as 20 nm which even starts to compare with the Ag thickness.

The major complexity of the treated geometry lies in its extremely high aspect ratio (lengths of several millimeters versus thicknesses of tens of microns) so that modelling geometries as such can be one of the more challenging tasks for the finite element analysts. This poses a challenge for an automatic or unstructured meshing where one strives to create an isotropic mesh distribution for high mesh quality. A strategy consists in subdividing the geometry, in a virtual manner, into vertical material layers with respect to the central normal block. A mapped mesh can then be generated on all the boundaries and distributed on the edges and peripheries. Next, one-to-one sweeping is used to map source surfaces mesh onto their target surfaces. Swept meshes are especially useful for thin geometries, as other tetrahedral and triangular meshes generate redundant elements than necessary, to account for the skewed dimensions existing within thin configurations. Swept meshing is a powerful technique for minimizing the computational complexity and leads to high-accuracy results quickly and at relatively lower computational costs in comparison with default mesh settings. By symmetry, we have simulated only one fourth of the model to make the computation even four times less expensive (Fig. 5). In such a way, the external boundaries of the irreducible geometry part can be maneuvered as symmetry planes in the computation. In our case, a qualitatively high resolution across the surfaces has been obtained using mapped mesh elements of minimal and maximal size of 40 nm and 0.1 mm, respectively. The surface mapped mesh has been swept through the substrate thickness using 20 elements with an element ratio of 30. Altogether, the high-resolution model involved of 172600 hexahedral elements, 42800 quadrilateral elements, 2066 edge elements, and 60 vertex elements, with quite a desirable average growth rate of nearly 1.161 (being not far from 1) that has yielded a
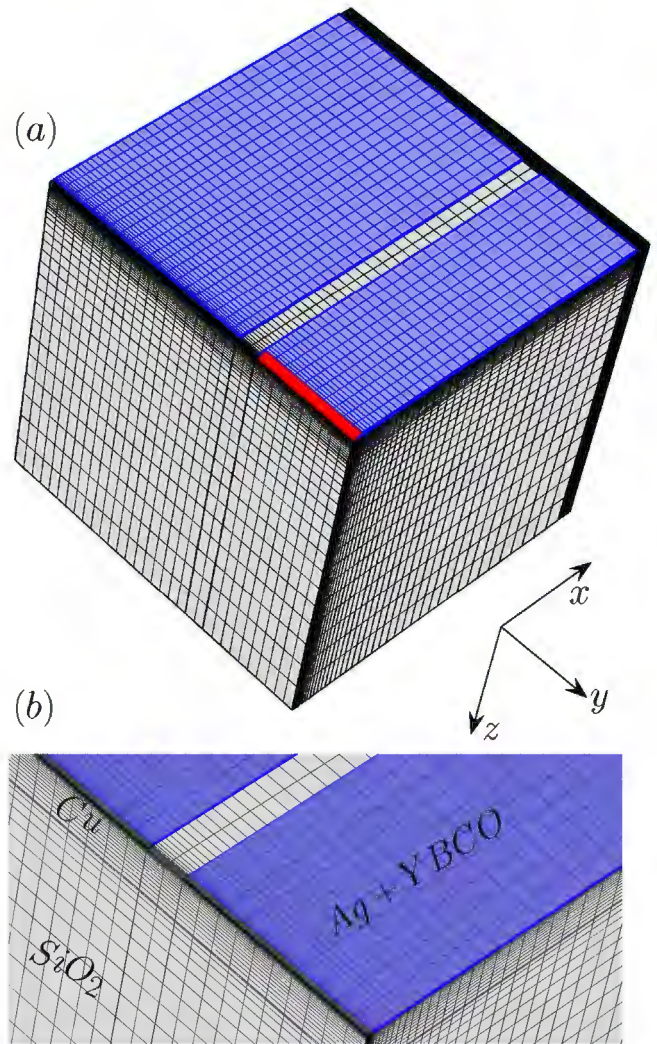
Fig. 5. Meshing discretization of one fourth of the geometry (a) predominantly made of hexahedral and quadrilateral elements. The coated superconducting lines are given in blue. The normal block drawn with red line is zoomed below (b) for better visualization of the mapped mesh distributed around it and further swept through three orthogonal directions: x, y, and z. The aspect ratio does not correspond to the realistic proportions. (For interpretation of the references to colour in this figure legend, the reader is referred to the web version of this article.)

reliable mesh statistics of solid mesh element quality.

The thermal contact of the interface between the superconducting lines and the underlying multi-structure represents a relevant parameter without which the heat propagation would become thoroughly adiabatic. Based on a novel characterization method reported in Ref. [22], the equivalent interface thermal conductance was guessed by experimental results for similar structures with a value estimated as 300 WK^{-1} cm^{-2}. If required by the experimental findings, this number might be modified. However, thus far it serves as a referential parameter with respect to which we will interpret our computational results. For further details with regards to a discussion on the equivalent interface conductance, the reader is kindly referred to [14]. The emissivity for the radiative heat transfer in the system amounts 30%, while the temperature dependent convection heat transfer coefficient has also been taken into account. We have stopped the simulations whenever the average temperature of the normal block exceeded 600 K. Only temperatures below this limit are admissible for high temperature operationality of RSFCLs [23].

2.3. Computation of normal zone propagation velocity

The key parameter which quantifies the quench propagation in RSFCLs is the normal zone propagation velocity. We have surveyed directional heat propagations along the coated YBCO line (longitudinal, x-axis) and sidewise (lateral, y-axis) with referential thermal front of $T_{NZ} \equiv T_C = 90$ K, the so-called normal zone. All the values found for NZPVs in the two directions are uniform over the whole geometry. This is in accordance with the picture of superconducting transition assisted heat propagation [19] which apparently dominates in our case. The computed NZPVs values were distilled directly from the COMSOL consoles, that gained an advantage over common post-simulated calculations of NZPVs. In other words, we have benefited from quick eliminations of disfavoured configurations with different geometries and materials in situ. The approach is based on solving numeric equation $T(x;t) = T_{NZ}$ (along x, for example) with respect to x for every time t. Fig. 6 delineates an integrational method in finding the NZPV numerical solution which consists of averaging out differently weighted solutions with a Gaussian enveloped ensemble of weights along a desired direction. Initially, a small tolerance $\delta_T(t)$ around T_{NZ} is set at time t. The thermal tolerance thus results in a set of the solutions dispersed with $\delta_x(t)$ around $\bar{x}(t)$, as is given in Fig. 6. Finally, the problem boils down to evaluating the time dependence of the expected value of spatial coordinate $\bar{x}(t)$, which is achieved by integrating along one half of the line (0<x<L/2). Alternatively, solving $T(x;t) = T_{NZ}$ can be inferred as a mapping of the temperature Gaussian distribution onto the spatial one at time t. For that reason, the highest weights in the integration have to be ascribed to the solutions sitting in a very close vicinity of $T(x;t) = T_{NZ}$. As a first time derivative of $\bar{x}(t)$, the NZPV can accordingly be written down as

$$v_{NZP} = \frac{\partial}{\partial t} \frac{\int_{x=0}^{x=L/2} x e^{-\frac{(T(x;t)-T_{NZ})^2}{2\delta_T^2(t)}} dx}{\xi + \int_{x=0}^{x=L/2} e^{-\frac{(T(x;t)-T_{NZ})^2}{2\delta_T^2(t)}} dx}. \quad (7)$$
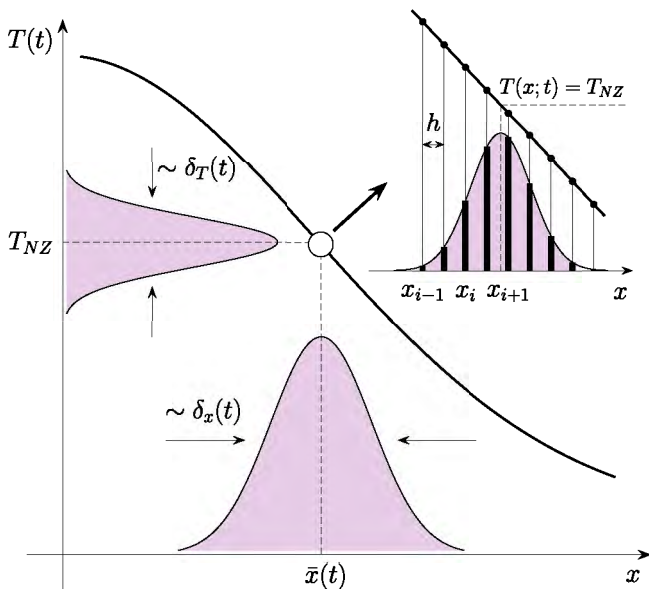
Fig. 6. 1D plot of a propagating temperature profile $T(x;t)$ which demonstrates an integrational approach to solving $T(x;t) = T_{NZ}$ in 1D, that is, a projection of the temperature Gaussian profile onto the spatial one with respect to this equation. $T(x)$ at time t is guessed linear (inset) over a domain containing large enough number of the mesh elements of size $h = x_{i+1}-x_i$.

This expression in general represents an efficient procedure for solving numerical equations based on Gaussian-weighted integration which finds its applicability to finite element method problems [24,25]. The integration is given by the Gauss-type quadrature formula, which runs some risk of containing division by zero. This can be skipped by inserting ξ as an internal COMSOL constant being a very small number on the order of 10^{-15}. Yet, one should use the nojac operator in COMSOL to make sure that the operating expression is excluded from the Jacobian computation. This is useful in the present case as the Jacobian contribution is not strictly necessary. Otherwise, the computational requirements for it would be considerably high.

Other x_i solutions, however lying in the vicinity of $T(x;t) = T_{NZ}$, are weighted with lower fractions falling off along the spatial Gaussian tail. Their contributions are limited due to the line-width of the temperature Gaussian function which has all the time been controlled with the characteristic size of the projected mesh element (h) in order to ensure the smoothness of generated $\bar{x}(t)$ function. Ideally, the single 100% weighted solution case would represent the exact analytical solution that cannot be conceived in FEM softwares because of the necessity for mesh discretization.

The integration step dx is equal to the characteristic size of meshing, h, which must satisfy the following condition for every t and all x's in vicinity of $T(x;t) = T_{NZ}$:

$$h \frac{\partial T(x;t)}{\partial x} \ll \delta_T(t) \ll T_{NZ}. \quad (8)$$

The condition follows from the linear approximation of the temperature profile around $T(x;t) = T_{NZ}$ as is shown in the inset of Fig. 6. Rationally, the temperature tolerance $\delta_T(t)$ must be much smaller than T_{NZ} and is projected linearly onto $\delta_x(t)$. There is also another way to rewrite the restriction in (8) as

$$h \ll \delta_x(t) \approx \frac{\delta_T(t)}{\partial T(x;t)/\partial x}. \quad (9)$$

The idea of this expression is to help us use correctly the integration tool for a reliable NZPV calculation. It lies in covering as large number of the mesh elements as possible, provided that $T(x;t)$ remains a smooth function over the domain of mesh elements. We have therefore carefully adjusted the characteristic mesh element size in order to ensure the required smoothness. In summary, the equations (8) and (9) are one another related by the fact that T_{NZ} is much larger than $\delta_T(t)$ which is linearly mapped onto $\delta_x(t)$ where this one must envelop a large number of the mesh elements (h).

3. Results and discussions

3.1. Comparison with the experiment

This part is devoted to the experimental verification of the numerical model put forward to study the heat propagation in the novel RSFCL. Although the thorough model has not been substantiated yet, it is important to assess the reliability of the simulations with respect to the method proposed for the heat generation evaluation. They have been validated for two cases with different RSFCL architectures and substrates, which could be parametrically tuned in the program. The two available experimental data approving the simulations deal with: 500 μm thick sapphire and 90 μm thick hastelloy substrates, with $J_{C77} = 3$ MA/cm^2, $J = 4.5$ MA/cm^2, and, $J_{C77} = 0.9$ MA/cm^2, $J = 1$ MA/cm^2, respectively [13,14,26]. The NZPV values which we have computed are 12 cm/s for hastelloy (90 μm) and 16 m/s for sapphire (500 μm) substrate. Exactly the same values of the NZPVs were reported in the corresponding measurements as well [26]. Generally, NZPVs are functions of both J

and J_{C77} for a given substrate. However, instead of looking at a dependence with respect to these variables individually, scaling the NZPV dependence down to a universal J/J_{C77} parameter has turned out to be quite level-headed. Thus, one should not be surprised if the NZPV dependence is represented as $v_{NZP}(J,J/J_{C77})$. With values falling into the range between 1 and 1.5, J/J_{C77} does not generate too much heat during the quench propagations. Our case concerns $J/J_{C77} = 1.25$ and can be considered safe against rapid overheatings. For already one micron of copper substrate, this ratio results in an NZPV value of nearly 4.5 m/s, a computational outcome which seems highly desirable to the market.

Nevertheless, the ultimate validation of the model for the novel RSFCL multi-structure is still in progress [16]. The experimental realization would certainly reconcile the low cost commercialization as one of the strongest feature of the proposed RSFCL and its apparently fast quench propagation required for thermal stability. For that reason we have adjusted the thickness of the copper layer to optimize the influence of the underlying fused silica substrate of which 100 μm of thermal inertia may well moderate the quench propagation. There is, on the other hand, a minuscule but still present thermal inertia coming from the copper itself.

3.2. Interpretation of the computational results

A visualized example of a temperature surface plot of the propagating normal zone across the three coated superconducting lines for $\delta_{Cu} = 1.5$ μm is given in Fig. 7. The upper figure (a) demonstrates in-plane propagation (x,y), while the lower one (b) provides the reader with a view in 3D (x,y,z). One can discriminate a 90 K border line of the propagating thermal front, which roughly demarcates the dark (at nearly 77 K) from light blue area at the moment when the hot spot reaches 214 K. The snapshot is taken 450 μs after the quench input. Only one fourth of the geometry has been simulated (Fig. 7(b)), while the entire geometry is given only in the plane on the top of the structure (Fig. 7(a)). The 3D presentation of the simulated segment allows us to grasp behaviour of the heat along z-direction during the propagation. It has been concluded that hardly few microns along the substrate thickness are affected by the heat propagation, whereas both longitudinal (x) and lateral (y) heat have already spread around at several mm scale. This means that the vertical heat penetration can be neglected as compared to the in-plane one that makes the process quasi-adiabatic. In such types of heat propagations one expects that for both J and J_{C77} fixed NZPV should poorly depend on the copper thickness values shorter than a characteristic thermal penetration depth of the vertically spreading heat. Indeed, we have computationally observed that the simulation results have not evolved beyond approximately 1 μm of copper thickness. Even up to 10 μm of Cu all the NZPV values have been found stable around 4.5 m/s. This leads us to a conclusion that the characteristic thermal penetration depth amounts nearly 1 μm. Variations of δ_{Cu} higher than this value have not brought about relevant changes in NZPVs.

There is also another parameter which has remained unchanged when δ_{Cu} is increased from 1 μm and higher. This parameter measures the time interval of the normal block temperature transition from 77 to 90 K and therefore quantifies the degree of operationality of the studied RSFCL device. The longer this transition time is the less homogenized the heat becomes and a severe damage may emerge. The transition time is in a direct relationship with thermodynamic stability of the RSFCL [23]. Shortening this time (t_{trans}) suppresses the normal block from reaching 600 K prior to the total transition of the three lines. For all $\delta_{Cu} \geq 1$ μm, t_{trans} is found to amount nearly 200 μs. However, this value starts to change for submicron δ_{Cu} values. The submicron variations of δ_{Cu} are therefore seen by the vertical heat penetration as they are shorter

(a)

(b)
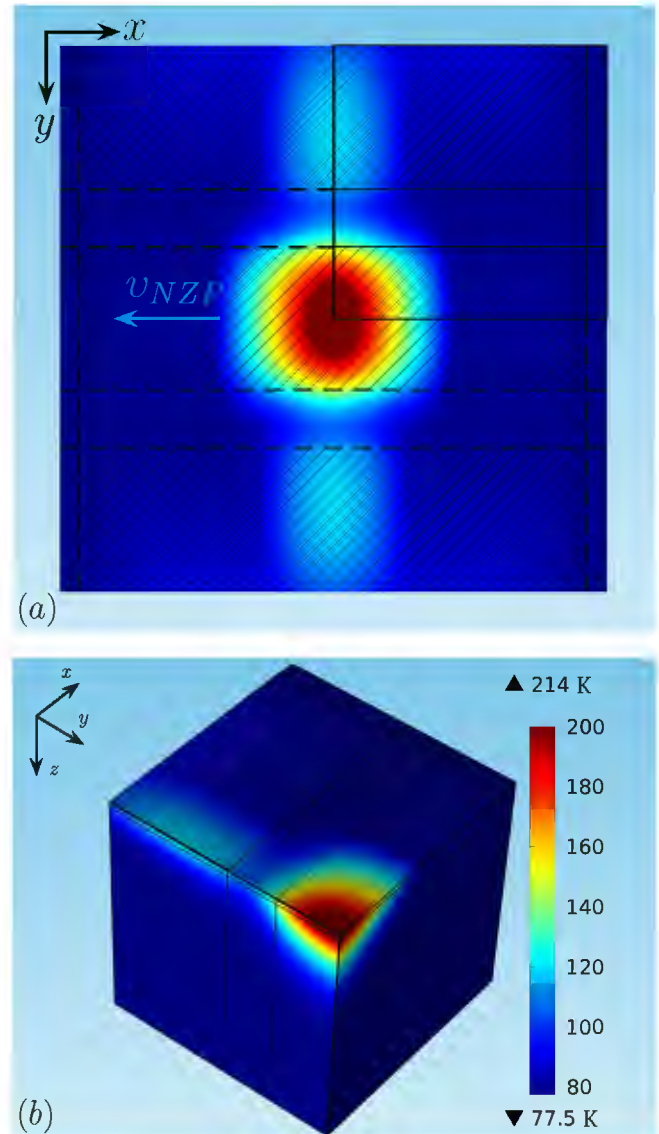
Fig. 7. Temperature profile of the normal zone propagation for the three superconducting lines in xy plane (a) and in 3D (b). The profile is taken at the moment of $450\mu s$ upon the quench initialization. For symmetry reasons, the lower figure (b) is chosen to demonstrate the 3D heat propagation over one quarter of the total geometry. The aspect ratio is different from the real proportions, but it helps the reader visualize the heat propagation in 3D.

than the characteristic thermal penetration depth. In such a way, the character of the heat transfer processes is no longer quasi-adiabatic so that the previous reasoning fails to apply for $\delta_{Cu} < 1$ μm. The evaluation of the heat propagation with respect to submicron δ_{Cu} variation is treated in the next section.

In addition, it is worth mentioning that due to the 3D (x,y,z) geometry, the temperature profiles centered in the middle line become softened to some extent, unlike the earlier studied 2D (x,z) computational models [13,14]. This further ensures thermal stability of RSFCL systems with increased geometries, such as ours, as a direct consequence of heat diffusions spreading along y, i.e. sidewise the middle line — a missing part in the 2D (x,z) simulated configurations. Yet, the existence of such an extra direction in temperature distribution leads to no important difference between the values in longitudinal (v_{NZP}^x) NZPVs computed respectively in the 2D (x,z) and 3D models. In the treated 3D case, we have also

noticed that the lateral (v_{NZP}^{y}) NZPV does not differ drastically from v_{NZP}^{x}. Because of their non-superconducting mediums, lateral heat propagations are commonly of diffusive nature. We have, however, found no significant discrepancy between v_{NZP}^{x} and v_{NZP}^{y}, that is most likely due to the very short non-superconducting space of 400 μm between the large superconducting lines of size $L \times d = 20 \times 6$ mm^2.

3.3. Submicron variation of the copper substrate thickness

In this section, we report and provide an answer of how to resolve the difficulties in computational convergences for submicron copper thickness variations. As has been pointed out in the previous section, there is a change in t_{trans} once δ_{Cu} is decreased from about one micron down to lower values. The reason for that lies in very fast temperature increase for the quasi-adiabatic regime in the case of submicron δ_{Cu} values. We have found that this problem can be solved if the transition time is kept at a certain minimal value to avoid the non-convergence difficulties. The t_{trans} value was determined with the maximal J value found experimentally ($J = 1$ MA/cm^2 for $\delta_{Cu} = 0$ [13,14]) in order to have a stable solution. The maximal injected current compatible with the stable solution is found to increase up to 2.5 MA/cm^2 for larger Cu thicknesses. Now the question is about the meaning of the thickness dependence of the NZP velocity. We can either keep the injected current at a constant value of 1 MA/cm^2 or determine the maximal NZP velocity according to the maximal allowed value of J. The Fig. 8 shows the results computed for each thickness with the maximal J value which results in the stable solution. Experimentally, this curve represents the real value for NZP velocity since RSFCL will operate on voltage source and never on current source. However, this presentation has a disadvantage as it compares NZP velocities computed at different injected current densities (J's). On the other hand, Dresner model [2], concerned with propagation of heat fronts under adiabatic conditions, predicts a velocity proportional to the injected current. From 1 MA/cm^2 to 2.5 MA/cm^2, the NZP velocity is expected to increase from 10 cm/s to 25 cm/s. We thus conjecture that the enormous increase of NZP velocity at Cu thickness of 1 μm, observed in our case, can be solely related to the improvement of the thermal properties of the multilayer structure.

As can be followed from Fig. 8, one observes a drop in the

maximal value of NZP velocity with decreasing δ_{Cu}, which is expected due the increasingly stronger influence of the thermal inertia of SiO$_2$. Fig. 8 also features the maximized v_{NZP} values achieved by departing from the simulation parameters which were employed in the quasi-adiabatic regime. At a copper thickness of about 1 μm, the gain in the NZP velocity is about 45 times its lowest value, which is achieved in the absence of Cu layer (~10 cm/s). The most optimal value for δ_{Cu} should therefore be close to one micron which would make the achievement of the multilayer structure easier, a realization which might be difficult to accomplish with larger Cu thicknesses.

4. Concluding remarks

In conclusion, the present computational work has made an important contribution to the development of high-temperature RSFCLs, which show a potential for use in medium voltage power applications. The FEM model, which we have developed using COMSOL Heat Transfer Module, is found quite accurate to simulate the 3D heat propagation in the YBCO-based CCs with a simplified meander geometry configured on a novel multistructure. We have demonstrated that varying the copper layer thickness (1–10 μm) has no impact on the NZPV values that is in accordance with a quasi-adiabatic picture of heat propagation. The computed NZPV values are of two magnitude order higher scale in comparison with an earlier studied RSFCL manufactured on a hastelloy substrate. The numerical approach developed in the present study to calculating NZPVs has been validated for two already realized configurations with sapphire [26] and hastelloy [13,14], while the FEM model in its entirety is yet to be verified experimentally for the proposed novel RSFCL architecture. With no loss of generality, we have summarized the overall thermal influence of the MgO/hastelloy buffer layers and remaining thin interlayers (such as Nb and TiO$_2$) into a single constant. Thermodynamical instabilities introduced by the submicron variation of copper thickness have been also scrutinized, that is nevertheless out of interest due to the required minimum of nearly one micron copper layer for experimental realizations.

Acknowledgment

Fig. 8. Dependence of the maximal value of NZP velocity on the copper thickness ranging from 0 up to 1400 nm (left side). The corresponding first derivative curve (right side) featuring the decrease of the NZP velocity rate. The derivative is obtained upon the data smoothing.

References

[1] Iwasa Y. Case studies in sSuperconducting Magnets: Design and Operational Issues. second ed. New York: Springer Science; 2009. http://dx.doi.org/10.1007/b112047.

[2] Dresner L. Stability of Superconductors. New York: Kluwer Academic Publishers; 2002. http://dx.doi.org/10.1007/b115033.

[3] Levin GA, Barnes PN, Bulmer JS. Current sharing between superconducting film and normal metal. Supercond. Sci Technol 2007;20:757–64. http://dx.doi.org/10.1088/0953-2048/20/8/006.

[4] Ishiyama A, Yanai M, Morisaki T, Ueda H, Shiohara Y, Izumi T, Iijima Y, Saitoh T. Normal transition and propagation characteristics of YBCO tape. IEEE Trans. Appl. Supercond. 2005;15:1659–62. http://dx.doi.org/10.1109/TASC.2005.849225.

[5] Hodge JD, Muller H, Applegate DS, Huang Q. A resistive fault current limiter based on high temperature superconductors. Appl. Supercond. 1995;3:469–82. http://dx.doi.org/10.1016/0964-1807(95)00074-7.

[6] Gurevich A. Thermal instability near planar defects in superconductors. Appl. Phys. Lett. 2001;78:1891–3. http://dx.doi.org/10.1063/1.1358361.

[7] Shapiro B, Bel G, Rosenstein B, Shapiro I. Hot spot in type-II Supercond.uctors: dynamics and instabilities. Phys. C Supercond. 2004;404:335–9. http://dx.doi.org/10.1016/j.physc.2003.11.032.

[8] Duron J, Grilli F, Antognazza L, Decroux M, Dutoit B, Fischer Ø. Finite-element modelling of YBCO fault current limiter with temperature dependent parameters. Supercond. Sci. and Technol. 2007;20:338–44. http://dx.doi.org/
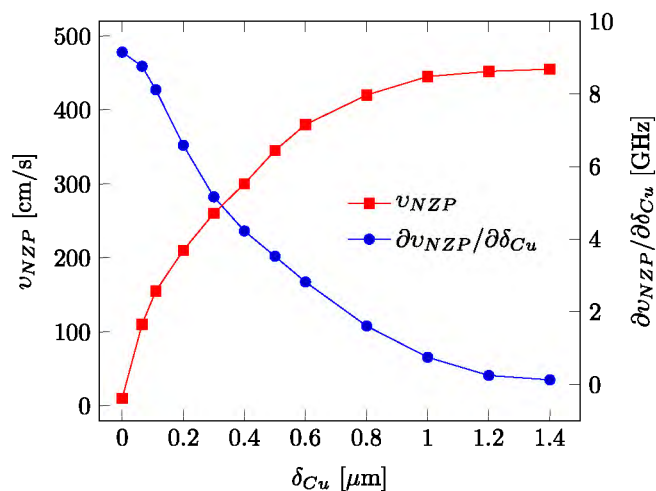
10.1088/0953-2048/20/4/007.

[9] Wang Y. Fundamental Elements of Applied Superconductivity in Electrical Engineering. Singapore: John Wiley & Sons; 2013. http://dx.doi.org/10.1002/9781118451151.

[10] Roy F, Pérez S, Therasse M, Dutoit B, Sirois F, Decroux M, Antognazza L. Quench propagation in coated conductors for fault current limiters. Phys. C Supercond. 2009;469:1462–6. http://dx.doi.org/10.1016/j.physc.2009.05.066.

[11] Decroux M, Antognazza L, Reymond S, Paul W, Chen M, Fischer Ø. Studies of YBCO strip lines under voltage pulses: optimization of the design of fault current limiters. IEEE Trans. Appl. Supercond. 2003;13:1988–91. http://dx.doi.org/10.1109/TASC.2003.812959.

[12] Tixador P, Villard C, Cointe Y. DC superconducting fault current limiter. Supercond. Sci Technol 2006;19:S118–25. http://dx.doi.org/10.1088/0953-2048/19/3/017.

[13] Badel A, Antognazza L, Decroux M, Abplanalp M. Hybrid model of quench propagation in coated conductors applied to fault current limiter design. IEEE Trans. Appl. Supercond. 2013;23:5603705–9. http://dx.doi.org/10.1109/TASC.2013.2247091.

[14] Badel A, Antognazza L, Therasse M, Abplanalp M, Schacherer C, Decroux M. Hybrid model of quench propagation in coated conductors for fault current limiters. Supercond. Sci Technol 2012;25:095015–23. http://dx.doi.org/10.1088/0953-2048/25/9/095015.

[15] Antognazza L, Decroux M, Therasse M, Abplanalp M, Fischer Ø. Test of YBCO thin films based fault current limiters with a newly designed meander. IEEE Trans. Appl. Supercond. 2005;15:1990–3. http://dx.doi.org/10.1109/TASC.2005.849434.

[16] D. M. Djokić, L. Antognazza, M. Decroux, Work in progress.

[17] MacManus-Driscoll JL. Recent developments in conductor processing of high irreversibility field superconductors. Annu. Rev. Mater. Sci. 1998;28:421–62. http://dx.doi.org/10.1146/annurev.matsci.28.1.421.

[18] Aytug T, Paranthaman M, Thompson JR, Goyal A, Rutter N, Zhai HY, Gapud AA, Ijaduola AO, Christen DK. Electrical and magnetic properties of conductive Cu-based coated conductors. Appl. Phys. Lett. 2003;83:3963–5. http://dx.doi.org/10.1063/1.1626263.

[19] D. M. Djokić, L. Antognazza, M. Abplanalp, M. Decroux, Heat propagation improvement in YBCO-coated conductors for superconducting fault current limiters, COMSOL Multiphysics, Cambridge, 2014, Excerpt from the Proceedings of the COMSOL Conference. URL https://www.comsol.com/paper/heat-propagation-improvement-in-ybco-coated-conductors-for-superconducting-fault-18187.

[20] Tarte EJ, Lean HW, Barber ZH, Waldram JR, Somekh RE. The resistance of YBCO-silver interfaces. Phys. C Supercond. 1991;185–189:2577–8. http://dx.doi.org/10.1016/0921-4534(91)91412-W.

[21] Stenvall A, Mikkonen R, Kováč P. Comparison of 1D, 2D, and 3D quench onset simulations. Phys. C Supercond. 2010;470:2047–50. http://dx.doi.org/10.1016/j.physc.2010.09.010.

[22] Antognazza L, Decroux M, Badel A, Schacherer C, Abplanalp M. Measurements of the DyBCO/substrate thermal conductance in coated conductors. Supercond. Sci Technol 2012;25:105002–9. http://dx.doi.org/10.1088/0953-2048/25/10/105002.

[23] Schwarz M, Schacherer C, Weiss K-P, Jung A. Thermodynamic behaviour of a coated conductor for currents above I_c. Supercond. Sci. Technol. 2008;21:054008–11. http://dx.doi.org/10.1088/0953-2048/21/5/054008.

[24] Ghanem R. Ingredients for a general purpose stochastic finite elements implementation. Comput Methods Appl. Mech. Eng. 1999;168:19–34. http://dx.doi.org/10.1016/S0045-7825(98)00106-6.

[25] Lu J, Darmofal DL. Higher-dimensional integration with Gaussian weight for applications in probabilistic design. SIAM J Sci. Comput. 2004;26:613–24. http://dx.doi.org/10.1137/S1064827503426863.

[26] Antognazza L, Decroux M, Reymond S, de Chambrier E, Triscone J-M, Paul W, Chen M, Fischer Ø. Simulation of the behavior of superconducting YBCO lines at high current densities. Phys. C Supercond. 2002;372–376:1684–7. http://dx.doi.org/10.1016/S0921-4534(02)01101-2.

Influence of antiferromagnetic spin ordering on the far-infrared active optical phonon modes of α-MnSe

D. M. Djokić[*] and Z. V. Popović

Centre for Solid State Physics and New Materials, Institute of Physics, Pregrevica 118, 11080 Belgrade, Serbia

F. R. Vukajlović

Institute for Nuclear Sciences-Vinča, P.O. Box 522, 11 001 Belgrade, Serbia

The effects of spin-phonon interaction and magnetic anisotropy on the temperature dependence of the infrared optical phonon modes in the antiferromagnetic α-MnSe are investigated by use of Green's function formalism within $1/z$ perturbation framework. The renormalization effects are calculated explicitly as a function of temperature, phonon-phonon, and spin-phonon interaction constants. Temperature dependence of the renormalized LO phonon frequencies of the F_{1u} infrared active and combinational phonon modes are calculated and compared with experimental data. We have shown that the inclusion of anisotropy is necessary in order to get a good quantitative agreement with the experiment.

PACS number(s): 63.20.kk, 75.30.Ds, 75.50.Ee, 78.30.Fs

I. INTRODUCTION

Effects of spin ordering on the microscopic and macroscopic dielectric properties are investigated for many magnetic crystals as a function of either temperature or magnetic field.[1–3] In the present theoretical study, the influence of the antiferromagnetic (AF) spin ordering on the observed far-infrared reflectivity spectra of α-MnSe is considered in detail. We apply the usual extension of Heisenberg model which includes the spin-phonon interaction terms and perform a low-density perturbation expansion.[4–6] The recent experimental findings[7] have guided us in that direction. It will be shown that simple noninteracting spin-wave theory is enough to account for the relevant physical properties of α-MnSe in far-infrared spectral region mainly because magnon-magnon interactions do not lead to the two-magnon bound states in this three-dimensional and high-spin AF system. In addition, it also happens that the *pseudodipolar* magnetic anisotropy is of the vital importance for the explanation of measured Raman scattering and infrared spectra.[7,8] The magnetic anisotropy has been taken into account in such a direct way in order to explain mechanical properties of some of the AF semiconductors. Because there is no structural phase transition in this ideal cubic antiferromagnet α-MnSe, no new phonon modes will appear below the magnetic transition temperature. Consequently, only magnetic degrees of freedom are responsible for suitable explanation of the observed spectra. In addition, we have extracted the exchange parameters for the first (J_1) and second (J_2) neighbors by making use of the magnetic susceptibility measurements of α-MnSe.[7]

The hardening of the optical phonon modes is one of the characteristic features of magnetic insulators (mainly antiferromagnets) in the low-temperature ordered phase (cf. Refs. 9 and 10 and references cited therein), but without appropriate microscopic explanation so far. Several earlier attempts were performed on purely phenomenological basis and only with a partial success.[3,9–11] We have shown in this investigation that the spin-phonon interaction, which arises due to a modulation of the exchange interaction by ionic vibrations,[12,13] can describe accurately such a temperature dependence of phonon frequencies. Note also that the occurrence of the mentioned hardening is very typical in systems with pronounced insulating properties, as α-MnSe is, in contrast to those systems exhibiting a metallic behavior.[14]

II. MAGNETIC HAMILTONIAN FOR THE ANTIFERROMAGNETIC α-MnSe

In order to treat the dynamical properties of a type II AF system such as α-MnSe (cf. Fig. 1), characterized by the high-spin value $\frac{5}{2}$ localized on manganese atoms and large number of interacting neighbors, we shall make an approximation which will enable us to use all benefits from representing spin operators in the spin-drone representation.[15,16] More precisely, we are using the following ansatz, which our further calculations will be relied on:

$$\hat{S}_{5/2}^z \approx 5\hat{S}_{1/2}^z, \tag{1}$$

where the $\frac{5}{2}$-spin states, $\left|\frac{5}{2}, +\frac{5}{2}\right\rangle$, and $\left|\frac{5}{2}, +\frac{3}{2}\right\rangle$, which are only relevant states in describing low-temperature magnon dynamics, can be drone mapped as spin-up and spin-down states of $S=\frac{1}{2}$, respectively. By this approximation, all the second and higher order spin-flip processes, related to magnon-magnon interactions, are neglected. In the temperature region below the Néel temperature, due to the condition $1/zS \ll 1$, where z (=18) is the number of spins interacting with any given spin of the absolute value $S=\frac{5}{2}$ (cf. Fig. 1), we do not need to perform calculations beyond the framework of linear spin wave theory and the introduced assumption is expected to be quite suitable.[17] A similar assumption was applied by Spencer[16] for the case of spin $S=1$. It was furthermore shown[18,19] that such an approach becomes highly favorable in weakly coupled systems, such as in our case (weak magnon- and magnon-phonon interaction).

Applying the ansatz [Eq. (1)], we can obtain the following relations for the modified spin-drone representation, on the lattice sites i,j belonging to two different sublattices:

$$\hat{S}_i^+ = \sqrt{5}\hat{c}_i^\dagger\hat{\varphi}_i, \quad \hat{S}_j^+ = \sqrt{5}\hat{\varphi}_j\hat{c}_j,$$

$$\hat{S}_i^z = 5\hat{c}_i^\dagger \hat{c}_i - \frac{5}{2}, \quad \hat{S}_j^z = \frac{5}{2} - 5\hat{c}_j^\dagger \hat{c}_j,$$

$$\hat{\varphi}_i = \hat{d}_i^\dagger + \hat{d}_i, \quad \hat{\varphi}_j = \hat{d}_j^\dagger + \hat{d}_j, \qquad (2)$$

where $\hat{c}$ and $\hat{d}$ are fermion anticommuting operators: $\{\hat{c}_i, \hat{c}_j^\dagger\} = \delta_{ij}$, $\{\hat{d}_i, \hat{d}_j^\dagger\} = \delta_{ij}$.

The Fourier transformation into reciprocal space is given by

$$\hat{c}_i^\dagger = \frac{1}{\sqrt{N}} \sum_{\mathbf{q}} e^{i\mathbf{q}\cdot\mathbf{l}_i} \hat{c}_{1\mathbf{q}}^\dagger, \quad \hat{\varphi}_i = \frac{1}{\sqrt{N}} \sum_{\mathbf{q}} e^{i\mathbf{q}\cdot\mathbf{l}_i} \hat{\varphi}_{1\mathbf{q}},$$

$$\hat{c}_j^\dagger = \frac{1}{\sqrt{N}} \sum_{\mathbf{q}} e^{-i\mathbf{q}\cdot\mathbf{l}_j} \hat{c}_{2\mathbf{q}}^\dagger, \quad \hat{\varphi}_j = \frac{1}{\sqrt{N}} \sum_{\mathbf{q}} e^{-i\mathbf{q}\cdot\mathbf{l}_j} \hat{\varphi}_{2\mathbf{q}}, \qquad (3)$$

where N is the number of sites in each sublattice (equal to number of unit cells).

We shall use the slightly modified Heisenberg Hamiltonian for $S = \frac{5}{2}$ which includes the exchange interaction between the nearest neighbors (nn), J_1, next-nearest neighbors (nnn), J_2, and small magnetic anisotropy term in addition,

$$\hat{H} = \sum_{\langle i,i'\rangle}^{nn} \hat{\mathbf{S}}_i \hat{J}_1 \hat{\mathbf{S}}_{i'} + \sum_{\langle j,j'\rangle}^{nn} \hat{\mathbf{S}}_j \hat{J}_1 \hat{\mathbf{S}}_{j'} + \sum_{\langle i,j\rangle}^{nn} \hat{\mathbf{S}}_i \hat{J}_1 \hat{\mathbf{S}}_j + \sum_{\langle i,j\rangle}^{nnn} \hat{\mathbf{S}}_i \hat{J}_2 \hat{\mathbf{S}}_j,$$

$$(4)$$

$$\hat{J}_i = J_i \times \begin{pmatrix} 1 & 0 & 0 \\ 0 & 1 & 0 \\ 0 & 0 & 1+g_i \end{pmatrix}, \quad i \in \{1,2\}, \quad g_1 \approx g_2 \equiv g.$$

$$(5)$$

According to Fig. 1, $\langle i,i'\rangle$ and $\langle j,j\rangle'$ indices correspond to spin-up and spin-down sublattices, respectively, while g denotes the pseudodipolar anisotropy contribution to the exchange constants.[20,21] Due to the fact that $g_{1,2} \ll 1$, the simplification we made, $g_1 \approx g_2 \equiv g$, is not seriously limiting our further conclusions.

By means of standard implementation of the spin-drone representation in the mean field approximation, one can obtain the sublattice magnetizations,[22,23]

$$\mathcal{M}_{1,2}(T) = \langle \hat{S}_{1,2}^z \rangle_T = 5(-1)^{1,2} \left\langle \frac{1}{2} + \hat{c}_{1,2}\hat{c}_{1,2}^\dagger \right\rangle_T$$

$$= \frac{5}{2} \tanh\left(\frac{5}{2}\frac{1}{k_B T} \mathcal{M}_{1,2}(T)[A(\mathbf{0}) - B(\mathbf{0})] \right), \quad (6)$$

where $A(\mathbf{q})$ and $B(\mathbf{q})$ are the off-diagonal and diagonal $\mathbf{q}$-space exchange interactions, respectively,

$$A(\mathbf{q}) = 2J_1 \left(\cos\frac{x+y}{2} + \cos\frac{y+z}{2} + \cos\frac{z+x}{2} \right)$$

$$+ 2J_2(\cos x + \cos y + \cos z),$$

$$B(\mathbf{q}) = 2J_1 \left(\cos\frac{x-y}{2} + \cos\frac{y-z}{2} + \cos\frac{z-x}{2} \right), \quad (7)$$
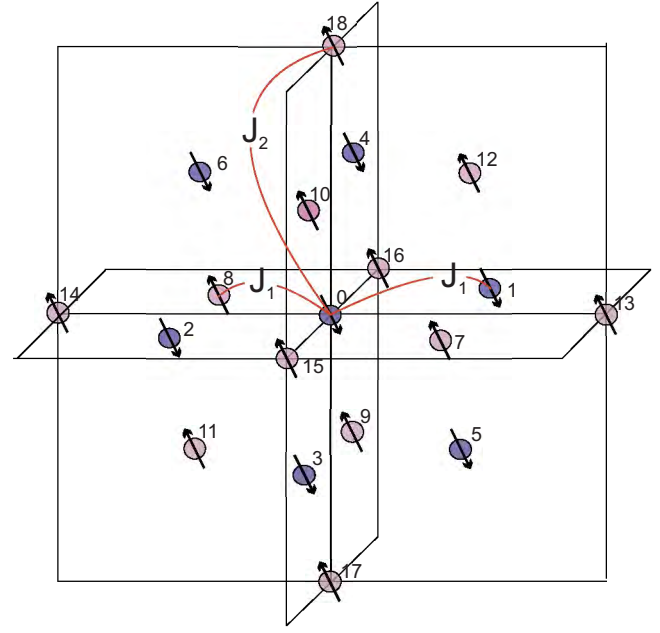
with

FIG. 1. (Color online) The fcc lattice of α-MnSe in the antiferromagnetic phase with an arbitrary spin direction. Here, 1–12 are the labels for the nearest-neighbor ions and 13–18 are respective labels for the next-nearest neighbors.

$$x = q_x a, \quad y = q_y a, \quad z = q_z a, \qquad (8)$$

where $a = 5.464$ Å, Ref. 24.

The Néel temperature is determined by solving Eq. (6) with respect to T when the sublattice magnetization becomes finite. Similarly, by converting $A(\mathbf{0})$ into $-A(\mathbf{0})$, we come up with θ temperature, which is an analog to the Curie-Weiss temperature when, hypothetically, all the spins in the system are turned to be ferromagnetically aligned. Then, one can easily obtain that

$$k_B T_N = \frac{75}{2}(1+g)J_2, \qquad (9)$$

$$-k_B \theta = \frac{75}{2}(1+g)(J_2 + 2J_1). \qquad (10)$$

Formulas (9) and (10) are in good agreement with the respective ones obtained by use of the Holstein-Primakoff representation for $\frac{5}{2}$ spins on manganese atoms in Ref. 25. This is the trump for the justification of our starting approximation [Eq. (1)].

Relying on the magnetic susceptibility measurements carried out in Ref. 7 and on the assumption that there are no structural changes below the magnetic phase transition temperature, one can come up with $\theta = -335$ K, $T_N = 130$ K, and the exchange interaction parameters, $J_1 = 1.94$ cm^{-1} and $J_2 = 2.46$ cm^{-1} as well. Respecting the fact that the AF exchange interaction J_2 stabilizes the system in some kind of AF ordered state, contrary to the AF interaction J_1 that

frustrates it, and bearing in mind the calculated ratio, $J_2/J_1 = 1.27 > 1/2$, the stability of the suggested AF ordering is maintained.[25,26]

After justifiably omitting all magnon-magnon interaction terms, the magnon dispersion relation can be calculated in the order of $(1/z)^1$ from the following transversal magnon propagator:[22,23]

$$\mathcal{T}_{mn}^{(1)}(\mathbf{k},\tau) = \langle \hat{\theta} \hat{S}_{m\mathbf{k}}^{-}(\tau) \hat{S}_{n\mathbf{k}}^{+}(0) \rangle, \tag{11}$$

where m,n are the sublattice indices (1 or 2) and $\hat{\theta}$ is the time ordering operator. Upon solving the corresponding Dyson's equation, the expression for this propagator in the imaginary time representation, $\mathcal{T}_{m,n}^{(1)}(\mathbf{k},i\omega)$, is given by

$$\hat{\mathcal{T}}^{(1)}(\mathbf{k},i\omega) = \frac{2\mathcal{M}}{E_{\mathbf{k}}^2 + \omega^2} \times \begin{pmatrix} \Xi^{+}(\mathbf{k},i\omega) & A(\mathbf{k})\mathcal{M} \\ A(\mathbf{k})\mathcal{M} & \Xi^{-}(\mathbf{k},i\omega) \end{pmatrix}, \tag{12}$$

where

$$\Xi^{\pm}(\mathbf{k},i\omega) = \pm i\omega + (1+g)[A(\mathbf{0}) + B(\mathbf{0})]\mathcal{M} - B(\mathbf{k}),$$
$$\mathcal{M} = |\mathcal{M}_{1,2}|, \tag{13}$$

and the magnon dispersion relation reads

$$E_{\mathbf{k}}(T) = \mathcal{M}(T)\sqrt{\{(1+g)[A(\mathbf{0}) + B(\mathbf{0})] - B(\mathbf{k})\}^2 - A^2(\mathbf{k})}. \tag{14}$$

The same dispersion relation can be found in Ref. 17. This is additional factor in favor of our starting ansatz [Eq. (1)].

Diagonalizing $\hat{\mathcal{T}}^{(1)}(\mathbf{k},i\omega)$ by means of the Bogoliubov's canonical transformation,

$$\tilde{T}(\mathbf{k},i\omega) = \mathcal{S}^{\dagger}(\mathbf{k})\hat{\mathcal{T}}^{(1)}(\mathbf{k},i\omega)\mathcal{S}(\mathbf{k}), \tag{15}$$

we come up with

$$\tilde{T}(\mathbf{k},i\omega) = 2\mathcal{M} \begin{pmatrix} \dfrac{1}{E_{\mathbf{k}} - i\omega} & 0 \\ 0 & \dfrac{1}{E_{\mathbf{k}} - i\omega} \end{pmatrix},$$

$$\mathcal{S}(\mathbf{k}) = \begin{pmatrix} \alpha_{\mathbf{k}} & -\beta_{\mathbf{k}} \\ -\beta_{\mathbf{k}} & \alpha_{\mathbf{k}} \end{pmatrix}, \tag{16}$$

$$\alpha_{\mathbf{k}}^2 = \frac{1}{2} \left\{ \left[1 - \left(\frac{A(\mathbf{k})}{(1+g)[A(\mathbf{0}) + B(\mathbf{0})] - B(\mathbf{k})} \right)^2 \right]^{-1/2} + 1 \right\},$$

$$\alpha_{\mathbf{k}}^2 - \beta_{\mathbf{k}}^2 = 1. \tag{17}$$

Unlike the transversal magnon propagator $\tilde{T}(\mathbf{k},i\omega)$, the longitudinal one does not have terms of the order of $(1/z)^1$. Even if one wanted to take into account longitudinal spin-fluctuation phenomena in higher orders $(1/z)^{n>1}$, such contributions would be irrelevant because of the $\delta_{\omega 0}$ factor involved in the longitudinal propagator, whereas we are interested in the finite frequencies optically active phonon modes.[22]

III. SPIN-PHONON INTERACTION IN α-MnSe

This section gives details of the spin system influence upon the lattice dynamics in the ordered phase of α-MnSe. Our calculations are carried out for the extended form of the Heisenberg Hamiltonian (4) that includes spin-phonon interaction terms in a standard way by expanding the exchange integrals in the powers of ionic displacements.[12,13] The spin-phonon interaction terms in the extended Heisenberg Hamiltonian are easily obtained by taking into account only the first derivative with respect to atomic displacements of the J_2 exchange integral. This is a consequence of the evident fact that, for the infrared active phonon modes[7] and the suggested magnetic ordering, all the (nn) contributions exactly cancel each other (every Mn ion is surrounded by the equal number of spin-up and spin-down ions). Thus, the spin-phonon interaction in α-MnSe with the suggested AF ordering is driven only by the last term in the modified Heisenberg Hamiltonian (4). The expansion of that term in ionic displacements gives

$$\hat{H}^{sp-ph} = \sum_{\langle i,j \rangle}^{nnn} \hat{\mathbf{S}}_i \{(\mathbf{x}_i - \mathbf{x}_j) \cdot \{\hat{\nabla}_{\mathbf{R}_i - \mathbf{R}_j} \hat{J}_2(\mathbf{R}_i - \mathbf{R}_j)\}|_0\} \hat{\mathbf{S}}_j, \tag{18}$$

where $\mathbf{l}_i$ and $\mathbf{l}_j$ enumerate equilibrium ionic position in up and down spin sublattices, and

$$\mathbf{R}_{i,j} = \mathbf{l}_{i,j} + \mathbf{x}_{i,j}, \tag{19}$$

$$\hat{J}_2(\mathbf{l}_i + \mathbf{x}_i - \mathbf{l}_j - \mathbf{x}_j) \approx \hat{J}_2(\mathbf{l}_i - \mathbf{l}_j) + (\mathbf{x}_i - \mathbf{x}_j)$$
$$\cdot \{\hat{\nabla}_{\mathbf{R}_i - \mathbf{R}_j} \hat{J}_2(\mathbf{R}_i - \mathbf{R}_j)\}|_0,$$

$$\hat{J}_2(\mathbf{l}_i - \mathbf{l}_j) \equiv \hat{J}_2. \tag{20}$$

The expansion of displacements $\mathbf{x}_i$ from their equilibrium position $\mathbf{l}_i$ in normal modes is given by

$$\mathbf{x}_i = \sqrt{\frac{\hbar}{2NM_i}} \sum_{\mathbf{q},\lambda} \frac{1}{\sqrt{\Omega_{\mathbf{q},\lambda}}} \mathbf{w}(\mathbf{q},\lambda) e^{i\mathbf{q}\cdot\mathbf{l}_i} (\hat{b}_{\mathbf{q},\lambda} + \hat{b}_{-\mathbf{q},\lambda}^{\dagger}). \tag{21}$$

Here, the phonon field operator is given by $\hat{\Phi}_{\mathbf{q},\lambda} = \hat{b}_{\mathbf{q},\lambda} + \hat{b}_{-\mathbf{q},\lambda}^{\dagger}$, $\Omega_{\mathbf{q},\lambda}$ is the normal mode frequency with wave vector $\mathbf{q}$ and branch index λ (LO, TO, TA,...), $\mathbf{w}(\mathbf{q},\lambda)$ is the polarization vector of the normal mode, $\hat{b}_{\mathbf{q},\lambda}^{\dagger}$ and $\hat{b}_{\mathbf{q},\lambda}$ are phonon creation and annihilation operators, N is the number of unit cells in the crystal, and M_i stands for the ionic mass.

Equations (18) and (21) give for the effective spin-phonon Hamiltonian,

$$\hat{H}^{sp-ph} = \sum_{\langle i,j \rangle}^{nnn} \sum_{\mathbf{q},\lambda} \hat{\Phi}_{\mathbf{q},\lambda} \hat{\mathbf{S}}_i \hat{\mathcal{K}}(\mathbf{l}_i,\mathbf{l}_j,\mathbf{q},\lambda) \hat{\mathbf{S}}_j, \tag{22}$$

with

$$\hat{\mathcal{K}}(\mathbf{l}_i,\mathbf{l}_j,\mathbf{q},\lambda) = \sqrt{\frac{\hbar}{2NM\Omega_{\mathbf{q},\lambda}}} (e^{i\mathbf{q}\cdot\mathbf{l}_i} - e^{i\mathbf{q}\cdot\mathbf{l}_j})$$
$$\times \{[\mathbf{w}(\mathbf{q},\lambda) \cdot \hat{\nabla}_{\mathbf{R}_i - \mathbf{R}_j}]\hat{J}_2(\mathbf{R}_i - \mathbf{R}_j)\}|_0. \tag{23}$$

Accordingly, for the infrared active phonon mode ($\mathbf{q} \approx 0$, $\Omega_{\mathbf{q},\lambda} \equiv \Omega$), we can write

TABLE I. The phonon-phonon and magnon-phonon fitting parameters of the LO phonon mode Ω_{01} and the one combinational two-phonon mode Ω_{02}. .

Phonon frequency (cm^{-1})	Phonon-phonon parameter (cm^{-1})	Magnon-phonon parameter (cm^{-1})
$\Omega_{01}=230.40$	$C_1=0.81$	$K_1=2.37$
$\Omega_{02}=224.60$	$C_2=1.78$	$K_2=2.33$

$$\mathcal{K}^{\mu\nu}(\mathbf{l}_i,\mathbf{l}_j,\mathbf{q},\lambda) \approx i\sqrt{\frac{\hbar}{2NM\Omega}}\mathbf{q}\cdot(\mathbf{l}_i-\mathbf{l}_j)$$

$$\times \{[\mathbf{w}(\mathbf{q})\cdot\hat{\nabla}_{\mathbf{R}_i-\mathbf{R}_j}]J_2^{\mu\nu}(\mathbf{R}_i-\mathbf{R}_j)\}|_{\mathbf{0}},$$

which after the Fourier transformation and in the limit of small phonon wave vectors becomes

$$\mathcal{K}^{\mu\nu}(\mathbf{Q},\mathbf{q}\approx 0) \sim i\left(\mathbf{q}\cdot\frac{\partial}{\partial\mathbf{Q}}\right)\{[\mathbf{w}(\mathbf{q})\cdot\mathbf{Q}]J_2^{\mu\nu}(\mathbf{Q})\}. \quad (24)$$

Finally, we are making an ultimate simplification which is expected to be appropriate for the optical infrared phonons we are dealing with in the present work. Instead of the **Q**-dependent spin-phonon interaction tensor, the constant diagonal tensor describing the magnon-phonon interaction is thus introduced as

$$\frac{1}{2}|\hat{\mathcal{K}}(\mathbf{Q},\mathbf{q}\approx 0)| \equiv \begin{pmatrix} K & 0 & 0 \\ 0 & K & 0 \\ 0 & 0 & (1+g)K \end{pmatrix}. \quad (25)$$

Magnon-phonon interaction constant K is expected to be much smaller than the characteristic frequency of optical modes in crystals (cf. Table I in the present work). The approximation [Eq. (25)] provides the simplest possible way of connecting the theory with the experimental data. This is allowed by the fact that Eq. (24) possesses very small q factor which smoothes the **Q** dependence of the whole expression.

The diagrammatic expression for the magnon-phonon interaction is given in Fig. 2, where the shaded circle represents the magnon-phonon interaction vertex with the additional vertex condition $m \neq n_1$, caused by the fact that the

$\mathcal{T}_{mn}(\mathbf{k}, i\omega + i\Omega)$

$\Pi^{(0)}(\mathbf{0},i\Omega)$

$\mathcal{T}_{m_1n_1}(\mathbf{k}, i\omega)$
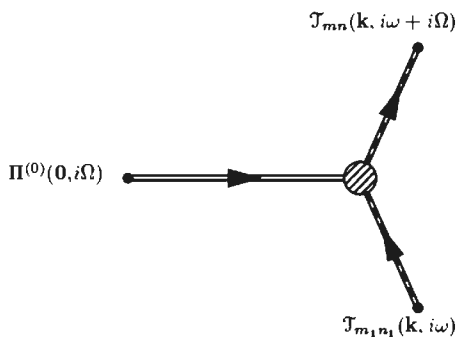
FIG. 2. The magnon-phonon interaction diagram.
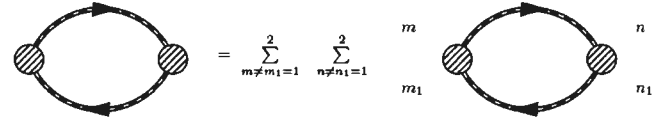
FIG. 3. The self-energy represented by four intersublattice pair-bubble parts.

magnon-phonon interaction has been obtained through the expansion of exchange interaction J_2 connecting different sublattices.

Renormalizing the bare optical phonon propagator $\Pi^{(0)}(\mathbf{q}\approx\mathbf{0},i\Omega)$ by the magnon-phonon interaction terms, we come up with the following Dyson's equation:

$$\Pi(\mathbf{0},i\Omega) = \frac{1}{\frac{1}{\Pi^{(0)}(\mathbf{0},i\Omega)} - \Sigma(\mathbf{0},i\Omega)}, \quad (26)$$

with the self-energy $\Sigma(0,i\Omega)$ represented by four intersublattice pair-bubble parts[27] in the diagram given in Fig. 3.

After straightforward, but analytically tedious manipulations, one can show that the explicit expression for the phonon self-energy operator is

$$\Sigma(\mathbf{0},i\Omega) = \frac{4K^2\mathcal{M}^2}{\beta N}\sum_{\mathbf{k}}\sum_{n=-\infty}^{n=+\infty}(\alpha_{\mathbf{k}}^2+\beta_{\mathbf{k}}^2)^2$$

$$\times\left(\frac{1}{i\omega_n+E_{\mathbf{k}}}\frac{1}{-i\omega_n-i\Omega+E_{\mathbf{k}}}\right.$$

$$+\frac{1}{-i\omega_n+E_{\mathbf{k}}}\frac{1}{i\omega_n+i\Omega+E_{\mathbf{k}}}\right)$$

$$+4\alpha_{\mathbf{k}}^2\beta_{\mathbf{k}}^2\left(\frac{1}{i\omega_n+E_{\mathbf{k}}}\frac{1}{i\omega_n+i\Omega+E_{\mathbf{k}}}\right.$$

$$+\frac{1}{-i\omega_n+E_{\mathbf{k}}}\frac{1}{-i\omega_n-i\Omega+E_{\mathbf{k}}}\right). \quad (27)$$

Performing the Matsubara summation over the imaginary boson frequencies by converting the sum to a contour integral[27] yields the result,

$$\Sigma[\mathbf{0},\Omega(T)] = -16K^2\mathcal{M}^2(T)\frac{1}{N}\sum_{\mathbf{k}}(\alpha_{\mathbf{k}}^2+\beta_{\mathbf{k}}^2)^2\coth\left(\frac{E_{\mathbf{k}}(T)}{2k_BT}\right)$$

$$\times\frac{E_{\mathbf{k}}(T)}{4E_{\mathbf{k}}^2(T)+[i\Omega(T)]^2+i\eta}, \quad (28)$$

where $\Sigma_{\mathbf{k}}$ represents summation over all the magnon degrees of freedom. Thus, we obtain the renormalized phonon frequency as

$$\Omega_R(T) = \Omega(T) + \Delta\Omega(T). \quad (29)$$

Here,
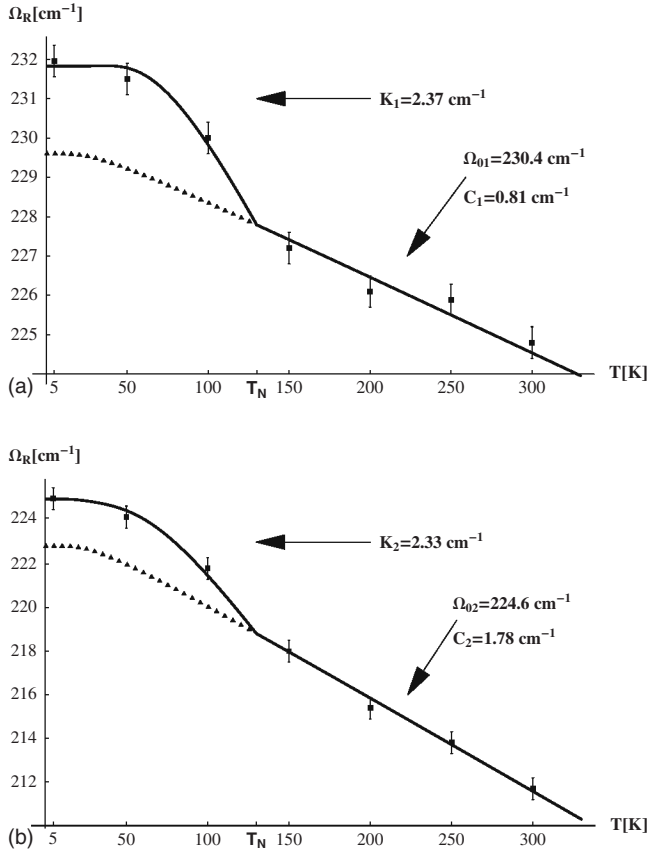
FIG. 4. (a) The visual survey of longitudinal optical phonon mode Ω_{01} and (b) combinational two-phonon mode Ω_{02} as a function of temperature. Squares with the error bars are the experimental results (Ref. 7), the full lines are our theoretical curves, whereas the triangles represent the residue of phonon hardening due to the phonon-phonon anharmonicity.

$$\Omega(T) = \Omega_0 - C\left(1 + \frac{2}{e^{(\hbar\Omega_0/2k_BT)} - 1}\right) \tag{30}$$

is the renormalized bare phonon frequency Ω_0 on the basis of the standard Balkanski's procedure which takes into account phonon-phonon interaction terms,[28] C is the phonon-phonon interaction strength, and

$$\Delta\Omega(T) = \text{Re}\{\Sigma[\mathbf{0}, \Omega(T)]\} \tag{31}$$

is presently calculated renormalization due to the magnon-phonon interaction. Note, just for completeness, that the renormalized optical phonon has the infinitesimally small damping up to the $i\eta$ factor.

IV. RESULTS AND DISCUSSION

Let us proceed further with the comparison of theoretical model presented in previous sections with the recent infrared reflectivity measurements in α-MnSe.[7] These experimental data clearly point to the additional phonon frequency hardening for temperatures below the AF transition temperature at 130 K (cf. Fig. 4). There are two basic fitting parameters: C and K which, as we already mentioned, represent the

phonon-phonon and magnon-phonon interaction strength constants, respectively. In addition, we have introduced the small anisotropy parameter g. It occurs that a slight extension of the the Heisenberg Hamiltonian (4), in order to include an anisotropy, is particularly relevant for getting quantitative agreement with the experiments. We have found that the anisotropy parameter should be $g \gtrsim 10^{-2}$, if one wanted to obtain suitable order of phonon hardening. This is in accordance with a common wisdom regarding the coupling of the magnetic system with the crystal lattice through the magnetic anisotropy energy. Using the one-magnon Raman excitation observed at ≈ 18 cm^{-1} in α-MnSe (Ref. 8) enables us to fix the true value of the anisotropy parameter, i.e., $g \approx 3 \times 10^{-2}$.

Note here that the anisotropies induced in the vibrational spectrum of transition-metal monoxide MnO (closely related to α-MnSe), solely by AF ordering, were investigated theoretically on the basis of accurate *ab initio* (mostly density-functional) and semiempirical calculations.[29] These authors found the anisotropy important both in the $\mathbf{q}=0$ optic phonon frequencies and in the dynamical charge tensor. They revealed that manganese monoxide MnO below T_N, despite having a cubic ionic arrangement and a practically cubic electron density, has a noncubic electronic response with strong enhancement of the weak anisotropy influenced by low-symmetry perturbations.

At last, we performed fitting the recently measured infrared phonon frequencies in the temperature range of 5–300 K (one LO phonon mode and one combinational two-phonon mode) using the microscopically calculated expression for the renormalized phonon frequencies $\Omega_R(T)$ [Eq. (29)]. Our results are presented in Fig. 4 and Table I. Almost perfect agreement with the experimental results, as well as the fitting parameters which have clear physical meaning, makes this straightforward approach very promising. One can infer from Table I that the fitting parameters take quite reasonable values. Thus, we have right to expect that the fitting function could also be useful for predicting eventual phonon softening in the region of phonon frequencies of the order of 100 cm^{-1} and less.

In conclusion, we have developed a microscopic approach for the renormalization of the phonon spectra due to the spin-phonon interaction terms. By means of detailed comparison between theory and experiment for the infrared optical phonon hardening in the antiferromagnetic phase of α-MnSe, the phonon-phonon and spin-phonon interaction parameters are estimated for this compound, as well as the exchange interactions for the nearest and next-nearest neighbors. We have found that the inclusion of the anisotropy has been essential for obtaining quantitative agreement with the experimental results.

*djokic@phy.bg.ac.yu

[1] R. Loudon, Adv. Phys. **17**, 243 (1968).

[2] E. Anda, J. Phys. C **9**, 1075 (1976).

[3] K. Wakamura and T. Arai, Phase Transitions **27**, 129 (1990).

[4] X. B. Wang, J. X. Li, Q. Jiang, Z. H. Zhang, and D. C. Tian, Phys. Rev. B **50**, 7056 (1994).

[5] D. U. Saenger, Phys. Rev. B **52**, 1025 (1995).

[6] A. Wurger, Phys. Rev. B **57**, 347 (1998).

[7] Z. V. Popović and A. Milutinović, Phys. Rev. B **73**, 155203 (2006).

[8] A. Milutinović, N. Tomić, S. Dević, P. Milutinović, and Z. V. Popović, Phys. Rev. B **66**, 012302 (2002).

[9] D. J. Lockwood and M. G. Cottam, J. Appl. Phys. **64**, 5876 (1988).

[10] D. J. Lockwood, Low Temp. Phys. **28**, 505 (2002).

[11] W. Baltensperger and J. S. Helman, Helv. Phys. Acta **41**, 668 (1968).

[12] G. Meissner, Z. Phys. **237**, 272 (1970).

[13] F. Vukajlović, H. Konwent, and N. M. Plakida, Theor. Math. Phys. **19**, 115 (1974).

[14] A. B. Migdal, Sov. Phys. JETP **34**, 996 (1958).

[15] D. C. Mattis, *Theory of Magnetism* (Harper, New York, 1965).

[16] H. J. Spencer, Phys. Rev. **167**, 430 (1968).

[17] R. J. Elliott and M. F. Thorpe, J. Phys. C **2**, 1630 (1969).

[18] B. J. McKenzie and G. E. Stedman, J. Phys. A **9**, 187 (1976).

[19] S. E. Barnes, J. Phys. C **5**, L178 (1972).

[20] S. Maekawa, T. Tohyama, S. E. Barnes, S. Ishihara, W. Koshibae, and G. Khaliullin, *Physics of Transition Metal Oxides* (Springer-Verlag, Berlin, 2004).

[21] K. Yosida, J. Appl. Phys. **39**, 511 (1968).

[22] M. G. Cottam and R. B. Stinchcombe, J. Phys. C **3**, 2283 (1970).

[23] M. G. Cottam and R. B. Stinchcombe, J. Phys. C **3**, 2305 (1970).

[24] T. Ito, K. Ito, and M. Oka, Jpn. J. Appl. Phys. **17**, 371 (1978).

[25] R. H. Swendsen, Phys. Rev. B **13**, 3912 (1976).

[26] M. C. Moron, J. Phys.: Condens. Matter **8**, 11141 (1996).

[27] R. D. Mattuck, *A Guide to Feynman Diagrams in the Many-Body Problem* (Dover, New York, 1992).

[28] R. F. Wallis and M. Balkanski, *Many-Body Aspects of Solid State Spectroscopy* (North-Holland, Amsterdam, 1986).

[29] S. Massidda, M. Posternak, A. Baldereschi, and R. Resta, Phys. Rev. Lett. **82**, 430 (1999).

Investigation of thermostability and phonon–phonon interactions in $Mo_6S_3I_6$ nanowires by Raman scattering spectroscopy

J. M. Todorović,[a] Z. D. Dohčević-Mitrović,[a]* D. M. Đokić,[a] D. Mihailović[b] and Z. V. Popović[a]

Detailed Raman scattering measurements were performed on molybdenum–sulfur–iodine nanowires ($Mo_6S_3I_6$). At room temperature, 21 well-resolved Raman modes were experimentally observed for the first time in this new compound. The phase stability and vibrational properties of the nanowires were investigated by different temperature treatments. High-temperature Raman spectra showed that the phase separation of $Mo_6S_3I_6$ nanowires took place between 573 and 673 K, followed by appearance of a new mode at 819 cm^{-1} characteristic of the MoO_3 phase. Low-temperature Raman scattering spectra showed a significant difference in phonon–phonon interactions between internal and external Raman modes of $Mo_6S_3I_6$ nanowires. These interesting vibrational properties can give new insights for improved material preparation and achievement of higher conductivity and other functional properties of these otherwise interesting materials. Copyright © 2009 John Wiley & Sons, Ltd.

Keywords: $Mo_6S_3I_6$ nanowires; Raman scattering; thermostability; phonon–phonon interactions

Introduction

The peculiar properties of $Mo_6S_3I_6$ nanowires have attracted much attention because of the numerous possible applications of this material for polyelectrolytes,[1] optical and chemisensors,[2] field emission tips,[3] field emission transistors and solid lubrication.[4] Furthermore, $Mo_6S_3I_6$ nanowire bundles can be connected with gold nanoparticles[5] in solutions to form networks,[6] meaning that they can be used as nanoconnectors at molecular level.

As previously reported,[1] $Mo_6S_3I_6$ nanowires can be synthesized in a single-step process directly from its component elements in the form of hair-like bundles. The individual bundles are of tens of nanometers in diameter and of the order of millimeters in length.[1,5] These bundles consist of weakly bound identical nanowires of 0.96 nm in diameter.[5] Although structurally identical, the wires are imperfect by nature, with the presence of vacancies, defects and impurities[1,3] such as $Mo_6S_6I_2$, Mo_2S_3 and MoS_2 inside the structure. Improved method of synthesis on molybdenum foils or on quartz plates as substrates enables more precise control over bundle synthesis parameters.[3] In such a way, $Mo_6S_6I_2$ single crystals grow in the form of cubes on the Mo substrate and act as the seed crystals from which $Mo_6S_3I_6$ bundles spontaneously form under specific external conditions.[3]

Van der Waals interaction among the wires has far-reaching implications affecting various aspects of physical properties of this material. The obvious consequences are imperfect ordering and possible bending or cross-linking of the wires inside a bundle. Moreover, the material can be easily dispersed in a variety of organic solvents without covalent functionalization[7,8] down to individual nanowires[9] using an ultrasonic bath. On the other hand, the spatial incoherence pose serious problems in the exact determination of the crystal structure and space group of the $Mo_6S_3I_6$ nanowires. Initially, transmission electron microscopy

revealed chain-like structures inside $Mo_6S_3I_6$ bundle[1] identified as individual wires. X-ray diffraction measurements alone were not enough to obtain unambiguous crystallographic unit cell,[1] but when accompanied by extended X-ray absorption fine structure measurements,[5] they indicated that the nanowire packing fitted to the hexagonal $P6_3$ space group taking into account the deviation of about 15% between the observed and the calculated diffraction patterns. However, recent high-resolution transmission electron microscopy data and annular dark-field imaging using an aberration-corrected scanning transmission electron microscope[10] proposed the triclinic $P\bar{1}$ space group crystal structure. These experiments have provided so far the best insight into the positions of the atomic species[10] in the definitely determined skeletal structure of a wire.[5,10]

In this work, we report Raman scattering experiments performed on $Mo_6S_3I_6$ nanowires over a wide range of temperatures, aimed at the investigation of vibrational properties and thermostability of these systems. Raman spectra of $Mo_6S_3I_6$ nanowires collected at room temperature resemble the typical spectra of molecular crystals with a frequency gap between the internal and the external Raman modes. Data obtained from the high-temperature measurements were consistent with earlier indication of phase separation above 300 °C in an oxygen environment.[1] We exper-

* Correspondence to: Z. D. Dohčević-Mitrović, Center for Solid State Physics and New Materials, Institute of Physics, 11080 Belgrade, Pregrevica 118, Serbia. E-mail: zordoh@phy.bg.ac.rs

a Center for Solid State Physics and New Materials, Institute of Physics, Pregrevica 118, P. O. Box 68, 11080 Belgrade, Serbia

b Department of Complex Matter, Jozef Stefan Institute, Jamova 39, 1000 Ljubljana, Slovenia

imentally observed 21 Raman active modes (from 45 predicted by factor group analysis for $P\bar{1}$ structure). Low-temperature Raman spectra revealed different anharmonic behavior of phonon frequencies belonging to external and internal Raman vibrations.

Experimental

$Mo_6S_3I_6$ nanowires were grown from $Mo_6S_6I_2$ single crystals which were formed on Mo substrate, as already described in Ref. [3] Raman spectra were acquired on a micro-Raman T64000 Jobin Yvon system using the 514.5 nm excitation line of Ar^+ laser in the backscattering geometry. Raman spectra of nanowires were recorded in three different manners: by increasing the incident laser power in the range 1–9 mW (by increasing power density at the sample in the range 0.24–2.19 kW/cm^2), by gradual heating from 297 up to 873 K, and by varying the temperature from 5 to 300 K. High-temperature measurements were performed using a Linkam THMS600 heating/cooling stage. In this set of measurements, the incident laser power was held at as low as 2 mW in order to minimize the local heating of the sample induced by the confocal focusing of the laser beam.

The Raman spectra in the temperature range from 5 to 300 K were obtained using a Cryovac Konti liquid helium microscope cryostat. The incident laser power was minimized and kept fixed (2 mW) during the measurements.

Results and Discussion

$Mo_6S_3I_6$ nanowires weakly bound in crystalline bundles have triclinic crystal structure with $P\bar{1}$ space group.[10] The unit cell consists of two $Mo_6S_3I_6$ formula units ($Z = 2$). The structure of $Mo_6S_3I_6$ nanowires is given in the literature.[10] The unit cell of the $Mo_6S_3I_6$ crystal structure contains six atomic planes of which four are mixed planes, each containing 3Mo atoms surrounded by 3I atoms, and two are linkage planes, each solely occupied by 3S atoms. Thus, the molybdenum octahedron Mo_6 is surrounded by 6I atoms in peripheral sites and by two linkage planes each containing 3S atoms. Adjacent $Mo_6S_3I_6$ molecules are rotated by $180°$ around long wire axis relative to each other. All atoms are in (2i) symmetry position of $P\bar{1}$ space group and the factor group analysis yields

$$\Gamma(P\bar{1}) = \underbrace{45A_g}_{\text{Raman active}} + \underbrace{42A_u}_{\text{IR active}} \qquad (1)$$

Thus, 45 Raman modes are expected to be seen in the Raman scattering experiment.

Room-temperature Raman spectrum of $Mo_6S_3I_6$ nanowires, measured on the bunch of bundles, is presented in Fig. 1.

In the spectral region 70–550 cm^{-1}, nearly 21 well-resolved Raman modes can be observed. Raman scattering spectra of $Mo_6S_3I_6$ nanowires have been published, to the best of our knowledge, only in Ref. [1] where only five Raman modes were observed in the same spectral range. In the inset of Fig. 1 is given a photo of the fairly well-oriented bundles from which the Raman spectrum was collected. As can be seen from Fig. 1, Raman spectrum of $Mo_6S_3I_6$ nanowires is very similar to the Raman spectra of the Chevrel phase crystals (Cu, Pb, Ba, Sn) Mo_6S_8, i.e. the vibrations of Mo_6S_8 clusters play a dominant role in the vibrational properties of $Mo_6S_3I_6$ nanowires.[11] The Raman spectrum from Fig. 1 is composed of two regions: the low-energy (below 175 cm^{-1}) region and high-energy region
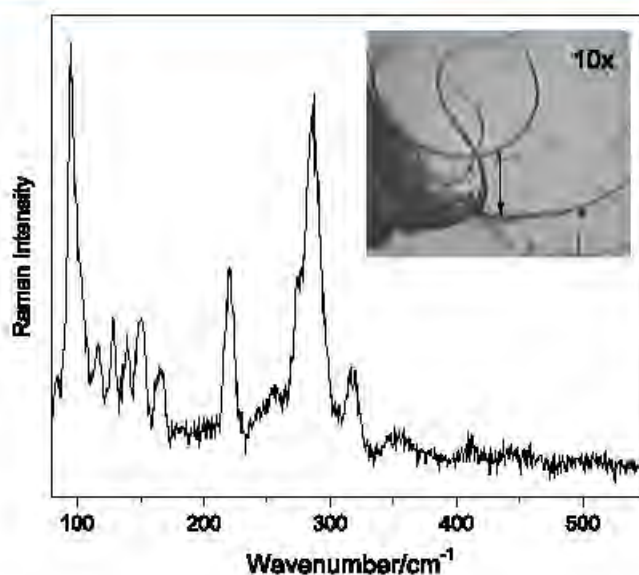
Figure 1. Room-temperature Raman spectrum of $Mo_6S_3I_6$ nanowires measured on a bunch of bundles. The inset shows the bundles.
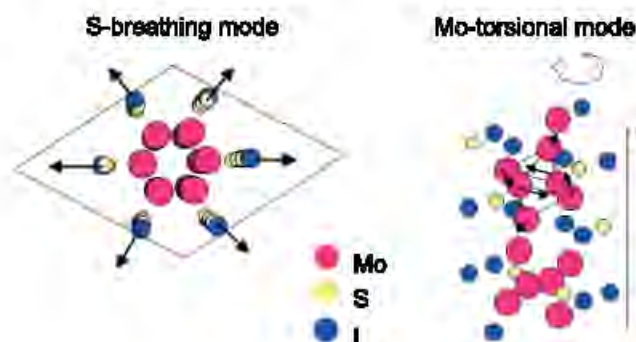
Figure 2. An illustration of nanowire vibrations for the breathing mode of S and torsional mode of Mo.

(above 200 cm^{-1}) separated by a frequency gap characteristic of crystals where molecular vibrations dominate. The low-energy modes can be classified as external modes originating mostly from the Mo–Mo vibrations. These modes exhibit predominantly torsional character. The most intense mode in this spectral region is centered at 95 cm^{-1}. The high-energy modes are classified as internal modes representing S–S breathing vibrations, and the most intense mode is positioned at 286 cm^{-1}.[1] A schematic illustration of breathing and torsional mode vibrations in the case of $Mo_6S_3I_6$ nanowires is presented in Fig. 2.

The deconvolution of internal and external Raman modes was performed using Lorentzian-type line profile. Examples of Lorentzian deconvolution of $Mo_6S_3I_6$ nanowire Raman modes in two different ranges are presented in Fig. 3.

Peak positions of the external and internal Raman modes thus obtained are summarized in Table 1.

In order to investigate the local heating effects on the structural stability of $Mo_6S_3I_6$ nanowires, we measured the Stokes and anti-Stokes Raman spectra by increasing incident laser power on the sample, Fig. 4.

It is possible to estimate the local temperature of the sample from the ratio of the Stokes and anti-Stokes Raman line intensity

979
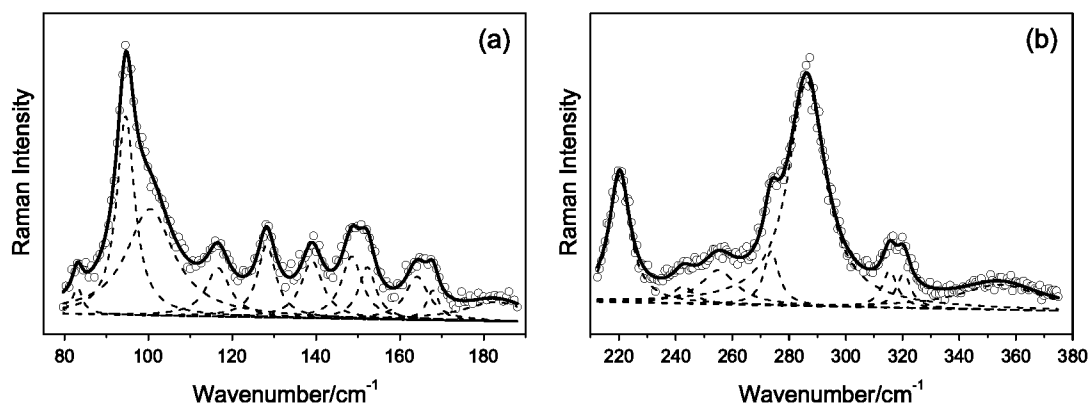
Figure 3. The deconvolution of the Raman spectra using Lorentzian functions for internal and external modes of $Mo_6S_3I_6$ nanowires.

Table 1. Raman mode wavenumbers obtained by Lorentzian deconvolution of the Raman spectrum from Fig. 1

External modes (cm^{-1})	Internal modes (cm^{-1})
83.1 ± 0.3	220.2 ± 0.1
94.60 ± 0.07	242.8 ± 0.9
100.5 ± 0.6	254.9 ± 0.8
116.6 ± 0.3	273.8 ± 0.2
128.2 ± 0.2	286.2 ± 0
139.0 ± 0.2	315.5 ± 0.5
148.5 ± 0.5	320.3 ± 0.6
152.2 ± 0.5	356 ± 2
164.1 ± 0.6	382 ± 3
167.8 ± 0.4	411 ± 1
183 ± 2	

using the formula:[12]

$$ T = \frac{\hbar \omega_s}{k_B} \left\{ \ln \left[\left(\frac{\omega_L + \omega_s}{\omega_L - \omega_s} \right)^4 \frac{I_{Stokes}}{I_{anti-Stokes}} \right] \right\}^{-1}, \qquad (2) $$

where ω_s and ω_L are phonon and excitation frequencies. Using the above formula, for the incident laser power of 2 mW from the Stokes and anti-Stokes mode intensity at 286 cm^{-1} we estimated that the average local temperature was around 450 K. As can be seen from Fig. 4, on gradually increasing the incident laser power up to 2 mW, there is no significant change in the Raman spectra. In the spectrum acquired at 3 mW, a new Raman mode at 819 cm^{-1} appears weakly, whereas at 4 mW this mode is clearly observed. This mode is characteristic of the molybdenum oxide (MoO_3) phase. The intensity of this mode increases with increasing incident laser power, and at 9 mW two additional modes of MoO_3 appear.[3] Due to the material decomposition by laser heating, the use of Stokes/anti-Stokes mode intensity ratio for temperature estimation was no longer possible. Because of that, it was necessary to perform high-temperature measurements in order to determine more precisely the temperature at which the nanowires started to decompose.

Raman spectra of the nanowires recorded at elevated temperatures are shown in Fig. 5.

As the temperature is increased, the Raman spectra undergo significant changes; i.e. intensities of all Raman modes decrease
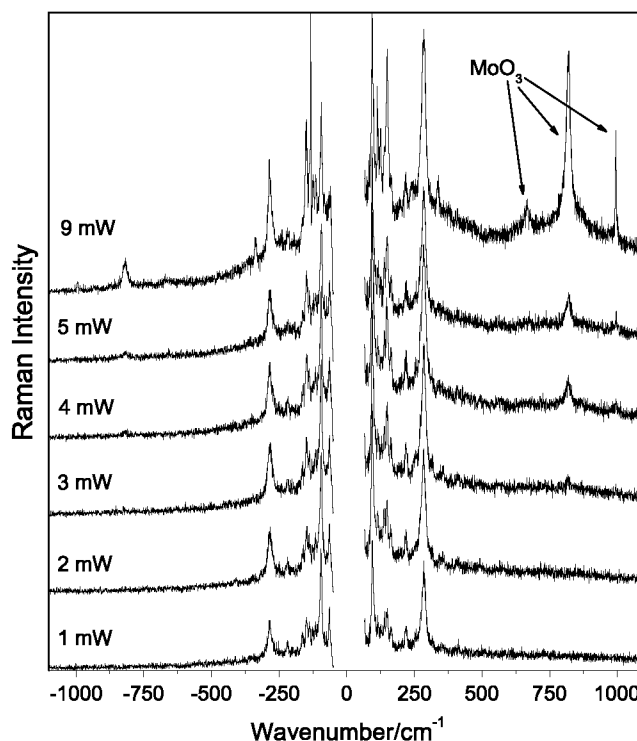
Figure 4. Raman spectra of $Mo_6S_3I_6$ nanowires in Stokes and anti-Stokes range measured by varying the incident laser power in the range 1–9 mW.

with the temperature rise. This is especially true for the most prominent external and internal Raman modes at 94 and 286 cm^{-1}. At 573 K, most of the Raman modes of nanowires have disappeared, whereas some modes at 274, 315.5 and 320 cm^{-1} have become barely visible. Such behavior can be ascribed to the structural transformation of $Mo_6S_3I_6$ nanowires and the initiation of Mo ion oxidation. At 673 K, an intense mode at 819 cm^{-1} indicates the formation of the molybdenum oxide phase. These results are in complete agreement with the data obtained from thermogravimetry measurements in an argon–oxygen environment.[1] Therefore, we concluded that $Mo_6S_3I_6$ nanowires started to decompose at temperatures between 573 and 673 K.

Furthermore, one can notice significant differences between the Raman spectra from Figs 4 and 5. As the laser power is increased, the nanowire Raman modes remain present in the spectra in Fig. 4 even when MoO_3 modes appear (starting at 3 mW), whereas in the
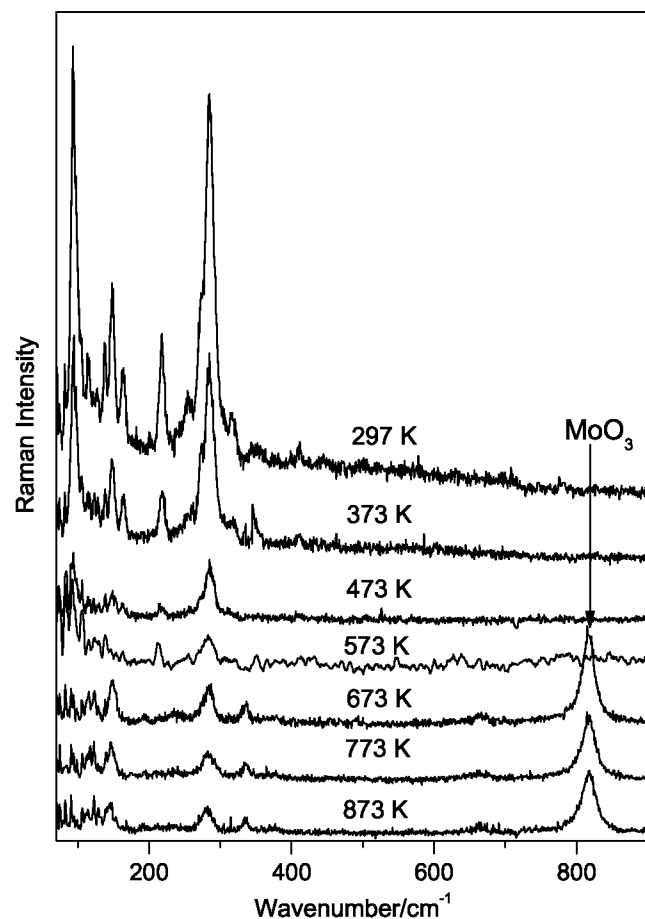
Figure 5. Raman spectra of Mo$_6$S$_3$I$_6$ measured in the temperature range 297–873 K.

Figure 6. Raman spectra of Mo$_6$S$_3$I$_6$ nanowires collected in the temperature range 5–300 K.

spectra in Fig. 5, most of the nanowire modes disappear already at 573 K whereas the other modes become considerably damped as temperature is increased. Laser heating (Fig. 4) substantially differs from standard heating (Fig. 5) in that the temperature starting from the laser spot center toward the edges of the compound may vary dramatically and can produce a temperature inhomogeneity. This temperature inhomogeneity influences the Raman spectra in such a way that MoO$_3$ forms in the micro-volume close to the center of the laser spot where the temperature is high enough to provoke the instability of nanowires and their oxidation. In the surrounding cooler domains, the nanowire bundles remain intact. On the other hand, in the case of homogeneous heating of the sample, MoO$_3$ layer forms as the nanowires decompose on a much larger scale.

Additionally, we noticed that phonon frequencies decrease with increase in temperature because of the anharmonic processes that become dominant at higher temperatures. Hence, we performed Raman measurements over the interval from 5 up to 300 K to study the temperature-induced changes of the vibrational properties of these materials.

The Raman spectra of Mo$_6$S$_3$I$_6$ acquired at temperatures from 5 to 300 K are represented in Fig. 6. To investigate the temperature influence on the phonon anharmonic coupling, we analyzed the wavenumber *versus* temperature mode behavior for the most intense external and internal Raman modes at 95 and 286 cm^{-1}.

The wavenumber shift and the variation of the half-width of the Raman modes in Mo$_6$S$_3$I$_6$ nanowires at constant pressure induced by temperature are a consequence of the anharmonicity. As

an effect of anharmonic interactions, the nonequilibrium phonon population decays into phonons of lower energy (downconversion process) or can be scattered by thermal phonons into phonons of different energy (upconversion processes). The variation of wavenumbers and half-widths of the Raman bands with temperature or pressure due to the anharmonicity is very well discussed in the paper of Lucazeau.[13] Klemens[14] and afterwards Balkanski[15] proposed that the optical phonon decays into two or three lower energy phonons due to the anharmonic interactions. In that case, temperature dependence of the Raman mode frequency including three and four phonon anharmonic processes, is given by:

$$\omega(q,T) = \omega_0(q) + \Delta\omega(T) \tag{3}$$

$$\Delta\omega(T) = C\left[1 + \frac{2}{e^{\frac{\hbar\omega_0}{2k_B T}} - 1}\right] + D\left[1 + \frac{3}{e^{\frac{\hbar\omega_0}{3k_B T}} - 1}\right.$$

$$\left. + \frac{3}{\left(e^{\frac{\hbar\omega_0}{3k_B T}} - 1\right)^2}\right], \tag{4}$$
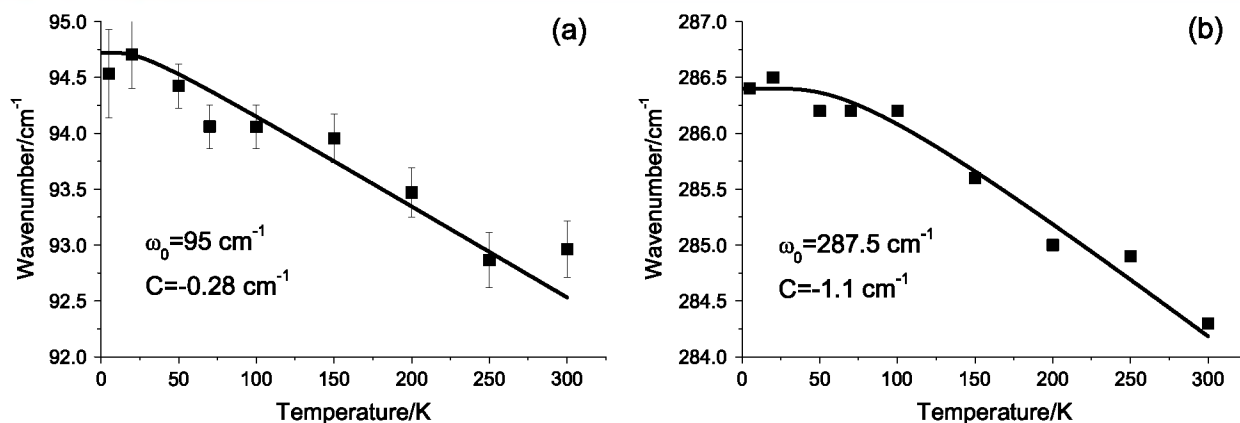
Figure 7. Wavenumber *versus* temperature dependence for the mode at (a) 95 cm^{-1} and (b) 286 cm^{-1}.

where ω_0 is harmonic frequency and C, D are anharmonic constants. The phonon–phonon interactions are of special interest in nanostructured systems when we consider that there is no adequate theory yet that describes the anharmonic effects in these systems. Hence, the above anharmonic model, which is valid for bulk phonons, is frequently applied to the nanostructured systems.[16–18] The wavenumber dependence of the most prominent external (95 cm^{-1}) and internal (286 cm^{-1}) Raman modes of nanowires on the temperature is shown in Fig. 7(a) and (b).

From Fig. 7 it can be seen that the wavenumbers of both modes decrease with increasing temperature. The best fit of the wavenumber (full line) during the gradual increase of the temperature up to room temperature was obtained including only the three-phonon anharmonic term from Eqn (4). On comparing the anharmonic constants for torsional and breathing modes, it is obvious that the anharmonic constant C for breathing mode is about 5 times greater than that for the torsional one. This implies that the phonon–phonon interaction for internal modes is much stronger than for the external Raman modes.

Conclusion

Vibrational properties of $Mo_6S_3I_6$ nanowires are very similar to Chevrel phase crystals where vibrations of Mo_6S_8 molecules are dominant. Nearly 21 well-resolved Raman modes are observed at room temperature. The $Mo_6S_3I_6$ nanowires decompose at temperatures between 573 and 673 K when the mode characteristic for the MoO_3 phase appears. The intensity of the MoO_3 mode rises with increasing temperature followed by the appearance of additional molybdenum oxide modes, pointing at the structural instability of these systems at higher temperatures. Phonon–phonon interactions investigated for the case of two most intense Raman internal and external modes in the temperature range 5–300 K showed that anharmonic coupling of phonons are almost 5 time stronger for the breathing (internal) modes than for torsional (external) ones. These vibrational properties may provide a stimulus to better understanding the lattice dynamics of $Mo_6S_3I_6$ nanowires, thus enabling improved functional properties of these otherwise interesting materials.

References

[1] D. Vrbanić, M. Remškar, A. Jesih, A. Mrzel, P. Umek, M. Ponikvar, B. Jančar, A. Meden, B. Novosel, S. Pejovnik, P. Venturini, J. C. Coleman, D. Mihailovic, *Nanotechnology* **2004**, *15*, 635.
[2] D. Mihailovic, *Prog. Mater. Sci.* **2009**, *54*, 309.
[3] D. Dvorsek, D. Vengust, M. Zumer, V. Nemanic, D. Mihailovic, *J. Appl. Phys.* **2007**, *102*, 114308.
[4] L. Joly-Pottuz, F. Dassenoy, J. M. Martin, D. Vrbanic, A. Mrzel, D. Mihailovic, W. Vogel, G. Montagna, *Trib. Lett.* **2005**, *18*, 385.
[5] A. Meden, A. Kodre, J. Padeznik Gomilsek, I. Arcon, I. Vilfan, D. Vrbanic, A. Mrzel, D. Mihailovic, *Nanotechnology* **2005**, *16*, 1578.
[6] M. I. Ploscaru, S. Jenko Kokalj, M. Uplaznik, D. Vengust, D. Turk, A. Mrzel, D. Mihailovic, *Nano Lett.* **2007**, *7*, 1445.
[7] V. Nicolosi, D. Vrbanic, A. Mrzel, J. McCauley, S. O'Flaherty, C. McGuinness, G. Compagnini, D. Mihailovic, W. J. Blau, J. N. Coleman, *J. Phys. Chem.* **2005**, *B109*, 7124.
[8] V. Nicolosi, D. Vrbanic, A. Mrzel, J. McCauley, S. O'Flaherty, D. Mihailovic, W. J. Blau, J. N. Coleman, *Chem. Phys. Lett.* **2005**, *401*, 13.
[9] V. Nicolosi, D. Vengust, D. Mihailovic, W. J. Blau, J. N. Coleman, *Chem. Phys. Lett.* **2006**, *425*, 89.
[10] V. Nicolosi, P. D. Nellist, S. Sanvito, E. C. Cosgriff, S. Krishnamurthy, W. J. Blau, M. L. H. Green, D. Vengust, D. Dvorsek, D. Mihailović, G. Campagnini, J. Sloan, V. Stolojan, J. D. Carey, S. J. Pennycook, J. N. Coleman, *Adv. Mater.* **2007**, *19*, 543.
[11] D. J. Holmgren, R. T. Demers, M. V. Klein, D. M. Ginsberg, *Phys. Rev.* **1987**, *B36*, 1952.
[12] H. Kuzmany, *Solid-State Spectroscopy*, Springer-Verlag, Berlin, **1999**, p. 186.
[13] G. Lucazeau, *J. Raman Spectrosc.* **2003**, *34*, 478.
[14] P. G. Klemens, *Phys. Rev.* **1966**, *148*, 845.
[15] M. Balkanski, R. F. Wallis, E. Haro, *Phys. Rev.* **1983**, *B28*, 1928.
[16] Z. V. Popović, Z. Dohčević-Mitrović, A. Cros, A. Cantarero, *J. Phys. Condens. Matter.* **2007**, *19*, 496209.
[17] Z. Dohčević-Mitrović, M. Radović, M. Šćepanović, M. Grujić-Brojčin, Z. V. Popović, B. Matović, S. Bošković, *Appl. Phys. Lett.* **2007**, *91*, 203118.
[18] K. Gao, *Phys. B* **2007**, *398*, 33.

Magnetism in nanoscale graphite flakes as seen via electron spin resonance

Luka Ćirić, Dejan M. Djokić,[*] Jaćim Jaćimović, Andrzej Sienkiewicz, Arnaud Magrez, and László Forró

Ecole Polytechnique Fédérale de Lausanne, ICMP, 1015 Lausanne, Switzerland

Željko Šljivančanin

Vinča Institute of Nuclear Sciences (020), RS-11001 Belgrade, Serbia

Mustafa Lotya and Jonathan N. Coleman

School of Physics, Trinity College Dublin, Dublin 2, Ireland

Magnetic properties of a large assembly of ultrathin graphitic particles obtained by heavy sonication of graphite powder dispersed in N-methylpyrrolidone were measured by electron-spin resonance (ESR). The ESR signal was decomposed into one narrow and one broad component. The narrow component was associated with localized Curie-type defects. The temperature dependence of the predominant broad component points to a transition to a superparamagnetic-like state at 25 K. By performing the density-functional-theory calculations for graphene with selected extended defects (the sheet edges, zigzag chains of chemisorbed H atoms, and pentagon-octagon rows), we found considerable magnetic moments at C atoms in their vicinities. We attribute the magnetism in the graphitic particles to the localized electronic states near the defects in the network of the π electrons of graphene. The ferromagnetic (FM) correlations among magnetic moments at carbon atoms near the edges are not able to give rise to a long-range FM order.

PACS number(s): 73.22.Pr, 75.70.Cn, 73.20.−r, 76.30.Pk

I. INTRODUCTION

After fullerenes and carbon nanotubes, the interest in an *old* polymorphism of carbon, graphene, is strongly increasing. This interest is due to the ease of its production and to the nonsophisticated theoretical modeling of its electronic structure. However, despite these simplicities graphene has many attractive features both in basic science and in applications. One of these possibilities is to use it in spintronics.[1] Theoretical modeling has shown that the localized states at the edges of graphene nanoribbons can have a long-range magnetic order, and as such, they can carry the spin information.[2] Furthermore, Son *et al.*[3] have predicted that the opposite edges have opposite spin configurations which could be tuned by electric field. This gives an additional control of the information transport.

Despite these spectacular theoretical predictions, the experimental demonstration of this long-range spin order in graphene and in graphene nanoribbons is still missing.[4] Very recent findings stemming from muon spectroscopy[5] have also eliminated the possibility of the formation of ferromagnetic (FM) or antiferromagnetic (AFM) ordering in defective graphene. Nevertheless, it has generated the revival of the investigation of ferromagnetism in graphite and in other carbon-based materials (CBMs). Already, the search for magnetism in CBMs has a long tradition. The interest was always to create nanoscale magnetic and spin-electronics devices. The light weight and the abundance of carbon would make CBMs ideal candidates, but one would need a FM state at room temperature (RT). There are only a few CBM ferromagnets, but their Curie temperatures (T_C) are well below RT. One prominent example is TDAE-C_{60} with a T_C of 12 K.[6] The FM state has been shown to be very fragile, depending on the thermal history of the sample. The exchange interaction (J) of the localized wave function of the electron on the C_{60} gives rise to a FM state only in a special mutual configuration

of the molecules because J depends on the overlap between adjacent sites.[7]

Most of the CBM-related ferromagnetism is reported for graphite and attributed to the presence of impurities or lattice imperfections like cracks, grain boundaries, and voids. Electron- and ion-irradiation-induced defects in graphite also can result in a FM state.[8] The underlying model in these cases relies on the defect-induced localized states at the Fermi level, leading to the existence of local moments. If these defects are aligned, e.g., on a grain boundary, direct exchange can give a FM state with a rather high T_C.[9] If the local moments are dispersed in space, then the Ruderman-Kittel-Kasuya-Yosida (RKKY) interaction is evoked for aligning the spins.[10] Nevertheless, in this case the T_C is rather low. Furthermore, it is debated in the literature whether the low carrier concentrations in CBMs, especially in graphene, are capable of producing sizable RKKY couplings between the localized spins.[11]

A mean-field theoretical study, carried out for randomly distributed magnetic defects in graphene,[12] has reported that FM correlations can coexist alongside an AFM exchange. On the other hand, the presence of AFM correlations in a magnetic phase induced by nonmagnetic structural defects in a single graphene sheet still remains less likely. This is because the antiferromagnetic-spin arrangements occur at special edge-defect configurations, such as edge segments separated by the turn of $120°$.[13]

Our work is a study of magnetism of nanographite with the philosophy that a deeper understanding of ferromagnetism in ultrathin graphitic systems will help to transfer this knowledge to graphene ribbons and to be useful in its spintronics applications. We report the detection of a superparamagnet-like state below 25 K in an assembly of nano-sized graphitic particles. These particles were created with a heavy sonication of graphitic powder in N-methylpyrrolidone (NMP). The

mechanical shock of the nanoparticles could produce structural defects which strongly perturb the electronic structure within graphene layers. The defect density, however, is not overwhelming; otherwise, the Raman study would notice it.[14]

The monoatomic-carbon vacancies are the simplest structural defects able to induce magnetism in graphene. We assume that the magnetism observed in the experiments described in this manuscript originates from structural imperfections more complex than monoatomic vacancies. Employing *ab initio* calculation, we identified several line defects which give rise to the magnetism in graphitic particles. The set of investigated defects includes the graphene edges, intrinsic structural defects in the honeycomb lattice, and zigzag chains of adsorbated H atoms. The calculations demonstrate that the emergence of defects in the π network of valence electrons gives rise to nonzero-spin density in a graphene sheet.

II. METHODS

A. Experiment

The nanographite sample was obtained as a by-product of graphite exfoliation in order to produce high-quality graphene.[15] A sieved graphite powder was dispersed in *N*-methylpyrrolidone by bath sonication. After sonication for 30 minutes, a gray liquid was obtained consisting of a large number of graphitic particles, including graphene flakes. The assembly was drawn through a filter paper, and a thick black deposit was obtained. Its characterization by scanning electron microscopy (SEM) is shown in Fig. 1. Most of the graphitic flakes are flat on the filter paper. A particle counting shows that more than 70% of the flakes have surface areas $\leqslant 1$ μm^2, and roughly 2% are $\geqslant 50$ μm^2.

The predominance of submicron-sized particles justifies the denomination *nanographite*. We do not have real statistics about the thicknesses of these particles, but independent study has shown that it contains a large number of graphene flakes.[15] The electron-spin-resonance (ESR) silent filter paper with the graphitic deposit was cut into 3.0×5.0 mm^2 rectangles, and approximately ten of them were piled up and introduced into
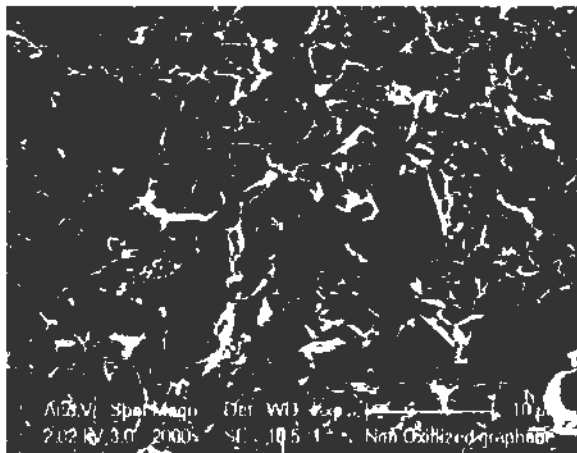
an ESR quartz tube which was evacuated, filed with 100 mbar of high-purity Helium gas, and sealed.

B. Theory

In order to examine prospects for defect-introduced magnetism in graphitic nanoparticles, we perform calculations of the electronic properties of graphene flakes and an infinite graphene layer with selected structural imperfections. The theoretical investigations are restricted to the structures containing a single graphene layer since the weak van der Waals forces between graphene sheets are not expected to substantially alter their magnetic properties. The structures considered in the present study are depicted in Fig. 2. The rationale which led to this choice of investigated structural defects in graphene is described in the next section together with the corresponding density-functional-theory (DFT) results.

All calculations are performed with the GPAW computer program[16,17] based on the real-space implementation of the projector-augmented-wave (PAW) method.[18] The electronic-exchange-correlation effects are described applying a Perdew-Burke-Ernzerhof exchange-correlation functional.[19] We used the grid spacing of 0.15 Å. The calculations for the graphene flake in Fig. 2(a) are performed employing open-boundary
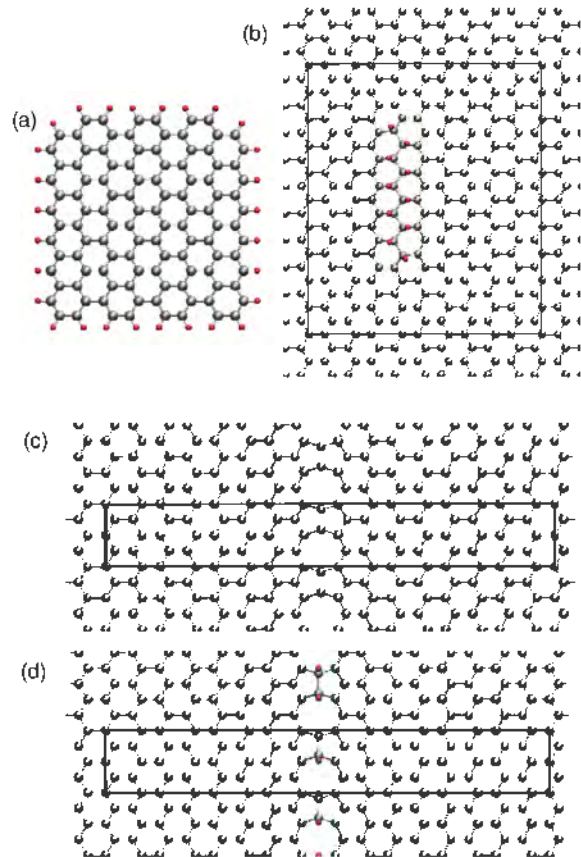
FIG. 2. (Color online) The atomic structure of (a) a small rectangular graphene flake, (b) a zigzag line of H adatoms on graphene, (c) a bare line defect containing carbon pentagons and octagons, and (d) a hydrogenated-line defect containing carbon pentagons and octagons. The H and C atoms are represented by red and gray spheres, respectively. For structures in (b)–(d), the surface unit cells are marked with black lines.

FIG. 1. Scanning-electron-microscopy (SEM) image of the large assembly of graphitic particles. At least 66% of the particles have a surface area $\leqslant 1$ mm^2.
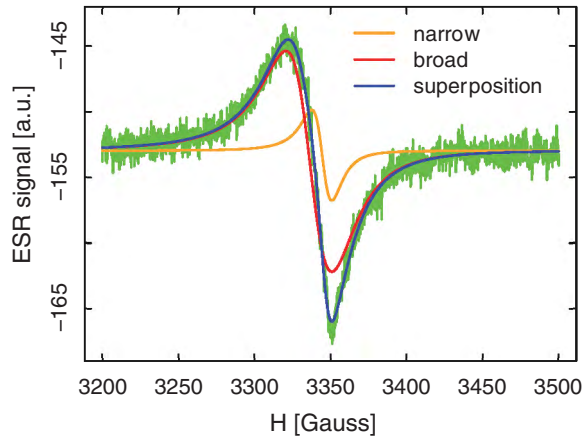
FIG. 3. (Color online) A typical ESR signal of the nanographite sample recorded at 100 K. The asymmetric signal is well fitted with a narrow and a broad component. The resonance field was roughly in the $H_0 \perp c$ configuration.

conditions. The H chains [Fig. 2(b)] and extended-line defects [Figs. 2(c)–2(d)] are examined using the supercell approach and applying periodic-boundary conditions in the graphene plane. The corresponding Brillouin zones are sampled with one (chains of H adatoms) and 16 Monkhorst-Pack **k** points (extended-line defects).

III. RESULTS

A. Experiment

At high temperatures the signal is Lorentzian while below 150 K it becomes asymmetric. An example of the signal recorded at 100 K is shown in Fig. 3. It can be fitted with two Lorentzian-absorption profiles as a sum of a broad and of a narrow component.

The narrow line could be followed up to 150 K. Its intensity obtained by the double integration of the ESR line is proportional to the spin susceptibility (χ) and shows a Curie behavior ($\chi \sim 1/T$).

It is worth mentioning that ESR spectra originating from conduction electrons are often asymmetric (Dysonian type). This effect is also observed in graphite and graphite-intercalation compounds (GIC)[20] but not in our sample consisting of nano-sized graphitic particles, and we will not discuss that matter in this paper.

The double-integrated broad line gives a Pauli-like susceptibility as in most of the graphite samples. This resemblance breaks at 25 K where the spin susceptibility starts to increase strongly on cooling (Fig. 4). This increase cannot be attributed simply to the appearance of a Curie tail since this increase is abrupt and much stronger than $\sim 1/T$.

This could be easily seen in the inset of Fig. 4 where the $\chi * T$ plot shows diverging behavior below 25 K, strongly suggesting the onset of FM correlations.

The g factor and the ESR linewidth (Fig. 5) corroborate with the behavior of the spin susceptibilities.

For the narrow-line component they reveal both the value and the featureless temperature dependence which is similar to that observed for defects in CBMs. However, the defects in our sample are not exactly the same as those

observed in electron- or ion-irradiated samples,[21] whose g factors are close to the free-electron value of 2.0023. In our case the g factor is higher (2.006), resembling the defects created by incomplete functionalization, e.g., oxidation or reduction.[22] The augmented g value could be observed for the broad component as well. In graphite in the static-resonance magnetic-field configuration H_0 parallel to the c axis, g has a strongly temperature-dependent value starting from 2.05 at 300 K and reaching 2.15 at 25 K.[23] In our nanographitic sample the g value is 2.011 at RT and shows practically no temperature dependence down to 25 K. At this transition g sharply decreases as the consequence of the onset of an internal magnetic field.

B. Theory

To investigate the possibility of the magnetism in graphene induced by structural imperfections more complex than monoatomic vacancies, we focus on three types of line defects depicted in Fig. 2: hydrogenated zigzag graphene edges, a zigzag chain of H adatoms at graphene, and a bare or hydrogenated intrinsic graphene line defect containing rows

FIG. 4. (Color online) The temperature dependence of the spin susceptibility corresponding to the broad component of the ESR line. The inset depicts the strong increase of both χ and $\chi * T$ below 25 K points to the onset of magnetic interactions.
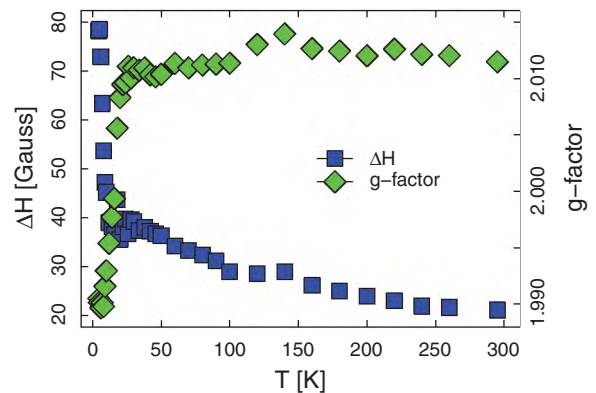
FIG. 5. (Color online) The ESR linewidth (left axis) and g factor (right axis) of the broad component of the ESR line as a function of temperature. At 25 K both quantities show the onset of magnetic correlations.

of carbon pentagons and octagons. All these defects can be modeled at modest computational cost applying DFT calculations and give rise to the zigzag boundaries in the π network of graphene valence electrons. Hence, these defects open the prospect for producing the spin-polarized-electron density in graphene following the same mechanisms described by Son *et al.* for zigzag graphene nanoribbons.[24]

The graphene edges are inevitable in any graphene sample of a finite size. Their effect on magnetism is modeled considering a nearly squared graphene nanoparticle in Fig. 2(a) since the majority of graphitic particles observed by SEM (Fig. 1) are of similar shapes. The DFT calculations of graphene flakes reveal that nonvanishing spin density is mostly located at C atoms near zigzag edges. The magnetic moment at the atoms along the same zigzag edge are ferromagnetically coupled with different signs for atoms near different zigzag edges [see Fig. 6(a)].

Thus, regarding ground-state magnetic properties, the graphene flake in Fig. 2(a) could be considered as a finite graphene nanoribbon.

The zigzag lines of H adatoms on graphene in Fig. 2(b) are among the favorable adsorption configurations of small hydrogen clusters on graphene[25] and, hence, could be produced during the process of graphite sonication in NMP. We examined the possibility to induce magnetism in graphene in the vicinity of the H-chain structure in Fig. 2(b) and found magnetic moments of $\sim$0.3 μ_B at C atoms near H adsorbates. The most favorable magnetic configuration corresponding to the H-zigzag chain on graphene is presented in Fig. 6(b).

The octagon-pentagon lines [Fig. 2(c)] are some of the simplest extended intrinsic line defects in graphene. They have been recently observed by Lahiri *et al.*,[26] who combined scanning transition microscopy (STM) with DFT calculations to resolve their structure at the atomic level. According to our
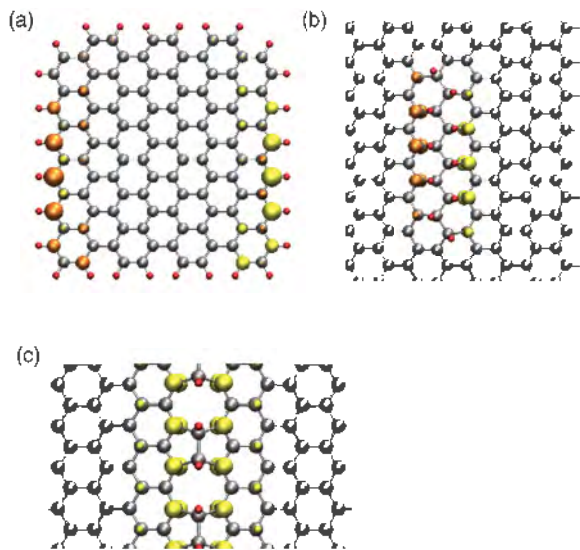

FIG. 6. (Color online) The isocontour plots of spin densities of (a) a small rectangular graphene flake, (b) a zigzag line of H adatoms on graphene, and (c) a hydrogenated-line defect containing carbon pentagons and octagons. Yellow and orange colors are used to represent spin densities generated from electron states with opposite spin orientations.

calculations, negligible spin polarization occurs in the bare lines of pentagons and octagons. However, the picture changes significantly when the H atoms are adsorbed at line defects as depicted in Fig. 2(d). For the H-adsorption configuration in Fig. 2(d), we calculated the binding energy of 2.49 eV per H atom. This value is 0.78 eV higher than that for H chains of defect-free graphene.[27] Thus, the line defect is likely to be hydrogenated if the source of H atoms is available. The spin-density plot in Fig. 6(c) clearly demonstrates that the hydrogenated-line defect induces significant magnetic moments at C atoms in its vicinity. The magnetic moments are ferromagnetically coupled, giving rise to the total magnetic moment of 1.22 μ_B per unit cell.

IV. DISCUSSION

The narrow line represents only $\sim$2% of the total intensity of the ESR signal. We attribute it to impurities in the sample. Its *g* factor and linewidth resemble the defects in graphene obtained by reduction of graphene oxide,[22] so we cannot exclude that they are situated in the exfoliated graphene flakes. Since there is no marked temperature evolution of this signal, we will disregard its further discussion.

The broad line coming from the majority phase shows in all physical quantities: intensity, linewidth, and *g* factor of the onset of the FM phase at 25 K. It manifests in the strong increase of the spin susceptibility and linewidth and in the abrupt decrease of the resonance field. Although these quantities show the appearance of a FM phase in the available temperature range, no long-range order emerges. The ESR line is still observable around a value of $g = 2$. This is explained by a FM transition in small domains at 25 K without interdomain interaction, and they could be considered as superparamagnetic clusters. They give an enhanced susceptibility and ESR-line broadening due to the distribution of local internal fields.

Since such a FM signal is absent in the graphite powder before sonication in NMP, the structure hosting the FM interaction was necessarily created during this procedure. One can suppose that the sonication creates defects such as vacancies or chemical functionalization. The model which accounts in this case for the FM state was elaborated by Yazyev and Helm.[28] It is based on the experimental STM observations[29] that a defect on a graphite surface causes the perturbation of the electronic structure in a large region. One can trace distinctive triangular patterns associated with individual quasilocalized states.[29] Evoking Lieb's theorem,[30] which relates the total magnetic moment of a half-filled bipartite system to the difference of the number of defects in the two sublattices, they could account for the FM signal in defected CBM systems. However, Lieb used the words *unsaturated ferromagnetism* to clarify that there is no spatial ordering.

An important question is the nature of the defects on the surface of nanographite, giving the local magnetic order. It is likely that they are extended defects which are created by the mutual shocks of the graphitic particles during the sonication. If the defects of different surface densities are produced in complementary sublattices not too close to each other, they show an enhanced magnetic moment. This is the scheme for ferromagnetism depicted in Refs. 28 and 31. However, based
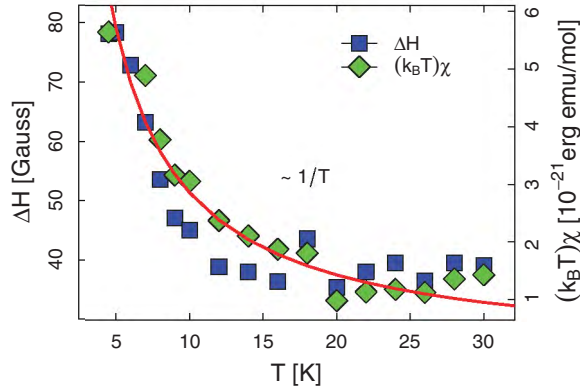
FIG. 7. (Color online) The linewidth and $(k_B T)$-multiplied susceptibility at low temperatures. The red curve represents the best fit ($\sim 1/T$) for both mutually scaling dependences.

on the g factors both for the narrow and broad lines, distinct from simple defects in a CBM (too big for both lines), we would like to suggest the possibility of NMP functionalization induced by sonication. This mechanical energy locally could enhance the probability of the chemical bonding of NMP with the sp^2 network. It is likely the NMP molecules attach preferentially to the sites which are already defected.

The NMP molecules perturb the electronic structure of graphite in the same manner as do vacancies. It is plausible that the stronger spin-orbit coupling of the NMP in respect to carbon gives an overall higher g factor for the assembly.

DFT calculations reveal that hydrogen functionalization leads to the magnetism. However, modeling the functionalization together with NMP is intricate and falls beyond the scope of the present study. Nevertheless, the NMP in graphene can also form covalent bonds to induce magnetism.

Our ESR data can be interpreted in terms of the onset of the two-dimensional (2D) ferromagnetic coupling between the spins emerging due to the H-saturated C atoms. As can be seen from Fig. 7, close to the ordering temperature (hypothetically speaking, $T_C = 0$ K) $\Delta H(T)$ broadens considerably below 25 K.

This type of behavior is generic for a 2D ferromagnet.[32] It is known that the dominant contribution to thermodynamic properties of weak ferro- and antiferromagnets above the transition temperature comes from diffusive magnetic excitations. In 2D systems with FM correlations, the $q = 0$ mode of the fluctuations grows considerably as temperature is lowered towards the critical temperature. In this case, the temperature dependence of ΔH follows the $\langle \hat{S}_{q=0}^z \hat{S}_{-q=0}^z \rangle \sim (k_B T)\chi(T)$ law rather than that of $\langle \hat{S}_{q=0}^z \hat{S}_{-q=0}^z \rangle^{-1}$, which is the case for a 3D ferromagnet.[32] The best fit for the temperature dependence of $\Delta H(T)$ was found to be $\sim 1/T$, thus meaning that as the temperature is lowered from 25 towards 0 K, $\chi(T)$ increases as $T^{-\gamma}$ with $\gamma \approx 2$. The high critical exponent $\gamma \approx 2$ points to the onset of the 2D ferromagnetic coupling. In particular, the Ising model of 2D ferromagnets predicts 7/4 for γ.[33]

Also, using the relation for the in-plane resonance field of 2D ferromagnets,[34] the g-factor temperature dependence below 25 K is given by

$$g(T) = g/\sqrt{1 + 4\pi \chi(T)\rho/M}, \qquad (1)$$
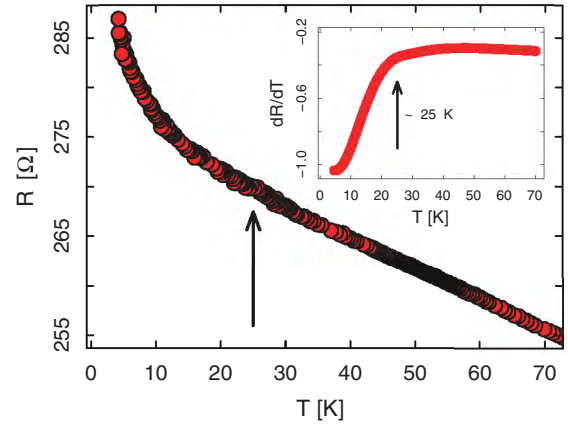
FIG. 8. (Color online) Resistance below 70 K of a thick film of nanographite (Fig. 1) as a function of temperature with weak nonmetallic temperature dependence. It shows a stronger increase below 25 K where the FM interaction is observed by ESR. The $R'(T)$ dependence presented in the inset clearly suggests a change at around 25 K.

where $M = 12$ g/mol, $\rho = 2.2$ g/cm^3, and $g = 2.011$. Based on Eq. (1), we find that the relative change of g with respect to $g(T)$ obtained at 4.5 K is $\delta g/g \approx 2\pi \chi \rho/M \approx 5 \times 10^{-6}$ ($\chi \gg \chi_{RT}$). The expression in Eq. (1) corroborates only qualitatively the related experimental value $\delta g/g \approx 10^{-2}$. We believe that the discrepancy between the estimated $\delta g/g \approx 5 \times 10^{-6}$ from expression (1) and the experimentally found $\delta g/g \approx 10^{-2}$ might be due to a very rough estimation of χ_{RT}. The corresponding susceptibility has been estimated as 7.5×10^{-8} emu/mol.[35] For example, assuming that $J \sim 50$ K, the temperature dependence of the susceptibility (Fig. 4) becomes consistent with the picture of ferromagnetic correlations at 1D graphene edges,[13] but this picture would then require χ_{RT} to be nearly three orders of magnitude bigger.

Resistance measurements of the thick film of the nanographite deposit (Fig. 8) signifies also the onset of the FM domains at 25 K. The resistance shows nonmetallic temperature dependence, a weak increase of R with decreasing temperature. This is consistent with a relatively easy hopping between the particles. However, as soon as the FM local order is established in the perturbed regions of the graphite layers, the resistance increases more strongly on lowering the temperature. This observation suggests that the clusters with a local magnetic order are extended structures and that it is not easy to short circuit them with the pristine regions.

If one admits the possibility that functionalization represents the defect sites, which induce magnetic moments in the graphitic structure, one could perform a targeted functionalization of graphene and study the appearance of FM correlations.

*dejan.djokic@epfl.ch

[1] P. Avouris, Z. H. Chen, and V. Perebeinos, Nat. Nanotechnol. **2**, 605 (2007).

[2] J. Fernández-Rossier and J. J. Palacios, Phys. Rev. Lett. **99**, 177204 (2007).

[3] Y. W. Son, M. L. Cohen, and S. G. Louie, Nature (London) **444**, 347 (2006).

[4] J. Barzola-Quiquia, P. Esquinazi, M. Rothermel, D. Spemann, T. Butz, and N. García, Phys. Rev. B **76**, 161403(R) (2007).

[5] M. Riccò, D. Pontiroli, M. Mazzani, M. Choucair, J. A. Stride, and O. V. Yazyev, Nano Lett. **11**, 4919 (2011).

[6] P. M. Allemand, K. C. Khemani, A. Koch, F. Wudl, K. Holczer, S. Donovan, G. Grüner, and J. D. Thompson, Science **253**, 301 (1991).

[7] B. Narymbetov, A. Omerzu, V. V. Kabanov, M. Tokumoto, H. Kobayashi, and D. Mihailović, Nature (London) **407**, 883 (2000).

[8] P. Esquinazi, D. Spemann, R. Höhne, A. Setzer, K. H. Han, and T. Butz, Phys. Rev. Lett. **91**, 227201 (2003).

[9] J. Červenka, M. I. Katsnelson, and C. F. J. Flipse, Nat. Phys. **5**, 840 (2009).

[10] M. A. H. Vozmediano, M. P. López-Sancho, T. Stauber, and F. Guinea, Phys. Rev. B **72**, 155121 (2005).

[11] S. R. Power, F. S. M. Guimares, A. T. Costa, R. B. Muniz, and M. S. Ferreira, e-print arXiv:1112.0205v1.

[12] Y. G. Semenov, J. M. Zavada, and K. W. Kim, Phys. Rev. B **84**, 165435 (2011).

[13] O. V. Yazyev and M. I. Katsnelson, Phys. Rev. Lett. **100**, 047209 (2008).

[14] U. Khan, A. O'Neill, M. Lotya, S. De, and J. N. Coleman, Small **6**, 864 (2010).

[15] Y. Hernandez *et al.*, Nat. Nanotechnol. **3**, 563 (2008).

[16] J. J. Mortensen, L. B. Hansen, and K. W. Jacobsen, Phys. Rev. B **71**, 035109 (2005).

[17] J. Enkovaara *et al.*, J. Phys.: Condens. Matter **22**, 253202 (2010).

[18] P. E. Blöchl, Phys. Rev. B **50**, 17953 (1994).

[19] J. P. Perdew, K. Burke, and M. Ernzerhof, Phys. Rev. Lett. **77**, 3865 (1996).

[20] M. Saint Jean, C. Rigaux, and J. Blinowsky, J. Phys. Radium **51**, 1193 (1990).

[21] F. Beuneu, C. l'Huillier, J. P. Salvetat, J. M. Bonard, and L. Forró, Phys. Rev. B **59**, 5945 (1999).

[22] L. Ćirić *et al.* (to be published).

[23] D. L. Huber, R. R. Urbano, M. S. Sercheli, and C. Rettori, Phys. Rev. B **70**, 125417 (2004).

[24] Y. W. Son, M. L. Cohen, and S. G. Louie, Phys. Rev. Lett. **97**, 216803 (2006).

[25] Ž. Šljivančanin, M. Andersen, L. Hornekær, and B. Hammer, Phys. Rev. B **83**, 205426 (2011).

[26] J. Lahiri, Y. Lin, P. Bozkurt, I. I. Oleynik, and M. Batzill, Nat. Nanotechnol. **5**, 326 (2010).

[27] L. Nilsson, Ž. Šljivančanin, R. Balog, T. R. Linderoth, E. Lægsgaard, I. Stensgaard, B. Hammer, F. Besenbacker, and L. Hornekær, Carbon **50**, 2052 (2012).

[28] O. V. Yazyev and L. Helm, Phys. Rev. B **75**, 125408 (2007).

[29] H. A. Mizes and J. S. Foster, Science **244**, 559 (1989).

[30] E. H. Lieb, Phys. Rev. Lett. **62**, 1201 (1989); **62**, 1927(E) (1989).

[31] O. V. Yazyev, Phys. Rev. Lett. **101**, 037203 (2008).

[32] P. M. Richards, *Proceedings of the International School of Physics "E. Fermi" Course LIX*, edited by K. A. Mueller and A. Rigamonti (North-Holland, Amsterdam, 1976), p. 538.

[33] D. B. Abraham, Phys. Lett. A **43**, 163 (1973).

[34] C. Kittel, *Introduction to Solid State Physics*, 4th ed. (Wiley, New York, 1971).

[35] O. Chauvet, G. Baumgartner, M. Carrard, W. Basca, D. Ugarte, W. A. de Heer, and L. Forró, Phys. Rev. B **53**, 13996 (1996).

Uncoupled photonic band gaps

Dj. Jovanović [a,*], B. Nikolić [b], T. Radić [c], D.M. Djokić [d], R. Gajić [a]

[a] Center for Solid State Physics and New Materials, Institute of Physics, University of Belgrade, Pregrevica 118, 11080 Belgrade, Serbia
[b] Faculty of Physics, University of Belgrade, P.O. Box 368, 11001 Belgrade, Serbia
[c] E-Search, Bulevar Mihaila Pupina 10z/IV, 11000 Belgrade, Serbia
[d] Institute of Condensed Matter Physics, EPFL, CH-1015 Lausanne, Switzerland

Abstract

We theoretically investigated the symmetry properties of the modes in two-dimensional square lattice photonic crystals in order to study phenomena that would enable new frontiers in the applications of photonic crystals. Using group theory, symmetry analysis of the photonic crystals bands has been done. Particular attention was given to the search for the uncoupled B modes that cannot be excited by the external plane wave because they are symmetry forbidden. The existence of the uncoupled modes enabled to define new physics phenomena: uncoupled photonic band gaps. For the frequency ranges inside the uncoupled photonic band gaps, zero transmission is obtained. Therefore, there are two different types of photonic gaps in the photonic crystals: photonic band gaps and uncoupled photonic band gaps. The appearance of uncoupled photonic band gaps in photonic crystals could at least improve the application of the existing photonic materials and structures or even enable the usage of new ones for devices like waveguides, filters, and lasers.

1. Introduction

Photonic crystals (PhCs) are periodic dielectric or metal structures that are designed to control the propagation of light [1]. In PhCs, it is well known that the absence of transmission is mostly the consequence of the presence of photonic band gaps [frequency ranges of the forbidden (not allowed) modes] [2,3]. Till now, well-known phenomena of the photonic band gaps (PBG) and especially the PhC

that are connected with it have been widely exploited. After the boom in the nineties, which was focused on research of these phenomena for obtaining PhCs with the biggest gaps in order to substitute semiconductors in industry, in this century photonic crystals was growing in the mature age and gave many applications and devices in the integrated optic and opto-electronic industry like lasers, waveguides, couplers, filters, LEDs, and fibers [1,4–8]. It can be said that the existence of the PBG most impacted the place that the PhCs has today.

On the other hand, in two-dimensional (2D) photonic crystals [9–21] and later in three-dimensional (3D) photonic crystals [22–24] experimentally and theoretically it was confirmed that the absence of the transmission also occurred for the frequency ranges out of the PBG. Robertson et al. [9,10] and later Sakoda

* Corresponding author. Tel.: +381 113713156;
fax: +381 113713190.
E-mail address: djordje@ipb.ac.rs (Dj. Jovanović).
URL: http://www.solid.ipb.ac.rs/graphenegroup

and co-workers [11,12] proved that this absence of transmission appeared because of the existence of electromagnetic modes which cannot be excited. The reason was the lack of coupling between incoming and correspondent Bloch plane waves (modes) in PhCs even for non-zero density of states (DOS). Namely, the authors concluded that the incoming plane waves and so called "uncoupled" modes have opposite plane symmetry under the mirror reflection at the plane (includes the incident wave vector and is perpendicular to the 2D plane), so the coupling between them is symmetry forbidden. The uncoupled modes are anti-symmetric while the incident waves are symmetric under that mirror reflection so the effective coupling between them is zero. In addition, according to group theory, it is shown that these antisymmetric uncoupled modes at high symmetry directions correspond to B modes, in contrast to the symmetric A modes that coupled with the incident wave and contributes to the transmission in PhCs [11].

In most previous investigations of the optical properties of the PhCs, the absence of transmission because of the uncoupled modes is preferably considered as the secondary reason in regard to the dominant PGB one, but as something that must be taken into account [9,12,13,17,22]. In some cases the existence of the uncoupled modes represented the problem regarding the phenomena connected with the transmission through the PhC [25–27]. Some researchers tried to remove this constraint (uncoupled modes) in order to get pronounced effects by creating anisotropies by the external electric field in liquid crystals [28] or changing the incident wave parameters [29]. The other researchers excited uncoupled modes by breaking the mirror symmetry (lowering the symmetry of the PhC) by sliding the surface layers in 3D FCC photonic crystals [23] or by the deformation (by introducing protrusion) of the PhC holes in 2D photonic crystals slabs [30]. Furthermore, excitation of the uncoupled modes can be also done by illuminating of the PhC at on oblique angle that is used in 2D square resonant gratings [30,31].

So far, the presence of uncoupled modes as the stop bands for the propagation of waves through the PhCs, despite the proven impact on the optical properties of the PhCs, unfortunately did not lead to a wide range of applications in contrast to the PBG. An exception is made in the construction of the surface emitting photonic crystal microcavity laser for sensor applications [32]. In addition, an opportunity existed for the filter application that has been done in resonant gratings by the construction of the unpolarized narrow-band filter [31]. The implementation of the new type of photonic band gap phenomenon, arising due to uncoupled modes, could have the important impact at least to improve the existing PhC materials and structures for applications. The deeper impact could be the use of new photonic materials, structures with improved functionality. Also it can be used in fundamental research for getting the real picture of the transmission properties of PhCs.

In this paper a new class of photonic band gaps that are based on the uncoupled modes is represented. The rest of the paper is organized as follows. In Section 2, the new class of the photonic band gaps is defined. Also, theoretical methods that are used for the observation of the symmetry properties of modes in the square two-dimensional photonic crystal made by GaAs infinite rods in air are briefly described. In Section 3 is confirmed the existence of the uncoupled modes and the corresponding photonic band gaps based on them. Finally, the summary of the main results are presented in Section 4.

2. Theory

In this paper the main two foci were the identification of the uncoupled modes and the photonic band gaps that are based on them. The main theoretical methods that are used for this are the plane wave expansion (PWE) method, group theory, similarity and projection methods and the finite-difference time-domain (FDTD) method. The first four methods are used for the calculation of the symmetry properties of the band structure of each band at the high symmetry points and directions of the first Brillouin zone. From these results it is possible to find the pronounced uncoupled modes and to obtain the frequency ranges of the correspondent photonic band gaps. The latter method is used for the numerical calculation of the transmission spectra in order to confirm the appearance of the photonic band gaps that emerge for the frequency ranges of the uncoupled modes. PWE and FDTD methods in this paper are implemented with commercial software packages BandSolve and FullWave [33]. The projection method is implemented through the non-commercial Mathematica package developed by Hergert and Däne [34].

The symmetry properties of the PhC bands (modes) can be obtained by the investigation of the symmetry properties of the solutions of the Maxwell equations [6,34]. More precisely, the symmetry properties of PhCs, expressed by the symmetry group (point group) and corresponding irreducible representations (IREPs), must be associated with the symmetry properties of the solutions of the Maxwell equations, i.e. specific field distributions of the modes [$E_y(x, z)$ and $H_y(x, z)$ for TE

and TM polarization, respectively, and for 2D PhCs]. For 2D PhC it is well-know that the dielectric function $\varepsilon(\boldsymbol{r})$ is invariant on any symmetry operator $R \in G_0$ (where G_0 is the point group of the PhC) [11]. It follows that the eigenfunction of the Maxwell operators is the eigenfunction of the symmetry operator R, so we can specify any band at $\boldsymbol{k}$ by the IREP of $G_0(\boldsymbol{k})$ (point group of the wave vector $\boldsymbol{k}$) [4,6]. Therefore, group theory, which holds for electronic band theory, is also applicable for the PhCs [35].

The assignation of the IREPs of the modes at the high symmetric points and directions are obtained by the similarity and projection methods. The similarity method determines the IREP of the particular PhC mode at $\boldsymbol{k}$ by comparing the known plane symmetries of allowed IREPs from $G_0(\boldsymbol{k})$ and the plane distribution of the PhC mode field at $\boldsymbol{k}$. The correct solution for the symmetry of the mode (IREP) is the one that is the same as the particular IREP. The second method, which is used for confirming the results obtained with the first one, determines the IREP of the PhC mode at $\boldsymbol{k}$ by affecting the character projection operator of the whole IREP from $G_0(\boldsymbol{k})$ on the plane field distribution of that mode [34]. The result is the decomposition of the plain field on irreducible components. If the projected field has a single non-zero component, then that field has well defined symmetry, corresponding to a single IREP.

As was earlier mentioned in the introduction, it is predicted that in PhCs, aside from classical PBG, photonic band gaps could also appeared for the frequencies ranges of the uncoupled modes. Based on their origin we define these additional gaps as uncoupled photonic band gaps (UPBG). Furthermore, if the uncoupled modes (B modes) appeared in certain frequency ranges and symmetry directions alone or with PBG, the additional classification of the UPBG could be made. Those UPBG that are composed of the B mode and PBG are defined as mixed UPBG (meaning that a B mode appears for one symmetry direction whereas a PBG exists for the other), while those composed only by the B mode (for both symmetry directions) are defined as pure UPBG. Therefore, in the PhC there could be two different types of the UPBG, the pure and mixed UPBG. These UPBG for the 2D square PhC and TM polarization are presented in Fig. 1. Involving the TE/TM polarization, it is possible to make the final classification of the UPBG:

1) pure
   a) full (partial) TE or TM gaps
   b) complete TE/TM gaps
2) mixed
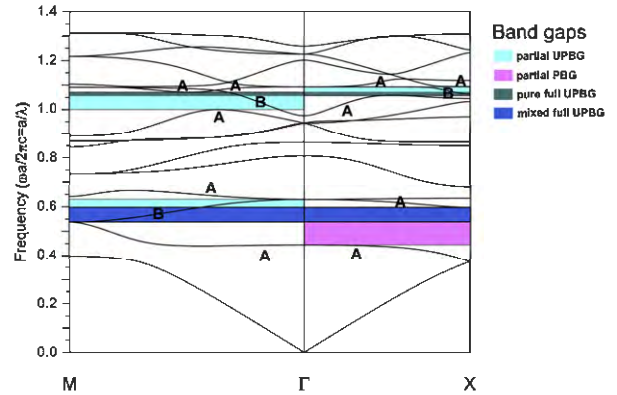
Fig. 1. The pure and mixed UPBG in the square PhC for the TM polarization with assigned IREPs at the high symmetry directions.

a) full TE or TM gaps
b) complete TE/TM gaps

The partial UPBG is equivalent to the uncoupled B mode for a symmetry direction. The full and complete UPBG correspond to UPBG that appeared for both high symmetry directions and particular (TE or TM) or both (TE and TM) polarizations respectively. Assigned IREPs (A and B modes) at the high symmetry directions (ΓM and ΓX) in Fig. 1 are obtained with group theory methods and present only partially results that will be discussed in detail in the next chapter. Furthermore, detailed analysis and the confirmation of the predicted UPBG will be also presented in the following chapter.

3. Results and discussion

The existence of the uncoupled modes and UPBG are analyzed in the 2D square PhC made of dielectric GaAs ($\varepsilon = 12.96$) rods in air ($r/a = 0.05$–0.50; r is the radius of the rods, a (=1 μm) is the lattice constant). The 2D square PhC was periodic in the x–z plane and infinite along the y-axis. This well known structure has the p4mm square plane symmetry group [36]. The high symmetry points of the I Brillouin zone are Γ, M and X whereas the high symmetry directions are $\Delta(\Gamma X)$, $\Sigma(\Gamma M)$ and Z(XM). The point groups $G_0(\boldsymbol{k})$ for the high symmetry points Γ, M and X are C_{4v}, C_{4v}, and C_{2v}, respectively and for the high symmetry directions Δ, Σ, and Z are C_{1h} [6]. In addition, this structure belongs to one of the eleven Archimedean structures whose optical properties have been very intensively studied [37,38].

The first goal was to obtain the symmetry properties of the bands in the PhC in order to find the uncoupled modes and corresponding UPBG. To perform this task it is necessary to determine whole IREPs in the analyzed
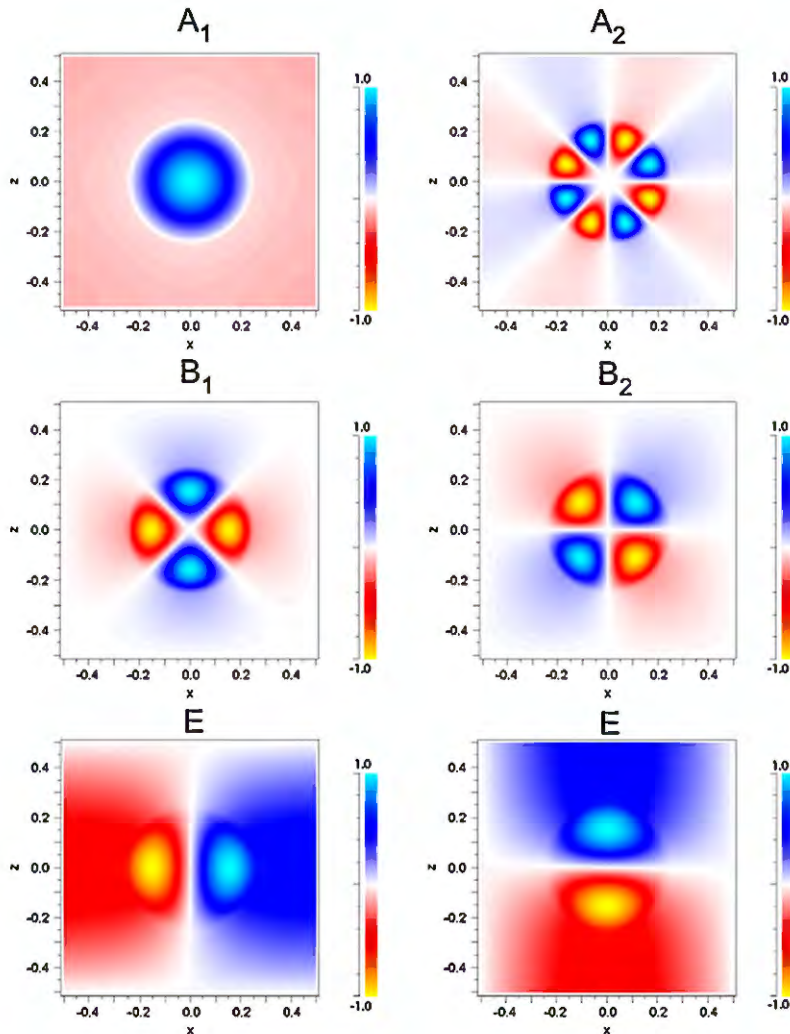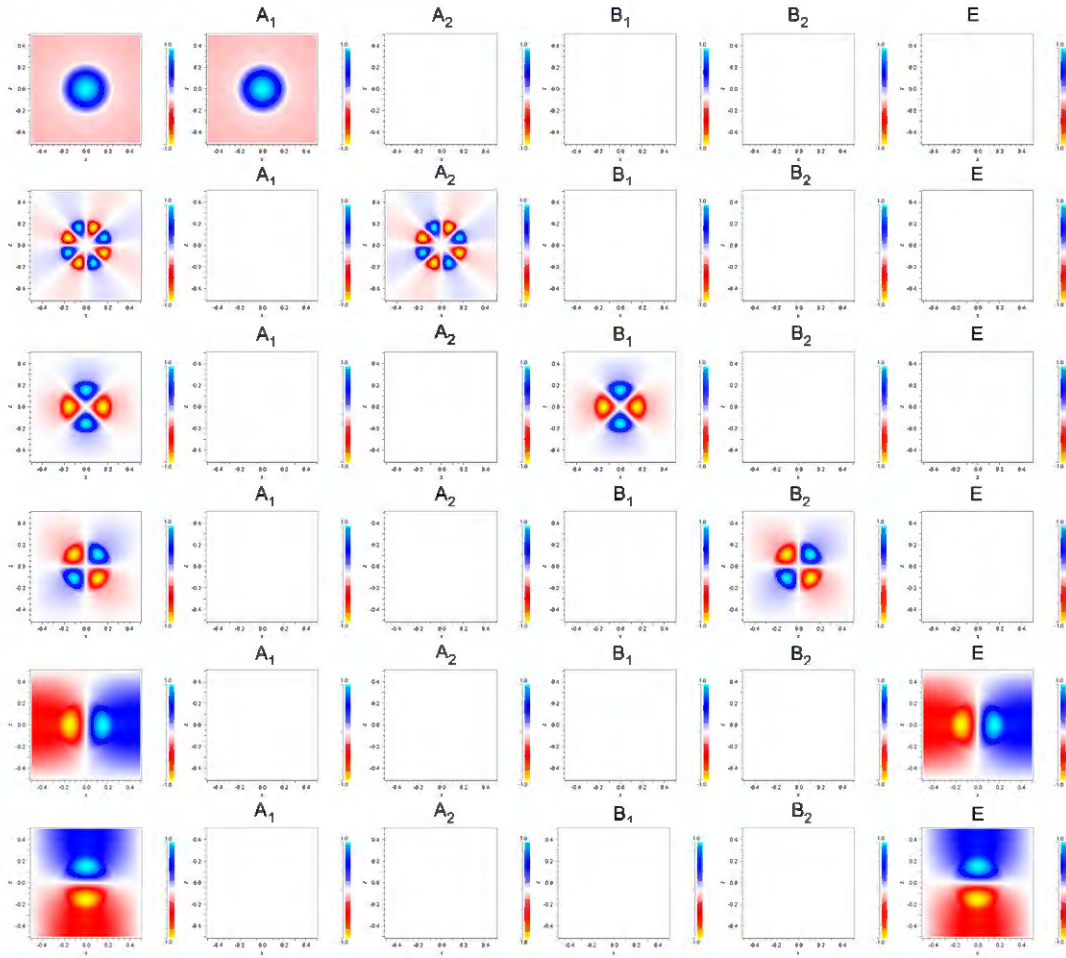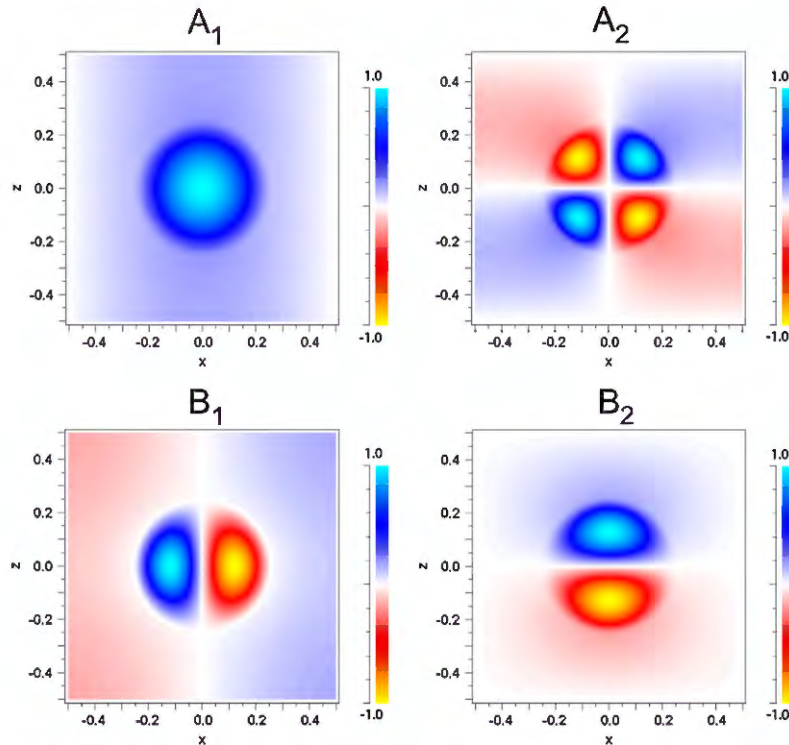
Fig. 2. The allowed A_1, A_2, B_1, B_2 and E modes of the TM bands at the Γ(M) symmetry point (C_{4v} point group) in the square PhC with GaAs rods ($r/a = 0.25$) in air. The colors determine amplitude values of the distribution of the fields for a primitive unit cells. Amplitude values of the field are normalized to unity. The IREPs and field distributions of the modes are obtained with similarity and PWE methods, respectively.

PhC at high symmetry points and directions (for allowed k and analyzed bands). By group theory and similarity/projection methods the symmetry analysis for the first 16 TE/TM modes in the 2D square PhCs with GaAs rods ($r/a = 0.05$–0.50) in air is performed. The TE and TM polarizations represent electric and magnetic field vectors normal to the plane of the wave propagation, respectively. The field distributions of the modes of unknown symmetries at high symmetry points and directions are obtained by the PWE method. Figs. 2 and 3 show all representative (allowed) IREPs of the TM modes at the Γ(M) point with the C_{4v} point symmetry group [30,39] that are obtained with the similarity and projection methods, respectively. These IREPs of the TM modes correspond to the square 2D

PhC ($r/a = 0.25$). The representative IREPs, presented in Fig. 2, are used for the determination of the whole IREPs of the 16 TE/TM bands, $r/a = 0.05$–0.50 at the Γ(M) points by the similarity method. Furthermore they can be used for the determination of the IREPs of the whole square PhCs modes at the Γ(M) points. The reason lies in the fact that these representative (Fig. 2) modes present all possible allowed states of the symmetry for $G_0(k)$ and can be used to determine the IREPs of other modes from the same $G_0(k)$. From both methods the same results (Figs. 2 and 3) for the IREPs of the modes of the 16 TE/TM bands and $r/a = 0.05$–0.50 at the Γ(M) points are obtained.

In order to obtain IREPs of the modes for the X symmetry point (C_{2v} point group) the same procedure as

Fig. 3. The allowed A$_1$, A$_2$, B$_1$, B$_2$ and E modes of the TM bands at the Γ(M) symmetry point (C_{4v} point group) in the square PhC with GaAs rods ($r/a = 0.25$) in air. The colors determine amplitude values of the distribution of the field for a primitive unit cell. Amplitude values of the field are normalized to unity. The modes of the unknown symmetry are presented in the first column and obtained with the PWE method. The other columns represent IREPs of the modes that are obtained with the projection method. The result is decomposition of the plain field on irreducible components. The correct solution is the IREP that has the same field distribution as the PhC mode. The other projections (empty squares) are zero field amplitudes.

for the Γ(*M*) points is repeated. The representative (allowed) IREPs of the modes at the *X* symmetry point, for the square PhC ($r/a = 0.25$) and TM polarization, that are obtained with the similarity and projection methods, are shown in Figs. 4 and 5, respectively. These representative IREPs of the TM modes (Fig. 4) are used for the determination of the whole IREPs of the 16 TE/TM bands, $r/a = 0.05$–0.50 at the *X* points by the similarity method. Furthermore, they can also be used for the determination of the IREPs of the whole square PhC modes at the *X* points. From both methods the same results (Figs. 4 and 5) for the IREPs of the modes are obtained.

The IREPs of the modes at the high symmetry directions ΓM and ΓX (C_{1h} point group) for the square PhCs ($r/a = 0.05$–0.50) are determined from known

tables of the compatibility relations for the square lattice [6,40,41] and from the obtained results for the high symmetry points (Γ, *M* and *X*). It is worth remembering, based on group theory, that in the square 2D PhC, the IREP at the high symmetry direction can be the *A* or pronounced uncoupled *B* mode [6]. From all these results the symmetry properties of the bands for the first 16 TE/TM modes at the high symmetry points and directions in square PhC with GaAs rods ($r/a = 0.05$–0.50) in air were determined.

The band structures of the first 16 bands with assigned IREPs at the high symmetry points and directions for the square PhC with GaAs rods $r/a = 0.15$ (TE polarization) and $r/a = 0.25$ (TM polarization) in air are presented in Figs. 6 and 7, respectively. Band structures are obtained with the PWE method. The main
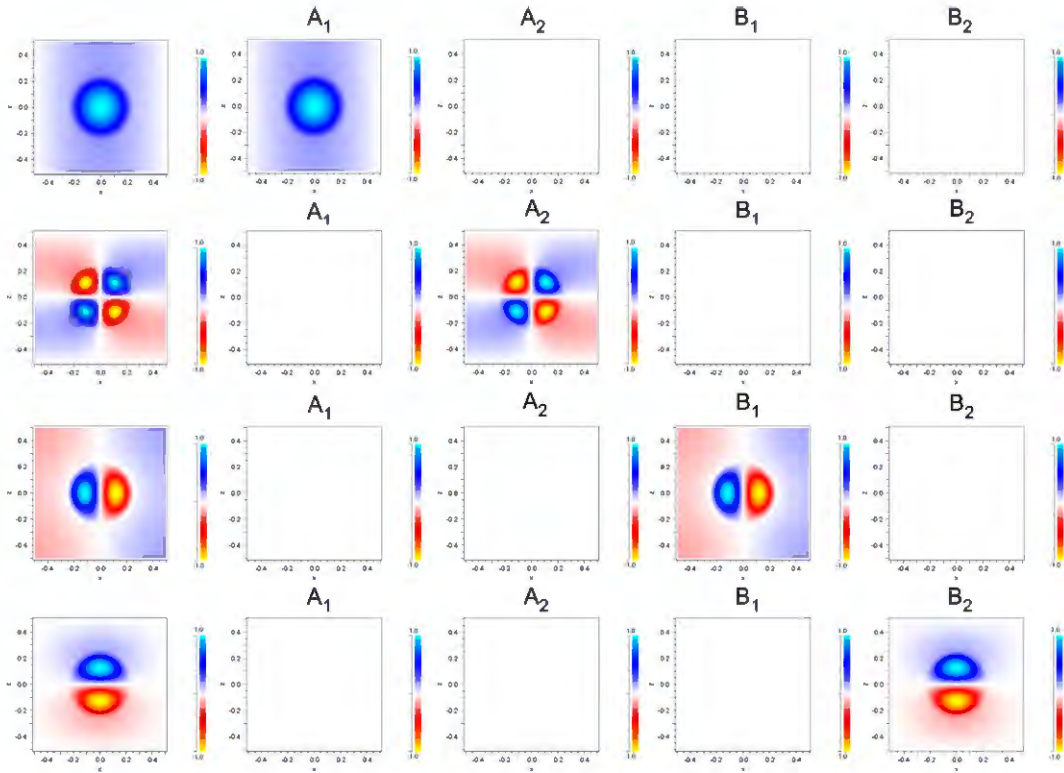
Fig. 4. The allowed A_1, A_2, B_1 and B_2 modes of the TM bands at the X symmetry point (C_{2v} point group) in the square PhC with GaAs rods ($r/a = 0.25$) in air. Presented colors, unit cells, IREP, modes and theoretical methods that are used in analysis are described the same as in Fig. 2.

aim was to define frequency ranges for which the mixed and pure UPBG emerge. From Fig. 6, it can be concluded that for the high symmetry directions (ΓM and ΓX) besides A modes, there are many pronounced B modes. Therefore, in addition to the PBG the mixed UPBG emerged (within the same frequency range of the B mode and partial PBG for the ΓX and ΓM symmetry directions, respectively). For this case there are two mixed UPBG that appears in the normalized frequency ranges $\bar{f}(\omega a/2\pi c) = a/\lambda$ from 0.596 to 0.677 and from 1.221 to 1.290, with $\Delta\bar{f} = 0.081$ and 0.069, respectively. The appearance of both gaps (PBG and UPBG) gives additional value and flexibility to PhC structure for possible applications.

From Fig. 7 it can be concluded that for the TM polarization besides the partial PBG and mixed UPBG a pure UPBG also appeared (within the same frequency range for both symmetry directions B modes appeared). The mixed and pure UPBG appeared in the normalized frequency ranges from 0.538 to 0.630 with $\Delta\bar{f} = 0.092$ and from 1.058 to 1.071 with $\Delta\bar{f} = 0.013$, respectively. Furthermore, the full PBG is not present in this structure for the TM polarization, but the existence of the UPBG enables control of the waves in the PhC and possible applications.

The appearance of the UPBG in the PhCs is confirmed by numerical simulations with FDTD and FFT calculations. The final goal was to confirm the assumption that transmission through the PhC is zero for the frequency ranges in the UPBG. In order to confirm the presence of the UPBG in the PhC, numerical simulations of the transmission in the square PhCs with GaAs rods ($r/a = 0.15$ and 0.25) in air, for the TE/TM modes and for both ($\Gamma M/\Gamma X$) directions of the incident wave were performed. Here, the PhCs with both ($\Gamma M/\Gamma X$) surface directions are constructed. The dimensions of the PhCs in the x–z plane were $19 \times 10 \times a$ (14 layers of rods) and $18 \times 12.3 \times a$ (10 layers of rods) for the ΓM and ΓX directions of the PhC surface, respectively, and infinite in the y-axis. In order to obtain the transmission spectra the detector was placed close to the rear of the PhC.

The confirmation of the existence of the mixed full UPBG, that is obtained with the previous symmetry analysis of the band structure, was performed by numerical FDTD simulations of the TE polarized wave transmission through the square PhC ($r/a = 0.15$), in the frequency range from 1.155 to 1.422 and for the $\Gamma M/\Gamma X$ incident wave directions (k is parallel to the $\Gamma M/\Gamma X$ directions). The excitation parameters represented a

Fig. 5. The allowed A_1, A_2, B_1 and B_2 mode of the TM bands at the X symmetry point (C_{2v} point group) in the square PhC with GaAs rods ($r/a = 0.25$) in air. Presented colors, unit cells, IREP, modes and theoretical methods that are used in analysis described here are the same as in Fig. 3. The correct solution is the IREP that has the same field distribution as the PhC mode. The other projections (empty squares) are zero field amplitudes.

Gaussian wave of width $15 \times a$ and $\bar{f}_{in} = 0.9$, whereas the numerical simulation parameters were: a) the dimension of the finite computation domains [(x, z) for both orientations of the PhC], $19 \times 13.5 \times a$; b) the spatial grid sizes (Δx and Δz), $0.02 \times 0.02 \times a$; c) temporal grid (time step, Δt) and the length of the simulation, 0.012 cT = $0.012 \times a$ and $3145.78 \times a$, respectively, and d) the boundary conditions concern

the perfectly matched layers (PML). The transmitted power was normalized to the power of the incident wave. The calculated values for the transmission in the ΓM (ΓX) directions presented in Fig. 8 are denoted with red and black lines, respectively. The mixed full UPBG (blue region) is obtained as the crossing of the frequency ranges of the two gaps [partial UPBG (light green region) and PBG (pink region) for the ΓM and ΓX
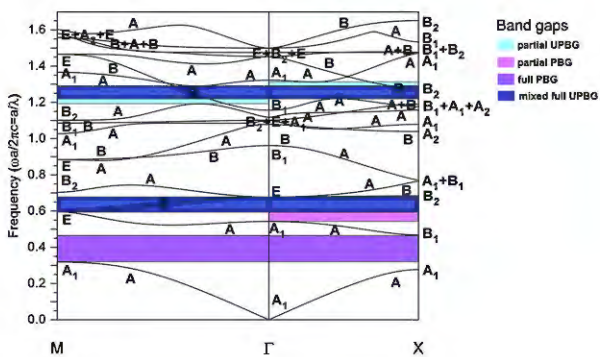
Fig. 6. The mixed full UPBG in the square PhC ($r/a = 0.15$) and for the 16 TE bands. The assigned IREPs of the modes are also illustrated.
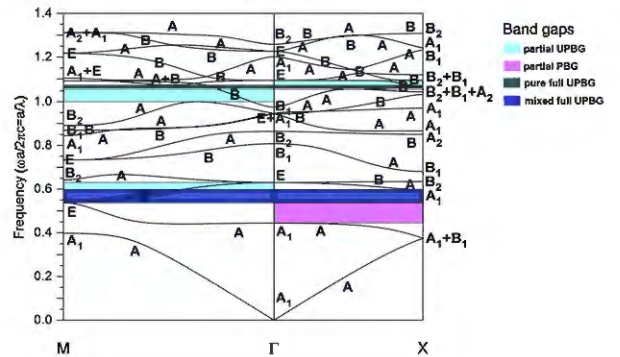
Fig. 7. The mixed and pure full UPBG in the square PhC ($r/a = 0.25$) and for the 16 TM bands. The IREPs of the modes are also illustrated.
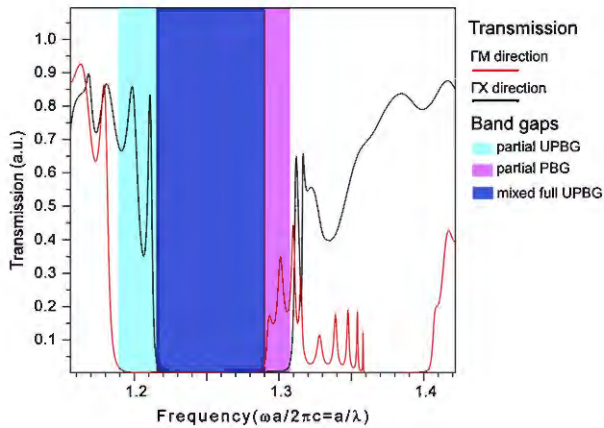
Fig. 8. The transmission spectra of the mixed full UPBG for the square PhC ($r/a = 0.15$), the TE polarization and ΓM (red line) and ΓX (black line) directed waves. The specific frequency gaps are denoted with different colors. (For interpretation of the references to color in this figure legend, the reader is referred to the web version of the article.)

directions, respectively]. For the normalized frequency range from 1.217 to 1.290 ($\Delta \bar{f} = 0.073$) of the mixed UPBG there is no transmission as was theoretically predicted earlier. There is an excellent agreement with the previous results obtained from the symmetry analysis within 5%. In addition, the appearance of the zero transmission for the ΓM direction in the frequency range from 1.359 to 1.403 is due to the presence of the B mode (Fig. 6) but it does not affect the mixed UPBG.
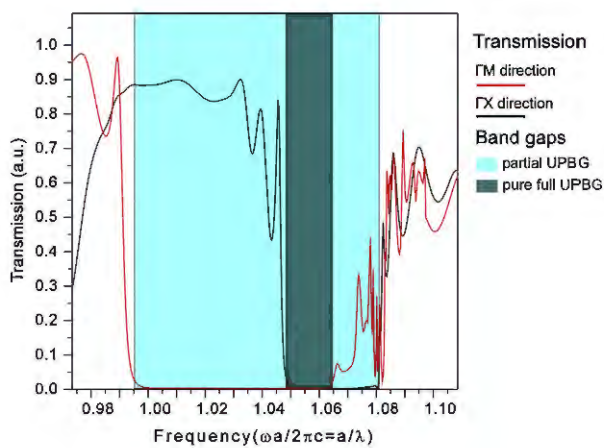
Fig. 9. The transmission spectra of the pure full UPBG for the square PhC ($r/a = 0.25$), the TM polarization and the ΓM (red line) and ΓX (black line) directed waves. The specific frequency gaps are denoted with different colors. (For interpretation of the references to color in this figure legend, the reader is referred to the web version of the article.)

The pure full UPBG, earlier predicted by the symmetry analysis, was verified by the numerical FDTD simulations of the TM polarized wave transmission through the square PhC ($r/a = 0.25$), $\bar{f}_{in} = 0.7$ (with a Gaussian profile of width $15 \times a$), in the frequency range from 0.973 to 1.109 and for the $\Gamma M/\Gamma X$ incident wave directions. The numerical simulation parameters were the same as in the previous case. The transmission spectrum of the PhC for both $\Gamma M/\Gamma X$ directions is presented in Fig. 9. The obtained transmission values are shown as red and black lines for the ΓM and ΓX direction, respectively. The pure full UPBG (green region) is obtained as the cross section of two partial UPBG (the B mode, depicted with light green region). It emerges, in the normalized frequency range, from 1.049 to 1.064 ($\Delta \bar{f} = 0.015$). For that range there is no transmission as was theoretically predicted earlier. There is a very good agreement with the previous results obtained from the symmetry analysis within 15%.

Furthermore, in the square PhC for the complete analyzed range of the GaAs rods ($r/a = 0.05$–0.50) in air and both TE/TM polarizations the mixed UPBG dominated. The appearance of the pure UPBG for the whole r/a range, let alone $r/a = 0.25$, also appeared for the $r/a = 0.1$ and 0.2. The mixed UPBG emerged mostly for the TM polarization. For the lower (higher) r/a the mixed UPBG appeared mostly for the TE (TM) polarization. For the whole r/a range of values and both TE/TM polarizations the mixed UPBG, composed by the B mode (3rd band, ΓM direction) and PBG (between 2nd and 3rd band, ΓX direction), dominated. Unfortunately, in the square PhC with GaAs rods in air, the complete (TE/TM polarization) pure or mixed UPBG of a significant width did not appear.

Finally, it is worth mentioning that the confirmed existence of the uncoupled modes in 2D slab and 3D photonic crystals [13,17,21–23] could also enable the appearance of the UPBG and usage of the presented group theory methods in those structures for their applications.

4. Conclusions

In this paper, the symmetry properties of the TE/TM bands of the square 2D PhC made by GaAs rods ($r/a = 0.05$–0.50) in air are theoretically studied. The symmetry analysis of the bands revealed the uncoupled modes that cannot propagate through the PhC. The existence of the uncoupled modes is used for defining a new class of the photonic band gaps–uncoupled photonic band gaps. It is concluded that besides PBG

in the PhCs, there is also the pure and mixed UPBG made by uncoupled modes (for both ΓM/ΓX high symmetry directions) or by the mixture of the uncoupled mode and PBG (for different high symmetry directions), respectively. Their appearance is confirmed by the transmission simulations through the PhC. Inside the frequency ranges of the UPBG (pure and mixed) the zero transmissions of the propagated waves are obtained. Therefore, there are two different types of photonic gaps in the PhC: PBG and UPBG. In addition, for the square PhC with rods (r/a = 0.05–0.50), mixed UPBG dominated. The existence of the UPBG in 2D and 3D PhCs could significantly improve the usage of the existing materials and photonic structures or enable new ones for applications in photonic devices like, for example waveguides, filters, and lasers. This will be one of the main topics in our future work.

Acknowledgments

References

[1] J.D. Joannopoulos, S. Johnson, J.N. Winn, R.D. Meade, Photonic Crystals, Molding the Flow of Light, second ed., Princeton University Press, New Jersey, 2008.

[2] E. Yablonovitch, Inhibited spontaneous emission in solid-state physics and electronics, Physical Review Letters 58 (1987) 2059–2062.

[3] E. Yablonovitch, T.J. Gmitter, K.M. Leung, Photonic band structure: the face-centered-cubic case employing nonspherical atoms, Physical Review Letters 67 (1991) 2295–2298.

[4] K. Inoue, K. Ohtaka, Photonic Crystals: Physics, Fabrication and Applications, Springer-Verlag, Berlin, 2004.

[5] K. Busch, S. Lolkes, R.B. Wehrspohn, H. Foll, Photonic Crystals: Advances in Design, Fabrication and Characterization, Wiley-VCH Verlag GmbH&Co., KGaA, Weinheim, 2004.

[6] K. Sakoda, Optical Properties of Photonic Crystals, second ed., Springer-Verlag, Berlin, 2005.

[7] J.M. Lourtioz, H. Benisty, V. Berger, J.M. Gerard, D. Maystre, A. Tchelnokov, Photonic crystals: Towards Nanoscale Photonic Devices, second ed., Springer-Verlag, Berlin, 2008.

[8] S. Noda, T. Baba, Roadmap on Photonic Crystals, Kluwer Academic Publishers, Dordrecht, 2003.

[9] W.M. Robertson, G. Arjavalingam, R.D. Meade, K.D. Brommer, A.M. Rappe, J.D. Joannopoulos, Measurement of photonic band structure in a two-dimensional periodic dielectric array, Physical Review Letters 68 (1992) 2023–2026.

[10] W.M. Robertson, G. Arjavalingam, R.D. Meade, K.D. Brommer, A.M. Rappe, J.D. Joannopoulos, Measurement of the photon dispersion relation in two-dimensional ordered dielectric arrays, Journal of the Optical Society of America B 10 (1993) 322–327.

[11] K. Sakoda, Symmetry, degeneracy, and uncoupled modes in two-dimensional photonic lattices, Physical Review B 52 (1995) 7982–7986.

[12] M. Wada, K. Sakoda, K. Inoue, Far-infrared spectroscopy study of an uncoupled mode in a two-dimensional photonic lattice, Physical Review B 52 (1995) 16297–16300.

[13] T.F. Krauss, R.M. De La Rue, S. Brand, Two-dimensional photonic-bandgap structures operating at near-infrared wavelengths, Nature 383 (1996) 699–702.

[14] M. Wada, Y. Doi, K. Inoue, J.W. Haus, Far-infrared transmittance and band-structure correspondence in two-dimensional air-rod photonic crystals, Physical Review B 55 (1997) 10443–10450.

[15] K. Sakoda, Transmittance, Bragg reflectivity of two-dimensional photonic lattices, Physical Review B 52 (1995) 8992–9002.

[16] V. Kuzmiak, A.A. Maradudin, Distribution of electromagnetic field and group velocities in two-dimensional periodic systems with dissipative metallic components, Physical Review B 58 (1998) 7230–7251.

[17] T. Ochiai, K. Sakoda, Dispersion relation and optical transmittance of hexagonal photonic crystal slab, Physical Review B 63 (2001) 125107.

[18] H.T. Zhang, D.S. Wang, M.L. Gong, D.Z. Zhao, Application of group theory to plane wave expansion method for photonic crystals, Optics Communication 237 (2004) 179–187.

[19] K. Busch, G. von Freymann, S. Linden, S.F. Mingaleev, L. Tkeshelashvili, M. Wegener, Periodic nanostructures for photonics, Physics Reports 444 (2007) 101–202.

[20] M. Sigalas, C.M. Soukoulis, E.N. Economou, C.T. Chan, K.M. Ho, Photonic band gaps and defects in two dimensions: studies of the transmission coefficient, Physical Review B 48 (1993) 14121–14126.

[21] J. Schilling, R.B. Wehrspohn, A. Birner, F. Müller, R. Hillebrand, U. Gösele, S.W. Leonard, J.P. Mondia, F. Genereux, H.M. van Driel, P. Kramper, V. Sandoghdar, K. Busch, A model system for two-dimensional and three-dimensional photonic crystals: macroporous silicon, Journal of Optics A: Pure and Applied Optics 3 (2001) S121–S132.

[22] K. Sakoda, Group-theoretical classification of eigenmodes in three-dimensional photonic lattices, Physical Review B 55 (1997) 15345–15348.

[23] V. Karathanos, Inactive frequency bands in photonic crystals, Journal of Modern Optics 45 (1998) 1751–1758.

[24] F. Lopez-Tejeira, T. Ochiai, K. Sakoda, J. Sanchez-Dehesa, Symmetry characterization of eigenstates in opal-based photonic crystals, Physical Review B 65 (2002) 195110.

[25] Z. Ruan, M. Qiu, S. Xiao, S. He, L. Thylén, Coupling between plane waves and Bloch waves in photonic crystals with negative refraction, Physical Review B 71 (2005) 045111.

[26] A. Martínez, J. Martí, Negative refraction in two-dimensional photonic crystals: role of lattice orientation and interface termination, Physical Review B 71 (2005) 235115.

[27] Đ. Jovanović, R. Gajić, K. Hingerl, Optical properties of the (3,12,12) hexagonal Archimedean photonic crystal, Acta Physica Polonica A 116 (2009) 642–644.

[28] H. Takeda, K. Yoshino, Disappearances of uncoupled modes in two-dimensional photonic crystals due to anisotropies of liquid crystals, Physical Review E 67 (2003) 056612.

[29] K.M. Lin, G.Y. Guo, Uncoupled modes and all-angle negative refraction in walled honeycomb photonic crystals, Journal of the Optical Society of America B 25 (2008) C75–C81.

[30] O. Kilic, M. Digonnet, G. Kino, O. Solgaard, Controlling uncoupled resonances in photonic crystals through breaking the mirror symmetry, Optics Express 17 (2008) 13090–13103.

[31] A.-L. Fehrembach, A. Sentenac, Unpolarized narrow-band filtering with resonant gratings, Applied Physics Letters 86 (2005) 121105.

[32] K. Srinivasan, O. Painter, R. Colombelli, C. Gmachl, D.M. Tennant, A.M. Sergent, D.L. Sivco, A.Y. Cho, M. Troccoli, F. Capasso, Lasing mode pattern of a quantum cascade photonic crystal surface-emitting microcavity laser, Applied Physics Letters 84 (2004) 4164–4166.

[33] RSoft Design Group, URL: http://www.rsoftdesign.com.

[34] W. Hergert, M. Däne, Group theoretical investigations of photonic band structures, Physica Status Solidi (a) 197 (2003) 620–634.

[35] J.F. Cornwell, Group Theory and Electronic Energy Bands in Solids, vol. 10, North Holland, Amsterdam, 1969.

[36] T. Hahn, International Tables for Crystallography, vol. A: Space-group Symmetry, fifth ed., Springer-Verlag, Berlin, 2005.

[37] Đ. Jovanović, R. Gajić, K. Hingerl, Refraction and band isotropy in 2D square-like Archimedean photonic crystal lattices, Optics Express 16 (2008) 4048–4058.

[38] Dj. Jovanović, R. Gajić, Optical properties of the (3.4.6.4) hexagonal Archimedean photonic crystal, Journal of Nanophotonics 5 (2011) 051820.

[39] T. Ito, K. Sakoda, Photonic bands of metallic systems. II. Features of surface plasmon polaritons, Physical Review B 64 (2001) 045117.

[40] D.B. Litvin, Compatibility relations for two-dimensional space groups, Journal of Physics C: Solid State Physics 17 (1984) L37–L39.

[41] T. Terzibaschian, R. Enderlein, The irreducible representations of the two-dimensional space groups of crystal surfaces, Physica Status Solidi (b) 133 (1986) 443–461.

Site-selective quantum correlations revealed by magnetic anisotropy in the tetramer system SeCuO₃

I. Živković,[1] D. M. Djokić,[2] M. Herak,[1,3] D. Pajić,[4,5] K. Prša,[2] P. Pattison,[6] D. Dominko,[1] Z. Micković,[2] D. Cinčić,[7]
L. Forró,[2] H. Berger,[2] and H. M. Rønnow[2]

[1]*Institute of Physics, Bijenička 46, HR-10000 Zagreb, Croatia*
[2]*Institute of Condensed Matter Physics, EPFL, CH-1015 Lausanne, Switzerland*
[3]*Jožef Stefan Institute, Jamova 39, SL-1000 Ljubljana, Slovenia*
[4]*Department of Physics, Faculty of Science, Bijenicka c.32, HR-10000 Zagreb, Croatia*
[5]*Institute of Mathematics, Physics and Mechanics, Jadranska c. 19, SL-1000 Ljubljana, Slovenia*
[6]*ESRF, SNBL, F-38042 Grenoble 9, France*
[7]*Department of Chemistry, Faculty of Science, Horvatovac 102A, HR-10000 Zagreb, Croatia*

We present the investigation of a monoclinic compound SeCuO₃ using x-ray powder diffraction, magnetization, torque, and electron-spin-resonance. Structurally based analysis suggests that SeCuO₃ can be considered as a three-dimensional network of tetramers. The values of intratetramer exchange interactions are extracted from the temperature dependence of the susceptibility and amount to ~ 200 K. The intertetramer coupling leads to the development of long-range antiferromagnetic order at $T_N = 8$ K. An unusual temperature dependence of the effective g tensors is observed, accompanied with a rotation of macroscopic magnetic axes. We explain this unique observation as due to site-selective quantum correlations.

I. INTRODUCTION

Since the first investigations of copper(II)-acetate,[1] magnetic properties of localized clusters of spins have attracted considerable interest. Recent discoveries of single-molecule magnets (SMMs) like Mn₁₂-acetate (Ref. [2]), V₁₅ (Ref. [3]), and Fe₈ (Ref. [4]) have revealed intriguing properties such as macroscopic quantum tunneling of magnetization, magnetic avalanches, and Berry-phase interference.[5] Since the magnetic interaction between the individual SMMs is very weak, they can be considered as isolated entities. On the other hand, many interesting phenomena can be observed when the intercluster interaction is increased, allowing the system to experience a collective behavior.

Recently, a system Cu₂Te₂O₅X_2 ($X =$ Br, Cl) composed of Cu²⁺ spins forming well-defined tetrahedra has been investigated in detail.[6–9] Due to the antiferromagnetic (AFM) intratetrahedron coupling ($J \sim 40$ K), the ground state of the localized cluster is a nonmagnetic singlet. The long-range ordered state is induced in both compounds (11 K and 18 K for Br and Cl, respectively) by the presence of the intertetrahedra interaction ($J/T_N \approx 2-3$). However, it has been shown[9] that the usual mean-field approach cannot satisfactorily explain the excitation spectrum from the inelastic neutron scattering. It has been suggested that the intercluster quantum effects should be taken into account in a development of a new theoretical approach.[9] In that context it is important to discriminate between the material-specific properties and a more general model.

The compound SeCuO₃, possessing a monoclinic space group $P2_1/n$ (Ref. [10]), can be considered as a potential candidate for the investigation of intercluster quantum effects. Magnetic clusters in this compound consist of four $S = 1/2$ spins with AFM intracluster coupling and a weak intercluster interaction that leads to long-range order. In SeCuO₃ the spins are arranged in linear segments—tetramers. We present the evidence that the intratetramer interactions are at the order of 200 K while the ordering takes place at $T_N = 8$ K. This implies

that the temperature range where the effects of intercluster quantum fluctuations could be investigated is considerably larger ($J/T_N \approx 20$) compared to Cu₂Te₂O₅X_2.

We have also discovered a unique influence of quantum correlations on the magnetic anisotropy of the system. The torque magnetometry revealed that the macroscopic magnetic axes are rotating with temperature and the ESR measurements showed a strong temperature dependence of the effective g factor along specific crystallographic directions. We show that both observations can be explained as a consequence of the singlet formation of the central copper pair within the tetramer.

II. EXPERIMENTAL DETAILS

Single crystals of SeCuO₃ have been grown by a standard chemical vapor phase method. Mixtures of analytical grade purity CuO and SeO₂ powder in molar ratio 4:3 were sealed in the quartz tubes with electronic grade HCl as the transport gas for the crystal growth. The ampoules were then placed horizontally into a tubular two-zone furnace and heated very slowly by 50°C/h to 500°C. The optimum temperatures at the source and deposition zones for the growth of single crystals have been 550°C and 450°C, respectively. After four weeks, many green SeCuO₃ crystals with a maximum size of 5 × 10 × 2 mm³ were obtained, which were identified on the base of x-ray powder diffraction data.

The temperature-dependent powder diffraction data were collected on beamline BM01A at the Swiss-Norwegian Beamline (SNBL) in the ESRF, Grenoble. A monochromatic wavelength of 0.6971 Å was selected, and the beam focused onto the sample using a combination of curved mirror and monochromator crystal. The sample of powdered single crystal of SeCuO₃ was loaded into a 0.3-mm diameter capillary. The experiment has been carried out on an MAR-Research mar345 image plate and the sample was rotated 30° during an exposure of 30 s per frame. The temperature was controlled by a cryostream N2 gas flow blower from Oxford Cryosystems.

The magnetic susceptibility of a powder was measured by a Faraday method in a home-built setup in applied dc magnetic field of 5 kOe. The measurements on single crystals were performed with a Quantum Design MPMS magnetometer.

Magnetic torque was measured with a home-built torque apparatus which uses a torsion of a thin quartz fiber for the torque measurement. The sample holder is made of an ultrapure quartz and has an absolute resolution of 10^{-4} dyn cm.

Temperature-dependent ESR spectra (5–300 K) were recorded using an ESR spectrometer, model E540 EleXys (Bruker BioSpin GmbH), operating in the microwave X band (9.4 GHz), and equipped with a cylindrical TE_{011} high-Q cavity. A continuous-flow helium cryostat, Oxford Instruments model ESR900, was connected. The spectrometer operates in reflection mode and modulation of the magnetic field H_0 was used for the signal enhancement. The 100-kHz modulation amplitude was kept at 10 G to avoid modulation broadening. The angular dependence was obtained using a one-axis goniometer.

III. EXPERIMENTAL RESULTS

A. Structure

In Fig. 1 we present the powder diffraction pattern of $SeCuO_3$. There exist several compounds with the same $SeCuO_3$ chemical formula but with different crystal structures. The observed powder pattern could be indexed to a monoclinic unit cell, space group $P2_1/n$, with unit cell parameters $a = 7.712$ Å, $b = 8.238$ Å, $c = 8.498$ Å, and $\beta = 99.124$ deg. Details of this structure have been published in Ref. 10 among other polymorphs and the structure has been designated with $Cu(SeO_3)$-III.

The temperature dependence of the unit cell parameters does not reveal any kind of structural phase transition down to 80 K (see Fig. 2). We attribute the small deviation from linearity seen for the c axis and the β angle around 150 K as an experimental artefact.

The monoclinic $SeCuO_3$ has two distinct copper sites, Cu1 and Cu2. Each site is composed of a central copper ion surrounded by six oxygen ions, forming a distorted octahedron
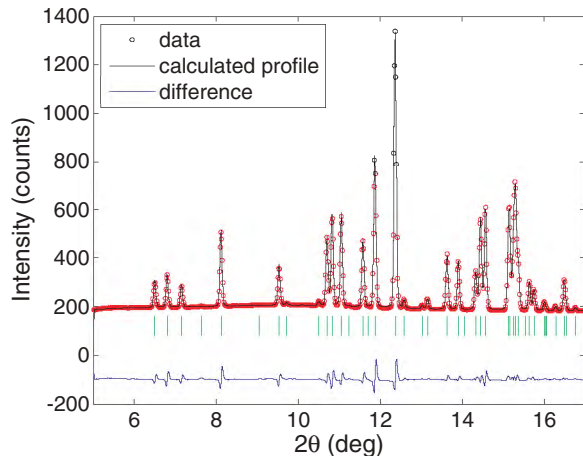
FIG. 1. (Color online) The x-ray powder pattern of $SeCuO_3$. The vertical markers correspond to the Bragg positions.
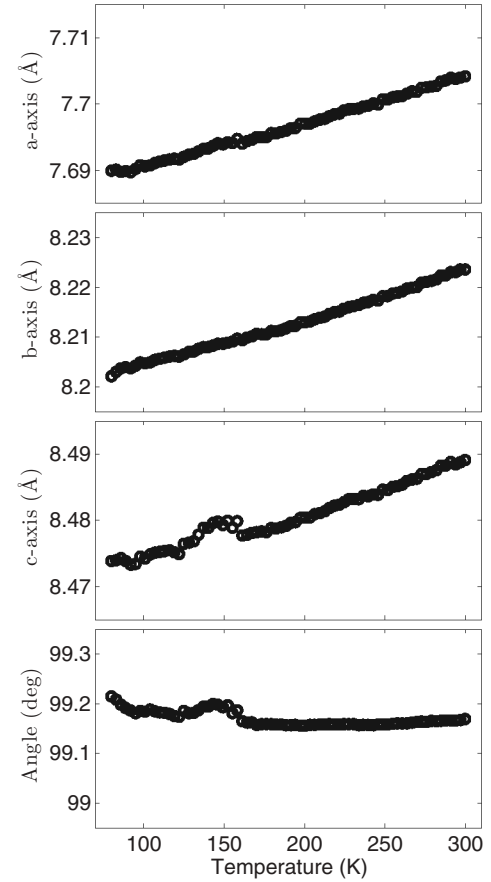
FIG. 2. The temperature dependence of unit cell parameters for the monoclinic $SeCuO_3$.

(Fig. 3). Selenium ions are placed in the center of a tetrahedron formed by three oxygens and a lone electron pair. Lone electron pairs act as chemical scissors, effectively reducing the number of magnetic exchange paths and forming low-dimensional magnetic subsystems.

In addressing the possible influence of the crystal structure on magnetic properties, it is important to consider how the local environment around the magnetic ion affects the energy levels of d orbitals. With a d^9 configuration on the copper ion, only the highest lying orbitals are magnetically active. In the (ideal) octahedral crystal field d orbitals are split into lower lying t_{2g} and higher lying e_g subsets. e_g consists of a planar $d_{x^2-y^2}$ and an elongated $d_{3z^2-r^2}$ orbital. From the list of all the distances between the copper and oxygen ions presented in Table I one can immediately notice that each copper ion has four oxygen ions at distances around 2 Å and two oxygen ions with distances much larger than 2 Å. Particularly, these two oxygen ions (O1 and O4 for the Cu1 ion and O4 and O5 for the Cu2 ion) are located on the opposite sides of the octahedron, making it elongated along the local z direction. This removes the degeneracy of the e_g subset in a way that leaves only $d_{x^2-y^2}$ as a highest lying orbital.

The superexchange interaction Cu–O–Cu between the magnetic moments should be strongest along the path $d_{x^2-y^2}-p_{x(y)}-d_{x^2-y^2}$. If only these paths are taken into account, then the structure can be represented as a weakly coupled three-dimensional (3D) network of tetramers, presented in
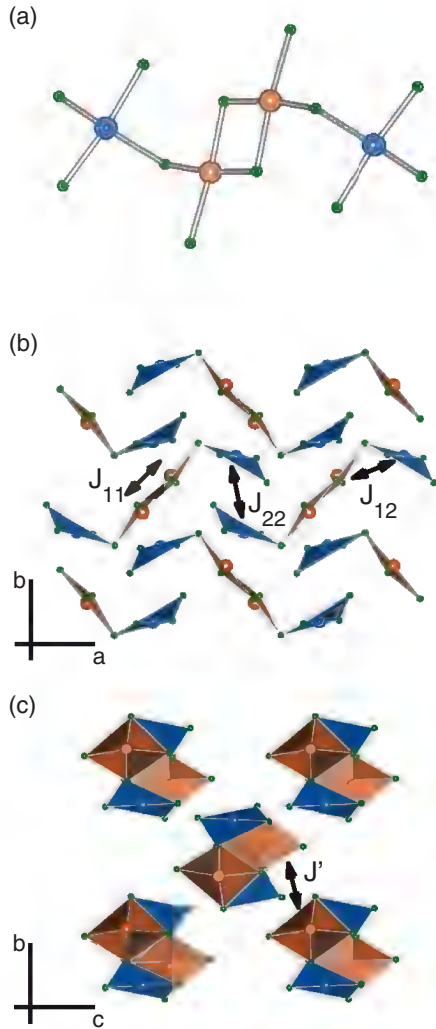
FIG. 3. (Color online) The sketch of the crystal structure of SeCuO₃ taking into account active $d_{x^2-y^2}$ orbitals.[11] (a) A single tetramer; view along the (b) c axis and (c) a axis. (Cu1, orange; Cu2, blue; O, green.)

Fig. 3 with views along the c and a axes. Tetramers are effectively forming two sets of chains running along the a axis, with tetramers in the neighboring chains related to each other by the 180° rotation around the b axis.

A single tetramer consists of a central Cu1–Cu1 dimer and two Cu2 ions on each end of the dimer. There are two Cu1–O–Cu1 paths with angles of 101.9° which contribute to the J_{11} interaction. On the other hand, there is a single Cu1–O–Cu2 path with an angle of 108.5° for the J_{12} interaction. Since these

TABLE I. Copper-oxygen distances (in Å).

Atoms	d(Cu1–O)	Atoms	d(Cu2–O)
Cu1–O1	2.38	Cu2–O1	1.98
Cu1–O3	1.95	Cu2–O2	1.96
Cu1–O3	1.96	Cu2–O4	1.95
Cu1–O4	2.42	Cu2–O4	2.71
Cu1–O5	2.02	Cu2–O5	2.36
Cu1–O6	1.95	Cu2–O6	1.98
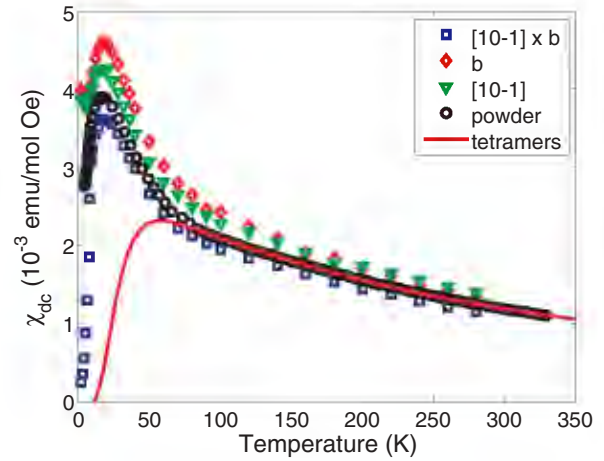
FIG. 4. (Color online) dc susceptibility vs temperature for the powdered sample and three orthogonal directions of the single crystal. The solid line is obtained using Eq. (2).

angles are significantly above 90°, one would expect medium strength AFM interactions between the neighboring moments.

Two types of intertetramer interactions can be expected. One is along the a axis between two Cu2 ions on the neighboring tetramers, J_{22}, and incorporates the $d_{3z^2-r^2}$ orbital. Since the octahedron is not ideal, there may be some mixing between $d_{3z^2-r^2}$ and $d_{x^2-y^2}$ orbitals, giving rise to a finite J_{22}. The second intertetramer interaction is the interchain interaction J' and it is mediated via Cu–O–Se–O–Cu paths.

B. Magnetization

The temperature dependence of the dc susceptibility $\chi_{dc} = M/H$ is presented in Fig. 4 for three different crystallographic directions and a powdered sample. Over the whole temperature range the susceptibility from the powdered sample follows the behavior expected from a direction-averaged measurement. At $T_N = 8$ K the transition to the long-range ordered state occurs (see Fig. 5).
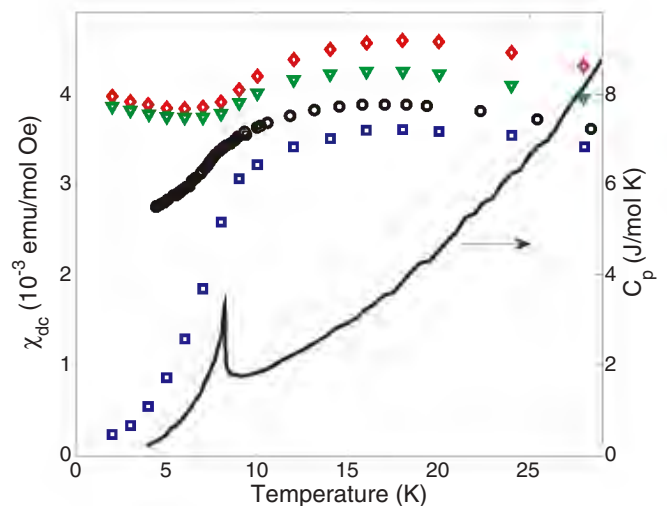
FIG. 5. (Color online) dc susceptibility around the transition. The markers are the same as in Fig. 4. The line shows the temperature dependence of the specific heat.

The dominant feature of the magnetic response of the SeCuO$_3$ compound is a broad maximum located around 18 K. The presence of such a maximum is usually related to the build-up of AFM correlations in the absence of long-range order due to the strong fluctuations present in low-dimensional systems. Following our structural analysis, the Hamiltonian that describes isolated tetramers is given by

$$\mathcal{H} = J_{12}(S_1 \cdot S_2 + S_3 \cdot S_4) + J_{11}(S_2 \cdot S_3), \qquad (1)$$

where S_2 and S_3 form the central pair coupled with the J_{11} exchange interaction and end spins are S_1 and S_4 coupled to the central pair with J_{12}.

Similar to the case of isolated tetrahedra in Cu$_2$Te$_2$O$_5$X$_2$, for $J_{11}, J_{12} > 0$ the ground state is a nonmagnetic singlet. The temperature dependence of the susceptibility is given by[12]

$$\chi = \frac{N_A g_{av}^2 \mu_B^2 \beta}{2} \frac{5\exp(\beta J(2+\gamma)) + \exp(\beta J \gamma) + \exp(\beta J K_+) + \exp(\beta J K_-)}{Z} + \chi_0, \qquad (2)$$

where

$$Z = 5\exp(\beta J(2+\gamma)) + 3\exp(\beta J \gamma) + 3\exp(\beta J K_+) + 3\exp(\beta J K_-) + 2\cosh(\beta J K^*),$$

and

$$\beta = 1/k_B T, \quad J = J_{12}/2, \quad \gamma = J_{11}/J_{12},$$
$$K_\pm = 1 \pm \sqrt{1 + \gamma^2}, \quad K^* = \sqrt{4 - 2\gamma + \gamma^2}.$$

Here N_A, g_{av}, and μ_B are Avogadro's number, average g factor, and Bohr magneton, respectively. χ_0 is a temperature-independent susceptibility. With $\gamma = 0$ one can recover the Bleaney-Bowers equation for a dimer system.[1]

As it turns out, it is not possible to model the experimental data with Eq. (2) in the whole temperature range using a single set of parameters. Moreover, our attempts to model it as a simpler low-dimensional system, like a one-dimensional (1D) magnetic chain or a magnetic dimer, also could not explain the magnetic behavior of SeCuO$_3$. We believe that this is due to the additional interaction in the system, not taken into account in the tetramer Hamiltonian Eq. (1). This is reflected in the measured susceptibility as a kink around 70 K below which the susceptibility starts to grow faster. For 90 K $< T < 330$ K one can successfully implement Eq. (2) with parameters $J_{11} = 225$ K, $J_{12} = 160$ K, $g_{av} = 2.25$, and $\chi_0 = -4 \times 10^{-5}$ emu/mol Oe. Here it is important to emphasize that neither a 1D magnetic chain model nor a magnetic dimer model can reproduce the susceptibility in this temperature range. The nature of the interaction that sets in around 70 K is unclear at the moment.

In Fig. 5 we present the results around the transition to the ordered state. All the curves exhibit a maximum around 18 K and at $T_N = 8$ K one of them (along the $\tau = [10\bar{1}] \times b$ direction) drops sharply towards zero. The susceptibility along two other crystallographic directions remains at the same level with a slight increase towards $T = 0$ K. This behavior is usually observed in systems with an uniaxial AFM arrangement of the magnetic moments where the susceptibility along the easy axis is greatly reduced compared to other two directions. Additionally, the specific heat measurement reveals a λ peak, supporting the conclusion that a 3D magnetic ordering takes place.

The AFM nature of magnetic order is further corroborated by the magnetization vs field scans along the three crystallographic directions (Fig. 6). The scans with $H \perp \tau$ show a

linear dependence of the magnetization at all temperatures. On the other hand, the scans along the τ direction are linear in the whole field range down to 10 K but below T_N there is a deviation from the linearity when the field is smaller than 2 T. This is a characteristic behavior for the spin-flop transition
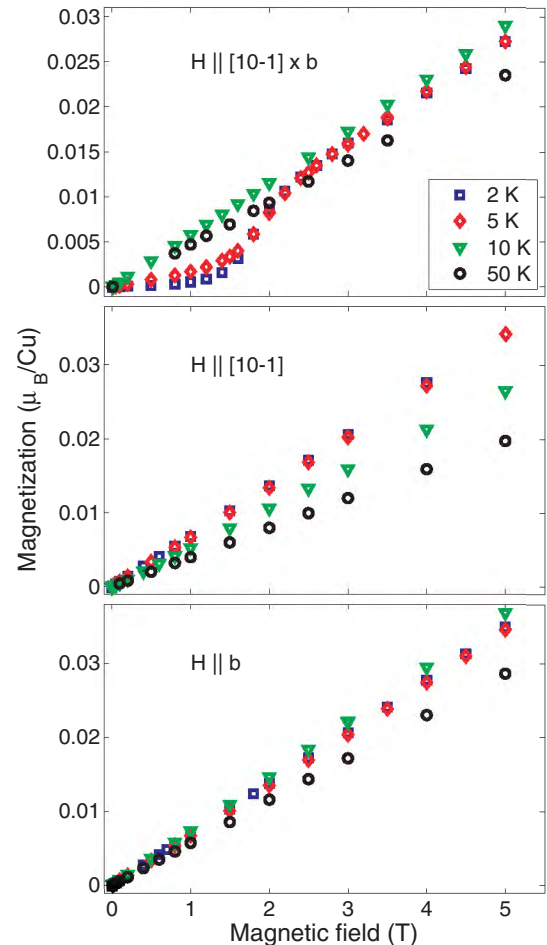

FIG. 6. (Color online) Magnetic field scans along three crystallographic directions.

where the moments switch their orientation from that parallel to the field to the one that is perpendicular to the field but still keeping the AFM alignment. The value of the spin-flop field is $\sim$1.7 T, similar to another case with the AFM ordering of Cu^{2+} spins in a 1D alternating chain $CuSb_2O_6$ (Ref. [13]).

C. Torque magnetometry

A subtle feature can be noticed around 200 K in Fig. [4]. Namely, single crystal susceptibilities along b and $[10\bar{1}]$ directions cross each other which indicates that the magnetic anisotropy of the system is changing with temperature. In order to investigate this feature more closely, we have performed torque measurements within two perpendicular planes: (010) plane (ac plane) and the one containing the b axis and the τ direction ($b\tau$ plane). The angular dependence of the measured torque component Γ_z in the case of a linear response is given by the expression,

$$\Gamma_z = \frac{m}{2M}H^2\Delta\chi_{xy}\sin(2\phi - 2\phi_0),\qquad(3)$$

where m is the mass of the sample, M the molar mass, H the magnetic field, and $\Delta\chi_{xy} = \chi_x - \chi_y$ is the susceptibility anisotropy in the xy plane (plane of rotation of the magnetic field). ϕ_0 is the phase shift with respect to the laboratory frame. From Eq. (3) we see that the torque is zero when the field is applied along ϕ_0 and $\phi_0 + 90°$. In addition, the torque is a sine curve with a positive amplitude if $\chi_x > \chi_y$. The measured angular dependence of torque in $SeCuO_3$ in $b\tau$ and ac planes at different temperatures is shown in Fig. [7]. In both the paramagnetic and the AFM state the measured torque obeys the above expression which means that the response to the magnetic field is linear. The angle in Fig. [7] is the goniometer angle.

One can immediately notice that for the $b\tau$ plane the zeros of the curves do not change as the temperature is lowered from the room temperature down to 4 K. In contrast, there is a substantial shift of magnetic axes within the ac plane. The temperature dependence of the phase shift is presented in Fig. [7(c)] with the inset showing the region around the transition. At 8 K there is a clear indication of the transition, and for temperatures below 5 K the easy axis approaches the τ direction, in accordance with the magnetization results.

D. Electron spin resonance

To further investigate the anisotropy, electron spin resonance measurements have been performed. The absorption profile of spectra obtained for various crystal orientations with respect to both sweeping H_0 and microwave H_1 magnetic field show a single, exchange-narrowed Lorentzian absorption line.[14,15] In Fig. [8] we present several spectra taken at different temperatures for the $H_0 \parallel [10\bar{1}]$ orientation. At room temperature we have observed a slight departure of the ESR lineshape from the Lorentzian absorption profile which is explained by the overlap of tails of the ESR line counterpart appearing in the negative magnetic field sector. The original line becomes so broad as to overlap via $H_0 = 0$ T with its negative magnetic field equivalent.
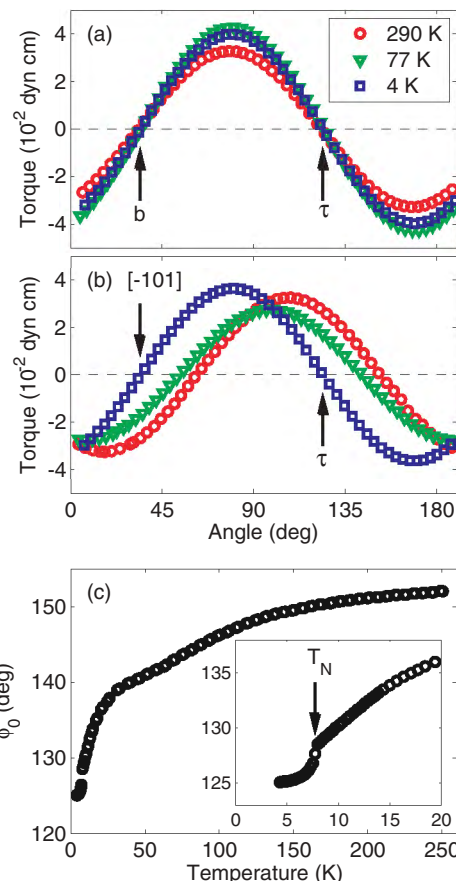

FIG. 7. (Color online) Torque measurements in (a) $b\tau$ plane and (b) ac plane. (c) Temperature dependence of the phase shift of magnetic axes in the ac plane.

Below T_N no AFM resonance absorption spectrum has been noticed to emerge at H_0 fields swept out from 50 up to 10 000 Gauss for different crystal orientations.

We have extracted the values of the g factor for each absorption spectrum and in Fig. [9] we present its temperature and angle dependence. Above $\sim$200 K the g factors saturate to values 2.23 and 2.26 for $H_0 \parallel [10\bar{1}]$ and $H_0 \parallel b$, respectively. Below 200 K, however, one discerns two contrary monotonic trends down to 40 K. Between 40 and 15 K the g factors retain almost constant values and in the vicinity of T_N both g factors are increasing. Such a strong temperature dependence of the g factor is usually associated with underlying structural changes, as evidenced in $CuSb_2O_6$ which exhibits a monoclinic-to-tetragonal phase transition below 400 K.[13]

The angular dependence at 15 and 100 K is presented in Figs. [9(b)] and [9(c)] for the ac and $b[10\bar{1}]$ plane, respectively. We have marked the position of the extrema for each curve and one can immediately notice that there is a clear phase shift in the ac plane, confirming the results from the torque magnetometry. On the other hand, when the anisotropy is measured in the plane that contains the b axis, there is no phase shift within the experimental error.

In Fig. [10] we present the temperature dependence of the linewidth ΔH for two crystal orientations. The linewidth is very broad and reaches nearly 150 mT at high temperatures. As the temperature is lowered, the line narrows with a broad
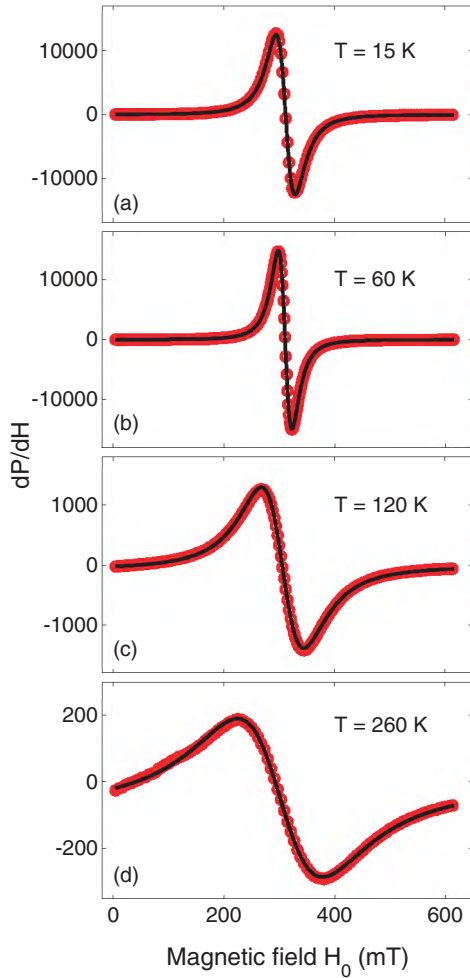
FIG. 8. (Color online) X band (9.4 GHz) ESR absorption spectra for $H_0 \parallel [10\bar{1}]$ (red) fitted with first derivative Lorentzian lines (black).
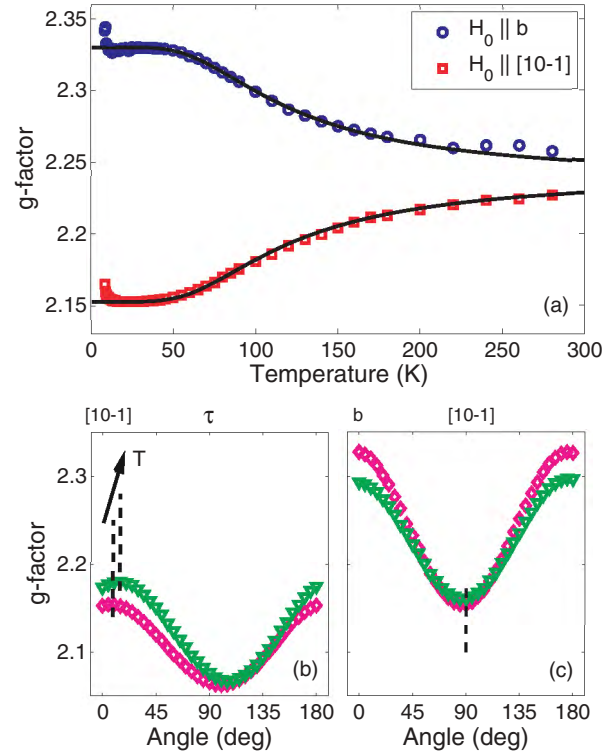

FIG. 9. (Color online) (a) Temperature dependence of the g factor with respect to two crystal orientations. The lines represent the fit using Eq. (5). Angular dependence of the g factor at 15 K (diamond) and 100 K (down triangle) (b) in the ac plane and (c) in the $b[10\bar{1}]$ plane. Vertical dashed lines mark the position of extrema.

minimum around 50 K below which ΔH tends to increase in the vicinity of the phase transition. It is interesting to note that at high temperatures $\Delta H^{[10\bar{1}]} > \Delta H^b$ while below the minimum $\Delta H^{[10\bar{1}]} < \Delta H^b$.

We can disregard the spin diffusion as a relaxation mechanism since no deviation from the Lorentzian profile has been noticed.[16–18] For classical 3D antiferromagnets ($T_N \sim J$) the Kubo-Tomita (KT) model[19] describes well the broadening of the absorption lines in the paramagnetic regime. However, the KT model is not applicable for the low-dimensional systems where long-range order is suppressed due to the AFM correlations in the range $T_N < T < J$. More recently Oshikawa and Affleck (OA) have developed a model to cover the deficiency of the KT theory at low T in $S = 1/2$ AFM Heisenberg chains.[20] Since SeCuO$_3$ has two distinct copper site, neither the OA model can be applied.

In a recent ESR investigation of the spin-Peierls compound CuGeO$_3$ very similar behavior of the ESR linewidth has been reported:[21] a significant decrease of the linewidth as the temperature is decreased with a broad minimum and a subsequent increase just above the transition. In an attempt to describe the high temperature behavior of the linewidth, Eremina and

coworkers used a semiphenomenological approach:[21]

$$\Delta H(T) = \Delta H(\infty) e^{-\frac{C_1}{C_2 + T}}. \qquad (4)$$

Here, C_1 corresponds to the exchange constant J, while C_2 is related to a transition temperature T_N and is therefore associated with the intertetramer interaction. The parameters extracted from the fit (see Table II) have reasonable values:
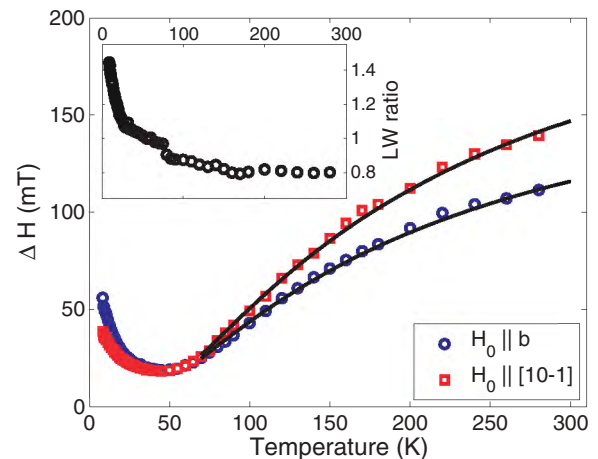
FIG. 10. (Color online) Temperature dependence of 9.4 GHz ESR linewidths obtained for two crystal orientations [$A(\phi = 0)$ and $B(\phi = 0)$]. The data are fitted (solid lines) using Eq. (4). The inset shows the ratio of two linewidths.

TABLE II. The fitting parameters for the linewidth behavior.

Orientation	C_1 (K)	C_2 (K)	$\Delta H(\infty)$ (mT)
$A(\phi = 0)$	175 ± 10	7 ± 3	260 ± 10
$B(\phi = 0)$	170 ± 10	12 ± 4	200 ± 10

$C_1 \approx 170$ K, close to J_{12} deduced from the tetramer fit, and $C_2 \approx 10$ K, close to the value of the 3D ordering.

It is significant that the phenomenological approach with Eq. (4) can be applied only down to 70 K, where the crossover in susceptibility has been observed and where the tetramer Hamiltonian Eq. (1) becomes insufficient. In the case of CuGeO$_3$ the increase of the linewidths close to the spin-Peierls transition (1–2 K) was attributed to the freezing of triplets, weakening the exchange narrowing.[21] SeCuO$_3$, on the other hand, shows a linewidth minimum around 50 K, much above T_N. In addition, at the same temperature the crossing of two linewidth curves occurs. Similarly broad minimum and subsequent increase of ΔH at lower temperatures has been observed in BaCu$_2$Ge$_2$O$_7$, another $S = 1/2$ AFM Heisenberg chain[22] which does not enter the spin-Peierls phase but orders at ≈ 8 K.

We also mention the contribution from the anisotropic Zeeman interaction to the ESR linewidth, due to the presence of two inequivalent g tensors. It has been shown[13,23] that in the high temperature limit that contribution is proportional to $(\Delta g)^2$. However, in SeCuO$_3$ the weakest coupling within the tetramer is $J_{12} \sim 160$ K and the high temperature limit refers to values much above our experimental window. To estimate the contribution from the anisotropic Zeeman interaction to ΔH one needs to know all the components of $\tilde{g}_1$ and $\tilde{g}_2$ so further investigation is desired.

IV. DISCUSSION

Let us first discuss the possible origins of the 70-K crossover. As mentioned in Sec. III B, no combination of parameters in Eq. (2) can reproduce the susceptibility in the range 10 K $< T <$ 70 K. Considering the structural arguments presented in Sec. III A, it is natural to assume that the crossover is a consequence of the intertetramer interaction along the a axis, J_{22}. It is expected that this interaction is rather weak compared to J_{11} and J_{12} due to the large elongation of the Cu2 octahedron [d(Cu2–O4) = 2.71 Å]. However, since the octahedron is not ideal, there may be some mixing of $d_{x^2-y^2}$ and $d_{3z^2-r^2}$ orbitals in the Cu2–O4 coupling, allowing for a finite J_{22}. The value of the angle $\angle$(Cu2–O4–Cu2) = 95° also suggests very weak J_{22} and even allows for both FM and AFM couplings to be realized. Such a scenario would mean that below 70 K SeCuO$_3$ should be regarded as a system of magnetic chains composed of three different couplings with very disproportionate values.

Since the strength of J_{22} sensitively depends on the exact values of d(Cu2–O4) and $\angle$(Cu2–O4–Cu2), one cannot disregard the possibility that a small structural change, particularly a shift of the ligand position(s), may occur around 70 K and enhance J_{22}. One possibility is that J_{22} becomes (more) ferromagnetic, which can come from the decrease of the $\angle$(Cu2–O4–Cu2) angle towards 90°, giving rise to an increase

of the susceptibility relative to the bare tetramer picture. Such a change can come from a lateral shift of the O4 apical ion relative to the $d_{x^2-y^2}$ orbital, thus pulling the neighboring tetramers closer along the a axis. However, this also reduces the distortion of the Cu2 octahedron which implies a smaller contribution from active $d_{x^2-y^2}$ orbitals and consequently a smaller J_{22}. In order to clarify this issue, further structural and theoretical studies are needed.

In addition to isotropic exchange interactions one needs also to consider the anisotropic ones, especially the Dzyaloshinskii-Moriya interaction (DMI). DMI mixes the singlet and the triplet states of localized spin clusters and is known to significantly influence the behavior of low-dimensional magnetic systems.[24,25] Taking into account the symmetry considerations, DMI is allowed only for the Cu1–Cu2 pair. The main influence of DMI is to cant the neighboring moments which produces the ferromagnetic component. However, due to the inversion symmetry in the center of the tetramer, it is expected that the ferromagnetic contributions from each end cancel each other.

It is important to emphasize that the temperature dependence of g factors and linewidths is not influenced by the feature around 70 K, indicating that the microscopic behavior is not greatly affected.

Secondly, we discuss the observed rotation of magnetic axes, presented in Fig. 7(c). The observed phase shift is a result of the rotation of local magnetic axes (i.e., the change of the total g tensor with temperature). Several origins can be considered. One could be the change of the ligand structure around the magnetic ion caused by a structural change. This type of change of the g tensor was observed in CuSb$_2$O$_6$ where the temperature dependence of the g tensor was triggered by structural changes in the wide temperature range.[13] However, our structural analysis down to 80 K does not indicate any significant structural alterations.

Another explanation could be that the g shift occurs due to present anisotropies induced by the increase of short-range correlations at temperatures $T < J$ in low-dimensional systems. Such g shifts have been observed in the one-dimensional system Cu-benzoate where the temperature dependence and a rotation of the g-tensor axis has been observed.[26] This was later explained as a consequence of the Dzyaloshinsky-Moriya interaction (DMI) within the Oshikawa-Affleck (OA) theory of ESR in spin $S = 1/2$ Heisenberg chains.[20,27] Similar g shift was documented and explained within the OA theory in 1D Cu pyrimidine dinitrate.[28] However, in SeCuO$_3$ the g shift saturates below 50 K only to increase again in the vicinity of the phase transition to long-range order. This saturation is not expected if the g shift is due to strengthening of anisotropic correlations.

Finally, a third, new scenario, which we argue is realized in SeCuO$_3$, can emerge in systems where there are at least two inequivalent sites contributing to the macroscopic anisotropy with different local magnetic axes and different temperature dependencies of magnetic susceptibility. In SeCuO$_3$ there are two copper sites, Cu1 and Cu2, with different values and orientations of their g tensors. Since they are exchange-coupled, the ESR experiment observes only one line with a total g tensor which nontrivially depends on g_1, g_2, J_{11}, and J_{12} (to a lesser extent even on J_{22}). From the present set of data

we are not able to fully model the system. In what follows we present a simple approach which depicts the essential nature of the physical processes.

Let us assume that individual tensors $\tilde{g}_1$ and $\tilde{g}_2$ are diagonal in a coordinate system defined by $\{[10\bar{1}],b,\tau\}$. Within our tetramer model we set $J_{12} = J_{22} = J' = 0$, $J_{11} > 0$, and we observe how the total g tensor depends on the temperature as the central Cu1–Cu1 pair experiences the singlet-triplet transformation. We use a simple averaging to get the total g tensor,

$$\tilde{g}_{\text{tot}} = \frac{\alpha\tilde{g}_1 + \beta\tilde{g}_2}{\alpha + \beta}, \tag{5}$$

where $\alpha = \alpha_T/\alpha_{\text{max}}$, $\alpha_{\text{max}} = 3/4$, $\beta = 1$, and α_T is the probability of finding the Cu1–Cu1 dimer in a triplet state,

$$\alpha_T = \frac{3e^{-J/T}}{1 + 3e^{-J/T}}. \tag{6}$$

In Fig. 9 we present the results of the above procedure for the $[10\bar{1}]$ and b directions using the values $\tilde{g}_1 = (2.335,2.14,2.07)$, $\tilde{g}_2 = (2.153,2.33,2.07)$, and $J_{11} = 290$ K. The agreement with the experimentally obtained values is surprisingly good, given the simplicity of the model, and the obtained value of J_{11} is very close to the one extracted from Eq. (2).

Within the choices of model parameters, it is not possible to describe the torque: no rotation of magnetic axes occurs since both g tensors are diagonal in the same coordinate system. A more realistic approach would take into account two g tensors for each copper site whose orientation is set by the local ligand environment. Since in that case the principal axes for $\tilde{g}_1$ and $\tilde{g}_2$ are pointing in different directions, the reduction of the Cu1 moment will also influence the direction of principal axes of the total g tensor. In Fig. 11 we demonstrate such a scenario for two temperatures with the emphasis on the rotation of the magnetic axes of the total g tensor as observed with torque measurements [see Fig. 7(c)].
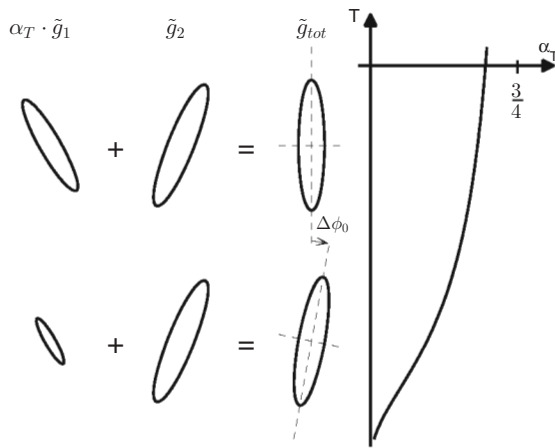
FIG. 11. Averaging the g tensors with varying contribution from $\tilde{g}_1$ which is proportional to the triplet probability (the graph on the right-hand side). As the temperature is lowered, the total g tensor effectively rotates by $\Delta\phi_0$. The semiaxis values are not scaled with the values from the text.

In SeCuO$_3$ this effect is not averaged out by the symmetry related sites. If the g tensor is diagonal in the experimental coordinates, the diagonal components remain dominant also in the crystal coordinate system. By using the symmetry operators of the space group of the crystal, it is straightforward to show that the g tensors at the symmetry-related sites within the tetramer do not cancel out: Actually the dominant diagonal values add up. In addition, the screw transformation maps tetramers from one chain to the other. Since g tensors are invariant under the 180° rotation, the contributions from four different Cu1 and Cu2 sites in the unit cell are adding up.

This simplified model demonstrates how effective magnetic axes can rotate when inequivalent sites experience different quantum correlations. However, to quantitatively fit our data, one would need the complete Hamiltonian, a theoretical method to treat it and a theory relating the calculated site-dependent susceptibilities to the observed ESR signal.

V. CONCLUSIONS

We have demonstrated that the tetramer model of SeCuO$_3$ can provide a good explanation for the observed high temperature behavior of the susceptibility and especially of the unusual temperature dependence of the g factor. The kink in the susceptibility around 70 K indicates that the tetramer Hamiltonian does not provide a complete set of interactions in the system. An additional coupling, most probably J_{22} which couples tetramers along the a axis, also influences the linewidth of the ESR spectra. Below 70 K the linewidths develop a minimum and the overall behavior is similar to the case of a 1D $S = 1/2$ AFM Heisenberg chain BaCu$_2$Ge$_2$O$_7$, although SeCuO$_3$ shows a large difference between various couplings ($J_{11} > 70$ K).

The intertetramer coupling, J', which is mediated via Cu–O–Se–O–Cu paths, drives the system into a long-range ordered state at $T_N = 8$ K. This provides a wide temperature window where the effects of intertetramer quantum fluctuations can be investigated. Compared to the incommensurate compounds Cu$_2$Te$_2$O$_5$X$_2$, SeCuO$_3$ shows a simpler magnetic structure with a relatively small spin-flop field ~ 1.7 T. This can enable an easier theoretical modeling of the magnetic structure and magnetic excitation with and without the magnetic field.

Finally, we have argued that the observed temperature dependence of magnetic axes is due to the inequivalent copper sites experiencing a different type of quantum correlations. Assuming temperature-independent g tensors, which is valid in most compounds, this effect can be inverted to a new experimental method of obtaining site-selective susceptibilities from bulk measurements.

[1]B. Bleaney and K. Bowers, Proc. R. Soc. London A **214**, 451 (1952).

[2]R. Sessoli, D. Gatteschi, A. Caneschi, and M. A. Novak, Nature (London) **365**, 141 (1993).

[3]Z. Salman, R. F. Kiefl, K. H. Chow, W. A. MacFarlane, T. A. Keeler, T. J. Parolin, S. Tabbara, and D. Wang, Phys. Rev. B **77**, 214415 (2008).

[4]A.-L. Barra, P. Debrunner, D. Gatteschi, Ch. E. Schulz, and R. Sessoli, Europhys. Lett. **35**, 133 (1996).

[5]J. R. Friedman and M. P. Sarachik, Annu. Rev. Condensed. Matter Phys. **1**, 109 (2010).

[6]P. Lemmens, K.-Y. Choi, E. E. Kaul, C. Geibel, K. Becker, W. Brenig, R. Valenti, C. Gros, M. Johnsson, P. Millet, and F. Mila, Phys. Rev. Lett. **87**, 227201 (2001).

[7]M. Prester, A. Smontara, I. Živković, A. Bilušić, D. Drobac, H. Berger, and F. Bussy, Phys. Rev. B **69**, 180401(R) (2004).

[8]O. Zaharko, A. Daoud-Aladine, S. Streule, J. Mesot, P.-J. Brown, and H. Berger, Phys. Rev. Lett. **93**, 217206 (2004).

[9]K. Prša, H. M. Rønnow, O. Zaharko, N. B. Christensen, J. Jensen, J. Chang, S. Streule, M. Jiménez-Ruiz, H. Berger, M. Prester, and J. Mesot, Phys. Rev. Lett. **102**, 177202 (2009).

[10]H. Effenberger, Z. Kristallogr. **175**, 61 (1986).

[11]K. Momma and F. Izumi, J. Appl. Crystallogr. **41**, 653 (2000).

[12]S. Emori, T. Tokii, and Y. Muto, Bull. Chem. Soc. Jpn. **48**, 1649 (1975).

[13]M. Heinrich, H.-A. Krug von Nidda, A. Krimmel, A. Loidl, R. M. Eremina, A. D. Ineev, B. I. Kochelaev, A. V. Prokofiev, and W. Assmus, Phys. Rev. B **67**, 224418 (2003).

[14]P. W. Anderson and P. R. Weiss, Rev. Mod. Phys. **25**, 269 (1953).

[15]P. W. Anderson, J. Phys. Soc. Jpn. **9**, 316 (1954).

[16]P. M. Richards, in *Local Properties at Phase Transitions*, Proceedings of the International School of Physics−Enrico Fermi, Course LIX, Varenna, 1973, edited by K. A. Müller and A. Rigamonti (North-Holland, Amsterdam, 1976), p. 539.

[17]D. L. Huber, J. Phys.: Condens. Matter **15**, L579 (2003).

[18]T. T. P. Cheung and Z. G. Soos, J. Chem. Phys. **69**, 3845 (1978).

[19]R. Kubo and K. Tomita, J. Phys. Soc. Jpn. **9**, 888 (1954).

[20]M. Oshikawa and I. Affleck, Phys. Rev. B **65**, 134410 (2002).

[21]R. M. Eremina, M. V. Eremin, V. N. Glazkov, H. A. Krug von Nidda, and A. Loidl, Phys. Rev. B **68**, 014417 (2003).

[22]S. Bertaina, V. A. Pashchenko, A. Stepanov, T. Masuda, and K. Uchinokura, Phys. Rev. Lett. **92**, 057203 (2004).

[23]B. Pilawa, J. Phys.: Condens. Matter **9**, 3779 (1997).

[24]J. Choukroun, J.-L. Richard, and A. Stepanov, Phys. Rev. Lett. **87**, 127207 (2001).

[25]M. Herak, A. Zorko, D. Arčon, A. Potocnik, M. Klanjšek, J. van Tol, A. Ozarowski, and H. Berger, Phys. Rev. B **84**, 184436 (2011).

[26]B. Pilawa, E. Herrling, and I. Odenwald, J. Magn. Magn. Mater. **226**, 417 (2001).

[27]M. Oshikawa and I. Affleck, Phys. Rev. B **76**, 109901(E) (2007).

[28]S. A. Zvyagin, A. K. Kolezhuk, J. Krzystek, and R. Feyerherm, Phys. Rev. Lett. **95**, 017207 (2005).

Quantum yield in polymer wrapped single walled carbon nanotubes: a computational model

Dejan M Djokić[1,2] and Aranya Goswami[1,3,4]

[1] Institute of Chemical Sciences and Engineering, Ecole Polytechnique Fédérale de Lausanne (EPFL), CH-1015 Lausanne, Switzerland
[2] Center for Solid State Physics and New Materials, Institute of Physics Belgrade, University of Belgrade, Pregrevica 118, 11 080 Belgrade, Serbia
[3] Electronics and Electrical Communication Engineering, Indian Institute of Technology (IIT), Kharagpur, India
[4] Department of Electrical and Computer Engineering, University of California, Santa Barbara, United States of America

E-mail: djokic@ipb.ac.rs

Abstract
Quantum yield in polymer wrapped single walled carbon nanotubes (SWCNTs) has been computationally investigated using a 2D model of exciton decay with non-radiative channels due to the diffusive motion across the nanotube surface. Beside the role of SWCNT's ends as the exciton quenchers, we have considered the influence of the wrapping polymer through its chemistry and wrapping angle. The model has been solved exactly for zero-angle wrapping, a particular case when the polymer interfaces the nanotube along its axis. The general case has been treated numerically and it has been concluded that the wrapping angle has no relevant influence upon the quantum yield values which are of experimental interest. A wide range of quantum yield values computed in the present contribution can be helpful in understanding potentially available photoluminescence data of SWCNTs wrapped with a variety of polymer families.

Keywords: carbon nanotubes, diffusion, quantum yield, fluorescence

(Some figures may appear in colour only in the online journal)

1. Introduction

Single walled carbon nanotubes (SWCNTs), as long hollow cylinders of carbon atom honeycomb lattice with extremely high aspect ratio, have continued to stay at the forefront of nanomaterial research for even longer than two decades [1]. They possess remarkable optoelectronic properties [2] which have captured the attention of researchers within multidisciplinary scientific communities [3, 4]. Semiconducting SWCNTs, in particular, are outstanding light-emitting materials capable of performing photoluminescence, a property which has been successfully implemented in a broad range of applications starting from realizations of nanoscale photonic devices in form of single-photon emitters [5] to near-infrared

optical biosensors for life sciences and biomedicine [6]. The key parameter relevant to such applications is the photoluminescence quantum yield the precise value of which in an individual SWCNT is difficult to measure since it is sensitive the nanotube's environment, chiral angle, defects, presence of different surfactants etc. The efficiency of the near-infrared photoluminescence spectra of solvent dispersed SWCNTs has been determined to be very poor with typical luminescence quantum yield values on the order of 0.1% and even lower [7–10], that classifies the nanotube photoluminescence as fluorescence. It has been well established that optical properties of SWCNTs even at room temperature are dominated by the exciton levels [11]. Both nature and dynamics of these excited states have a huge impact on the functionality of

SWCNT-based optolectronic applications [12]. The quantum yield is in direct relationship with the radiative and non-radiative exciton lifetimes, the latter being much shorter. This results in photoluminescence lifetimes on the order of a few (10) picoseconds since nonradiative exciton recombination processes dominate [13–15]. A considerable improvement of the quantum yield is therefore required that can be achieved by noncovalent polymer functionalizations of SWCNTs [16], wrapped, for example, by phospholipids, DNA, μ-RNA, polyacrilic acid, etc. Furthermore, SWCNTs coated with biological polymer wrappings to control the sensor's selectivity by modulating the surface coverage of the nanotube in the presence of an analyte can be used as sensors with single-molecule sensitivities [17]. Single-molecule adsorption and desorption events on the funtionilised nanotube surface result in stochastic changes in SWCNT photoluminescence efficiency [18].

In this theoretical account we explore 2D exciton dynamics of polymer wrapped SWCNTs in order to understand both geometrical effects of wrapping and influence of polymer type upon the quantum yield. The excitons have been treated classically as point-like particles at room temperature. Surface random walk analysis in the diffusion limit of the fluorescence emission has been used to provide a physical assessment of the quantum efficiency of light emission as a function of both radiative and diffusion induced non-radiative, environmentally dependent, exciton lifetimes. The exciton dynamics in polymer-wrapped nanotubes is therefore assumed to follow 2D diffusion dynamics on the surface [19], challenging conventional underlying assumptions of uni-dimensionality [20, 21] which consider the effects of nanotube defected ends only. The model is able to predict a strong polymer type dependence of quantum yield as a result of the contribution of the chemistry of polymer to SWCNTs photoluminescence spectra. On the other hand, for measurable quantum yield values, we have observed the extremely weak dependence on the wrapping angle that is ascribed to the very high aspect ratio of SWCNTs. An appreciable angular dependence has been noticed in the case of extremely low quantum yield values being lower than ca 0.01%, that is out of experimental focus. In such a way, it is sufficient to use the simplified model only which is solvable analytically and concerns the so-called zero angle wrapping where polymers interface the nanotube along its axis without wrapping.

2. Computational details

We have used a 2D thermal diffusion model to study the exciton dynamics by relying on two approaches, analytic and numeric. The model assumes the random walk of delocalized bounded electron–hole pairs which move diffusively in the continuous limit. The excitons are considered as point-like classical particles at room temperature capable of spreading along the nanotube axis and circumferentially. This assumption is corroborated by the fact that room temperature fluctuations dephase the quantum nature of the excitons which thereby lose their wave-packet properties. Accordingly, an extra spatial

degree of freedom is introduced to exciton motion ensuring the 2D treatment. The dephasing arises from extremely frequent exciton–phonon scattering events with τ_{deph} of nearly 75 fs [22]. The effective exciton mass m_{exc} is estimated like $0.17m_e$ [23], that brings about the diffusion constant value of $D = 20\ \mathrm{cm^2\ s^{-1}}$ at room temperature. The diffusion constant estimation is based on Einstein–Smoluchowski relation, $D = \mu_{\mathrm{exc}}k_B T$, where the exciton mobility, $\mu_{\mathrm{exc}} = \tau_{\mathrm{deph}}/m_{\mathrm{exc}}$, is in accordance with a Boltzmann probability distribution of point-like particles [24]. As an outcome of *ab initio* calculations [25], the effective radiative decay rate, χ_r, is taken to be nearly 1 ns^{-1}.

The computational working area concerns the surface of the nanotube demarcated by the nanotube ends and the interfacing line-like polymer, which is, for simplicity, assumed to have no thickness. There are two cases which have been considered. The first is related to the so-called zero angle wrapping in which the polymer is aligned on the surface along the nanotube axis. This case has been solved analytically and is based on the method of separation of variables with two types of boundary conditions: (1) perfect exciton quenchers at the nanotube ends in which the concentration is kept to zero and (2) absorption radiative condition at the polymer sites characterized by a constant γ which relates the exciton flux to its concentration at the boundary. The second case is a rather generalized one which involves the non-zero angle wrapping ($\phi \neq 0$). The working computational area is a skewed rectangle on the surface of the nanotube. Because of complexity of the boundary conditions on the polymer site we have mapped out the problem onto the skew coordinate system in which the boundary conditions become quite simplified. However, the price to be paid is the transformation of the diffusion equation into an elliptic differential equation of the second order. This equation has been treated numerically in R using a finite difference method that will be explained later throughout the text in detail. Finally, using the diffusion survival probability we have integrated all the solutions of the exciton concentrations over time and space for all possible initial exciton distributions in order to compute the photoluminescence quantum yield depending on both γ and ϕ.

3. Results and discussions

We present results of the 2D exciton diffusion model developed on the nanotube surface. There are two cases considered: $\phi = 0$ and $\phi \neq 0$. The former has been solved analytically, whereas the latter has been treated numerically due to its complexity arising from the boundary conditions which mix x and y contributions to the exciton fluxes as soon as ϕ moves away from zero. We propose the application of the analytic approach ($\phi = 0$) to solving exciton dynamics only regardless of the angular value. This is based on the fact that no significant angular dependence has been proven to contribute to experimentally distilled quantum efficiency of SWCNT photoluminescence. The properties and/or type of the polymer affect the exciton motion in a manner that results in the following two types of events: a mobile exciton can be
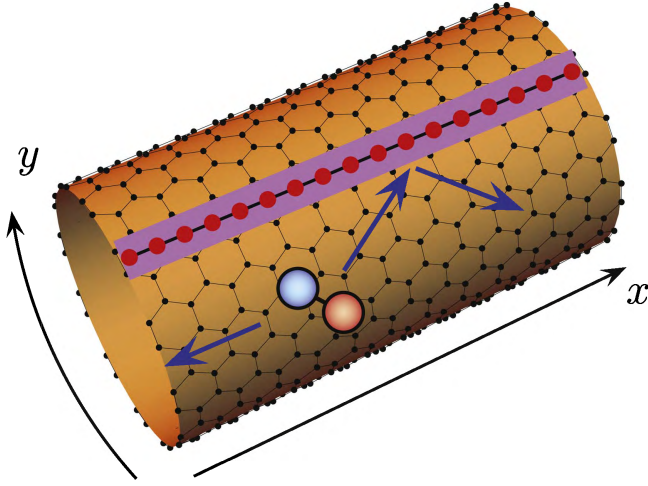
Figure 1. An exciton (red-blue pair) moving by random walk across the illuminated surface of a SWCNT. There is a polymer attached to the surface alongside the nanotube. The motion of the exciton is confined by the nanotube ends, as well as, polymer barrier that can either absorb or reflect the exciton.

completely destroyed at the barrier or partially bounced back to continue performing its random walk motion. Our main assumption is that the polymer wraps the nanotube by functionalizing the surface of the nanotube noncovalently [26]. SWCNTs are cylindrical graphene tubes with a quasi one-dimensional π-conjugated structure so that the noncovalently realized functionalization commonly goes via enthalpy-driven interactions, such as π-π or CH$-\pi$, and/or entropy-driven hydrophobic interactions [27]. In such a way, there is a minimum damage in the nanotube band structure that allows the generation of the excitons across the entire surface upon illumination. However, this is not the case in the immediate vicinity of the polymer which due its strong local dielectric screening potential of the exciton binding energy can lead to exciton recombination. There is also a possibility of the exciton survival at polymer sites which is manifested through its reflection by the barrier. Evidently, dielectric mediums functionalizing the nanotube surface substantially modify the electron–hole interaction potential decreasing the optical transition energies as has been verified experimentally in resonant Raman spectroscopy [28]. On the other hand, the complete quenching of the exciton occurs only at the ends of the nanotube which are considered as strong defect sites. Tight-binding modeling [29] together with experimental results based on scanning tunneling spectroscopy [30] indicate substantial alterations in the local electronic band structure close to the carbon nanotube ends which cause the permanent exciton loss.

3.1. The case $\phi = 0$

In this section we investigate the influence of the polymer as a diffusion barrier on the exciton dynamics in the case of zero angle wrapping of SWCNT. Figure 1 delineates a mobile exciton on a nanotube surface. The area of interest for studying the exciton motion is bordered with the nanotube ends along x-direction and with both sides of the polymer

along the circumference (y-direction). No diffusive passage of exciton through the barrier is taken into account. In the actual fact, the surface of the area is equal to $L \times \pi d$, where L and d are the nanotube length and diameter, respectively. The concentration of the exciton, $f(x, y, t)$, is fixed to zero at $x = 0, L$ all the time during the exciton motion, whereas the two polymer sides ($y = 0, \pi d$) allow the existence of excitons in their vicinity up to a condition imposed on the exciton flux. This condition is nothing but the so-called 'radiation' boundary condition that reads as

$$\frac{\partial f}{\partial y} = \pm \gamma f, \ \text{ at } y = 0, \pi d. \tag{1}$$

The constant of proportionality, γ, between the exciton flux $\left(\frac{\partial f}{\partial y}\right)$ and concentration measures the extent to which an exciton is absorbed/reflected by the polymer [31]. This constant encapsulates the chemical property of the polymer. In $\gamma \rightarrow \infty$ limit, the condition (1) boils down to the Smoluchowsky boundary condition ($f \rightarrow 0$ at $y = 0, \pi d$) which completely favors the exciton destruction (absorption) over its reflection. In other terms, polymers with large γ's values behave rather like defects resembling very much the effects of the nanotube ends. On the other hand, polymers with low γ values promote the survival of the exciton, which is essential for an improved photo-luminescence spectra.

The exciton dynamics governed with time-dependent diffusion equation with the above-mentioned boundary conditions and diffusion constant D on a rectangle $[0, L] \times [0, \pi d]$ in xy-plane can be solved analytically. The rectangle is obtained by unzipping the nanotube along the polymer and represents the working computational area on the cylinder. We apply the method of separation of variables by extending the one-dimensional approach developed in [32, 33] to 2D. Thus, the complete generalized solution of the exciton concentration can be written down in the following closed form:

$$f(x, y, t; x_0, y_0) = \sum_{m=1}^{\infty} \sum_{n=1}^{\infty} A_m(x, x_0) B_n(y, y_0) e^{-D(\alpha_m^2 + \beta_n^2)t},$$

$$\tag{2}$$

where, for an exciton initially generated at a point (x_0, y_0) with Dirac-δ distribution:

$$A_m(x, x_0) = (2/L)\sin(\alpha_m x_0)\sin(\alpha_m x),$$
$$B_n(y, y_0) = 2(\beta_n \cos(\beta_n y_0) + \gamma \sin(\beta_n y_0))$$
$$\times \frac{\beta_n \cos(\beta_n y) + \gamma \sin(\beta_n y)}{(\beta_n^2 + \gamma^2)\pi d + 2\gamma}. \tag{3}$$

Implementing the imposed boundary conditions at the polymer sites (1) together with the zero exciton concentrations at $x = 0, L$ one automatically comes up with the following expressions for α_m and β_n:

$$\alpha_m = m\pi/L,$$
$$2\cot(\beta_n \pi d) = \beta_n/\gamma - \gamma/\beta_n. \tag{4}$$

Note that for $\gamma \rightarrow \infty$, β_n takes on a similar form like α_m. In general, the solution to β_n is deduced numerically from the second relation given in (4). There is exactly one root per
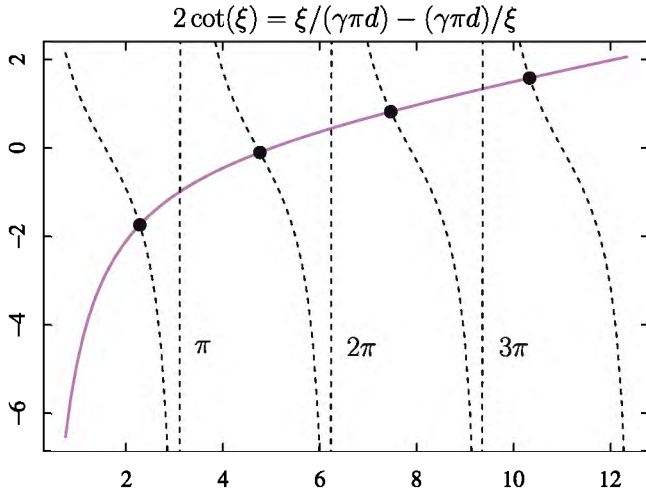
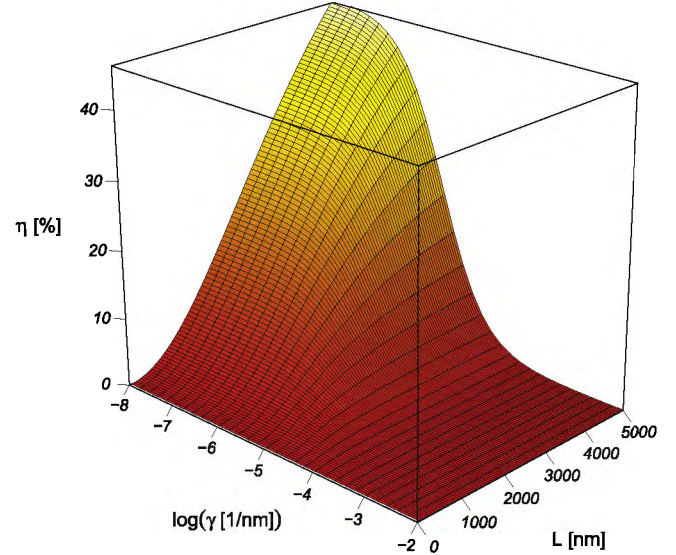**Figure 2.** Several crossing points between functions $2\cot(\xi)$ (dashed curve) and $\xi/(\gamma\pi d) - (\gamma\pi d)/\xi$ (in violet). The points represent the solutions $\xi_n \equiv \beta_n\pi d$ which are confined within the intervals $((n-1)\pi, n\pi]$.

Figure 3. 2D surface plot of the quantum yield spanned over $\log(\gamma)$ and L. The dependence has been calculated for $m = n = 50$ terms of the sum in (6) ensuring the convergence of the result.

$((n-1)\pi, n\pi]$ interval resulting in n-solutions to $\beta\pi d$, where $n = 1, 2, \ldots$. In praxis, it is quite sufficient to determine few tens of such roots in order to achieve a solid convergence in the concentration exciton value. Figure 2 demonstrates the crossing points of two functions $2\cot(\xi)$ and $\xi/(\gamma\pi d) - (\gamma\pi d)/\xi$. One can see that for very large γ's values, $\xi \equiv \beta\pi d$ tends to $\pi, 2\pi, 3\pi$ and so on. Otherwise, the solutions fall within the mentioned intervals.

In order to compute the quantum yield of nanotube fluorescence using exciton levels one must allow for all the possible initial exciton concentrations generated randomly across the surface of the nanotube. This means that we adopt a conventional approach [34] based on the calculation of the survival exciton probability with the area of interest: $[0, L] \times [0, \pi d]$. The survival probability computation implies averaging out over all the possible initial positions (x_0, y_0), as well as, a spatial integration of the exciton concentration. This probability is time dependent and contains an extra term, $e^{-\chi_r t}$, originating from the exciton consumption rate term, $-\chi_r f(x, y, t)$, that can be added to the diffusion equation. The consumption is stimulated through the radiative decay channel with a decay rate of nearly 1 ns^{-1} as has been discussed earlier. Finally, the quantum yield, η, represents the inverse of total luminescence rate scaled with radiative life time. The inverse of total luminescence rate is obtained by integrating the time decaying survival probability function from 0 to ∞. Therefore,

$$\eta = \frac{\chi_r}{L\pi d} \int_0^\infty dt$$
$$\times \int_0^L dx_0 \int_0^{\pi d} dy_0 \int_0^L dx \int_0^{\pi d} dy f(x, y, t; x_0, y_0).$$
(5)

Inserting $f(x, y, t; x_0, y_0)$ into this equation leads to the final expression of the quantum yield which, unlike the 1D case, now contains the contribution of the polymer property via γ

parameter. That is,

$$\eta = \sum_{m=1}^{\infty} \frac{2}{1 + \frac{D}{\chi_r}\frac{(2m-1)^2\pi^2}{L^2}} \frac{4}{(2m-1)^2\pi^2}$$
$$\times \sum_{n=1}^{\infty} \frac{2}{1 + \frac{D}{\chi_r}\beta_n^2} \frac{(\gamma - \gamma\cos(\beta_n\pi d) + \beta_n\sin(\beta_n\pi d))^2}{\beta_n^2((\beta_n^2 + \gamma^2)\pi^2 d^2 + 2\gamma\pi d)}.$$
(6)

This expression is properly normalized as in the limits: $\gamma \to \infty$ (complete exciton quenching) and $D \to 0$ (absence of diffusion) η becomes 1, according to the fact that the value of the infinite sum of reciprocal of squares of odd numbers is equal to $\pi^2/8$. However, in the treated case, diffusion constant has been estimated as 20 cm^2 s^{-1}, while χ_r amounts nearly 1 ns^{-1}. By fixing these values one can look at behavior of the quantum yield with respect to three different parameters: L, γ, and d. Upon a careful inspection, we have noticed that η does not vary on nanotube diameter, d, which commonly takes values between 0.5 and 1 nm [35]. We will henceforth fix the diameter value to 1 nm so as to vary two parameters L and γ only which reflect the influence of the ending defects and polymer sitting on the nanotube, respectively. The case of nanotube length contribution to the quantum yield has already been studied using a 1D exciton dynamics approach [20, 21]. Here we are able to examine the influence of the polymer property on photoluminescence spectra of SWCNTs based on our 2D exciton dynamics on the surface.

The (γ, L) dependence of quantum yield is featured in figure 3. Although, the sum in (6) quickly converges after few tens of (m, n) terms, we have calculated the sum up to 50×50 terms It has turned out that γ dependence of η becomes noticeable as soon as γ is varied at logarithmic scale, implying that the quantum yield is affected by γ at its large scales. The decrease in the quantum yield with increasing γ is evident. This represents a natural outcome given that the

destruction of the exciton is favored for large γ's values, whereas there is an increase in the exciton survival as $\gamma \to 0$, the so-called total exciton reflection case. For potential experimental data on quantum yield, we have presented wide intervals for both $\gamma \in (10^{-8}, 10^{-2})$ nm^{-1} and $L \in (50, 5000)$ nm to cover a broad range of η's values. It reaches its minimum of nearly $10^{-4}\%$ for the highest γ and shortest L. On the other hand, the maximum value of nearly 45% is reached in the opposite limit.

　　As far as the variation of the nanotube length is concerned, there is an increase in the quantum yield for long nanotubes, that is expected because the ratio of defected sp^3 over sp^2 states tends to vanish in this limit. In such a way, we are able to reproduce the results based on the 1D model [20, 21]. Moreover, we have observed a slight saturation with growing L. Relying on the 1D model this can be only explained by limited exciton diffusion length due to the radiative life time of excitons. However, the proposed 2D model clearly demonstrates that such a leveling off effect with respect to increasing length occurs at much lower values of about a few hundred nm's not only because of χ_r but also due to the large γ's values reflecting the strong polymer influence. As a well-known parameter characterizing SWCNTs, the d/L ratio does influence the quantum yield values. Yet, this dependence largely originates from L but only a little from d due to its minor variation as compared to the scale at which L is varied.

　　Note that L should be scaled appropriately in experimental configurations which include bulk samples when the nanotubes assume both length distribution and random orientation. Actually, the length must be averaged over a known distribution in the sample and hence replaced with $\langle L \rangle$ wherever it figures. On the other hand, the exciton decay rate may depend on the orientation of each individual nanotube in the sample. However, near-infrared pulse spectroscopy [36] suggests the lack of anisotropy in the exciton decay, whereas slight discrepancies between the isotropic and anisotropic results on bundles are attributed to inter-tube exciton migration which is far beyond the scope of the present study. Another cause to averaging the nanotube length can originate from a defect distribution across the nanotube surface. In this case finding the effective nanotube length boils down to determining the mean free path of the excitons which scatter by such defects on the surface. For a known average density of randomly distributed defects on a individual nanotube, n, the effective length distribution takes on an exponential shape $p(L) = ne^{-nL}$ to yield $1/n$ for $\langle L \rangle$ [21]. Nevertheless, such exponential distributions might be troublesome to employ as there is also a foremost length distribution of the nanotubes themselves in an ensemble.

3.2. The case $\phi \neq 0$

A more interesting case concerns polymer wrappings with finite angles (figure 4(a)). The wrapping angle ϕ is spanned between the nanotube axis and surface tangent of the polymer as is demonstrated in figure 4(b). The nanotube is unzipped along the polymer whereby the cylindrical surface gets
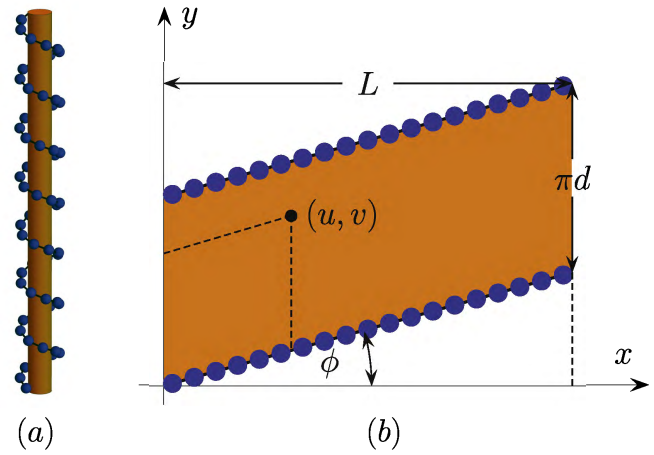
Figure 4. Line polymer wrapping a SWCNT (a) with an angle ϕ. The surface of the tube cut along the polymer line is unrolled into a parallelogram (b) confined between the nanotube ends of circumference πd along y and two sides of the polymer (blue dots), which make an angle ϕ with the nanotube axis x. The parallelogram is spanned in the skew coordinate system (u, v).

unwrapped in the plane whose borders confine the motion of the excitons. The unzipping line is skewed towards the nanotube axis (x-direction) with an angle ϕ.

　　Mathematically, the angle may vary between $0°$ and $90°$. However, angles close to $90°$ are not of physical interest given that they are related to extremely dense wrappings. Moreover, we have refrained from analyzing angles greater than $70°$ since the simulations show instability at those large angles.

　　We have transformed (x, y) Cartesian coordinates into the skew coordinates (u, v) which read as follows [37]:

$$u = x/\cos\phi, \quad v = y - x\tan\phi. \tag{7}$$

The main reason for doing so lies in the fact that the boundary conditions at the polymer sites become troublesome since there is a term for the exciton flux $\overrightarrow{n} \cdot \overrightarrow{\nabla} f$ mixing x and y coordinates, where $\overrightarrow{n}$ stands for the unit vector perpendicular to the polymer line. Working within the skew coordinate system successfully circumvents such an issue that leads to the following boundary conditions:

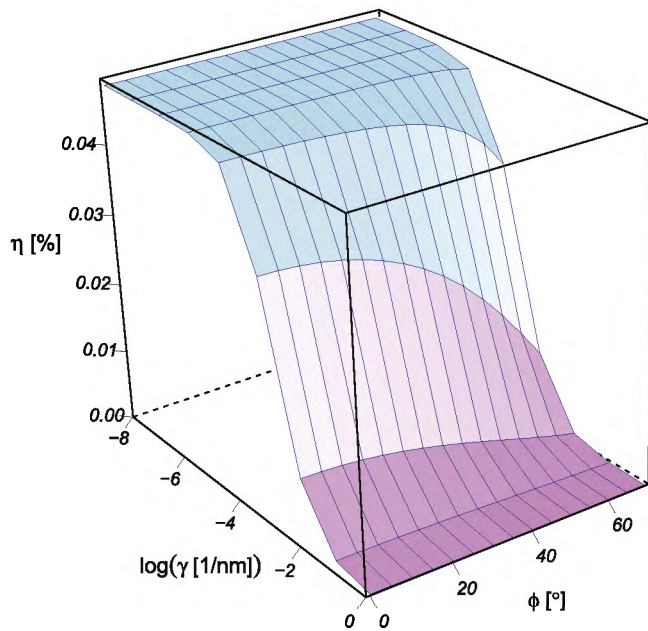$$\frac{\partial f}{\partial v} = \pm\gamma f, \text{ at } v = 0, \pi d \tag{8}$$

and

$$f = 0, \text{ at } u = 0, L/\cos\phi. \tag{9}$$

Nevertheless, simplifying the boundary conditions transforms the (x, y) diffusion equation into the second order elliptic partial differential equation which depends on the wrapping angle ϕ. This equation looks like

$$\frac{\partial f}{\partial t} = \frac{D}{\cos\phi^2}\left[\frac{\partial}{\partial u}\left(\frac{\partial f}{\partial u} - \sin\phi\frac{\partial f}{\partial v} \right) + \frac{\partial}{\partial v}\left(\frac{\partial f}{\partial v} - \sin\phi\frac{\partial f}{\partial u} \right) \right] \tag{10}$$

and it boils down to the 2D diffusion equation in the limit $\phi \to 0$.

Figure 5. Surface plot of the quantum yield depending on both γ and ϕ for a 100 nm long SWCNT. The γ variation is presented at logarithmic scale.


Figure 6. The evolution of the quantum yield with wrapping angle up to 70° at two different γ's values: 10^{-8} (blue) and 10^{0} nm^{-1} (red) for a 100 nm long nanotube. The former case shows no angular dependence, whereas the latter clearly demonstrates a drop in quantum yield values.

Differential equation in (10) has been treated numerically due to the complexity of finding the analytic solution. We have applied the finite difference method using R, explicitly Runge–Kutta method implemented in package deSolve [38], to compute the exciton concentrations at their uniform initial values for different L, γ, d and ϕ. The diameter has been kept to 1 nm because no particular dependence on d has been found out in this case as well. The working computational area has the same surface ($L\pi d$) as in the $\phi = 0$ case. Yet, in the present case the skew coordinate domain is $(u, v) \in [0, L/\cos\phi] \times [0, \pi d]$ with the Jacobian of transformation being $\cos\phi$. The quantum yield has been computed in the same manner as in the zero-angle case apart from the fact that we have guessed the uniform normalized exciton concentrations in order to speed up the convergence of the simulations.

Figure 5 shows the evolution of the quantum yield depending on (γ, ϕ) for a nanotube length of 100 nm. There is an evident drop in quantum yield values with increasing γ. The same feature has been seen in the $\phi = 0$ case meaning that polymers with large absorption coefficients tend to lessen the photoluminescence efficiency by consuming large concentrations of photo-generated excitons. On the other hand, no notable angular dependence has been evidenced over a wide range of γ's which result in measurable quantum yield values greater than ca 0.03%. A similar finding has been concluded for various nanotube lengths of 50, 500, 1000, 2000, and 5000 nm. There is a large saturation plateau of η's values as γ is decreased from ca 10^{-4} nm^{-1}, and in this region little variation of η with growing ϕ can be observed. Such extremely slight variations fall inside a few percents of the quantum yield values which are, however, estimated as the computational precision.
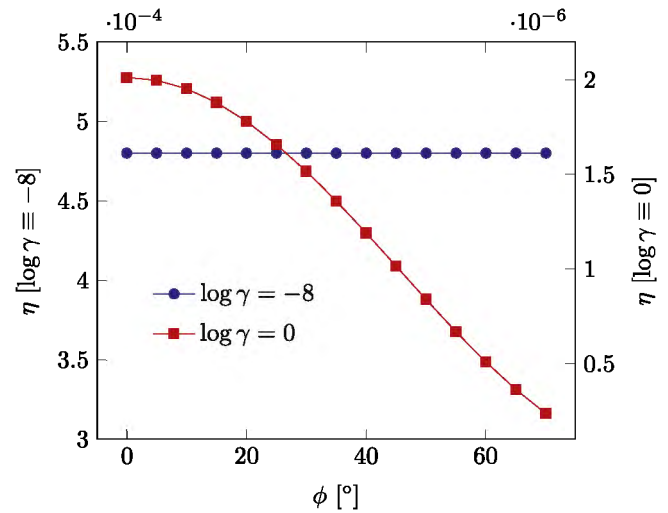
For large γ's values, which are greater than 10^{-4} nm^{-1}, implying a strong polymer exciton absorption contribution, a clear decrease in the quantum yield can be followed as the angle is increased up to 70°. In this case, there is an angular evolution of the quantum yield. Yet, its values enormously diminish down to 10^{-6}. This computational result would pose a serious challenge to experimentalists to distill the evolution of such a tiny number of the photoluminescence efficiency. Nonetheless, relying on the proposed 2D skew coordinate model we are able to follow the angular evolution numerically up to 70°. As is demonstrated in figure 6 (data in red), there is a noticeable drop in η as the wrapping angle is increased, that is an expected outcome since dense wrappings should decrease photoluminescence quantum efficiency. However, we attach no particular importance to such angular alterations as this case is concerned with practically immeasurable η's values. For low enough γ's (figure 6 (data in blue)), no marked change in η could be traced out with the increasing wrapping angle. This case is found rather applicable knowing that the related quantum yield takes on reasonable values which can be encountered in literature [39]. A plausible explanation comes from the fact that SWCNTs possess extremely high aspect ratio which screens the angular variations on the surface. Accordingly, it turns out that one can rely on the zero-angle approach in order to properly describe the influence of the wrapping polymer upon the photoluminescence quantum efficiency of SWCNTs.

Figure 7 features behavior of the quantum yield obtained numerically for $\phi = 0$ versus nanotube length which is scalled logarithmically with various γ values. Even within the numeric treatment, one can observe that the leveling off in the η values occurs at different lengths for different γ values. That is, lower γ values tend to push the saturated η values towards longer nanotube lengths. Such a saturation of η has already been seen in the 1D model [21], but due to different D/χ_r
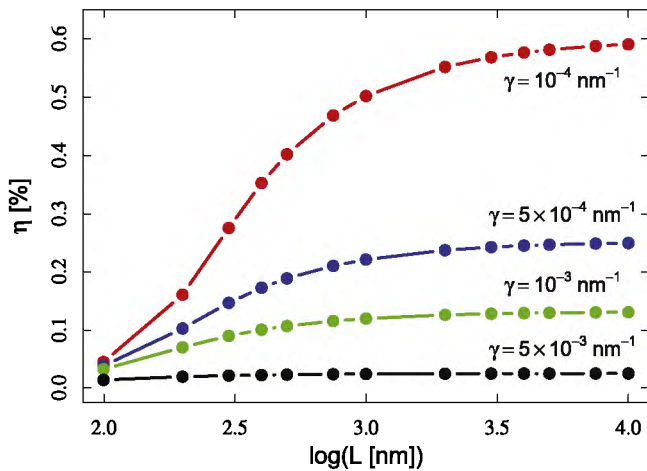
Figure 7. Numerically calculated quantum yield versus SWCNT length at logarithmic scale for various values of γ at $\phi = 0$. The saturation plateaus in η values are shifted towards right with decreasing γ.

values. Clearly, here we are able to tune the saturation plateau of η by switching from one polymer to another due to its influence on photoluminescence spectra through different γ values. Experimentally [39], the η leveling off has been evidenced to emerge at L values shorter than a micron, other than what the 1D model is able to predict [21].

3.3. Physical meaning of γ

In a particle diffusion model, the diffusion constant represents a measure of how large the variance of jumping particles is. Thus, it is possible to compute the average diffusion length at a given time. As with our case, we are interested in establishing a relationship between parameter γ (expressed in nm^{-1} as a unit of an inverse length) and a rather physical microscopic constant. Expressed in spatial units, this length (γ^{-1}) tells us how often the exciton becomes destroyed when encountering the barrier. The shorter the length is the higher the probability of exciton absorption is. Knowing that the excitons obey diffusion law, we can estimate rate τ^{-1} of the exciton loss at the polymer barrier. Namely, as

$$\gamma^{-1} = \sqrt{D\tau}, \tag{11}$$

the life time of the exciton, τ, limited by the interaction with the polymer becomes $1/\gamma^2 D$. Following the results presented in figure 3, one observes a considerable drop in the quantum yield beyond γ's values greater than 10^{-3} nm^{-1} for $D = 20$ cm^2 s^{-1}. This corresponds to τ's values that are shorter than a nanosecond, which is comparable to the radiative life time of excitons. To put it another way, the scattering events at the polymer sites start to dominate (by its high absorption rate) over the radiative processes important for photoluminescence, thus degrading the spectra. This explains why the quantum yield goes significantly low at τ's values shorter than χ_r^{-1}. The exciton life time at the polymer barrier can be computed directly if the dielectric function is known along the polymer. The dielectric screening by the polymer leads to lowering exciton binding energy that consequently makes τ's values shorter [40].

4. Concluding remarks

In conclusion, we have put forward a 2D classical diffusion model to describe the influence of polymer wrapping on the exciton dynamics in SWCNTs. Understanding exciton migration over the nanotube surface, whose nonradiative quenchings and scatterings are introduced in our model through appropriate boundary conditions at both nanotube ends and polymer sites, is central to computing quantum yield, η. The model is able to predict a strong γ dependence of η which incorporates the contribution of the chemistry of polymer into SWCNTs photoluminescence spectra. Yet, no significant dependence on the wrapping angle ϕ for experimentally accessible η's values has been found out, most likely due to the very high aspect ratio of SWCNTs. The ultimate outcome of the present theoretical analysis is that it is sufficient to rely on the proposed analytic model only ($\phi = 0$, no wrapping angle dependence) in order to properly fit the evolution of potentially available experimental quantum yield data with respect to a type of wrapping polymer, no matter what the wrapping angle is. The results should be verifiable by experimental means such as tip-enhanced fluorescence spectroscopy in conjunction with atomic force microscopy.

Acknowledgments

ORCID iDs

Dejan M Djokić ⓘ https://orcid.org/0000-0002-6265-2843

References

[1] Iijima S 1991 *Nature* **354** 56–8
[2] Avouris P, Marcus F and Perebeinos V 2008 *Nat. Photon.* **2** 341–50
[3] Barone P W, Baik S, Heller D A and Strano M S 2005 *Nat. Mater.* **4** 86–92
[4] Jain A, Homayoun A, Bannister C W and Yum K 2015 *Biotechnol. J.* **10** 447–59
[5] Miyauchi Y, Iwamura M, Mouri S, Kawazoe T, Ohtsu M and Matsuda K 2013 *Nat. Photon.* **7** 715–9
[6] Iverson N M *et al* 2013 *Nat. Nanotechnol.* **8** 873–80
[7] Miyauchi Y 2013 *J. Mater. Chem.* C **1** 6499–521
[8] Shaver J, Kono J, Portugall O, Krstić V, Rikken G L J A, Miyauchi Y, Maruyama S and Perebeinos V 2007 *Nano Lett.* **7** 1851–5
[9] Schöppler F, Mann C, Hain T C, Neubauer F M, Privitera G, Bonaccorso F, Chu D, Ferrari A C and Hertel T 2011 *J. Phys. Chem.* C **115** 14682–6
[10] Hain T C, Kröker K, Stich D G and Hertel T 2012 *Soft Matter* **8** 2820–3
[11] Wang F, Dukovic G, Brus L E and Heinz T F 2005 *Science* **308** 838–41
[12] Gabor N M, Zhong Z, Bosnick K, Park J and McEuen P L 2009 *Science* **325** 1367–71

[13] Miyauchi Y, Matsuda K, Yamamoto Y, Nakashima N and Kanemitsu Y 2010 *J. Phys. Chem.* C **114** 12905–8

[14] Iwamura M, Akizuki N, Miyauchi Y, Mouri S, Shaver J, Gao Z, Cognet L, Lounis B and Matsuda K 2014 *ACS Nano* **8** 11254–60

[15] Park J, Deria P, Olivier J H and Therien M J 2014 *Nano Lett.* **14** 504–11

[16] Strano M S 2006 *Nat. Mater.* **5** 433–4

[17] Zhang J *et al* 2011 *J. Am. Chem. Soc.* **133** 567–81

[18] Boghossian A A *et al* 2011 *J. Chem. Phys.* **135** 084124

[19] Pedersen T G 2003 *Phys. Rev.* B **67** 073401

[20] Rajan A, Strano M S, Heller D A, Hertel T and Schulten K 2008 *J. Phys. Chem.* B **112** 6211–3

[21] Harrah D M and Swan A K 2011 *ACS Nano* **5** 647–55

[22] Cognet L, Tsyboulski D A, Rocha J D R, Doyle C D, Tour J M and Weisman R B 2007 *Science* **316** 1465–8

[23] Pedersen T G 2004 *Carbon* **42** 1007–10

[24] Crochet J J, Duque J G, Werner J H, Lounis B, Cognet L and Doorn S K 2012 *Nano Lett.* **12** 5091–6

[25] Spataru C D, Ismail-Beigi S, Capaz R B and Louie S G 2005 *Phys. Rev. Lett.* **95** 247402

[26] Backes C 2012 *Noncovalent Functionalization of Carbon Nanotubes—Fundamental Aspects of Dispersion and Separation in Water* (Berlin: Springer)

[27] Fujigaya T and Nakashima N 2015 *Sci. Technol. Adv. Mater.* **16** 024802

[28] Walsh A G, Vamivakas A N, Cronin Y Y S B, Ülmü M S, Goldberg B B and Swan A K 2007 *Nano Lett.* **7** 1485–8

[29] Vita A D, Charlier J C, Blase X and Car R 1999 *Appl. Phys.* A **68** 283–6

[30] Kim P, Odom T W, Huang J L and Lieber C M 1999 *Phys. Rev. Lett.* **82** 1225–8

[31] Szabo A, Schulten K and Schulten Z 1980 *J. Chem. Phys.* **72** 4350–7

[32] Carslaw H S and Jaeger J C 1986 *Conduction of Heat in Solids* 2nd edn (Oxford: Oxford Science Publications)

[33] Hahn D W and Özisik M N 2012 *Heat Conduction* 3rd edn (New York: Wiley)

[34] Redner S 2001 *A Guide to First-Passage Processes* (Cambridge: Cambridge University Press)

[35] Weisman R B and Bachilo S M 2003 *Nano Lett.* **3** 1235–8

[36] Lüer L, Hoseinkhani S, Polli D, Crochet J, Hertel T and Lanzani G 2009 *Nat. Phys.* **5** 54

[37] Lebedev L P and Cloud M J 2003 *Tensor Analysis* (London: World Scientific)

[38] Soetaert K, Cash J and Mazzia F 2012 *Solving Ordinary Differential Equations in R* (Berlin: Springer)

[39] Hertel T, Himmelein S, Ackermann T, Stich D and Crochet J 2010 *ACS Nano* **4** 7161–8

[40] Singh J 2006 *Optical Properties of Condensed Matter and Applications* (New York: Wiley)

Infrared reflectivity spectra of η-Na$_{1.3}$V$_2$O$_5$ in the charge disordered and ordered phase

Z.V. Popović[1,a], D.M. Đokić[1], Z. Dohčević–Mitrović[1], M. Isobe[2], and Y. Ueda[2]

[1] Center for Solid State Physics and New Materials, Institute of Physics, Pregrevica 118, 11080 Belgrade, Serbia
[2] Materials Design and Characterization Laboratory, Institute for Solid State Physics, The University of Tokyo, 5-1-5 Kashiwanoha, Kashiwa, Chiba 277-8581, Japan

Abstract. We have measured the far-infrared reflectivity spectra of the sodium vanadium oxide η-Na$_{1.3}$V$_2$O$_5$ polycrystals in the wide temperature (80–300 K) and frequency (150–1500 cm^{-1}) range. Appearance of new phonon oscillators, phonon oscillator mode splitting and step-like shift of TO and LO frequencies at low temperatures are correlated with the charge-ordering phase transition, which takes place at about 120 K in this vanadium oxide.

PACS. 78.30.Hv Other nonmetallic inorganics – 63.20.D- Phonon states and bands, normal modes, and phonon dispersion – 71.30.+h Metal-insulator transitions and other electronic transitions – 71.27.+a Strongly correlated electron systems; heavy fermions

1 Introduction

In the sodium-vanadium oxide system Na$_x$V$_2$O$_5$, there exist seven phases denoted by α-, β-, δ-, τ-, α'-, η-, and κ-phases in the ascending order of x. They are mixed-valence compounds of V^{4+} (d^1, S = 1/2) and V^{5+} (d^0, S = 0) ions, among which α'-Na$_x$V$_2$O$_5$ ($x = 1.0$) has been studied most intensively for its anomalous phase transition like a spin – Peierls transition [1,2]. Recently, it has been reported [3] that the η-phase Na$_x$V$_2$O$_5$ ($x \sim 1.3$) exhibits low-dimensional behavior of the magnetic susceptibility. Two models have been proposed to explain the spin gap in this oxide. First one is based on fused chain model [4] of ten-node rings with the spin gap, taking into account the V$_{10}$O$_{30}$ chains as a basic unit in η-phase. Second model is based on low-temperature structural measurements [5], which have revealed the existence of a structural second-order phase transition in this oxide, associated with a concomitant charge ordering. A doubling of the b lattice parameter observed below 100 K signifies that each magnetic unit contains, at low temperature, 2×9 S = 1/2 spins. Hence the origin of the spin gap can be related to the formation of this superstructure below 100 K in the system.

Many of the physical properties of η-Na$_{1.3}$V$_2$O$_5$, including lattice dynamics, are unknown. The X-band electron-spin resonance [6] and complementary magnetic susceptibility data [5] give additional evidence for the transition around 100 K and confirm the existence of the spin gap, which is estimated to be of the order of

35 K. NMR study of spin gap in the vanadium bronze η-Na$_{1.286}$V$_2$O$_5$ [7] revealed that spin gap energy is vanadium site dependent. They estimated the gap value of 152 K, 54 K and 174 K for vanadium V(4)A, V(4)B and V(7)A sites, respectively.

In the Raman scattering measurements [8] on single crystal vanadium bronze samples the 27 first-order Raman active modes were observed, as well as their overtones and combinational lines. The appearance of new phonon or spin-related modes is not registered in the low temperature phase. This is explained as a consequence of their small intensity, sample heating by laser irradiation or due to small normal vibrational coordinate change by crystal structure transformation. The temperature dependence of Raman active phonon mode frequency and damping shows step-like shift at low temperatures in the charge ordered phase.

In this paper we measured the infrared reflectivity spectra of polycrystalline η-Na$_{1.3}$V$_2$O$_5$ in the charge disordered and ordered phase. We found new phonon oscillators, oscillator splitting and step-like frequency shift of infrared active modes by lowering the temperature below the charge ordering temperature (T$_{CO}$), i.e. the phase transition has a rather strong influence on the phonon dynamics of η-Na$_{1.3}$V$_2$O$_5$.

2 Experiment

The present work was performed on powder samples. The details of the sample preparation were published elsewhere [3]. The infrared measurements were carried out

a e-mail: zoran.popovic@phy.bg.ac.yu

with a BOMEM DA-8 FTIR spectrometer. A DTGS pyroelectric detector was used to cover the wave number region from 100 to 700 cm^{-1}; a liquid nitrogen cooled HgCdTe detector was used from 500 to 5000 cm^{-1}. Spectra were collected with 2 cm^{-1} resolution, with 1000 interferometer scans added for each spectrum. For low-temperature measurements a Janis STDA 100 cryostat was used.

3 Results and discussion

The η-phase, which can also be denoted by the stoichiometric formula Na$_9$V$_{14}$O$_{35}$, crystallizes at room temperature in the monoclinic system (space group $P2/c$) with an original structure built up of layers consisting of VO$_5$ square pyramids sharing edges and corners, with their apical oxygens pointing up and down alternately to form double zigzag chains in the [100] direction, Figure 1. These double chains are bridged by VO$_4$ tetrahedra to form the V$_2$O$_5$ layers. A peculiarity of the Na$_9$V$_{14}$O$_{35}$ crystal structure is shearing of VO$_5$ chains at every five V(5)O$_5$–V(5)O$_5$ units, as it is illustrated in Figure 1. The Na atoms are located between the layers. The V$_2$O$_5$ layers contain V^{4+}, V$^{4.5+}$, and V^{5+} ions. Each V(i)O$_4$ ($i = 4, 7$) tetrahedron has a V^{5+} ion (d^0), each V(i)O$_5$ ($i = 1, 2, 3, 6$) square pyramid has a V^{4+} (d^1) ion, and each V(5)O$_5$ square pyramid has a V$^{4.5+}$ ion. The low-temperature structure remains centrosymmetric with space group $P2/c$ but with a doubled b lattice parameter, as we have already mentioned. Two vanadium sites which host V$^{4.5+}$ ions at room temperature become stabilized as one V^{4+} and one V^{5+} at low temperature.

The P-centered monoclinic unit cell [3] of Na$_9$V$_{14}$O$_{35}$ consists of two formula units ($Z = 2$) comprising 116 atoms in all. Since there is a large number of atoms in the unit cell and low symmetry of $P2/c$ (C$_{2h}^4$) space group we can expect a large number of optically active modes. The factor-group-analysis [8] yields the total number of optical active phonons in Na$_9$V$_{14}$O$_{35}$:

$$\Gamma_{Na_9V_{14}O_{35}}^{opt.} = 86A_g(xx, yy, zz, xz) + 88B_g(xy, yz)$$
$$+ 85A_u(\mathbf{E}||\mathbf{y}) + 86B_u(\mathbf{E} \perp \mathbf{y}).$$

According to this representation one can expect totally 171 infrared active modes to be observed in the infrared experiment.

Figure 2 shows the unpolarized reflectivity spectra of η-Na$_{1.3}$V$_2$O$_5$ polycrystalline samples measured at room and liquid nitrogen temperatures in the spectral range from 150 to 1150 cm^{-1}. These spectra contain both the A_u and B_u symmetry modes. We have observed 30 oscillators at room temperature and additional 6 more oscillators at 80 K (in the charge ordered state). The frequencies of TO and LO modes are given in Table 1. These frequencies were obtained by Kramers-Kronig Analysis (KKA) and first derivative (FD) of the reflectivity spectra. Because of many very weak oscillators in relatively narrow spectral range or weak intensity oscillators close to high intensity one the KKA turned to be insensitive to detect TO and LO frequencies of all observed oscillators. Therefore, we
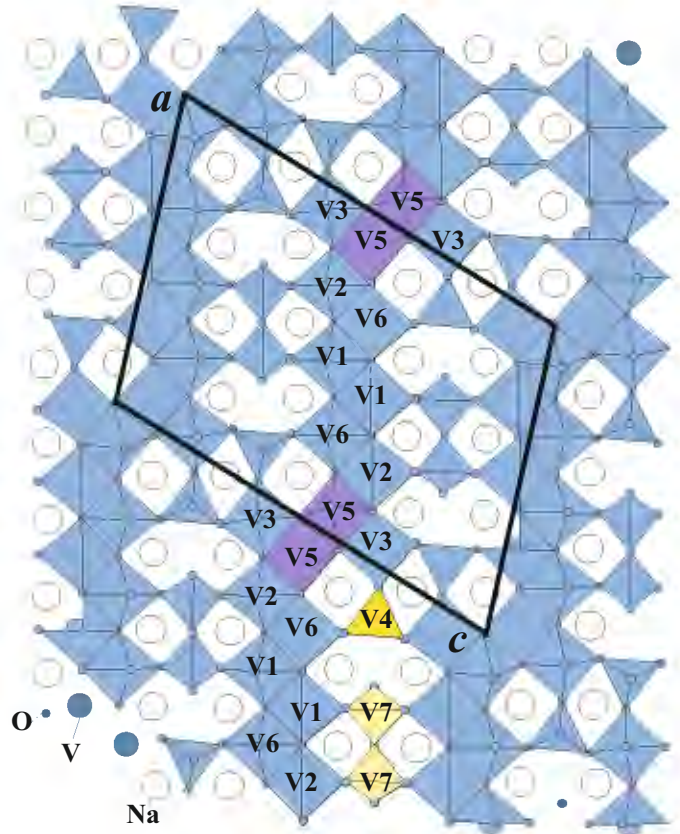

Fig. 1. Crystal structure of η-Na$_{1.3}$V$_2$O$_5$ projected on the (ac) plane. The VO$_5$-chains running parallel to the a-axis.
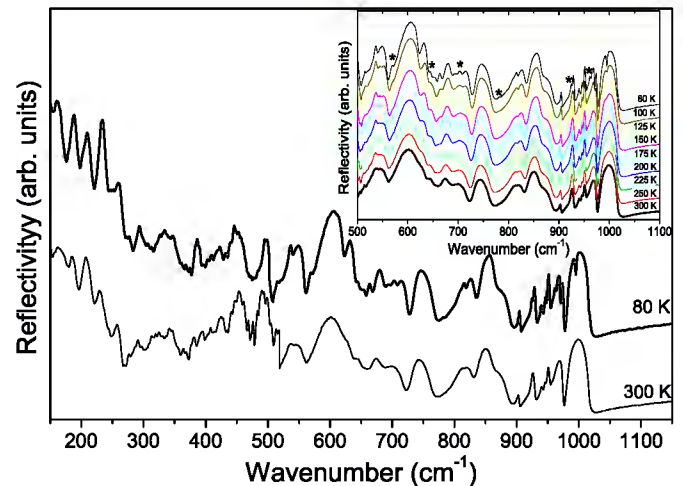

Fig. 2. Unpolarized far-infrared reflectivity spectra of η-Na$_{1.3}$V$_2$O$_5$ measured at room and liquid nitrogen temperature. Inset: Infrared reflectivity spectra at different temperatures.

calculated FD of the reflectance data as a complementary method. The advantage of using the derivative technique is well documented in references [9,10]. In Figure 3, for the highest frequency oscillators, we have compared the derivative spectrum with the optical conductivity and loss function data obtained from KKA. It is obvious that maxima (minima) of the DT spectrum correspond to maxima

Table 1. Phonon mode frequencies (in cm^{-1}) of η-Na$_{1.3}$V$_2$O$_5$.

Raman [8]		Infrared		Tentative assignment
A_g	B_g	TO	LO	
162		159.4	174.0	
213		180.0	191.1	
232		199.7	216.8	
250		227.1	238.3	
309		252.8	263.1	
321		274.3	277.7	O–V–O bending
333		288.8	293.1	
355		340.0	348.0	
377		374.6	383.1	
400		419.1	429.4	
439		438.0	462.8	
466				
484		486.0	501.4	
514		511.7	518.6	
527		531.3	554.4	
565		585.3	615.2	
648		625.8	634.7	V–O$_5$ stretching in the basal plane
		640.3	648.0	
		668.2	680.0	
		694.3	716.4	
		730.9	759.8	
		803.2	813.8	
811	817	817.7	826.4	
823				
849		867.8	884.2	
900		900.6	904.5	V–O$_4$ stretching
931		923.8	928.6	
		938.2	941.1	
943		944.0	946.9	
948		949.0	952.7	
964		961.4	973.9	V–O$_5$ stretching
990		979.7	1016.3	

of the optical conductivity – TO modes (loss function – LO modes). Since reflectivity measurements carried out on powder samples give good results for TO and LO mode frequencies in the case of isolated oscillators only, the obtained frequencies from Table 1 should be taken as tentative ones, only. Namely, two or more oscillators from different symmetries can appear as multi-peak-structure in the reflectivity spectra of powder samples [11]. Because of that, the assignment of the infrared-active modes is practically impossible without polarized measurements on single crystals.

If we compare this reflectivity spectra with the infrared reflectivity spectra of other vanadates [11,12], we can conclude that the two highest frequency modes, as well as the modes between 500 and 700 cm^{-1}, represent the vibration of VO$_5$ pyramid. The modes between 750 and 950 cm^{-1} are bond stretching vibrations of VO$_4$ tetrahedra. In the
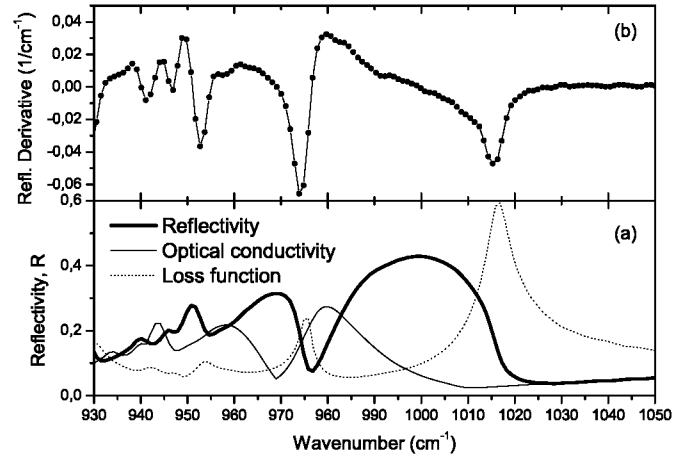
Fig. 3. (a) Unpolarized infrared reflectivity spectra of η-Na$_{1.3}$V$_2$O$_5$ in the 930–1050 cm^{-1} spectral range together with optical conductivity and loss function ($-$Im$[1/\epsilon(\omega)]$), obtained using KKA of the reflectivity data. (b) First derivative of the reflectivity spectrum of η-Na$_{1.3}$V$_2$O$_5$.

spectral range below 500 cm^{-1} there are many modes that originate from V–O bond bending vibration. As in the case of Raman spectra [8] the more precise assignment of infrared active modes is not possible without single crystal measurements.

By lowering the temperature the observed modes harden and strong phonon oscillators start decomposing into several modes. At temperatures below 125 K new modes appear (denoted by asterisk in the inset of Fig. 2), as a consequence of phase transition. This finding is in accordance with the X-ray measurements of η-Na$_{1.3}$V$_2$O$_5$ in the charge ordered state [5]. Namely, due to the doubling of the b-axis below phase transition temperature it is natural to expect an appearance of new phonon oscillators.
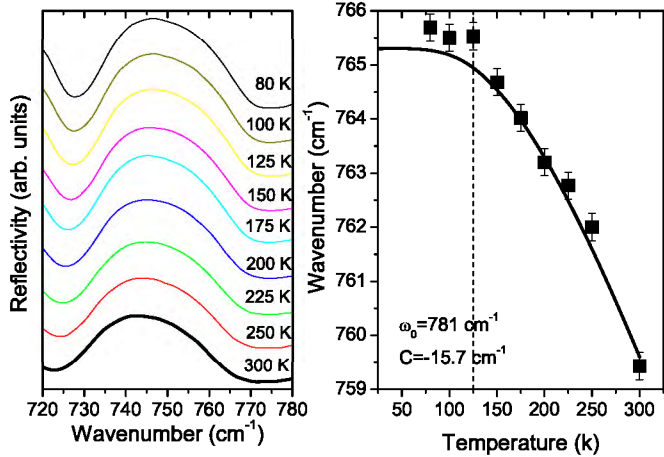
Figure 4 (left panel) presents the infrared reflectivity spectra of Na$_9$V$_{14}$O$_{35}$ in the spectral range between 955 and 1030 cm^{-1} at different temperatures. The decomposition of the 970 and 1000 cm^{-1} oscillators into several other ones starts at temperatures lower than 200 K, see Figure 4, right panel. Because these new oscillators appear at temperatures much higher than the critical temperature T_{CO} we concluded that they were masked by stronger oscillators at room temperature and became observable due to reduction of broadening of stronger oscillators with temperature decrease. At temperatures close to the phase transition temperature the only one additional mode appears in this spectral range, which is denoted by asterisk in Figure 4.

In order to examine the influence of the phase transition to the phonon properties of Na$_9$V$_{14}$O$_{35}$ we analyzed LO mode frequency vs temperature change of an isolated oscillator, Figure 5. With temperature lowering LO mode frequency increases monotonously from room temperature to the phase transition temperature, when a change of frequency is observed. The drastic frequency variation is a consequence of the charge ordering, i.e. the change of crystal and magnetic structure at the phase
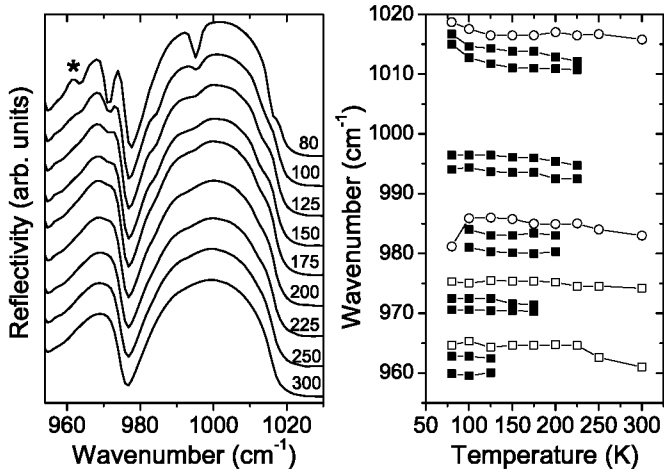
Fig. 4. Left panel: unpolarized infrared reflectivity spectra of η-Na$_{1.3}$V$_2$O$_5$ in the 955–1030 cm^{-1} spectral range. Right panel: temperature dependence of TO and LO mode frequency of several oscillators in the 955–1030 cm^{-1} spectral range.

Fig. 5. Left panel: unpolarized infrared reflectivity spectra of η-Na$_{1.3}$V$_2$O$_5$ in the 720–780 cm^{-1} spectral range. Right panel: temperature dependence of LO mode frequency of the phonon oscillator from the left panel. Solid line represents the anharmonic phonon-phonon interaction spectrum, equation (1).

transition due to the spin gap opening. In order to distinguish the phonon-phonon contribution due to the anharmonic effects from charge ordering-related contribution we have fitted the high temperature part of the frequency versus temperature dependence using a model for the anharmonic phonon-phonon interaction [13]:

$$\omega_{ph}(T) = \omega_0 + C[1 + 2/(e^{\omega_0/2kT} - 1)], \qquad (1)$$

where ω_0 and C take the values 781 cm^{-1} and –15.7 cm^{-1},

for the LO mode under consideration. The calculated spectra are represented by solid line in Figure 5 (right panel). It is obvious that the dominant contribution in the frequency versus temperature dependence of this LO mode below the phase transition arises from charge ordering and not only from phonon-phonon interaction due to the anharmonic effects.

In conclusion, we have measured unpolarized far-infrared reflectivity spectra of η-Na$_{1.3}$V$_2$O$_5$ polycrystals in the wide temperature and frequency range. The appearance of new infrared active phonon modes, mode splitting and the phonon frequency variation, below 120 K, are interpreted as a consequence of the change of crystal structure at the phase transition due to the charge ordering.

References

1. M. Isobe, Y. Ueda, J. Phys. Soc. Jpn. **65**, 1178 (1996)
2. M. Isobe, Y. Ueda, K. Takizawa, T. Goto, J. Phys. Soc. Jpn. **67**, 755 (1998)
3. M. Isobe, Y. Ueda, Y. Oka, T. Yao., J. Solid State Chem. **145**, 361 (1999)
4. M.-H. Whangbo, H.-J. Koo, Solid State Commun. **115**, 115 (2000)
5. F. Duc, P. Millet, S. Ravy, A. Thiollet, F. Chabre, A.M. Ghorayeb, F. Mila, A. Stepanov, Phys. Rev. B **69**, 094102 (2004)
6. F. Chabre, A.M. Ghorayeb, P. Millet, V.A. Pashchenko, A. Stepanov, Phys. Rev. B **72**, 012415 (2005)
7. T. Hayashi, T. Nakamura, T. Kozuka, M. Itoh, M. Isobe, J.I. Yamura, Y. Ueda, J. Mag. Mag. Materials **310**, 1224 (2007)
8. Z.V. Popović, V.V. Moshchalkov, M. Isobe, Y. Ueda, Solid State Commun. **142**, 385 (2007)
9. D.J. Lockwood, G. Yu, N.L. Rowell, Solid State Commun. **136**, 404 (2005)
10. G. Yu, N.L. Rowell, D.J. Lockwood, Z.R. Wasilewski, Appl. Phys. Lett. **83**, 3683 (2003)
11. Z.V. Popović, M.J. Konstantinović, R. Gajić, V.N. Popov, M. Isobe, Y. Ueda, V.V. Moshchalkov, Phys. Rev. B **65**, 184303 (2002)
12. Z.V. Popović, V. Stergiou, Y.S. Raptis, M.J. Konstantinović, M. Isobe, Y. Ueda, V.V. Moshchalkov, J. Phys.: Cond. Matter **14**, L583 (2002)
13. M. Balkanski, R.F. Wallis, E. Haro, Phys. Rev. B **28**, 1928 (1983)

Size dependence of the magnetic response of graphite oxide and graphene flakes – an electron spin resonance study

Luka Ćirić[*,1], **Andrzej Sienkiewicz**[1], **Dejan M. Djokić**[1], **Rita Smajda**[1], **Arnaud Magrez**[1], **Tommy Kaspar**[2], **Reinhard Nesper**[2], and **László Forró**[1]

[1] Laboratorys of Physics of Complex Matter, EPFL, Lausanne, Switzerland
[2] Laboratorium for Inorganic Chemistry, ETH Zurich, Switzerland

[*] Corresponding author: e-mail luka.ciric@epfl.ch, Phone: +41216937936, Fax: +41216934470

We employed electron spin resonance (ESR) technique in the investigation of a series of graphene flakes with different size distributions. Graphene oxide (GO) samples with three distinct size distributions were prepared by the Brodie method. Large flakes of $\sim$2500 μm^2, intermediate size flakes of $\sim$1 μm^2, and small ones of $\sim$500 nm^2 have been characterized by ESR in the 4–295 K temperature range. Already for GO flakes the magnetic response strongly varies with their size. Large GO flakes are inhomogeneous, revealed by the presence of both Pauli and Curie components in the overall signal. In small GO flakes ESR spin susceptibility reveals superparamagnetic behavior

ascribed to interaction between localized spins. The intermediate flakes show a standard Curie behavior showing a uniform oxidation and the concomitant non-interacting localized spins. On this batch a thermal method of reduction was applied such that in polar solvent the suspension of GO was heat treated at temperatures below 200 °C. ESR susceptibility shows that this reduction can recover some of the Pauli-like contribution of the pristine graphene. However, our study shows that the full optimization of oxidation/reduction parameters is yet to be achieved.

1 Introduction Graphene has stimulated vast theoretical and experimental research activities in recent years. Having a gapless and a linear band dispersion in the vicinity of the Fermi level, graphene shows many outstanding properties such as exceptionally high carrier mobility, unconventional quantum Hall effect, resilience to very high electrical current densities [1], *etc*. These properties open a wide range of potential applications. Nevertheless, for some of them, like new generation of integrated circuits and quantum computational devices, the full implementation and realization is still missing. One of the reasons is the absence of a production route which might give high quality graphene flakes with a good control of size and the type of the edge termination (zigzag or armchair).

Concerning large scale production of graphene one of the most promising methods is the so called graphene oxide (GO) route. There are several variants of making of GO [2, 3] with a common expectation to recover the pristine properties of graphene simply by reducing formerly oxidized graphite

[4]. However, the optimization of the oxidation/reduction parameters is still in progress. Our previous electron spin resonance (ESR) study (Ciric et al., submitted) of reduced graphene oxide (RGO) has reported a relatively large amount of defects which may hinder the advantageous properties of graphene.

Recently, the GO route has been applied and the GO flakes were then thermally reduced in a polar solvent without using hydrazine or hydrogen plasma [4]. With these chemicals it is difficult to control the degree of reduction. The size distribution of GO and RGO samples was different, ranging from $\sim$2500 μm^2 to below 500 nm^2. This also means that the flakes had a different "edge contribution". The variation in the sample size is especially important considering theoretical predictions which claim that alignment of the localized spins along the zigzag edges of graphene [5] might result in a long range ferromagnetic order usable in spintronics applications. Both the precursor (GO) and the final material (RGO) were studied and characterized

Original

Paper

Phys. Status Solidi B **247**, Nos. 11–12 (2010)

2959

by ESR in a broad temperature range (4–295 K). ESR is able to separate the contributions of localized and conduction electrons from the overall magnetic response and to detect magnetic correlations. For the structural characterization and the size distribution of the flakes atomic force microscopy (AFM), scanning electron microscopy (SEM), and high resolution transmission electron microscopy (HRTEM) were used.

In this paper we show that the magnetic response of graphene flakes, even in the oxidized form, strongly depends on their size. Nevertheless, for all cases examined we have not found signs of the predicted long range ferromagnetic order. That may be due to the formation of inner edges by holes generation through the oxidation process. The susceptibility measurements show that the reduction method is promising, the optimization of which might result in a higher quality graphene.

2 Experimental In the first step graphite oxide was prepared according to the method of Brodie [2] using technical graphite that was treated with fuming nitric acid and sodium chlorate: 10 g graphite powder (Alfa Aeser GmbH & Co KG; natural, universal grade, −200 mesh, 99.9995%, metal basis) were mixed with 85 g sodium chlorate (Fisher Scientific AG, powder, analytical grade) and cooled down to *ca.* −20 °C. Under constant stirring 60 mL of fuming nitric acid (VWR, Nitric acid fuming, 100% GR for analysis ACS) are being added over a period of 6 h. Stirring is continued for another 12 h at room temperature and for 10 h at 60 °C. The brown product was isolated and analyzed. Depending on the starting material, large flakes of $\sim$2500 μm^2, intermediate size flakes of $\sim$1 μm^2, and small ones of $\sim$500 nm^2 have been obtained (Figs. 1a and b). These surfaces represent the most frequent size in a given batch based on SEM images. A detailed histogram giving the size-distribution in each batch is in progress.

The GO can then be dispersed in selected polar solvents *i.e.*, water [6] at less than 1% carbon per liter. Dependent on the solvent boiling point heat treatment between 100 and 200 °C in an open or a pressurized system yields a blackish
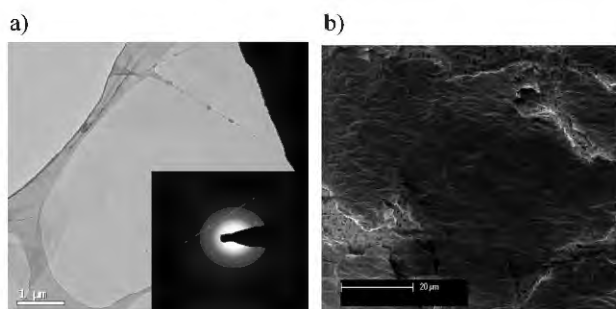
dispersion of reduced GO. The dispersion contains single graphene layers. This can be seen by settling small amounts of the dispersion on a TEM grid and by subsequent electron diffraction. Most of the graphene sheets exhibit only *h* and *k* Bragg reflections, without the *l* ones which would be characteristic for stacking of several layers (Fig. 1a).

The sample preparation for ESR measurements was done by drawing aqueous solutions of GO/RGO material through an ESR silent PVDF filter paper. The thin deposits with the filter paper were cut, piled up, and placed in a 2.9 mm ID and 4 mm OD quartz tube which was evacuated and filled with 300 mbar of He prior to sealing. Temperature dependent ESR measurements were performed using a standard X-band ESR spectrometer.

3 Results on graphene oxide (GO) Before we analyze the ESR results of RGO, it is important to understand the characteristics of its precursor – GO. We have characterized the three batches of large, intermediate, and small GO flakes. The typical morphology of large GO flakes is shown on the representative scanning electron microscope (SEM) image (Fig. 1b).

The ESR measurement of the large GO flakes was performed in the 4–295 K temperature range. A representative ESR spectrum is shown in Fig. 2. One can identify two distinct magnetic contributions in the overall response: a narrow and a broad line. The broad line has a Gaussian lineshape, whereas the narrow can be fitted with a Lorentzian line, shown in Fig. 2. The spin susceptibility, proportional to the double integrated ESR line, reveals Curie temperature dependence for the broad component (red dots in Fig. 3). It is attributed to defects and localized states in the sample. The narrow line has a Pauli susceptibility seen as a temperature independent contribution to χ (blue dots, inset Fig. 3). Although ESR can resolve different magnetic species, it is lacking of spatial resolution. It cannot be known whether the
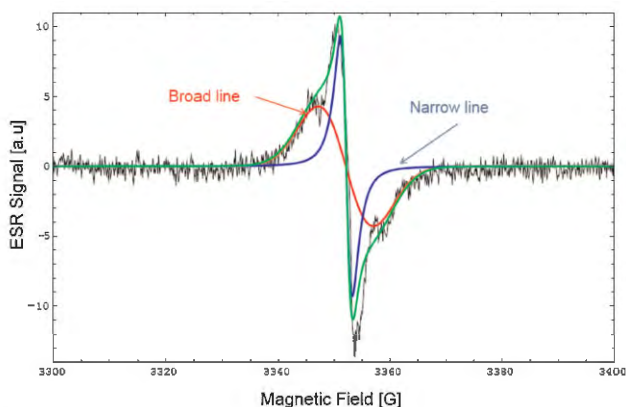

Figure 1 (a) TEM image of GO flakes deposited on TEM grid. Inset reveals electron diffraction pattern characteristic for a single layer of graphene. (b) SEM image of GO with large flakes (see text) deposited on the filter paper.

Figure 2 (online color at: www.pss-b.com) Two components ESR spectrum recorded at 6 K, fitted by Gaussian and Lorentzian functions. The narrow Lorentzian line ($\Delta H = 3.4$ G) is associated with conduction electrons, while the broad one ($\Delta H = 11$ G) corresponds to defects.
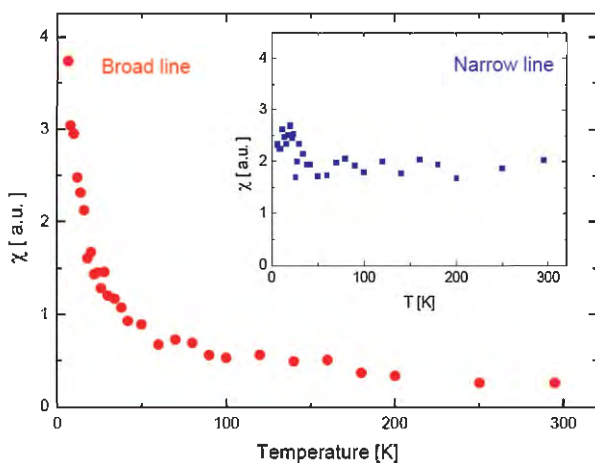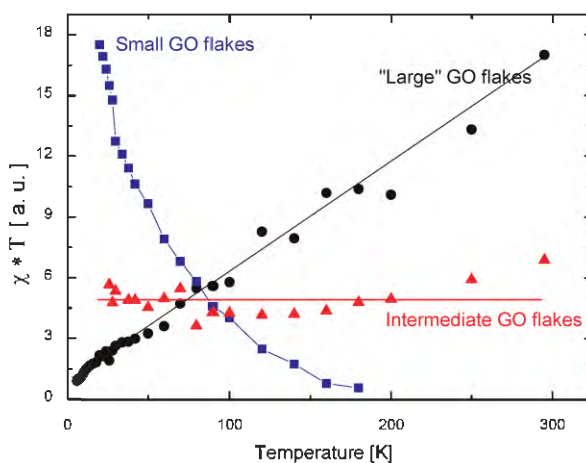
Figure 3 (online color at: www.pss-b.com) Spin susceptibility *versus* temperature for large GO flakes. The broad component (red) reveals Curie-like behavior associated with defects and localized states while the narrow component (inset, blue) is assigned to conduction electrons and has characteristic Pauli behavior.

Figure 4 (online color at: www.pss-b.com) T^*spin susceptibility plot for large flakes (average surface $\sim 2500\,\mu m^2$), intermediate flakes ($\sim 1\,\mu m^2$), and small-size ($\sim 500\,nm^2$) GO flakes. For a better comparison the, curves were normalized together at 80 K. The signal varies with flake size from metallic through simply Curie to superparamagnetic response, respectively. The solid lines are eye-guides.

two signals are coming from the same flake or from different flakes.

The latter possibility would suggest incomplete exfoliation, and the broad component would be ascribed to thicker, graphitic flakes. However, the spin susceptibility of this signal displays Curie-like behavior contrary to that of graphite. Because of this discrepancy, we have a slight preference for attributing both ESR lines to the same flake which would suggest the presence of conductive islands in the otherwise insulating GO flakes. This would suppose that the oxidation process of the starting material is fundamentally inhomogeneous [7]. Nevertheless, the presence of non-oxidized parts does not prevent exfoliation of GO flakes from the graphite oxide. For the GO flakes that are sufficiently large the contribution of these unoxidized graphene-like islands can become significant enough and therefore can give a distinct ESR signal.

To understand further the origin of the metallic contribution to the spin susceptibility in large GO flakes we have performed measurements on intermediate and small-sized GO flakes. In these latter cases only a single Lorentzian line was observed. Its double integration gives the overall susceptibility of the samples. Their spin susceptibility, together with that of the large flakes is shown in Fig. 4. In the case of intermediate-size GO flakes the observed ESR spin susceptibility displays a standard Curie behavior coming from non-interacting localized moments solely. In the case of small flakes the spin susceptibility follows an anomalous Curie law with temperature dependent Curie constant, *i.e.*, susceptibility drops faster than $1/T$, [8]. One could imagine that this behavior is due to small clusters in which spin defects interact ferromagnetically but long range ferromagnetism cannot be established because the thermal energy is sufficient to average out the net magnetization to zero. By lowering the temperature the
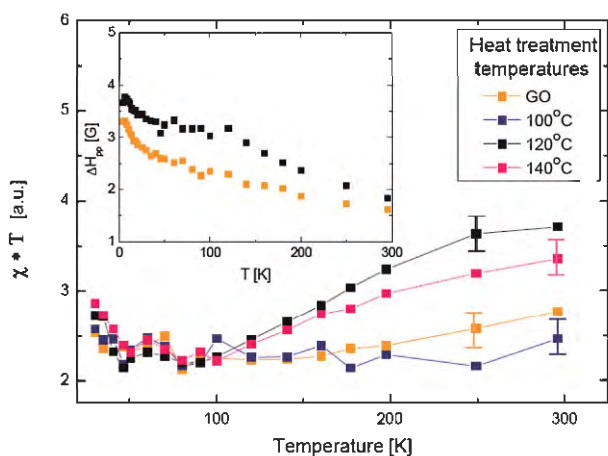
effective magnetic moment hence the Curie constant increase. The resulting temperature dependence, stronger than that of a paramagnet, is often called as superparamagnetic. However, the low value of the measured magnetic moment in our sample may ask for another scenario. We have to mention, that similar behavior was observed in electron irradiated carbon nanotubes [9]. In that case it was attributed to interaction of quasi-delocalized electrons with ferromagnetic catalytic particles. This explanation does not apply in the case of graphene. The departure from the typical Curie law might come either from increasing interaction between localized moments on decreasing temperature or from thermal excitation of weakly localized spins into the conduction band. In this latter case, the intensity of the Pauli contribution to the susceptibility would be too low to be observable.

4 Results on reduced graphene oxide (RGO) flakes In order to restore the pristine graphene from GO flakes, the intermediate-sized flakes were chosen as showing a "standard" behavior. They were exposed to subsequent thermal treatment in polar solvents. Depending on the solvent boiling point the reduction was done at the following temperatures: 100, 120, and 140 °C. The effect of all reduction treatments are characterized by ESR.

The ESR spectrum is a single Lorentzian line with a room temperature *g*-factor of ~ 2.003 and linewidth $\Delta H_{pp} \approx 3$ G. The presence of a single ESR line is interpreted as a strong coupling between localized paramagnetic spins and conduction electrons in RGO. In this case the linewidth is expressed in the following form [10]:

$$\Delta H = (\Delta H_1 \chi_1 + \Delta H_2 \chi_2)/(\chi_1 + \chi_2), \tag{1}$$

Phys. Status Solidi B **247**, Nos. 11–12 (2010)

2961

Original

Paper

Figure 5 (online color at: www.pss-b.com) Temperature dependence of the T^* spin susceptibility of GO (orange squares), and RGO for different reduction temperatures 100 °C (blue squares), 120 °C (black squares), 140 °C (pink squares). The $\chi^* T$ plot illustrates how the Pauli component develops in the function of temperature of the reduction. The inset shows the evolution of the ESR linewidth with temperature. Its increase for the RGO sample suggests the contribution of conduction electrons to the spin relaxation, see Eq. (1).

where ΔH_1 and ΔH_2 are the linewidths of localized spins and conduction electrons, respectively. Their contribution to the observed linewidth is weighted by their respective spin susceptibilities (χ_1 and χ_2). ΔH_1 has the characteristic temperature dependence of a dipolar linewidth. Upon reducing GO, with the creation of conduction electrons, the contribution of ΔH_2 to the linewidth is visible (Fig. 5 and its inset).

In the overall susceptibility the increasing weight of χ_2 with reduction is noticed in the $\chi^* T$ product. By plotting the $\chi^* T$ as a function of temperature one can clearly distinguish the Curie-term ($\sim T$ independent value) and the Pauli contribution (T dependent term) to the overall susceptibility (Fig. 5). In this plot one can follow the evolution of the spin susceptibility upon changing the conditions of the reduction. At low temperature heat treatment (100 °C) in polar solvent the dominant contribution comes from localized states like in the untreated GO sample. For heat treatments at higher temperatures, although χ always decreases with T, one can

follow a clear development of a Pauli component to the spin susceptibility in the $\chi^* T$ plots.

By comparing the slopes of the $\chi^* T$ plots for various reduction temperatures one can conclude that the reduction is starting to be efficient above 120 °C (the difference between black and pink symbols in Fig. 5 is not significant). Although the dominant response is still coming from the localized spins related to defects, this is highly encouraging result concerning future applications because it shows that the restoration of the conductivity of graphene is feasibly with a mild reduction step.

However, there is plenty of room for improvement. One has to optimize the flake size, to insure good exfoliation but not to have too small flakes where disorder and quantum size effects would localize the charge carriers. Furthermore, the choice of the polar solvent and the optimal heat treatment will be examined in the near future.

References

[1] A. H. Castro Neto et al., Mod. Phys. **81**, 109–162 (2009).
[2] M. B. C. Brodie, Ann. Chim. Phys. **59**, 466–472 (1860).
[3] W. S. Hummers and R. E. Offeman, J. Am. Chem. Soc. **80**, 1339 (1958).
[4] Y. Zhu, M. D. Stoller, W. Cai, A. Velamakanni, R. D. Piner, D. Chen, and R. S. Ruoff, ACS Nano **4**, 1227–1233 (2010).
[5] Y. W. Son, M. L. Cohen, and S. G. Louie, Nature **444**, 347–3349 (2006).
[6] J. I. Paredes, S. Villar-Rodil, A. Martinez-Alonso, and J. M. D. Tascon, Langmuir **24**, 10560–10564 (2008).
[7] Z. Y. Li, W. H. Zhang, Y. Luo, J. L. Yang, and J. G. Hou, J. Am. Chem. Soc. **131**, 6320 (2009).
[8] B. Náfrádi, N. M. Nemes, T. Fehér, L. Forró, Y. Kim, J. E. Fischer, D. E. Luzzi, F. Simon, and H. Kuzmany, Phys. Status Solidi B **243**, 3106–3110 (2006).
[9] J.-P. Salvetat, T. Fehér, C. L'Huillier, F. Beuneu, and L. Forró, Phys. Rev. B **72**, 075440 (2005).
[10] Y. Tomkiewicz, A. R. Taranko, and J. B. Torrance, Phys. Rev. Lett. **36**, 751 (1976).

Waveguiding Effect in GaAs 2D Hexagonal Photonic Crystal Tiling

Đ. Jovanović[a,*], R. Gajić[a], D. Djokić[a] and K. Hingerl[b]

[a]Institute of Physics, P.O. Box 68, 11080, Belgrade, Serbia

[b]Zentrum für Oberächen- und Nanoanalytik und Universität Linz

Altenbergerstr. 69, A-4040 Linz, Austria

In this paper we theoretically study (with plane wave expansion and finite-difference time-domain models) waveguiding effect of the 2D hexagonal dielectric photonic crystal tiling. The structure is made of GaAs dielectric rods in air. We perform the calculations of the band structures, equi-frequency contours and electromagnetic propagation through the new type of the photonic crystal and self-collimation waveguides making it possible for application.

PACS numbers: 42.25.Bs, 42.70.Qs, 42.82.Et

1. Introduction

Photonic crystals (PC) are artificial structures that have a periodic dielectric constant. They are designed to control photons in the same way that crystals in solids control electrons. Some specific PC possess energy ranges, called the photonic band gap (PBG), where light propagation is completely prohibited. If linear defects are introduced in such PC, light propagation can be completely guided along a path of the linear defects, in what is called a PC waveguide (PCW), even when it largely bends. PCW advantages are low losses, high confinement and the fact that they can be fabricated in actual materials already used in electronic industry.
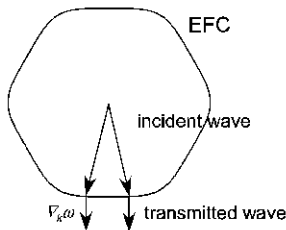
Fig. 1. Illustration of the self-collimation phenomena for an EFC. $\nabla_k \omega$ is the group velocity.

Also, it is well known that for specific frequencies and PC lattices light can propagate without diffraction, which can leads to the phenomenon that is of the special interests of our research in this paper, self-collimation (for

some authors self-collimation is also known as super--collimation) [1–3]. The self-collimation effect relies on the special dispersion properties of the Bloch waves in PC, where the curvature of the equifrequency contours (EFC) departs from the normally circular curvature in free space. As the direction of a propagating Bloch mode is always normal to the EFC, the self-collimation is achieved when they are as flat as possible (Fig. 1). Self-collimation, also known as auto-collimation or self--guiding allows a narrow beam to propagate in the photonic crystal without any significant broadening or change in the beam profile, and without relying on the light intensity, bandgap or engineered defects, such as waveguides (advantage over the PCW). This property can be used for waveguiding and dense routing of optical signals.

2. Structure

We analysed the structure which belongs to class of the Archimedean lattices [4] (Fig. 2) and by notation of Grünbaum and Shephard [5] is named by $(3, 12^2)$. In contrast to our previous work with square Archimedean lattices [6, 7] this structure falls in the hexagonal crystal system with the *P6mm* plane symmetry group according to the *International Tables for Crystallography* [8]. The primitive unit cell and the first Brillouin zone with symmetry points are presented in Fig. 2. It has 6 atoms per unit cell. Structural motiv is dodecagon which is placed in the structure like hexagonal lattice.

3. Results

In this paper we present research of the waveguide effect (by the self-collimation and the presence of PBG)

———

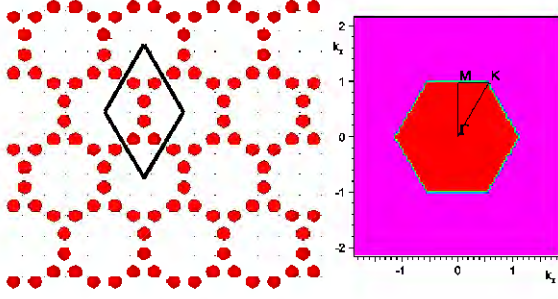* corresponding author; e-mail: djordje@phy.bg.ac.yu

Fig. 2.   Crystal lattice, primitive unit cell and the first Brillouin zone with symmetry points of the $(3, 12^2)$.
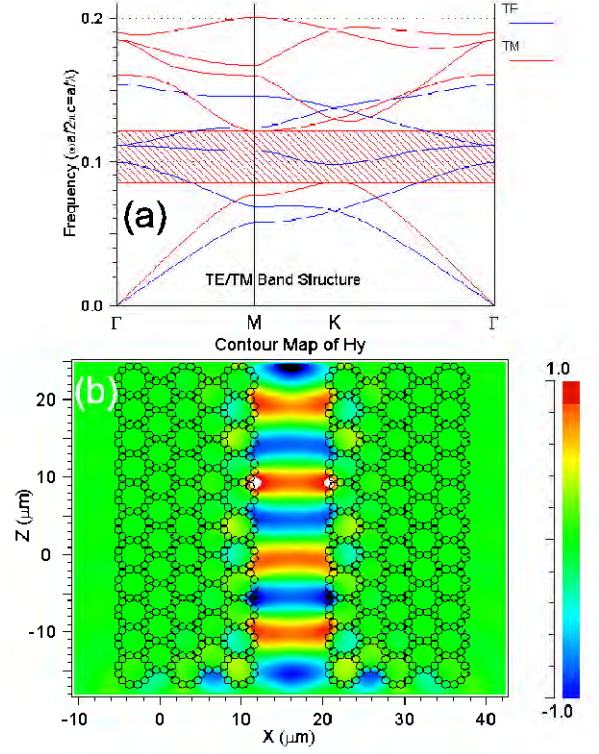

Fig. 3.   (a) Band structure of the first five bands, $r/a = 0.48$ and TE/TM polarization. (b) Propagation of wave through the PCW for the band gap frequency $\bar{f} = 0.1$ ($\lambda/a = 10$) and TM polarization.

in the PC lattice which is made of the GaAs 2D dielectric cylinders ($\varepsilon = 12.96$) in air ($r/a = 0.48$, where r is the rod radius and a is smallest distance between the rods). Also, it is assumed that material is homogeneous, linear and lossless. As a tool for the analysis we used RSOFT [9] to calculate band structures, EFC and for the wave propagation through PC. The theoretical models are well known plane wave expansion (PWE) method for the first two calculations and a finite-difference time-domain (FDTD) method for the latter.

In Fig. 3a there is presented the band structure (obtained with PWE model) of the first five bands, TE/TM polarization (TE and TM polarizations means that electric and magnetic field vectors are normal to the plane of the wave propagation, respectively) and $r/a = 0.48$ (the rods almost touch). From this picture, one can see wide gap for TM polarization that emerges between first and the second TM band for normalization frequency range $\bar{f}$ ($= \omega a/2\pi c$) $= 0.085$–0.121. For these frequencies, there is no propagation of the light in material which leads to waveguiding effect in PCW structures [10].

As the application of the $(3, 12^2)$ lattice we construct a PCW. The PCW is formed by removing two rows of dodecagons from the original structure which creates line defect (Fig. 3b). The dimensions of this structure with the M interface are $37a \times 42.5a$. The FDTD model simulates propagation of the wave through the line defect. For the wide continuous Gaussian beam, band gap frequency ($\bar{f} = 0.1$, $\lambda/a = 10$) and TM polarization we obtained clear guiding without losses.

The next phenomenon which we study in $(3, 12^2)$ structure, as suitable for application in guiding waves, is self-collimation. To find propagation direction of the light through the PC, with PWE model, we analyze EFC for different bands and polarizations. The results are presented in Fig. 4 for the TE2 band. According to appropriate interface of the structure, full normal and parallel line are normal and parallel component of k wave vector. The parallel component of k is conserved in refraction (the Snell law). The first Brillouin zone of $(3, 12^2)$ lattice is shown by the broken line. The symmetry points, Γ, K and M of the first Brillouin zone are also marked.
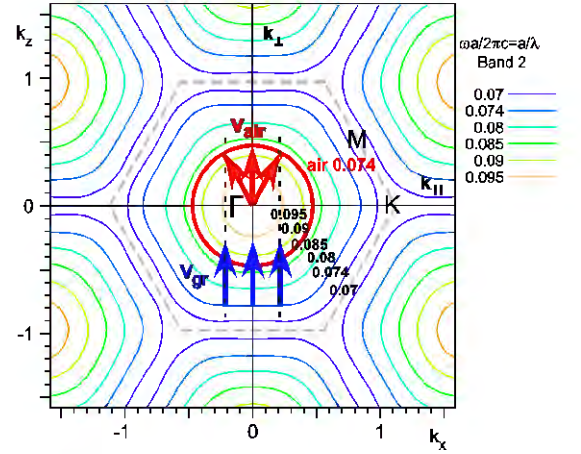
Fig. 4.   The EFC plot for the TE2 band and the $r/a = 0.48$. The orange circle and upper arrows indicate incident air wave ($\bar{f} = 0.074$, $\lambda/a = 13.51$) in the range of angles (0–28°). For these conditions, part of the corresponding PC EFC is virtually straight (almost flat) and the group velocities are almost the same (lower arrows). This is the reason for the self-collimation effect to emerge.

From the figure one can see that contures are very flat for the frequencies near the end of the first Brilloiun zone and around M symmetry point (necessary condition for the self-collimation effect). We can predict that the self--collimation effect will emerge for $\bar{f} = 0.07$–0.08. To confirm that assumption, we construct an air frequency contour for frequency $\bar{f} = 0.074$ ($\lambda/a = 13.51$) to find the directions of the group velocity (to tell us about wave propagation) in PC. For that frequency, incident angles up to 28° (0–28°) and from the well known formula, for group velocity, $\boldsymbol{v}_g = \nabla_k \omega$ we concluded that transmitted wave inside the PC will propagate without dispersion (the refracted angle is almost zero). For $k_x = 0$ ($\theta_{in} = 0°$) we find flatness EFC (the curvature of the couture is extremely small) which is fundamental for good collimation and application. For the flattest EFC the beam is traveling to longest distances without dispersion (so-called super-collimation [2]). Similar situation emerges in the TM2 band.

In order to confirm the self-collimation effect made by analysis of the EFC, we analyzed, with FDTD model, propagation of the wave through the $(3, 12^2)$ structure. The structure, which we call self-collimation waveguide (SCW), as potential application for integrated optic devices, is made of the 21 layers of dodecagons with K interface. The dimensions of the structure are $42a \times 69.5a$ which is small enough for integrated optical circuits and also large enough for good guiding of wave. For best performances (long dispersionless propagated beam), parameters for simulation of the continuous Gaussian incident wave are $\bar{f} = 0.074$ ($\lambda/a = 13.51$) and $\theta_{in} = 0°$. The results are presented in Fig. 5. As we predicted in the EFC analysis we got clear self-collimation inside the structure even for the oblique incidence. The wave inside the PC propagates without dispersion.

Also, from the figure, one can see that for this interface major part of the field is located in the walls made of dielectric cylinders which can be desirable for good waveguiding. To fit operating wavelength at 1.55 μm (telecommunication wavelength) the lattice constant and the radius of the dielectric rods must be $a = 0.115$ μm and $r = 0.055$ μm.

4. Conclusions

In this paper, we present our research of the waveguiding effect in the less known 2D hexagonal lattice tiling made by dielectric GaAs rods in air. We investigated possibilities of the waveguiding effect for applications of the $(3, 12^2)$ Archimedean PC lattice. We propose the new type of the PCW and SCW devices for integrated optics applications based on the PBG and self-collimation effect, respectively.

Acknowledgments

References

[1] H. Kosaka, T. Kawashima, A. Tomita, M. Notomi, T. Tamamura, T. Sato, S. Kawakami, *Appl. Phys. Lett.* **74**, 1212 (1999).

[2] P.T. Rakich, M.S. Dahlem, S. Tandon, M. Ibanescu, M. Soljacic, G.S. Petrich, J.D. Joannopoulos, L.A. Kolodziejski, E.P. Ippen, *Nature Mater.* **5**, 93 (2006).

[3] D.W. Prather, S. Shi, J. Murakowski, G.J. Schneider, A. Sharkawy, C. Chen, B. Miao, R. Martin, *J. Phys. D, Appl. Phys.* **40**, 2635 (2007).

[4] J. Kepler, *Harmonices Mundi*, Linz 1619.

[5] B. Grünbaum, G. Shephard, *Tilings and Patterns*, Freeman, New York 1987.

[6] R. Gajić, D. Jovanović, K. Hingerl, R. Meisels, F. Kuchar, *Opt. Mater.* **30**, 1065 (2008).

[7] D. Jovanović, R. Gajić, K. Hingerl, *Opt. Express* **16**, 4048 (2008).

[8] T. Hahn, *International Tables for Crystallography, Volume A: Space-group symmetry*, Springer, Netherlands 2005, p. 105.

[9] BandSOLVE, FullWave, RSoft Design Group Inc., URL: http://www.rsoftdesign.com .

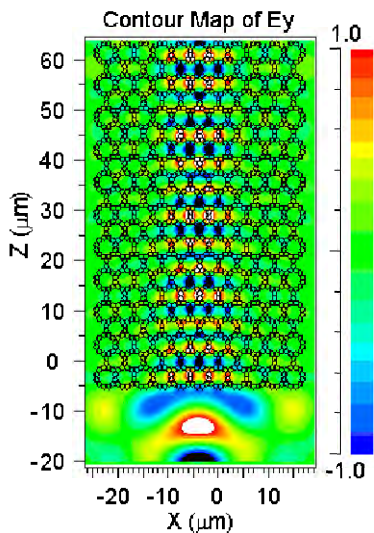[10] R. Meisels, P. Oberhumer, F. Kuchar, F. Aldrian, R. Gajic, *J. Appl. Phys.* **102**, 094106 (2007).

Fig. 5. Propagation of the self-collimated TE beam through $(3, 12^2)$ structure without dispersion. Incident wave parameters are $\bar{f} = 0.074$ ($\lambda/a = 13.51$) and $\theta_{in} = 0°$.

Heat Propagation Improvement in YBCO-Coated Conductors for Superconducting Fault Current Limiters

D. M. Djokić[*1], L. Antognazza[1], M. Abplanalp[2], and M. Decroux[1]

[1]Department of Quantum Matter Physics, University of Geneva, Switzerland
[2]ABB Corporate Research Center, Dättwil, Switzerland
*Corresponding author: dejan.djokic@unige.ch

Abstract: YBCO Coated Conductors (CCs), used for applications in Resistive Superconducting Fault Current Limiters (RSFCLs), are known to have insufficiently high Normal Zone Propagation Velocity (NZPV) during quench events. The improvement can be made by enhancing the thermal conductivity of YBCO-CCs with no decrease in the electrical resistivity. We studied the advantage of multi-layered structures grown on a cheap fused silica with thickness of 90 μm. The multilayer is composed of: a several microns thick copper layer to enhance the thermal conductivity, a layer to prevent the inter-diffusion, and a Hastelloy top layer. We carried out 3D FEM simulations in COMSOL Multiphysics on a meander configuration to calculate NZPV. The simulation results show a marked improvement as compared to the earlier cases [1, 2].

Keywords: Resistive Fault Current Limiters, YBCO Thin Films Applications, Cryostability of High-Temperature Superconductors, Heat Transfer and Phase Change Modelling, Medium Voltage Grids.

1. Introduction

In order to engineer superconducting cable applications, such as RSFCLs, the adequate protection from their quench damages represents one of the crucial parameters. Over the past half-century, low temperature superconductors have already proven effective in the field of cryogenic stability with reference to the operation of devices they are used for. On the other hand, high temperature superconductor applications, based on YBCO-CCs for example [3], possess quite different physical properties, with expectancy to operate within much higher temperature ranges. As their measure of cryostability, YBCO-CCs' quench propagation velocities fall into the three magnitudes lower range (of the order of cm/s) as compared to low temperature superconductors. For that reason, the use of YBCO-CCs entails high risk for damages due to eventual hot spot proliferations [4, 5]. Cabling such systems has become a subject to extensive investigations, both experimental and theoretical [6], to ensure quite a high degree of the operational stability of YBCO-CCs' devices. For example, RSFCLs made of YBCO on sapphire substrates [7] have been recognised as a possible alternative. However, these suffer from a disadvantage by virtue of their considerable costs for commercialization purposes.

In this account, our attention is devoted to numerical simulations on YBCO-CCs based RSFCLs integrated in real grid configurations. Our goal is to improve the thermal property of such superconducting devices, as well as, to optimize their designs in order to guarantee the safe integration. There are two ways of doing so: by (i) lessening the thermal influence of a massive lowermost substrate (such as SiO_2) to make the heat propagation dominated by the properties of a thermally conductive layer (such as Cu) and (ii) increasing the dimensionality up to a meander configuration. We have also raised the question of how much of the copper layer is sufficient for, in an effective sense, decoupling the YBCO-CC from the thermally inertial SiO_2. The proposed numerical model safely assumes the current transport in YBCO-CCs only and joule heating sources due to the local perturbations across the high temperature superconductor, and in the same manner, allows the variation of all the geometrical parameters relevant for the heat propagation improvement.

2. Multi-Layered Superstructure and Computational Details

We have carried out heat transfer time dependent finite element simulations in COMSOL on a simple 3D meander geometry of a novel RSFCL which is demonstrated in Figure 1. The RSFCL consists of a 40 nm Ag-coated 300 nm YBCO bonded to a multi-layered superstructure sitting

on a cheap fused silica substrate with thickness of 90 microns. The multilayer is composed of the following elements: (1) a several microns thick copper layer (varied from 0 up to 5 microns) designated to enhance the thermal conductivity of the structure, (2) a layer to prevent the inter-diffusion with (3) the Hastelloy top layer of 1 μm essential for the deposition of 2 μm thick MgO buffer layer and for avoiding the copper contamination. The realisation of the envisaged structure is well in progress [8], and yet, piloted by the simulation outcomes. Most conventionally, three experimental techniques are adopted to build up such a novel RSFCL: (1) DC magnetron sputtering system for the multilayer deposition, (2) co-evaporation technique for Ag coating and deposition growth of YBCO thin films (critical temperature T_C =92 K and critical current J_C=2 MAcm^{-2} at 77 K), and (3) ion-beam assisted deposition for bi-axially alignment of the MgO template.
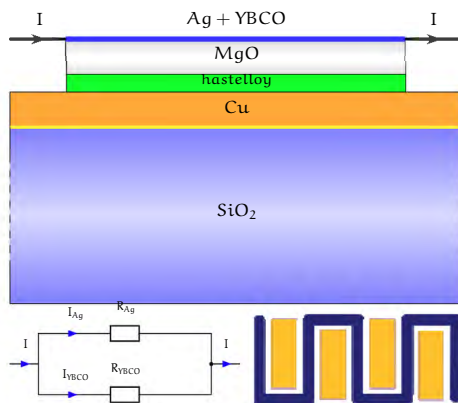
Figure 1. Novel multi-layered superstructure (upper panel) configured into a meander geometry (down right) of an YBCO-based CC lying on the copper+SiO$_2$ substrate. The superconducting line is electrically isolated from the substrate so that the current is shared in YBCO-based CC only (down left).

Without loss of generality, the simulated geometry of the meander (Fig. 1 down right panel) has been streamlined to comprise only three superconducting lines (each 6 mm×20 mm), separated by 0.4 mm lying on the top of the copper layer. The entire configuration is immersed into a thermal bath of liquid nitrogen (77 K). The dissipation initialization is achieved by locally weakening the critical current density.

Therefore, the central 6 mm × 50 μm block (T_C=92 K and J^B_C=0.1 MAcm^{-2}) of the middle line (Fig. 2) is taken to be in the normal state even well below 92 K and represents the T-J dependent heat source which is, accordingly, time dependent too. Once a DC current is switched on, the initial normal block, as a hot spot naturally existing in such systems [5], is gradually spreading along the line like an avalanche due to the assisted superconducting transition. The operational current is shared in the Ag-coated YBCO layer only (Fig. 1 down left panel) with its constant density of J=2.5 MAcm^{-2}. Although, the realistic RSFCL applications are designed for current limitations in AC networks, the typical thermal times of both diffusive and superconducting transition assisted heat propagations [9] are much shorter than common AC periods (25 ms for 50 Hz), as will be verified later in the text. Because of computational convergence issues on one hand side and meshing distribution on the other, the size of the normal block has been cautiously tuned to ultimately yield an optimal length of 50 μm for the present case [1].
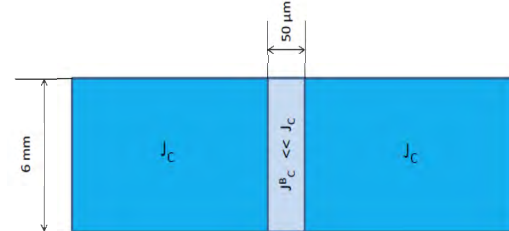
**Figure 2.** A scetch of the central 6 mm × 50 μm block with the critical current much lower as compared to the reamaing superconductiong parts. The block is extremely resistive even at 77 K for operational currents of 1 MAcm^{-2}.

As a heat source input, the T-J dependent power density function (Fig. 4) has been evaluated numerically in R based on the so-called current sharing function (Fig. 3). Observing the complexity of the problem with regards to mixing instantaneously temperature and current dependencies of YBCO resistivity, the solution in the circuit element (Fig. 1 down left panel) has been achieved self-constituently with several short time consuming loops. It assumes the following temperature dependent form of the YBCO flux flow resistivity which can be encountered elsewhere [10]:

$$\rho(J,T) = \rho_0 \cdot \left(\frac{J}{J_c(T)} - 1 \right)^n, \text{ with } J_c(T) = J_{c0} \cdot \left(1 - \frac{T}{T_c} \right)^{1/2} \cdot \left(1 - \left(\frac{T}{T_c} \right)^4 \right)^{1/2}$$

where, ρ_0 is the equivalent resistivity at $2J_C$ and n stands for the order of the power law. The two parameters must fit the properties of the superconductor for a given underlying substrate. J_{C0} represents the critical current predicted at 0 K in the self-field and it is deduced from the J_C measurement at 77 K. The size of the circuit element for current sharing has been adjusted automatically in COMSOL to the optimised meshing element distribution. There has been therefore no need for block fragmentation of the coated conductor as was an earlier computationally rather time consuming approach [1, 2].
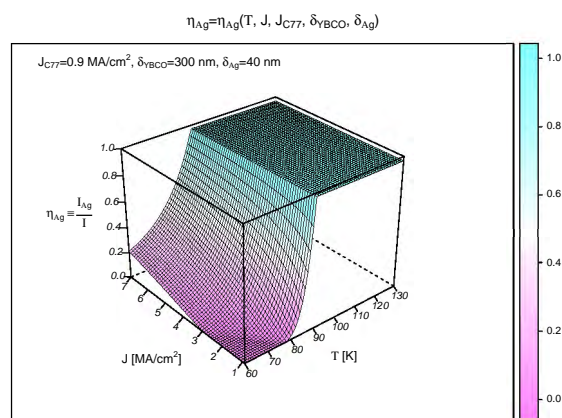
Figure 3. T-J dependent complex current sharing function reaching the plateau of height 1 above 92 K.

Finite element meshing was used to discretize the material distribution. Still, the major difficulty of the treated geometry lies in its extremely high aspect ratio that can be a challenge for an automatic or unstructured meshing where the goal is to create an isotropic mesh distribution for high mesh quality. The strategy was to subdivide the geometry into material layers with respect to the central normal block. A mapped mesh was then created on all the boundaries and distributed on the edges and peripheries. By symmetry, only one fourth of the

model was simulated to speed up the computation. Thus, the symmetry boundaries were considered as nothing but the external boundaries in such a shrunken geometry.
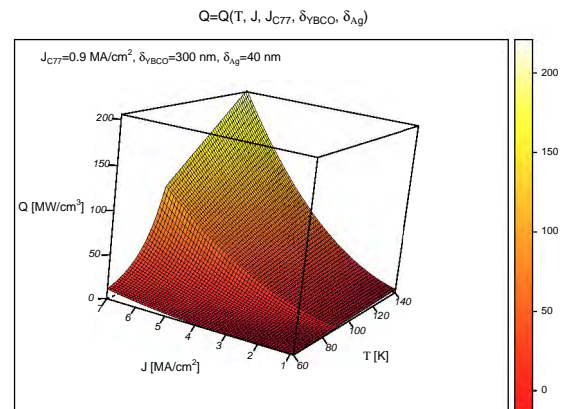
Figure 4. T-J dependent complex heat source function directly imparted from the current sharing function.

The material properties data for thermal conductivity, specific heat capacity, and convection heat transfer coefficient, all the three being isotropic and temperature dependent, were adopted from [1, 2]. The spatial dependence of YBCO resistivity along the line was not considered directly. Namely, it was incorporated implicitly through J_C spatial dependence that has a sudden drop at the position of the normal block which is a solely new layer of the same material. As with the thermal contact between the superconducting lines and the underlying multi-structure, the equivalent interface conductance was guessed from experimental results for similar structures based on a novel characterization method reported in [11]. The estimated value was taken to be 300 W $K^{-1}cm^{-2}$. For further details with regards to a discussion on the equivalent interface conductance the reader is kindly referred to [1].
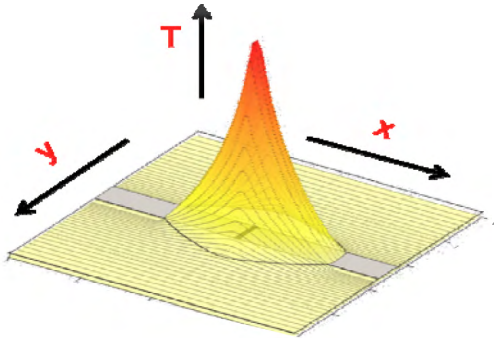
Figure 5. A temperature profile featuring longitudinal (x) and lateral (y) normal zone propagation across a single line sitting on a substrate. The figure is partially borrowed from [1].

The simulations were not of real-time type and were terminated as soon as the transition had spread out over the entire superconducting volume. Such moments were translated into real times (t_{final}) which regularly took shorter than a millisecond. Until t_{final} is reached, the average temperature of the normal block, T_{block}, was followed in order to quantity the high temperature operationality of the RSFCL. Admissible temperatures are supposed to be lower than 600 K [12] for that purpose. The heat propagation was also monitored through other referential points in time (i.e. temperature) evolution, such as: t_{trans} which represents the moment of the very first 92 K transition occurred within the normal block, and t_{600} which measures the time interval until T_{block} reaches 600 K, provided it does. Directional heat propagations along the line (longitudinal, x-axis) and sidewise (lateral, y-axis) were surveyed too (Fig. 5), with particular reference to propagating fronts of T_{NZ}=92 K, the so-called normal zones. Apart from several initial microseconds, all the values for NZPVs in the two directions of interest were found uniform over the whole interval. This is in accordance with the picture of superconducting transition assisted heat propagation [8]. The character of such a type of heat propagation is prevailing in the y-direction too knowing that the lateral NZPV is averaged out over the narrow space of the underlying layer favouring diffusive-like transport and fairly larger space of the adjacent superconducting line. Leading

contributions of the diffusive-like propagations would be expected at, if of interest, larger distances between the lines.

Generally, the NZPV is a function of both J and J_C for a given substrate. However, rather than looking at the dependence with respect to these variables individually, one is usually interested in scaling the NZPV dependence down to the universal parameter J/J_C. With its values falling into the range between 1 and 1.5, it generates no extensive heating during the quench propagations. Our case is concerned with J/J_C=1.25 and can be considered rationally safe in connection with the issues with rapidly overheated RSFCLs.

The 3D model has even allowed an observation, yet only qualitative, of the heat penetration into the substrate along z-axis within few first microseconds. All the relevant times were measured from the moment the hot spot proliferation had been launched at.

3. Results and Discussions

This section is devoted to a discussion on the FEM computational results which are presented in Table 1 and obtained for the following parameters: δ_{Ag}=40 nm, δ_{YBCO}=300 nm, δ_{MgO}= 2 μm, δ_{Hast}=1 μm, δ_{Cu}=0.5-5 μm, δ_{SiO2}=90 μm, J_C=2 MAcm^{-2}, J=2.5 MAcm^{-2}, and K_{inter}=300 WK^{-1}cm^{-2}. To ensure the reliability of the simulations, the model has been successfully validated with available experimental data for both 500 μm thick sapphire and 90 μm thick hastelloy substrate; the former with J_C=3 MAcm^{-2} and J=4.5 MAcm^{-2}, while the latter with J_C=0.9 MAcm^{-2} and J=1 MAcm^{-2}. The computed values for the relevant times and temperatures were distilled directly from the COMSOL consoles, whereas the values for NZPVs were calculated based on the first derivative conditions for the normal zone time propagating path averaged along a desired direction. These conditions vary from one spatial coordinate to another depending on the mesh element distribution. The problem boils down to solving a numerical equation with respect to x for which $T(x) = T_{NZ}$. One way of doing so, that has turned out to be extremely straightforward in COMSOL, is to evaluate the expected value of the spatial coordinate $<x(t)>$ along the line (0<x<L, for example) using an

integration method. It consists in centring a Gaussian density distribution peak on $T(x) = T_{NZ}$ (Fig. 6) to guarantee the highest probability for events satisfying $T(x) = T_{NZ}$. The NZPV therefore reads as follows:

$$\upsilon_{NZP} = \frac{\partial}{\partial t} \frac{\int_{x=0}^{L} x\, e^{\frac{(T(x)-T_{NZ})^2}{2\delta^2}}\, dx}{\left(\varepsilon + \int_{x=0}^{L} e^{\frac{(T(x)-T_{NZ})^2}{2\delta^2}}\, dx \right)}$$

Other solutions, however lying in the close vicinity, are weighted with less significant fractions to the integration which fall off along the Gaussian tail. Their contributions are limited due to the line-width of the Gaussian density function (δ_T) which is further controlled with the size of the projected mesh element (h) in order to provide a satisfactory smoothness of generated $<x(t)>$ function. Ideally, the case $\delta_T=0$ would represent the exact analytical solution that can be treated in none of FEM software because of the hypothesised mesh fragmentation. The confidence intervals varied with respect to the integration direction, as well as, the available space for the integration. One must bear in mind that $L_x=20$ mm (length of the line), while $L_y=0.4$ mm (space between the lines). Such an evidently anisotropic ratio in geometry necessarily leads to the difference in relative errors for NZPV values along x, i.e. y, such that they are of 1 %, i.e. 7 %, respectively. In addition, we do not place our confidence in lateral NZPV values given that such propagations are rather of diffusive nature that may entail time dependence. Nevertheless, the order of the magnitude for lateral NZPVs appears very sensible with reference to the values for longitudinal ones.

As is shown in Figure 6, the idea of properly using the integration as a reliable NZPV calculation tool lies in covering as large number of mesh elements as possible, provided that $T(x)$ remains a smooth function over a domain of the mesh elements. Our simplification, without loss of generality however, was to guess the linearity over one such domain that has led to the following condition: $h \times T_x' << \delta_T << T_{NZ}$, where T_x' represents the slope of $T(x)$. A thorough description of the introduced condition is delineated in Figure 6.
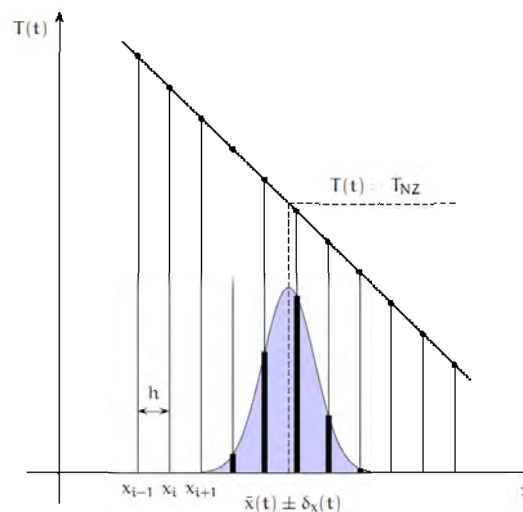

Figure 6. NZPV smoothness condition, $h << \delta_T/T_x'$, controlling the mesh size element. $T(x)$ is guessed linear over a domain containing a large enough number of the mesh elements.

The integration runs some risk of containing division by zero. This can be escaped by inserting ϵ as an internal COMSOL constant that is a very small number of the order of 10^{-15}. Yet, one should use the *nojac* operator in COMSOL to make sure that the operating expression is excluded from the Jacobian computation. This is useful in the present case as the Jacobian contribution is not strictly necessary and the computational requirements for it are considerably high.

δ_{Cu} [µm]	0.5	1	2	3	4	5
υ_x [m/s]	3.5	4.50	4.60	4.65	4.70	4.70
υ_y [m/s]	3.5	4.0	4.0	4.0	4.1	4.1
t_{fin} [µs]	900	840	850	870	880	890
t_{trans} [µs]	40	25	30	43	55	72
t_{600} [µs]	$>t_{fin}$	$>t_{fin}$	$>t_{fin}$	$>t_{fin}$	$>t_{fin}$	$>t_{fin}$
T_{block} [K]	590	540	540	500	520	500

Table 1. The longitudinal (υ_x) and lateral (υ_y) NZPV values, relevant time parameters, and T_{block} with respect to the Cu thickness varied (δ_{Cu}). J=2.5 MAcm^{-2} and J/J$_C$=1.25.
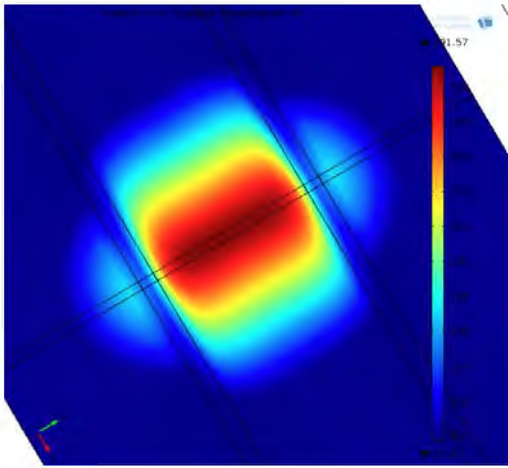
Figure 7. Temperature profile for the three superconducting lines (δ_{Cu}=2 μm) measured at 340 μs after the transition (30 μs).

The NZPV values are found quite level-headed if compared with far 13 cm/s for hastelloy and close 10 m/s for sapphire substrate at J/J_C=1.25 [12]. It is also worth noting here that this comparison is made at the fixed value of J/J_C which is the most relevant parameter for the evaluation of heat propagations in different systems. However, the complete validation of the model for the multi-structure in question is still well under way [8]. In such a manner, reconciliation can be effected between the low cost commercialisation as the strongest feature of the former and fast quench propagation as the most appealing property of the latter. For that reason one must adjust the thickness of the copper layer in order to optimize, on one hand, the influence of the underlying fused silica substrate of which 90 microns of thermal inertia may well moderate the quench propagation, and miniscule but still present thermal inertia coming from the copper itself, on the other. Saturation in the NZPV values with respect to copper thickness variation is therefore expected, as is implied from Table 1.

It is worth mentioning that there are also FEM measurements made for copper substrates thinner than 0.5 μm down to zero. It has been found that a substantial drop in the NZPV values occurs below 100 nm at which they fall in the range of the order of 10 cm/s (7 cm/s for 0 μm). The errors in the simulation measurements for such

thin layers are considerably large if one bears in mind the difficulty with the mesh quality due to the extremely high aspect ratio. Nevertheless, it is of experimental interest to study only those copper layers which are thicker than a micron since acquiring the reliable experimental data on the effective thermal conductivity may become troublesome for thinner copper layers. As a result, a deposition of one up to two microns at most of copper layer would prove quite sufficient for the desirable heat propagation improvement in the proposed structure.

As with the remaining computed values at δ_{Cu}>0.5 μm, t_{trans} and t_{fin} are both found corroborative with the behaviour of the NZPVs. t_{trans} should increase with the increase of thickness of a good thermal conductor such as copper because the system gains some tendency to become robust towards the very first transition. On the other hand, t_{final} was measured as a time for which the point with the lowest temperature reaches 92 K. This point may not be kept at the same position as the copper thickness is varied. For that reason, this parameter is not quite corresponding to the time for which the normal zone extents over the entire system. Nevertheless roughly speaking, according to the relevant spatial dimensions and NZPV values, t_{final} is supposed to be of the order of 10^3 μs or less that is the case in the treated coated conductor. The thorough discussion above does not apply for δ_{Cu}<1 μm since this case starts to extend the influence of the fused silica.

In addition, none of the t_{600} values could be measured for all the six copper thicknesses as it goes beyond t_{fin} values. This further ensures the operationality of the studied RSFCL device. The heat propagation is desirably homogenised over the system upon a quench initialisation, before any eventual severe damage is inflicted [13]. That is, T_{block} as the highest temperature has always been found to be below 600 K for finite Cu thicknesses.

An example of the COMSOL temperature surface plot of the propagating normal zone over the three superconducting lines for 2 μm thick copper layer is given in Figure 7. One can delineate a 92 K border line of the propagating profile, which roughly demarcates dark blue from light blue area, at the moment when the hot

spot reaches 292 K. There is substantial heat diffusion sidewise the middle line that to some extent softens the temperature profile. Such extra temperature distribution has, however, led to no significant difference between the longitudinal NZPVs computed in 2 and 3D.

4. Concluding Remarks

In conclusion, the present computational work has made a valuable contribution to the development of superconducting high current cables with YBCO coated conductors that can be used for medium voltage power applications. The FEM model, which we have developed in COMSOL Heat Transfer Module, has been found quite accurate to simulate the 3D transition-induced heat propagation in YBCO-based CCs used for RSFCLs with simple meander geometry on a novel multi-structure (on-going experiment [8]). The computational results, which are given in the present study, have been employed to optimally moderate the experimental assortment of both thermally conductive and single crystalline substrates down to the use of copper. We have demonstrated that varying the Cu-substrate thickness above 0.5 μm has no considerable impact on longitudinal/lateral NZPVs. This means that a copper layer not thicker than a micron is sufficient to come up with an already desirable degree of the RSFCL operationality. The obtained NZPV values have proven to fall into the almost two magnitude higher range as compared to the earlier studies [2] that is promising for commercialization purposes.

5. References

[1] A. Badel, L. Antognazza, M. Therasse, M. Abplanalp, C. Schacherer, and M. Decroux, Hybrid Model of Quench Propagation in Coated Conductors for Fault Current Limiters, *Supercond. Sci. Technol.* **25**, 095015 (2012).
[2] A. Badel, L. Antognazza, M. Decroux, and M. Abplanalp, Hybrid Model of Quench Propagation in Coated Conductors Applied to Fault Current Limiter Design, *IEEE Trans. Appl. Supercond.* **23**, 5603705 (2013).
[3] J. D. Hodge, H. Muller, D. S. Applegate, and Q. Huang, A Resistive Fault Current Limiter Based on High Temperature Superconductors, *Appl. Superconductivity* **3**, 469 (1995).

[4] A. Gurevich, Thermal Instability Near Planar Defects in Superconductors, *Appl. Phys. Lett.* **78**, 1891 (2001).
[5] B. Shapiroa, G. Bela, B. Rosensteinb, and I. Shapiroa, Hot Spot in Type-II Superconductors Dynamics and Instabilities, *Physica C: Superconductivity* **404**, 335 (2004).
[6] Y. Wang, *Fundamental Elements of Applied Superconductivity in Electrical Engineering*, John Wiley & Sons, Singapore (2013).
[7] J. Duron, F. Grilli, L. Antognazza, M. Decroux, B. Dutoit, and Ø. Fischer, Finite Element Modelling of YBCO Fault Current Limiter with Temperature Dependent Parameters, *Supercond. Sci. Technol.* **20**, 338 (2007).
[8] D. M. Djokić, L. Antognazza, M. Abplanalp, and M. Decroux, *in preparation* (2014).
[9] D. M. Djokić, L. Antognazza, M. Abplanalp, and M. Decroux, Improved Heat Propagation in Coated Superconducting Fault Current Limiters, *EuCAS Conference Poster*, Genoa (2013).
[10] L. Dresner, *Stability of Superconductors*, Kluwer Academic Publishers, New York (2002).
[11] L. Antognazza, M. Decroux, A. Badel, C. Schacherer, and M. Abplanalp, Measurement of the DyBCO Substrate Thermal Conductance in Coated Conductors, *Supercond. Sci. Technol.* **25**, 105002 (2012).
[12] L. Antognazza, M. Decroux, S. Reymond, E. de Chambrier, J. M. Triscone, W. Paul, M. Chen, Ø. Fischer, Simulation of the Behaviour of Superconducting YBCO Lines at High Current Densities, *Physica C* **372–376**, 1684 (2002).
[13] M. Schwarz, C. Schacherer, K. P. Weiss, and A. Jung, Thermodynamic Behaviour of a Coated Conductor for Currents Above I_C, *Supercond. Sci. Technol.* **21**, 054008 (2008).

6. Acknowledgements

Carbon / organic spintronics

115. *Investigations of N@C60 and N@C70 Stability Under High Pressure and High Temperature Conditions*
A. Iwasiewicz-Wabnig, K. Porfyrakis, G.A.D. Briggs, B. Sundqvist

116. *Hot-electron spin transport in Graphite*
T. Banerjee

117. *Localized Magnetic State and Induced Magnetic Moment in Graphene*
M. Inglot

118. *Spin-orbit coupling and spin relaxation in grapheme*
S. Konschuh, M. Gmitra, C. Ertler, J. Fabian

119. *Magnetism and Correlations of Fractionally Filled Edge-states in Graphene Quantum Dots*
A. D. Guclu, P. Potasz, O. Voznyy, M. Korkusinski, P. Hawrylak

120. *Electron Spin Resonance Study of Graphene-like Materials Suitable for Spintronics Applications*
L. Ćirić, A. Magrez, A. Sienkiewicz, L. Forró

121. *Enhanced magnetoresistance in self-assembled monolayer of oleic acid molecules on Fe3O4 nanoparticles*
S. Wang, F. J. Yue, **D. Wu**, F. M. Zhang, W. Zhong, Y. W. Du

122. *Magnetic Measurements and Modeling of the Anisotropic Molecular-Based Ring Cr7Cd*
P. Kozlowski, G. Kamieniarz, **M. Antkowiak**, F. Tuna, G. A. Timco, R. E. P. Winpenny

123. *High field ESR temperature study on (EDT-TTF-CONH)6Re under pressure*
D. Djokic, A. Olariu, P. Batail, L. Forro

124. *Electrostatic Spin Crossover Effect in magnetic molecules*
N. Baadji, S. Sanvito

125. *Magnetic Exchange in Porphyrin-based Molecular Structures*
D. Sankar Kesanakurthi, N. Baadji, S. Sanvito

126. *Spin-Polarized Transport through a Single-Molecule Magnet*
M. Misiorny, I. Weymann, J. Barnaś

(Ga,Mn)As and related systems

127. *Influence of Annealing on Mn Implanted GaAs Films*
D. Bürger, S. Zhou, J. Grenzer, H. Reuther, W. Anwand, M. Pandey, V. Gottschalch, M. Helm, H. Schmidt

128. *The combined method of MOC-hydride epitaxy and laser deposition for formation of structures with ferromagnetic semiconductor layers*
B. N. Zvonkov, **Y. A. Danilov**, M. V. Dorokhin, Y. N. Drozdov, A. V. Kudrin, M. V. Sapozhnikov, O. V. Vikhrova

129. *Modeling of Mn-doped III-V Nanowires*
M. Galicka, M. Bukała, R. Buczko, P. Kacman

49	Thursday	Larrea	Julio	Julio Larrea, H. Ronnow, M. El-Zayed, M. de Vires, J. Piatek, R. Lortz and C. Ruegg	Lab.Quantum Magnetism, EPFL Lausanne, Dpt Physics-Hong Kong University of Science & Technology, London Center NanoTechnology, University College London	*High pressure induce phase transition in 2D spin-dimmer system SrCu2(BO3)2*
50	Wednesday	Tsyrulin	Nikolay	Nikolay Tsyrulin, Xiao F., Pardini T, Singh R. R. P., Schneidewind A, Link P, Rønnow H. M., Gavilano J., Landee C. P., Turnbull M. M. and Kenzelmann M.	Lab. Solid State Physics and Lab.Neutron Scattering, ETH Zürich & PSI, Dpt Physics, Clark University - Massachusetts - USA	*Quantum effects in a weakly-frustrated two-dimensional S=1/2 antiferromagnet Cu(pz)2(ClO4)2*
51	Thursday	Viciu	Liliana	Liliana Viciu, Francesco Canonaco, Nikolai Zhigadlo, Janusz Karpinski, Michael Worle and Reinhard Nesper	Lab.of Inorganic Chemistry and Dpt of Physics - ETH Zurich	*Structure and Basic Properties of the Tetrahedral Coordinated Fe2+ Based Compounds SrFeSO and SrFe2S2O*
52	Wednesday	Ubaldini	Alberto	Alberto Ubaldini, Enrico Giannini, Romain Viennois and Dirk van der Marel	DPMC, Geneva University	*New materials with structure related to Iron oxypnictides: synthesis and physical properties*
53	Thursday	Le Dréau	Loïc	L. Le Dréau, W. Paulus, J. Shefer, O. Hernandez	University of Rennes-France, Paul Scherrer Institut, Villigen-Switzerland	*Oxygen diffusion and ordering in La2CoO4+d*
54	Wednesday	Aguirre	Myriam H.	Myriam H. Aguirre, Andrey Shkabko, Laura Bocher, Anke Weidenkaff, Peng Wand and Ursel Bangert	Solid State Chemistry & Catalysis, Empa - Duebendorf, SuperSTEM Daresbury Lab., UK, School of Materials. University of Manchester	*EELS/EDX study on SrTiO3-xNy single crystal obtained by microwave plasma ammonolysis.*
55	Thursday	Elia	Jack	Jack Elia, Romain Viennois, Jeremie Teyssier, Alberto Ubalidini, Enrico Giannini, Dirk van der Marel and Joachim Deisenhofer	DPMC - Geneva University, Center Electronic Correlations & Magnetism, University of Augsburg - Germany	*Two-dimensional orbital ordering and ferromagnetism in d1 Mott insulator Sr2VO4*
56	Wednesday	Pomjakushina	Ekaterina	Ekaterina Pomjakushina, Kazimierz Conder, Vladimir Pomjakushin, Markus Bendele, and Rustem Khasanov	Lab. Developmts & Methods and Lab. Neutron Scattering, ETHZ & PSI, Physik-Institut der Universitat Zurich, Lab.Muon Spin Spectroscopy	*Synthesis, crystal structure and chemical stability of the superconductor FeSe1-x*
57	Thursday	Arsenijevic	Stevan	Stevan Arsenijevic, Richard Gaal and László Forró	Inst. Condensed Matter Physics, EPFL Lausanne	*Pressure effects on the transport properties of BaFe2As2 and Ba(Fe0.9Co0.1)2As2*
58	Wednesday	Scherwitzl	Raoul	Raoul Scherwitzl, Pavlo Zubko, Celine Lichtensteiger and Jean-Marc Triscone	DPMC - Geneva University	*Growth and characterization of epitaxial LaNiO3 electrodes*
59	Thursday	Jacimovic	Jacim	J. Jacimovic, R. Gaal, C. Vaju, H Berger, L. Forro, V. Stevanovic and R. Zikic	EPFL, School of Basic Sciences-Lausanne, Inst. of Physics, Belgrade, Serbia	*High pressure transport study of anatase TiO2*
60	Wednesday	Olariu	Areta	Areta Olariu, Dejan Djokic, Patrick Batail, Stephane Baudron and Laszlo Forro	Inst. of Condensed Matter Physics, Lab. of Nanostructures & Novel Electronic Materials - EPFL Lausanne, Lab. de Chimie, Ingénierie Moléculaire et Matériaux d'Anangers - France	*High frequency Electron Spin Resonance study of the organic kagome compound (EDT-TTF-CONH2)6[Re6Se8(CN)6] under hydrostatic pressure*
61	Thursday	Dejan	Djokic	Djokic Dejan, Sienkiewicz Andrzej, Olariu Areta, Gaal Richard, Batail Patrick and Forro Laszlo	Inst. of Physics of Condensed Matter, EPFL Lausanne, Lab. Chimie, Ingénierie Moléculaire & Matériaux Angers, CNRS-Université Angers	*Electron Spin Resonance study of kappa -(EDT-TTF-CO-NH-CH2-CO2H)2[HSO4-] organic charge transfer salt*
62	Wednesday	Xie	Hangxing	Hangxing Xie, Helena Alves and Alberto Morpurgo	Kavli Inst. NanoScience - Delft University of Technology-TheNetherlands, DPMC -Geneva University, INESC MN and IN, Portugal	*Intrinsic Mobility, Shallow Traps and Deep Traps in TMTSF Single-Crystal Transistors*
63	Thursday	Ono	Shimpei	Shimpei Ono,Kazumoto Miwa, Shiro Seki, Jun Takeya and Alberto Morpurgo	Central Research Inst. of Electric Power Industry Osaka University, Geneva University	*High density carrier doping by electrolyte; Application to organic FETs*
64	Wednesday	Zhigadlo	N.D.	N.D. Zhigadlo, J. Karpinski, S. Katrych, Z. Bukowski and B. Batlogg	Lab.Solid State Physics, ETH Zurich	*Exploratory Synthesis and Crystal Growth of FeAs Based Superconductors*

High field ESR temperature study of $(EDT\text{-}TTF\text{-}CONH)_6Re_8Se_6(CN)_6$ under pressure

D. Djokić^a, A. Olariu^a, L. Forró^a, P. Batail^b

^{a}*Institute of Physics of Condensed Matter, Ecole Polytechnique Fédérale de Lausanne, Lausanne, Switzerland*
^{b}*aboratoire de Chimie, Ingénierie Moleculaire et Matériaux d'Angers, CNRS-Université d'Angers, Angers, France*

The 210 GHz high field temperature dependent ESR measurements under hydrostatic pressure have been done on $(EDT\text{-}TTF\text{-}CONH)_6Re_6Se_6(CN)_6$ charge transfer organic single crystal with nearly free electron g-factor. The ESR spectra were recorded across the wide temperature range from 300 down to 2 K at various pressure values up to 15 kbar. This material has proven exceptional for probing bosonisation techniques at one spatial dimension, on one, and highly 2D *kagome* physics on the other hand. Its high temperature rhombohedral crystal phase is accompanied with the lightly metallic state having one half spin *kagome* topology, unprecedentedly emerged in the chemistry of TTF family. Such a strong planar character has been verified by means of transport measurements at room temperature [1]. The structural phase transition towards low triclinic symmetry, occurring around 180 K at ambient pressure, drives the system into the Mott insulating state. To the fit of spin susceptibility data [1], this state is well modelled by quasi-one-dimensional Heisenberg $S = 1/2$ chain with AF coupling of *ca* 65 K. Whether or not the structural phase transition affects the present Mott transition and *vice versa* is nevertheless a contentious issue to deal with. Upon examining the ESR line-width temperature behaviour versus the pressure rise, one finds the phase transition shifted towards higher temperatures. As the system is cooled down, a considerable decrease of the line-width value has also been perceived in almost one order of magnitude (250 G$\rightarrow$ 50 G), owing to the exchange narrowing and localisation. The question to be addressed here is whether the low exchange coupling of the spin chain evolves with respect to the pressure applied, relying on the approach due to Oshikawa and Affleck [2] which, in addition, observes the interchain coupling and exchange anisotropy.

References

[1] S. A. Baudron *et al.*, J. Am. Chem. Soc. **127**, 11785 (2005).
[2] M. Oshikawa and I. Affleck, Phys. Rev. **65**, 134410 (2002).

ID	MᴀNEP Poster
6001	$Fe_{1+y}Se_xTe_{1-x}$ superconductors: phase diagram, crystal growth, structural and magnetic properties *Ekaterina Pomjakushina*
6002	Evidence for large electric polarization from collinear commensurate magnetism in multiferroic $TmMnO_3$ *Vladimir Y. Pomjakushin*
6003	Optical Investigation of the Charge Dynamics in $Ba(Co_xFe_{1-x})_2As_2$ *Andrea Lucarelli*
6004	Morphology, Elasticity and Slow Dynamics of Superconducting Vortex Lattices Investigated with Time Resolved Stroboscopic Neutron Scattering. *Sebastian Mühlbauer*
6005	Influence of doping on the strong rail spin ladder compound $(2,3\text{-dmpyH})_2CuBr_4$ *Sebastian Mühlbauer*
6006	Electron paramagnetic resonance investigation of $EuFe_{2-x}Co_xAs_2$ (x=0, 0.1, 0.2) single crystals *Zurab Guguchia*
6007	Muon spin rotation study of the CaC_6 superconductor at low temperatures *Ferenc Muranyi*
6008	Metallic-like temperature dependence of the mobility in n-type organic single-crystal field effect transistors *Nikolas Minder*
6009	Equilibrium and out of equilibrium studies of ultracold fermions in an optical lattice *Thomas Uehlinger*
6010	MuSR studies of the heavy fermion $CeRhSi_3$ *Nikola Egetenmeyer*
6011	Graphene based devices on top of single crystal $SrTiO_3$ substrates *Nuno J. G. Couto*
6012	Dissipation-driven phase transitions in superconducting wires *Alejandro M. Lobos*
6013	Dynamical correlation functions in spin-1/2 ladders under a magnetic field *Pierre Bouillot*
6014	Anisotropic properties of superconducting single crystals of $La_{2-x}Sr_xCuO_4$ *Saskia Bosma*
6015	Ferromagnetic spin resonance in $EuTiO_3$ probed by time-domain THz ellipsometry *J. L. M. van Mechelen*
6016	Evidence for extended magnetic interactions in the cuprates from the magnon dispersion of $Sr_2CuO_2Cl_2$ *Marco Guarise*
6017	Low energy muon spin rotation study of the Meissner effect in $La_{2-x}Sr_xCuO_4$ heterostructures *Bastian M. Wojek*
6018	Spectroscopy of cold bosonic atoms by periodically phase-modulation of optical lattice potential *Akiyuki Tokuno*
6019	Semimetal to semiconductor phase transition in $1T\text{–}TiS_2$ induced by Nb doping studied by angle resolved photoemission spectroscopy *Miguel A. Valbuena*
6020	Threshold Voltage and Space Charge in Organic Transistors *Ignacio Gutiérrez Lezama*
6021	Pseudogap and anisotropic far-infrared optical conductivity of URu_2Si_2 *Julien Levallois*
6022	Giant spin orbit splitting from band topology: Experiment and tight-binding approach to the Bi/Si(111) bandstructure *Emmanouil Frantzeskakis*
6023	High Field ESR Study of $(\text{EDT-TTF-CONH})_6Re_6Se_8(CN)_6$ Under Pressure *Dejan Djokic*
6024	Pseudogap Phase of High-Temperature Superconductors Studied by ARPES *Elia Razzoli*
6025	When Superconductivity meets Magnetism: Angle Resolved Photoemission Spectroscopy and Polarized Neutron Reflectometry studies on $YBa_2Cu_3O_{7-x}/La_{0.7}Sr_{0.3}MnO_3$ Bilayers *Milan Radovic*
6026	Magnetically-driven electric polarization in a magneto-electric organo-metallic magnet *M. Kenzelmann*
6027	Manganese silicide nanowires on the Si(001) surface induced by Bi nanolines *James H. G. Owen*
6028	Pauli paramagnetic effects on the flux line lattice in $CeCoIn_5$ *Jonathan S. White*
6029	Anisotropic properties and multi-gap superconductivity in $SmFeAsO_{1-x}F_y$ *Stephen Weyeneth*
6030	Proximal detection of magnetism near the surface of YBCO films using β-NMR *Hassan Saadaoui*
6031	The phase diagram of precursor superconductivity as obtained from the infrared c-axis conductivity of $RBa_2Cu_3O_{7-\delta}$ *Adam Dubroka*
6032	Heat propagation velocities in coated conductors for fault current limiter applications. *Louis Antognazza*
6033	Magnetic and superconducting properties of electron doped $La_{2-x}Ce_xCuO_4$ epitaxial thin films *Hubertus Luetkens*
6034	Effect of a staggered spin-orbit coupling on the occurrence of a nematic phase in $Sr_3Ru_2O_7$ *Mark H. Fischer*
6035	Collective Mode Energy Measured by Scanning Tunneling Spectroscopy Does Not Follow T_c in $Bi_2Sr_2Ca_2Cu_3O_{10+\delta}$ *Nathan Jenkins*
6036	Structural Studies of the Interfaces Between Insulating Metal Oxides *Stephan A. Pauli*
6037	Ultrafast laser-induced spin-reorientation in the heterostructure $Co/SmFeO_3$ *Loic Le Guyader*
6038	High oxygen pressure single crystal growth of spin ladder superconductor $Sr_{14-x}Ca_xCu_{24}O_{41}$ by optical floating zone technique *Guochu Deng*
6039	The spin-mediated pairing interaction of high T_c superconductors: clues from scanning tunneling spectroscopy on $YBa_2Cu_3O_{7-\delta}$ single crystals *Ivan Maggio-Aprile*
6040	Study of magnetoelectric effects (parity and time odd) by resonant x-ray diffraction techniques in $GaFeO_3$ *Urs Staub*
6041	Strong-coupling signatures in the tunneling spectra of metals and superconductors: the role of dimensionality *Christophe Berthod*
6042	Structural and magnetic properties of the parent compound $T'\text{-}La_2CuO_4$ of electron-doped cuprates *Gwendolyne Pascua*
6043	Electronic Structure of Superconducting iron-chalcogenide studied by angle-resolved photoemission spectroscopy *Ping-Hui Lin*

1003	**Electron Spin Resonance Study of SeCuO$_3$**

1003

Electron Spin Resonance Study of SeCuO$_3$

Dejan Djokic [1], Zlatko Mickovic [1], Ivica Zivkovic [2], Kurt Schenk [3], Henrik Ronnow [4], Laszlo Forro [1]
[1] EPFL SB ICMP LPMC, Station 3 – Boîte A, Bâtiment PHD, CH-1015 Lausanne
[2] Institute of Zagreb, Bijeniika 54, HR-10000 Zagreb
[3] EPFL SB IPSB LCR, CH-1015 Lausanne ; [4] EPFL SB ICMP LQM, CH-1015 Lausanne

We carried out 9.4 GHz ESR temperature dependent measurements on a single crystal of SeCuO$_3$ at three crystal orientations. The spectra originating from Cu^{2+} S=1/2 consist of a broad Lorentzian. The extracted spin susceptibility was found to be in good agreement with SQUID data. SeCuO$_3$ undergoes the antiferromagnetic (AF) phase transition at T_N=8 K as was evidenced through the disappearance of the spectra below T_N and seen from the distilled AF correlations in the Curie-Weiss behaviour of the susceptibility. The linewidth behaviour obeys the Kubo-Tomita temperature law of spin relaxation from room temperature down nearly to 50 K below which it starts to diverge and finally vanishes at T_N. Based on the behaviour of the g-factor, linewidth, and susceptibility, magnetic fluctuations were conjectured to lower the mean-field transition temperature. The system belongs to the CuO based family possessing magneto-electric coupling and promises to be exploited for multiferroic applications.

1004

~~Magnetoresistance effects in nanocontacts - studying the dependency on constriction width~~

~~Jakoba Heidler [1], Arndt Von Bieren [2], Ajit Patra [3], Jan Rhensius [1], Laura Heyderman [1], Regina Hoffmann-Vogel [4], Mathias Kläui [2]~~
~~[1] Paul Scherrer Institut, WBBA, CH-5232 Villigen PSI~~
~~[2] Ecole Polytechnique Fédérale de Lausanne, PHH, CH-1015 Lausanne~~
~~[3] Universität Konstanz, Universitätsstr 10, DE-78464 Konstanz~~
~~[4] Karlsruher Institut für Technologie, 4/19, DE-76128 Karlsruhe~~

~~Nanocontacts of variable cross-section fabricated by UHV deposition and in-situ electromigration are used study the evolution of the magnetoresistance from the diffusive to the ballistic regime. We determine the resistance values with and without a magnetic domain wall at zero field as a function of contact size. In the ballistic transport regime the magnetoresistance reaches up to 50% and exhibits a sign change. Atomistic theoretical calculations of the conductance for different atomic configurations of the nanocontact qualitatively reproduce our results highlighting the importance of the detailed atomic arrangement for the magnetoresistance effect.~~

CANCELLED

1005

Thermally activated domain wall depinning: Extraction of the non-adiabatic contribution

Jan Heinen [1], Olivier Boulle [2], Gregory Malinowski [3], Christian Ulysse [4], Giancarlo Faini [4], Mathias Kläui [5]
[1] Fachbereich Physik, Universität Konstanz, Universitätsstr. 10, DE-78457 Konstanz
[2] INAC, CEA, 17 Rue des Martyrs, FR-38054 Grenoble
[3] Lab. de physique des solides, Univ. Paris-sud, Rue Georges Clemenceau, FR-91405 Orsay
[4] Phynano Team, Lab. de Photonique et de Nanostructures, CNRS, Rue Nozay, FR-91460 Marcoussis
[5] Laboratory for Nanomagnetism and Spin Dynamics, EPFL, CH-1015 Lausanne

We report time resolved measurements of the extraordinary hall effect (EHE) on perpendicularly magnetized nanowires with narrow domain wall (DW) structures. Using Co/Pt multilayer nanowires, we have previously shown that despite Joule heating effects it is possible to deduce the non-adiabacity factor beta [1] and determined the contribution of spin torque and Oersted field effects from DW depinning experiments [2].
Time resolved experiments to measure the extraordinary hall voltage of a Hall cross show the existance of multiple metastable pinning sites, which can be used to study thermally activated depinning. The variation of an applied external field and the variation of current allows us to extract of the non-adiabaticity factor beta.

[1] O. Boulle et al., Phys. Rev. Lett. 101, 216601 (2008).
[2] J. Heinen et al., Appl. Phys. Lett. 96, 202510 (2010).

1006

Micromagnetic simulations of depinning process of the magnetic domain wall by propagating spin waves on a magnetic thin film

June-Seo Kim [1], Luis Lopez-Diaz [2], Eduardo Martinez [2], Jungbum Yoon [3], Chun-Yeol You [3], Mathias Kläui [4]
[1] Department Physik, Universität Konstanz, Universitätsstr. 10, DE-78457 Konstanz
[2] Universidad de Salamanca, Plaza de la Merced s/n, ES-37008 Salamanca
[3] Department of Physics, Inha University, 402751 Incheon, Republic of Korea
[4] Laboratory for Nanomagnetism and Spin Dynamics, EPFL, CH-1015 Lausanne

The recent discovery that a propagating spin-wave moves a domain wall has created a new possibility to

Poster N°	Name	Firstname	Authors	Affiliations	Title
65	WANG	Zhiwei	Zhiwei Wang, Enrico Giannini, Alberto Ubaldini, Jacim Jacimovic and Dirk van der Marel	Département de Physique de la Matière Condensée, University of Geneva, Switzerland	Superconductivity and metal-insulator transition in Ca-doped $(Bi_{1-x}Cax)_4O_4S_3$
66	Gerber	Simon	Simon Gerber, Marek Bartkowiak, Jorge L. Gavilano, Eric Ressouche, Nikola Egetenmeyer, Christof Niedermayer, Andrea D. Bianchi, Roman Movshovich, Eric D. Bauer, Joe D. Thompson and Michel Kenzelmann	Laboratory for Neutron Scattering, Paul Scherrer Institut, Villigen, Switzerland Laboratory for Developments and Methods, Paul Scherrer Institut, Villigen, Switzerland SPSMS, INAC, UMR-E CEA/UJF-Grenoble 1, France Deptart ement de Physique & RQMP, Universit e de Montr eal, Quebec, Canada Condensed Matter & Magnet Science, Los Alamos National Laboratory, New Mexico, USA	Switching of magneto-superconducting domains reveals triplet admixing in CeCoIn5
67	Stilp	Evelyn	Evelyn Stilp, Andreas Suter, Elvezio Morenzoni, Thomas Prokscha, Zaher Salman, Hugo Keller, Patrick Pahlke, Ruben Hühne, Jordan C. Baglo, Ruixing Liang and Robert F. Kiefl	Laboratory for Muon Spin Spectroscopy, Paul Scherrer Institut, Villigen PSI, Switzerland Physik-Institut der Universitat Zürich, Switzerland Dresden University of Technology, Department of Physics, Institute for Physics of Solids, Germany Leibniz Institute for Solid State and Materials Research Dresden, Germany Department of Physics and Astronomy, University of British Columbia, Vancouver, Canada	Influence of photo illumination on the Meissner screening profile of underdoped $YBa_2Cu_3O_{7-\delta}$
68	Chang	Johan	Johan Chang, Elizabeth Blackburn, Alex Holmes, Markus Hucker, Niels Bech Christensen, Ruixing Liang, Doug Bonn, Walter Hardy, Uta Ruett, Olof Gutowski, Martin von Zimmermann, Ted Forgan and Stephen Hayden	Institut de la mati ere complexe, Ecole Polytechnique F ederale de Lausanne (EPFL), Switzerland Swiss Light Source, Paul Scherrer Institut, Villigen PSI, Switzerland School of Physics and Astronomy, University of Birmingham, United Kingdom Condensed Matter Physics Materials Science Department, Brookhaven National Laboratory, Upton, New York , USA Department of Physics, Technical University of Denmark, Kongens Lyngby, Denmark Department of Physics Astronomy, University of British Columbia, Vancouver, Canada Canadian Institute for Advanced Research, Toronto, Canada Deutsches Elektronen-Synchrotron DESY, Hamburg, Germany H. H. Wills Physics Laboratory, University of Bristol, United Kingdom	Direct observation of charge-density-wave order in underdoped $YBa_2Cu_3O_{7-x}$
69	Zhigadlo	N.D.	N.D. Zhigadlo, P.J.W. Moll, S. Weyeneth, S. Katrych, K Rogacki, S. Bosma, R. Puzniak, J. Karpinski and B. Batlogg	Laboratory for Solid State Physics, ETH Zurich, Switzerland Physik-Institut der Universitat Zurich, Zurich, Switzerland Institute of Condensed Matter Physics, EPFL, Lausanne, Switzerland Institute of Low Temperature and Structure Research, Wroclaw, Poland Institute of Physics, Polish Academy of Sciences, Warsaw, Poland	Improved growth of $Ln1111$ crystals from $NaAs/KAs$ flux
70	Amundsen	Thomas Brecke	Thomas Brecke Amundsen, Alexandre Piriou, Ivan Maggio Aprile and Oystein Fischer	Université de Genève, Switzerland	Transition from the superconducting to the pseudogap phase in $Bi_2Sr_2Ca_2Cu_3O_{10+d}$ studied by Scanning Tunneling Spectroscopy
71	Pisoni	Andrea	A. Pisoni, R. Gaál, S. Katrych, J. Karpinski and L. Forró	Laboratory of Physics of Complex Matter, EPFL, Switzerland	Physical Properties of a New Iron-Based Superconductor: $Pr_4Fe_2As_2Te_{1-x}O_4$
72	Pascua	Gwendolyne	Gwendolyne Pascua, Hubertus Luetkens, Erwin Wiesenmayer, Zurab Shermadini, Rustem Khasanov, Alex Amato, Hemke Maeter, Hans-Henning Klauss, Hugo Keller, Elvezio Morenzoni and Dirk Johrendt	Laboratory for Muon Spin Spectroscopy, Paul Scherrer Institute, Villigen PSI, Switzerland Institut für Festkörperphysik, Technische Universität Dresden, Germany Physik-Institut der Universität Zürich, Switzerland Department Chemie, Ludwig-Maximilians-Universität München, Germany	Microscopic Coexistence and Competition of Magnetism and Superconductivity in $Ba_{1-x}K_xFe_2As_2$: A Structural, Magnetic, and Superconducting Phase Diagram
73	Legner	Markus	Markus Legner and Titus Neupert	Institut für theoretische Physik, ETH Zürich, Switzerland Condensed Matter Theory Group, Paul Scherrer Institute, Villigen PSI, Switzerland	Interlinkage of the entanglement spectrum, quantum geometry and topology in noninteracting fermionic systems
74	Couto	Nuno	Nuno Couto, Davide Costanzo, Dong-Keun Ki and Alberto Morpurgo	Départment de Physique de la Matiére Condensée (DPMC) and Group of Applied Physics (GAP), University of Geneva	Graphene devices on h-BN substrates
75	Kuzmenko	Alexey	Alexey Kuzmenko, Iris Crassee, Markus Ostler, Thomas Seyller, Jianing Chen and Rainer Hillenbrand	Département de Physique de la Matière Condensée, Université de Genève, Switzerland Lehrstuhl für Technische Physik, Universität Erlangen-Nürnberg, Germany CIC nanoGUNE Consolider, Donostia-San Sebastian, Spain	Optical excitation of plasmons at nano-scale defects in graphene
76	Antognazza	Louis	Louis Antognazza, Michel Decroux, Arnaud Badel and Markus Abplanalp	Université de Genève, DPMC, Switzerland ABB Corporate Research Centre, Baden-Dättwil, Switzerland	A new way to measure the thermal conductance of the DyBCO/substrate interface in coated conductors.
77	Djokic	Dejan	Djokic Dejan, Badel Arnaud, Antognazza Louis, Abplanalp Markus and Decroux Michel	DPMC, University of Geneva, Switzerland ABB Corporate Research Centre, Baden-Dättwil, Switzerland	Hybrid Model of Quench Propagation in Coated Conductors Applied to Fault Current Limiter Design
78	Larose	Daniel	Edmond Koller, Daniel Larose, Jean-Philippe Rapin and Oystein Fischer	Université de Genève, Switzerland	New thin film hydrogen detector device

Ultrafast Electro-modulated Differential Absorption Spectroscopy of Methylammonium Lead Iodide Perovskite Thin Films: Evidence for Carriers Trapping and Accumulation at the Surface [PC-104]
Arun Aby Paraecattil, *Jacques-E. Moser,* EPF Lausanne

Cold ion spectroscopy reveals the exact structure of protonated helical peptides in the gas-phase. [PC-105]
Chiara Masellis, *Thomas R Rizzo,* EPF Lausanne

Femtosecond transient absorption spectroscopy of CsPbX$_3$ perovskite nanoparticles [PC-106]
F. G. Santomauro, *Majed Chergui,* EPF Lausanne

Photoinduced charge transfer mechanism in Diketopyrrolopyrrole(DPP) dye-sensitiezed solar cell [PC-107]
Heewon Bahng, EPF Lausanne

Spectroscopic studies of kinetically trapped conformations in the gas phase: the case of triply protonated bradykinin [PC-108]
Liudmila Voronina, *Thomas R Rizzo,* EPF Lausanne

State-to-state scattering of CH$_4$(v$_3$) from Ni(111) and LiF(100) surfaces. [PC-109]
Maarten van Reijzen, *Rainer Beck,* EPF Lausanne

Infrared spectroscopy of mobility-selected H$^+$-Gly-Pro-Gly-Gly (GPGG) [PC-110]
Michael Z Kamrath, *Thomas R Rizzo,* EPF Lausanne

Electronic energy transfer in model peptides [PC-111]
Valeriu Scutelnic, *Thomas R. Rizzo,* EPF Lausanne

Pushing the limits of cold ion spectroscopy: structural characterization of protonated ubiquitin in the gas phase [PC-112]
Vladimir Kopysov, *Oleg V Boyarkin,* EPF Lausanne

Photoassociation of cesium atoms upon Rydberg excitation in a dense ultracold gas [PC-113]
Heiner Saßmannshausen, *Frédéric Merkt,* ETH Zurich

Precision Spectroscopy in Cold Molecules: The First Rotational Intervals of He$^+_2$ by High-Resolution Spectroscopy and Rydberg-Series Extrapolation [PC-114]
Luca Semeria, *Frédéric Merkt,* ETH Zurich

Continuous trap loading of Rydberg-Stark decelerated metastable helium using overlaid electric and magnetic traps [PC-115]
Matija Zesko, *Frédéric Merkt,* ETH Zurich

MQDT-assisted high-resolution spectroscopy of the Rydberg states of H$_2$ - ionization energy of H$_2$ and rovibrational structure of H$_2$+ [PC-116]
Maximilian Beyer, *Frédéric Merkt,* ETH Zurich

High-Resolution VUV-Absorption Spectroscopy using Phase Modulation [PC-117]
U. Hollenstein, *Frédéric Merkt,* ETH Zürich

Mapping the electronic states of small transition metal clusters by nonlinear spectroscopy [PC-118]
Martin Beck, *Peter Pal Radi,* PSI Villigen

Dissociation dynamics of dissolved CH$_3$I studied with time-resolved resonant inelastic X-ray scattering [PC-119]
Rok Bohinc, PSI Villigen

Femtosecond Time-resolved Spectroscopy in the Extreme Ultraviolet Spectral Range [PC-120]
Jakob Grilj, Stanford University School of Medicine, *Majed Chergui, EPF Lausanne*

Quantum-Logic Spectroscopy for Single Trapped Molecular Ions [PC-121]
Gregor Hegi, *Stefan Willitsch*, University of Basel

Towards hybrid trapping of cold molecules and cold molecular ions [PC-122]
Dominik Haas, *Stefan Willitsch,* University of Basel

Cold Ion-Neutral Reactions in Next-Generation Ion-Atom Hybrid Traps [PC-123]
Pascal Eberle, *Stefan Willitsch,* University of Basel

Ionic Liquids based on crown ether as electrolytes for batteries [PC-124]
Hervé YAO, *Katharina M. Fromm,* University of Fribourg

Electrons and ionic liquids - a novel approach to study electron scattering from nonvolatile compounds [PC-125]
Khrystyna Regeta, *Michael Allan,* University of Fribourg

Ligand exchange reactions with Palladium, Platinum doped Au25(SR)18 clusters [PC-126]
Annelies Sels, *Thomas Bürgi,* University of Geneva

Tracking Solvent Controlled Photoinduced Electron Transfer Using Broadband Fluorescence Up-Conversion [PC-127]
Arnulf Rosspeintner, *Eric Vauthey* University of Geneva

Ligand exchange reaction of chiral Pd$_2$Au$_{36}$(SR)$_{24}$ cluster [PC-128]
Bei Zhang, *Thomas Bürgi,* University of Geneva

Chiral Recognition in Bimolecular Photoinduced Electron Transfer [PC-129]
Christoph Nançoz, *Eric Vauthey,* University of Geneva

Excited-state dynamics of radical ions [PC-130]
Joseph Samuel Beckwith, *Eric Vauthey,* University of Geneva

Separation of chemical shifts and J-couplings using homodecoupled-DIAG spectra [PC-131]
Marta Brucka, *Damien Jeannerat,* University of Geneva

Ultrafast Intersystem-crossing Dynamics and Breakdown of the Kasha-Vavilov's Rule of Naphthalenediimides [PC-132]
Oleksandr Yushchenko, *Eric Vauthey,* University of Geneva

Time Resolved infrared spectroscopy of Ruthenium(II) tris-bipyridyl complexes [PC-133]
Qinchao Sun, *Andreas Hauser,* University of Geneva

Structural investigation of the HS to LS relaxation dynamics on the porous coordination network [Fe(pz)Pt(CN)$_4$]·xH$_2$O [PC-134]
Teresa Delgado, *Andreas Hauser,* University of Geneva

Marangoni flow driven maze solving [PC-135]
Rita Toth, EMPA

Identification of Gas-Phase-Active Reactive Intermediates in Thermal Decomposition of Organophosphorus Compounds [PC-136]
Shuyu Liang, EMPA, *Hansjörg Grützmacher, ETH Zurich*

Exact versus approximate methods for nonadiabatic quantum molecular dynamics induced by the interaction with the electromagnetic field [PC-137]
Aurélien Patoz, *Jiri Vanicek,* EPF Lausanne

Hyperpolarized *para*-ethanol [PC-138]
Daniele Mammoli, *Geoffrey Bodenhausen,* EPF Lausanne

Excitonic Effects and Optical Spectra of Single Walled Carbon Nanotubes for Biosensor Applications in Life Sciences and Medicine [PC-139]
Dejan M Djokic, *Ardemis A. Boghossian*, EPF Lausanne

Studying Xe Migration in Truncated Hemoglobin with Molecular Dynamics Simulations [PC-140]
Polydefkis Diamantis, EPF Lausanne, *Markus Meuwly, University of Basel*

Electron Spin Resonance Study of SeCuO$_3$

D. M. Djokić[*], Z. Micković[*], I. Živković[†], K. Schenk[*], H. Rønnow[*] and L. Forró[*]

[*]*Ecole Polytechnique Fédérale de Lausanne, Lausanne, Switzerland*
[†]*Institute of Physics, Zagreb, Croatia*

Abstract. We have carried out 9.4 GHz ESR temperature dependent $(5 - 300 \text{ K})$ measurements on a single crystalline sample of SeCuO$_3$ for three different crystal orientations. The ESR spectra originating from $S = 1/2$ of Cu^{2+} consist of a single broad exchange narrowed Lorentzian absorption profile. The extracted temperature dependence of absolute spin susceptibility was found to be in good agreement with SQUID data. The compound undergoes the antiferromagnetic (AF) phase transition at $T_N = 8$ K as was evidenced through the disappearance of the ESR spectra below T_N as well as seen from the distilled AF correlations inferred from the Curie-Weiss behaviour of the susceptibility. The line-width behaviour obeys the Kubo-Tomita temperature law of spin relaxation from room temperature down nearly to 50 K below which it starts to diverge and finally vanishes at T_N. Based on the behaviour of the g-factor, line-width, and susceptibility, magnetic fluctuations have been conjectured to lower the mean-field transition temperature drastically. The system belongs to the Cu-O based family possessing magneto-electric coupling induced by the magnetic fluctuations and promises to be exploited for multiferroic applications.

Carbon / organic spintronics

115. *Investigations of N@C60 and N@C70 Stability Under High Pressure and High Temperature Conditions*
A. Iwasiewicz-Wabnig, K. Porfyrakis, G.A.D. Briggs, B. Sundqvist

116. *Hot-electron spin transport in Graphite*
T. Banerjee

117. *Localized Magnetic State and Induced Magnetic Moment in Graphene*
M. Inglot

118. *Spin-orbit coupling and spin relaxation in grapheme*
S. Konschuh, M. Gmitra, C. Ertler, J. Fabian

119. *Magnetism and Correlations of Fractionally Filled Edge-states in Graphene Quantum Dots*
A. D. Guclu, P. Potasz, O. Voznyy, M. Korkusinski, P. Hawrylak

120. *Electron Spin Resonance Study of Graphene-like Materials Suitable for Spintronics Applications*
L. Ćirić, A. Magrez, A. Sienkiewicz, L. Forró

121. *Enhanced magnetoresistance in self-assembled monolayer of oleic acid molecules on Fe3O4 nanoparticles*
S. Wang, F. J. Yue, **D. Wu**, F. M. Zhang, W. Zhong, Y. W. Du

122. *Magnetic Measurements and Modeling of the Anisotropic Molecular-Based Ring Cr7Cd*
P. Kozlowski, G. Kamieniarz, **M. Antkowiak**, F. Tuna, G. A. Timco, R. E. P. Winpenny

123. *High field ESR temperature study on (EDT-TTF-CONH)6Re under pressure*
D. Djokic, A. Olariu, P. Batail, L. Forro

124. *Electrostatic Spin Crossover Effect in magnetic molecules*
N. Baadji, S. Sanvito

125. *Magnetic Exchange in Porphyrin-based Molecular Structures*
D. Sankar Kesanakurthi, N. Baadji, S. Sanvito

126. *Spin-Polarized Transport through a Single-Molecule Magnet*
M. Misiorny, I. Weymann, J. Barnaś

(Ga,Mn)As and related systems

127. *Influence of Annealing on Mn Implanted GaAs Films*
D. Bürger, S. Zhou, J. Grenzer, H. Reuther, W. Anwand, M. Pandey, V. Gottschalch, M. Helm, H. Schmidt

128. *The combined method of MOC-hydride epitaxy and laser deposition for formation of structures with ferromagnetic semiconductor layers*
B. N. Zvonkov, **Y. A. Danilov**, M. V. Dorokhin, Y. N. Drozdov, A. V. Kudrin, M. V. Sapozhnikov, O. V. Vikhrova

129. *Modeling of Mn-doped III-V Nanowires*
M. Galicka, M. Bukała, R. Buczko, P. Kacman

Technology - Netherlands, [3]Istituto di Fotonica e Nanotecnologie, CNR, Roma - Italy

3P-EL3-11

Superconducting Nanowire Single Photon Detectors with Reduced Area for energy-efficient Optical-to-Electrical Converters
Kajino K.[1], Yamashita T.[1], Miki S.[1], Terai H.[1], Wang Z.[1]
[1]NICT - Japan

3P-EL3-12

Approaching the theoretical depairing current in YBCO nanowires
Arpaia R.[1], Nawaz S.[1], Bauch T.[1], Lombardi F.[1]
[1]Chalmers University of Technology - Sweden

3P-EL3-13

Photoresponse experiments on parallel superconducting YBCO nanowires
Arpaia R.[1], Arzeo M.[1], Nawaz S.[1], Bauch T.[1], Lombardi F.[1], Ejrnaes M.[2], Cristiano R.[2], Pepe G.P.[3], Parlato L.[3], Tafuri F.[4]
[1]Chalmers University of Technology - Sweden, [2]Istituto di Cibernetica "E. Caianiello" del Consiglio Nazionale delle Ricerche - Italy, [3]University of Naples Federico II - Italy, [4]Università degli studi di Napoli Federico II - Italy

3P-LS1: Fault Current Limiters II
Wednesday, September 18 @ 14:15 in Poster Area
Chair: *Carlos Baldan, Daniele Colangelo*

3P-LS1-01

Electromagnetic Characteristics Analysis of 500kV Single Phase Saturated core Type Superconducting Fault Current Limiter
Meng S.[1]
[1]Yunnan Power Grid Corp. - China

3P-LS1-02

Hysteretic Dependence of Magnetic Flux Density on Primary AC Current in Flat-Type Inductive Fault Current Limiter with YBCO Thin Film Discs.
Harada M.[1], Okuda K.[1], Yokomizu Y.[1], Matsumura T.[1]
[1]Nagoya University - Japan

3P-LS1-03

Improved Heat Propagation in Coated Superconducting Fault Current Limiters
Djokic D.[1], Antognazza L.[2], Badel A.[3], Decroux M.[1], Abplanalp M.[4]
[1]DPMC, University of Geneva - Switzerland, [2]University of Geneva - Switzerland, [3]CRETA, G2Elab, Grenoble - France, [4]ABB Research Center, Baden-Dätwil - Switzerland

ID	MaNEP Poster
6001	$Fe_{1+y}Se_xTe_{1-x}$ superconductors: phase diagram, crystal growth, structural and magnetic properties *Ekaterina Pomjakushina*
6002	Evidence for large electric polarization from collinear commensurate magnetism in multiferroic $TmMnO_3$ *Vladimir Y. Pomjakushin*
6003	Optical Investigation of the Charge Dynamics in $Ba(Co_xFe_{1-x})_2As_2$ *Andrea Lucarelli*
6004	Morphology, Elasticity and Slow Dynamics of Superconducting Vortex Lattices Investigated with Time Resolved Stroboscopic Neutron Scattering. *Sebastian Mühlbauer*
6005	Influence of doping on the strong rail spin ladder compound $(2,3-dmpyH)_2CuBr_4$ *Sebastian Mühlbauer*
6006	Electron paramagnetic resonance investigation of $EuFe_{2-x}Co_xAs_2$ (x=0, 0.1, 0.2) single crystals *Zurab Guguchia*
6007	Muon spin rotation study of the CaC_6 superconductor at low temperatures *Ferenc Muranyi*
6008	Metallic-like temperature dependence of the mobility in n-type organic single-crystal field effect transistors *Nikolas Minder*
6009	Equilibrium and out of equilibrium studies of ultracold fermions in an optical lattice *Thomas Uehlinger*
6010	MuSR studies of the heavy fermion $CeRhSi_3$ *Nikola Egetenmeyer*
6011	Graphene based devices on top of single crystal $SrTiO_3$ substrates *Nuno J. G. Couto*
6012	Dissipation-driven phase transitions in superconducting wires *Alejandro M. Lobos*
6013	Dynamical correlation functions in spin-1/2 ladders under a magnetic field *Pierre Bouillot*
6014	Anisotropic properties of superconducting single crystals of $La_{2-x}Sr_xCuO_4$ *Saskia Bosma*
6015	Ferromagnetic spin resonance in $EuTiO_3$ probed by time-domain THz ellipsometry *J. L. M. van Mechelen*
6016	Evidence for extended magnetic interactions in the cuprates from the magnon dispersion of $Sr_2CuO_2Cl_2$ *Marco Guarise*
6017	Low energy muon spin rotation study of the Meissner effect in $La_{2-x}Sr_xCuO_4$ heterostructures *Bastian M. Wojek*
6018	Spectroscopy of cold bosonic atoms by periodically phase-modulation of optical lattice potential *Akiyuki Tokuno*
6019	Semimetal to semiconductor phase transition in $1T–TiS_2$ induced by Nb doping studied by angle resolved photoemission spectroscopy *Miguel A. Valbuena*
6020	Threshold Voltage and Space Charge in Organic Transistors *Ignacio Gutiérrez Lezama*
6021	Pseudogap and anisotropic far-infrared optical conductivity of URu_2Si_2 *Julien Levallois*
6022	Giant spin orbit splitting from band topology: Experiment and tight-binding approach to the Bi/Si(111) bandstructure *Emmanouil Frantzeskakis*
6023	High Field ESR Study of $(EDT-TTF-CONH)_6Re_6Se_8(CN)_6$ Under Pressure *Dejan Djokic*
6024	Pseudogap Phase of High-Temperature Superconductors Studied by ARPES *Elia Razzoli*
6025	When Superconductivity meets Magnetism: Angle Resolved Photoemission Spectroscopy and Polarized Neutron Reflectometry studies on $YBa_2Cu_3O_{7-x}/La_{0.7}Sr_{0.3}MnO_3$ Bilayers *Milan Radovic*
6026	Magnetically-driven electric polarization in a magneto-electric organo-metallic magnet *M. Kenzelmann*
6027	Manganese silicide nanowires on the Si(001) surface induced by Bi nanolines *James H. G. Owen*
6028	Pauli paramagnetic effects on the flux line lattice in $CeCoIn_5$ *Jonathan S. White*
6029	Anisotropic properties and multi-gap superconductivity in $SmFeAsO_{1-x}F_y$ *Stephen Weyeneth*
6030	Proximal detection of magnetism near the surface of YBCO films using β-NMR *Hassan Saadaoui*
6031	The phase diagram of precursor superconductivity as obtained from the infrared c-axis conductivity of $RBa_2Cu_3O_{7-\delta}$ *Adam Dubroka*
6032	Heat propagation velocities in coated conductors for fault current limiter applications. *Louis Antognazza*
6033	Magnetic and superconducting properties of electron doped $La_{2-x}Ce_xCuO_4$ epitaxial thin films *Hubertus Luetkens*
6034	Effect of a staggered spin-orbit coupling on the occurrence of a nematic phase in $Sr_3Ru_2O_7$ *Mark H. Fischer*
6035	Collective Mode Energy Measured by Scanning Tunneling Spectroscopy Does Not Follow T_c in $Bi_2Sr_2Ca_2Cu_3O_{10+\delta}$ *Nathan Jenkins*
6036	Structural Studies of the Interfaces Between Insulating Metal Oxides *Stephan A. Pauli*
6037	Ultrafast laser-induced spin-reorientation in the heterostructure $Co/SmFeO_3$ *Loic Le Guyader*
6038	High oxygen pressure single crystal growth of spin ladder superconductor $Sr_{14-x}Ca_xCu_{24}O_{41}$ by optical floating zone technique *Guochu Deng*
6039	The spin-mediated pairing interaction of high T_c superconductors: clues from scanning tunneling spectroscopy on $YBa_2Cu_3O_{7-\delta}$ single crystals *Ivan Maggio-Aprile*
6040	Study of magnetoelectric effects (parity and time odd) by resonant x-ray diffraction techniques in $GaFeO_3$ *Urs Staub*
6041	Strong-coupling signatures in the tunneling spectra of metals and superconductors: the role of dimensionality *Christophe Berthod*
6042	Structural and magnetic properties of the parent compound T'-La_2CuO_4 of electron-doped cuprates *Gwendolyne Pascua*
6043	Electronic Structure of Superconducting iron-chalcogenide studied by angle-resolved photoemission spectroscopy *Ping-Hui Lin*

1003	**Electron Spin Resonance Study of SeCuO$_3$**

Dejan Djokic [1], Zlatko Mickovic [1], Ivica Zivkovic [2], Kurt Schenk [3], Henrik Ronnow [4], Laszlo Forro [1]
[1] EPFL SB ICMP LPMC, Station 3 – Boîte A, Bâtiment PHD, CH-1015 Lausanne
[2] Institute of Zagreb, Bijeniika 54, HR-10000 Zagreb
[3] EPFL SB IPSB LCR, CH-1015 Lausanne ; [4] EPFL SB ICMP LQM, CH-1015 Lausanne

We carried out 9.4 GHz ESR temperature dependent measurements on a single crystal of SeCuO$_3$ at three crystal orientations. The spectra originating from Cu^{2+} S=1/2 consist of a broad Lorentzian. The extracted spin susceptibility was found to be in good agreement with SQUID data. SeCuO$_3$ undergoes the antiferromagnetic (AF) phase transition at T$_N$=8 K as was evidenced through the disappearance of the spectra below T$_N$ and seen from the distilled AF correlations in the Curie-Weiss behaviour of the susceptibility. The linewidth behaviour obeys the Kubo-Tomita temperature law of spin relaxation from room temperature down nearly to 50 K below which it starts to diverge and finally vanishes at T$_N$. Based on the behaviour of the g-factor, linewidth, and susceptibility, magnetic fluctuations were conjectured to lower the mean-field transition temperature. The system belongs to the CuO based family possessing magneto-electric coupling and promises to be exploited for multiferroic applications.

1004	~~**Magnetoresistance effects in nanocontacts -**~~ ~~**studying the dependency on constriction width**~~

~~*Jakoba Heidler [1], Arndt Von Bieren [2], Ajit Patra [3], Jan Rhensius [1], Laura Heyderman [1],*~~
~~*Regina Hoffmann-Vogel [4], Mathias Kläui [2]*~~
~~*[1] Paul Scherrer Institut, WBBA, CH-5232 Villigen PSI*~~
~~*[2] Ecole Polytechnique Fédérale de Lausanne, PHH, CH-1015 Lausanne*~~
~~*[3] Universität Konstanz, Universitätsstr 10, DE-78464 Konstanz*~~
~~*[4] Karlsruher Institut für Technologie, 4/19, DE-76128 Karlsruhe*~~

~~Nanocontacts of variable cross-section fabricated by UHV deposition and in-situ electromigration are used study the evolution of the magnetoresistance from the diffusive to the ballistic regime. We determine the resistance values with and without a magnetic domain wall at zero field as a function of contact size. In the ballistic transport regime the magnetoresistance reaches up to 50% and exhibits a sign change. Atomistic theoretical calculations of the conductance for different atomic configurations of the nanocontact qualitatively reproduce our results highlighting the importance of the detailed atomic arrangement for the magnetoresistance effect.~~

CANCELLED

1005	**Thermally activated domain wall depinning: Extraction of the non-adiabatic contribution**

Jan Heinen [1], Olivier Boulle [2], Gregory Malinowski [3], Christian Ulysse [4], Giancarlo Faini [4], Mathias Kläui [5]
[1] Fachbereich Physik, Universität Konstanz, Universitätsstr. 10, DE-78457 Konstanz
[2] INAC, CEA, 17 Rue des Martyrs, FR-38054 Grenoble
[3] Lab. de physique des solides, Univ. Paris-sud, Rue Georges Clemenceau, FR-91405 Orsay
[4] Phynano Team, Lab. de Photonique et de Nanostructures, CNRS, Rue Nozay, FR-91460 Marcoussis
[5] Laboratory for Nanomagnetism and Spin Dynamics, EPFL, CH-1015 Lausanne

We report time resolved measurements of the extraordinary hall effect (EHE) on perpendicularly magnetized nanowires with narrow domain wall (DW) structures. Using Co/Pt multilayer nanowires, we have previously shown that despite Joule heating effects it is possible to deduce the non-adiabacity factor beta [1] and determined the contribution of spin torque and Oersted field effects from DW depinning experiments [2].
Time resolved experiments to measure the extraordinary hall voltage of a Hall cross show the existance of multiple metastable pinning sites, which can be used to study thermally activated depinning. The variation of an applied external field and the variation of current allows us to extract of the non-adiabaticity factor beta.

[1] O. Boulle et al., Phys. Rev. Lett. 101, 216601 (2008).
[2] J. Heinen et al., Appl. Phys. Lett. 96, 202510 (2010).

1006	**Micromagnetic simulations of depinning process of the magnetic domain wall by propagating spin waves on a magnetic thin film**

June-Seo Kim [1], Luis Lopez-Diaz [2], Eduardo Martinez [2], Jungbum Yoon [3], Chun-Yeol You [3], Mathias Kläui [4]
[1] Department Physik, Universität Konstanz, Universitätsstr. 10, DE-78457 Konstanz
[2] Universidad de Salamanca, Plaza de la Merced s/n, ES-37008 Salamanca
[3] Department of Physics, Inha University, 402751 Incheon, Republic of Korea
[4] Laboratory for Nanomagnetism and Spin Dynamics, EPFL, CH-1015 Lausanne

The recent discovery that a propagating spin-wave moves a domain wall has created a new possibility to

SAO/NASA ADS **Physics Abstract Service**

· **Find Similar Abstracts** (with **default settings below**)

· **Electronic On-line Article (HTML)**

· **Reads History**

·

· **Translate This Page**

Title:	Magneto-Electric Coupling in Single Crystal Cu_2OSeO_3 Studied by a Novel Electron Spin Resonance Technique
Authors:	Maisuradze, Alexander ; Shengelaya, Alexander ; Berger, Helmuth ; Djokić, Dejan ; Keller, Hugo
Publication:	American Physical Society, APS March Meeting 2013, March 18-22, 2013, abstract #F21.009
Publication Date:	03/2013
Origin:	APS
Bibliographic Code:	2013APS..MARF21009M

Abstract

The magneto-electric (ME) coupling on spin-wave resonances in single-crystal Cu_2OSeO_3 was studied by a novel technique using electron spin resonance combined with electric field modulation. An external electric field E induces a magnetic field component $\mu_0 H^i = \gamma E$ along the applied magnetic field H with $\gamma = 0.7(1)\ \mu T/(V/mm)$ at 10 K. The ME coupling strength γ is found to be temperature dependent and highly anisotropic. $\gamma(T)$ nearly follows that of the spin susceptibility $J^M(T)$ and rapidly decreases above the Curie temperature T_c. The ratio γ/J^M monotonically decreases with increasing temperature without an anomaly at T_c.

Bibtex entry for this abstract   **Preferred format for this abstract** (see **Preferences**)

Add this article to private library	Remove from private library

| Submit corrections to this record | View record in ADS Bumblebee | NEW! |

Find Similar Abstracts:

Use: ☐ Authors

        ☑ Title

        ☑ Abstract Text

Return: ● Query Results Return `100` items starting with number `1`

        ○ Query Form

Database: ☐ Astronomy

        ☑ Physics

        ☐ arXiv e-prints

| Send Query | Reset |

Heat Propagation Improvement in YBCO-Coated Conductors for Superconducting Fault Current Limiters

D. M. Djokic[1], L. Antognazza[1], M. Abplanalp[2], M. Decroux[1]
[1]DPMC, University of Geneva, Geneva, Switzerland
[2]ABB Corporate Research Centre, Dättwil, Switzerland

YBCO Coated Conductors (CCs), used for applications in Resistive Superconducting Fault Current Limiters (RSFCLs), are known to have insufficiently high Normal Zone Propagation Velocity (NZPV) during quench events. The improvement can be made by enhancing the thermal conductivity of YBCO-CCs with no decrease in the electrical resistivity. We studied the advantage of multilayered structures grown on a cheap fused silica with thickness of 90 µm. The multilayer is composed of: a several microns thick copper layer to enhance the thermal conductivity, a layer to prevent the inter-diffusion, and a Hastelloy top layer. We carried out 3D FEM simulations in COMSOL Multiphysics® on a meander configuration to calculate NZPV. The simulation results show a marked improvement as compared to the earlier cases.

Download

djokic_poster.pdf (/paper/download/199691/djokic_poster.pdf) - 0.79MB
djokic_paper.pdf (/paper/download/199689/djokic_paper.pdf) - 0.47MB
djokic_abstract.pdf (/paper/download/199687/djokic_abstract.pdf) - 0.02MB

Dear Dejan,

Thank you for your participation in the COMSOL Conference 2014 Cambridge. Your work titled "Heat Propagation Improvement in YBCO-Coated Conductors for Superconducting Fault Current Limiters" has been approved and will be scheduled in the poster presentation session.

If you haven't registered for the conference, please do so as soon as possible so we can post your abstract on the web. Here is the link to register: http://www.comsol.com/conference2014/europe/register/.

You are also encouraged to submit a full length paper that will be published in the Conference Proceedings. Please use the paper template to prepare your paper. The paper can be uploaded online through "My Conference" by logging into your COMSOL Access account. You can find the paper template here: http://www.comsol.com/conference2014/europe/instructions/.

Your contribution to the COMSOL Conference is deeply appreciated. We look forward to seeing you at the conference!

Best Regards,
Robbie Balcombe, PhD
COMSOL Ltd.
Tel: +44 (0) 1223 451580
Fax: +44 (0) 1223 367361

Electron Spin Resonance of Novel Materials

THÈSE N^O 5537 (2012)

PRÉSENTÉE LE 2 NOVEMBRE 2012
À LA FACULTÉ DES SCIENCES DE BASE
LABORATOIRE DE PHYSIQUE DE LA MATIÈRE COMPLEXE
PROGRAMME DOCTORAL EN PHYSIQUE

ÉCOLE POLYTECHNIQUE FÉDÉRALE DE LAUSANNE

POUR L'OBTENTION DU GRADE DE DOCTEUR ÈS SCIENCES

PAR

Dejan DJOKIĆ

acceptée sur proposition du jury:

Prof. N. Grandjean, président du jury
Prof. L. Forró, directeur de thèse
Prof. H. Keller, rapporteur
Prof. Ph. Turek, rapporteur
Prof. O. Yazyev, rapporteur

ÉCOLE POLYTECHNIQUE
FÉDÉRALE DE LAUSANNE

Suisse
2012

Contents

Abstract

Novel magnetic materials are constantly emerging. This thesis reports an Electron Spin Resonance (ESR) study on three novel materials of great scientific interest: monoclinic $SeCuO_3$ compound representing a network of tetramers, large assembly of ultrathin graphitic nanoparticles obtained by heavy sonication of graphite powder, and newly synthesized organic system $(EDT-TTF-CONH_2)_6Re_6Se_8(CN)_6$ which spans a kagomé topology above 200 K. Respecting the order of the selected materials, the following phenomena have been observed. The inter tetramer antiferromagnetic coupling in $SeCuO_3$ was found responsible for the development of a fluctuating long-range antiferromagnetic order at $T = 8$ K with an unusual temperature dependence of the effective g-tensors. These observations were explained by site selective quantum correlations. In consistency with the picture of magnetic correlations at 1D graphene edges, the temperature dependence of the ESR spectra in the graphitic sample signified the onset of ferromagnetic correlations below 25 K, but the true long-range ferromagnetic ordering was missing and the magnetic state was interpreted as a superparamagnetic like phase. Through ESR measurements at low and high frequencies, the temperature and pressure dependence of the magnetic response of $(EDT-TTF-CONH_2)_6Re_6Se_8(CN)_6$ were investigated. The major finding was the cohabitation of correlations and metallicity in a dynamically disordered kagomé lattice at high temperatures. Below 200 K the system looses the kagomé geometry and an antiferromagnetic spin exchange stabilizes the system. Conclusively, the thesis also demonstrates the powerfulness of ESR spectroscopy to link and combine different physical phenomena in emergent magnetic materials that is of great fundamental

and of possibly practical significance.

Version abrégée

De nouveaux matériaux magnétiques sont découverts constamment. Cette thèse présente une étude de résonance paramagnétique électronique (RPE) sur trois nouveaux matériaux qui sont de grand intérêt scientifique: le composé monoclinique $SeCuO_3$ représentant un réseau de tétramères, les assemblages de nanoparticules ultra fine graphitique obtenus par forte sonication de poudre de graphite, et le système organique nouvellement synthétisé $(EDT-TTF-CONH_2)_6Re_6Se_8(CN)_6$ qui adopte une topologie de kagomé au dessus de 200 K. En respectant l'ordre des matériaux sélectionnés, ce qui suit a été observée. Le couplage entre tétramères antiferromagnétiques dans $SeCuO_3$ a été démontré responsable du développement d'un ordre fluctuant antiferromagnétique à longue distance à $T = 8$ K avec une dépendance inhabituelle des g-tenseurs effectifs observés avec la température. Ceci a été expliqué par les corrélations quantiques de site sélectifs. De facon cohérente avec l'image des corrélations magnétiques aux bords de graphène 1D, la dépendance en température des spectres RPE dans l'échantillon graphitique a signifié le début de corrélations ferromagnétiques en dessous de 25 K, mais il n'y a pas du véritable ordre longue-distance ferromagnétique qui a été observée et l'état magnétique était interprété comme une phase superparamagnétique. Grâce aux mesures RPE basses et hautes fréquencse, le comportement de $(EDT-TTF-CONH_2)_6Re_6Se_8(CN)_6$ avec la température et sous pression a été étudié avec les principales conclusions d'une cohabitation entre corrélations et métallicité à haute température, qui a été interprété par la présence d'un échange de chaînes de spins anitferroagnétiques déstabilisant le système en dessous de 200 K et une topologie de kagomé dynamiquement désordonnée. En

conclusion, la thèse démontre aussi la puissance de la spectroscopie RPE pour lier et combiner différentes physiques observées dans les divers matériaux magnétiques émergents qui sont d'une importance fondamentale et éventuellement pratique.

mots-clés : résonance magnétique; oxides cuivriques multiferriques; graphène avec défection; conducteurs organiques à faible dimension.

Acknowledgments

Introduction

Exploiting Spin in Novel Materials

This dissertation deals with magnetism. Using a special technique called Electron Spin Resonance (ESR) I was exploring the magnetic properties of novel materials to learn how the spin, a tiny compass in exotic, novel materials behaves. What are the conditions to align them to create a magnet; how does the geometry of the crystal influences it; can one manipulate their ordering by electric current, etc? This research is of strongly fundamental character; nevertheless I hope that the knowledge obtained this way will be one day useful in some applications.

Magnetism has started in the ancient times as a curiosity, a stone which attracts iron, but it has developed into an applied science, with its use in compass for orientation, to inform the sailors about the directions, one can say that into the information technologies (IT) of those days (Fig. 1a). Today, magnetism is at the heart of IT, for the time being as the working principle of the most powerful memory devices, magnetic random access memories, or MRAMs (Fig. 1b). The central unit in both cases, compass and hard disc is the electron, with its magnetic moment, its spin (Fig. 1c).

Figure 1a	Figure 1b	Figure 1c

The way was long to understand the connection between spin and magnetism. The treatment of magnetism has started in the 16th century by William Gilbert, who was revolted by the occult use of magnetite in everyday life, and who wrote his treaty *De Magnete* in 1600 which was the first scientific approach to it. A further big step was the recognition of the connection between electric charge and magnetism in the 19th century. The culmination of the classical description of this connection were the Maxwell equations which gave not only the unification of the two phenomena, electricity, and magnetism, but it had also a predictive power, to give the speed of light.

A radically new look on magnetism was started with quantum mechanics at the beginning of the 20th century. It was realized that the magnetic moment of an electron is much more than just a minute compass; it is a complex quantum mechanical property of electron, which creates a tiny magnetic field. For the sake of simplicity, spin is given a direction, either *up* or *down*. Just as the low resistance or high resistance values used to encode data as the 0s and 1s of the binary system used in our computers. But unlike charge-based data storage, spin-based storage does not disappear when the electrical current stops.

The expectations are much higher than just not to lose the information in a switched-off state! Researchers think that the spin can revolutionize IT by spintron-

ics and quantum computing. It is widely known not only for those who work in IT technology that Moore's law, which states that computing power doubles every eighteen months, will come to an end very soon. It is due to the fact that one cannot miniaturize ad absurdum, making smaller and smaller structures for storing more and more information per cm^2. Moore's law will be replaced by some other theory that will take into account the immense capabilities of the quantum character of spin. This is offered by the new platforms of spintronics and quantum computing.

Spintronics is an emerging area of solid-state physics that attempts to use the spin as well as the charge of electrons to process data more efficiently. Electron spin is already making its mark on the computer industry with the development of magnetic random access memory chips, or MRAMs. MRAM can also store data in a much smaller space and access it much more quickly, while consuming far less power than today's charge-based memory. Spin also has some potential benefits for speed. In charge-based electronics, the speed is set by the RC time constants. In utilizing spin, it may be possible to circumvent this general rule. There is a great opportunity to make high speed, low power applications based on spins, but novel circuit architectures need to be developed to bring this to realization. But for computing there is a problem: electron spins have a fairly short lifetime, which in practice would lead to corrupt data. For this reason scientists have been looking for new and better ways to store and retrieve information and this is quantum computing (QC).

Quantum computers may represent the next major paradigm shift in technology. In theory, such computers could perform faster and more complex computations using a fraction of the energy. The basic principle of QC is the following. While conventional computers store data as *bits* with value 1 or 0, in quantum computing data
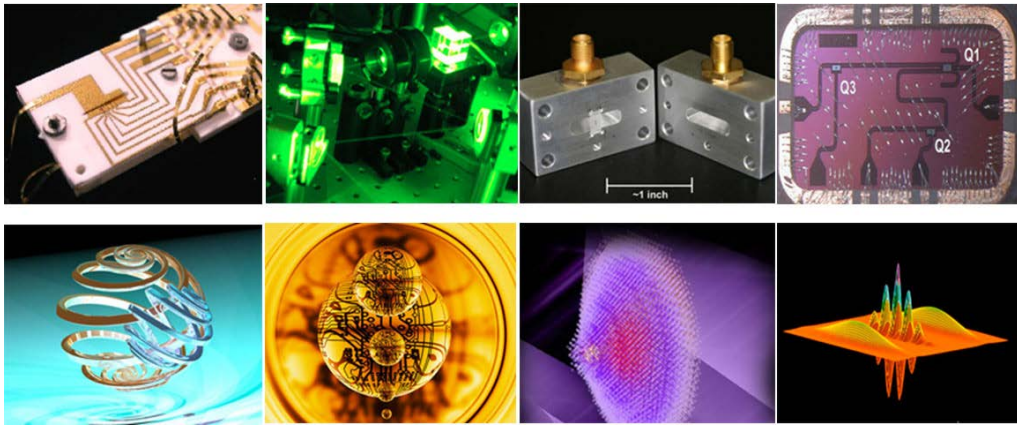
Figure 2: Upper row: Few trial for the realization of a quantum computer: Trapped ions, optical lattices, cavity-based quantum electrodynamics, superconductor-based quantum device. Lower row: Artistic visions of quantum entanglement and quantum computing.

is stored as *qubits*, which can hold more than one value at the same time. Qubits are quantum states stored in particles (photons, electrons, atoms) that can become *entangled* with other quantum states, allowing them to transfer information instantaneously regardless of their separation distance. This is difficult to grasp with our experience in macroscopic world, but this is inherent to the quantum world. The special properties of qubits will allow quantum computers to work on millions of computations at once. A single 250-qubit state contains more bits of information than there are atoms in the universe!

There are many physical systems, not only spins, to realize the qubits. Trapped ions, cavity-based quantum electrodynamics, optical lattices, nuclear magnetic resonance on molecules in solution, superconductor-based quantum computers etc (see upper row of Figure 2). As one can see, these devices are far from being small, nano-

metric. For the time being, the goal is to create qubits and to demonstrate the proof of principles. However, in practice, building a QC is a very tricky engineering challenge. In art-work (lower row in Figure 2) the realization of QC is "more advanced" than in manufacturing it.
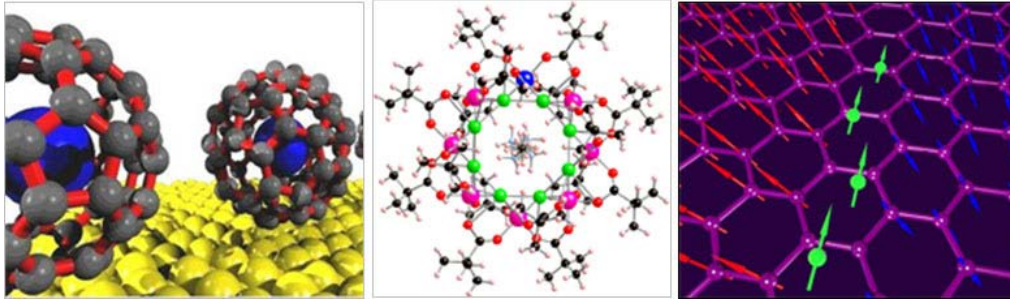
Figure 3: Few materials which are considered for quantum computing and spintronics: endohedral fullerenes, molecular magnets and graphene.

The problem is that qubits are very gossamer. One should be able to interact with them, to write in the information, but they evaporate quickly before the read-out if they are slightly perturbed by the environment. Across all areas of nanotechnology research and broader, there is a great effort to find new kinds of materials which allow easy inscription but they could keep the coherence of quantum states for a long enough time.

Figure 3 gives few examples of materials' classes which are considered for QC (and spintronics) applications. These are fullerene-based materials (endohedral fullerenes or peapods), molecular magnet, graphene and much more. In these materials the major questions are: what is the lifetime of a given spin state; what is the interaction between spins, can one stabilize a long range order; what is the role of defects; how

does geometrical frustration, low-dimensionality of the structure influence the spin life-time, can one influence spin interactions by electric field? In a broad sense, these questions were the leitmotif of my PhD training.

Structure and Subject of the Thesis

The impetus of this thesis has emerged from a need to understand the properties of some of the current novel materials by means of Electron Spin Resonance spectroscopy. Novel and emergent magnetic materials are attracting major interest in condensed matter research as their wide ranging novel properties seem to be not only important for basic research but also for various applications. The primary purpose of this thesis is to present and discuss experimental results obtained by ESR on cutting-edge novel materials which include: $SeCuO_3$ − a cupric oxide quantum antiferromagnet with an indicative multiferroicity, defected graphene bottled-up in a nanographitic sample, and $(EDT\text{-}TTF\text{-}CONH_2)_6Re_6Se_8(CN)_6$ − an organic, charge transfer, possibly low dimensional topological insulator with kagomé geometry. Graphene and organic topological insulators, in particular, constitute a novel class of materials in condensed matter physics whose low energy quasiparticles follow Dirac-like, rather than Schrödinger-like, equation.

The central experimental technique employed to complete the aim of the thesis is ESR. As very sensitive and informative, it continues to find important applications not only in solid state but also in biomedical and environmental sciences. Given that it directly measures the spin response, ESR spectroscopy is certainly one of the most powerful tools to investigate magnetic properties of dense both 3D and low

dimensional spin systems, as well as magnetically diluted compounds. Also, ESR is noninvasive and contactless probe with ability to analyze directly the nature and dynamics of charge carriers in conductive systems. Employing high field ESR is particularly useful in obtaining improved resolution of overlapping signals and the proper interpretation of acquired data.

Nearly seven decades have elapsed since the very first observation of ESR by USSR scientist Zavoisky in 1944. Over that period till now, many monographs, several textbooks, a large number of reviews, and a few hand books, have been revealed including a great deal of achievements in theory, instrumentation, as well as application to an enormous amount of materials. The ESR repository in literature is immense, and comprehensive treatments on ESR can be found elsewhere. Following citations, two pioneering books are singled out: *Electron Paramagnetic Resonance* by S. A. Al'tschuler and B. M. Kozyarev (1964), and *Electron Paramagnetic Resonance of Transition Ions* by A. Abragam and B. Bleaney (1970). For more details regarding ESR, the reader is kindly asked to refer to the two outstanding books.

As a brief overview, this thesis falls into three chapters and is organized as follows.

In Chapter 1, a 9.4 GHz ESR study, carried out on antiferromagnetic (AF) $SeCuO_3$ insulator, is presented. Unlike other polymorphs which are ferromagnets, the crystal structure of the studied compound obeys $P2_1/n$ monoclinic space group symmetry. It has been proven that $SeCuO_3$ stands for a solid quantum antiferromagnet according to the existing AF correlations which extend well above $T_N \simeq 8$ K to nearly 170 K. This temperature emerges from one of the isotropic AF exchange interactions in the system that has been deduced from the temperature behaviour of both measured linewidth and g-factor. The temperature dependence of the linewidth has been successfully

7

fitted using a semi-empirical model for spin relaxation. In this respect, there are two approaches of interest this model relies on: Kubo-Tomita and Oshikawa-Affleck. Analyzing g-factor behaviour and ESR spin susceptibility, we have also concluded that ferromagnetic and antiferromagnetic interactions compete in $SeCuO_3$ above T_N. This is connected with opening up a broad temperature sector $T_N \ll T \ll \theta \sim J$, which very often takes place in frustrated antiferromagnets. In addition, temperature dependence of the measured g-factor has been observed that is due to the inequivalent copper sites which experience different type of quantum correlations. We have made a reasonable assumption that the on-site g-tensors are temperature independent. The assumption has proven valid in most of akin compounds. Monoclinicity of the $SeCuO_3$ crystal symmetry has also been attested by ESR assessing the principal values of the g-factor tensor at 50 K. Finally, ESR has provided an indication of a likely existence of multiferroicity in $SeCuO_3$ around T_N. The related results were published in *Physical Review B*.

In Chapter 2, we have made an interesting observation on spin ordering phenomena in a nanographitic sample by X-band ESR. Following the high-yield production of the sample, it contains a considerable quantity of graphene, based on which we have interpreted the data. Carbon spins have been found to align ferromagnetically below 25 K in accordance with the Lieb's theory for a bipartite 2D lattice. These findings squarely follow from the temperature behaviour of g-factor, linewidth, and susceptibility. Both g-factor and linewidth have been analyzed in terms of 2D ferromagnetism which requires the extension of the Kubo-Tomita theory up to accounting for spin 2D diffusion phenomena. The temperature dependence of ESR extracted susceptibility exhibits a Pauli like paramagnetism down to 25 K below which a nearly

Ising type enhancement is noticed. The ferromagnetic interaction is found to origi-nate from defects created during the sonication of the graphitic powder. Although a ferromagnetic coupling is present, the system is not capable of forming the true ferromagnetic state, rather superparamagnetic one. The accompanied transport data have also corroborated the emergence of such magnetism together with DFT calcula-tions. These calculations reveal that hydrogen functionalization is responsible for the existence of the ferromagnetic coupling. The corresponding results were published in *Physical Review B.*

In Chapter 3, through X-band ESR and 210 GHz ESR measurements under pres-sure we have studied the $(EDT-TTF-CONH_2)_6Re_6Se_8(CN)_6$ system in which the or-ganic dimers are organized into a kagomé network in the high temperature regime above 200 K. The kagomé topology is unprecedented for any TTF-based material ever studied. The ESR measurements, together with associated transport data, have clearly shown the existence of metallic behaviour at high temperature. The observed metallic state has been found to have a strong two-dimensional character, in co-herence with the kagomé lattice symmetry at a third filling. The ESR data have, surprisingly, revealed the presence of correlations at high temperature, through the large value of the magnetic susceptibility and its Curie-Weiss temperature depen-dence. By means of ESR, the evolution of the structure under hydrostatic pressure has been additionally tracked out and has revealed a shift of a dimensional crossover towards higher temperatures, occurring around 8 kbar. In literature, the coexistence of magnetism and metallic behaviour in the high temperature regime has already been predicted theoretically for the kagomé lattice at a third filling by accounting for correlations − correlated topological insulator. At low temperature insulator phase,

9

we have demonstrated a quantitative agreement with the Oshikawa-Affleck model for antiferromagnetic spin 1/2 chains with dipolar exchange anisotropy and staggered field. The related results combined with the theory of dense dynamic disorder are to be submitted to *Nature Materials*.

Finally, the summary and concluding remarks of the thesis outline the main results and provide perspectives for future investigations.

Chapter 1

Electron Spin Resonance of Tetramer SeCuO$_3$ System

1.1 Introduction

With unstoppably accelerating trends towards device miniaturization, there has always been increasing interest in tracing a self-generated effect to combine electric and magnetic degrees of freedom − the so-called magnetoelectric effect. It was even discovered more than a century ago [1]. Materials bearing such an effect, in which electric and magnetic dipole order become naturally coupled, are termed as multiferroics. In the past few years, a novel class of multiferroic materials has been proposed, such as copper(II)-oxides. They have been found to possess large magnetic superexchange interactions and stand as good candidates for multiferroicity with relatively high transition temperatures. These systems are continuously attracting mainstream interest and provoking much research activity driven by the profound physics, as well

as potential applications in novel multifunctional devices such as sensors, transducers, memories, and ultimately spintronics [2]. However, beside this resurgence driven by long-term aspirations, improved theoretical models to be added to the design of new multiferroics would certainly help us understand the origin of the coupling between magnetic and ferroelectric orders. To this effect, it is of cardinal importance to investigate long range ordering phenomena emerging from both spin and charge degrees of freedom. It turns out that most of the relevant attention has just been concentrated around spin dynamics in the copper(II)-oxides at the genuine quantum level [3].

Indeed, classic examples of a variety of quantum spin phenomena are compounds containing divalent copper Cu^{2+} with $S = 1/2$. For example, the effects of quantum antiferromagnetism (AF) present in copper-oxide-based compounds, which have been extensively studied since the time high-T_C superconductivity was discovered [4], remain an unlocked puzzle within the community of condensed matter physics. That is why the quest for a credible explanation as to why these compounds are so particular is greatly intensified, especially after the finding that Cu-O type multiferroics also go high-T_C [5, 6] (see Figure 1.1). In such oxides the multiferroicity [7] is magnetically driven, meaning that macroscopic/local electric polarization is induced by magnetic long-range order, or very often by competing interactions which are able to prevent it. Definitely, the emergence of magneto electric phenomena has been evidenced in a great deal of copper-oxide-based systems with competing magnetic interactions [8]. Somewhat detailed insight into such magnetic interactions reveals that they are, unexpectedly due to the quenched orbital angular momentum in $3d^9$ configuration of magnetic Cu^{2+}, far from being magnetically isotropic. Whether the present anisotropy is relevant depends on the effective magnetic dimensionality. While

12
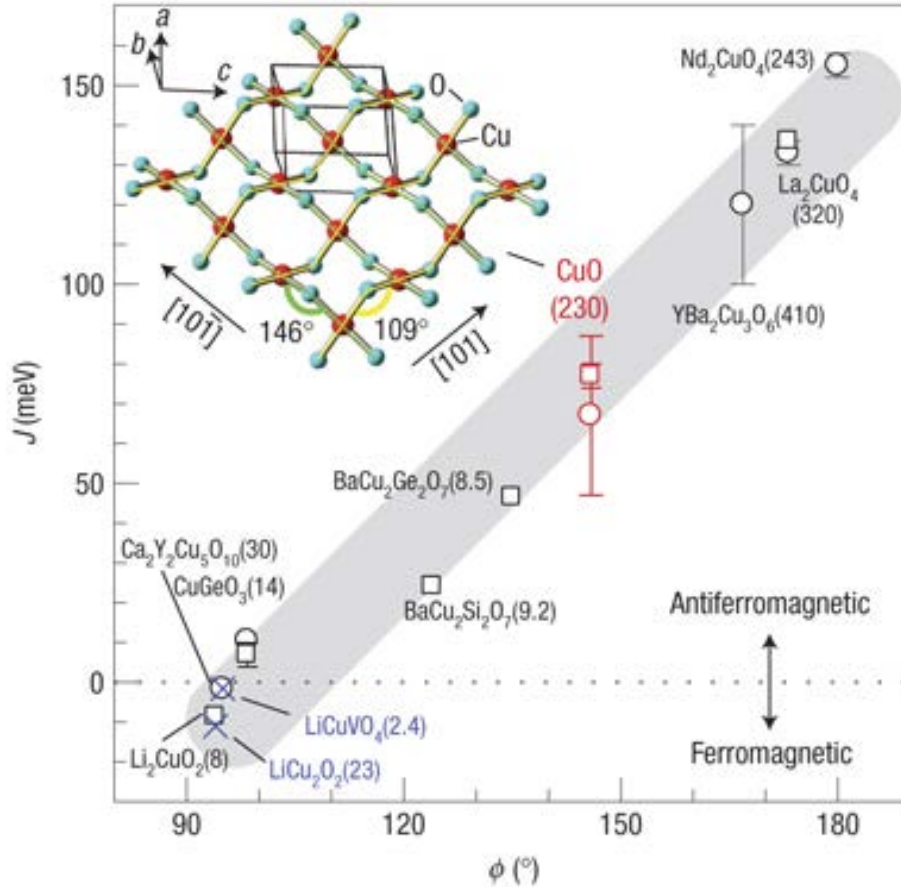
Figure 1.1: Cupric oxides as magnetically driven multiferroics with high T_C. The figure is taken from [5].

$2D$ magnetic structures of Cu-O based compounds are known for their considerably isotropic magnetic structures, such $1D$ systems usually do not share similar properties [9]. This is due to the fact that the exchange interactions are mediated via Cu-O-Cu bonds with different φ angles. In $2D$, an exchange interaction typically runs via 180°. The mediation favours the dominance of the isotropic exchange over the anisotropic one, unlike the $1D$ case. In this case the diminishing of the leading isotropic exchange becomes severe because the condition, $90° < \varphi < 180°$, is very often satisfied. The

conclusion squarely follows from the Goodenough-Kanamori-Anderson rules (GKA) [10]. They are applicable to a great number of Cu-O based compounds. Yet, not all of them observe the rules. In the $ACuO_3$ (A=Se^{4+}, Te^{4+}) family for instance, the GKA rules are not adhered by the oxygen mediated exchange interactions [11].

$ACuO_3$s are insulators with the orthorhombic/monoclinic crystal system and have highly distorted perovskite structures due to the small ionic radius of closed shell Se^{4+}/Te^{4+}. The magnetic structures in them may vary from anti- to ferromagnetic ordered lattices, and *vice versa*, that can be adjusted by fine tuning φ [12]. The tuning is equivalent to substituting one A element for another. The role of the lone-pair A cations is not only to create new magnetic structures but, interestingly, also to chemically tailor the magnetic dimensionality [13]. Such chemical scissors have therefore the dual act − driving competing interactions by tuning φ as well as lessening magnetic dimensionality. Both roles tend to be cooperative in fostering quantum spin effects that is, in the actual fact, a subject of the quantum magnetism [14].

Over the time, techniques used in the quantum magnetism have proven suitable not only in studying correlated electron materials ranging from local spin clusters to novel superconductors, but also in understanding phenomena which emerge beyond the low energy physics [15, 16]. This advantage comes from the sensible experimental accessibility in solid state sciences. In quantum magnetism, one commonly explores the potentiality of quantum fluctuations to spoil a long range magnetic ordering. They can be a cooperative outcome of magnetic frustration, dimensionality, and/or spin magnitude. Such a magnetism, AF notably, is thus said to be suppressed by the quantum spin effects. The relevance of the effects can be assessed by comparing

14

the ordering temperature, T_N, to the Curie-Weiss temperature, θ_{CW} [17]. Considerable suppression of T_N, relative to θ_{CW}, opens up a broad temperature sector: $T_N \lesssim T \lesssim \theta_{CW}$, within which the fluctuations, apart from temperature ones, become dominating [18]. This happens because of geometry and/or competing interactions in the system that makes magnetic frustration. To estimate its strength one introduces $f \equiv \theta_{CW}/T_N$, the so-called frustration parameter. In highly frustrated systems for example [19], it may reach values as high as 20. On the other hand, very often due to the fluctuations T_N is lower as compared to the leading AF exchange integral value J in the system. Along this line, there are two paramagnetic sectors of interest: $T \gg J$ and $T \ll J$. They can become remarkably separated in $S = 1/2$ systems with low dimensions [20].

As highly sensitive to magnetic environments, ESR [21] seems to be an essential tool in probing quantum magnetism. Indeed, because of the two mentioned temperature sectors, the physics of the related spin relaxation mechanisms at the resonance differ one from another. In this case, there are two suggested models in service of tracing the origin of the relaxations: one due to Kubo and Tomita (KT) [22] being exact for $T/J \to \infty$, and the other, after Oshikawa and Affleck (OA) [23] developed to cover the low T sector. Both models apply to the magnetically disordered phase and are concerned with two limits of an universal mechanism which has been so far understood only phenomenologically [24, 20]. In such a way, it is possible to uncover the influence of quantum correlations as a consequence of potential spin singlet formations.

As a member of the $ACuO_3$ family, type-III $SeCuO_3$ (only $SeCuO_3$ henceforth) compound offers a fertile playground for exploring the two models. Despite the fact

that no evident multiferroicity has been reported so far in $SeCuO_3$, there is an ongoing endeavour to resolutely inscribe it into multiferroics or to definitely ignore such a possibility. Quite recently, a novel ESR approach to be used in the case of $SeCuO_3$ would certainly help us clarify the present puzzle [25].

$SeCuO_3$ is an insulator whose crystal structure obeys $P2_1/n$ monoclinic space group symmetry with the following lattice parameters: $a = 7.725(1)$ Å, $b = 8.241(1)$ Å, $c = 8.502(1)$ Å, and $\beta = 99.16(2)°$. Details of this structure have been published in [26] among other existing polymorphs.

1.2 Experimental Details

Single crystals of $SeCuO_3$ have been grown by a standard chemical vapor phase method. Mixtures of analytical grade purity CuO and SeO_2 powder in molar ratio 4 : 3 were sealed in quartz tubes with electronic grade HCl as the transport gas for the crystal growth. The ampoules were then placed horizontally into a tubular two-zone furnaces and heated very slowly by 50 C°/h to reach 500 C°. The optimum temperatures at the source and deposition zones for the growth of single crystals were 550 C° and 450 C°, respectively. After four weeks, many green $SeCuO_3$ crystals with a maximum size of $5 \times 10 \times 2$ mm^3 were obtained, which were identified on the basis of X-ray powder diffraction data.

ESR measurements were performed on single crystalline samples of fairly regular shape − transparently green plate like samples of which the longest crystal edges are along b-axis and the largest faces are coincident with $(10\bar{1})$ (See Figure 1.2). The crystal orientation measurement was carried out using a Laue X-ray diffractome-

ter. By means of SQUID, heat capacity, and neutron diffraction measurements, the
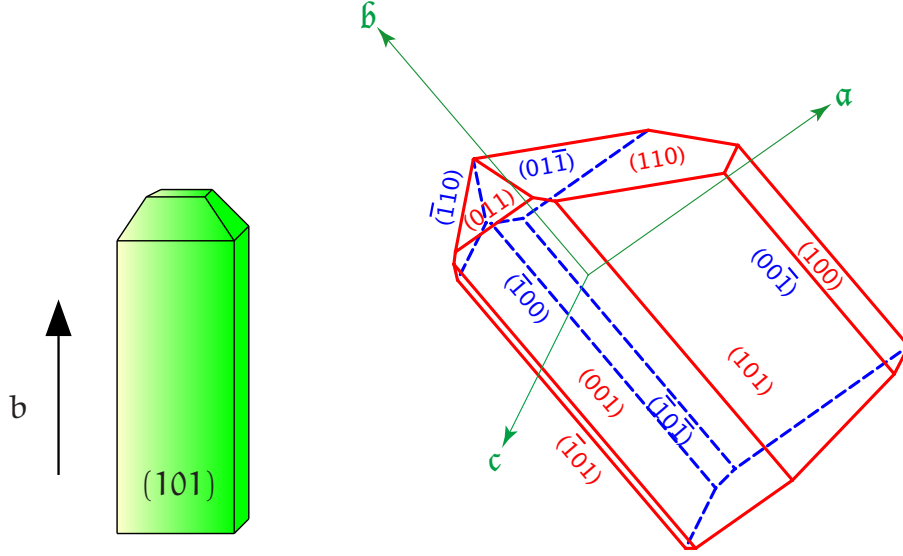
Figure 1.2: A common shape of oriented single-crystalline samples of $SeCuO_3$ (left). A detailed drawing of the oriented crystal faces.

$SeCuO_3$ system was resolved to be an AF with $T_N \simeq 8$ K and correspondingly high $\theta_{CW} \sim 200$ K [27]. Temperature $(5 - 300$ K$)$ as well as angular $(0 - 360°)$ dependent ESR spectra were recorded using a Bruker ESR spectrometer E500 EleXsys Series (Bruker Biospin GmbH) housing a one axis $\pm 2°$ incertitude goniometer and equipped with a continuous wave Gunn diode-based microwave bridge (model SuperX, 9.402 GHz), a Bruker ER 4122 SHQE cylindrical TE_{011} high-Q cavity, and an Oxford Instruments Helium-gas continuous flow cryostat (ESR900). The 100 kHz modulation amplitude was kept at 1 mT to improve signal-to-noise ratio and avoid modulation broadening. The related absorption profile of spectra obtained for various crystal orientations with respect to both sweeping H_0 and microwave H_1 magnetic field (Figure

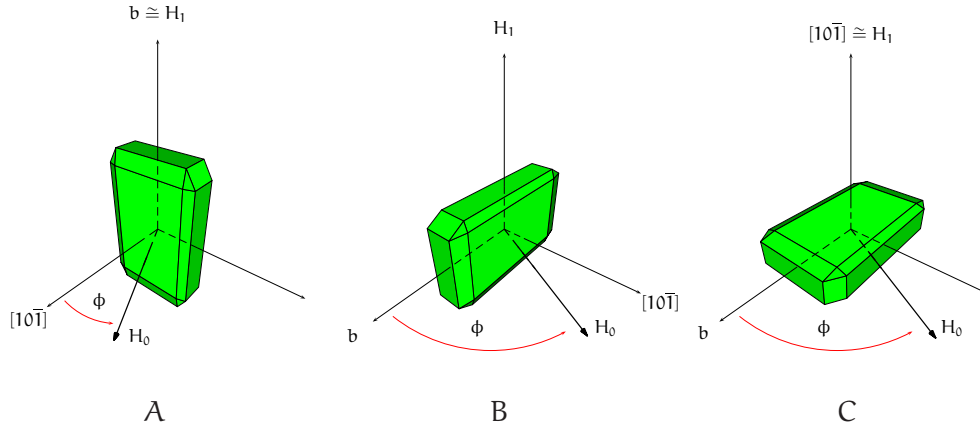Figure 1.3: Three different crystal orientations (A, B, and C) with respect to both H_0 and H_1. The ϕ rotation axis is coincident with the axis of the cylindrical cavity that is also the azimuthal axis of the goniometer.

1.3), from room temperature down to nearly 8 K, was found to consist of a broad Lorentzian first derivative exchange narrowed [28, 29] single line, as is presented in Figure 1.4.

Below *ca* 8 K, apart from the the background signal, no AF resonance absorption spectrum was identified at H_0 fields swept out from 50 up to 10000 Gauß for different crystal orientations. We can ascribe the absence of the resonant signal to the restricted magnetic field accessibility of X-band spectrometers and in order to observe AF resonance an accessibility measured in Tesla units would be required. Slightly above 8 K the spectra experience a severe disruption down to their disappearance as can be followed from Figure 1.5. On approaching T_N from above the resonant signal becomes permeated with a growing noise which rather seems regular and intrinsic to the AF transition than an overwhelming background. The isolated phenomenon has shown to have no notable angular dependence and might be understood as an
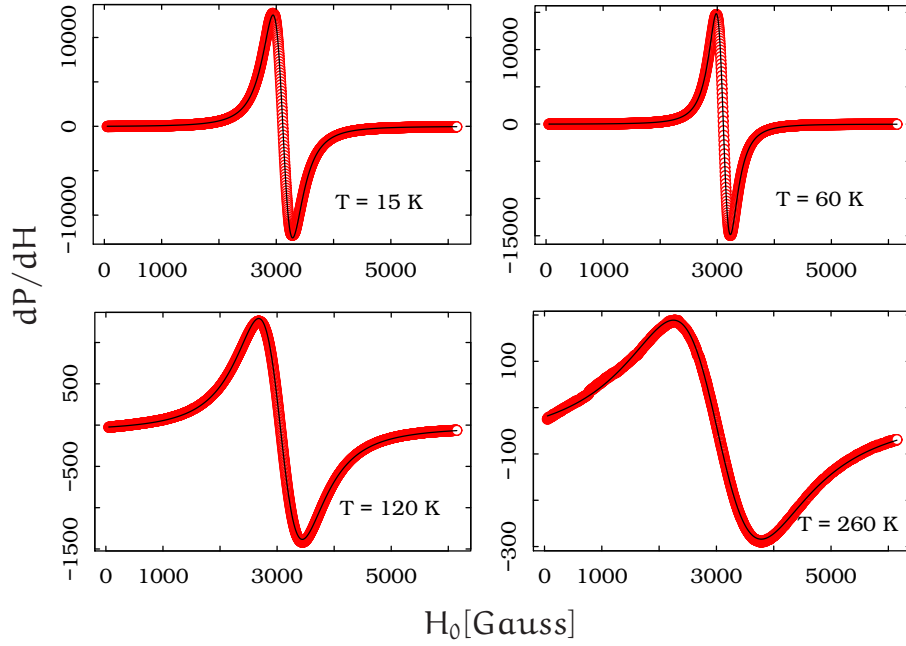
Figure 1.4: X-band ($A(\phi = 0)$ crystal orientation) ESR absorption spectra (red) fitted with first derivative Lorentzian lines (black).

upturn in the dielectric constant in the vicinity of the magnetic phase transition that may spoil the resonant condition within the cavity. Possibility of having a permanent macroscopic or local electric polarization below T_N due to the coupling between dielectric and magnetic degrees of freedom is not discarded. The manifestation of such coupling is a natural concomitant of copper-oxide-based compounds [5, 6], particularly in some of the $ACuO_3$ family, as was well reported by Lawes *et al.* [8].

On the other hand, the ESR has displayed no sign of the interaction between the microwave ($\vec{H}_1$) and an eventual electric polarization ($\vec{P}$). This has been proven by turning $\vec{P}$ around $\vec{H}_0$ (See Figure 1.6). Exploring all possible angles between these two vectors would cancel the interaction once the angle becomes 90° [30] that has
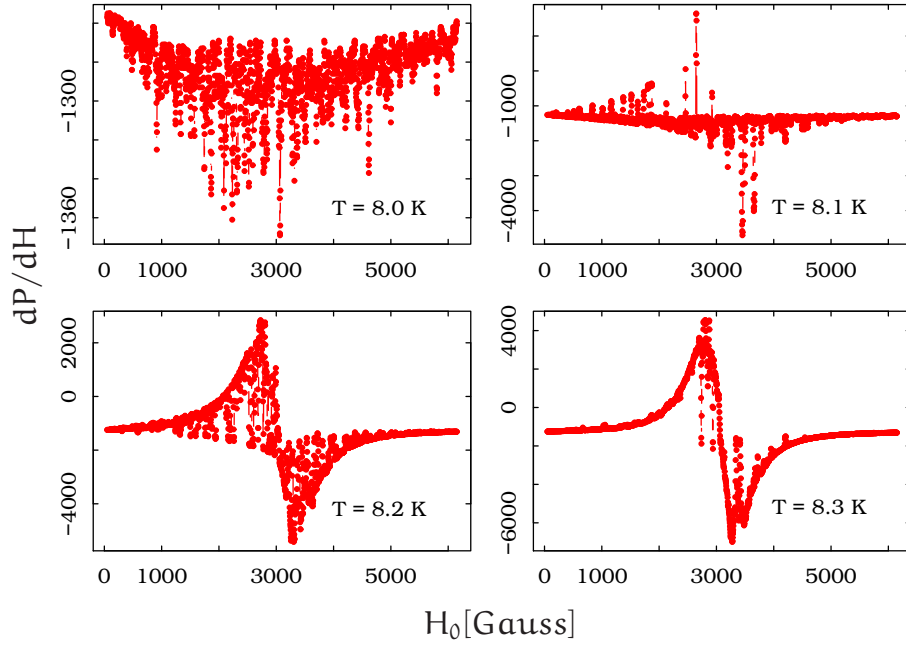
Figure 1.5: Antiferromagnetic phase transition followed by the disruption of the X band ($A(\phi = 0)$ crystal orientation) ESR spectra near 8 K.

never been the case as the spectra have always stayed disrupted close to T_N as is shown in Figure 1.5. Yet, it remains uncertain whether this anomaly is related to some of the instrumental details.

At room temperature, however, a slight departure of the ESR lineshape from the Lorentzian absorption profile has been observed that is explained by the involvement of tails of the ESR line counterpart appearing in the negative magnetic field sector. The original line becomes so broad as to overlap via $H_0 = 0$ T with its negative field equivalent.
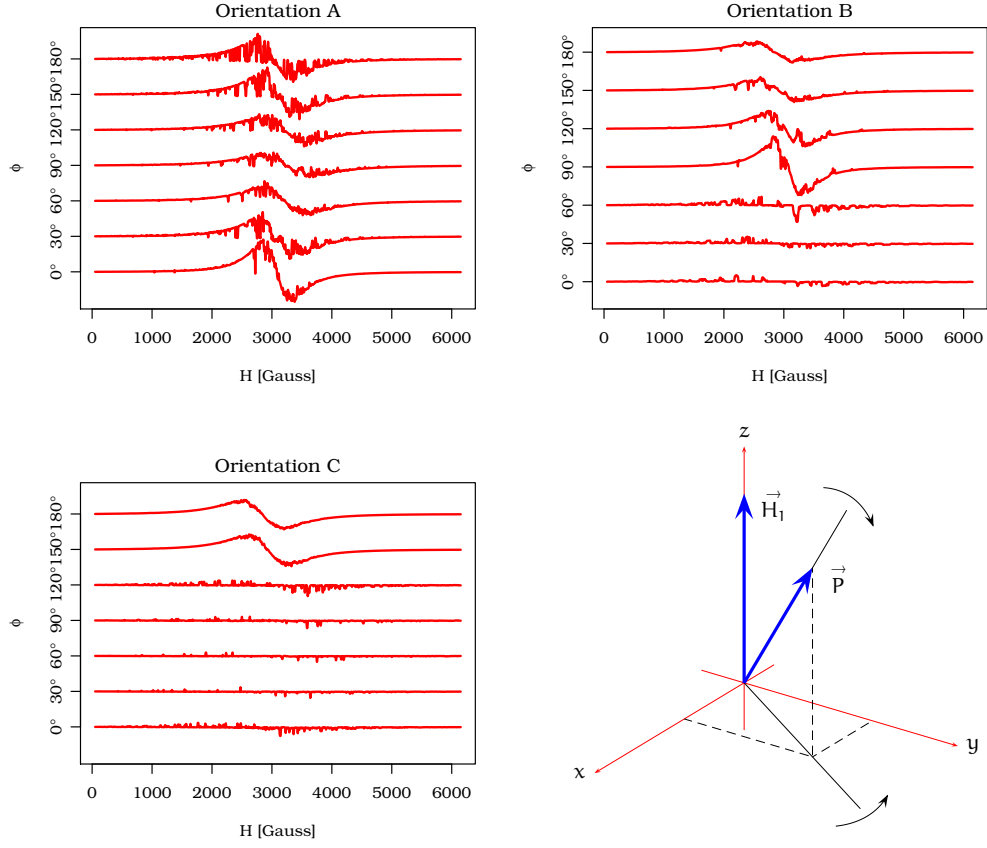
Figure 1.6: Evolution of the ESR spectra with respect to ϕ at (8.10 ± 0.05) K for all the three orientations. Changing the orientation enables $\vec{P}$ to move freely with respect to fixed $\vec{H_1}$.

1.3 Results and Discussions

1.3.1 Electronic and Spin Configuration

To address a possible influence of the crystal structure upon the magnetic properties of SeCuO$_3$, it is important to understand how the local environment around the magnetic ion affects the energy levels of d-orbitals. With a d^9 configuration on Cu^{2+}, only the highest lying orbitals become magnetically active. In an ideal octahedral
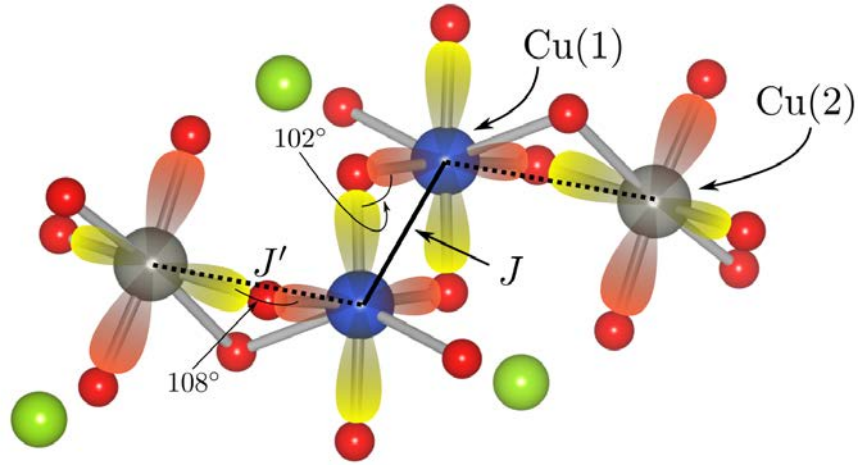
Figure 1.7: The sketch of the orbital configuration of $SeCuO_3$ with the magnetically active d-orbitals (a single tetramer).

crystal field d-orbitals are split into lower lying t_{2g} and higher lying e_g subsets. From the sketch representing a configuration between the copper and oxygen ions (Figure 1.7) one notices that each copper ion has 4 oxygen ions nearly in a plane and 2 oxygen ions out of it. The former are positioned at distances of about 2 Å away from the copper ion and the latter much larger than 2 Å. Particularly, these two oxygen ions are located at the opposite sides of the octahedron, making it elongated along the local z-direction. This removes the degeneracy of the e_g subset in a manner that leaves only $d_{x^2-y^2}$ as the highest lying orbital.

The superexchange interaction $Cu-O-Cu$ between the magnetic moments should be the strongest along the path $d_{x^2-y^2} - p_{x(y)} - d_{x^2-y^2}$. If only these paths are taken into account, then the structure can be represented as a weakly-coupled 3D network

of tetramers (Figure 1.7). Tetramers effectively form two sets of chains running along the a-axis, with tetramers in the neighboring chains related to each other by the $180°$ rotation [27].

A single tetramer consists of a central $Cu(1)-Cu(2)$ dimer and two copper ions on each end of the dimer. There are two $Cu(1)-O-Cu(1)$ paths with angles of $102°$ which contribute to J interaction. On the other hand, there is a single $Cu(1)-O-Cu(2)$ path with an angle of $108°$ for the J' interaction. As these angles are quite above $90°$, one would expect medium strength AF interactions between the neighboring moments.

Two types of inter-tetramer interactions can be also expected. One is along the a-axis between two $Cu(2)$ ions on the neighboring tetramers, and incorporates the $d_{3z^2-r^2}$ orbital. Since the octahedron is not ideal, there may exist a mixing between $d_{3z^2-r^2}$ and $d_{x^2-y^2}$ orbitals, giving rise to a finite exchange. The second possible inter-tetramer interaction is the inter-chain interaction and it runs via via $Cu(1)-O-Se-O-Cu(2)$ paths. However, observing their strengths, these types of the exchanges can safely be disregarded in the system. Their presence, albeit minuscule, drives the system into the long range ordered state. This provides a wide temperature range in which the effects of inter-tetramer quantum fluctuations spread considerably [27].

1.3.2 ESR Susceptibility (χ), Linewidth (ΔH), and g-factor

With the aid of ESR tool three relevant pieces of information can be distiled: χ, ΔH, and g. Double integrating ESR spectra over the magnetic field corresponds to the spin

susceptibility [31]. The extracted ESR susceptibility ($\chi_{ESR}(T)$) has been found to be in good agreement with the related SQUID results [27], i.e. dc magnetic susceptibility ($\chi_{dc}(T)$). This means that the response which is probed by ESR is pertinent to nothing but ALL paramagnetic spin species in the system. The agreement between $\chi_{ESR}(T)$ and $\chi_{dc}(T)$ was ensured using tempol as a room temperature standard in the X-band spectrometer. The dominant feature of the magnetic response of the $SeCuO_3$ compound is a broad maximum located around 18 K [27]. The presence of such a maximum is usually related to the formation of AF correlations in the absence of long-range order due to the strong fluctuations present in low-dimensional systems. The absence of ferromagnetic correlations, which were seen in other $SeCuO_3$ polymorphs [12], was corroborated with the $M(H)$ dependence (Figure 1.8). No hysteresis in $M(H)$ has been observed below and above T_N.

Following our structural analysis, the Hamiltonian describing isolated tetramers can be postulated

$$\mathbf{H} = J'(\mathbf{S_1} \cdot \mathbf{S_2} + \mathbf{S_3} \cdot \mathbf{S_4}) + J\mathbf{S_2} \cdot \mathbf{S_3}, \tag{1.1}$$

where $\mathbf{S_2}$ and $\mathbf{S_3}$ form the central pair coupled with the J exchange interaction and end spins are $\mathbf{S_1}$ and $\mathbf{S_4}$ coupled to the central pair with J'. For $90\,\mathrm{K} < T < 330\,\mathrm{K}$ one can successfully implement a model for magnetic susceptibility, applied to a similar compound $Cu_2Te_2O_5X_2$ [32], to yield the following parameters: $J = 225$ K, $J' = 170$ K, and $g_{av} = 2.25$ [27]. Here it is important to stress that neither a 1D magnetic chain model nor a magnetic dimer model can reproduce the magnetic susceptibility in this temperature range. The nature of the interaction that sets in around 70 K remains somewhat unclear and further investigations are required [27].
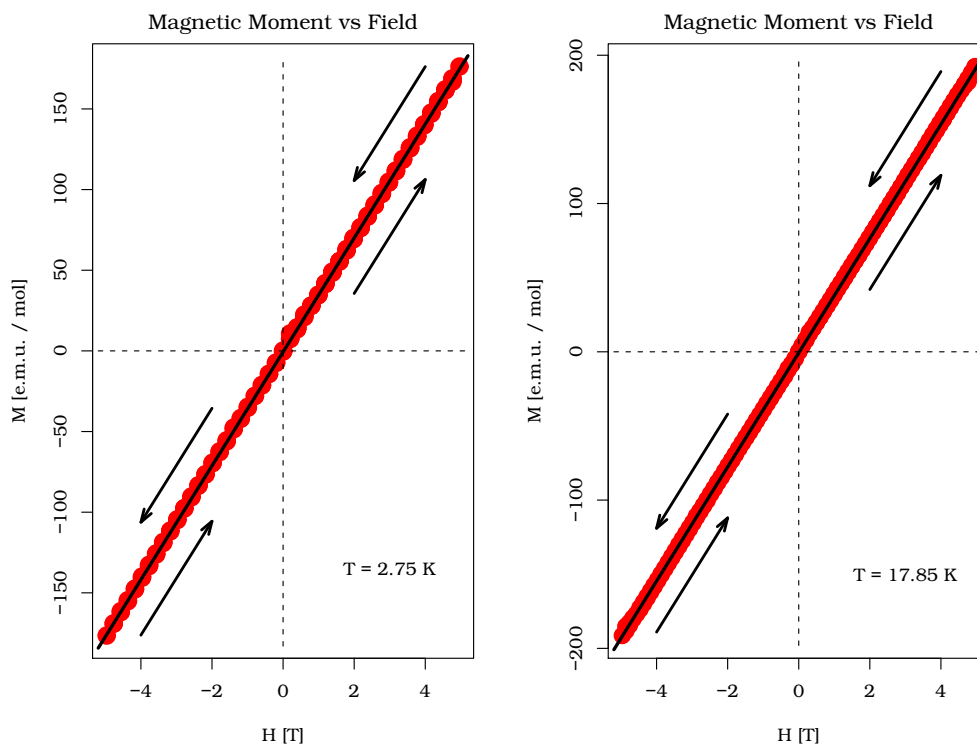
Figure 1.8: Magnetic moment plotted against magnetic field for H_0 parallel to $(10\bar{1})$ at the two relevant temperatures.

Nevertheless, at high temperature, we verify CW behaviour in $\chi_{ESR}(T)$, which strongly indicates that the spins are prevailingly AF coupled. Its reciprocal value versus temperature is plotted in Figure 1.9 for two crystal orientations ($A(\phi = 0)$ and $B(\phi = 0)$). The two dependences follow the linear law in temperature from 100 to 300 K and are nicely fitted within this range. The abscise intercepts extrapolated from the fits lead to the following CW temperatures: $\theta_A = (280\pm10)$ K and $\theta_B = (320\pm10)$ K. Their values are both significantly high as compared to T_N. In this respect we draw a conclusion that there is a presence of quantum fluctuations in the system. The controlling parameter of frustration after Ramirez [17], f, is of order of ~ 30 and unveils a potential existence of competing magnetic interactions and/or reduced

dimensionality in the spin connectivity. The slopes inferred from the two fits are found to amount $k_A = (1.14 \pm 0.04)$ molK^{-1}emu^{-1}and $k_B = (0.67 \pm 0.07)$ molK^{-1}emu^{-1}. These respectively yield $g_A = (2.21 \pm 0.1)$ and $g_B = (2.27 \pm 0.1)$ clearly suggesting that the entire magnetism is spanned by an anisotropic 1/2 spin network formed out of Cu^{2+} ions. The two g-factor values were computed from the mean-field magnetic moments for $S = 1/2$ [33] and do not depart markedly from those which the respective ESR spectra center around at high temperature. This point will be further elaborated later throughout the paragraph devoted to the temperature dependent g-factor.
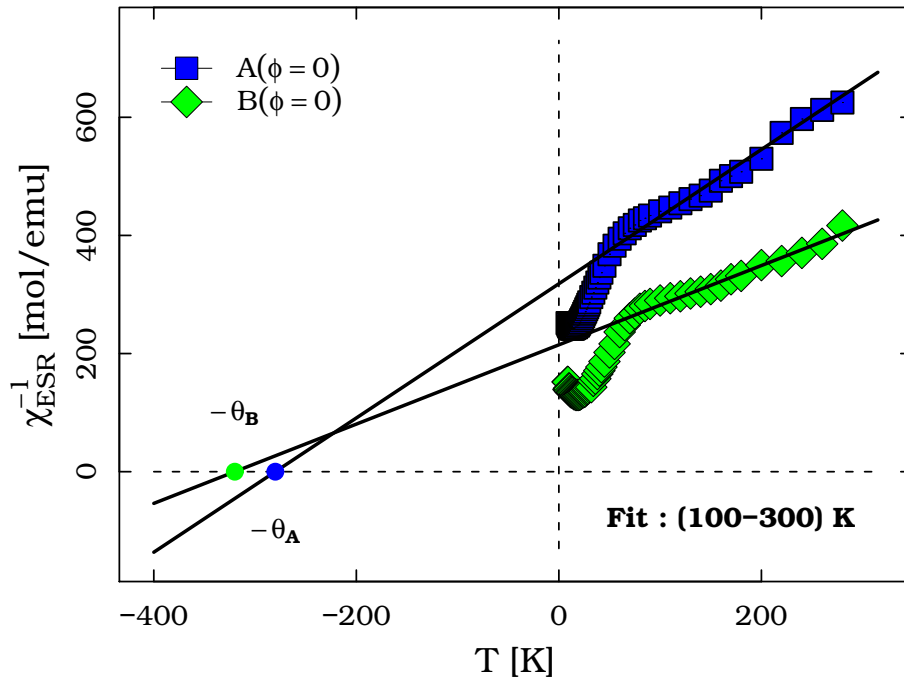

Figure 1.9: Temperature dependence of inverse 9.4 GHz ESR susceptibility obtained for two crystal orientations ($A(\phi = 0)$ and $B(\phi = 0)$). The data are fitted (straight black lines) within $(100 - 300)$ K range. CW temperatures are $\theta_A = (280 \pm 10)$ K and $\theta_B = (320 \pm 10)$ K.

In majority of Cu-O based compounds the ESR spectrum is a single resonance line due to the strong oxygen mediated isotropic exchange coupling between Cu^{2+} spins. This coupling (like J') can become very pronounced when Cu^{2+} ions cluster like in the case of $SeCuO_3$. It may amount to as much as few hundreds K and even higher [34]. On the other hand, a Cu^{2+} ion has its nuclear spin (3/2) that can realize a hyperfine coupling to its electronic spin (1/2). The corresponding hyperfine coupling is usually of order of ~ 1 K or lower and is obviously overwhelmed by the exchange interaction. $SeCuO_3$ is a spin dense system so that the hyperfine splittings are irrelevant. Furthermore, the unit cell of $SeCuO_3$ contains four Cu^{2+} ions subdivided into two crystallographically inequivalent pairs. However, the exchange interaction (J') between the spins sitting on inequivalent ions $Cu^{2+}(1)$ and $Cu^{2+}(2)$ is sufficiently strong to cause these two ESR active species to coalesce into single one in the spectra. As $J' = 170$ K, the static magnetic field at the X band spectrometer (~ 0.3 T$\ll J'$) seems to be unsubstantial to resolve the line into two. Indeed, we *did* observe the only one ESR absorption line for all temperature dependent spectra, instead of, possibly, $2 \times ((2 \times \frac{3}{2} + 1) + 1) = 10$ lines. Given they are tightly coupled, the $Cu^{2+}(1)$ and $Cu^{2+}(2)$ spin species through their ΔHs, gs, and χs contribute on equal footing to the total ESR spectra. We naturally assume that $\mid H_0^{(1)} - H_0^{(2)} \mid \ll J'$. In this respect, total linewidth ΔH is arithmetic mean of $\Delta H^{(1)}$ and $\Delta H^{(2)}$ so that there is no additional line broadening caused by the g-factor difference between the inequivalent magnetic centers [24]. The line-width is extremely broad and reaches nearly 150 mT at high temperatures. Its temperature dependence for both crystal orientations is presented in Figure 1.10. At low temperatures, ΔH tends to diverge in the vicinity of the phase transition. Qualitatively, there is some universal behaviour displayed in

27

the temperature dependence near the phase transition in both cases: $A(\phi = 0)$ and $B(\phi = 0)$. The mechanism of the line broadening is related to the critical fluctuations and certain magnon contributions. At higher temperatures far from the transition,
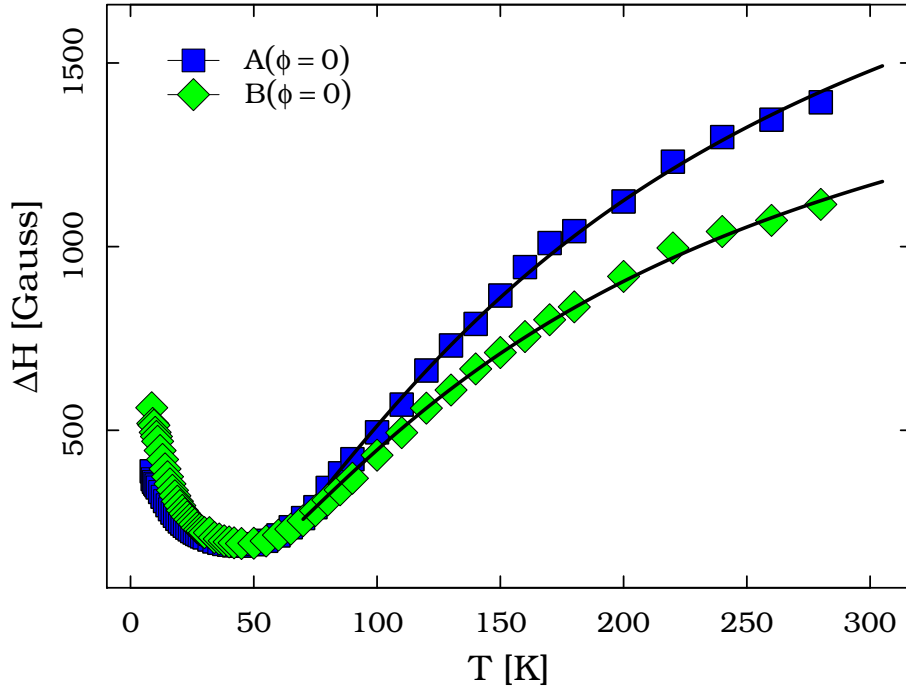
Figure 1.10: Temperature dependence of 9.4 GHz ESR line-width obtained for two crystal orientations ($A(\phi = 0)$ and $B(\phi = 0)$). The data are neatly fitted (black curves) with temperature dependent law $\Delta H(\infty)e^{-\frac{C_1}{C_2+T}}$ at high T.

the line broadens due to the presence of the magnetic anisotropy. In fact, it is well known in literature (see [24] with all references therein) that for spin systems having isotropic exchange interactions, given in the standard $SU(2)$ Heisenberg form, there is no relaxation in the total magnetization no matter how strong or weak the coupling is. This is no longer correct in the presence of an even infinitely small anisotropy which violates $SU(2)$ so that the ESR line is not absolutely narrowed in the para-

magnetic phase, but narrowed enough to fit Lorentzian (the fast modulation case, $H_0 \ll J$). The broadening mechanism of the linewidth at high T is explained by the Kubo-Tomita (KT) model [22], which is an exact theory for $T \gg J$. In 3D and/or classical antiferromagnets $T_N \sim J$ and the KT model becomes applicable to the entire paramagnetic sector. The opposite limit concerns 1D magnets in which long-range order may merely exist due to the weak interchain interactions ($T_N \sim 0$). As for this case, there is a wide temperature range ($T \ll J$) in the paramagnetic phase where AF correlations are pronounced enough to make the KT model inapplicable. Very recently, however, Oshikawa and Affleck (OA) [23] have developed a model to cover the deficiency of the KT theory at low T in $S = 1/2$ AF Heisenberg chains. The OA field theoretical approach accounts successfully $\Delta H(T)$ for $T \ll J$ in the fast modulation regime. The same analogy fits for J' as it is unclear how the interactions (J and J') dominate one over another in forming the AF ordering.

In this study, nevertheless, we favour a semi-phenomenological approach, put originally forward in [24, 20], to fit the linewidth above the transition by the following expression

$$\Delta H(T) = \Delta H(\infty) e^{-\frac{C_1}{C_2 + T}}. \tag{1.2}$$

Here C_1, C_2, and $\Delta H(\infty)$ stand for the fitting parameters. C_1 relates to the order of magnitude of J (however rather J'), while C_2 indicates the influence of the transition temperature T_N upon the broadening. $\Delta H(\infty)$ is proportional to M_2/J. M_2 represents the so-called second moment. According to the KT theory in $T \to \infty$, $M_2 \propto (\delta J)^2$ where δJ corresponds to the so-called symmetric anisotropic exchange interaction or pseudo-dipolar exchange [35, 36]. Unlike $\Delta H(\infty)$, parameters C_1 and

29

C_2 have no angular dependence as is extrapolated from the OA theory. Being a small parameter, δ is the only term depending on the crystal orientation with respect to H_0 and originates from the second order perturbation of the spin-orbit coupling. The first order contribution, antisymmetric Dzyaloshinskii-Moriya interaction, (DM) should be identically equal to zero in the case of $SeCuO_3$ because its crystal lattice possesses the centre of inversion. Still, DM is likely to occur inside $Cu(1)-Cu(2)$ pairs which are coupled together in the ESR spectra.

The $SeCuO_3$ system is neither a totally classic 3D nor purely quantum 1D antiferromagnet so that relation (1.2), as an empirical extension to both KT and OA theory, remains quite convenient for the interpretation of the linewidth behaviour. Also, we discard the possibility that the line can broaden due to the spin diffusion relaxation mechanism [37, 38, 39]. Explicitly, no deviation from the Lorentzian profile has been noticed in the lineshape. The fitting parameters are given in Table 1.1 and point out that $\Delta H(\infty)$ is the only angular dependent parameter as is indeed required by the model. Also, $T_N \sim C_2$. Estimated J' should amount nearly like $C_1 = 170$

Table 1.1: The fitting parameters for the linewidth behaviour.

Orientation	C_1[K]	C_2[K]	$\Delta H(\infty)$[mT]
$A(\phi = 0)$	170 ± 10	7 ± 3	260 ± 10
$B(\phi = 0)$	170 ± 10	12 ± 4	200 ± 10

K which is indeed the case. δs were found to have reasonable values amounting less than 0.5 % for both crystal orientations. Above $T \sim 170$ K the linewidth starts to mimic behaviour dictated by the KT mechanism. Below this temperature there is a

wide sector which is dominated by magnetic fluctuations. We, therefore, count the SeCuO$_3$ compound into potential quantum and/or frustrated antiferromagnets. The existence of such a sector offers a very corroborative evidence regarding the quantum nature of the fluctuations.

The temperature dependence of g-factor is plotted in Figure 1.11 for $A(\phi = 0)$ and $B(\phi = 0)$. Above ~ 170 K g-factors saturate to values 2.23 and 2.26 for $A(\phi = 0)$ and $B(\phi = 0)$, respectively. This is in accordance with the KT approach ($T \gg 170$ K) which predicts no eventual temperature dependence for g-factor. In the low T sector, however, one discerns two contrary monotonic trends, $g_{A(\phi=0)}(T)$ and $g_{B(\phi=0)}(T)$, down nearly to T_N in which vicinity both gs have a tendency to diverge towards their higher values. As the temperature falls off from 170 K, there is a clear drop/upturn in $g_{A(\phi=0)}(T)/g_{B(\phi=0)}(T)$ which we find to be in good agreement with respective $\chi^{-1}(T)$ ($\chi(T) \propto g$) obtained at the SQUID [27]. The decrease of $g_{A(\phi=0)}(T)$ on one hand, and the increase of $g_{B(\phi=0)}(T)$ on the other, indicate that magnetic moments polarized along $[10\bar{1}]/b$-axis experience a rise in anti/ferromagnetic interaction with falling temperature. An admissible interpretation is that there are simultaneously existing ferromagnetic and antiferromagnetic, most likely competing, interactions in the system leading to the frustration. Thence, yet another evidence in favour of the quantum magnetism in SeCuO$_3$.

In addition to the symmetric anisotropic exchange (δJ) one needs also to consider the antisymmetric one, such as DM. DM is capable of mixing the singlet and triplet states of localized spin clusters and may have a marked impact upon the behaviour of low dimensional magnetic systems [40]. Bearing in mind the symmetry considerations, DM is allowed only for Cu(1)$-$Cu(2) pairs. The main influence of DM is to cant the
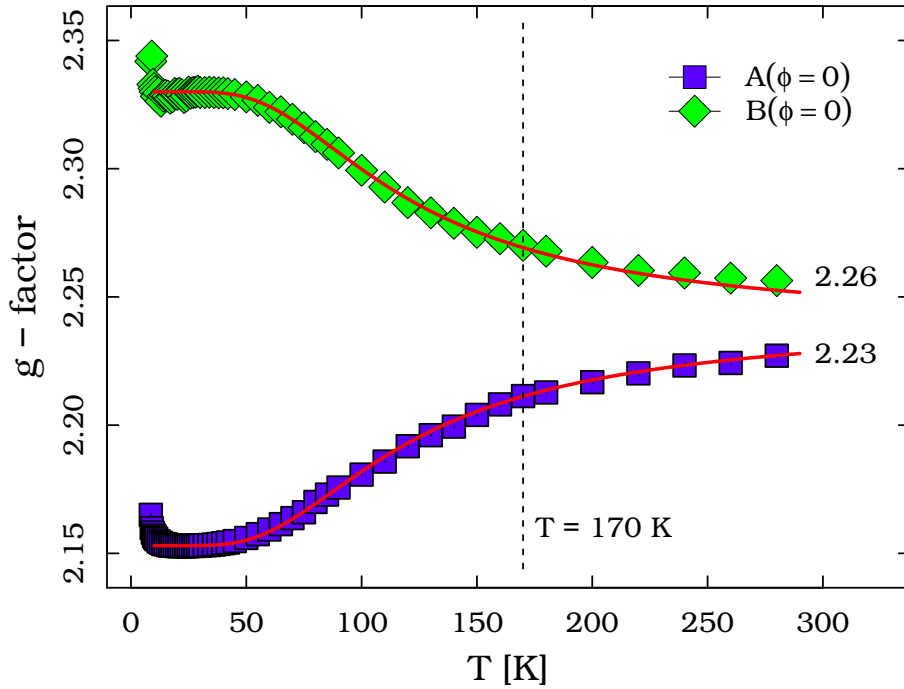
Figure 1.11: Temperature dependence of g-factor with respect to two crystal orientations ($A(\phi = 0)$ and $B(\phi = 0)$). Fitting functions are given in red.

neighboring moments which produces the ferromagnetic component. However, due to the inversion symmetry in the center of the tetramer, it is expected that there are ferromagnetic contributions from the ends which should cancel each other.

To qualitatively describe the g-factors behaviours depicted in Figure 1.11 we assume that individual tensors, g_1 and g_2, are diagonal in a coordinate system defined as $\{\frac{1}{\sqrt{2}}[10\bar{1}], [010] \equiv b, \frac{1}{\sqrt{2}}[10\bar{1}] \times [010]\}$ as well as temperature independent. The subindices in the g-factors are correspondingly connected to the copper sites. The reason why such a basis is introduced to represent g-tensors will be later elaborated in the subsequent subsection. Within the tetramer model one sets that $J > 0$. In doing so, it can be observed how the total g-tensor depends on the temperature given

32

that the central Cu(1)−Cu(1) pair experiences the singlet-triplet transformation. To
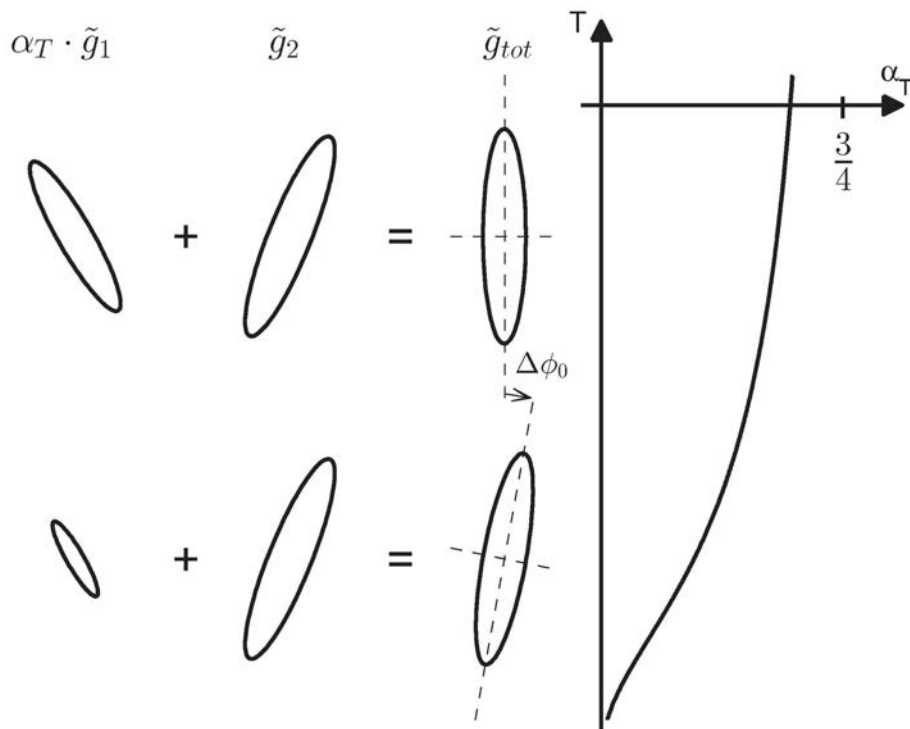
Figure 1.12: Averaging the g-tensors with varying contribution from g_1 which is proportional to the triplet probability (the graph on the right-hand side). As temperature is lowered, the total g tensor effectively rotates by $\Delta\phi$ [27].

obtain the measured total temperature dependent g-tensor a simple averaging is used such as

$$g_{tot} = \frac{\alpha g_1 + \beta g_2}{\alpha + \beta},$$

(1.3)

where $\alpha = \alpha_T/\alpha_{\max}, \alpha_{\max} = 3/4, \beta = 1$. α_T represents the probability of finding Cu(1)−Cu(1) dimer in the triplet state,

$$\alpha_T = \frac{3e^{-J/T}}{1 + 3e^{-J/T}}.$$

(1.4)

33

Figure 1.12 depicts the results of the above procedure for the $[10\bar{1}]$- and b-directions using the values $g_1 = (2.335, 2.14, 2.07)$, $g_2 = (2.153, 2.33, 2.07)$, and $J = 290$ K. The agreement with the experimentally obtained values is surprisingly good, given the simplicity of the model, and the obtained value of J is quite close to that extracted earlier.

1.3.3 ESR Consistency with X-Ray Diffraction

To compute the principal components of the $\hat{\mathfrak{g}}$ tensor as well as to attest the monoclinicity from the ESR data of $SeCuO_3$ recorded at 50 K we exploit a conventional method for obtaining the principal components of the second rank symmetric tensors [41]. The data involve the three crystal rotations about the orthogonal axes (A, B, and C orientations) (see Fig. 1.3). Such a computational treatment is commonly limited to the $S = 1/2$ Hamiltonians and is not applicable to systems having $S > 1/2$. Shortly, it consists in what follows.

The Zeeman Hamiltonian can be written down as

$$\mathbf{H} = \mu_B \vec{H} \cdot \hat{\mathfrak{g}} \cdot \vec{S}, \tag{1.5}$$

where $\vec{H} \equiv H_0 \hat{\mathbf{e}}_H$ and $\vec{S}$ are magnetic field and spin operator, respectively, while $\hat{\mathfrak{g}}$ represents the symmetric g-factor second rank tensor. In the principal coordinate system of the tensor, $\{u_1, u_2, u_3\}$, the Hamiltonian takes a far simpler form

$$\mathbf{H} = \mu_B(\mathfrak{g}_{u_1} H_{u_1} S_{u_1} + \mathfrak{g}_{u_2} H_{u_2} S_{u_2} + \mathfrak{g}_{u_3} H_{u_3} S_{u_3}). \tag{1.6}$$

As the direction of the principal coordinates relative to the crystal axes can be inferred from the symmetry properties of the crystal, the determination of the principal values

becomes quite straightforward. However, in majority of the cases the orientation of the principal coordinate system is not suggested by the crystal symmetry and every attempt to analyze the data becomes correspondingly troublesome. Implied by the symmetry, on the other hand, our case boils down to taking the following coordinate system $\left\{ \frac{1}{\sqrt{2}}[101], ca\ \frac{1}{\sqrt{2}}[10\bar{1}], b \equiv b^* \right\} \rightarrow \{x, y, z\}$ for the orthogonal reference axes. It is taken to obtain numerical values $(\hat{\mathfrak{g}}^2)_{ij}$ for the components of the symmetric tensor $\hat{\mathfrak{g}}$ as well as the orientation of the principal axes relative to the reference system. To this effect, the Zeeman Hamiltonian is further rewritten as

$$\mathbf{H} = \mu_B(\vec{H} \cdot \hat{\mathfrak{g}}) \cdot \vec{S} = \mu_B(\vec{H^*} \cdot \vec{S}), \tag{1.7}$$

where $\vec{H^*}$ represents the transformation of $\vec{H}$ by $\hat{\mathfrak{g}}$, no matter what adjungated sense is assumed. Alternatively, the energy of the ESR absorption is always

$$\hbar\omega = \mu_B |(\hat{\mathfrak{g}} \cdot \vec{H})|, \tag{1.8}$$

from which

$$(\hbar\omega)^2 = \mu_B^2(\hat{\mathfrak{g}} \cdot \vec{H})^2 \Rightarrow g^2 = (\hat{\mathfrak{g}} \cdot \hat{\mathbf{e}}_H)^2. \tag{1.9}$$

Here g is the effective value defined as $\hbar\omega/\mu_B H_0$. The value is measured at all the three rotations. To exemplify, we consider a rotation around the z axis. In such a way

$$\hat{\mathbf{e}}_H = \hat{\mathbf{e}}_{\phi_z} = (\cos(\phi_z), \sin(\phi_z), 0) \tag{1.10}$$

and

$$g_{(z)}^2 = (\hat{\mathfrak{g}}^2)_{xx} \cos^2(\phi_z) + (\hat{\mathfrak{g}}^2)_{yy} \sin^2(\phi_z) + 2(\hat{\mathfrak{g}}^2)_{xy} \cos(\phi_z) \sin(\phi_z) \tag{1.11}$$

that leads to the general formula

$$g^2 = \gamma_{11} \cos^2(\phi) + \gamma_{22} \sin^2(\phi) + 2\gamma_{12} \cos(\phi) \sin(\phi). \tag{1.12}$$

35

The related matrix $\hat{\mathfrak{g}}^2$ can thus be diagonalized by the common methods for extracting the principal components. Their square roots are the principal components of $\hat{\mathfrak{g}}$, and the transformation which diagonalizes the experimental $\hat{\mathfrak{g}}^2$ gives the correct

Table 1.2: Matrix elements of g^2 with respect to the three orientations.

Orientation	γ_{11}	γ_{22}	γ_{12}
A$[\vec{z}(\phi)]$	4.6112 ± 0.0008	4.2596 ± 0.0009	0.0684 ± 0.0009
B$[\vec{y}(\phi)]$	5.4092 ± 0.0009	4.6112 ± 0.0008	0.0042 ± 0.0008
C$[\vec{x}(\pi/2 - \phi)]$	4.2596 ± 0.0009	5.4092 ± 0.0009	0.0081 ± 0.0008

relationship between xyz and $u_1 u_2 u_3$. Along these lines, the fitting parameters pertinent to the ESR data (Figure 1.13) were extracted using R (*Mixed Effects Models*). The parameters' values were found to share one common value of their incertitudes of nearly 10^{-3} (Table 1.2).

Figure 1.13 shows the angular dependence of g-factor square at 50 K for the three crystal rotations ($A(\phi)$, $B(\phi)$, and $C(\phi)$). The dependences were obtained at rotations around three orthogonal axes ξ_A, ξ_B, and ξ_C, which relate to $[010] \equiv b$, $\frac{1}{\sqrt{2}}[10\bar{1}] \times [010]$, and $\frac{1}{\sqrt{2}}[10\bar{1}]$, respectively. Also, $\{u_1, u_2, u_3\} \equiv \{\xi_B, \xi_C, \xi_A\}$. The crystal system is monoclinic so that $[10\bar{1}] \times [010]$ somewhat differs from $[101]$. The rotations were made with step of $(10 \pm 2)°$ from $0°$ up to $360°$ where the attendant incertitude was fueled by handling the goniometer. The approach predicts the squares
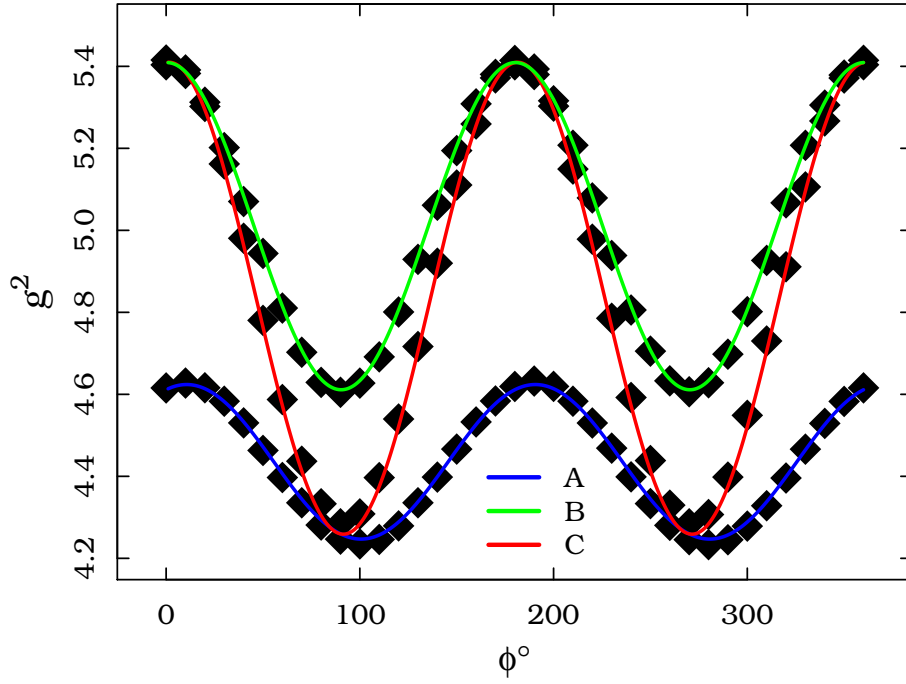
Figure 1.13: Angular dependence of g^2 for three different rotations $A(\phi)$, $B(\phi)$, and $C(\phi)$ at 50 K. The data are successfully fitted (yellow, green, and red curve) with law $g^2 = \gamma_{ii} \cos^2(\phi) + \gamma_{jj} \sin^2(\phi) + 2\gamma_{ij} \cos(\phi) \sin(\phi)$.

of g-factor to take on the following forms for the three rotations

$$A(\phi) \quad : \quad g^2 = \gamma_{CC} \cos^2(\phi) + \gamma_{BB} \sin^2(\phi) + 2\gamma_{CB} \cos(\phi) \sin(\phi), \qquad (1.13)$$

$$B(\phi) \quad : \quad g^2 = \gamma_{AA} \cos^2(\phi) + \gamma_{CC} \sin^2(\phi) + 2\gamma_{AC} \cos(\phi) \sin(\phi),$$

$$C(\phi) \quad : \quad g^2 = \gamma_{AA} \cos^2(\phi) + \gamma_{BB} \sin^2(\phi) + 2\gamma_{AB} \cos(\phi) \sin(\phi),$$

where γ_{ij} $(i, j = A, B, C)$ represent matrix elements of the square of g-factor tensor expressed in $\{\xi_A, \xi_B, \xi_C\}$. These elements are distilled as fitting parameters (Table 1.2) from the fits given in Figure 1.13.

Accordingly,

$$
\hat{\mathfrak{g}}^2 \equiv
\begin{pmatrix}
(\hat{\mathfrak{g}}^2)_{xx} & (\hat{\mathfrak{g}}^2)_{xy} & (\hat{\mathfrak{g}}^2)_{zx} \\
(\hat{\mathfrak{g}}^2)_{xy} & (\hat{\mathfrak{g}}^2)_{yy} & (\hat{\mathfrak{g}}^2)_{yz} \\
(\hat{\mathfrak{g}}^2)_{zx} & (\hat{\mathfrak{g}}^2)_{yz} & (\hat{\mathfrak{g}}^2)_{zz}
\end{pmatrix}
=
\begin{pmatrix}
4.6112 & 0.0684 & 0.0042 \\
0.0684 & 4.2596 & 0.0081 \\
0.0042 & 0.0081 & 5.4092
\end{pmatrix}.
\tag{1.14}
$$

The square root is reminiscent of a second rank monoclinic tensor (not necessarily metric),

$$
\hat{\mathfrak{g}} =
\begin{pmatrix}
2.14731 & 0.01624 & 0.00093 \\
0.01624 & 2.06382 & 0.00159 \\
0.00093 & 0.00159 & \mathbf{2.32577}
\end{pmatrix}
\tag{1.15}
$$

$$
\simeq
\begin{pmatrix}
a^2 & ac\cos(\pi - \beta) & 0 \\
ac\cos(\pi - \beta) & c^2 & 0 \\
0 & 0 & b^2
\end{pmatrix},
$$

and the computed principal values are

$$
\hat{\mathfrak{g}} =
\begin{pmatrix}
2.15035 & 0 & 0 \\
0 & 2.06076 & 0 \\
0 & 0 & \mathbf{2.32578}
\end{pmatrix}.
\tag{1.16}
$$

Following this calculus, the corresponding principal vectors are found to be

$$
\vec{u_1} = (0.98284, 0.18435, -0.00692), \tag{1.17}
$$

$$
\vec{u_2} = (0.18439, -0.98284, 0.00534),
$$

$$
\vec{u_3} = (0.00582, 0.00652, 0.99996),
$$

or estimated within fidelity of 10^{-2}

$$
\vec{u_1} \approx (0.98, 0.18, 0), \vec{u_2} \approx (0.18, -0.98, 0), \vec{u_3} \approx (0, 0, 1). \tag{1.18}
$$
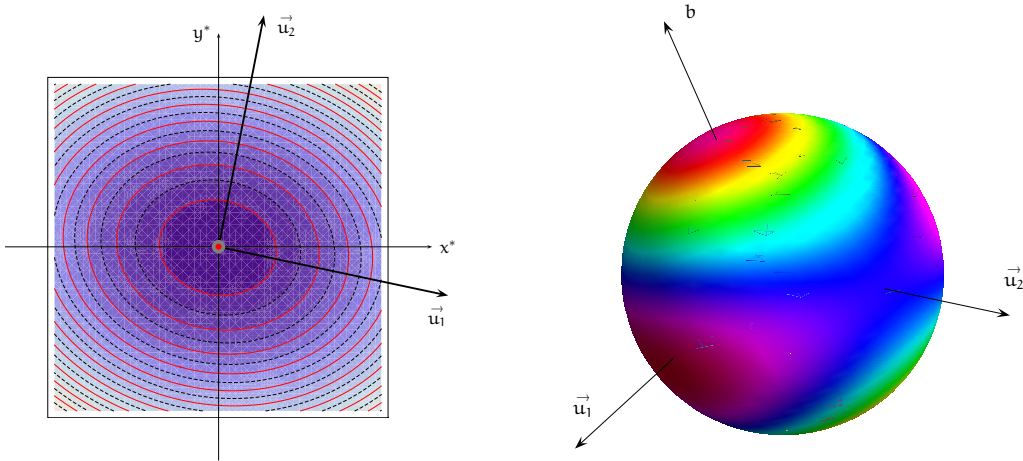
Figure 1.14: Principal coordinates and spatial distribution of the g-factor with respect to xyz $(x^* \Leftrightarrow x, -y^* \Leftrightarrow y)$ both in plane (left) and in 3D (right).

One can see that the u_3 principal axis is coincident with b. This simply means that the $\hat{\mathfrak{g}}$-factor behaves as a scalar along b-axis and, even more, is invariant in the sense of $C_{2h} \equiv \sigma_h \otimes C_2 = \{e, C_2, \sigma_h, i\}$ symmetry point group. It is exactly this point group that is required for the monoclinic crystal system. As a mere restriction in general, one principal value of every second rank monoclinic tensor must be aligned along the twofold axis (b in the treated case). The spatial distribution of the g-factor can also corroborate the symmetry visually (Figure 1.14). The plots have been constructed following a procedure which was given in [42].

1.4 Concluding Remarks

In conclusion, through ESR we provide an evidence that the $SeCuO_3$ compound can be considered as a solid quantum antiferromagnet based on the existing AF

correlations which extend well above T_N to nearly 170 K. This temperature is found to correspond to the isotropic AF exchange interaction (J') in the system. The exchange has been deduced from the temperature behaviour of both linewidth and g-factor. The temperature dependence of the linewidth has been successfully fitted using a semi-empirical model for spin relaxation. The model fuses two limiting approaches: Kubo-Tomita and Oshikawa-Affleck. Likewise, the conclusion about the presence of competing interactions (ferromagnetic and antiferromagnetic) has been drawn by analyzing g-factor behaviour and ESR spin susceptibility. We also conclude that there is opening of a broad temperature sector $T_N \ll T \ll \theta \sim J$, which frequently occurs in frustrated antiferromagnets. The observed temperature dependence of g-factors is due to the inequivalent copper sites experiencing different type of quantum correlations. Assuming temperature independent g-tensors that is valid in most of akin compounds, this effect can be inverted to a new experimental method of obtaining site selective susceptibilities from bulk measurements. In addition, monoclinicity of the $SeCuO_3$ crystal symmetry has been attested by assessing the principal values of g-factor tensor at 50 K.

Bibliography

[1] W. C. Röntgen, Annalen der Physik **271**, 264 (1888).

[2] Y. Wang, J. Hu, Y. Lin, and C. W. Nan, NPG Asia Materials **2**, 61 (2010).

[3] M. A. Kastner, R. J. Birgeneau, G. Shirane, and Y. Endoh, Rev. Mod. Phys. **70**, 897 (1998).

[4] J. G. Bednorz and K. A. Müller, Z. Physik B: Condensed Matter **64**, 189 (1986).

[5] T. Kimura, Y. Sekio, H. Nakamura, T. Siegrist, and A. P. Ramirez, Nature Materials **7**, 291 (2008).

[6] G. Giovannetti, S. Kumar, A. Stroppa, J. van den Brink, S. Picozzi, and J. Lorenzana, Phys. Rev. Lett. **106**, 026401 (2011).

[7] S. W. Cheong and M. Mostovoy, Nature Materials **6**, 13 (2007).

[8] G. Lawes, A. P. Ramirez, C. M. Varma, and M. A. Subramanian, Phys. Rev. Lett. **91**, 257208 (2003).

[9] S. Tornow, O. Entin-Wohlman, and A. Aharony, Phys. Rev. **B60**, 10206 (1999).

[10] B. H. Kim, H. Choi, and B. I. Min, Chemistry of Materials **12**, 2853 (2000).

[11] A. Villesuzanne, M. H. Whangbo, M. A. Subramanian, and S. F. Matar, Chemistry of Materials **17**, 4350 (2005).

[12] M. A. Subramanian, A. P. Ramirez, and W. J. Marshall, Phys. Rev. Lett. **82**, 1558 (1999).

[13] M. Johnsson, K. W. Törnroos, F. Mila, and P. Millet, Chemistry of Materials **12**, 2853 (2000).

[14] P. Fazekas, *Lecture Notes on Electron Correlation and Magnetism*, Series in Modern Condensed Matter Physics, Vol. 5, World Scientific Publishing, Singapore (1999).

[15] S. Sachdev, Nature Physics **4**, 173 (2008).

[16] L. Balents, Nature **464**, 199 (2010).

[17] A. P. Ramirez, Annual Review of Materials Science **24**, 453 (1994).

[18] D. Bergman, J. Alicea, E. Gull, S. Trebst, and L. Balents, Nature Physics **3**, 487 (2007).

[19] N. Tristan, J. Hemberger, A. Krimmel, H. A. Krug von Nidda, V. Tsurkan, and A. Loidl, Phys. Rev. **B72**, 174404 (2005).

[20] D. Zakharov, H. A. Krug von Nidda, M. Eremin, J. Deisenhofer, R. Eremina, and A. Loidl, *Anisotropic Exchange in Spin Chains*, p. 193 in NATO Science for Peace and Security Series B: Physics and Biophysics, ed. B. Barbara, Y. Imry, G. Sawatzky, and P. C. E. Stamp, Springer Netherlands (2008).

[21] A. Bencini and D. Gatteschi, *EPR of Exchange Coupled Systems*, Springer-Verlag, Berlin Heidelberg (1990).

[22] R. Kubo and K. Tomita, J. Phys. Soc. Jpn. **9**, 888 (1954).

[23] M. Oshikawa and I. Affleck, Phys. Rev. **B65**, 134410 (2002).

[24] R. M. Eremina, M. V. Eremin, V. N. Glazkov, H. A. Krug von Nidda, and A. Loidl, Phys. Rev. **B68**, 014417 (2003).

[25] A. Maisuradze, A. Shengelaya, H. Berger, D. M. Djokić, and H. Keller, Phys. Rev. Lett. **108**, 247211 (2012).

[26] H. Effenberger, Z. Kristallographie **175**, 61 (1986).

[27] I. Živković, D. M. Djokić, M. Herak, D. Pajić, K. Prša, P. Pattison, D. Dominko, Z. Micković, D. Cinčić, L. Forró, H. Berger, and H. Rnnow, Phys. Rev. **B86**, 054405 (2012).

[28] P. W. Anderson and P. R. Weiss, Rev. Mod. Phys. **25**, 269 (1953).

[29] P. W. Anderson, J. Phys. Soc. Jpn. **9**, 316 (1954).

[30] G. Srinivasan, A. S. Tatarenko, Y. K. Fetisov, V. Gheevarughese, and M. I. Bichurn, Mater. Res. Soc. Symp. Proc. **966**, 14 (2007).

[31] B. Cowan, *Nuclear Magnetic Resonance and Relaxation*, Cambridge University Press, New York (2005).

[32] S. Emori, T. Tokii, and Y. Muto, Bull. Chem. Soc. Jpn **48**, 1649 (1975).

[33] J. S. Smart, *Effective Field Theories of Magnetism*, W. B. Saunders Company, Philadelphia (1966).

[34] S. K Hoffmann and L. S. Szczepaniak, J. Magn. Res. (1969) **52**, 182 (1983).

[35] H. A. Krug von Nidda, N. Büttgen, and A. Loidl, European Phys. J. : Special Topics **180**, 161 (2009).

[36] J. Deisenhofer, R. M. Eremina, A. Pimenov, T. Gavrilova, H. Berger, M. Johnsson, P. Lemmens, H. A. Krug von Nidda, A. Loidl, K. S. Lee, and M. H. Whangbo, Phys. Rev. **B74**, 174421 (2006).

[37] P. M. Richards, *Proceedings of the International School of Physics*, "Enrico Fermi" Course LIX, North-Holland, Amsterdam (1976).

[38] D. L. Huber, J. Phys: Condensed Matter **15**, L579 (2003).

[39] T. T. P. Cheong and Z. G. Soos, J. Chem. Phys. **69**, 3845 (1978).

[40] J. Choukroun, J. L. Richard, A. Stepanov, Phys. Rev. Lett. **87**, 127207 (2001).

[41] J. E. Geusic and L. C. Brown, Phys. Rev. **112**, 64 (1958).

[42] H. Manaka, K. Masamoto, and S. Maehata, J. Phys. Soc. Jpn. **76**, 023002 (2007).

Chapter 2

Electron Spin Resonance Evidence for Magnetism in Nano-Sized Graphite and Graphene

2.1 Introduction

2.1.1 The Realm of Graphene

Carbon is one among the most fascinating elements in the Periodic Table. As a building brick, it takes variety of forms such as diamond, charcoal, fossil fuels, CO_2, graphite, including an endless list of compounds that has this element in common. Its presence can be traced in about 10 million compounds and is very abundant element in our lives. With exceptionally complex behaviour it has been extensively studied over decades and even centuries. For example, the knowledge about diamond, as one of the elementary carbon allotropes, dates back to ancient times, but the relevance

of graphite had been only identified two millennia later on, until correspondingly late, in XVIII century. Nowadays, carbon has been recognized as a central element in processes such as photosynthesis and natural acids such as DNA. Astonishingly, the entire Universe is permeated with reactions which carbon takes part in; just mention collisions of alpha particles, diamond stars, etc. Also, nanoscale science as a growing new focus of scientific interest has stepped into the realm of novel carbon based materials (CBM). A myriad of diverse studies continue to elaborate on the properties of carbon allotropes at nanoscale levels. For instance, diamond nanorod was evidenced to be the hardest material ever reported. Quite the opposite, graphite, as a bulk material on the other hand, is known to be the softest one. It would be no exaggeration to state that the CBM wonderland (see Figure 2.1) is one of the hottest new playgrounds for both researchers and engineers to career around.

Crucial discoveries with regard to CBM includes that of fullerenes [1] as well as the very first fabrication of carbon nanotubes [2]. The two carbon polymorphs have altogether led to a new perception of the material science applications. The quest for a revolution in this field has had considerable repercussions on practical applications of CBM, transistors in particular. The impact of such discoveries upon the scientific community is entirely unprecedented. The straightforward explanation is concerned with the outstanding properties of novel CBM.

Following fullerenes and carbon nanotubes, the interest for an old polymorphism of carbon, graphene, has continued to grow exponentially. The interest lies in the ease in its production and is sparked off by the non-sophisticated theoretical modeling of the electronic structure of graphene. However, despite these simplicities, it possesses as many attractive features, both in basic science and applications. Structurally,
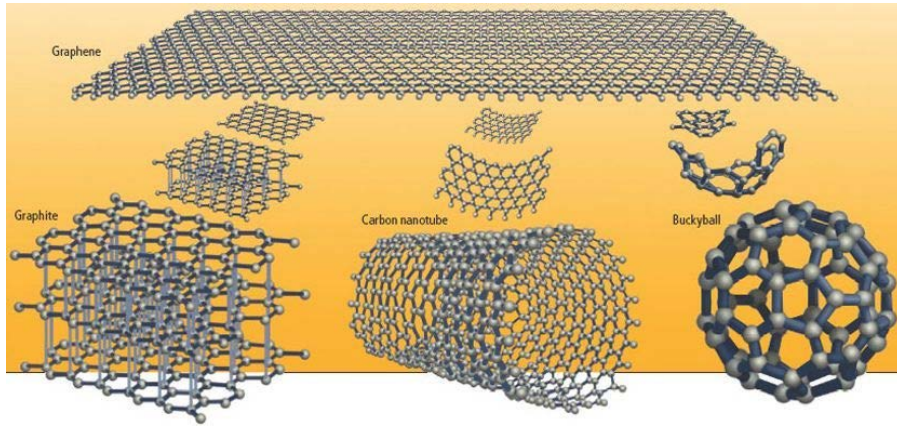
46

Figure 2.1: Graphene wrapped into rounded forms − *Carbon Wonderland.* The forms include honeycombed cylinders known as carbon nanotubes and soccer-ball shaped molecules known as fullerene, as well as various shapes which combine the two forms. The figure is adopted from Scientific American [3].

graphene is a pure 2D form of carbon and has been used and studied for even several decades as an elementary building block to CBM (Fig. 2.1). Such a two dimensional configuration consists of a real atomic monolayer of carbon atoms, which are organized into a honeycomb lattice.

Beyond the 90s, carbon allotropes were made available throughout 3D, 1D, and amazingly, 0D. As Figure 2.1 depicts, graphene is, unambiguously, the building block of each of these compounds − stacking several graphene layers yields graphite, rolling a graphene layer along a longitudinal axis yields a nanotube, and wrapping it as a ball will lead to a fullerene. As a consequence, the theory for graphene has been well developed even for sixty years, at the first place to explain the properties of the other dimensionalities and, second of all, as a model borrowed from quantum electrodynamics. Although graphene is known to inhere in graphite, for quite a long

47

period the thorough solid state community have adhered to a belief that it would be impossible to ever single out graphene as a stable atomic monolayer. In 1930s Landau and Peierls [4, 5] were (independently!) first to put forward theoretical arguments that 2D crystals should remain thermodynamically unstable and thereby could not exist as free standing systems. Predicted by the theory, thermal fluctuations would bring about a divergent contribution in systems with low dimensions. Concretely, the displacements of the lattice vibrations would approach the interatomic distances whereby the system would start melting at any finite temperature. Mermin further advanced this theory in 1968. He made a comparison to experimental results and successfully validated the hypothesis [6]. Regardless of the theoretical speculations, in praxis a single layer graphene subsists in crystalline form exhibiting only random microscopic curvatures [7]. Still, it was not these authors who were to make the unexpected discovery. "Mechanical analysis" of graphite has proven to be the most convenient way for "graphene synthesis".

Graphite, a material which has been studied for quite so long due to its fascinating mechanical properties, contains its relative graphene encapsulated as its building brick and can apparently be used to isolate graphene. It is only recently [8] that a free-standing stable atomic monolayer of carbon has been singled out as well as observed. The remarkable discovery disproved what was proposed by Landau and Peierls [4, 5]. Despite a certain amount of skepticism, numerous endeavours to make graphene have taken place over decades and mostly chemical exfoliations had been used for a long time − but with no unprecedented success. Such exfoliations consisted in implementing molecules into graphite samples in a chemical manner so as to separate single carbon monolayers, which are coupled together by van der Waals forces. Geim

and Novoselov, however, demonstrated in their remarkable Science paper [8] that it is possible to isolate graphene mechanically in different environments. The ease of the approach they favoured seems to have caused the scientific community to lessen the impact of the discovery. Nevertheless, it remains both unexpected and revolutionary − there have been many attempts of chemical preparing graphene which had failed until Geim and Novoselov.

The experimental discovery of graphene, which has turned out to contradict the entangling theory, has brought about a full revolution in the condensed matter world as well as beyond it, even towards high energy physics. Graphene does not stand only for the thinnest solid ever fabricated, but has also incredible properties. Some of the hot topics on the subject of pristine graphene samples are given in what follows.

Highly ordered graphene crystals are very stable at room temperature. Its inter-atomic bonds are covalent, thence both strong and flexible that may accommodate certain deformations leading to the fascinating mechanical properties of graphene. Exhibiting such properties, it may permit appreciable flexibility during experiments. Its crystalline form is a layer structure of benzene rings that commonly contains few defects.

The other important factor responsible for the growing excitement on graphene consists in its exceptional electronic properties. It is known to have good electric conductivity, which with great surprise never approaches zero irrespective of how low the concentration of free carriers is present in [7, 9]. The charge carriers in graphene are actually relativistic particles with their speed of about 1/300 of the speed of light. In literature, these are termed as massless Dirac fermions. When teaching physics of graphene, the famous Shrödinger equation is replaced by Dirac's for an appropriate

description of graphene behaviour that clearly has profound consequences upon the graphene properties. In fact, it seems not that common to trace an exception to the universal Shrödinger equation. However, it is important to know that the periodic potential generated by the honeycomb lattice in graphene is what constitutes the source of such exotic graphene behaviour. In other terms, carbon atoms themselves and their electrons moving around have no relativistic behaviour a priori. Graphene, represented as a system built of two honeycomb sublattices which involve both electrons and holes, forms a new type of quasiparticles, which are considered relativistic at low energy scale (Figure 2.2). The energy bands of the electronic structure are as-
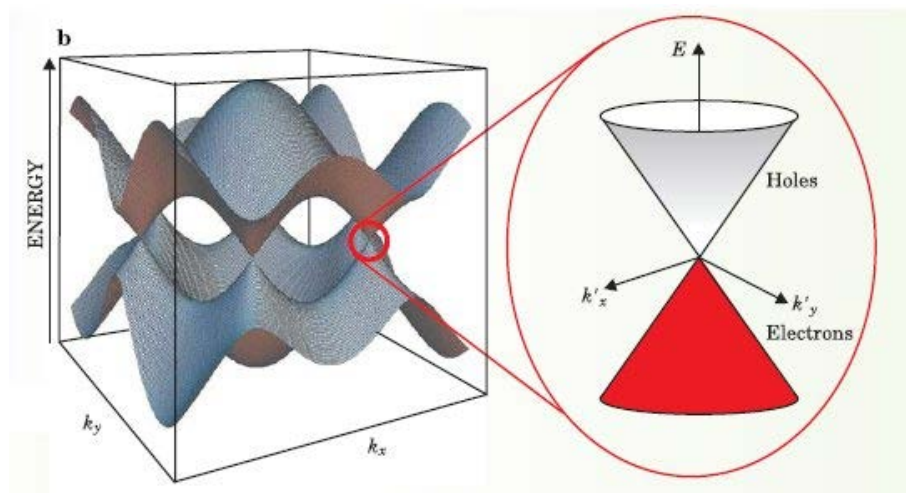

Figure 2.2: Electronic structure of graphene. The related dispersion relation is linear along the corners of the BZ.

sociated with the sublattices. The bands intersect at zero energy at K and K', which are located on the edges of the Brillouin Zone (BZ). The dispersion relation is linear across these points that introduces the quantum electrodynamics (QED), $E(k) \propto k$.

Although this theory was initially formulated around the 1920s, it remains on the verge of a new era. Thus, QED is not new, but probing it in solid state is. Complex phenomena predicted by this theory have always required giant laboratories for high energy physics. Moreover, eventually fairly weak responses are reached in such labs. With graphene on the other hand, QED is made possible to observe even on an office table. Low energy, relatively simple preparations, and setups are merely required. QED seems to go rather cheap. That is a giant step for QED that had always been related to black holes, cosmology, high energy particle accelerators, nuclear weapons, and the like, before graphene was paid attention to.
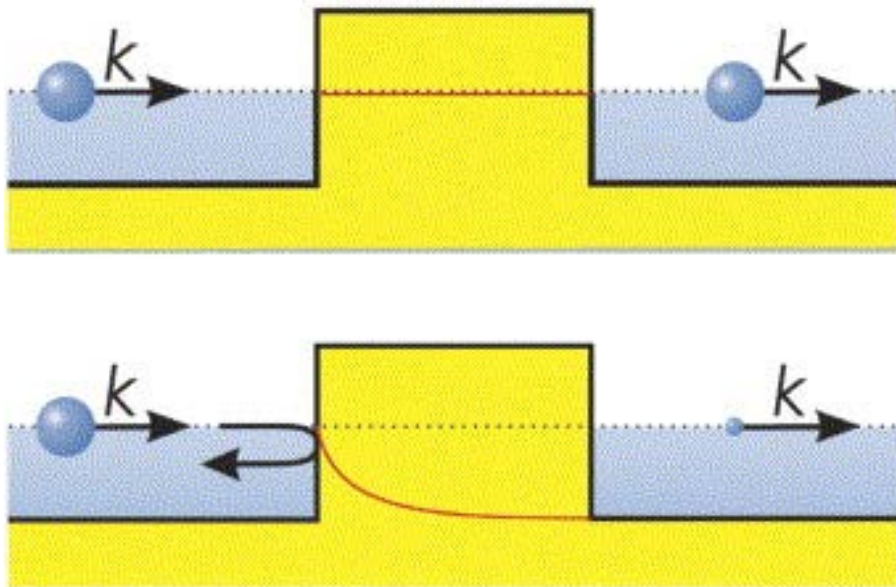

Figure 2.3: Klein paradox in massless Dirac fermions in graphene. Tunneling in graphene (top) and conventional tunneling (bottom). The figure is taken from [10].

The difference between classical and nonrelativistic quantum mechanics as well as QED is simply highlighted in Figure 2.3. Commonly, a low energy particle, ex-

periencing a high potential, can be safely treated classically and the corresponding model would imply that it will bounce back on the wall. This happens because the energy of the particle can provide no hopping over the top of the barrier. In the case of nonrelativistic quantum mechanics, there is a finite probability that the particle can be located on the other side of the potential barrier, according to the tunnelling principle. The probability depends on both height and width of the potential barrier. Entirely unexpectedly, QED imposes that a relativistic particle exhibits an ideal tunnelling, through a creation of a new but anti particle, no matter what characteristics the potential barrier possesses. This is known as the Klein paradox [10] which still continues to cause some confusion within the QED community.

2.1.2 Relevant Measurements, Growth, and Potential Applications

Novel electronic properties of graphene have been well documented by various experimental techniques [11]. Though nowadays one can encounter in the literature AFM, TEM, and SEM studies on graphene flakes, such techniques are unlikely to be useful for both locating graphene and estimating its thickness or number of layers. As far as the related optical spectroscopy measurements are concerned, it seems not trivial to achieve all the required parameters for these studies, such as thicknesses and cleanliness of the layers that also concerns used substrates. For instance, 315 nm of SiO_2 wafer makes the graphene invisible as compared to that of 300 nm instead [12]. Also, recently, as yet another optical tool, Raman spectroscopy on graphene has been successfully reported (see Malard *et al.* [13] and all the references therein).

These findings allow the identification and help determine the number of graphene layers which are present in the flakes (see Figure 2.4). The extensive use of Raman
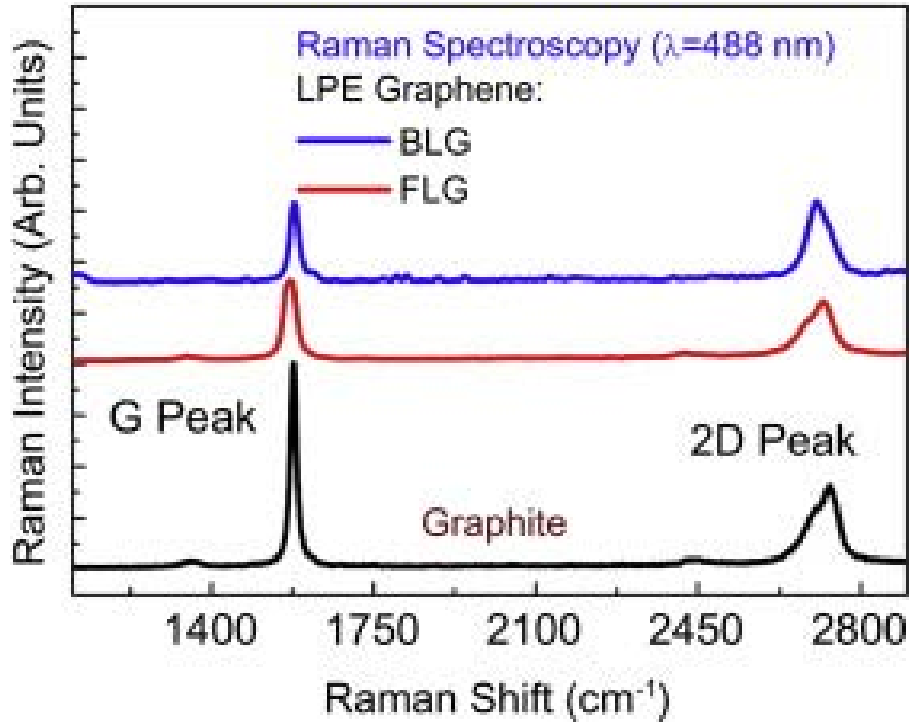
Figure 2.4: Room temperature Raman spectra of bilayer graphene (BLG) and few-layer graphene (FLG) flakes extracted from a solution. The figure is adopted from [14].

spectroscopy for graphene characterization is enabled by the fact that this material is entirely composed of symmetric sp^2 bonded carbons. However, imperfections it may have can be traced by Raman precisely, observing the violation of the optical selection rules. The Raman still remains the best technique for the graphene characterization. In order to establish a full repository of experiments for graphene it is important to have access to an optical tool such as Raman.

Graphene is also firmly assumed to be an eventual solution to some of the limits of the Si-based semiconductors. It appears feasible to improve the performance of the devices by reducing their size when using graphene. Moore's law, if believed, sets down such requirements.

Graphene based devices are predicted to exhibit remarkable properties that raises the expectation for graphene to be used in transistors. For this reason, a significant amount of work is necessary in order to come up with the most suitable characterization tools to use for graphene. Photo Electron Spectroscopy (PES), Low Energy Electron Diffraction (LEED), Angle Resolved Photon Spectroscopy (ARPES), as well as Raman Spectroscopy, seem to provide the effective solutions [15]. See Figure 2.5.

Fabrication of graphene goes with an astonishing ease and is well suited for both research and applications. However, it still does not meet prime requirements for large scale commercial production, nor for eventually patterned devices. An interesting study carried out by Kim *et al.* [16] tackles these issues which are associated with large scale pattern growth. To circumvent the obvious obstacles, it has been suggested to employ chemical vapor deposition of graphene [16] as well as graphene layers chemically exfoliated from graphite in organic solvents [17]. Both prove to exhibit properties even comparable to "ideal" or mechanically cleaved graphene: large electron mobility at room temperature, optical transparency, low sheet resistance, and at last but not least, the anomalous half-integer quantum Hall (Figure 2.6). By this effect, which is concerned with two-dimensional electron and hole gas, one can assess high quality graphene samples. Unusual half-integer quantum Hall effect and a non-zero Berry's phase discovered in graphene provide the unambiguous evidence of the existence of Dirac fermions in graphene and distinguish it from other conventional
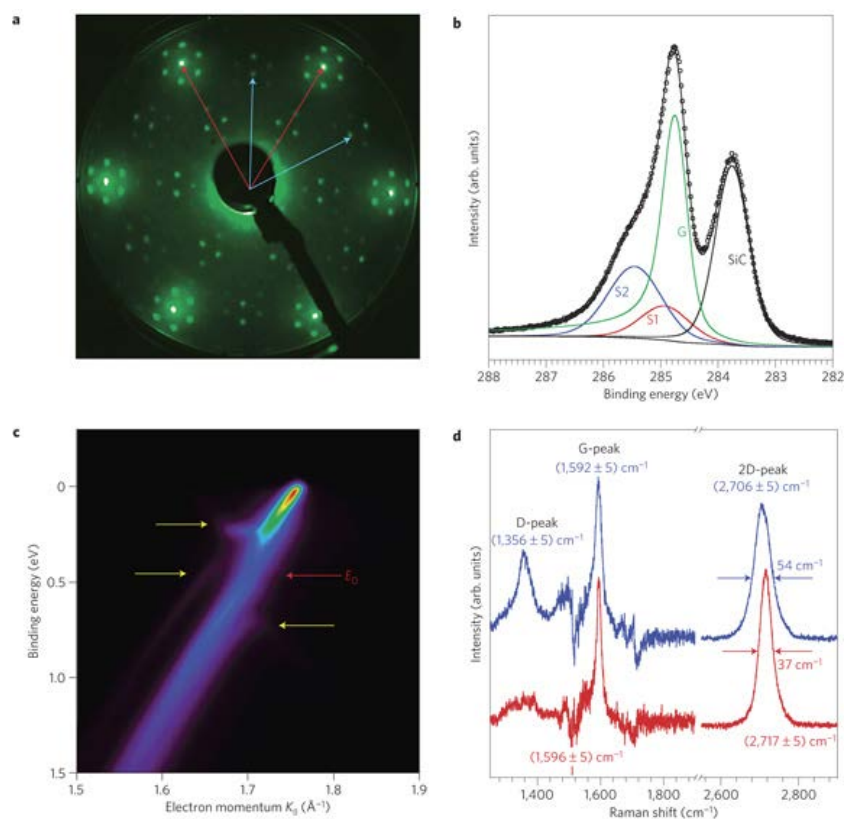
54

Figure 2.5: Various optical experimental characterization tools used for examining graphene (LEED, PES, ARPES, Raman). The figure is taken from [15].

2D electronic systems with a finite carrier mass. Observing the quantum Hall effect in graphene features very well its intrinsic electronic properties. The high-quality material could therefore be used not only for device applications, but also for many other fundamental studies. Still hitherto, the uniform growth of graphene single layers of at large scales remains challenging. Importantly, apart from the so-called "peel-off" technique, a giant chemistry endeavour, such as a method with colloidal suspensions [18], is ahead to make graphene layers at an appropriate macroscale.

It is interesting to note that one of the pioneering papers, regarding the graphene isolation based on micromechanical exfoliation, had no restrictions to carbon only
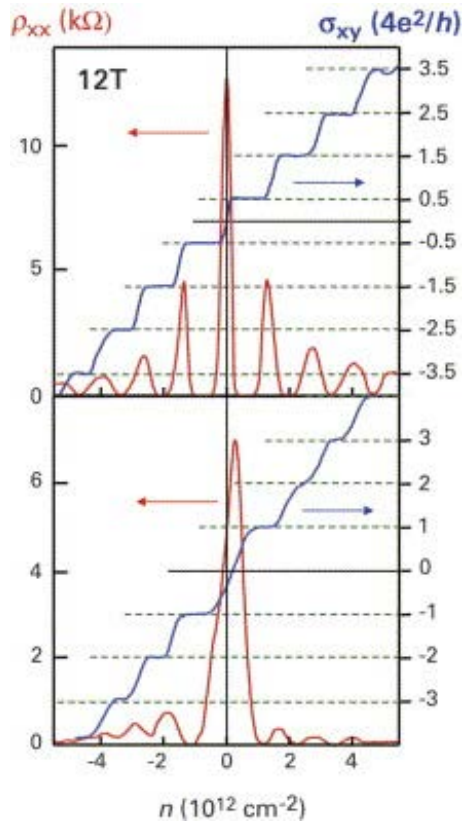
Figure 2.6: Quantum Hall effect in graphene (top) and bilayer graphene (bottom) as a function of carrier concentration. The peak at $n = 0$ displays a Landau level at zero energy where no states exist in zero field. The figure is taken from [10].

[19]. Notably elegant is the idea of attaching hydrogen atoms to each site of the graphene in order to create *graphane* (Figure 2.7), which alters the hybridization of carbon atoms from sp^2 into sp^3, thus removing the conducting *pi*-bands and opening up an energy gap. Partial hydrogenation can break the delocalized π bonding network of graphene, leaving the electrons in the unhydrogenated carbon atoms localized and unpaired. The magnetic moments at these sites may couple ferromagnetically. This is also found in widely studied finite graphene nanostructures, such as one-dimensional

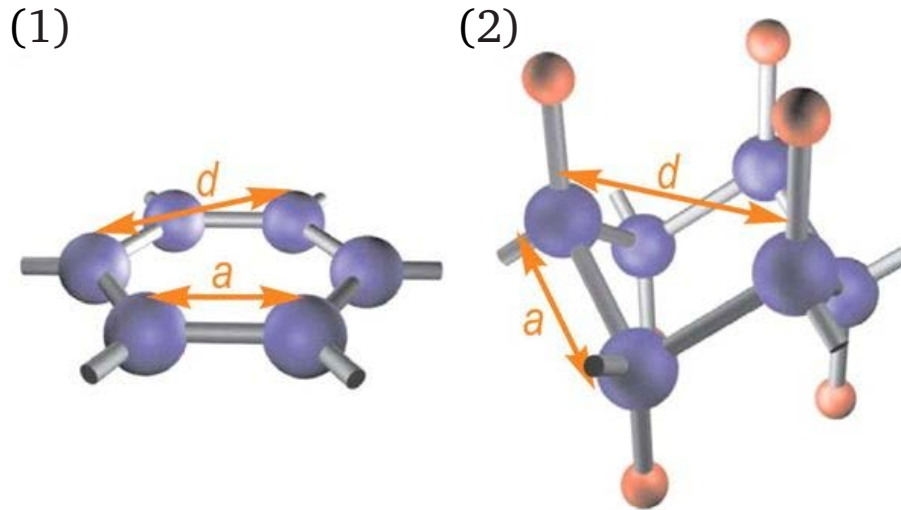Figure 2.7: The sp^2 (1) and sp^3 (2) hybridized C atoms in graphene. The latter hybridization comes from the bond saturation induced by hydrogen [19].

nanoribbons, where zigzag edges lead to the magnetism. From graphene to graphane, there is an evolution from metallic to semiconducting and from nonmagnetic to magnetic. Hydrogenation provides a novel manner to tune even magnetic properties with unprecedented potentials for applications, particularly in spintronics.

2.1.3 Magnetism in Graphene

2.1.3.1 General Introduction

The search for magnetism in CBM has a long tradition, in graphene in particular. Ideal graphene is nonmagnetic per se like other CBM [20]. Naturally, one relates the emergence of magnetism to transition metals, which originates from their partially filled d-electron bands. The light p-block elements belonging to the second period of the periodic table are, on the other hand, known for exhibiting no magnetic behaviour. However, as these elements are light, carbon based magnetism would attract

an enormous attention in technology. Diverse possible scenarios of such magnetism are anticipated to occur in nanostructured graphene as well as in its derivatives [21]. One of these possibilities is to use it in spintronics [22], which, unlike traditional electronics exploiting only charge degrees of freedom, makes use of spin. Indeed, theoretical modelings have shown that the localized states at the edges of graphene nanoribbons can have a long range magnetic order and as such they can carry the spin-information [23]. In addition, Son *et al.* [24] have predicted that the opposite edges have opposite spin configuration which could be tuned by electric field. This gives an additional control of the information transport.

Despite these spectacular theoretical predictions, the experimental demonstration of the long-range spin order in graphene and in graphene nanoribbons is still missing [25]. Very recent findings stemming from the muon spectroscopy [26] have also eliminated the possibility of formation of FM or antiferromagnetic (AFM) ordering in defective graphene. Nevertheless, it has generated the revival of the investigation of ferromagnetism in graphite or in other CBM. The interest has always been to create nanoscale magnetic and spin electronics devices. The light weight and the abundance of carbon would make CBM ideal candidates, but one would need a FM state at room temperature (RT). There are only few CBM ferromagnets, but their Curie temperature (T_C) is well below RT. One prominent example is TDAE-C_{60}, with a T_C of 12 K [27]. The FM state has shown to be very fragile, depending on the thermal history of the sample. The exchange interaction (J) of the localized wave-function of the electron on the C_{60} gives rise to FM state only in a special mutual configuration of the molecules because J depends on the overlap between adjacent sites [28].

Most of the CBM related ferromagnetism is reported for graphite and attributed

to the presence of impurities or lattice imperfections like cracks, grain boundaries, voids. Electron or ion irradiation induced defects in graphite also can result in a FM state [29]. The underlying model in these cases relies on the defect induced localized states at the Fermi level which leads to the existence of local moments. If these defects are aligned, e.g., on a grain boundary, direct exchange can give a FM state, with a rather high T_C [30]. If the local moments are dispersed in space then the RKKY interaction is evoked for aligning the spins [31]. Nevertheless, in this case the T_C is rather low. Furthermore, it is debated in the literature whether the low carrier concentration in CBM, especially in graphene, is capable to produce a sizable RKKY coupling between the localized spins [32].

A mean field theoretical study, carried out for randomly distributed magnetic defects in graphene [33] has reported that FM correlations can coexist alongside an AFM exchange. On the other hand, the presence of AF correlations in magnetic phase induced by non-magnetic structural defects in a single graphene still remains less likely. This is because the antiferromagnetic spin arrangements occur at special edge defect configurations, such as edge segments separated by the turn of 120° [34].

The present investigation inscribes in a study of magnetism of nano-graphite with the philosophy that a deeper understanding of ferromagnetism in ultra-thin graphitic systems will help to transfer this knowledge to graphene ribbons and to be useful in its spintronics applications. Temperature dependent Electron Spin Resonance provides a precious piece of information imparted from the spin paramagnetic sector only that is of the key relevance to tracing magnetism in CBM, which are notorious for large diamagnetism. By means of 9.4 GHz ESR, a superparamagnetic like state below 25 K in an assembly of nano-sized graphitic particles has been observed. These particles

were created with a heavy sonication of graphitic powder in N-methylpyrrolidone (NMP). The mechanical shock of the nanoparticles could produce structural defects which strongly perturb the electronic structure within graphene layers. The defect density, however, is not overwhelming, otherwise the Raman study would notice it [35], but its significance lies in the explanation of the magnetism.

The monoatomic carbon vacancies are the simplest structural defects able to induce magnetism in graphene. The magnetism observed in the experiments originates from structural imperfections more complex than monoatomic vacancies. Employing *ab initio* calculation several line defects can be identified, which give rise to the magnetism in graphitic particles through a finite density of states (DOS) near the Dirac point (see the subsection below). The set of investigated defects includes the graphene edges, intrinsic structural defects in the honeycomb lattice, and the zigzag chains of adsorbated H atoms. The calculations demonstrate that the emergence of defects in the π network of valence electrons gives rise to non-zero spin density in graphene sheet.

The ESR results presented throughout the thesis have been revealed in a cooperation with Dr. Luka Ćirić. The reader is kindly referred to the recently published work by L. Ćirić *et al.* [36].

2.1.3.2 Density of States in Defected Graphene

To understand the emergence of the magnetism in defected graphene it is important to compute its DOS. Density of states of a graphene nanodisk can be decomposed into the DOS due to the edge states (Dirac δ) and the DOS due to the bulk (smooth function). The bulk DOS per unit cell, $\rho_B(\epsilon)$, can be derived as an analytical expression

[37], which has the form

$$\rho(\epsilon) = \frac{4}{\pi^2} \frac{|\epsilon|}{t^2} \frac{1}{Z_1} K\left(\sqrt{\frac{Z_2}{Z_1}}\right), \tag{2.1}$$

with

$$Z_1 = \begin{cases} (1 + |\epsilon/t|)^2 - ((\epsilon/t)^2 - 1)^2/4; & -t \le \epsilon \le t \\ 4|\epsilon/t|; & -3t \le \epsilon \le -t \vee t \le \epsilon \le 3t \end{cases}, \tag{2.2}$$

$$Z_2 = \begin{cases} 4|\epsilon/t|; & -t \le \epsilon \le t \\ (1 + |\epsilon/t|)^2 - ((\epsilon/t)^2 - 1)^2/4; & -3t \le \epsilon \le -t \vee t \le \epsilon \le 3t \end{cases}, \tag{2.3}$$

where $K(x)$ is the complete elliptic integral of the first kind, while t is the bandwidth. In such a way, near the Dirac point,

$$\rho_B(\epsilon) \to \frac{2A_C}{\pi v_F^2} |\epsilon| \tag{2.4}$$

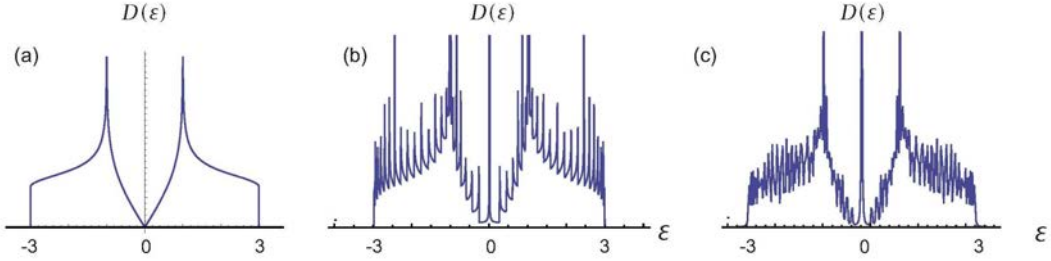where A_C stands for the unit cell area, $A_C = 3\sqrt{3}a^2/2$.

Figure 2.8: DOS of graphene (a), graphene nanoribbon (b), and graphene nanodisk (c), with respect to ϵ. The numerical results are taken from [37].

Therefore, near the Fermi energy, the DOS consists of that of the bulk graphene and an additional peak at zero energy due to the edge states for large number of

defects (N), as illustrated in Figure 2.8. Hence, together with spin degrees of freedom ($2S + 1$), the DOS behaves as

$$D(\epsilon) = \rho_B(\epsilon) + 2N\delta(\epsilon), \tag{2.5}$$

The crucial point is that the edge state peak is clearly distinguished from the DOS due to the bulk part. It is sufficient to take into account only the low energy sector to analyze physics near the Fermi energy, as the contribution from the edge states is always dominant. A finite DOS at the Fermi level is also a requirement imposed by the Stoner model for itinerant ferromagnetism.

2.2 Experimental and Theoretical Details

The nanographite sample was obtained as a side-product of graphite exfoliation in order to produce high quality graphene [17]. A sieved graphite powder was dispersed in N-methylpyrrolidone (NMP) by bath sonication. After sonication for 30 minutes a gray liquid was obtained consisting of a large number of graphitic particles including graphene flakes. The assembly was drawn through a filter paper and a thick black deposit was obtained. Its characterization by SEM is shown in Figure 2.9. Most of the graphitic flakes are residing flat on the filter paper. A particle counting shows that more than 70 % of the flakes have a surface area $\leq 1~\mu\text{m}^2$ and roughly 2 % are $\geq 50~\mu\text{m}^2$. The predominance of submicron sized particles justifies the denomination *nanographite*. Real statistics about the thickness of these particles is missing, but independent study has shown that it contains a large number of graphene flakes [17]. The ESR silent filter paper with the graphitic deposit was cut into $3.0 \times 5.0~\text{mm}^2$ rectangles and ~ 10 of them were piled up and introduced into an ESR quartz tube
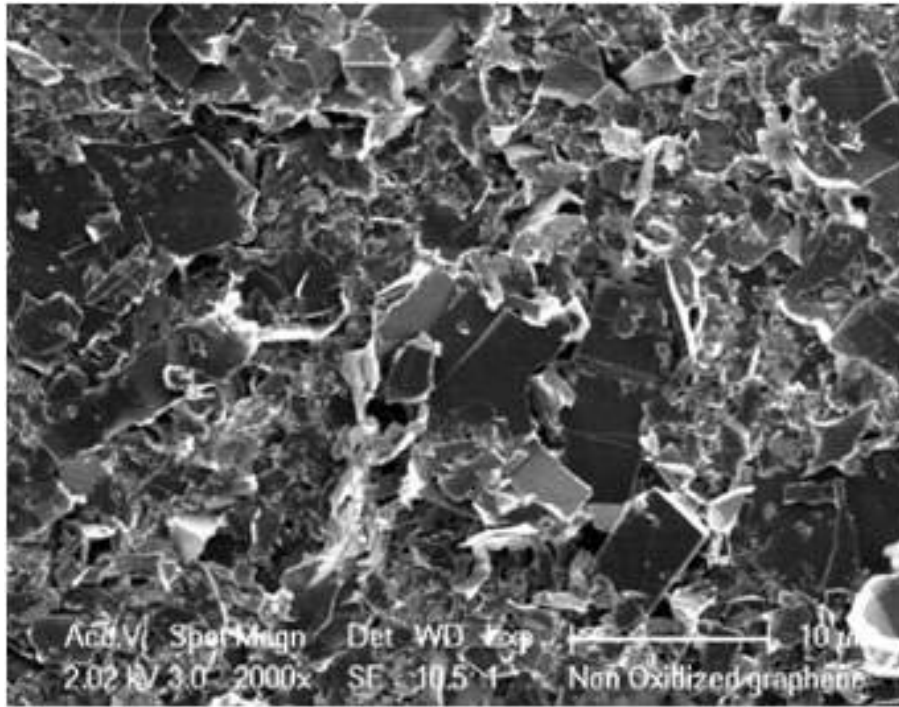
Figure 2.9: Scanning Electron Microscopy (SEM) image of the large assembly of graphitic particles. At least 66 % of the particles have a surface area ≤ 1 mm^2.

which was evacuated, filed with 100 mbar of high purity Helium gas and sealed. Temperature $(5-300$ K$)$ dependent ESR spectra were recorded using a Bruker ESR spectrometer E500 EleXsys Series (Bruker Biospin GmbH) which is equipped with a continuous wave Gunn diode, Bruker ER 4122 SHQE cylindrical TE$_{011}$ high-Q cavity, and an Oxford Instruments Helium-gas continuous flow cryostat (ESR900).

In order to examine prospects for defect-introduced magnetism in graphitic nanoparticles we perform calculations of the electronic properties of graphene flakes and an infinite graphene layer with selected structural imperfections. The theoretical investigations are restricted to the structures containing a single graphene layer since the weak van der Waals forces between graphene sheets are not expected to substan-

63

tially alter their magnetic properties. The structures considered in the present study are depicted in Figure 2.10. The rationale which led to this choice of investigated structural defects in graphene is described in the next section together with the corresponding DFT results. The calculations are performed with the GPAW computer
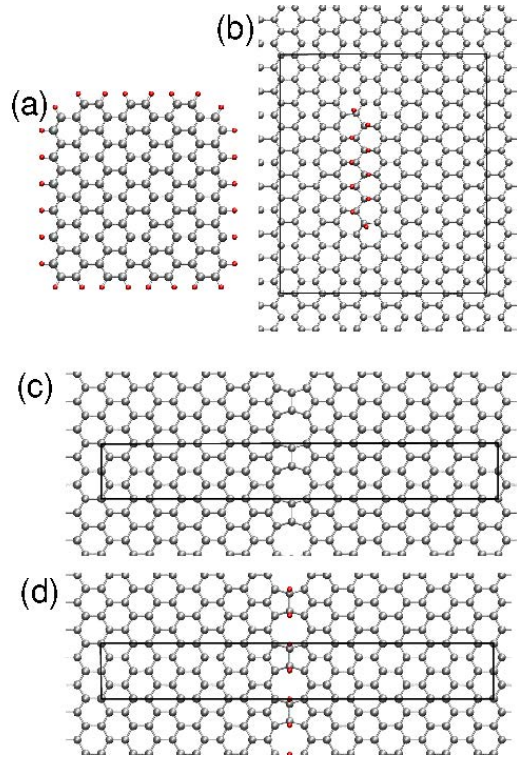
Figure 2.10: The atomic structure of (a) small rectangular graphene flake; (b) zigzag line of H adatoms on graphene; (c) bare line defect containing carbon pentagons and octagons; (d) hydrogenated line defect containing carbon pentagons and octagons. The H and C atoms are represented by red and gray spheres, respectively. For structures in (b)-(d) the surface unit cells are marked with black lines.

program [38, 39] based on the real space implementation of the projector augmented wave (PAW) method [40, 41]. All the credits for the numerical calculations go to Dr.

Željko Šljivančanin from the Institute of Vinča in Belgrade.

2.3 Results and Discussions

The obtained temperature dependent ESR spectra at 9.4 GHz consist in the following. At high temperature the signal is Lorentzian, while below 150 K it becomes asymmetric. An example of the signal recorded at 100 K is shown in Figure 2.11. It can be fitted with two Lorentzian absorption profiles as a sum of a broad and of a narrow component. The narrow line could be followed up to 150 K. Its intensity obtained by
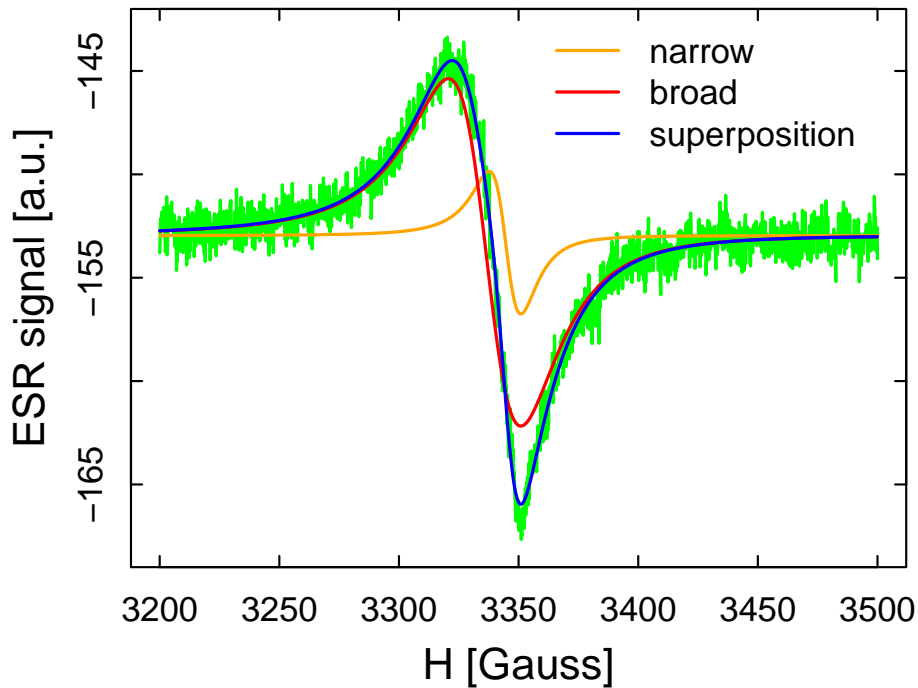

Figure 2.11: A typical ESR signal of the nano-graphite sample recorded at 100 K. The asymmetric signal is well fitted with a narrow and a broad component. The the resonance field was roughly in the $H_0 \perp c$ configuration.

the double-integration of the ESR line is proportional to the spin susceptibility (χ) and shows a Curie behaviour ($\chi \sim 1/T$).

It is worth mentioning that ESR spectra originating from conduction electrons are often asymmetric (Dysonian type). This effect is also observed in graphite and graphite intercalation compounds (GIC) [42], but not in our sample consisting of nano-sized graphitic particles, and we will not discuss that matter in this paper.

The double integrated broad line gives a Pauli-like susceptibility as in most of the graphite samples. This resemblance breaks at 25 K where the spin susceptibility starts to increase strongly on cooling (Fig. 2.12). This increase cannot be attributed simply to the appearance of a Curie tail since this increase is abrupt and it is much stronger than $\sim 1/T$. This could be easily seen in the inset to Figure 2.12 where the $\chi * T$ plot shows diverging behaviour below 25 K, strongly suggesting the onset of FM correlations.

The g-factor and the ESR line width (Fig. 2.13) corroborate with the behaviour of the spin susceptibilities. For the narrow line component they reveal both the value and the featureless temperature dependence which is similar to that observed for defects in CBM. However, the defects in our sample are not exactly the same as those observed in electron or ion irradiated samples [43], whose g-factor is close to the free electron value 2.0023. In our case the g-factor is higher (2.006), which resembles to defects created by incomplete functionalization, e.g., oxidation or reduction [44]. The augmented g value could be observed for the broad component, as well. In graphite in the static resonance magnetic field configuration H_0 parallel to c axis, g has a strongly temperature dependent value starting from 2.05 at 300 K and reaching 2.15 at 25 K [45]. In the present nanographitic sample the g value is of 2.011 at RT and shows
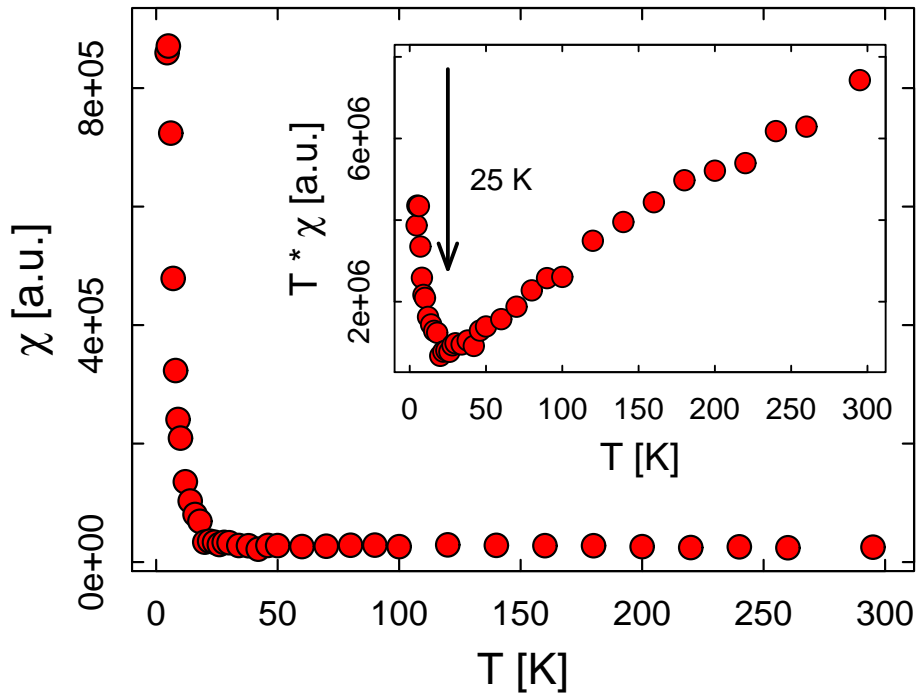
66

Figure 2.12: The temperature dependence of the spin susceptibility corresponding to the broad component of the ESR line. The strong increase of both χ and $\chi * T$ below 25 K points to the onset of magnetic interactions (inset).

practically no temperature dependence down to 25 K. At this transition g sharply decreases as the consequence of the onset of internal magnetic field.

2.3.1 DFT Calculations

To investigate possibility of the magnetism in graphene induced by structural imperfections more complex than monoatomic vacancies we focus on three types of line defects depicted in Figure 2.10: hydrogenated zigzag graphene edges, a zigzag chain of H adatoms at graphene, and a bare or hydrogenated intrinsic graphene line defect containing rows of carbon pentagons and octagons. All these defects can be modeled
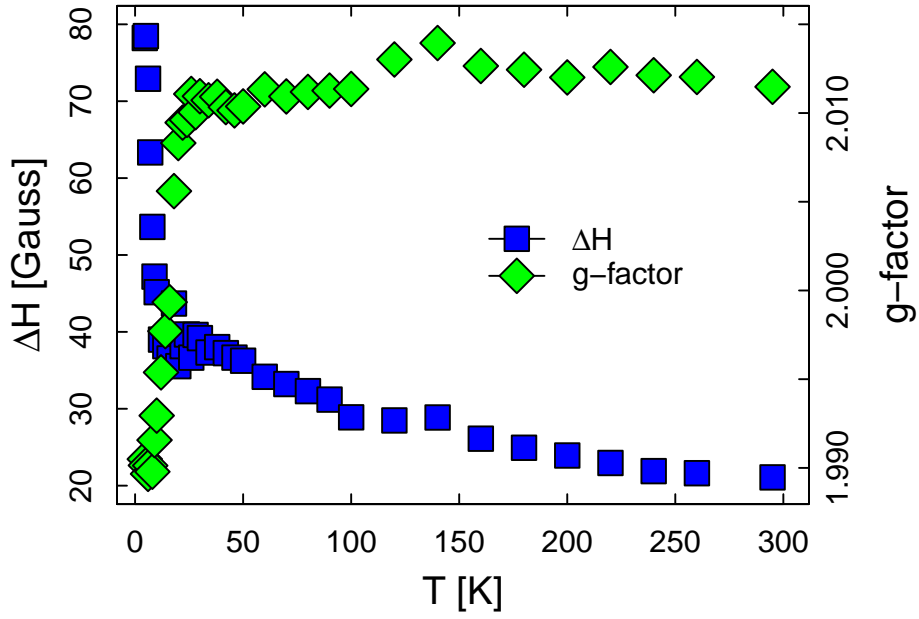
Figure 2.13: The ESR line width (left scale) and *g*-factor (right scale) of the broad component of the ESR line as a function of temperature. At 25 K both quantities show the onset of magnetic correlations.

at modest computational cost applying DFT calculations and give rise to the zigzag boundaries in the π network of graphene valence electrons. Hence these defects open prospect for producing the spin-polarized electron density in graphene following the same mechanisms described by Son *et al.* for zigzag graphene nanoribbons [46].

The graphene edges are inevitable in any graphene sample of a finite size. Their effect on magnetism is modeled considering a nearly squared graphene nanoparticle in Figure 2.10a since majority of graphitic particles observed by SEM (Fig. 2.9) are of similar shapes. The DFT calculations of graphene flake reveal that non-vanishing spin density is mostly located at C atoms near zigzag edges. The magnetic moment at the atoms along the same zigzag edge are ferromagnetically coupled, with different

signs for atoms near different zigzag edges (see Fig. 2.14a). Thus, regarding ground
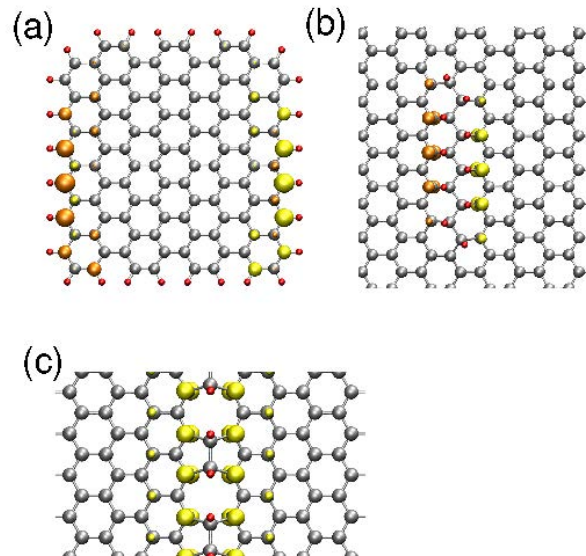
Figure 2.14: The isocontour plots of spin densities of (a) small rectangular graphene flake; (b) zigzag line of H adatoms on graphene; (c) hydrogenated line defect containing carbon pentagons and octagons. Yellow and orange colors are used to represent spin densities generated from electron states with opposite spin orientations.

state magnetic properties the graphene flake in Figure 2.10a could be considered as a finite graphene nanoribbon.

The zigzag lines of H adatoms on graphene in Figure 2.10b are among favorable adsorption configurations of small hydrogen clusters on graphene [47] and hence could be produced during the process of graphite sonication in NMP. A possibility of inducing magnetism in graphene in vicinity of the H chain structure (Figure 2.10b) is examined and magnetic moments were found to be of nearly $\sim 0.3\mu_B$ at C atoms near H adsorbates. The most favorable magnetic configuration corresponding to the

H zigzag chain on graphene is presented in Figure 2.14b.

The octagon-pentagon lines (Fig. 2.10c) are one of the simplest extended intrinsic line defects in graphene. They have been recently observed by Lahiri *et al.* [48] who combined STM with DFT calculations to resolve their structure at the atomic level. According to our calculations negligible spin polarization occurs in bare lines of pentagons and octagons. However, the picture changes significantly when the H atoms are adsorbed at line defects, as depicted in Figure 2.10d. For the H adsorption configuration in Figure 2.10d we calculated the binding energy of 2.49 eV per H atom. This value is by 0.78 eV higher than for H chains at defect free graphene [49]. Thus, the line defect is likely to be hydrogenated if the source of H atoms is available. The spin density plot in Figure 2.14c clearly demonstrates that the hydrogenated line defect induces significant magnetic moments at C atoms in its vicinity. The magnetic moments are ferromagnetically coupled giving rise to the total magnetic moment of 1.22 μ_B per unit cell.

2.3.2 Interpretation of ESR and Transport Data

The narrow line represents only $\sim$ 2 % of the total intensity of the ESR signal. This is attribute to impurities in the sample. Its g-factor and linewidth resemble to the defects in graphene obtained by reduction of graphene oxide [44], so we cannot exclude that they are situated in the exfoliated graphene flakes. Since there is no marked temperature evolution of this signal, we will disregard its further discussion.

The broad line coming from the majority phase shows in all physical quantities: intensity, linewidth, and g-factor the onset of the FM phase at 25 K. It manifests

in the strong increase of the spin susceptibility and linewidth, and in the abrupt decrease of the resonance field. Although these quantities show the appearance of a FM phase in the available temperature range no long range order emerges. The ESR line is still observable around $g = 2$ value. This is explained by a FM transition in small domains at 25 K, without interdomain interaction, and they could be considered as superparamagnetic clusters. They give an enhanced susceptibility and ESR line broadening due to the distribution of local internal fields.

Since such a FM signal is absent in the graphite powder before sonication in NMP, the structure hosting the FM interaction was necessarily created during this procedure. One can suppose that the sonication creates defects such as vacancies or chemical functionalization. The model which accounts in this case for the FM state was elaborated by Yazyev and Helm [50]. It is based on the experimental, STM observations [51] that a defect on graphite surface causes the perturbation of the electronic structure in a large region. One can trace distinctive triangular patterns associated with individual quasi-localized states [51]. Evoking the Lieb's theorem [52], which relates the total magnetic moment of a half-filled bipartite system to the difference of number of defects in the two sublattices, they could account for the FM signal in defected CBM systems. However, Lieb used the word *unsaturated ferromagnetism* to clarify that there is no spatial ordering.

Important question is the nature of the defects on the surface of nano-graphite which gives the local magnetic order. It is likely that they are extended defects which are created by the mutual shocks of the graphitic particles during the sonication. If the spatially close defects of different surface densities are produced in the complementary sublattices, they show an enhanced magnetic moment. This is the scheme

71

for ferromagnetism depicted in Ref. [50, 53]. However, based on the g -factors both for the narrow and broad lines, distinct from simple defects in a CBM (too big for both lines), we would like to suggest the possibility of NMP functionalization induced by sonication. This mechanical energy locally could enhance the probability of chemical bonding of NMP with the sp^2 network. It is likely, the NMP molecules attach preferentially to the sites which are already defected. The NMP molecules perturb
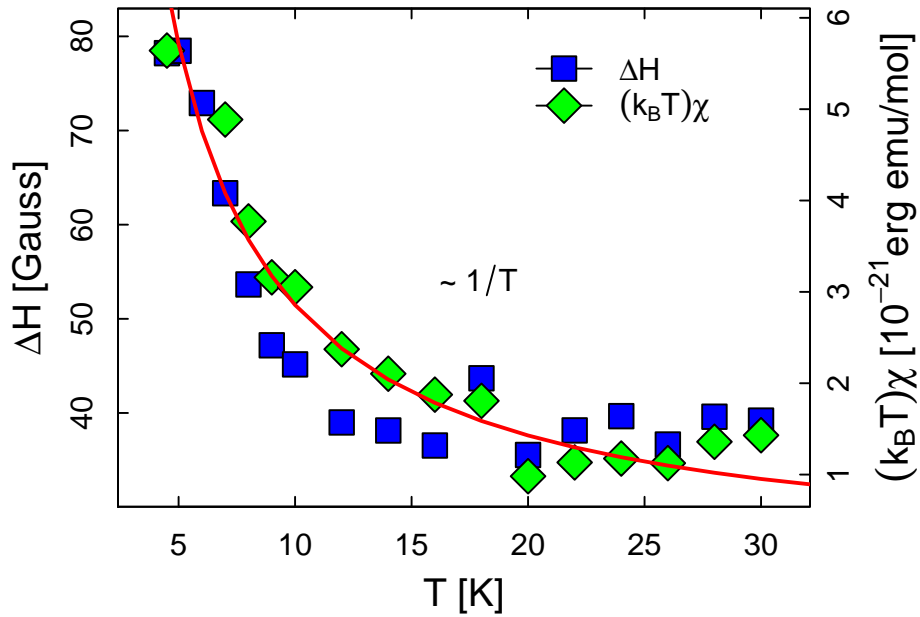
Figure 2.15: The line width and $(k_B T)$ multiplied susceptibility at low temperature. The red curve represents the best fit ($\sim 1/T$) for both mutually scaling dependences.

the electronic structure of graphite in the same manner as do vacancies. It is plausible that the stronger spin-orbit coupling of the NMP in respect to carbon gives an overall higher g-factor for the assembly.

The ESR data can be interpreted in terms of the onset of the 2D ferromagnetic coupling between the spins emerging due to the H-saturated C-atoms. As can be seen

from Figure 2.15, approaching the ordering temperature (hypothetically speaking $T_C = 0$ K) $\Delta H (T)$ broadens considerably below 25 K. This type of behaviour is generic for a 2D ferromagnet [54]. It is known that the dominant contribution to thermodynamic properties of weak ferro- and antiferromagnets above the transition temperature comes from diffusive magnetic excitations. In 2D systems with FM correlations, the $q = 0$ mode of the fluctuations grows considerably as temperature is lowered towards the critical temperature. In this case, the temperature dependence of ΔH follows

$$\left\langle \hat{S}^z_{q=0} \hat{S}^z_{-q=0} \right\rangle \sim (k_B T) \chi (T) \tag{2.6}$$

law rather than that of $\left\langle \hat{S}^z_{q=0} \hat{S}^z_{-q=0} \right\rangle^{-1}$, which is the case for a 3D ferromagnet [54]. The best fit for the temperature dependence of $\Delta H (T)$ was found to be $\sim 1/T$, thus meaning that, as the temperature is lowered from 25 towards 0 K, $\chi (T)$ increases as $T^{-\gamma}$ with $\gamma \approx 2$. The high critical exponent $\gamma \approx 2$ points to the onset of the 2D ferromagnetic coupling. In particular, the Ising model of 2D ferromagnets predicts 7/4 for γ [55]. The thorough explanation of the temperature dependent ΔH (2.6), which is generated by spin diffusion processes in 2D, is given in the subsequent section.

Also, using the relation for the in-plane resonance field of 2D ferromagnets [56], the g-factor temperature dependence below 25 K is given by

$$g(T) = g/\sqrt{1 + 4\pi \chi (T) \rho/M}, \tag{2.7}$$

where $M = 12$ g/mol, $\rho = 2.2$ g/cm^3, and $g = 2.011$. Based on Eq. (2.7) we find that the relative change of g with respect to $g(T)$ obtained at 4.5 K is $\delta g/g \approx 2\pi \chi \rho/M \approx 5 \times 10^{-6}$ ($\chi \gg \chi_{RT}$). The expression in (2.7) corroborates only qualitatively the related experimental value, $\delta g/g \approx 10^{-2}$. We believe that the discrepancy between

the estimated $\delta g/g \approx 5 \times 10^{-6}$ from the expression (2.7) and the experimentally found $\delta g/g \approx 10^{-2}$ might be due to a very rough estimation of χ_{RT}. The corresponding susceptibility has been estimated as 7.5×10^{-8} emu/mol [57]. For example, assuming that $J \sim 50$ K, the temperature dependence of the susceptibility (Fig. 2.13) becomes consistent with the picture of ferromagnetic correlations at 1D graphene edges [34], but this picture would then require a χ_{RT} to be nearly three orders of magnitude bigger.
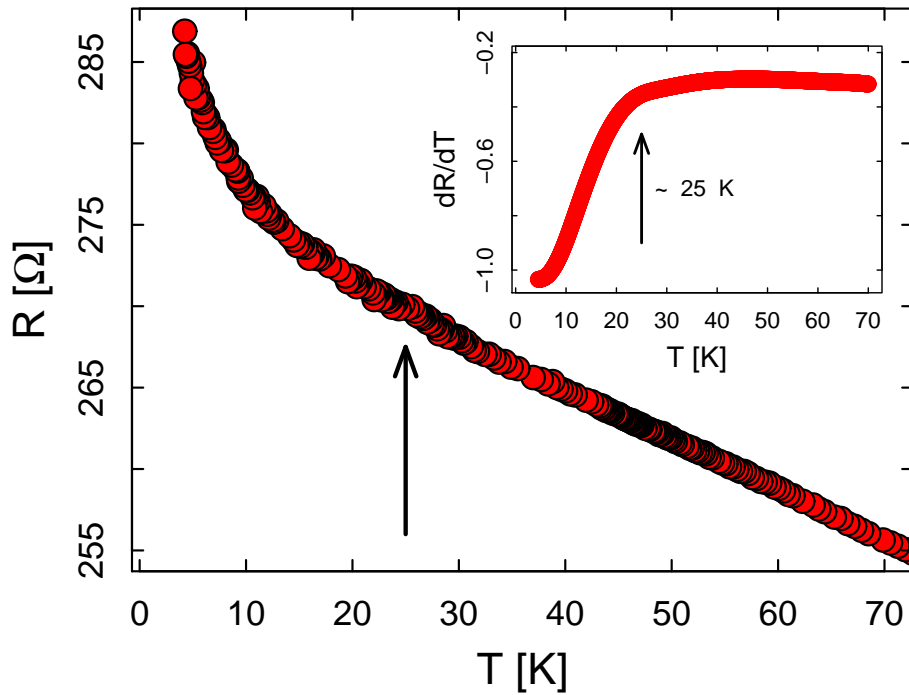

Figure 2.16: Resistance below 70 K of a thick film of nanographite (Fig. 2.9) as a function of temperature with weak non-metallic temperature dependence. It shows a stronger increase below 25 K where the FM interaction is observed by ESR. $R'(T)$ dependence presented in the inset clearly suggests a change at around 25 K. The data were acquired by Jaćim Jaćimović.

Resistance measurement of the thick film of the nano-graphite deposit (Fig. 2.16) signifies also the onset of the FM domains at 25 K. The resistance shows non-metallic temperature dependence, a weak increase of R with decreasing temperature. This is consistent with a relatively easy hopping between the particles. However, as soon as the FM local order is established in the perturbed regions of the graphite layers, the resistance increases stronger on lowering temperature. This observation suggests that the clusters with a local magnetic order are extended structures, it is not easy to short circuit them with the pristine regions.

2.3.3 Temperature Dependence of ESR Linewidth in 2D Ferromagnets

Strictly speaking, 2D ferromagnetically coupled systems should exhibit no phase transition at finite temperatures [58]. Still, as far as 2D Heisenberg magnets are concerned, there might exist phase transitions, albeit not of the conventional type, rather like one proposed by Lieb [52].

The well known magnetic transition occurs in 2D is Ising's. However, Ising magnets are generally not amenable to study by magnetic resonance due to the strong magnetic anisotropy which is generally present in their realizations causing spins to relax quite fast. This means that a minuscule anisotropy may eventually lead to transitions in 2D Heisenberg systems whose critical temperatures are considerably lowered due to the quantum fluctuations. The fluctuations bear a wave meaning and are therefore commonly specified by wave vector mode q. The effects of these modes are the major point about low dimensional Heisenberg magnets − for ferromagnets,

$q = 0$, in particular.

In 3D coupled systems on the other hand, the isotropic Heisenberg exchange, J, leads to an exchange narrowing of the ESR spectrum, which is usually described by the Kubo-Tomita model [59]. To obtain ΔH, the model involves: the second moment M_2 of the resonance line and exchange field $H_{ex} \propto J$,

$$\Delta H \simeq M_2/H_{ex}. \tag{2.8}$$

In such a way, the temperature dependence of the linewidth can be given in the high temperature approximation as

$$\Delta H(T) = \frac{\chi_0(T)}{\chi(T)} \Delta H_\infty. \tag{2.9}$$

where $\chi_0(T)$ is the free Curie susceptibility

$$\chi_0(T) = N g^2 \mu_B^2 S(S+1)/3k_B T$$

with $S = 1/2$, and $\chi(T)$ denotes the measured susceptibility. As $\chi_0(T)/\chi(T) \to 1$ for $T \to \infty$, the temperature independent parameter ΔH_∞ can be identified with the high temperature limit of the ESR linewidth. On can notice then that

$$\Delta H \sim \frac{1}{(k_B T) \chi(T)}$$

for 3D Heisenberg magnets.

ESR normally provides striking evidences from the importance of $q = 0$ modes in 2D systems and demonstrates rather directly the existence of spin diffusion which is central to the spin dynamics even above transient temperatures. It is well accepted that spin diffusion characterizes [54, 60] the static q behaviour at temperatures sufficiently above the transitions in which propagating spin waves become quite irrelevant.

76

Formally speaking, by spin diffusion one means that the spin correlation function, $\left\langle \hat{S}_i^z(\tau)\hat{S}_j^z \right\rangle \equiv \Sigma(\vec{r},\tau)$, obeys a diffusion equation ($\tau \to \infty$ or alternatively $\omega \to 0$), that is

$$\frac{\partial \Sigma(\vec{r},\tau)}{\partial t} = D\nabla^2 \Sigma(\vec{r},\tau). \tag{2.10}$$

The spatial Fourier transform gives the solution to (2.10) as

$$\left\langle \hat{S}_q^z(\tau)\hat{S}_{-q}^z \right\rangle = \left\langle \hat{S}_q^z \hat{S}_{-q}^z \right\rangle e^{-Dq^2|\tau|} \tag{2.11}$$

Since (2.10) is expected to be valid only for large $\vec{r}$, it follows that (2.11) holds only for small q. Insertion [61] of (2.11) into
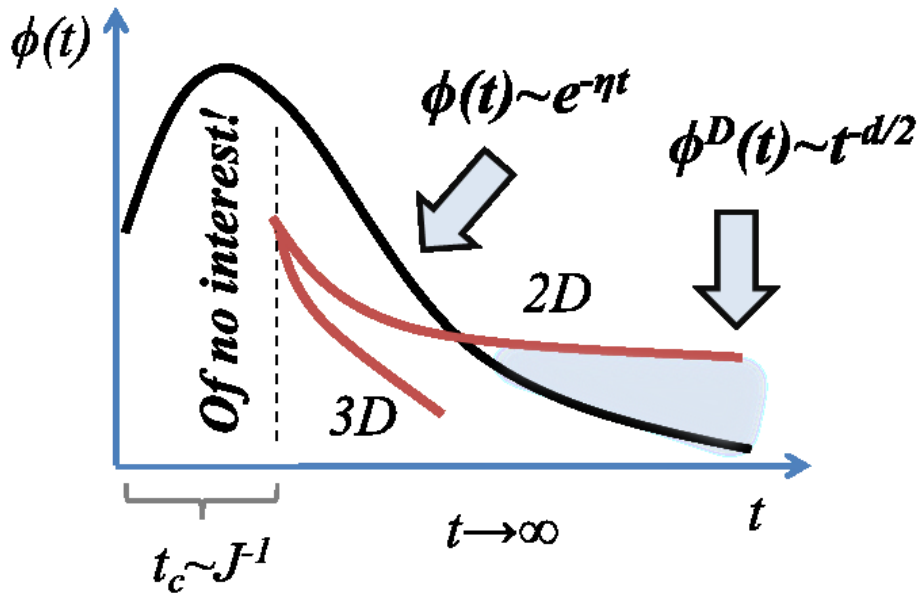

Figure 2.17: The figure demonstrates the relevance of the relaxation (red curves) due to the spin diffusion in 2D and 3D. Black curve represents the common nonspatial relaxation function. The τ_C sector is of no interest because of the strong exchange narrowing.

$$\left\langle \hat{S}_i^z(\tau)\hat{S}_j^z \right\rangle \propto \int q^{d-1} \left\langle \hat{S}_q^z(\tau)\hat{S}_{-q}^z \right\rangle dq, \tag{2.12}$$

where $d = 2$, leads to

$$\left\langle \hat{S}_i^z(\tau)\hat{S}_j^z \right\rangle \overset{\tau \to \infty}{\Rightarrow} \tau^{-1} \tag{2.13}$$

This is exactly the contribution to the spin relaxation function in 2D coming from the spin diffusion (see Figure 2.17). Spin relaxation is understood through its relaxation function $(\phi(t))$, which is defined as

$$\phi(t) \equiv \frac{\left\langle \hat{S}^+(t)\hat{S}^-(0) \right\rangle}{\left\langle \hat{S}^+(0)\hat{S}^-(0) \right\rangle}. \tag{2.14}$$

Nonspatial $\phi(t)$ is usually proportional to $e^{-\eta t}$ and it dominates over the spin diffusion part in 3D (Figure 2.17) leaving it practically irrelevant. Namely, the relaxation of spins due to the spatial transfer of the magnetization $(qa \ll 1)$ by virtue of the coupling between the spins takes place within a short time that is out of an experimental observation. In 2D, however, this is not the case.

Naturally, linewidth corresponds to the negative value of the inverse $\frac{\partial ln(\phi(t))}{\partial t}$ function whereby the spin diffusion part is involved. It turns out that using the general RPA (Random Phase Approximation) approach after Richards [54] uncovers the spin diffusion evident. This approach predicts that

$$\Delta H \sim (k_B T)\chi(T) \tag{2.15}$$

This relation stands opposite to the 3D case yielded from the Kubo-Tomita approach. Of course, the present calculation of the temperature dependence of the spin resonance linewidth (2.15) is indeed based on the Kubo-Tomita relaxation function, but somewhat generalized up to accounting for spin diffusion phenomena.

2.4   Concluding Remarks

In conclusion, ESR on the nanographitic sample has provided an evidence of a 2D ferromagnetic ordering of the Lieb type below 25 K. The FM interaction is found to originate from defects created during the sonication of the graphitic powder in NMP. The transport data have also corroborated the emergence of such a magnetism together with the DFT calculations. These reveal that hydrogen functionalization is responsible for the magnetism. However, modelling the functionalization together with NMP has turned out to be intricate and falls beyond the scope of the present study − the NMP in graphene can also form covalent bonds to induce the magnetism. At last, one can admit a possibility that the functionalization represents the defect sites, which induce magnetic moments in the graphitic structure, so that a targeted functionalization of graphene and study the appearance of FM correlations could be further carried out.

Bibliography

[1] H. W. Kroto, J. R. Heath, S. C. O'Brien, R. F. Curl, and R. E. Smalley, Nature **318**, 162 (1985).

[2] S. Iijima, Nature **354**, 56 (1991).

[3] K. G. Geim and P. Kim, Scientific American **298**, 90 (2008).

[4] L. D. Landau, Phys. Z. Sowjetunion **11**, 26 (1937).

[5] R. Peierls, Helv. Phys. Acta **7**, 81 (1934).

[6] N. D. Mermin, Phys. Rev. **176**, 250 (1968).

[7] J. C. Meyer, A. K. Geim, M. I. Katsnelson, K. S. Novoselov, D. Obergfell, S. Roth, C. Girit, and A. Zettl, Solid State Communications **143**, 101 (2007).

[8] K. S. Novoselov, A. K. Geim, S. V. Morozov, D. Jiang, Y. Zhang, S. V. Dubonos, I. V. Grigorieva, and A. A. Firsov, Science **306**, 666 (2004).

[9] M. I. Katsnelson, K. S. Novoselov, and A. K. Geim, Nature Physics **2**, 620 (2006).

[10] M. I. Katsnelson, Materials Today **10**, 20 (2007).

[11] A. K. Geim and K. S. Novoselov, Nature Materials **6**, 183 (2007).

[12] K. S. Novoselov, D. Jiang, F. Schedin, T. J. Booth, V. V. Khotkevich, S. V. Morozov, and A. K. Geim, PNAS **102**, 10451 (2005).

[13] L. M. Malard, M. A. Pimenta, G. Dresselhaus, and M. S. Dresselhaus, Physics Reports **473,** 51 (2009).

[14] K. M. F. Shahil and A. A. Balandin, Solid State Communications **152**, 1331 (2012).

[15] K. V. Emtsev, A. Bostwick, K. Horn, J. Jobst, G. L. Kellogg, L. Ley, J. L. McChesney, T. Ohta, S. A. Reshanov, J. Röhrl, E. Rotenberg, A. K. Schmid, D. Waldmann, H. B. Weber, and T. Seyller, Nature Materials **8**, 203 (2009).

[16] K. S. Kim, Y. Zhao, H. Jang, S. Y. Lee, J. M. Kim, K. S. Kim, Jong-Hyun Ahn, P. Kim, Jae-Young Choi, and B. H. Hong, Nature **457**, 706 (2009).

[17] Y. Hernandez, V. Nicolosi, M. Lotya, F. M. Blighe, Z. Sun, S. De, I. T. McGovern, B. Holland, M. Byrne, Y. K. Gun'Ko, J. J. Boland, P. Niraj, G. Duesberg, S. Krishnamurthy, R. Goodhue, J. Hutchison, V. Scardaci, A. C. Ferrari, and J. N. Coleman, Nature Nanotechnology **3**, 563 (2008).

[18] S. Park and R. S. Ruoff, Nature Nanotechnology **4**, 217 (2009).

[19] D. C. Elias, R. R. Nair, T. M. G. Mohiuddin, S. V. Morozov, P. Blake, M. P. Halsall, A. C. Ferrari, D. W. Boukhvalov, M. I. Katsnelson, A. K. Geim, and K. S. Novoselov, Science **323**, 610 (2009).

[20] R. C. Haddon, Nature **378**, 249 (1995).

[21] O. V. Yazyeɣ, Rep. Prog. Phys. **73**, 056501 (2010).

[22] P. Avouris, Z. H. Chen, and V. Perebeinos, Nature Nanotechnology **2**, 605 (2007).

[23] J. Fernández-Rossier and J. J. Palacios, Phys. Rev. Lett. **99**, 177204 (2007).

[24] Y. W. Son, M. L. Cohen, and S. G. Louie, Nature **444**, 347 (2006).

[25] J. Barzola-Quiquia, P. Esquinazi, M. Rothermel, D. Spemann, T. Butz, and N. García, Phys. Rev. **B76**, 161403(R) (2007).

[26] M. Riccò, D. Pontiroli, M. Mazzani, M. Choucair, John A. Stride, and O. V. Yazyev, Nano Letters **11**, 4919 (2011).

[27] P. M. Allemand, K. C. Khemani, A. Koch, F. Wudl, K. Holczer, S. Donovan, G. Grüner, and J. D. Thompson, Science **253**, 301 (1991).

[28] B. Narymbetov, A. Omerzu, V. V. Kabanov, M. Tokumoto, H. Kobayashi, and D. Mihailović, Nature **407**, 883 (2000).

[29] P. Esquinazi, D. Spemann, R. Höhne, A. Setzer, K. H. Han, and T. Butz, Phys. Rev. Lett. **91**, 227201 (2003).

[30] J. Červenka, M. I. Katsnelson, and C. F. J. Flipse, Nature Physics **5**, 840 (2009).

[31] M. A. H. Vozmediano, M. P. López-Sancho, T. Stauber, and F. Guinea, Phys. Rev. **B72**, 155121 (2005).

[32] S. R. Power, F. S. M. Guimares, A. T. Costa, R. B. Muniz, and M. S. Ferreira, http://arxiv.org/abs/1112.0205v1 (2011).

[33] O. V. Yazyev and M. I. Katsnelson, Phys. Rev. Lett. **100**, 047209 (2008).

[34] Y. G. Semenov, J. M. Zavada, and K. W. Kim, Phys. Rev. **B84**, 165435 (2011).

[35] U. Khan, A. O'Neill, M. Lotya, S. De, and J. N. Coleman, Small **6**, 864 (2010).

[36] L. Ćirić, D. M. Djokić, J. Jaćimović, A. Sienkiewicz, A. Magrez, L. Forró, Ž. Šljivančanin, M. Lotya, and J. N. Coleman, Phys. Rev. **B85**, 205437 (2012).

[37] M. Ezawa, *Physics of Triangular Graphene*, in Physics and Applications of Graphene - Theory, ed. by S. Mikhailov, InTech Publisher (2011).

[38] J. J. Mortensen, L. B. Hansen, and K. W. Jacobsen, Phys. Rev. **B71**, 35109 (2005).

[39] C. Rostgaard, J. J. Mortensen, J. Chen, M. Dułak, L. Ferrighi, J. Gavnholt, C. Glinsvad, V. Haikola, H. A. Hansen, H. H. Kristoffersen, M. Kuisma, A. H. Larsen, L. Lehtovaara, M. Ljungberg, O. Lopez-Acevedo, P. G. Moses, J. Ojanen, T. Olsen, V. Petzold, N. A. Romero, J. Stausholm-Møller, M. Strange, G. A. Tritsaris, M. Vanin, M. Walter, B. Hammer, H. Häkkinen, G. K. H. Madsen, R. M. Nieminen, J. K. Nørskov, M. Puska, T. T. Rantala, J. Schiøtz, K. S. Thygesen, and K. W. Jacobsen, J. Phys.: Condens. Matter **22**, 253202 (2010).

[40] P. E. Blöchl, Phys. Rev. **B50**, 17953 (1994).

[41] J. Perdew, K. Burke, and M. Ernzerhof, Phys. Rev. Lett. **77**, 3865 (1996).

[42] M. Saint Jean, C. Rigaux, and J. Blinowsky, J. Phys. France **51**, 1193 (1990).

[43] F. Beuneu, C. L'Huillier, J. P. Salvetat, J. M. Bonard, and L. Forró, Phys. Rev. **B59**, 5945 (1999).

[44] L. Ćirić *et al.*, *unpublished.*

[45] D. L. Huber, R. R. Urbano, M. S. Sercheli, and C. Rettori, Phys. Rev. **B70**, 125417 (2004).

[46] Y. W. Son, M. L. Cohen, and S. G. Louie, Phys. Rev. Lett. **97**, 216803 (2006).

[47] Ž. Šljivančanin, M. Andersen, L. Hornekær, and B. Hammer, Phys. Rev. **B83**, 205426 (2011).

[48] J. Lahiri, Y. Lin, P. Bozkurt, I. I. Oleynik, and M. Batzill, Nature Nanotechnology **5**, 326 (2010).

[49] L. Nilsson, Ž. Šljivancanin, R. Balog, T. R. Linderoth, E. Laegsgaard, I. Stensgaard, B. Hammer, F. Besenbacker, and L. Hornekaer, Carbon **50**, 2052 (2012).

[50] O. V. Yazyev and L. Helm, Phys. Rev. **B75**, 125408 (2007).

[51] H. A. Mizes and J. S. Foster, Science **244**, 559 (1989).

[52] Elliott H. Lieb, Phys. Rev. Lett. **62**, 1201 (1989); **62**, 1927(E) (1989).

[53] O. V. Yazyev, Phys. Rev. Lett. **101**, 037203 (2008).

[54] P. M. Richards, *Proceedings of the International School of Physics*, "Enrico Fermi" Course LIX, North-Holland, Amsterdam (1976).

[55] D. B. Abraham, Phys. Lett. **43A**, 163 (1973).

[56] C. Kittel, *Introduction to Solid State Physics*, (4th edition) Wiley, New York (1971).

[57] O. Chauvet, G. Baumgartner, M. Carrad, W. Basca, D. Ugarte, Walt A. de Heer, and L. Forró, Phys. Rev. **B53**, 13996 (1996).

[58] H. E. Stanley and T. A . Kaplan, Phys. Rev. Lett. **16**, 981 (1966).

[59] R. Kubo and K. Tomita, J. Phys. Soc. Jpn. **9**, 888 (1954).

[60] J. P. Boucher, F. Ferrieu, and M. Nechtschein, Phys. Rev. **B9**, 3871 (1974).

[61] P. K. Leichner and P. M. Richards, Phys. Rev. **B7**, 453 (1973).

Chapter 3

Itinerant Magnetism in Organic Kagomé $(EDT\text{-}TTF\text{-}CONH_2)_6Re_6Se_8(CN)_6$ System as Seen via Electron Spin Resonance

3.1 Introduction

Low-dimensional organic conductors, a subclass of organic compounds, are considered to have potential applications in molecular electronics, spintronics, and optoelectronics [1]. However, for the time being they are still model compounds, subjects of basic research. Chemists and solid state physicists make a joint effort to learn the basic

physical properties and to explore the tunability of these compounds for achieving a desired function. Along these lines there is a strong activity for designing and synthesizing molecular systems based on electron donor (D) and acceptor (A) building units. Amongst many kinds of molecular electron donor moieties, tetrathiafulvalene (TTF Fig. 3.1) and its derivatives are known to be strong π-donors, capable of forming
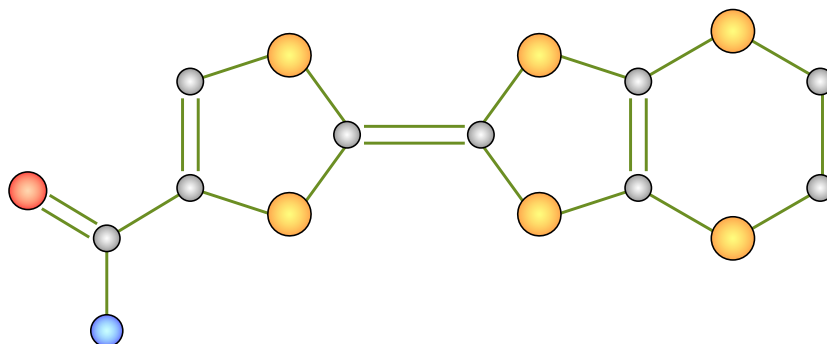

Figure 3.1: A simple sketch of a tetrathiafulvalene (TTF) derivative. The atoms are given in standard CPK color convention.

stable cation radical and dication species upon oxidation, thus leading to a number of conducting and superconducting materials.

Even at the present time, much interest in studying TTF derivatives has been well evinced. Their astonishing facets of physical properties emerging from *reduced dimensionality* keeps enjoying constantly a special place in the hearts of both experimental and theoretical solid state scientists [2]. The interest is mostly due to the fact that a great deal of TTF compounds crystallize in the form of linear stacks of large planar organic molecules. These strongly overlap via π-orbitals in one particular plane. It is in general perpendicular to the molecular planes in-between which no significant overlap takes place. As a result of such a crystallization and π-orbital overlapping,

the electron transport goes easiest in the plane and becomes considerably prevented perpendicularly.

The traditional band structure theory used to describe such compounds has, however, met strenuous objections from both experimental and theoretical side [3]. The major theoretical objection comes from the paper by Anderson [4]. Detailed insights into corresponding experimental data of π-conjugated organic systems reveal that their actual behaviour markedly differs from that predicted by the band structure theory. For example, their spin susceptibility can sizably be enhanced over its Pauli value, a feature that is absolutely inappropriate for normal metals [5].

One quite astonishing recently synthesized compound constituted of TTF derivatives is $(EDT-TTF-CONH_2)_6Re_6Se_8(CN)_6$, in which the organic dimers form a kagomé lattice that is unprecedented for any organic material [6]. Kagomé networks, composed of corner-sharing interlaced triangles are nowadays at the heart of intense research due to the possibility of generating new and original electronic ground states. Many studies have been devoted to the case of systems with localized moments and antiferromagnetic correlations, in which the following geometry highly frustrates spin interactions to induce fluctuating behaviour. The case of localized spins has thus been enormously studied in the literature, whereas the area of itinerant kagomé systems has remained less explored. Theoretical calculations have demonstrated grotesque properties of these systems [7]. Half electron filling in such geometries appears to insure the stability of the Mott insulating state with help of relatively high values of the onsite Coulomb repulsion (U).

On the other hand, itinerant electrons in 2D kagomé lattice with third fillings form a Dirac semimetal, similar to graphene [8]. A simple tight-binding model for electrons
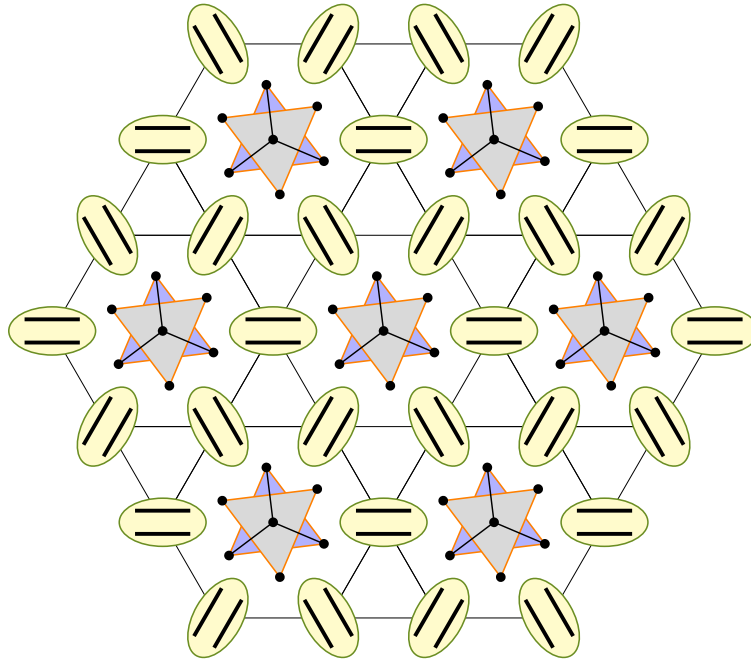
88

Figure 3.2: The kagomé network in $(EDT-TTF-CONH_2)_6Re_6Se_8(CN)_6$ at high temperature. The organic dimers are given in yellow ovals. The inorganic spinless anionic octahedra are situated in the centers of hexagons.

on kagomé lattice at both 1/3 and 2/3 filling leads to the topological insulating behaviour upon inclusion of the spin-orbit coupling [9]. For Dirac kagomé semimetals at 1/3 filling, a finite interaction strength U of order t is needed to open up a gap [10]. At 2/3 filling, however, the band crossing is quadratic and the instability towards the insulating phase occur at infinitesimal repulsive interaction, making such system a promising candidate for a 2D topological insulator.

In the $(EDT-TTF-CONH_2)_6Re_6Se_8(CN)_6$ crystal the TTF-based molecules form kagomé topology in the metallic state at high temperature as is sketched in Figure 3.2. The kagomé unit cell contains three crystallographic sites: A, B, and C (Fig. 3.3). Four holes are shared by the three sites leading to 2/3 hole (1/3 electron) filling. The
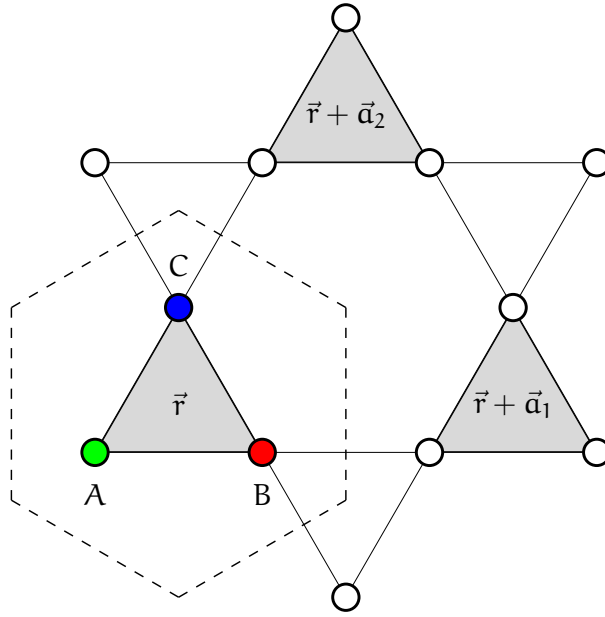
Figure 3.3: The kagomé unit cell delineated with the dashed hexagon. The cell basis is spanned by three crystallographic sites: A, B, and C, each belonging to its triangular network.

metallic state observed in the $200 - 300$ K temperature range has been found to have a strong two-dimensional character, in coherence with the kagomé lattice symmetry [6]. The same authors have reported a structural instability towards a distorted form of the kagomé topology of lower symmetry at ca 200 K. As with the low-temperature structure, it is associated with a localized, electrically insulating electronic ground state which restores Mott half filling scenario. Its magnetic susceptibility can be accounted for by uniform Heisenberg chains of localized $S = 1/2$ spins at low temperature. The two phases could be nicely followed via ESR spectra (including linewidth, g-factor, and A/B) recorded at 9.4 GHz with some considerations listed in [6].

In this part of the thesis, a succession of the previous comprehensive study of $(EDT-TTF-CONH_2)_6Re_6Se_8(CN)_6$ [6] is reported according to pressure and temper-

ature dependence of 210 GHz ESR spectra in combination with the X-band ESR. For completeness, transport measurements have been involved that was borrowed by courtesy of Jaćim Jaćimović. Dr. Areta Olariu is greatly acknowledged for having taken a considerable part in acquiring the ESR data.

3.2   Experimental Details

Measurements were made on $(EDT\text{-}TTF\text{-}CONH_2)_6Re_6Se_8(CN)_6$ single crystals of nearly 1 mm^3 in size. Although they were of complicated shapes, few were synthesized with (111) face and then used for ESR measurements. A high field ESR spectrometer [11] (210, 315, and 420 GHz) was used with the configuration that allows easy adaptation of a high pressure cell operating up to 15 kbar. The high field ESR spectrometer is equipped with a superconducting magnet which reaches maximal field of 16 T corresponding to resonant frequency of 420 GHz for systems with g factors ~ 2. The spectrometer operates in the frequency range of $210 - 420$ GHz and in the temperature range of $2 - 300$ K. Quasi-optical techniques were exploited to include the use of a homodyne reference arm, induction operation, corrugated wave guide, and the use of linearly polarized light. As far as the 9.4 GHz ESR temperature $(5 - 300$ K$)$ dependent measurements are concerned, they were recorded using a Bruker ESR spectrometer E500 EleXsys Series equipped with a standard continuous wave Gunn diode, Bruker ER 4122 SHQE cylindrical TE_{011} high-Q cavity, and an Oxford Instruments He gas continuous flow cryostat.

3.3 Results and Discussions

Since organic materials are in general quite susceptible to hydrostatic pressure, one of our aims is to study and understand the kagomé to 1D spin chain transition by ESR as a function of pressure and temperature. Further goal is also to grasp the spin dynamics of the 1D Heisenberg chains as a function of pressure at low temperature.

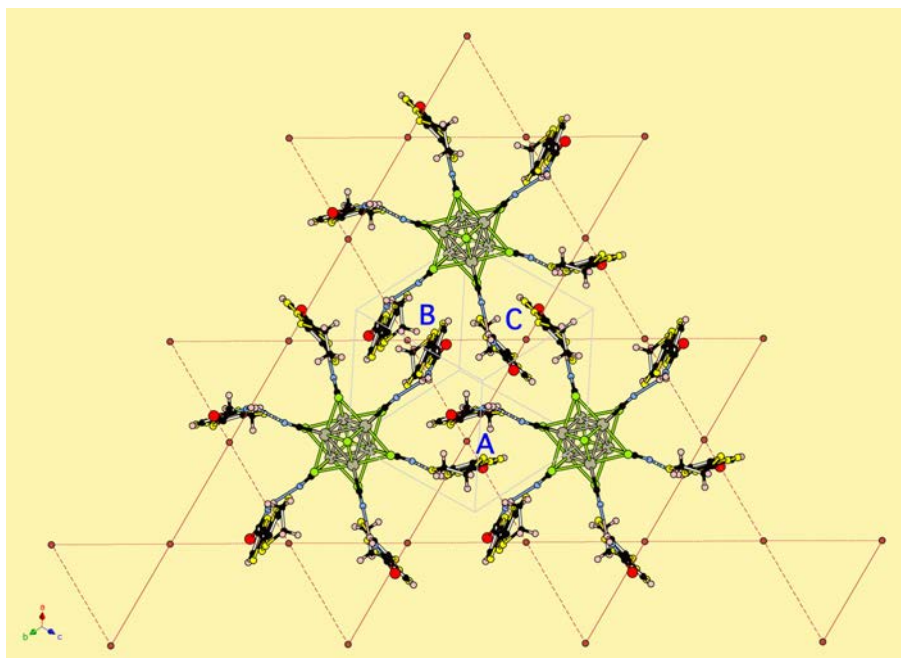### 3.3.1 Evolution of the Crystal Structure

Figure 3.4: Projection onto a kagomé layer illustrating its distortion of the crystal structure at ambient pressure (by courtesy of P. Batail).

The high temperature rhombohedral unit cell of $R\bar{3}$ symmetry contains one independent EDT-TTF-CONH$_2$ in general position which forms centrosymmetric dimer.

Sizable displacements of EDT-TTF-CONH$_2$ molecules occur at the transition (below 200 K) so that the three dimers: A, B and, C (Figure 3.4) become inequivalent as the three-fold crystallographic axis disappears and the symmetry is reduced down to the triclinic one. As exemplified in Figure 3.5, molecules in dimer B rotate around their short in-plane molecular axes in a direction opposite to that of the rotation of molecules in A and C. Deviations from the room temperature positions of the molecular planes amount to $2-4°$ at 100 K. As a result, the pattern of overlap within dimer B (Fig. 3.5a) differs from that within A and C (Fig. 3.5b).
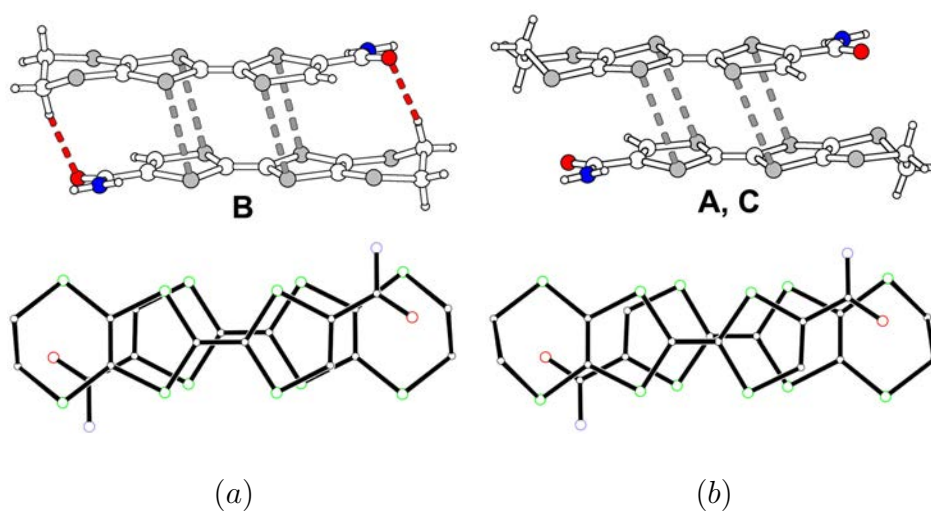

(a) (b)

Figure 3.5: The 3-fold axial symmetry breaking in the triclinic structure reveals a set of $2 + 1$ centrosymmetric dimers A$^{•+}$, C$^{•+}$, and B^{2+} described here: (a) Side and top views of intermolecular overlap modes inside B and (b) A, C dimers [6].

The symmetry of the kagomé net in the rhombohedral room temperature structure shown in Figure 3.4 becomes broken in the triclinic structure below 200 K. The distortion essentially results from significant molecular motions and change of conformations of dimers A, B, and C [6] . The concomitant structural and electronic

transitions leave one single direction of 1D uniform chains of spins 1/2, materialized by the parallel solid red lines connecting dimers $A^{\bullet+}$ and $C^{\bullet+}$; charge ordering has occurred along the two broken red line directions where $A^{\bullet+}$ (or $C^{\bullet+}$) and B^{2+} alternate (Figure 3.4).
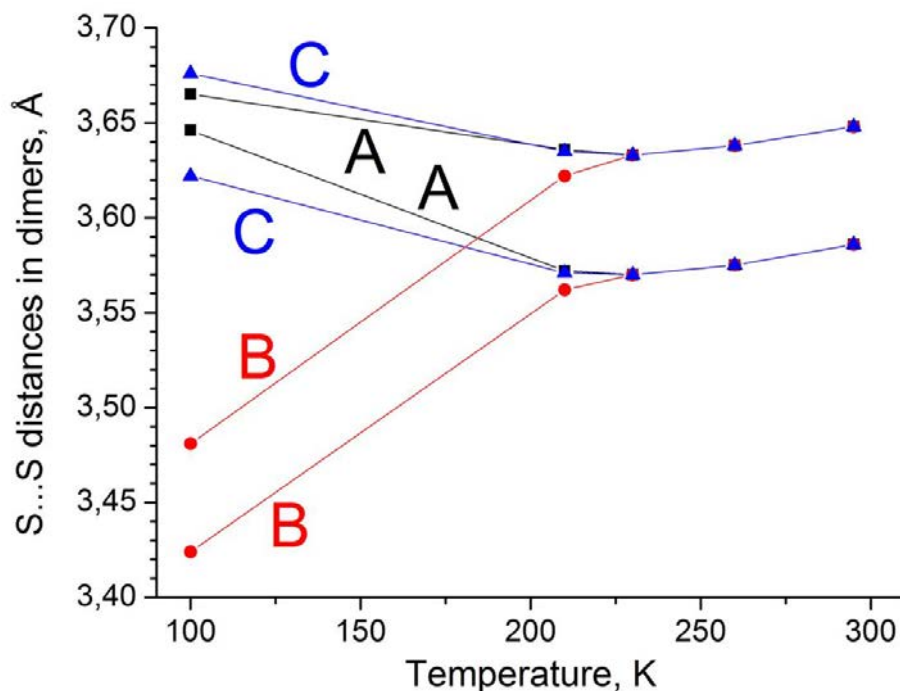

Figure 3.6: Temperature dependence of S$\cdots$S distances in the TTF dimers. The material of this figure is provided by courtesy of P. Batail.

At room temperature, all EDT-TTF-CONH$_2$ molecules in the $4+/4-$ state are identical, bearing a uniform charge of $+2/3$. At the transition, the charge of EDT-TTF-CONH$_2$ molecules within dimer B increases up until close to being fully oxidized $(+1)$ radical cations while the charge for molecules within dimers A and C is reduced to close to $+0.5$ (charge calculation using empirical formula based on the bond lengths in TTF-type organic donors at 100 K gives values of $+0.65$ for molecules within A,

+0.91 for molecules within B, +0.59 for molecules within C) [6]. This unambiguously qualifies a case of charge localization with one hole on both dimers A and C and two holes on dimer B. The localization of one extra hole on dimer B^{2+} brings the molecules closer in this dimer with interplanar separations at 3.45(2), 3.38(1) and 3.41(2) Å for A, B and, C, respectively, and S$\cdots$S orbital overlap interactions become noticeably stronger in B^{2+} than in A $^{\bullet+}$ and $C^{\bullet+}$ (Figure 3.6) [6].

3.3.2   X-Band ESR Measurements

The X-band ESR spectra recorded at all temperatures are composed of two components (Fig. 3.7). One narrow line, of width of nearly 10 Gauß originating from low percentage of defects, and one broad component (of width of $200 - 300$ Gauß at room temperature), which has been found dominant in intensity. Quite surprisingly, the defect line exhibits no variation with the rotating static magnetic field is rotated in (111). In such a way, the defects are deduced to belong to the plane. However, the defect presence does not influence the intrinsic ESR properties. Henceforth, the broad component is referred to as the intrinsic one.

The ESR lineshape is the first derivative of Lorentzian. At all temperatures and for all the possible orientations of the resonant magnetic field with respect to the crystal no asymmetry has been observed. An exception (Fig. 3.7), however, has come out at temperatures above the transition for the configuration in which the microwave magnetic field is in the kagomé plane. In this case the line is no longer a symmetric first derivative of Lorentzian, but takes on Dysonian shape, because of the conduction in (111) plane. This provides a clear-cut signature of the metallic character that is
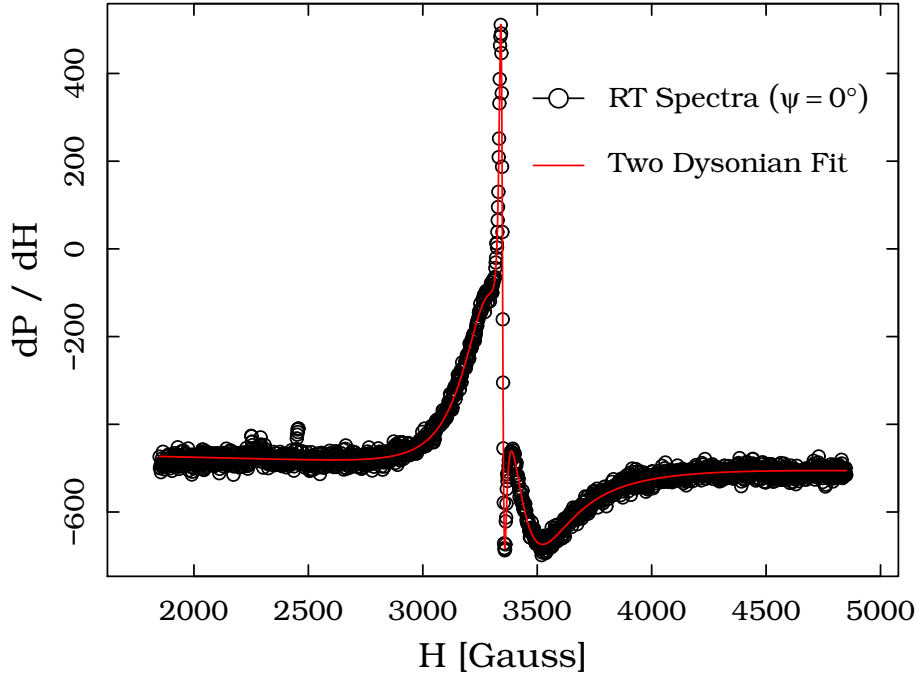
Figure 3.7: Room temperature 9.4 GHz ESR spectra composed of two asymmetric lines. The resonant field is parallel to [111] ($\psi = 0°$) that is equivalent to the configuration in which the microwave lies in plane (111). The fit is presented with the red line.

also in good qualitative agreement with the temperature dependence of the resistivity (Fig. 3.8).

The spin susceptibility, χ, is obtained by double integrating the ESR line. The calibration was made by means of the DPPH reference. At room temperature, χ amounts to $(1.3 \pm 0.2) \times 10^{-3}$ emu/mol. This value in susceptibility is unexpectedly large for metallic systems. Also, the ESR susceptibility has been found to be in good agreement with the SQUID data recorded on the powder [6], implying that ESR probes the response from all the spins in the system. The inverse temperature dependence of the susceptibility ($1/\chi$) distilled for the intrinsic line is presented in Figure
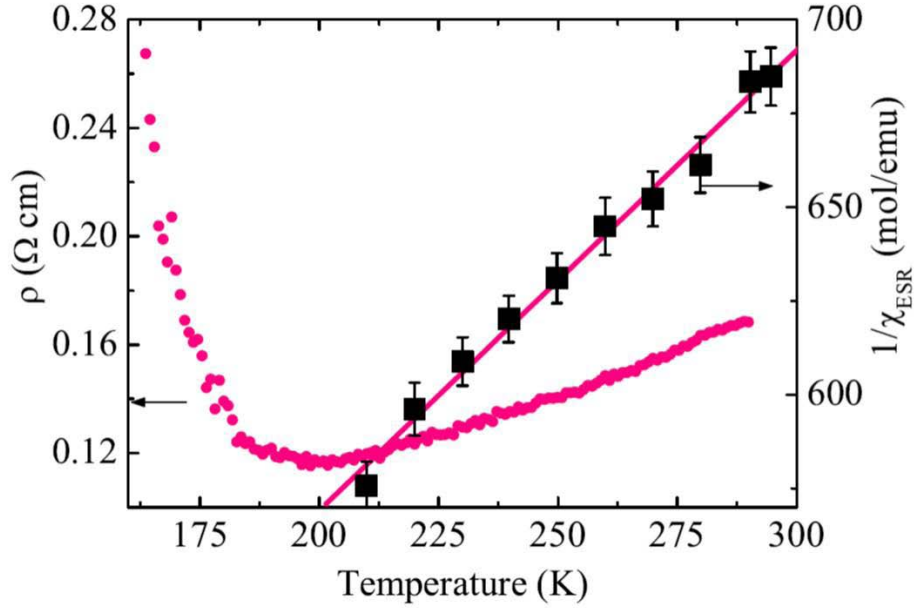
Figure 3.8: Left: resistivity of the kagomé plane as a function of temperature evidencing metallic behaviour above 200 K. Right: temperature dependence of the $1/\chi$, extracted from the X-band ESR spectra for the resonant magnetic field perpendicular to (111) plane. Material for this figure has been provided by courtesy of Jaćim and Areta.

3.8. In the high temperature kagomé phase, $1/\chi$ behaves linearly with the temperature, exhibiting Curie-Weiss behaviour with deduced antiferromagnetic correlations. The effective magnetic moment has been estimated as 2.5 μ_B, while the Curie-Weiss temperature has reached nearly 250 K. These findings clearly demonstrate the presence of the correlations in the high temperature phase. Note that most of organic conductors have temperature independent susceptibilities which are typically an order of magnitude lower than in the present case. Both resistivity and susceptibility reveal the puzzling coexistence of metallicity and magnetic correlations, perhaps even localized moments coming from the itinerant electron sector. This might be explained

97

by the presence of the correlations (U) in the kagomé Dirac semimetal at 2/3 hole filling, where a finite interaction strength U of order t opens up a gap at the Dirac point [10] and thus enhances the susceptibility. Nevertheless, this explanation meets an objection observing the relatively high temperature resistivity value of nearly 0.17 Ωcm. The major objection is raised by Anderson Fermi glass model [4] in which the presence of disorder, either static (standard defects) or dynamic (polarons), properly relates large χ to small ρ in disordered metals.
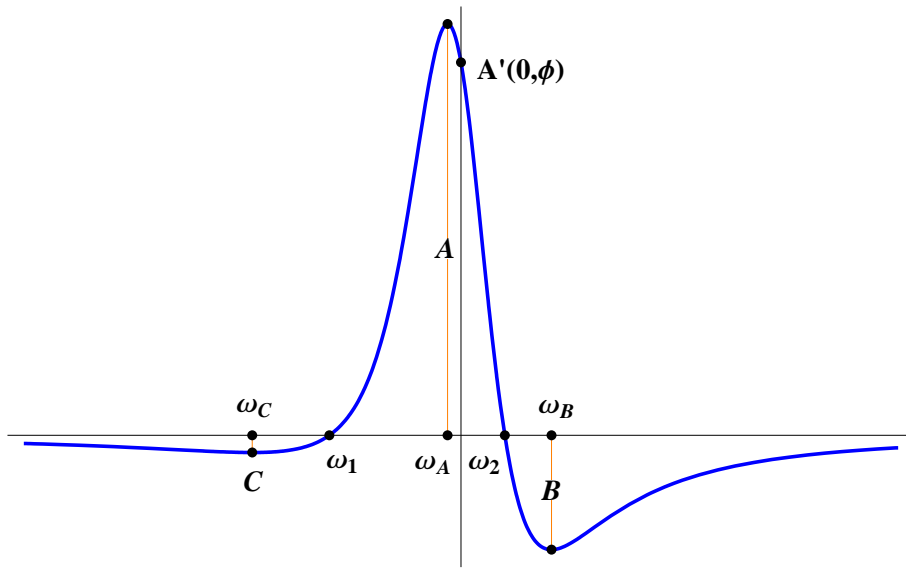
Figure 3.9: Lorentzian first derivative profile possessing both absorption and dispersion with the relevant points and lengths presented [17].

Both ESR lines were fitted with the asymmetric Lorentzian ESR profiles. The asymmetry emerging from the defect line is ascribed to localized spin species due to the imperfections in the crystallinity. The broad intrinsic line represents the genuine Dysonian as has already been corroborated in [6] . The observed asymmetry comes

98

from the shape and conductivity of the sample. The concept of the Dysonian shape profiles is well worked out in literature [12, 13, 14, 15, 16].

In general, the asymmetric Lorentzian ESR profile (Figure 3.9) consists of dispersion and absorption term as follows

$$A(\omega, \phi) = N(\omega_0)\rho(\phi)(\chi''(\omega)\cos(\phi) + \chi'(\omega)\sin(\phi)), \tag{3.1}$$

where

$$\chi''(\omega) = \frac{\Delta H}{\pi} \frac{1}{(\omega - H_0)^2 + \Delta H^2} \tag{3.2}$$

and

$$\chi'(\omega) = \frac{\omega - H_0}{\pi} \frac{1}{(\omega - H_0)^2 + \Delta H^2} \tag{3.3}$$

Here, $N(\omega_0)$ stands for the number of active spins probed at resonance. $N(\omega_0)$ reflects on how susceptible a spin system is, while $\rho(\phi)$ describes the microwave loss and depends on the crystal properties and temperature. Once the fitting parameter ϕ is extracted, the asymmetry parameter, A/B, can be calculated by the following expression

$$\frac{A}{B} = \frac{\left(1 + 2\cos\left(\frac{2\phi}{3}\right)\right)\left(3\cos\left(\frac{\pi}{6} - \frac{\phi}{3}\right) + \sin(\phi)\right)}{4\cos\left(\frac{\pi}{6} - \frac{\phi}{3}\right)\left(1 + \sin\left(\frac{\pi}{6} - \frac{2\phi}{3}\right)\right)^2}. \tag{3.4}$$

In general, response functions in conduction ESR may have particular mathematical restrictions to ϕ and thence A/B ($A/B \leq 8$). Also, physically $A/B \rightarrow (5+3\sqrt{3})/4 \approx$ 2.54904 for highly conductive samples. Beyond this value, A/B starts to loose its physical meaning.

The ESR function profiles can alternatively be written down as $x\chi''(\omega) + y\chi'(\omega)$, where x and y are the absorption and dispersion fractions. $\rho(\phi)$ is thus identified

as $\sqrt{x^2 + y^2}$, while ϕ takes on $\arctan(y/x)$. This transcription of the ESR Dysonian profile is helpful in quantitatively interpreting the A/B asymmetry in terms of the conductivity.

To relate ESR to the transport data, consider now a particular geometry that roughly fits the kagomé sample. Let's take a considerably thin metallic crystal plate geometry of thickness d. One important parameter of the conductive crystal is the skin depth δ, which screens the AC magnetic field. δ falls off with increasing frequency ω of the microwave, and if not anomalous [17] depends on the crystal conductivity explicitly (implicitly on temperature). For the above assumed geometry, the absorption and dispersion fractions in the ESR response read as follows [18]:

$$
\begin{aligned}
x(\eta) &= \frac{\sinh(\eta) + \sin(\eta)}{2\eta(\cosh(\eta) + \cos(\eta))} + \frac{1 + \cosh(\eta)\cos(\eta)}{(\cosh(\eta) + \cos(\eta))^2} \geq 0, \qquad (3.5) \\
y(\eta) &= \frac{\sinh(\eta) - \sin(\eta)}{2\eta(\cosh(\eta) + \cos(\eta))} + \frac{\sinh(\eta)\sin(\eta)}{(\cosh(\eta) + \cos(\eta))^2} \geq 0.
\end{aligned}
$$

where $\eta \equiv d/\delta$ [18].

In our case, we estimate d roughly as 300 μm. The fitting parameter ϕ was found to be 24° that corresponds to $A/B \simeq 1.63$ according to (3.4). Furthermore, $\eta = 1.13$ and based on (3.5) and the relation for the skin depth [17] at 9.4 GHz we find the resistivity value of nearly 0.2 Ωcm. This value agrees well with that obtained by the transport measurement at room temperature. However, the geometry we have taken here might depart from the realistic one. One has to bear in mind that the sample was indeed thin, but as large as 2 mm, that may not fit perfectly the geometry of a considerably thin metallic plate.

3.3.3   210 GHz ESR Temperature and Pressure Dependent Measurements

Driven by the structural phase transition from rhombohedral to triclinic phase at low temperatures, the changes in the electronic properties and spin dynamics in the organic kagomé system $(EDT\text{-}TTF\text{-}CONH_2)_6Re_6Se_8(CN)_6$ can be followed by the behaviour of the 210 GHz ESR linewidth (Figure 3.10). The Elliott-Yafet mechanism
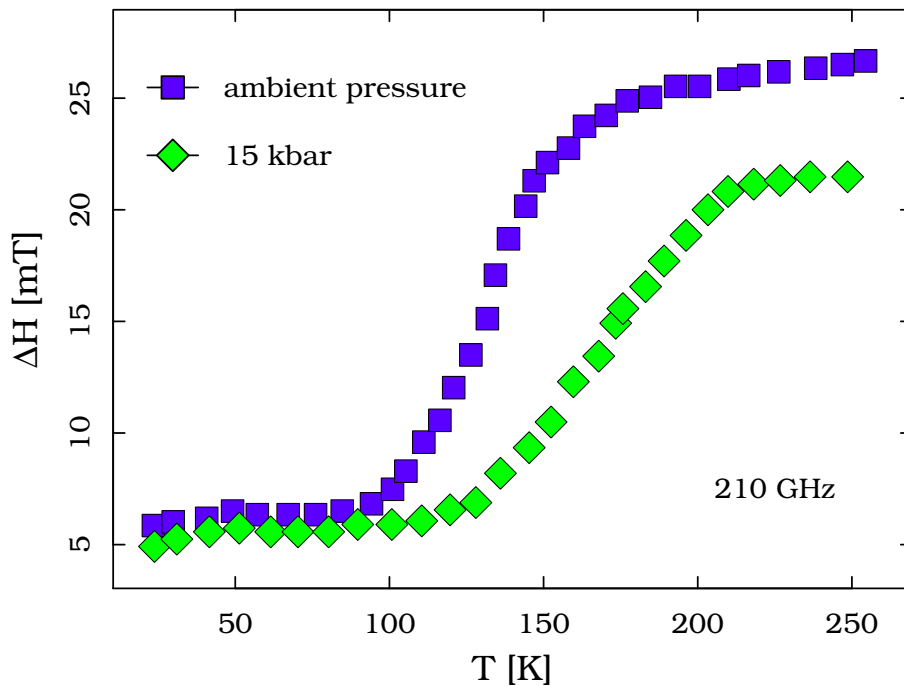

Figure 3.10: Temperature dependence of the linewidth at 210 GHz. The resonant magnetic field is perpendicular to (111) plane. Blue squares (green diamonds) represent the measurements carried out at ambient pressure (under 15 kbar hydrostatic pressure).

[19, 20] for spin relaxation, characteristic for metals, is assumed to be valid in the

high temperature rhombohedral phase with the kagomé topology. That is

$$\Delta H = \frac{\hbar}{g\mu_B} \left(\frac{\Delta g}{g}\right)^2 \frac{1}{\tau_c}.$$ (3.6)

This mechanism relates the linewidth (ΔH) with the momentum relaxation rate ($1/\tau_c$). τ_c regularly becomes longer with raising pressure as the statistics of phonons becomes diminished. Indeed, in the kagomé phase the linewidth decreases with pressure that is in accordance with the mechanism. Also, when compared to 9.4 GHz linewidth [6] with the respective crystal orientation, there has been no scaling with resonant frequency traced in ΔH. After the model by Bloembergen, Purcell, and Pound [21], the spin relaxation time in metals is insensitive towards frequency variations. At 15 kbar, the linewidth behaviour in the high temperature regime is qualitatively the same as at ambient pressure, with the difference that the curve appears to be shifted to the right in temperature.

An important decrease occurs below 200 K, that follows quite well the deformation of the structure seen in X-ray [6]. In the triclinic state, there is an evident narrowing in the linewidth emerged due to the localization and physics which is dominated by the antiferromagnetic exchange. Weak temperature dependence is observed above 15 K. Below this value, the linewidth decreases linearly, but does not tend to zero, unlike in the 9.4 GHz case. The linewidth behaviour below 15 K will be later elaborated at both 9.4 and 210 GHz. Albeit the initial idea was to apply pressure in an attempt to stabilize the rhombohedral phase down to lower temperatures, the pressure turns out to shift the structural phase transition to higher temperatures and consequently extends the temperature range of the nonmetallic behaviour. This behaviour suggests that, under hydrostatic pressure, the dimensional crossover shifts to higher
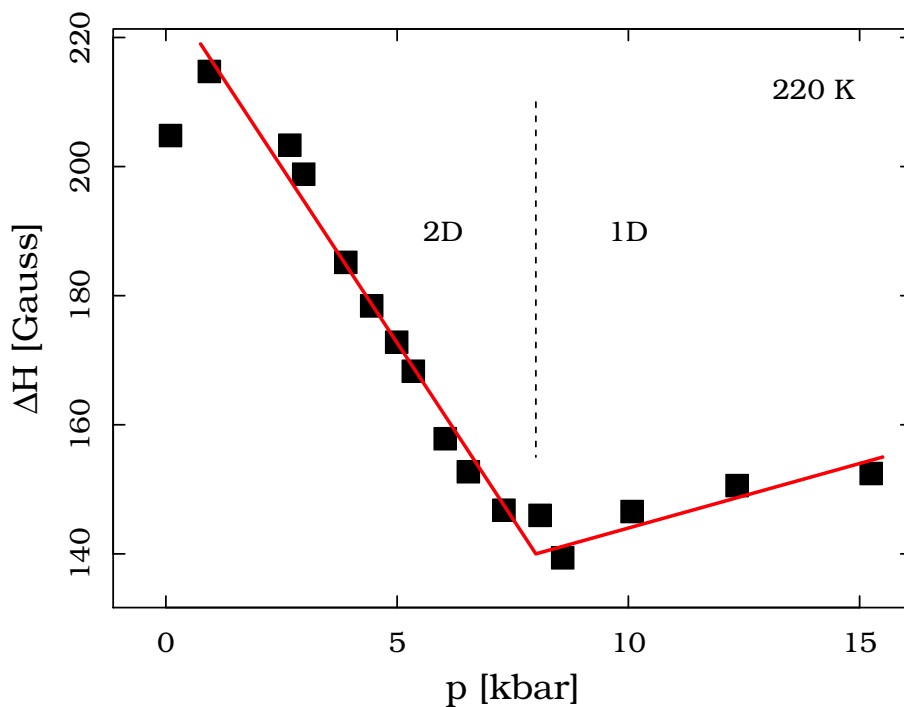
102

temperatures.

Figure 3.11: The evolution of the ESR linewidth with the pressure showing the 2D towards 1D crossover at 220 K and 210 GHz. The resonant magnetic field is perpendicular to (111) plane.

The evolution of the structure with the pressure can be nicely traced from Figure 3.11 representing the 210 GHz ESR pressure dependent measurements performed at 220 K. At this temperature, the system is still in the rhombohedral phase at atmospheric pressure. The pressure dependence of the linewidth tracks the deformation of the structure from rhombohedral to triclinic. The linewidth decreases progressively for pressures up to 8 kbar. Above this value, the linewidth presents only little variation with the pressure. This leads to an pressure induced dimensional crossover from

2D (kagomé) to 1D (spin chain). Below 8 kbar the linewidth narrowing is expected due to the Elliott-Yafet spin relaxation mechanism. However, above the crossover temperature a slight increase in the linewidth with pressure guarantees the spin localization. Most likely, the slight broadening arises because of the pressure increased dipole-dipole interaction. This interpretation is in accordance with an ongoing temperature and pressure dependent X-ray study to be revealed soon by P. Batail e*t al.*

Such crossovers are quite common in organic conductors due to their compressibility. One can even expect that a mild hydrostatic pressure on the order of 10 kbar may have an impact on the electronic properties, because it is capable of finely tuning the overlap between orbitals.

3.3.4 Low Temperature Triclinic Phase

The low temperature phase of $(EDT\text{-}TTF\text{-}CONH_2)_6Re_6Se_8(CN)_6$ is a Mott insulator state, which magnetically (see Figure 3.12) can be described by 1D Heisenberg model of $S = 1/2$ spins with $J \approx 65$ K, as has already been adopted in the literature [6]. However, such idealistic spin chain systems are never encountered in the nature and are supposed to incorporate small perturbation parameters within their Hamiltonians, such as staggered field h, Ising-like exchange anisotropy δ, and interchain coupling γ [22]. These parameters give rise to the widths of ESR lines. γ is very often responsible for driving spin chains into the antiferromagnetic ordering. The greater the value of γ the higher the transition temperature, that might be tuned by applying pressure, for instance. In our case, no signature of the ordering has been evidenced at all.
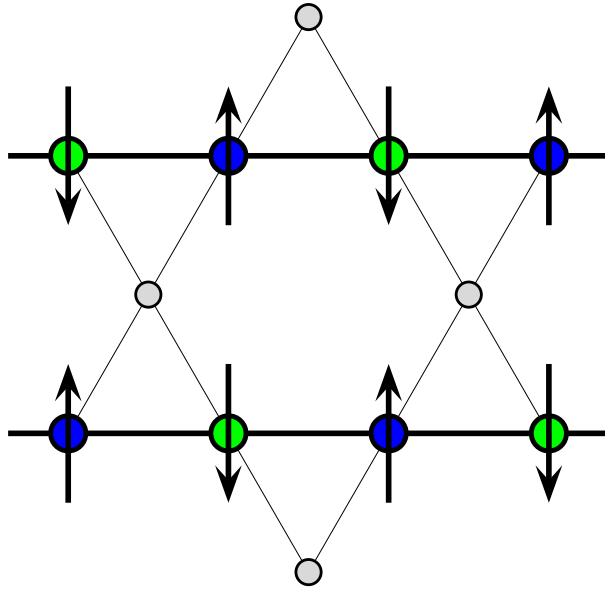
Figure 3.12: The sketch of the 1D AF state at low temperature. Four holes are so distributed that two of them populate one single site (B - gray circle, spinless), while the other two go separately to the two remaining sites (A - green circle and C - blue circle, half filled).

However, the behaviour of ΔH below nearly 15 K at 9.4 GHz (ambient pressure) and at 210 GHz under 15 kbar indicates a tendency towards ordering at zero temperature. Given that the condition 15 K$\ll J$ is fulfilled, one can straightforwardly apply the model after Oshikawa and Affleck [22] in this temperature region.

To use this model, yet another important condition has to be satisfied. Namely, the resonant field H must be much less than J. This condition provides the Lorentzian profile in the spectra, which has been indeed observed at low temperature. H is uniform magnetic field and as such has no influence upon the spectra. The only impact H may have goes via its staggered component h, because of the off-diagonal terms of g tensor at a spin chain site. All what H does directly is drifting the resonant

frequency ω ($\omega = H$ in the paramagnetic case) given that the $SU(2)$ symmetry of the system remains unaffected for $H \ll J$.

Both h and γ contribute to ΔH in the same manner. As was discussed in the paper [22], a staggered field h could effectively arise from a staggered g tensor or else from a staggered Dyaloshinsky-Moriya (DM) interaction. Whether either of these is present can be determined by careful symmetry considerations. Without loss of generality, DM interaction will be disregarded throughout the consideration and analyzing the symmetry of g might be one of further goals. The treated system does have the centre of inversion and therefore is an unlikely candidate to drive the DM anisotropy term into its Hamiltonian. As for γ, it is also staggered in the sense of relation (3.7, see below) like h. Moreover, one can claim that γ has to increase by applying pressure because the interchain distance is correspondingly diminished.

The model Hamiltonian which serves as a starting point to developing the bosonisation techniques given in [23] for a $S = 1/2$ chain under uniform magnetic field H reads as

$$\mathcal{H} = J\sum_j \vec{S}_j \cdot \vec{S}_{j+1} + h\sum_j (-1)^j S_j^x + \delta \sum_j S_j^z S_{j+1}^z - H \sum_j S_j^z. \qquad (3.7)$$

This model also considers the pressure influence which is realized by simply replacing h with $h + \gamma$.

After series of tedious transformations elaborated in [22] one comes up with the $\Delta H(T)$ dependence as follows

$$\begin{aligned}
\Delta H(T) &= \frac{1}{16}\sqrt{\frac{\pi}{2}}\left(\frac{\Gamma(\frac{1}{4})}{\Gamma(\frac{3}{4})}\right)^2 \frac{Jh^2}{T^2}\left(\ln\frac{J}{\max(T,H)}\right)^{1/2} \\
&\quad + \frac{4}{\pi^3}\left(\frac{\delta}{J}\right)^2\left(\ln\frac{J}{\max(T,H)}\right)^2 T.
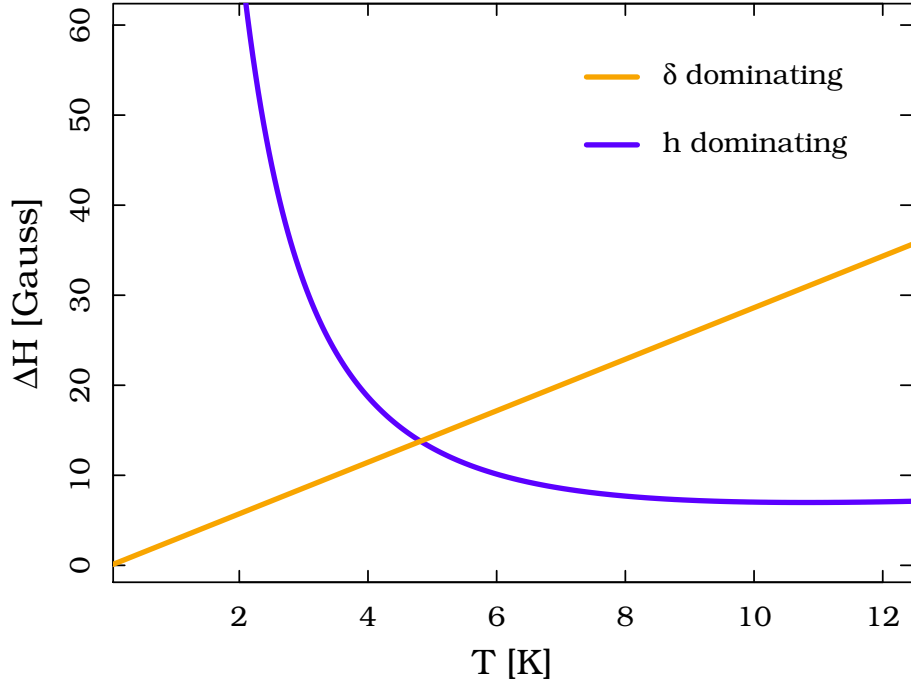\end{aligned} \qquad (3.8)$$

106

Figure 3.13: Arbitrarily taken behaviour of $\Delta H(T)$ for two extreme cases of the perturbation parameters in relation (3.8).

Here δ acts as an irrelevant operator and leads to the ΔH narrowing, unlike h which affects ΔH the other way round. Plus, h's, or eventually $(h + \gamma)'$s, influence on the broadening can well be intensified with increasing either H or p. A sketch of theoretical predicted temeparture dependence of ΔH is given in Figure 3.13 for two opposite limits in h and δ.

Table 3.1: The extracted fit parameters for the linewidth temperature dependences.

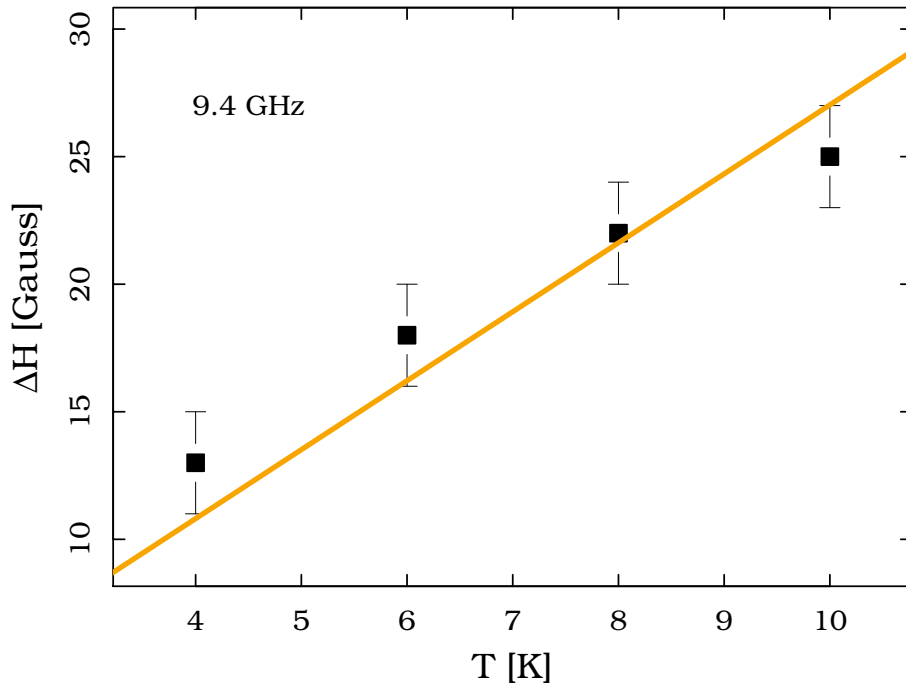| Resonant ω at p	J [K]	h [K]	δ [K]
9.4 GHz at ambient pressure	175 ± 5	0.001 ± 0.001	2.6 ± 0.1
210 GHz at 15 kbar	185 ± 5	0.0189 ± 0.0004	3.7 ± 0.1

Figure 3.14: The 9.4 GHz ambient pressure ESR linewidth data fitted with function in (3.8).

The data are fitted for two diverse ΔH behaviours as is shown in Figures 3.14 and 3.15. The fitting parameters are given in Table 3.1.

The measured temperature dependences of ΔH below 15 K ($T \ll J$) have indicated to follow the behaviours similar to those presented in Figure 3.13. Two different trends in the line width behaviour can be seen. First, $\Delta H \uparrow$ when $T \uparrow$ at the low field (Fig. 3.13, orange curve). Second, $\Delta H \uparrow$ when $T \downarrow$ under the highest pressure applied (15 kbar) at high field. This is expected knowing that $h \uparrow$ when $H \uparrow$ ($h \propto H$), so that ΔH behaviour should be predominantly determined by h at high frequency, rather than by δ. The regime given in Figure 3.13 (orange curve) turns into the other regime (blue curve) once both field H and pressure p becomes correspondingly high.
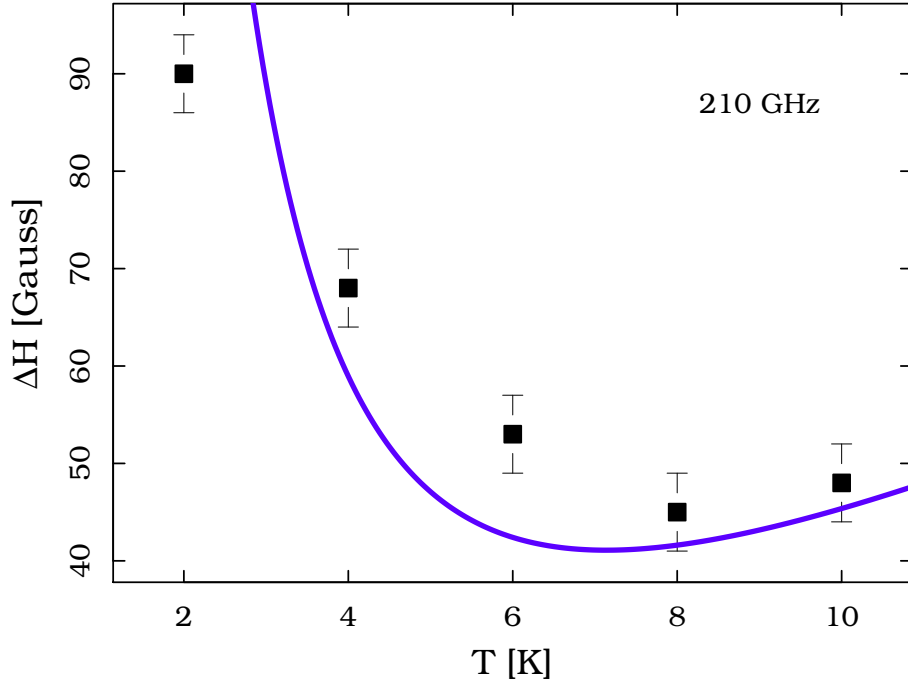
Figure 3.15: The 210 GHz 15 kbar ESR linewidth data fitted with function in (3.8).

One can notice that the extracted h and δ are markedly small compared to J that is required by the theory. Surprisingly, J is notably large as compared to the predicted 65 K. Furthermore, ratio h/H is of order of 10^{-3} at both resonant frequencies that is attributed to the nature of the off-diagonal matrix elements in g factor. Also, J (and thence δ) undergoes a slight increase with p whose value, in all likelihood, is not high enough to drive the interchain physics (γ seems to be small) and generate the ordering. In addition, $h(210\text{GHz})/h(9.4\ \text{GHz})$ is nearly as much as $210/9.4$, meaning that h does depend on H linearly that is indeed suggested by the model.

In addition, the fits display somewhat departure from the original data, but nevertheless, they demonstrate a lot of meaningful physics at micro level. The deduced spin dynamics based on the distilled parameters goes along the predictions of half

spin chains made in [6].

3.4 Recent Theoretical Findings and Further Perspectives

Fair number of theoretical investigations on third filled kagomé lattices is progressively growing [8, 9, 10]. The impetus has emerged due to the one-to-one correspondence to graphene which spans the half filled honeycomb lattice. These investigations have raised questions as to an experimental realization of such itinerant kagomé systems that would certainly support their predicted phenomena. The (EDT-TTF-CONH$_2$)$_6$Re$_6$Se$_8$(CN)$_6$ organic compound is bound to fulfill the ambition of the theory, whose exotic behaviour is attested by ESR and transport in this thesis.

An interesting recently reported theoretical study [24], focusing on filling fractions which involve a pair of Dirac points in the 1/3 filling kagomé system, has presented a Hartree-Fock mean-field tight-binding approach to demonstrate various possible symmetry-broken states and phase diagrams as well as highlight the competition between them. The study employs some fine tuning interaction parameters, such as t and U (common Hubbard parameters), and V which stands for the nearest-neighbour repulsion. There are other V-like parameters which were involved [24], however without loss of generality the inclusion of next nearest-neighbour V terms was not found cardinal to constructing the generic phase diagram. In that respect, the employed model Hamiltonian for spin polarized fermions in the 1/3 filled kagomé

system is taken to be as

$$H = -t \sum_{\langle i,j \rangle \sigma} c_{i\sigma}^\dagger c_{j\sigma} + U \sum_i n_{i\uparrow} n_{j\downarrow} + V \sum_{\langle i,j \rangle} n_i n_j, \qquad (3.9)$$

where $c_{i\sigma}^{(\dagger)}$ annihilates (creates) a fermion on site i with spin $\sigma = \uparrow, \downarrow$, $n_{i\sigma} = c_{i\sigma}^\dagger c_{i\sigma}$, and $n_i = \sum_\sigma n_{i\sigma}$.

Based on the Hamiltonian in (3.9), there are three phases emerging as a result of the special filling fraction, the nature of the kagomé lattice, and the additional spin degrees of freedom (Figure 3.16). The semimetal state (SM) is favoured in the
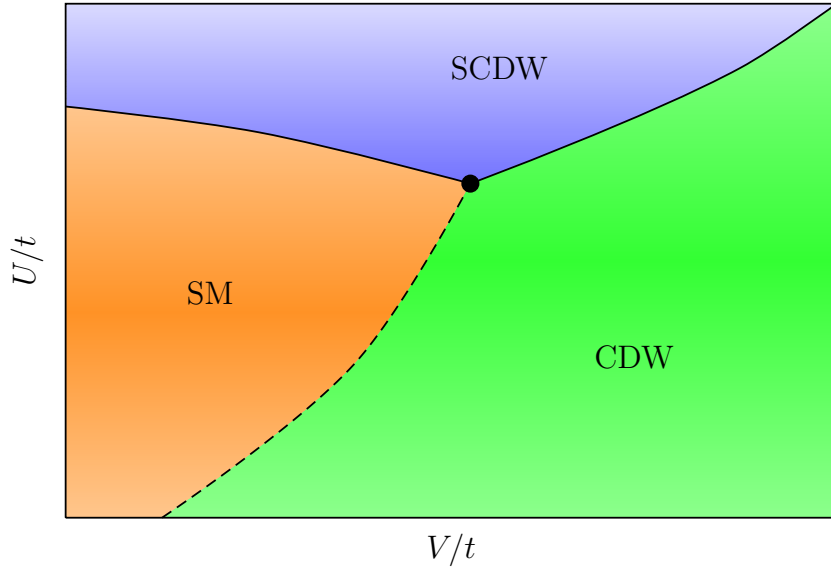
Figure 3.16: Generic phase diagram of the 1/3 filled kagomé lattice with three crucial tuning parameters: t, U, and V. Solid lines indicate first-order and dashed lines second-order transitions.

noninteracting regime and can be destabilized by increasing either U or V. This phase is in the coherence with the kagomé topology. An increase in U, brings about the instability towards the so-called spin-charge-density-wave (SCDW) phase which

in our case represents the insulating AF spin chain state (Figure 3.12). According to the mean-field calculations, this phase does break the translational symmetry, leading to the structural changes. Indeed, in the $(EDT\text{-}TTF\text{-}CONH_2)_6Re_6Se_8(CN)_6$ system this instability occurs through the structural phase transition at around 200 K. The correlations (U) above this temperature remain suppressed due to the temperature fluctuations that stabilizes the SM phase.

On the other hand, an increase in V drives the SM state into the so-called charge-density-wave (CDW) state. The state is supposed to preserve the kagomé symmetry, but it is insulating unlike the SM. The CDW phase is distinguished with the triple degeneracy as is shown in Figure 3.17, given that there are three equivalent sites in the kagomé plane: A, B, and C. The CDW-SM instability is found to be a second-order phase transition at a critical interaction strength V_C. In the case of $(EDT\text{-}TTF\text{-}CONH_2)_6Re_6Se_8(CN)_6$ this transition can be understood as the crossover observed at around 8 kbar. The pressure most likely serves as a parameter that tunes V. Although the CDW-SM transition predicts no dimensional alterations, it still remains uncertain whether the ESR data given in Fig. 3.11 can support the concept of the preserved dimensionality.

It should be also noted that the CDW phase carries similarities with one found for the Kekulé texture on the honeycomb lattice [24]. In analogy with these examples, topological defects of the CDW pattern are expected to appear in the form of a Z_3 vortex configuration (Figure 3.17). This picture can give rise to interesting physics; potentially including charge fractionalization and anyon statistics. The vortices are not spinless and can freely move unless they are pinned due to the defects. This can explain the cohabitation between the magnetism and itinerancy at high temperatures
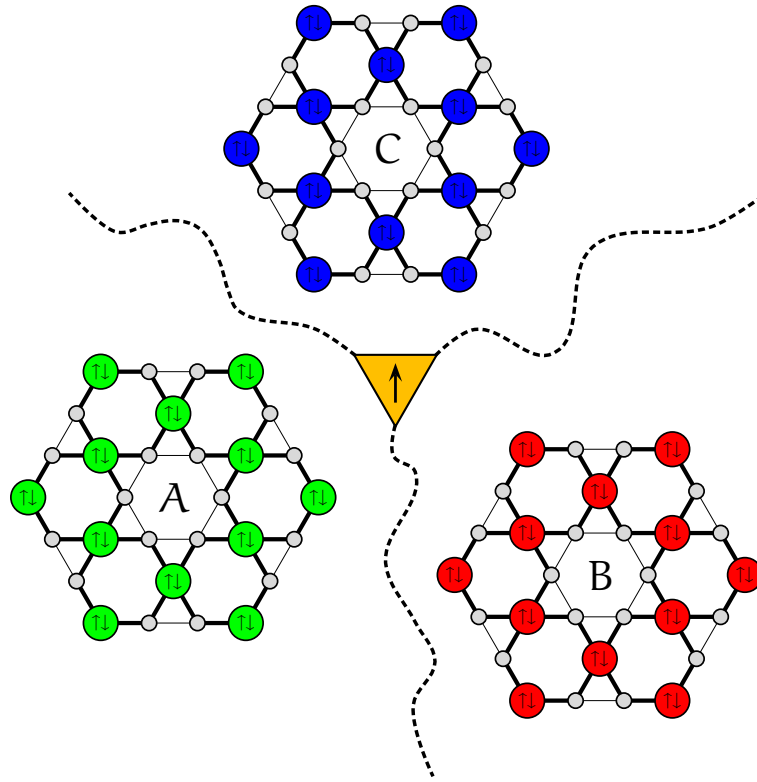
Figure 3.17: Magnetic vortex (spin in triangle) of the CDW phase possessing triple degeneracy in the kagomé plane: A, B, and C.

in $(EDT\text{-}TTF\text{-}CONH_2)_6Re_6Se_8(CN)_6$. However, the high value in the resistivity is not compatible with the SM nor with CDW state. Further extension of the investigations, in which the electron-phonon coupling (g) is included, is needed for reaching the proper quantitative interpretation. According to numerical calculations, recently made by Prof. Dr. Eduard Tutiš, the involvement of g leads to the replacement of the CDW by a bipolaron lattice state that provides a good estimation of both spin susceptibility and resistivity at room temperature. The influence of the phonon dynamics upon the electronic sector is quite considerable in organic systems and generates dynamic polaronic disorder at high temeparture. The following outcome explains the

bad metallicity and itinerant magnetism appropriately. The related results are in the preparation stage and are going to be submitted to *Nature Materials.*

3.5   Concluding Remarks

In summary, the X-band ESR and 210 GHz ESR measurements under pressure made on the $(\text{EDT-TTF-CONH}_2)_6\text{Re}_6\text{Se}_8(\text{CN})_6$ system have been presented. In this organic system, TTF-dimers are organized into a kagomé geometry at high temperature above 200 K. The ESR data, together with associated transport measurements, have clearly demonstrated the existence of metallic behaviour at high temperature, in coherence with the kagomé lattice symmetry with 2/3 hole filling. Also, by ESR, the presence of magnetic correlations at high temperature has been detected, based on the large value of the spin susceptibility and its Curie-Weiss temperature dependence. The changes in the electronic properties and spin dynamics have been followed by the behaviour of the 210 GHz ESR linewidth. These changes are driven by the structural phase transition from rhombohedral to triclinic phase at low temperatures. The evolution of the structure under hydrostatic pressure has been additionally followed by the 210 GHz ESR. A dimensional crossover at higher temperatures has been observed to occur at around 8 kbar. At low temperature insulator phase, the Oshikawa-Affleck model for antiferromagnetic spin 1/2 chains with dipolar exchange anisotropy and staggered field has been successfully applied. The coexistence of magnetism and metallic behaviour in the high temperature regime has already been predicted theoretically for third filled kagomé lattices accounting for: t, U, V. However, the thorough interpretation requires the inclusion of the electron-phonon coupling which leads to the

114

polaronic picture.

Bibliography

[1] G. Saito and Y. Yoshida, Bull. Chem. Soc. Jpn. **80**, 1 (2007).

[2] L. P. Gor'kov, Sov. Phys. Usp. **27**, 809 (1984).

[3] I. A. Misurkin and A. L. Tchougreeff, J. Chem. Phys. **100**, 2223 (1994).

[4] P. W. Anderson, Comments Solid State Phys. **2**, 193 (1970).

[5] L. Forró, J. R. Cooper, B. Rothaemel, J. S. Schilling, M. Weger, D. Schweitzer, H. J. Keller, and K. Bechgaard, Synth. Metals **19**, 339 (1987).

[6] S. A. Baudron, P. Batail, C. Coulon, R. Clérac, E. Canadell, V. Laukhin, R. Melzi, P. Wzietek, D. Jérome, P. Auban-Senzier, and S. Ravy, J. Am. Chem. Soc. **127**, 11785 (2005).

[7] T. Ohashi, N. Kawakami, and H. Tsunetsugu, Phys. Rev. Lett. **97**, 066401 (2006).

[8] Z. Wang and P. Zhang, New Journal of Physics **12**, 043055 (2010).

[9] H. M. Guo and M. Franz, Phys. Rev. **B80**, 113102 (2009).

[10] S. Nishimoto, M. Nakamura, A. O'Brien, and P. Fulde, Phys. Rev. Lett. **104**, 196401 (2010).

[11] B. Náfrádi, *Multi Frequency High Pressure Electron Spin Resonance Study of Low Dimensional Organic Conductors*, EPFL PhD Thesis (2008).

[12] G. Feher and A. F. Kip, Phys. Rev. **98**, 337 (1955).

[13] F. J. Dyson, Phys. Rev. **98**, 349 (1955).

[14] J. H. Pifer and R. Magno, Phys. Rev. **B3**, 663 (1971).

[15] A. H. Kahn, Phys. Rev. **B16**, 64 (1976).

[16] J. P. Joshi and S. V. Bhat, J. Magn. Res. **168**, 284 (2004).

[17] R. N. Edmonds, M. R. Harrison, and P. P. Edwards, Annual Reports C: Phys. Chem. **82**, 265 (1985).

[18] A. C. Chapman, P. Rhodes, and E. F. W. Seymour, Proc. Phys. Soc. **B70**, 345 (1957).

[19] R. J. Elliott, Phys. Rev. **96**, 266 (1954).

[20] Y. Yafet, Solid State Phys. **14**, 1 (1963).

[21] N. Bloembergen, E. M. Purcell, and R. V. Pound, Phys. Rev. **73**, 679 (1948)

[22] M. Oshikawa and I. Affleck, Phys. Rev. **B65**, 134410 (2002).

[23] I. Affleck, in *Fields, Strings and Critical Phenomena, Les Houches, Session XLIX*, edited by E. Brézin and J. Zinn-Justin (North-Holland, Amsterdam, 1988).

[24] J. Wen, A. Rüegg, C. C. J. Wang, and G. A. Fiete, Phys. Rev. **B82**, 075125 (2010).

Conclusions and Perspectives

This thesis inscribes into a study of novel magnetic materials. Its aim was to present an overview on the abilities of ESR as a microscopic, yet bulk, probe for spin dynamics phenomena in some of the topic emergent novel materials with interesting magnetic properties. They included: $SeCuO_3$ − a cupric oxide quantum antiferromagnet with potential multiferroic properties, defected graphene bottled-up in nanographite, and $(EDT-TTF-CONH_2)_6Re_6Se_8(CN)_6$ − an organic, charge transfer, low dimensional most likely topological insulator with unprecedented kagomé geometry thus far known for TTF derivatives. Direct information on the magnetic susceptibility, local dominant magnetic interactions, as well as spin relaxation were imparted from the respective parameters: double integrated ESR intensity, g-value, and linewidth. Powerfulness of this technique reflects in its ability to unite and complement different physics observed in different systems that is of great fundamental and practical importance. Both low and high temperature behaviours of the three novel materials were understood and interpreted quantitatively, with special emphasis to their ability to undergo phase transitions in spin dynamics. This could be of value to a wide range of solid state physicists dealing with ESR technique and engaged in designing other families of emergent magnetic materials akin to those presented throughout the

thesis. By means of ESR, the thesis was also intended to illustrate a rich variety of magnetism scenarios, starting from quantum fluctuations in a low dimensional spin dense system with promising multiferroicity, over emerging, theoretically ever sought, magnetism in defected nanographite and nanographene, towards itinerant correlations in an organic low dimensional topological insulator experiencing a phase transition with tuning both temperature and pressure. These were explained and understood in terms of simple physical models such as: the generic theory by Kubo and Tomita (very often argued to break down in low dimensional antiferromagnetic systems), then an alternative model to the former after Oshikawa and Affleck to account successfully for the low temperature dependence of the measured linewidths, and ultimately Elliot-Yafet spin flip mechanism employed in the case of the conduction ESR.

Beyond the presented deliberation, the field of novel magnetic materials faces a number of challenges. The most important issues are concerned with the experimental side. In particular, the physics of defect-induced genuinely ferromagnetic graphene at room temperature has already attracted a large number of computational and theoretical researchers. However, no direct experimental evidence has been reported regarding the saturated ferromagnetism (in Landau sense) at the time the thesis was written. This thesis attempted to tackle the desirable magnetism from the Lieb point of view. Other leading directions in research of this field would include understanding itinerant magnetism in bulk organic systems with Dirac point and frustrated geometry. This would be of real help to experimental bulk probes which suffer from limits in sensitivity. For instance, investigating an atomic scale layer such as graphene by ESR poses challenges in respect of quantity and available space.

In addition, as a future task for searching novel multiferroic materials, which can

realize low dimensional antiferromagnetic frustration scenarios, the family of correspondingly doped selenium cupric oxides appears as a prominent candidate. Understanding the mechanism of the appearance of magneto electric coupling due to the quantum fluctuations at micro level, would certainly require a succession of the study given in this thesis, using complementary experimental techniques. These would include: neutron diffraction and elastic neutron scattering, far infrared reflection and transmission under high magnetic fields, capacitance versus magnetic field measurements, and the like.

Dejan M. Djokić

~ Curriculum Vitae ~

Work and Training Experience

October 2008 – hitherto

Ecole Polytechnique Fédérale de Lausanne (EPFL)
Laboratory of Physics of Complex Matter

Developed knowledge and expertise: CW Electron Spin Resonance (ESR), resonant microwave structures (X/Q-band, 110-420 GHz), ESR under pressure (up to 1.6 GPa), cryogenics, high magnetic fields (up to 16 T), SQUID, neutron diffraction (TriCS - PSI), low dimensional organic conductors and superconductors, graphene, fullerenes, spin diffusion and relaxation phenomena, quantum magnetism, magneto-electric coupling.

Autumn 2011

Le Centre d'Imagerie Bio-Médicale (CIBM)
Fundamentals of Biomedical Imaging

Certificate training: Magnetic Resonance Imaging (MRI), RF pulse NMR, tomography, MRI contrast enhancing agents, biological safety.

October 2009 – June 2010

Conférence Universitaire de Suisse Occidentale
Statistical Field Theory

Certificate course: Feynman's functional integral, domain walls in magnetic and ferroelectric materials, disorder and glasses, dissipative quantum systems, quantum and classical phase transitions, coherence and systems out of equilibrium, macroscopic quantum tunneling.

January 2006 – September 2008

Center for Solid State Physics and New Materials
Research Assistantship

Acquired knowledge and experience: optical transmission and reflectivity (far-IR to UV), Brillouin and Raman scattering, nanostructured systems, strongly correlated materials (vanadates and manganites), magnon-phonon coupling, factor group analysis, 2D photonic crystals and meta-materials.

International Awards and Certificates

September 2010

Teaching Certificate, Swiss Federal Institute of Technology

January 2006

Scholarship of Foundation for Talented Young Scientists, Ministry of Education of Serbia

October 2004

Royal Norwegian Grant, for Exceptional Academic Results

Computer Skills

Considerably Skilled: PSTricks, $\mathbb{R}$, MATLAB, LaTeX
Intermediate Knowledge: Word, PowerPoint, Python, $\mathbb{C}$
Proficient: Cryptography & Boolean Functions in $\mathbb{R}$

✉ | Ramière 4, CH-1028 Préverenges
Switzerland
Born in Valjevo, Serbia (ex SFRY)
February 07, 1980
☎ | +41 (0)78 692 15 59
@ | dejan.m.djokic@gmail.com

Education

October 2012	Doctor of Philosophy in Physics **EPFL**, Lausanne, Switzerland 17/12 ECTS Major: Magnetic Resonance
February 2008	Magister of Science in Physics Faculty of Physics, Belgrade University of Belgrade 120 ECTS *summa cum laude* Major: Raman/Infrared Spectroscopy
September 2005	Diploma in Physics Faculty of Physics, Belgrade University of Belgrade 300 ECTS *summa cum laude* Major: Theoretical and Experimental

Languages

Serbian	Mother Tongue
English	Fluent
French	Solid Knowledge

Interests and Activities

Minimal and Early Music
Paradoxes in Statistical Mechanics
Number Theory
Wireless Quantum Watermarking
Swimming and Rowing
Etymology

Publications and Recommendation Letters

Pub.pdf — Published Works and Conferences
App.pdf — Publications to Appear
Lett.pdf — Recommendation Letters

Scientific Metier

Solid State Spectroscopy
Teaching in Condensed Matter Physics
Novel Carbon Based Materials
Spintronics
Strongly Correlated Electron Systems
Multiferroics

Published Works and Conferences

[1] Site Selective Quantum Correlations Revealed by Magnetic Anisotropy in the Tetramer System SeCuO$_3$; I. Živković, D. M. Djokić, M. Herak, D. Pajić, K. Prša, P. Pattison, D. Dominko, Z. Micković, D. Cinčić, L. Forró, H. Berger, and H. Rønnow, Physical Review **B86**, 054405 (2012).

[2] Uncoupled Photonic Band Gaps; Dj. Jovanović, B. Nikolić, T. Radić, D. M. Djokić, and R. Gajić, Photonics and Nanostructures - Fundamentals and Applications **10**, 657 (2012).

[3] Magnetoelectric Coupling in Single Crystal Cu$_2$OSeO$_3$ Studied by a Novel Electron Spin Resonance Technique; A. Maisuradze, A. Shengelaya, H. Berger, D. M. Djokić, and H. Keller, Physical Review Letters **108**, 247211 (2012).

[4] Magnetism in Nanoscale Graphite Flakes as Seen Via Electron Spin Resonance; L. Ćirić, D. M. Djokić, J. Jaćimović, A. Sienkiewicz, A. Magrez, M. Lotya, J. N. Coleman, Ž. Šljivančanin, and L. Forró, Physical Review **B85**, 205437 (2012).

[5] Electron Spin Resonance Study of SeCuO$_3$; D. M. Djokić, Z. Micković, I. Živković, K. Schenk, H. Rønnow, H. Berger, and L. Forró, Joint Annual Meeting of Swiss Physical Society and Austrian Physical Society - Condensed Matter Physics, Lausanne (2011).

[6] Size Dependence of the Magnetic Response of Graphite Oxide and Graphene Flakes - an Electron Spin Resonance Study; L. Ćirić, A. Sienkiewicz, D. M. Djokić, R. Smajda, A. Magrez, T. Kaspar, R. Nesper, and L. Forró, Phys. Status Solidi **B247**, 2958 (2010).

[7] Investigation of Thermostability and Phonon-Phonon Interactions in Mo$_6$S$_3$I$_6$ Nanowires by Raman Scattering Spectroscopy; J. M. Todorović, Z. D. Dohčević-Mitrović, D. M. Djokić, D. Mihailović, and Z. V. Popović, J. Raman Spectroscopy **41**, 978 (2010).

[8] Metallicity in the Organic Kagomé (EDT-TTF-CONH$_2$)$_6$Re$_6$Se$_8$(CN)$_6$ Compound as Seen Via Electron Spin Resonance; D. M. Djokić, A. Olariu, P. Batail, and L. Forró, European Science Foundation Meeting - Highly Frustrated Magnetism, Kranjska Gora (2010).

[9] Electron Spin Resonance Study of 1D κ-[(EDT-TTF-CO-NH-CH$_2$-CO$_2$H)$_2$]$^{\bullet+}$[HSO$_4$]$^-$ Organic Charge Transfer Salt; D. M. Djokić, A. Sienkiewicz, A. Olariu, R. Gaál, A. El-Ghayoury, S. Simonov, P. Batail, and L. Forró, MaNEP Swiss Workshop Meeting on Basic Research and Applications, Les Diablerets (2009).

[10] High Pressure ESR Study of the Organic Kagomé (EDT-TTF-CONH$_2$)$_6$Re$_6$Se$_8$(CN)$_6$; D. M. Djokić, A. Olariu, P. Batail, and L. Forró, Fifth International School and Conference on Spintronics and Quantum Information Technology - SPINTECH V, Kraków (2009).

[11] Waveguiding Effect in GaAs 2D Hexagonal Photonic Crystal Tiling; Dj. Jovanović, R. Gajić, D. M. Djokić, and K. Hingerl, Acta Physica Polonica **A116**, 55 (2009).

[12] Investigation of Thermostability of Mo$_6$S$_3$I$_6$ Nanowires by Means of Raman Spectroscopy; J. M. Todorović, D. M. Djokić, Z. D. Dohčević-Mitrović, D. Mihailović, and Z. V. Popović, Hem. Ind. **63**, 217 (2009).

[13] Influence of Antiferromagnetic Spin Ordering on the Far-Infrared Active Optical Phonon Modes of α-MnSe; D. M. Djokić, Z. V. Popović, and F. R. Vukajlović, Phys. Rev. **B77**, 01430 (2008).

[14] Effects of Spin Correlations of the Antiferromagnetically Ordered State on the Infrared Spectra of of α-MnSe; D. M. Djokić, Magister Thesis, University of Belgrade (2008).

[15] Infrared Reflectivity Spectra of η-Na$_{1.3}$V$_2$O$_5$ in the Charge Disordered and Ordered Phase; Z. V. Popović, D. M. Djokić, Z. D. Dohčević-Mitrović, M. Isobe, and Y. Ueda, Eur. Phys. J. **B65**, 1 (2008).

[16] High-Order Temperature Corrections to the Liquid Drop Model; D. M. Djokić, Diploma Work, University of Belgrade (2005).

Publications to Appear

[1] Evidence for Fermi Glass Behaviour of κ-[(EDT-TTF-CO-NH-CH$_2$-CO$_2$H)$_2$]$^{\bullet+}$[HSO$_4$]$^-$ Organic Charge Transfer Salt; D. M. Djokić, A. Sienkiewicz, A. El-Ghayoury, S. Simonov, P. Batail, and L. Forró, Physical Review **B**, *to be submitted*.

[2] Absence of Ferromagnetism in Mn^{2+} Doped Both H$_2$Ti$_3$O$_7$ and TiO$_2$ Nanotubes Synthesized by the Hydrothermal Method; Z. Mickovic, P. Szirmai, D. M. Djokić, E. Horváth, R. Smajda, L. Forró and A. Magrez, Journal of Physical Chemistry **C**, *to be submitted*.

[3] Strong Evidence for Metallic Behaviour of the (EDT-TTF-CONH$_2$)$_6$Re$_6$Se$_8$(CN)$_6$ Kagomé System; J. Jaćimović, D. M. Djokić, A. Olariu, P. Batail, E. Tutiš, and L. Forró, Nature Physics, *to be submitted*.

[4] Infrared Reflectivity and Transmissivity Spectra of SeCuO$_3$; K. Miller, D. M. Djokić, H. Berger, and D. Tanner, Physical Review **B**, *to be submitted*.

[5] Electron Spin Resonance of Novel Materials; D. M. Djokić, EPFL PhD Thesis, *to be defended*.